Technische Universität München
Fakultät für Elektrotechnik und Informationstechnik
Lehrstuhl für Elektrische Antriebssysteme und Leistungselektronik

Multidisciplinary Optimization of Drag Power Kites

Florian Bauer

Vollständiger Abdruck der von der Fakultät für Elektrotechnik und Informationstechnik der Technischen Universität München zur Erlangung des akademischen Grades eines

Doktor-Ingenieurs (Dr.-Ing.)

genehmigten Dissertation.

Vorsitzender:		Prof. Dr. rer. nat. Thomas Hamacher
Prüfer der Dissertation:	1.	Prof. Dr.-Ing. Dr. h. c. Ralph M. Kennel
	2.	Assoc. Prof. Dr.-Ing. Roland Schmehl Delft University of Technology, Niederlande

Die Dissertation wurde am 18.04.2019 bei der Technischen Universität München eingereicht und durch die Fakultät für Elektrotechnik und Informationstechnik am 24.01.2021 angenommen.

Abstract

A drag power kite belongs to the class of crosswind kite power- and airborne wind energy systems. It is a tethered electric aircraft, which flies figure eights or circles, and harvests wind energy with small onboard wind turbines. High altitudes with strong and steady winds are reachable, while only a small amount of construction material is required. Electrical power is transferred between kite and ground in conductors integrated in the tether. The kite launches and lands like a multicopter by re-using the onboard wind turbines as propellers. A solution, applications, and the benefits for multidisciplinary optimizations of such systems are presented.

To allow for fast optimizations and parameter studies, but simultaneously obtain reasonable results by considering all important domains and dominant effects, a multidisciplinary steady systems engineering model is derived. It consists of several submodels, taken or extended from literature, or derived from scratch. In particular, the kite dynamics model is based on an extension of Loyd's model, the kite's aerodynamics model is based on a solution from lifting-line theory, the tether is modeled as straight and is dimensioned in accordance with the nominal mechanical and electrical loads together with an electrical cables model, the rotors are modeled with Betz' model as actuator disks, the powertrain is modeled with efficiencies, costs, and mass, the atmosphere is modeled with a wind shear and wind probability distribution, the kite's control is modeled by an analytically optimized complete power curve, and the economics is modeled with interest rate as well as capital and operational cost contributions. The model equations are arranged into a sequence of (mostly) explicit analytical equations. A key idea for that is to not estimate the total costs and mass, but instead to compute the maximum allowed ones. Therefore, no rough assumptions on cost- and mass factors are introduced.

The derived model is validated among others against the measured power curve of Makani's Wing 7 and against simulations of a higher fidelity point-mass model. For that, a control scheme which includes limitations of force, speed, and power over the whole wind speed range is derived.

Optimizations are conducted with the genetic algorithm CMA-ES. One result is that a 40 m wing span biplane kite optimized for an onshore site is expected to achieve $\approx 4\,\mathrm{MW}$ nominal electrical power with $\approx 50\,\mathrm{kW/m^2}$ power density. Monoplane, offshore, and small-scale variants are also investigated. Results include that a biplane is expected to outperform a monoplane, offshore sites can significantly improve important figures of merit like the energy yield, and a good scalability can be assessed. Sensitivities for vast changes of almost every model parameter are computed. The mean wind speed is the most important parameter of a deployment site. All economic and kite aerodynamics parameters have a high sensitivity on the power plant economics. Particularly important are a high nominal airfoil lift coefficient, achievable through multi-element airfoils, and thus a high wing loading, as well as a high wing span efficiency. Therefore, a biplane, with its truss-like structure and thus high strength as well as a possibly very high aspect ratio, is an interesting concept for a drag power kite. Conversely, the majority of the tether parameters, even the nominal tether voltage, hardly affect any of the important figures of merit.

Keywords: Airborne wind energy, crosswind kite power, drag power, drag mode, wind turbine, multidisciplinary, optimization, model, systems engineering, techno-economic analysis, Loyd, Betz, aerodynamics, multi-element airfoil, high lift, tether, cable, voltage, efficiency, cost, economics, materials, validation, Makani, genetic algorithm, swarm optimization, CMA-ES, parameter study, sensitivity analysis, figure of merit.

Preface and Acknowledgements

The present dissertation is the result of my doctoral research. It was conducted under the supervision of *Univ.-Prof. Dr.-Ing. Dr. h. c. Ralph M. Kennel* at the *Chair of Electrical Drive Systems and Power Electronics* of the *Technical University of Munich (Germany)* from 2013 to 2021. This dissertation was mainly written from early 2017 to mid 2018 and is therefore based on the state of the art at that time. More recent developments are not included in the considerations of this dissertation, e.g. the publications of Makani Power/Google in 2020 or details on the meanwhile founded spin-off kiteKRAFT with its successful crosswind flights of a prototype, which are partly based on the results of this dissertation.

This journey began very differently than I imagined. I started with an idea for the autonomous launch and landing of flexible kites. Simulations seemed promising. We received research grants, so it was time to test the idea in reality. At that time, I also received the opportunity to spend almost two years at the University of California, Irvine at Prof. Smedley's Power Electronics Lab, which I gratefully accepted. That seemed to be an ideal place for experiments, because Irvine is close to the sea with much more wind than in Munich (of course, with the other nice side effects California offers). Unfortunately, building a demonstrator was much more challenging than I expected and I realized that I had to adjust my goals. I first built a simple ground station and left autonomous launch and landing aside. Already that was challenging and time consuming, even without starting to consider implementing any autonomous launch and landing. Every single actuator and sensor required its own very detailed attention. Eventually, we were able to fly the kite autonomously in figure of eights, at least for a few minutes (a photograph of the successful experiment is included in this dissertation).

That experience made me question the technology as a whole. After one and a half year into the doctoral research project, I had to return to square one: Is a flexible kite really meaningful for a power plant? Is this concept with generators on ground really that good? Is it not a great benefit to use a rigid kite with onboard generators and wind turbines which can be reused as propellers for a relatively simple and proven multicopter launch and landing? Is airborne wind energy at all a meaningful concept for power plants, which require a long lifetime and high reliability? I critically asked those questions and compared all airborne wind energy concepts (the full comparison is included in this dissertation). My conclusion was and still is, that airborne wind energy is clearly very interesting, but the drag power concept, i.e. rigid kite with onboard turbines, is by far the most promising concept. Interestingly, at that time only a single group, Makani Power/Google, pursued this concept, even though they probably made the greatest progress as they already had the fully autonomous Wing 7 system.

The question then was, what are the challenges to be solved and what can I contribute? Achieving the required high tether voltage seemed to be one such challenge. I came up with the idea to connect low-voltage and thus high-efficient electrical drives partly in series on the DC-side. That required a voltage stabilization and simultaneous control of the overall rotor forces and moments. I developed a control scheme, at least for the hovering case, and verified it with experiments. Despite that success, the concept had critical drawbacks: First, the control is nonlinear and complicated. Second, the fault tolerance is reduced. A further general flaw is that all known powertrain concepts cannot cope with a short circuit in the tether, questioning if the required reliability for a commercializable power plant can be achieved.

After comparing the airborne wind energy concepts, I wondered what an optimal kite looks like and what the design sensitivities are. For example, is a high voltage in the order of 8 kV, which results from a tether mass minimization, really required? After I returned from Irvine to Munich, I began to model the whole system, with a comprehensive but still relatively simple modeling approach. I found that a much lower voltage is also fine, because the tether voltage turned out to have a low sensitivity on the overall system performance. So neither a series connection, which requires a complicated control and compromises the fault tolerance, nor DC-DC converters or similar might be required. With these analyses, I noticed another interesting result: a rather high number of electrical cables around the tether core is optimal. So one day I had the idea, how to cope with a short circuit in the tether. One just should not parallelize the electrical cables on the ground and on the kite, but instead leave them isolated for each rotor drivetrain. If there is a short circuit in the tether, at the most only two rotors could be affected. A little later, I also found a fuse and converter shutoff-control scheme, with which for any fault at the most a single rotor drivetrain fails. Key parts of that concept were than also proven experimentally. Later, a patent application on that was submitted and a paper was published.

As result of that side project of modeling and optimizing the complete drag power kite plant, there is now a concept available for a fault tolerant powertrain for drag power kites without single point of failure. However, with that I had several unambiguous arguments making my previous series connection concept obsolete. The question then was, what should my dissertation be about? Making that series connection as main topic seemed pointless (even though that concept remains academically interesting) and I felt little motivation for the work still ahead (e.g. extending the controller for crosswind flight). The fault tolerant powertrain as main topic seemed too little for a dissertation, also in view that this solution is relatively simple (although this is actually a big advantage for this concept). The most interesting main topic was the drag power kite plant modeling, optimizations, and parameter studies. Maybe I find further interesting sensitivities or results which are counterintuitive? However, a drawback of this topic is that it can almost only be of simulative- and thus theoretical nature. The compromise was to also include a focus on the validation e.g. by means of comparison with measurements from Makani. Additionally, a sensitivity analysis for almost each model parameter is conducted, particularly for the ones that are hard to estimate. This is exactly the essence of the present dissertation.—Nevertheless, I also wanted to validate the results I found from my optimizations. We started to build a tiny-scale kite (maybe a few kilowatts power) and submitted proposals to build larger demonstrators. Since conducting the analyses with high accuracy and writing the dissertation was the priority, it was not expected that any reasonable demonstrator results could be included into this dissertation.

The derivations, discussions, and analyses are presented in relatively high detail. The goal was, that as many readers as possible can make use of and build upon my works as much as possible, so that we have soon many kite power plants deployed worldwide, have stopped the anthropogenic global warming, and saved our planet earth—this is my fundamental motivation (besides that I am fascinated by power generating kites, i.e. electric aircraft which generate clean energy). *Because of that, the page count of this dissertation is relatively high, but the reader should not be repelled by that:* Particularly the validations, parameter studies, and sensitivity analyses involve many full-page tables and figures as well as intentionally partly left plank pages, so that text and corresponding figures and tables are close to each other.

Besides this doctoral research, I assisted and was responsible for the lecture materials, tutorials, and exams of the chair's course "Antriebsregelung für Elektrofahrzeuge" (Engl. "drive control for electric vehicles").

I would like to express my deep gratitude to all people I have worked with, supported me, or simply chatted or discussed with me.—This doctoral research was a journey with ups, but also deep downs, visualized almost exactly by the image on the next page, which I first saw in the AWEC2017 talk of Fort Felker (head of Makani). The reassurance of my colleagues and friends,

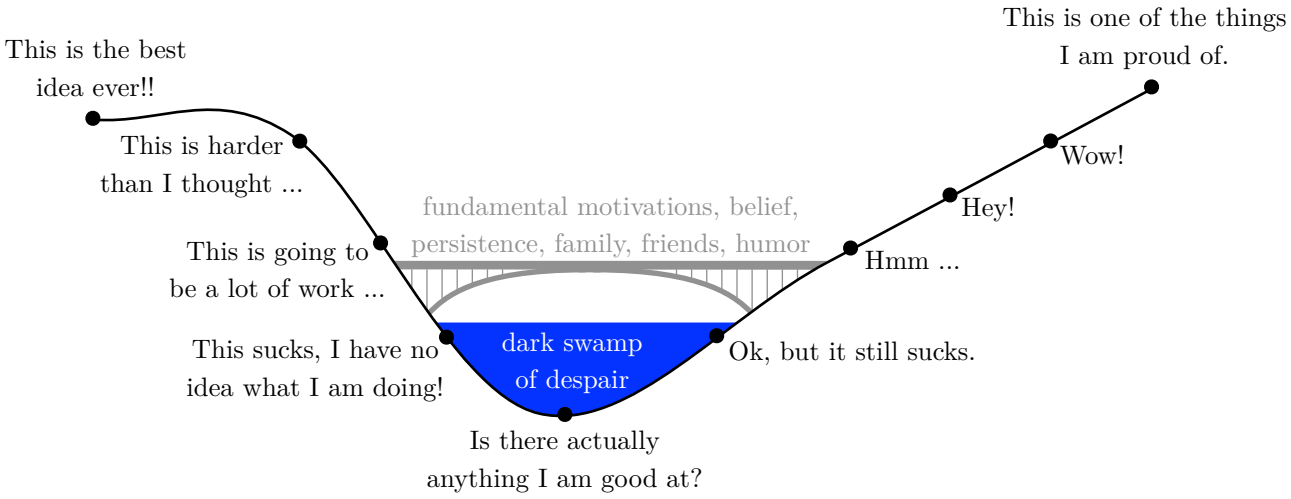

Figure: Emotional journey.
Image inspired by https://i2.wp.com/john.do/wp-content/uploads/2016/12/emotional-journey-of-creating-anything-great-infographic-large.jpg (visited on March 29, 2018).

as well as exemplifying that I was not alone in the "dark swamp of despair", really helped me to get through it, and this was heart-balm. I also want to pass on this helpful message to doctoral students or anyone else who finds himself or herself currently in a "dark swamp of despair": it is normal to be there for some time! Although it was hard to get out, it did teach me to overcome overwhelming hurdles, to become realistic, and to get focused.—First of all, I thank Prof. Kennel for his openness in accepting my relatively crazy research topic which was rather off-topic for the chair, for giving me all the freedom I had for both, in my daily work and changing the research focus when it appeared necessary, for giving me advice and motivation when I needed it, and for giving me the opportunities for extensive international collaborations. I thank Prof. Schmehl, not only for being the second examiner of my dissertation, but also for the many interesting discussions and collaborations on publications and proposals. I thank Prof. Smedley for the interesting collaboration in Irvine as well as for her advice and motivation when I was depressed from failed experiments. I thank all my colleagues I met and worked with in Munich and in Irvine, in particular: Roozbeh Naderi and Tim Schmidt for motivating me when I struggled, for discussions, and for the nice board game nights; Christoph Hackl and Filippo Campagnolo for the fruitful discussions and collaborations, their expertise and mentoring; Hannes Börngen for the interesting discussions on power electronics and his help during tests; Dietmar Schuster for making parts for test setups and helping me in the workshop; Wolfgang Ebert for ensuring a smooth functioning of the IT infrastructure; the students I supervised in their seminar works and theses (most listed within this dissertation), particularly Zhenhan Xu for his excellent work on the octocopter and PCB debugging, Benjamin Prünster among others for his work on the comparative kite concept simulations, Mengjie Zhao for her work on the airfoil CFDs and wind tunnel test, and Moritz Blasche for his excellent work on building parts of the tiny-scale kite demonstrator; and everyone else I forgot to mention. I thank Max Isensee, André Frirdich and Christoph Drexler, who joined me on the way to continue working on the topic beyond this dissertation with our planned spin-off kiteKRAFT. At the time of finalizing this dissertation, we already accomplished to build a 2.4 m wing span biplane/boxplane kite, based on the results of this dissertation, shown in the photograph on the next page. I am really looking forward to this new just started journey!

Figure: The founder team of the planned spin-off kiteKRAFT with the first demonstrator with 2.4 m wing span and 5 kW power. From left to right: Max Isensee (business development), Florian Bauer (electronics & software), André Frirdich (aerodynamics), Christoph Drexler (mechanics).
This image is a high resolution version of the one in the kiteKRAFT blog entry https://medium.com/kitekraft/kitekraft-unveils-5-kw-kite-c7851f7dad8 (visited on Apr. 7, 2019).

I thank the whole airborne wind energy community for their openness and interesting discussions at conferences. I am also thankful for the financial funding I received, particularly from the *Department of Electrical and Computer Engineering of the Technical University of Munich*, from the *Bund der Freunde der Technischen Universität München e.V.*, from the *European Union's Horizon 2020 research and innovation programme*, and therefore not least from the German and European government and people. I hope that my research contributions, my help to educate engineers, and soon my workforce and knowledge in the industry return all the funding invested in me. Finally, I thank my family and my wonderful girlfriend Nadine Stappenback for her endless love and support.

Munich, 21st March 2021
Florian Bauer

Contents

List of Figures

List of Tables

List of Abbreviations and Terms

Abbreviation/term	Meaning
AC	alternating current
airborne wind turbine	airborne wind energy plant, drag power kite, or onboard wind turbines of a drag power kite
airflow speed	speed of the air as experienced by an object (e.g. by the kite); an alternative term is apparent wind speed or airspeed (albeit the latter is usually defined in opposite direction of the airflow velocity direction)
CAD	computer aided design
CF	carbon fiber(s)
cf.	confer, compare
CFD	computational fluid dynamics
chap., chaps.	chapter, chapters
CMA-ES	Covariance Matrix Adaptation Evolution Strategy
CNT	carbon nanotube(s)
DC	direct current
dimensioning parameter	a parameter of the kite power plant, whose optimal value is obscure and is optimized in a superimposed optimization
DOI	digital object identifier
drag power	crosswind kite power concept
EEG	"Erneuerbare Energien Gesetz", German renewable energies law
e.g.	exempli gratia, for example
electrical drive	combination of electrical machine (i.e. motor or generator, depending on the instantaneous control mode or power flow direction), its power electronics, and basic controllers such as current controller, torque controller, and angular speed controller
EMI	electromagnetic interference
eq., eqs.	equation, equations
et al.	et aliae, and co-authors
FAA	Federal Aviation Administration
FEM	finite element method
fig., figs.	figure, figures
figure of merit	performance value, which is usually suitable for comparisons; examples for a power plant include LCOE, nominal power, energy yield, and capacity factor
fixed parameter	a parameter of the kite power plant, which cannot be optimized reasonably, e.g. because it is defined out of scope of a kite power plant manufacturer
i.e.	id est, that is, that means
ISSN	International Standard Serial Number
ISBN	International Standard Book Number
LCOE	levelized cost of energy, or levelized cost of electricity
lift power	crosswind kite power concept

Abbreviation/term	Meaning
MPC	model predictive control
MPP	maximum power point
MPPT	maximum power point tracking
p., pp.	page, pages
p.a.	per annum, per year
P-controller	proportional controller
PCB	printed circuit board
PE	polyethylene
PI-controller	proportional-integral controller
RC	remote control(led)
RPM(s)	revolutions per minute
sect., sects.	section, sections
SI-units	International System of Units, from the French Système international (d'unités)
s.t.	subject to
tab., tabs.	table, tables
UPS	uninterruptible power supply
URL	uniform resource locator, internet address, web address
w.r.t.	with respect to

List of Symbols

Symbol	Meaning
General nomenclature.	
$\#, x, y$	general example- or placeholder variables
x	constants and function names are written normal
x	scalars are written italic
$\boldsymbol{x}$	vectors are written bold; the length/magnitude/Euclidian norm/2-norm is written with the same symbol in normal (because it is a scalar)
$\boldsymbol{X}$	matrices are written bold (and always upper-case)
$\mathbf{1}$, $\mathbf{1}_x$	row vector or matrix of ones, explicitly with x rows (and columns)
$\mathbf{I}$, $\mathbf{I}_x$	identity matrix, explicitly with x rows and x columns
x'	(un)corrected or alternative version of x; per unit version of x
x^*	optimal value of x
$\boldsymbol{x}^\top$	transpose of $\boldsymbol{x}$
$\boldsymbol{x}^{\mathrm{y}}$	vector described in the reference frame y
$\overline{x}$	upper bound (or maximum) of x
$\underline{x}$	lower bound (or minimum) of x
$\hat{x}$	maximum allowed or maximum available value of x
$\tilde{x}$	(un)corrected or alternative version of x; mean of x
Δx	change of x
$\mathrm{d}x$	infinitesimal change of x
$\frac{\mathrm{d}}{\mathrm{d}t}x = \dot{x}$	first time derivative of x
$\frac{\mathrm{d}^2}{\mathrm{d}t^2}x = \ddot{x}$	second time derivative of x
$x \approx y$	x is approximately equal to y, written explicitly, which may also be written as equality $x = y$
$x := y$	x is defined by y, which also implies $x = y$
$x \leftarrow y$	y is assigned to x
$x \sim y$	x is proportional to y
$x \lesssim y$	x is smaller than approximately y
$x \gtrsim y$	x is greater than approximately y
$xy = x \cdot y$	x multiplied by y
$\boldsymbol{x} \bullet \boldsymbol{y}$	scalar product of $\boldsymbol{x}$ and $\boldsymbol{y}$
$\boldsymbol{x} \times \boldsymbol{y}$	vector product of $\boldsymbol{x}$ and $\boldsymbol{y}$
$x \in Y$	x is element of set Y
$x \in [x_1, x_2)$	x is element of the range $x_1 \leq x < x$
$\{[()]\}$	mathematical brackets
$x(y)$	x is a function of y, which is however only written so explicitly instead of just "x" if it is necessary to avoid ambiguity or for highlighting purposes
x[y]	x given in unit y
$[x]$	unit of x
$\lfloor x \rfloor$	rounded-off- or "floor"-value of x
$\lvert x \rvert$	absolute value of x

Symbol	Meaning
$\|\|\boldsymbol{x}\|\|$	magnitude/Euclidian norm/2-norm of $\boldsymbol{x}$, i.e. $\|\|\boldsymbol{x}\|\| := \sqrt{\boldsymbol{x}^\top \boldsymbol{x}} =: x$
Special functions.	
$\arctan_2(y,x)$	multi-valued inverse tangent function of y and x, defined by $\arctan_2(y,x) := \begin{cases} \arctan\left(\frac{y}{x}\right) & \text{if } x > 0, \\ \arctan\left(\frac{y}{x}\right) + \pi & \text{if } x < 0 \text{ and } y \geq 0, \\ \arctan\left(\frac{y}{x}\right) - \pi & \text{if } x < 0 \text{ and } y < 0, \\ +\frac{\pi}{2} & \text{if } x = 0 \text{ and } y > 0, \\ -\frac{\pi}{2} & \text{if } x = 0 \text{ and } y < 0, \\ 0 & \text{if } x = 0 \text{ and } y = 0 \end{cases}$
arg	argument
$\mathrm{dir}(\boldsymbol{x})$	direction of $\boldsymbol{x}$, defined by $\mathrm{dir}(\boldsymbol{x}) := \begin{cases} \frac{\boldsymbol{x}}{\|\|\boldsymbol{x}\|\|} & \text{for } \|\|\boldsymbol{x}\|\| \neq 0, \\ \boldsymbol{0} & \text{otherwise} \end{cases}$
f	generic function, placeholder function
force	computation of tangential force, see Appendix C.2.4.1 for details
$\mathrm{limit}(x_{\min}, x, x_{\max})$	limitation/saturation of x between $x_{\min}$ and $x_{\max}$, defined by $\mathrm{limit}(x_{\min}, x, x_{\max}) := \begin{cases} x_{\min} & \text{if } x < x_{\min}, \\ x_{\max} & \text{if } x > x_{\max}, \\ x & \text{otherwise} \end{cases}$
linpol	linear interpolation, see Appendix C.2.4.2 for details
$\max\{x_1, x_2, ...\}$	maximum of $x_1, x_2, ...$
$\max_y x$	maximum of x w.r.t. y
$\min\{x_1, x_2, ...\}$	minimum of $x_1, x_2, ...$
$\mathrm{normalized}(x)$	angle x wrapped into the interval $[-\pi, \pi]$, defined by $\mathrm{normalized}(x) := x - 2\pi \left\lfloor \frac{x+\pi}{2\pi} \right\rfloor$
quadpol	quadratic interpolation, see Appendix C.2.4.3 for details
$\Gamma(x)$	gamma function of value x
Latin symbols.	
A	area [m^2]
$\boldsymbol{A}$	area multiplied by its unity normal vector [$\mathbf{1}\mathrm{m}^2$]
a	glide angle [rad] (or [°]); axial induction factor [1]
AR	aspect ratio [1]
b	wing span [m]
C	aerodynamic coefficient (3D, whole wing or kite) [1]; heat capacity [J/K]
c	aerodynamic coefficient (2D, e.g. airfoil) [1]; speed of sound [m/s]
D	electric displacement field magnitude [$\mathrm{C/m}^2$]; damping constant of a second order delay
$\boldsymbol{D}$	electric displacement field vector [$\mathbf{1}\mathrm{C/m}^2$]
d	diameter, thickness [m]
E	electric field magnitude, electric field/dielectric strength [V/m]; energy [Ws]; annual energy yield [Wh/yr]
$\boldsymbol{E}$	electric field vector [$\mathbf{1}\mathrm{V/m}$]
e	span efficiency factor [1]
$\boldsymbol{e}$	unit vector (possibly of a reference frame) [$\mathbf{1}$]
F	force magnitude [N]
$\boldsymbol{F}$	force vector [$\mathbf{1}\mathrm{N}$]
f	generic function, placeholder function

Symbol	Meaning
f	factor (e.g. correction factor)
G	controller gain
g	gravitational acceleration [m/s^2]
H	capacity factor [1] (or [%]); heat dissipation factor [W/K]
h	altitude (above ground) [m]
I	electric current [A]; interest rate [1/yr] (or [%/yr])
i	counter, placeholder
K	cost(s) [EUR]
k	specific cost(s) [EUR/#]; placeholder
L	total length [m]
l	length [m]
$\boldsymbol{l}$	length multiplied by its unity tangential vector [$\mathbf{1}$m]
M	moment [Nm]
m	(effective) mass [kg]
N	number [1]
n	amount [1]
P	power [W]
p	specific power [W/#]; probability [1]; parameter/placeholder
$\boldsymbol{p}$	momentum [kg m/s]
Q	charge [C]
R	electric resistance [Ω]
$\boldsymbol{R}$	rotation matrix [$\mathbf{1}$]
r	radius [m]; ratio [1]
$\boldsymbol{r}$	position [$\mathbf{1}$m]
S	safety factor [1]
s	complex frequency (Laplace domain) [Hz]
T	life time, (dynamic) amortization time [yr]; time constant [s]
$\boldsymbol{T}$	orientation matrix, transformation matrix [$\mathbf{1}$]
t	time [s]
U	voltage [V]
u	control or actuation variable
$\boldsymbol{u}$	control or actuation variables summarized as vector
V	volume [m^3]
v	speed, velocity vector magnitude [m/s]
$\boldsymbol{v}$	velocity [$\mathbf{1}$m/s]
w	width, thickness [m]
x	position in x-direction [m]; placeholder
$\boldsymbol{x}$	vector of state variables; axis unit vector of the x-axis of a cartesian reference frame [$\mathbf{1}$]
Y	Young's modulus [Pa]
y	position in y-direction [m]; placeholder
$\boldsymbol{y}$	vector of optimization variables; axis unit vector of the y-axis of a cartesian reference frame [$\mathbf{1}$]
z	position in z-direction [m]; z_0 is the roughness length [m]
$\boldsymbol{z}$	vector of (interesting) results; axis unit vector of the z-axis of a cartesian reference frame [$\mathbf{1}$]
Greek symbols and other symbols.	
α	angle of attack [rad] (or [°]); α_H is the Hellmann exponent [1]
$\Gamma(x)$	gamma function of value x

Symbol	Meaning
γ	specific mass [kg/#]; course angle or sometimes also called velocity angle [rad] (or [°])
δ	distance between the center of two neighboring electrical cables in the tether [m]
ϵ	permittivity, ϵ_r is the relative permittivity [1], $\varepsilon_0 = 8.854187817...\cdot 10^{-12}\,\mathrm{F/m}$ is the vacuum permittivity; angle between two electrical cables in the tether [rad] (or [°])
ζ	power harvesting factor [1]
η	efficiency [1] (or [%])
ϑ	elevation (angle) [rad] (or [°])
κ	specific electrical conductivity [S/m]
λ	shape parameter of Weibull distribution [1]
μ	scale parameter of Weibull distribution [m/s]
ξ	damper constant of a spring-damper [N/(m/s)]
π	the number pi, $\pi = 3.14159265359\ldots$
ρ	density [kg/m^3]; air density [kg/m^3]; charge density [C/m^3]
ϱ	penalty cost contribution
σ	yield strength [Pa]
ς	spring constant of a spring-damper [N/m]
τ	temperature [K] (or [°C])
ϕ	angle integration variable [rad] (or [°])
φ	azimuth (angle) [rad] (or [°])
ψ	roll (angle) [rad] (or [°])
Ω	control volume
ω	angular speed [rad/s] (or [°/s])
$\boldsymbol{\omega}$	angular velocity vector [**1**rad/s] (or [**1**°/s])
#	placeholder
Latin indices.	
A	w.r.t. area
a	aerodynamic; air, apparent; airborne; actuation, actuated
acc	acceleration
af	airframe
af&o	airframe and other
Al	aluminum
am	static amortization
an	annuity
avail	availability
b	w.r.t. wing span
c	electrical cable (of tether)
cen	centripetal/centrifugal
CF	carbon fiber(s)
CNT	carbon nanotube(s)
cor	correction
cos	cosine
Cu	copper
cut-in	cut-in, start
cut-out	cut-out, stop
D	drag
design	design

Symbol	Meaning
disk	disk
dist	disturbance
Dyn	Dyneema
el	electric(al)
eq	equivalent
F	filter
fdn&to	foundation and tower
flight	crosswind flight
flt	system fault, rotor failure
fut	future
g	gravity, gravitation; ground; gear(box)
g-m	gearbox-machine combination
H	Hellmann
hov	hover(ing)
I, II, ...	power curve Region I, II, ...
I $\leftrightarrow$ II, II $\leftrightarrow$ III, ...	transition between power curve Regions I and II, Regions II and III, ...
i	induced
ideal	ideal
in	inner
inertia	inertia, inertial
infeas	infeasibility
ins	insulation, insulator
inv	investment
j	jacket
k	kite
Kev	Kevlar, Aramid
kin	kinematic reference frame
L	lift; w.r.t. length
land	landing
LCOE	levelized cost of energy, levelized cost of electricity
loss	loss
M	w.r.t. torque
m	electrical machine(s)
m-te	tether mass
max	maximum; nominal maximum; instantaneous maximum
max-F	w.r.t. maximum force
max-op	operational maximum
mech	mechanic(al)
mid	middle
min	minimum
min-op	operational minimum
mw	main wing(s)
n	nominal
n-ins	installed nominal
n(1)	first nominal point
n(2)	second nominal point
now	now, present
o	other parts; offset

Symbol	Meaning
o&p	in $K_{\mathrm{inv,o\&p}}$: investment costs of airframe, tether, ground station, and other parts, includes also development costs, as well as the profit margin of the power plant manufacturer
ok	system ok, no rotor failure
op	operating, operational
out	outer
over-F	force overloading
over-P	power overloading
over-v	speed overloading
P	power; proportional
p	parasitic
P&U	w.r.t. power and voltage
PE	polyethylene
pe	power electronics
pt	powertrain
r	radial; relative, ϵ_r is the relative permittivity
Re	Reynolds
ref	reference
rot	rotor
S	side
s	shaft (of electrical machine); single; slope
sav	savings
sd	spring-damper
SE	small earth reference frame
set	set value, target value
sh	shield (of electrical cable of tether)
shear	shear
snd	sound
St	steel
tan	tangential
te	tether
te-loss	tether loss
Tef	Teflon
th	threshold
tip	(rotor blade) tip
to	tower
turn	turn
UPS	uninterruptible power supply
V	w.r.t. volume
v	w.r.t. speed
w	wind; weight; wire (of electrical cable of tether)
x	x-value, about x-axis
x	w.r.t. a variable x
y	y-value, about y-axis
yr	yearly, annual
z	z-value, about z-axis
Greek indices and other indices.	
γ	w.r.t. course angle
ϑ	into the ϑ-direction

Symbol	Meaning
Π	total, sum/product (expressed explicitly)
Σ	total, sum (expressed explicitly)
τ	w.r.t. temperature
φ	into the φ-direction
0	zero; initial; $c_{\mathrm{D},0}$ is the zero-lift drag; ε_0 is the vacuum permittivity
1	one; single
2	two; $c_{\mathrm{D},2}$ is the drag coefficient slope w.r.t. the lift coefficient squared
∞	ambient; lying figure eight flight path
$\circ$	closed loop; circular flight path
$+$	positive, generative
$-$	negative, consumptive
$\|\|$	parallel (to the tether)
#	placeholder
Superscripts.	
k	in coordinates of the kite reference frame
kin	in coordinates of the kinematic reference frame
SE	in coordinates of the small earth frame
0	baseline value, value of reference scenario

Chapter 1

Introduction

1.1 Motivation

Energy is the basis of modern societies. It is the requirement for turning on a light, having a warm home and warm water, taking a ride in a car or train, or running a computer. The most versatile form of energy is electricity, because it can be transported and converted relatively easily into any other form of energy with a high efficiency. Its importance for modern societies becomes clear when imagining what happens without it: A blackout just for a few days can cause economic costs in the order of billions of euros, and a wide-range blackout lasting a few weeks is expected to be catastrophically [1].

Today, most of the energy demand is supplied by conventional resources based on fossil fuels like coal, oil, or gas, which have a number of shortcomings:

- Fossil fuel resources are limited, and therefore alternatives must take over—sooner or later.
- Fossil fuel resources are distributed heterogeneously over the planet, including in politically unstable regions, which is why a decrease of their dependence is desired.
- The environmental impact of fossil fuels is rather large, both locally and globally. In particular, the CO_2 emissions are made responsible for global warming [2].

To overcome those shortcomings, renewable energy technologies are being developed. Wind energy has been particularly successful in terms of installed power, generated energy, and low costs, cf. e.g. [3]. However, renewable energies are still not competitive with conventional sources, apart from some exceptions like wind energy in windy near-shore regions: Fig. 1.1 compares the *levelized cost of energy (LCOE)*[1] for important conventional and renewable energy technologies. Only onshore wind energy can generate electricity at similar costs as brown coal at some sites. Considerable efforts are required to further drive down the costs, but the cost decreases have slowed down over the past years, cf. e.g. [5, Fig. C.1], and are not expected to drop fast, cf. e.g. [4, Fig. 17]. Wind turbine manufactures try to reduce costs e.g. with even higher towers and larger turbine diameters, which on the other hand impose logistic challenges. Offshore is still not mature enough to generate energy at lower costs. On the contrary, offshore is significantly more expensive, as visualized in Fig. 1.1, caused by the relatively big foundations and the higher development and maintenance costs. Fast cost decreases for offshore wind are not expected either [5, Fig. C.2], although some recent bids for offshore wind parks were "surprisingly" low [6]. Even if general cost reductions become real, fossil fuel might become cheaper because of a high supply-demand-imbalance of energy [7], which in turn increases the pressure on the LCOE for renewables. On the other hand, massive amounts of fossil generation capacities need to be

[1] The LCOE, levelized cost of energy (or electricity), is the sum of all costs for a unit of energy which is, for electricity, usually given in USD or EUR per kilowatt hour, i.e. it includes the capital or investment costs for the construction of the power plant, running expenses such as maintenance costs, fuel costs, CO_2 certificates costs, permit costs, etc. Therefore, the LCOE allows meaningful comparisons between any energy generation systems.

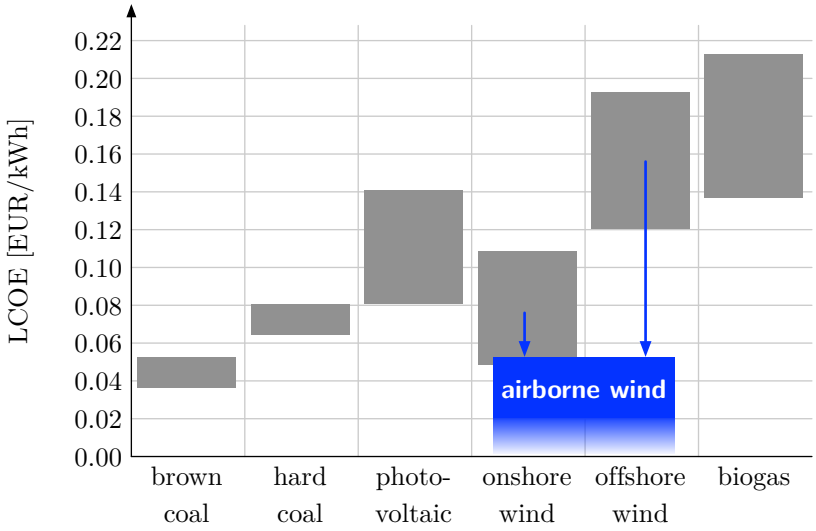

Figure 1.1: Comparison of LCOEs for different electricity generation technologies in Germany in 2013. Data reproduced from [4, Fig. 6].

replaced and new demands may arise from electric vehicles and in general from global economic growth in emerging and developing countries.

Airborne wind energy is expected to bring a disruptive change into the energy market, cf. e.g. [8]: To reduce significantly the power plant's construction material demand while tapping higher altitudes with stronger and steadier winds, an airborne object is used to convert the energy of the wind flow into mechanical energy and then into electrical energy. As visualized in Fig. 1.1, it is expected, that airborne wind energy can generate electricity at an LCOE in the magnitude of brown coal or below without subsidies. This is a great motivation for a number of reasons:

- The technology is less dependent on political goodwill on releasing subsidy funds. Therefore, the financial burden to the public is lower and the risks for investors are more predictable.
- If airborne wind energy becomes more competitive than other technologies, it will be the default choice for a power plant investor and automatically replace fossil fuel based technologies, possibly without a need for (additional) penalization of these technologies, which would also depend on volatile political decisions.
- The LCOE, or dependent economical values such as return on investment or interest rate, are amongst the most important figures of merit[2] for an energy generation technology, because electricity is a commodity which is not differentiable from its generation source. In fact, the investment into a power plant is similar to the investment into a financial product, for which the interest rate and the risk are the most important figures of merit.

Numerous airborne wind energy concepts are proposed and developed, cf. e.g. [9–12]. Some concepts use lighter-than-air blimps and employ onboard wind turbines or the Magnus effect, others use kites, i.e. tethered wings, made from flexible materials similar to surf kites or from rigid materials similar to airplanes. The generator is either placed on the ground or onboard

[2] A figure of merit is a performance value or index value, which is usually suitable for comparisons. Besides economical values such as the LCOE, also the nominal power, energy yield, or maintenance costs may be important figures of merit for a power plant.

the airborne object. Among the most promising concepts are the *crosswind kite power* concepts, which can be classified among *lift power* and *drag power* concepts[3] [13], both visualized in Figs. 1.2 and 1.3:

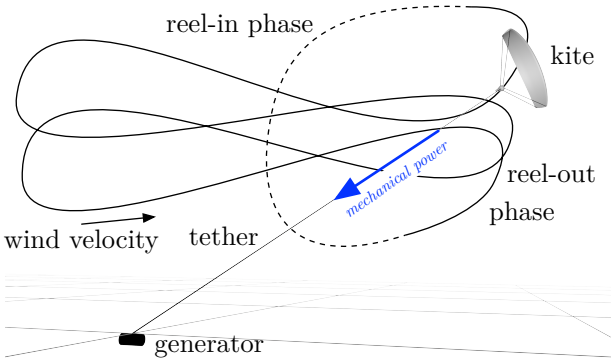

Figure 1.2: Visualization of the lift power concept. Similar image published by the author already e.g. in [14, Fig. 18.2].

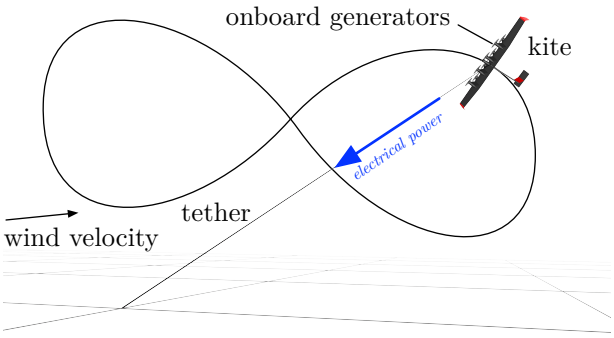

Figure 1.3: Visualization of the drag power concept. Similar image published by the author already e.g. in [14, Fig. 18.1].

Lift Power: The kite is tethered to a winch on the ground. The winch is connected to an electrical drive[4] which can be operated as motor or as generator. The kite is flown in crosswind motions like figure eights or circles, i.e. it is flown (almost) perpendicular to the wind vector which is similar to the wing tips of a rotor of a conventional wind turbine. Therefore, the airflow speed[5] is about a magnitude higher than the actual wind speed. The high airflow

[3] The terminology "lift power" and "drag power" is introduced in the first publication about crosswind kite power by Miles Loyd in [13], which is also used throughout this dissertation. Alternative terms for "lift power" are "traction power", "ground generation", "pumping mode power generation", "pumping kite generator", or "ground-gen". Alternative terms for "drag power" are "onboard generation", "continuous power generation", "fly-gen", or "airborne wind turbine", but the latter is sometimes also used for other airborne wind energy concepts or only for the onboard turbines of a drag power kite.

[4] The term "electrical drive" denotes the combination of electrical machine (i.e. motor or generator, depending on the instantaneous control mode), its power electronics, and basic controllers such as current-, torque- and speed controllers.

[5] The term "airflow speed" is used throughout this dissertation. An often used alternative term is "apparent wind speed" or "airspeed" (albeit the latter is usually defined in opposite direction of the airflow velocity direction).

speed generates a high lift force with which the tether is pulled from the winch. The winch drive counteracts by generative braking, i.e. it is operated as generator and electrical energy is generated. Before the tether is pulled off entirely, the kite is flown towards a low force position like the zenith and then reeled-in. Some flexible kites can also be depowered and a rigid kite can dive towards the ground station for minimal reel-in time and force. During this reel-in phase the ground winch drive is operated in motor mode, but only a fraction of the generated energy is used. When the tether length is short enough, the pumping process restarts. As essentially the lift of the kite is used to generate power, this concept is called lift power [13].

Drag Power: Wind turbines with electrical drives are attached to a rigid kite or to an airborne unit beneath a flexible kite. The kite is also flown in crosswind motions with a high airflow speed, but with a constant tether length. The turbines generate electrical power, i.e. the turbines brake the kite generatively. This is similar to a conventional wind turbine's generator, which brakes the wing tips of the rotor blades generatively. As the airflow speed is about a magnitude higher than the actual wind speed, the turbines can be relatively small. The electrical power is transmitted to the ground via medium-voltage electrical cables which are integrated into the tether. As the turbines add drag to the kite, with which power is generated, this concept is called drag power[6] [13].

It is not yet clear if a flexible kite or a rigid kite and if the lift power or the drag power concept is overall the best choice, or if several approaches can be viable solutions. Virtually all researchers and developers start with flexible kites and most of them focus on the lift power concept. A number of successes have been achieved, e.g. the company SkySails pulled a container ship with a $320\,\mathrm{m}^2$ flexible kite and a mechanical power of 2 MW [15]. However, flexible kites and the lift power concept have a number of disadvantages compared to rigid kites and compared to the drag power concept, despite their higher airborne mass: For instance, the durability of flexible kites is rather low and lift power kites are hard to launch and land autonomously. Maybe the biggest advantage of drag power kites is the simplicity of their operation: For launch and landing the kite is operated like a multicopter just by operating the onboard rotors as propellers and the electrical machines and power electronics in motor mode, there is no reel-in phase during power generation which simplifies the control and design of the kite, and the kite can be kept in crosswind flight even at low and zero wind due to the rotors. Recently, great successes for the drag power concept have been achieved: In 2012, Makani Power/Google/X Development (in the following denoted in short as Makani) flew a 20 kW demonstrator fully autonomously in all flight maneuvers, including launching and landing [16, 17]. At that time, this kite achieved the highest power density w.r.t. the kite area [18]. In 2016, a scaled-up 600 kW version was flown successfully in crosswind maneuvers [19, 20]. Fig. 1.4 shows a photograph of the Makani M600 system.—Those are motivations for this dissertation to focus on the drag power concept. A more detailed comparison and assessment of the airborne wind energy technologies as well as more reasons for the motivation for the drag power concept are given in Appendix A.

Developing and commercializing drag power kite plants impose numerous interdisciplinary challenges. A development team needs deep insights in the various engineering disciplines. Experimental verifications of new designs and ideas are necessary, but with a model-based design new ideas can be pre-assessed quickly at low cost by simulations and the full potential of kite power can be utilized through model-based optimizations. For that, either simple or rather sophisticated kite power plant models are available. With the first, only rough estimates on the expected power output can be made with limited force of expression. With the latter, usually only one or

[6] Note however, that both crosswind kite power concepts are based on the lift principle and that usually also lift-type turbines are used onboard a drag power kite, because of their higher efficiency compared to drag-type turbines.

Figure 1.4: Photograph of the Makani M600 system [21].

a few specific phenomenons are highly resolved and only for a certain kite design. Significant efforts are required for the model setup. The model execution is computationally expensive, which makes it unsuitable for optimizations. Specifically no drag power kite systems engineering model is available, i.e. a multidisciplinary model which covers the dominant phenomenons of all involved disciplines, with which electrical energy outputs and the economic performance can be predicted, a good or optimal design of a drag power kite plant can be found, and sensitivities on design choices can be investigated, with which e.g. the importance of the detailed design of a component can be assessed. A prominent example question is: what is the sensitivity of the tether transmission voltage on the figures of merit? If the sensitivity is low, a much smaller off-optimal voltage could be used to greatly simplify the design of the power electronics. There are many more similar questions a research and development team asks in the design process. To enable agile decisions, such questions must be answered fast. Therefore, the systems engineering model and optimization procedures must be simple enough.—Those are motivations for this dissertation's research focus: First, a systems engineering model is derived with a good trade-off between accuracy and computational cost. This is approached with a multidisciplinary steady drag power kite model, because it can fulfill this trade-off well. That is shown in a second step by validating the model. Third, an optimization procedure is utilized to finally execute various optimizations and parameter studies such as sensitivity analyses.

1.2 Related Works: Literature Review

Early Research and Development, First Models

In 1980, Miles Loyd published the paper "Crosswind Kite Power" [13] as one of the first publications about airborne wind energy [22, 23]. Only a few earlier patents and other publications can be associated with that topic [23], but in which no crosswind kite power model is derived. Loyd's paper is referenced in almost every work about airborne wind energy, making it probably the most cited publication on this subject. In particular, he was the first who derived the potential of

crosswind kite power with the power equation

$$P = \frac{2}{27}\rho v_{\mathrm{w}}^3 A \frac{C_{\mathrm{L}}^3}{C_{\mathrm{D}}^2}, \tag{1.1}$$

where ρ is the air density, v_{w} is the wind speed (at the kite's altitude), A is the kite's reference area (usually the projected wing area), and C_{L} and C_{D} are the (total) lift and drag coefficients of the kite. Eq. (1.1) is based on a few assumptions, e.g. that the aerodynamic forces are dominant, but it is valid for both, lift power and drag power. By inserting reasonable values into (1.1), it becomes obvious why crosswind kite power is so interesting: For instance, assuming $\rho = 1.225\,\mathrm{kg/m^3}$ (standard atmosphere), $v_{\mathrm{w}} = 15\,\mathrm{m/s}$ (similar to nominal wind speed of a conventional wind turbine), $A = 100\,\mathrm{m^2}$ (medium kite size), $C_{\mathrm{L}} = 1.5$ and $C_{\mathrm{D}} = 0.1$ (conventional airfoil plus some drag accounting for other system parts), then the result is $P \approx 10.6\,\mathrm{MW}$, or, w.r.t. the wing area, $P/A \approx 106\,\mathrm{kW/m^2}$. This is a more than hundred times higher power density compared to photovoltaics. Compared to a conventional three-bladed wind turbine, the potential is also enormous, considering that the kite's mass and size are much smaller than that of a conventional wind turbine of similar power, and that no tower and a much smaller foundation are required.

Today's Research and Development

Loyd also filed a patent [24], but, after the oil crises of the 1970s and 1980s ended, the concept received almost no attention until the 2000s years, cf. e.g. [23]. Reasons may include that the need to shift the energy supply towards renewable energies became more evident due to the new price increase of fossil fuels and due to the evidence of the anthropogenic global warming. Moreover, the costs for the required sensors and computational power to execute the fully autonomous flight control algorithms dropped significantly and numerous flight control algorithms became available. During the past few years, a number of researchers and developers have published refined models, have developed control algorithms, have built demonstrators, and have been working on commercial-scale systems. A general overview of airborne wind energy systems, their development status, and modeling concepts are given e.g. by Fagiano and Milanese [9], the "Airborne Wind Energy" book from 2013 edited by Ahrens, Diehl, and Schmehl [10], or, more recently, the overview by Cherubini [11], the new "Airborne Wind Energy" book from 2018 edited by Schmehl [12], or the overview about scientific and patent literature by Mendonça et al. [23]. Those references provide also an overview about the companies and research groups involved in airborne wind energy. The two biggest research groups are the KitePower research group at Delft University of Technology lead by Prof. Dr.-Ing. Roland Schmehl [25], focusing mainly on lift power kite modeling, control, and design of flexible kites, and the Systems Control and Optimization Laboratory at University of Freiburg lead by Prof. Dr. rer. nat. Moritz Diehl [26], focusing mainly on nonlinear model predictive control. Worth to be mentioned (startup) companies include the already in the previous section mentioned Makani [27] focusing on rigid drag power kites, Ampyx Power [28] focusing on rigid lift power kites with a catapult-like launch and landing, EnerKite [29] focusing on semirigid lift power kites with a rotational (or helical) launch and landing, SkySails [30] and KitePower [31] focusing on lift power flexible kites, or TwingTec [32] focusing on a semirigid lift power kite with multicopter launch and landing.

Advanced Dynamic Models

In 2017, in total only a few hundred scientific works and patents about airborne wind energy in general are published [23], which include also those publications which focus not only on crosswind kite power, but on other airborne wind energy concepts. An early publication on crosswind kite

power, which further refines Loyd's model, is Diehl's dissertation [33] in which he modeled the kite as point-mass and applied model predictive control to stabilize the kite's trajectory. The model was later refined by Houska and Diehl and the controller was optimized for towing [34] and lift power operation [35]. Their kite model refinements include a logarithmic wind shear for the wind field, a reduction of the air density for increasing altitudes with a barometric equation, and the consideration of a tether drag force lumped to the kite. These modeling approaches have then been used by many authors e.g. for performance estimations and the development of control algorithms, cf. e.g. [10, 12, 36–41] and references therein. Other authors further refined the kite dynamics, tether dynamics, and aerodynamics models: Instead of a point-mass for the kite and a straight massless tether, the kite and tether have been modeled with rigid bodies, different types of multibodies, and with finite element-like methods, cf. e.g. [10, 12, 42] and references therein. Moreover, wake effects of the kite are attempted to be included into the model [43, 44]. Such model refinements improve the accuracy of the system dynamics with higher resolution of instantaneous forces and extracted power, but the computational load and efforts for the model-setup are high and other important disciplines to evaluate the technological potential, such as economics, are usually neglected.

Advanced Steady Models

Researchers also tried to reduce the complexity of the dynamics model, while still obtaining the dominant effects of the dynamics. The available computational resources are then used e.g. to compute the complete power curve, i.e. the power for all wind speeds, with which e.g. economic performance estimations can be made. For the reel-out phase of lift power kites and generally for drag power kites, one approach to approximate the dynamics is to use a representative position of the kite in which the computed power is equal to the average power the kite harvests within a complete figure eight or circular flight path. This steady or "average" modeling approach adds only the cube of the cosine of the (average or effective) azimuth angle and the cube of the cosine of the (average or effective) elevation angle as factors to Loyd's power equation (1.1). Argatov [39], Luchsinger [45], Fechner and Schmehl [46], Fechner [47, Chap. 3], Schmehl et al. [48–50], and some therein referenced works use such approaches for lift power kites, albeit a good model for the reel-in phase is only "quasi"-steady. Costello et al. [51] generalize this approach, include the airborne mass, and proof that an averaged model gives a best-case result. De Lellis et al. [52] include into the model a by the kite itself reduced wind speed in the wind field (wake effects) and compare the wind power extraction efficiency of the lift power and drag power concepts with conventional wind turbines.

Steady Drag Power Kite Model

Vander Lind [16] uses a similar approach to model Makani's drag power kite. This study is particularly interesting, because a power curve for the kite is derived and compared to the power curve computed with a higher fidelity kite dynamics model and with measurements: Although the kite's mass is almost completely neglected, the computed power curve of the steady model matches well with the higher fidelity model and with the measurements. Vander Lind also shows that the actuator disk efficiency of the onboard wind turbines can be rather high, much higher than the Betz efficiency value of 16/27 for tower based wind turbines, in part because the optimal induction factor for the onboard wind turbines of a drag power kite is usually low. However, the total lift and drag coefficients were simply given as numbers. No reasons for their choice or origin are given. Moreover, no electrical power output and no economic values are given.

Economics

The economics of lift power kites is touched by Luchsinger [45] by computing the annual energy yield, similar to conventional wind turbines, by integrating the power curve of a lift power kite with a wind probability distribution over all wind speeds. Heilmann [53] and Heilmann and Houle [54] use a similar approach, but additionally derive cost models for the different parts of the system. Fechner [55] compares the costs for different system sizes, but uses a similar cost modeling approach as Heilmann and Houle [53, 54]. Argatov and Shafranov [56] investigate the economics of small-scale pumping kite wind generators. Grete [57], Faggiani [58], Faggiani and Schmehl [59], and De Lellis et al. [60] use a quasi-steady kite model or a point-mass kite model for optimizations and sensitivity analyses of a lift power flexible kite and a wind farm thereof to analyze economics. All these works have in common that they focus on lift power kites only and consider only airfoils with a rather low lift coefficient around one, although e.g. Heilmann [53] concludes that the maximum lift coefficient has a high impact on the system performance.—It should be noted that indeed much higher lift coefficients *are* possible with multi-element airfoils, i.e. airfoils with slats and flaps, which are being used in commercial airliners for many decades [61].—Moreover, many rather rough assumptions are made for the cost factors for the different system components.

Power Plant Design and Optimization

The design of a kite is still immature, which is expressed by Gohl and Luchsinger: "[a] general guideline for designing kites does not exist and makes the design of kites so far to a large extent a trial and error process" [62]. Breukels and Ockels [63] tested a "kiteplane" made of foam, but they considered no crosswind flight operation. In [64] the same authors compare a foam structure with an inflatable structure and conclude that the latter provides a lower mass. Lansdorp et. al [65] discuss the design of the actuators of a remotely controlled surf kite. In [66], Lansdorp and Ockels detail the design of a large-scale "laddermill", i.e. several "simple kites" in Loyd's terminology on a single tether. With his Ph.D. thesis, Breukels [42] developed a methodology to design and analyze flexible lift power kites. Two technology demonstrators for flexible lift power kites are described by van der Vlugt et al. [67] and Milanese et al. [68]. Dunker [69] and Paulig et al. [70] describe the design of flexible kites. Some authors discuss the design optimization of a power generating kite, but it is usually limited to optimizing the tether length and investigating scaling-up effects, cf. e.g. [71, 72] and references therein. Gohl and Luchsinger [62] describe a simulation tool and compare kites with arc-shaped wings and flat wings. They conclude, that the latter provides considerably higher performance, particularly for the reel-in phase. Venturato [73] optimized a single-element airfoil for kite power applications, but he neglected the tether drag, which in fact is a non-negligible drag contributor [35], and therefore his results are only of limited applicability. Coenen et al. [74] designed a kite within a student design challenge. All these works have in common, that again only simple kites (in Loyd's terminology) or lift power kites and only airfoils with a rather low lift coefficient around one are considered, although Coenen et al. concluded in their conference poster "[i]t turns out that $C_{\mathrm{L,max}}$ of the wing is the driving coefficient to design for" [74]. Only Vander Lind [16] gives some reasoning for the choice of designing Makani's kite with a high wing aspect ratio by comparing the performance to a low aspect ratio flexible kite. This is also one of the few publications which considers a higher lift coefficient around two by using a multi-element airfoil which is shown in the patent [75]. Moreover, the patents filed by Makani disclose some of the design choices for the Makani kite, cf. e.g. [75].

Very recently, Kruijff and Ruiterkamp [76] sketch the optimization procedure employed for Ampyx Power's kite with dynamic simulations and economic models and also mention a lift coefficient of 2.4 achieved with a multi-element airfoil. Though, they focus on a specific lift power concept and use dynamic simulations, which are likely inevitable because of the reel-in phase

and the catapult launch and landing, therefore the computational load for an optimization is rather high compared to a steady model. Also very recently, Ranneberg et al. [77] describe a procedure to compute the power curve of a lift power kite for energy yield estimations by solving force equilibria for a discretized flight path. Again, the computational load is high compared to a steady model and lift power instead of drag power is the focus of their work.

Another very recent work is Tucker's talk at the Airborne Wind Energy Conference 2017 [78], in which he sketches Makani's approach to design its kite through a techno-economical optimization with different modeling levels. This work has the closest relation to this dissertation. However, only a few details are disclosed (but which are used within this dissertation in Chap. 3).

The early patent "Self-erecting windmill" by Payne and McCutchen [79] from 1976 is the first proposal of a system configuration with two kites connected to a shared and possibly very long tether, but seemingly without realizing the main advantage of the system. Houska and Diehl [35] analyze and optimize such a configuration for lift power kites and later other authors e.g. [72] adapt for drag power kites. They highlight the advantage of such configurations, that the tether drag is significantly lower compared to a system with a single kite, because the long shared tether hardly moves. However, again all studies consider only a rather low maximum lift coefficient around one. Moreover, only a single wind speed and, in case of drag power kites, no details about the electrical transmission over the tether are considered. Only Cherubini [80] derives a simplified model which takes also the significant transmission losses and a worst-case power curve into account. A considerable disadvantage of such systems is the increased complexity as two kites have to be controlled simultaneously. Moreover, with the long shared tether, a considerable air volume is occupied compared to a single-kite system on a much shorter tether. Therefore, it is questionable if such systems can be economically viable.

Electrical System of Drag Power Kites

The electrical system of drag power kites is investigated by Kolar et al. in [81]. By considering a certain system size and power, they discuss interconnection concepts of the power electronic components, optimize the tether sizing and tether voltage which is modeled by empiric relations, optimize the machine design, and optimize the power electronic converters. The optimal tether voltage is found at 8 kV for a 100 kW system. On the kite, the proposed optimal system configuration consists of low-voltage machines with low-voltage three-phase AC-DC converters, connected to low-voltage DC to high-voltage DC dual active bridge converters, which are finally connected to the tether terminals. In further studies, the design and optimization of many system components are further detailed by Kolar and members of his group [82–87] and other authors [88–90]. Makani filed a few patents with different system approaches with AC transmission [91] and with series connections [92, 93]. However, these publications do not consider back-coupling effects: For instance, in [81] the tether is optimized for weight and efficiency in the electrical domain only without considering that a changed tether diameter significantly affects the captured wind power because of the changed tether drag. Moreover, the tether length is not optimized and instead left at a constant (and arguable) value, only a specific system size is considered, and again only a low lift coefficient around one is considered.

Applicability of Lift Power Findings to Drag Power, Further Information on Drag Power from Makani

Although some results from publications about lift power kites are applicable also for drag power kites, the systems do have considerable differences. Most importantly, drag power kites do not have a reel-in phase which simplifies the design, control, and analysis at first sight, but they have medium-voltage electrical cables integrated into the tether, which increase the tether diameter

and thus the tether drag, increase the tether weight, and introduce power transmission losses. Moreover, the onboard turbines and the whole powertrain with a number of electrical power conversions affect the efficiency, costs, and mass of the kite power plant. Therefore, only a few results from lift power kites are also applicable to drag power kites, e.g. the crosswind flight control in a circular or figure eight path.

In 2018, Makani is the most important company which focuses on drag power kites. Only two other small startup companies began to also go into that direction [94, 95], and the former company Joby Energy [96] also focused on drag power kites. No research group known to the author of this dissertation focuses on drag power kites, apart from side-projects or small investigations. All the few publications about drag power kites available are mentioned in this section. Besides Vander Lind's book chapter [16], Makani published only limited details, which is understandable for a company. Some further information could be extracted from the recent paper [97] by Wijnja et al. about aeroelastic analyses. Some further information, but mostly photographs and videos from successful experiments, are given in conference talks, cf. e.g. [19, 78, 98, 99], their website [27], on their Google+ account [100], on their Youtube channel [101], and in a response to the Federal Aviation Administration (FAA) [102]. Further information and some interesting details can be extracted from the many filed patents, cf. [23] and references therein. For instance, in a recent patent, published in July 2017, a two element airfoil is disclosed which achieves a maximum lift coefficient of up to four [103], though, as usual for patents, it is left uncertain which concrete lift coefficient is best and why. Those communication channels are not used for further details on the modeling and optimization of drag power kites.

1.3 Goals

Quite an amount of work has been conducted on the modeling and optimization of kites. However, most works focus on lift power kites and the previously published models are either too rough to derive a good (or optimal) preliminary kite design or too complex and highly resolve only specific phenomenons (e.g. kite dynamics) while neglecting other dominant and important phenomenons (e.g. the power transmission). Moreover, many works optimize the flight path which is indeed part of the power plant, but design variables such as the lift coefficient are set to some value, although e.g. the choice of the airfoil and its lift coefficient might have a much higher impact on the overall system performance. The major sensitive design variables for a drag power kite are unknown.

A first and important goal of this dissertation can therefore be stated as follows:

Goal 1: *Derive a multidisciplinary steady model of a drag power kite, which combines models for the important and dominant phenomenons of all involved disciplines (systems engineering model) and which is suitable for fast performance estimations, fast parameter studies, and fast (preliminary) kite power plant design optimizations.*

With the focus on a steady model it is ensured that the model complexity is limited. The word "fast" refers to the model setup, the parameter estimations, and the model execution. Hence, the steady models referred to in the previous section are used as basis for further submodel extensions.

Before the targeted model is derived, it should be recalled what a model is: Any model is a simplification of a real world phenomenon or object. For sake of simplicity and to keep the modeling manageable and mathematically solvable, always only the important and dominant phenomenons are considered in a model. The advantage of mathematical models is that deep insights for mathematical relationships can be gained and design improvements or control algorithms can be developed with first validations in software at low costs. All variables are available in a simulation model, even though they might not be measurable at reasonable costs or at all.

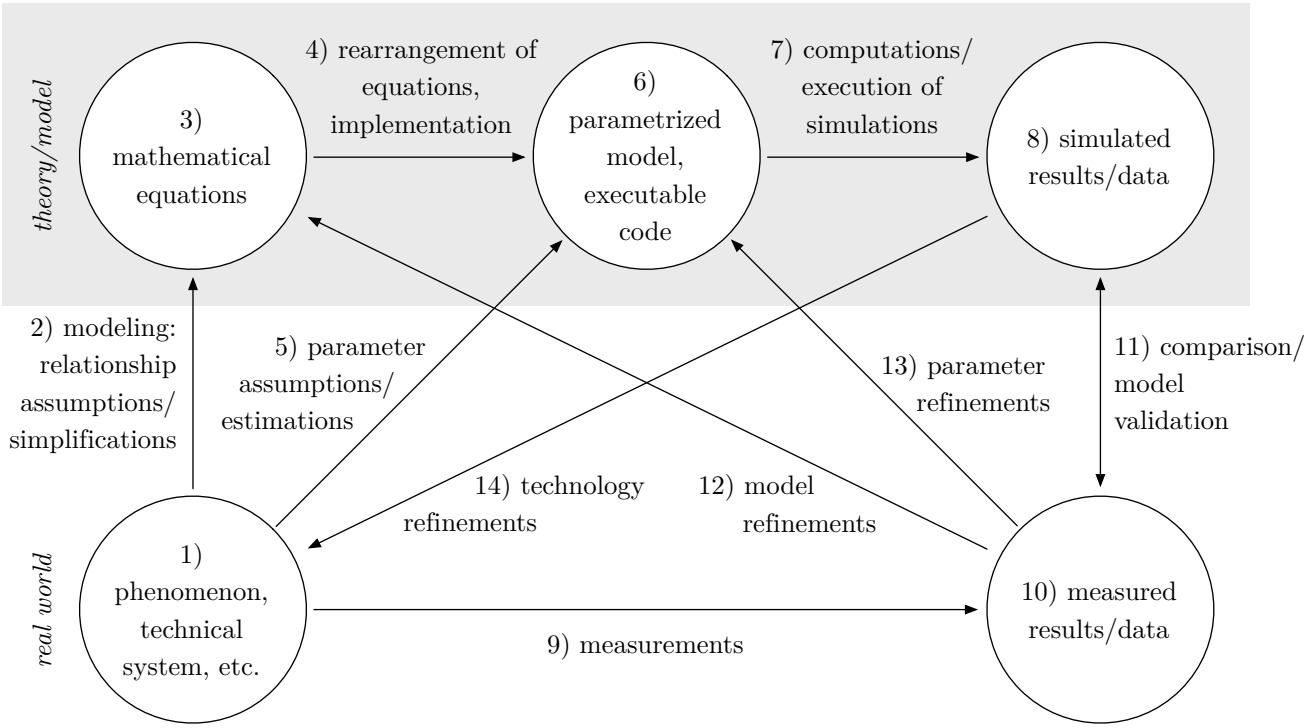

Figure 1.5: Process of model derivation and model-based design.

Fig. 1.5 is a visualization of the model derivation and model-based design process: Important aspects of the real world 1) are transformed into mathematical equations 3) by imposing assumptions or simplifications (in the following always called: assumptions) on the relationships 2) between quantities (variables and parameters). As a simple example, the relationship between force, mass, and acceleration can be described by Newton's second axiom, where force and acceleration can be interpreted as variables and the mass can be interpreted as a constant parameter. The equations are then (re)arranged and implemented 4) on a computer 6). The model is parametrized with measured, estimated, assumed, or guessed parameter values 5). In the just mentioned example, the mass might be a measured model parameter. The model code is then executed 7) to generate simulated data 8). Measurements 9) are conducted to generate measured data 10), which are compared 11) to the simulated data to validate the model. If measurements and simulations do not agree sufficiently well, model refinements 12) or parameter refinements 13) are necessary. When the model can reproduce real world results sufficiently well, new ideas can be developed and tested within the model, i.e. optimizations and parameter studies can be performed. Finally technology refinements 14) can be proposed and implemented. The process then might be restarted over and over again.

Deriving the model with reasonable assumptions 2), which include all relevant dominant effects, is one of the most challenging tasks. First, general limitations on the considered system are made, i.e. the general scope of the model is defined. An example for kite power, which is also made in this dissertation, is, that only rigid drag power kites are considered. Second, a possibly high number of assumptions with different degrees of roughness are made. Each assumption tells implicitly, under what circumstances the model is valid. The more assumptions made and the rougher the assumptions are, the lower is the expected accuracy. Note that not the total

number of assumptions is a measure of the overall model accuracy, but the assumptions and their roughness altogether. However, the roughness of an assumption may be obscure and ultimately only be evaluated by comparing the computed results of the model (predictions) with real world achieved (measured) results. With the imposed limitations and assumptions, the model is only valid for certain designs or configurations of the system of interest and parameter ranges.

In a continued work, some in this dissertation derived submodels might need refinements. To make the derived models and the results of this dissertation accessible and usable as simple as possible to other researches and developers, a second goal is:

Goal 2: *State and highlight all imposed assumptions as clearly as possible.*

The general scope of the model derived in this dissertation is further narrowed below, in Sect. 1.5. In the model derivation chapter, each assumption is highlighted where it is first needed, such that the reader can quickly catch each assumption. If one assumption is too rough for the work of a reader, the assumption and the corresponding equations could be replaced with finer ones.

For the modeling strategy 2) there are generally three different options:

- White-box modeling: The model is derived based on fundamental physical relationships. In its ideal form, the model is based solely on first principles. The generality of white-box models is usually high. All parameters, all variables, and all internal model states and intermediate values have a physical meaning. Particularly predictions of changes in results for changes of (design) parameters can be made.
- Black-box modeling: The model is a mathematical function with unknown parameters. Neither the mathematical function, nor the parameters may have a physical meaning, and so do the internal model states and intermediate values. The parameters are fitted, such that the input-output characteristic of the model agrees well with *certain* empiric data or measurements. Therefore, the generality of black-box models is only as good as the available fitting data. Predictions on performance results for changes of design parameters are impossible, unless those design parameters are inputs to the black-box model.
- Grey-box modeling: The model is a mixture of white- and black-box models, i.e. it is in part derived by first principles and in part by fitted parameters. The generality is given within certain parameter ranges, in which it can be used for predictions on changes of results for changes of (design) parameters.

A pure white-box model has the highest generality, but also the highest complexity. The rougher a model is, the simpler, the fewer the number of parameters, and the faster the computation of results or predictions, respectively. Fig. 1.6 visualizes that trade-off for different kite dynamics models. Loyd's model, i.e. (1.1), is simple, has a low number of parameters, but also a low accuracy. For instance, the actual flight path is not resolved at all or an estimation of the value of C_D, which includes all drag contributions including that of the tether, is difficult. If the kite is modeled as point-mass, rigid body, multi body, or finally with a finite element model (FEM), the model accuracy in terms of the dynamics or structural loads increases, but so do the model complexity and the number of parameters, e.g. for a FEM the geometry of the kite is required. The model complexity and computational cost tend to increase even exponentially with the model accuracy. In Fig. 1.6, "model accuracy" refers only to the resolution of the dynamics or structural loads of the kite or closely related values like the prediction of the instantaneous power extraction over the crosswind flight path. However, the model accuracy for other disciplines, e.g. the economic performance, might be hardly increased, i.e. the model accuracy can be interpreted to have multiple dimensions, one for each phenomenon or discipline.

For the modeling strategy and complexity, the following goal is set in this dissertation, with which Goal 1 is further specified:

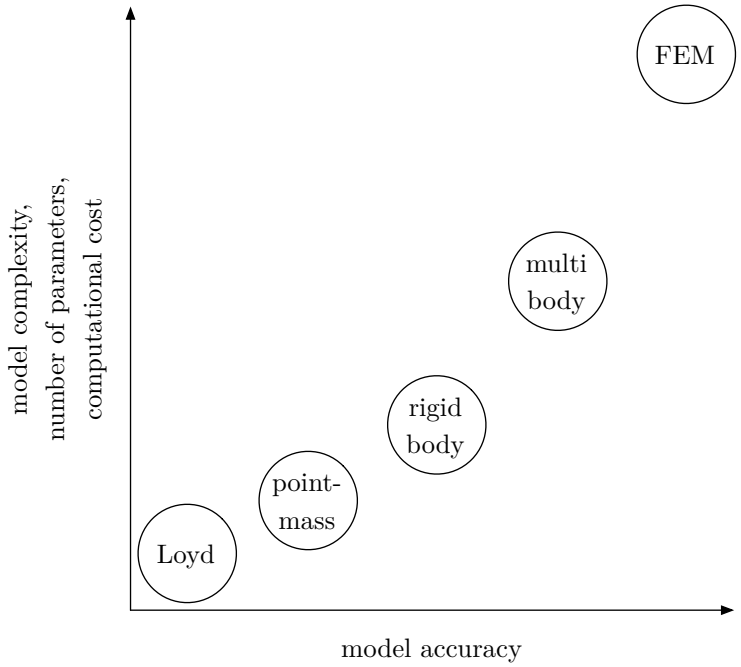

Figure 1.6: Example of a typical relationship between model accuracy and model complexity, number of parameters, as well as computational cost.

Goal 3: *Develop a white-box drag power kite plant model as far as possible for all relevant dominant effects of all involved disciplines for a sufficiently high model accuracy and generality, while the model uncertainty and complexity are limited, but, for sake of simplicity, black-box and grey-box submodels are allowed if the model would become too complex otherwise, i.e. the model as a whole is allowed to be a grey-box model. To ensure that the overall model is simple for a fast model setup and fast computations, it shall be steady and ideally explicitly analytically solvable. The relevant dominant effects include the kite dynamics, kite and tether aerodynamics, rotor aerodynamics, electro-mechanical power conversions, electrical power transmission over the tether, thermodynamics, reliability, and economics.*

As visualized in Fig. 1.5, the validation of a model is an important step and must therefore be also a goal of this dissertation. However, the full design and construction of a whole drag power kite plant is a time consuming and difficult task, which is tried to be accomplished by whole development teams in different kite power research groups and startup companies. For manageable validations for a single doctoral research project, the model validations must be limited to comparisons to published measurements (e.g. by Makani) and higher fidelity models:

Goal 4: *Validate the model by comparing results to measured published data and higher fidelity models.*

Once the model is derived and validated, optimizations and parameter studies can be executed, with which improvements to the technology can be proposed:

Goal 5: *Execute optimizations and parameter studies and give answers to questions such as: How should an optimal drag power kite plant look like? What are the most sensitive design parameters?*

This goal is maybe also the most interesting part, as it gives important answers to research and development teams.

1.4 Methodology

To solve the set goals, the following methodology (or materials and methods) is chosen straightforwardly: All steps in Fig. 1.5, apart from the implementation of technology refinements, are conducted in the presented order, in a multidisciplinary fashion for a drag power kite plant.

1.5 Scope

Based on the previous discussions, the scope of this dissertation is the derivation and validation of a multidisciplinary steady drag power kite model and execution of optimizations and parameter studies, or in short the *multidisciplinary optimization of drag power kites*, the title of this dissertation. The scope of the validations is further narrowed to comparisons with published measurements and comparisons to higher fidelity models.

The scope of the considered drag power kite plant concept and design is further specified as follows, cf. Fig. 1.7: A drag power kite, which is made from a rigid material such as light

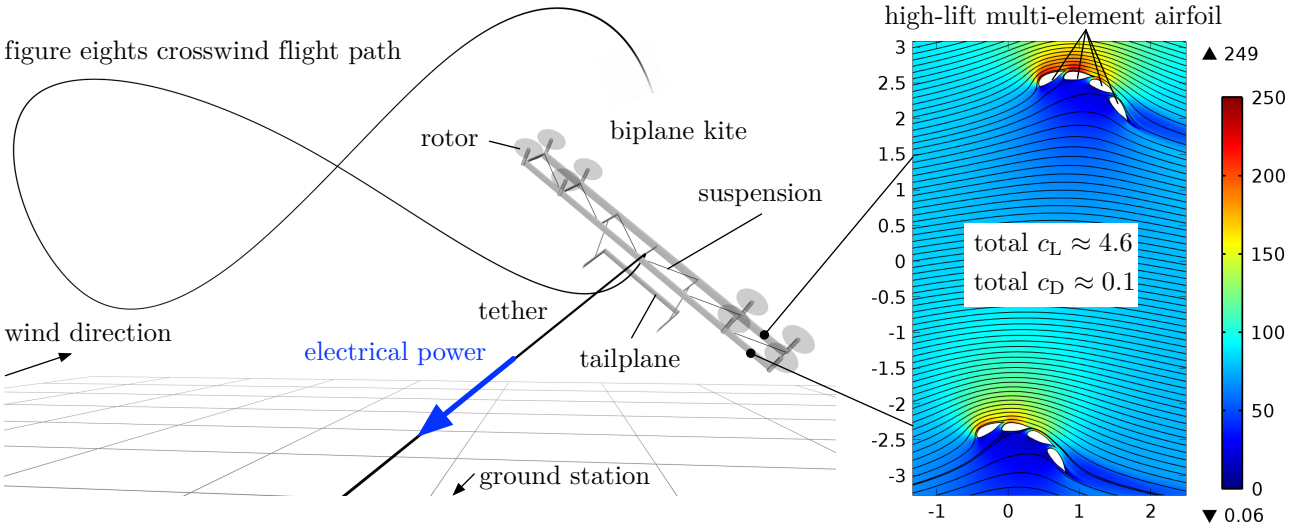

Figure 1.7: Exemplary embodiment of the considered drag power kite concept: Biplane kite flying in figure eights (left) with a high-lift multi-element airfoil (right). Similar image published by the author already in [104, p. 72].

metals or composites, is considered. It has a number of onboard rotors which can be operated in wind turbine mode (generator mode) for power generation and in propeller mode (motor mode) to maintain crosswind flight, to hover during launching and landing maneuvers, or to transit between hovering and crosswind flight. For efficient operation, lift-type rotors are considered. The rotors are considered to be identical apart from the rotation direction and mounted firmly to the kite's frame, i.e. the rotors are not tiltable. Fixed pitch rotors are considered for their simplicity, robustness, and low-cost. The kite is considered to have onboard control surfaces such as ailerons, flaps, rudders, elevators, air brakes, or combinations thereof such as flaperons, with

which not only lift and drag are controlled directly or indirectly via angle of attack and angle of sideslip, but also the flight path via a roll moments and a roll angle are controlled. The kite is considered to have a number of identical main wings, whereby usually only a number of one or two is considered, i.e. either monoplane or biplane (or box wing) configurations. The kite is considered to have one tether with integrated electrical cables. Via a number of bidirectional power conversions, the electrical power is transmitted over the electrical tether cables and fed into the grid or demanded from the grid.

The considered tether design is shown in Fig. 1.8, which is similar to [81] and [105]: In the

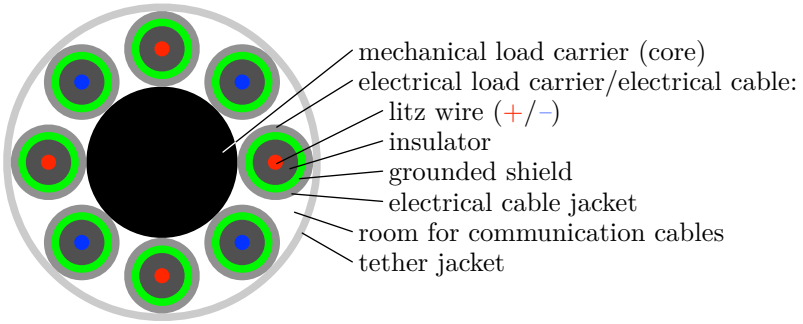

Figure 1.8: Considered cross section design of the tether. Image published by the author already in [106, Fig. 8].

center, the tether has a core (black) which is preferably made from a material with a very high strength-to-weight ratio (e.g. Dyneema) to carry the complete mechanical load. The core is surrounded by electrical cables to carry the electrical load. The electrical cables are considered to be placed in a helix along the tether. Each electrical cable consists of litz wires (red for DC-positive or first AC-life wire, blue for DC-negative or second AC-life wire; in the following only denoted as positive and negative wires), surrounded by an insulator (dark grey), surrounded by a grounded shield (also called screen or sheath, green), and surrounded by a jacket (grey) for mechanical protection of the shield or of the electrical cable, respectively. For sake of symmetry and simplicity, identical electrical cables and the same amount of positive and negative electrical cables are considered. The final tether layer is the tether jacket (light grey) which surrounds the electrical cables to provide mechanical and weather protection. As in [81] and [105], a medium voltage DC or AC transmission is considered. Unless denoted otherwise, if more than two electrical cables are used (as in Fig. 1.8), then all positive cables are connected together on the kite and on the ground, respectively, and so are the negative ones. For a minimal insulation width, the transmission voltage is "centered around ground", i.e. the voltage rating of one electrical cable against ground is only half of the transmission voltage (plus safety margin). Under stress, the core strains and constricts, while the helically placed electrical cables can follow the strain like a spring with low stress. The tether jacket is considered flexible enough under such strain. In-between the electrical cables, also optical or conductive communication cables can be placed. As the tether cross section is round, its drag is independent from the airflow direction, and the tether can be wound easily on a drum. The considered design is thermally beneficial, e.g. compared to a coaxial electrical cable in the center surrounded by mechanical load carriers as in [107], because conduction loss heat has a short escape path to ambient air.

The shields of the electrical cables are beneficial for a thin insulation layer: Fig. 1.9 compares the norm of the electric field of two close electrical cables in air, one time without shield in Fig. 1.9 (top) and one time with shield in Fig. 1.9 (bottom). In the variant without shield, the electric field has a significantly higher maximum, which occurs even outside the insulation layer

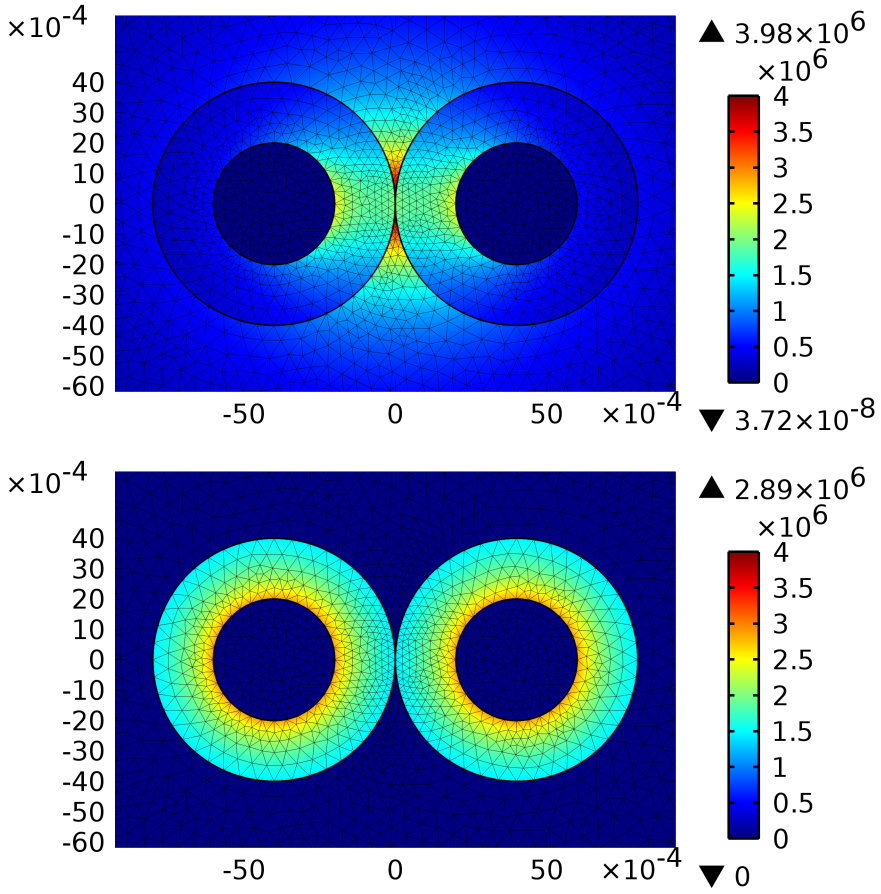

Figure 1.9: FEM results of the norm of the electric field of two electrical cables in air. Each cable consists of a 4 mm diameter copper litz wire, and 2 mm thick PTFE insulation. In the top figure, there is no shield. In the bottom figure, the insulation is surrounded by a thin layer of grounded shield. The voltage of the litz wires is ±4 kV. The space dimensions and electric field dimensions are in SI-units.

in air. This can lead to interferences or arcs and thus damage the insulation, cause a short circuit, or cause a fire. To keep the electric field strength at a harmlessly low level, the insulation layer needs to be thicker than in the variant with shield. In the latter, the electric field is purely radial with known value everywhere in the insulation for the known voltage and geometry. The required insulation thickness is much easier modeled than for cables without shield, as it can be described by a rather simple analytical equation. Outside the shielded cables, the electric field strength is zero. Shields are also a common design approach for high-voltage cables, cf. e.g. [108, Chap. 9]. Further reasons for a shield of the electrical cables for drag power kites are to ground the kite's frame without additional grounding wire or the suppression of electromagnetic interference (EMI), which is e.g. caused by the power electronics.

1.6 Hypotheses

Based on the stated goals and scope, a hypothesis to be confirmed is:

Hypothesis 1: *It is possible to derive a simple multidisciplinary drag power kite plant model which covers all relevant effects of all disciplines, such that fast optimizations and parameter studies are possible.*

However, this hypothesis is a bit artificial. With the optimizations and parameter studies, a number of more interesting hypotheses can be targeted to be confirmed or disconfirmed. In the following, such hypotheses are stated, which can be considered as common sense at the beginning of this doctoral research in spring 2014:

Hypothesis 2: *A kite can have a much higher power density than a conventional wind turbine w.r.t. the overall construction mass and therefore it can obtain a much lower LCOE, or, vice versa, much higher profits while achieving a certain LCOE.*
(Source: This results from a general consideration and is in agreement among kite power researchers and developers, cf. e.g. Diehl's comparison of kite power with conventional wind turbines in [18] or also [9–12].)

Hypothesis 3: *A kite can have a much higher capacity factor than a conventional wind turbine.*
(Source: From a general consideration, a kite can tap stronger and steadier winds in higher altitudes and thus achieve a higher capacity factor. This is also usually mentioned as one of the advantages of kite power over conventional wind power.)

Hypothesis 4: *A single-element airfoil with a high glide ratio is optimal, while the value of the lift coefficient is of less importance.*
(Source: A single-element airfoil with a lift coefficient around one is considered in most publications, cf. Sect. 1.2.)

Hypothesis 5: *The optimal tether transmission voltage is about* $8\,\mathrm{kV}$.
(Source: Ref. [81].)

Hypothesis 6: *The optimal tether inclination is about* $20\,^\circ$, *the optimal tether length is up to about* $1000\,\mathrm{m}$, *and, by combining those two values, the optimal altitude above ground is about* $350\,\mathrm{m}$.
(Source: Cf. e.g. [16, 51, 72].)

Hypothesis 7: *Tethering the kite to a tower is not meaningful.*
(Source: From a general consideration, a tower would significantly increase the construction material demand and construction efforts. The fact that a tower is not a requirement is one of the prominent statements for the kite power technology and is therefore not considered by any researcher and developer known to the author, cf. e.g. [9–12].)

Hypothesis 8: *The achievable power density does not exceed about* $40\,\mathrm{kW/m^2}$. *(Source: Cf. e.g. [18] or other chapters in [10], or cf. e.g. [72].)*

Hypothesis 9: *A biplane kite is not beneficial, e.g. due to the aerodynamic interference of the two wings.*
(Source: Most researchers and developers consider monoplane kites only, cf. e.g. [10, 12].)

Hypothesis 10: *A kite made from metal is too heavy.*
(Source: All researchers and developers known to the author consider lighter materials only, such as carbon fiber, flexible materials, or combinations thereof, cf. e.g. [10, 12, 81, 102].)

Hypothesis 11: *A drag power kite is not beneficial, because the kite is heavier due to the onboard generators, the tether is thicker and heavier because of the integrated electrical cables, the efficiency is low e.g. because of the power transmission loss, and the Betz-limit of the onboard turbines, and most components must be custom-made because of the high transmission voltage in the tether.*
(Source: Most researchers and developers focus on lift power and mention such reasons against drag power e.g. in conversations on conferences, cf. also e.g. [18].)

Hypothesis 12: *A steel tether is too heavy and too thick compared to synthetic materials such as Dyneema, and is therefore not meaningful for kite power applications.*
(Source: Virtually all researchers and developers consider materials with very high strength-to-weight ratio such as Dyneema, Kevlar, or Carbon Fiber, cf. e.g. [9–12, 102].)

Hypothesis 13: *A tether made of carbon nanotubes can increase the system performance significantly.*
(Source: This is a common sense expectation, because carbon nanotubes are expected to have a much higher strength-to-weight ratio than any other today available material, cf. e.g. [109] and references therein.)

Hypothesis 14: *A high aspect ratio is optimal, as it minimizes the induced drag.*
(Source: Cf. e.g. [16].)

Hypothesis 15: *Drag power kites are scalable.*
(Source: This is a common sense expectation among kite power researchers and developers. Most researchers and developers first develop small kites as technology demonstrators and plan to scale them up stepwise, cf. e.g. [10, 12, 18, 102].)

Hypothesis 16: *A region in the power curve, in which the force is constant but the power increases with wind speed, is meaningful.*
(Source: This is a common sense expectation, because the maximum power is high while the maximum force of all system parts can be kept relatively low; a similar approach is also considered for lift power kites, cf. e.g. [16, 45].)

Hypothesis 17: *An offshore system is more performant than an onshore system.*
(Source: This is a common sense expectation for kite power, despite the likely increased construction and maintenance costs.)

Hypothesis 18: *A high reliability for a drag power kite, e.g. in which a short circuit in the tether is unproblematical, is not possible.*
(Source: No published solution to overcome this challenge is available at the time around 2014.)

1.7 Contributions

The contributions of this dissertation can be summarized as follows:

Contribution 1: *Loyd's model [13] is extended, not only by a steady misalignment model for force and wind speed (as e.g. in [50] and referenced works), an atmosphere model, and a tether drag model (as in [34, 35] and in a number of later works), but also by an airfoil polar model, a 3D wing model, an economics model, a model for the electrical cables of the tether and their sizing based on first principles (instead of empiric correlations as in [81]), an actuator*

disk model for the rotors for crosswind flight in turbine and propeller mode as well as for hovering and in case of rotor failures (i.e. reliability issues are covered), and a powertrain model with all power conversion subsystems between the rotors and the grid connection.

Contribution 2: *The power curve with all meaningful regions is derived and optimized analytically. In particular, it includes a region were only the force and airflow speed are at the upper limit, while power is still increased. In addition to [16], all specific actuations, including rotor drag coefficient and induction factor, lift coefficient, actuated drag, and actuated flight path changes, to obtain that complete power curve, are derived.*

Contribution 3: *The model equations are coupled for fast performance computations, virtually entirely based on explicit analytical equations.*

Contribution 4: *The model is validated against the measured power curve recorded with Makani's Wing 7 demonstrator, against expectations of Makani's M600 and M5, and against a higher fidelity model.*

Contribution 5: *With the developed code of the multidisciplinary model, the plant parameters are optimized with a genetic algorithm for a number of different drag power plant variants, including small-scale and utility-scale systems, onshore and offshore. An optimal novel kite design with a high-lift multi-element airfoil and a biplane is proposed. Numerous parameter studies and sensitivity analyses are performed. With that, the hypotheses formulated in Sect. 1.6 are checked.*

1.8 Structure

This dissertation has the following structure:

- In Chap. 2, the multidisciplinary steady drag power kite plant model, i.e. the systems engineering model, is derived, and the submodels are coupled by arranging the equations into a (mostly) explicit analytical order.
- Chap. 3 presents validations of the model with data from Makani and with higher fidelity models. The derivation of the higher fidelity model, as extension to the steady model, is presented in Appendix C. That model is also validated against the measurements of Makani.
- Chap. 4 presents the optimization procedure and the selected optimization algorithm.
- Chap. 5 presents the optimizations and parameter studies including sensitivity analyses.
- Finally, Chap. 6 draws conclusions and gives an outlook.

The appendices contain information which are less relevant or less related to the main part, or provide more details and insights which are not necessary to understand the main part.

1.9 Prior Publications and Talks

This dissertation is in part the combination of the prior paper [110], talk [104], paper [106], conference poster [111], and paper [112] by the author of this dissertation: Ref. [110], entitled "Drag Power Kite with very High Lift Coefficient", co-authored by Ralph M. Kennel, Christoph M. Hackl, Filippo Campagnolo, Michael Patt, and Roland Schmehl, and published in Elsevier's "Renewable Energy" journal, derives a steady drag power kite model and, among others, derives an optimal kite design. Ref. [104], entitled "Power Curve and Design Optimization of Drag Power

Kites", co-authored by the same co-authors as for Ref. [110], is a talk given at the "Airborne Wind Energy Conference 2017" in which the steady drag power kite model of [110] is further refined, a model validation against the measured power curve of Makani's Wing 7 is performed, and preliminary parameter study results are presented. Ref. [106], entitled "Fault Tolerant Power Electronic System for Drag Power Kites", co-authored by Ralph M. Kennel, and published in Hindawi's Open Access Journal of "Renewable Energy", proposes a fault tolerant powertrain design for drag power kites, for which also a patent application is filed. This paper includes a derivation of an analytical tether model with integrated electrical cables, which was also utilized in the talk [104]. Ref. [111], entitled "Design Sensitivities of Drag Power Kites", co-authored by Ralph M. Kennel, and presented on the "Advances in Energy Transition – 8th Colloquium of the Munich School of Engineering", shows first results from design sensitivity analyses. Ref. [112], entitled "Control of a Drag Power Kite over the Entire Wind Speed Range", co-authored by Daniel Petzold, Ralph M. Kennel, Filippo Campagnolo, and Roland Schmehl, and submitted to the "AIAA Journal of Guidance, Control, and Dynamics", presents a control scheme to control a drag power kite at all wind speeds. The results are validated against the measured power curve of Makani's Wing 7.

Main concepts and major parts of those five references are used for this dissertation in all remaining chapters. However, the analyses are in part further refined and extended to meet the goals and contributions stated in the previous sections. To make this dissertation self-contained and simple to read, all relevant results are derived again in this dissertation and adapted to the dissertation's nomenclature and structure.

During the doctoral research time, a number of further contributions were published by the author prior to this dissertation, which in part also have a relation to the dissertation content. Appendix E lists all other publications by the author. Moreover, students' works, supervised by the author, are listed in Appendix F.

Chapter 2

Derivation of a Systems Engineering Model

In this chapter, a multidisciplinary steady drag power kite model—a systems engineering model—is derived. Fig. 2.1 provides an overview of the submodels which are detailed in the following sections. At the end of this chapter, in Sect. 2.9, the submodels are coupled by arranging the equations into a mostly explicit order, with which the complete model is also summarized.

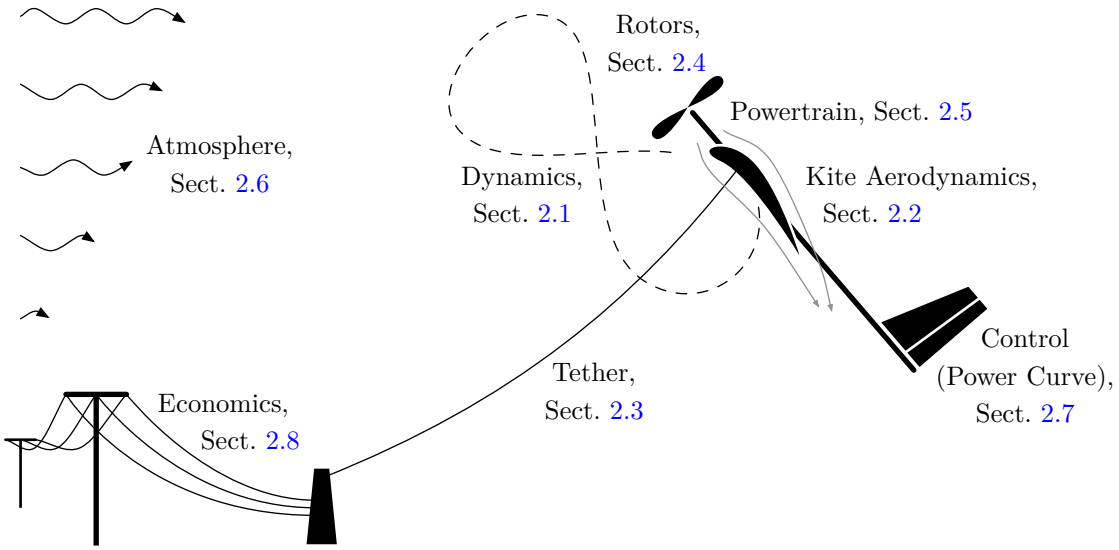

Figure 2.1: Model overview.

Each quantity is introduced when it is first used. If not stated otherwise, all quantities are in SI-units and any quantity x is possibly a function of one or more other quantities y, but "$x(y)$" is written instead of just "x" if it is necessary to avoid ambiguity or for highlighting purposes. Vectors are written in bold, e.g. $\boldsymbol{x}$, while scalar quantities are written normal, e.g. x (which may be the magnitude of vector $\boldsymbol{x}$). Further details on the nomenclature and a complete list of symbols is given on pp. xxv.

2.1 Dynamics Model

The employed dynamics model is an extension of Loyd's model [13] similar to e.g. [16, 39, 45–50] and is similarly employed by the author of this dissertation in [104, 110].

2.1.1 Crosswind Flight Dynamics

For crosswind flight, the following assumptions are imposed:

Assumption 2.1: *The kite's aerodynamic force and the counter-acting tether force are dominant.*

Assumption 2.2: *The kite does not fly through its own wake.*

Assumption 2.3: *The tether is straight.*

Assumption 2.4: *The tether is stiff.*

Even for a relatively heavy rigid drag power kite, Assumption 2.1 is justified due to the usually high airflow speed and thus high lift during crosswind flight. Because the kite's flight path swept area is usually large, Assumption 2.2 is justified. Assumption 2.3 is justified by the high tether force compared to the tether's mass and drag, which limit the tether sagging to a small extend. This is supported e.g. by the photographs and videos from Makani which show a straight tether [17, 20]. Assumption 2.4 is justified by usually used tether core materials with a very high elastic modulus like Dyneema. Moreover, all four assumptions are justified by comparing experimental results to results of simulations, which are based on the same assumptions, cf. [16] or below, Chap. 3.

With Assumptions 2.1–2.4, the "crosswind flight law" can be derived:

Theorem 2.1 (Crosswind Flight Law of a Drag Power Kite): *Consider a drag power kite with total lift and drag coefficients C_L and C_D in a wind field with an azimuth φ and an elevation ϑ w.r.t. the vector of the wind speed v_w at the kite. If Assumptions 2.1–2.4 apply, then the airflow speed at the kite is*

$$v_\mathrm{a} = \cos(\varphi)\cos(\vartheta) v_\mathrm{w} \frac{\sqrt{C_\mathrm{L}^2 + C_\mathrm{D}^2}}{C_\mathrm{D}}. \tag{2.1}$$

Proof. Due to Assumptions 2.1 and 2.3, the kite's aerodynamic force $\boldsymbol{F}_\mathrm{a}$ and tether force $\boldsymbol{F}_\mathrm{te}$ are in balance

$$\boldsymbol{0} = \boldsymbol{F}_\mathrm{a} + \boldsymbol{F}_\mathrm{te}. \tag{2.2}$$

Therefore their magnitudes are equal

$$F_\mathrm{te} = F_\mathrm{a} \tag{2.3}$$

and the aerodynamic force is parallel to the tether. This is visualized in Fig. 2.2.

The aerodynamic force can be decomposed into a drag force component $\boldsymbol{F}_\mathrm{D}$, which is parallel to the airflow velocity $\boldsymbol{v}_\mathrm{a}$, and a lift force component $\boldsymbol{F}_\mathrm{L}$, which is perpendicular to $\boldsymbol{v}_\mathrm{a}$. Similarly, the airflow vector can be decomposed into a radial component $\boldsymbol{v}_\mathrm{a,r}$, which is parallel to the tether, and a tangential component $\boldsymbol{v}_\mathrm{a,tan}$, which is tangential to the sphere defined by the tether ("wind window"). As shown in Fig. 2.2, the force and velocity diagrams with these vectors are in the same plane and are similar, such that one finds the fundamental relationship between force magnitudes and velocity magnitudes (i.e. speeds)

$$\frac{v_\mathrm{a,r}}{v_\mathrm{a}} = \sin(a) = \frac{F_\mathrm{D}}{F_\mathrm{a}}, \tag{2.4}$$

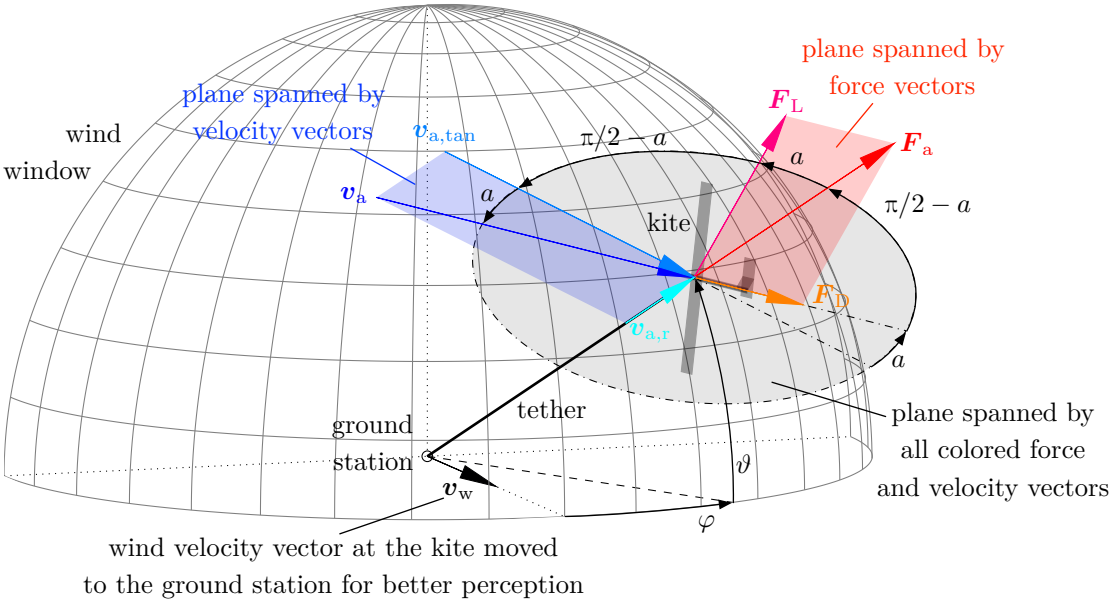

Figure 2.2: Similarity of force and velocity vector diagrams of a kite with dominant aerodynamic force (and counteracting tether force).

where the angle a can be defined as glide angle[7].

The force magnitudes are generally given by

$$F_a = \sqrt{F_L^2 + F_D^2}, \tag{2.5}$$

$$F_L = \frac{1}{2}\rho v_a^2 A C_L, \tag{2.6}$$

$$F_D = \frac{1}{2}\rho v_a^2 A C_D, \tag{2.7}$$

where ρ is the air density (at the kite's position), A is the kite's reference area (most commonly and also throughout this dissertation: the projected wing area), and C_L and C_D are the total lift and drag coefficients (w.r.t. A).

Due to Assumptions 2.2 and 2.4, and because a drag power kite is considered which implies a constant tether length during crosswind flight, the radial component of the airflow velocity originates only from the wind velocity $\boldsymbol{v}_w$, which is in view of Fig. 2.2 given by

$$v_{a,r} = \cos(\varphi)\cos(\vartheta)v_w. \tag{2.8}$$

Substituting (2.5)–(2.8) into (2.4) gives

$$\frac{\cos(\vartheta)\cos(\varphi)v_w}{v_a} = \frac{\frac{1}{2}\rho v_a^2 A C_D}{\sqrt{\left(\frac{1}{2}\rho v_a^2 A C_L\right)^2 + \left(\frac{1}{2}\rho v_a^2 A C_D\right)^2}}$$

[7] This glide angle is defined in analogy to conventional aircraft glide. Note that the glide angle a is only equal to the angle of attack α, if the kite's pitch angle, i.e. the angle between the kite's reference chord line and a line perpendicular to the tether, is zero.

$$= \frac{C_\mathrm{D}}{\sqrt{C_\mathrm{L}^2 + C_\mathrm{D}^2}}. \tag{2.9}$$

Solving that for v_a results in (2.1). ■

It should be noted that a real kite must be rolled consistently to tilt the lift vector and generate a centripetal force which is required for the turns in a figure eight or circular flight path.[8] This reduces the aerodynamic force component parallel to the tether or, in other words, reduces the in (2.1) effective lift coefficient C_L. However, Assumptions 2.1 and 2.2 already imply comparatively small inertial and gravitational forces as well as wide turns to obtain a large flight path, which in turn implies a small roll angle.

2.1.2 Averaged Crosswind Flight

The kite is flown on a crosswind flight path and therefore the instantaneous azimuth and elevation angles change consistently, and so do the instantaneous airflow speed (2.1), forces (2.5)–(2.7), and further derived values such as altitude, power, etc. However, φ, ϑ, and all further dependent values, can also be considered as *effective* constant values which yield the average (thus constant) power that is generated within a full figure eight or circular path for the given wind speed and given aerodynamic coefficients:

Assumption 2.5: *Azimuth φ and elevation ϑ are the effective constant values which yield the average power during the given commanded flight path.*

The effective values φ and ϑ can originate from a data fit with measurements or can be estimations as in Fig. 2.3: For a figure eight flight path, a good estimate for φ is the center point of a turn,

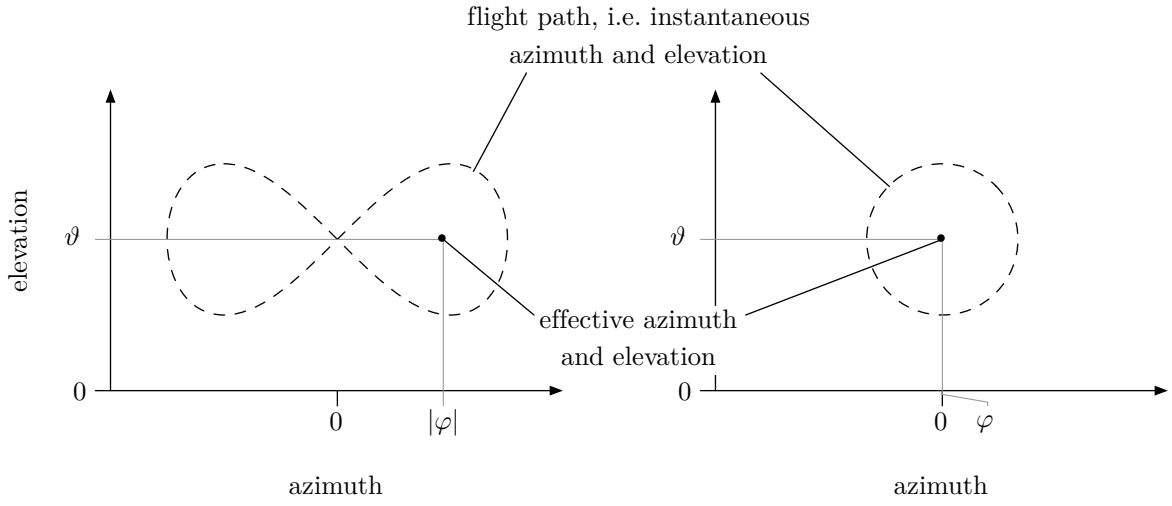

Figure 2.3: Effective azimuth and elevation (black dot) from figure eight (left) and circular (right) flight paths (dashed). The absolute value $|\varphi|$ is written for the figure eight to indicate that the azimuth of the left or right turn is used, whatever is further away from zero.

[8] It should be noted that the centripetal force can also be generated by vertical wings and sideslipping, with which however the kite mass may be increased substantially (for having long enough vertical wings) and the drag is generally increased. However, this is not considered in the scope of this dissertation, cf. Sect. 1.5.

i.e. half of the width from the intersection point to the maximum azimuth point, and a good estimate for ϑ is the elevation of the intersection point [49, 50]. For a circular flight path, a good estimate for φ and ϑ are the azimuth and elevation of the circle's center [16].

2.1.3 Aerodynamic Coefficients

An aerodynamic coefficient relates a force to the dynamic pressure $\frac{1}{2}\rho v_\mathrm{a}^2$ and a reference area of an object in a flow. The flow around the object is generally complex and time dependent. An aerodynamic coefficient is generally a function of the geometry of that object, of the airflow direction (or the angle of attack and angle of sideslip), of the airflow speed value itself (or their non-dimensional counterparts Reynolds number and Mach number), and a function of time (caused by time variations, i.e. instabilities, of the flow at constant geometry, such as unstable vortexes, which in turn may depend on the airflow speed magnitude and airflow direction). For crosswind kite power, usual airflow speeds are subsonic at a low Mach number and within a narrow range, and thus within a narrow Reynolds number and Mach number range. Instabilities of the flow for usually employed airfoils are not dominant, or have a high frequency but low amplitude and thus cause only negligible fluctuations in the resulting forces. Therefore, the following assumption can be made:

Assumption 2.6: *An aerodynamic coefficient depends only on the geometry and airflow direction.*

The contributions to the total lift and drag coefficients C_L and C_D originate from the kite's airframe, from the tether, and from the rotors, i.e. generally

$$C_\mathrm{L} = C_\mathrm{L,k} + C_\mathrm{L,te} + C_\mathrm{L,rot}, \tag{2.10}$$

$$C_\mathrm{D} = \underbrace{C_\mathrm{D,k} + C_\mathrm{D,te}}_{=: C_\mathrm{D,eq}} + C_\mathrm{D,rot}, \tag{2.11}$$

where index "k" is for kite (or its airframe), index "te" is for tether, and index "rot" is for rotors, and where the sum of $C_\mathrm{D,k}$ and $C_\mathrm{D,te}$ is also called equivalent drag coefficient,

$$C_\mathrm{D,eq} := C_\mathrm{D,k} + C_\mathrm{D,te}. \tag{2.12}$$

For the lift contributions, the following assumption can be imposed:

Assumption 2.7: *The kite's main wings dominate the lift contribution.*

This assumption is justified, because the kite's fuselage is small (no lifting body design is considered, cf. Sect. 1.5) and the kite's empennage is mainly responsible for the kite's stability and therefore has a negligible lift contribution, the tether's aerodynamic load is almost entirely parallel to the airflow direction, and the rotors' disk normal vector is exactly parallel or almost parallel to the airflow direction while additionally the rotors' total force is much lower than the lift force (in crosswind flight). Therefore, with Assumption 2.7,

$$C_\mathrm{L,te} = 0 \tag{2.13}$$

$$C_\mathrm{L,rot} = 0 \tag{2.14}$$

and (2.10) becomes

$$C_\mathrm{L} = C_\mathrm{L,k} = C_\mathrm{L,k,mw} \tag{2.15}$$

where $C_\mathrm{L,k,mw}$ is the total lift coefficient of the main wings.

The lift coefficient $C_\mathrm{L,k,mw}$ and the drag coefficients $C_\mathrm{D,k}$, $C_\mathrm{D,te}$, and $C_\mathrm{D,rot}$ remain to be further specified in the subsequent sections.

2.1.4 Resulting Forces and Aerodynamic Power

With the definition of the rotor drag coefficient $C_{\mathrm{D,rot}}$ (i.e. the drag contribution of all rotors) in (2.11), the rotors' thrust force is

$$F_{\mathrm{rot}} = \frac{1}{2}\rho v_{\mathrm{a}}^2 A C_{\mathrm{D,rot}} \tag{2.16}$$

and their power is

$$P_{\mathrm{a}} = v_{\mathrm{a}} F_{\mathrm{rot}}, \tag{2.17}$$

which becomes by inserting (2.16) with (2.1) and (2.11)

$$\begin{aligned} P_{\mathrm{a}} &= \frac{1}{2}\rho v_{\mathrm{a}}^3 A C_{\mathrm{D,rot}} && (2.18)\\ &= \frac{1}{2}\rho \cos^3(\varphi)\cos^3(\vartheta) v_{\mathrm{w}}^3 A \frac{\sqrt{C_{\mathrm{L}}^2 + (C_{\mathrm{D,eq}} + C_{\mathrm{D,rot}})^2}^3}{(C_{\mathrm{D,eq}} + C_{\mathrm{D,rot}})^3} C_{\mathrm{D,rot}}. && (2.19) \end{aligned}$$

Here, this power is called "aerodynamic power" and generative power is defined positive while consumed[9] power is defined negative. The term $\cos^3(\vartheta)$ in (2.19) may be called cosine efficiency (or $\eta_{\cos}$, cf. the prior work of the author of this dissertation [14]). It should be noted, that the rotor drag coefficient $C_{\mathrm{D,rot}}$ must not be confused with the rotor thrust coefficient. Those are only identical if the total rotor area is identical to the kite's reference area A.

Combining (2.1), (2.3), (2.5), and (2.11), the tether force is given by

$$\begin{aligned} F_{\mathrm{te}} &= F_{\mathrm{a}} \\ &= \frac{1}{2}\rho v_{\mathrm{a}}^2 A \sqrt{C_{\mathrm{L}}^2 + (C_{\mathrm{D,eq}} + C_{\mathrm{D,rot}})^2} && (2.20)\\ &= \frac{1}{2}\rho \cos^2(\varphi)\cos^2(\vartheta) v_{\mathrm{w}}^2 \frac{\sqrt{C_{\mathrm{L}}^2 + (C_{\mathrm{D,eq}} + C_{\mathrm{D,rot}})^2}^2}{(C_{\mathrm{D,eq}} + C_{\mathrm{D,rot}})^2} A \sqrt{C_{\mathrm{L}}^2 + (C_{\mathrm{D,eq}} + C_{\mathrm{D,rot}})^2} \\ &= \frac{1}{2}\rho \cos^2(\varphi)\cos^2(\vartheta) v_{\mathrm{w}}^2 A \frac{\sqrt{C_{\mathrm{L}}^2 + (C_{\mathrm{D,eq}} + C_{\mathrm{D,rot}})^2}^3}{(C_{\mathrm{D,eq}} + C_{\mathrm{D,rot}})^2}. && (2.21) \end{aligned}$$

With (2.21), the aerodynamic power (2.19) can also be expressed by

$$P_{\mathrm{a}} = F_{\mathrm{a}} \cos(\varphi)\cos(\vartheta) v_{\mathrm{w}} \frac{C_{\mathrm{D,rot}}}{C_{\mathrm{D,eq}} + C_{\mathrm{D,rot}}}. \tag{2.22}$$

2.1.5 Minimum Aerodynamic Force During Crosswind Flight

During crosswind flight, a certain minimum aerodynamic force must hold for Assumptions 2.1 and 2.3 as well as to keep the kite airborne after all. To estimate that, Fig. 2.4 shows a sketch of a sidewards flying kite from the side. Unlike Fig. 2.2, it does not neglect the gravitational force which has to be balanced by the aerodynamic force. Herein, ψ_{w} is the roll angle (w.r.t. the tether) to balance the weight. By invoking the law of sines, one finds

$$\frac{F_{\mathrm{a}}}{\sin\left(\vartheta + \frac{\pi}{2}\right)} = \frac{F_{\mathrm{g}}}{\sin(\psi_{\mathrm{w}})}, \tag{2.23}$$

[9] Physically, power or energy cannot be consumed but only converted. However, for sake of brevity, the wording "consumed" and "consumptive" power are used here as alternative e.g. for "from the grid demanded" power.

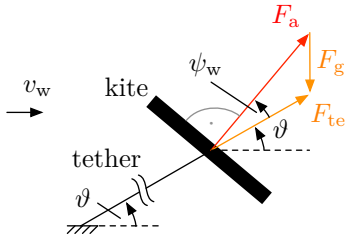

Figure 2.4: Sketch of a sidewards flying kite with gravitation, seen from the side. Image published by the author already in [110, Fig. 3].

where

$$F_\mathrm{g} = m_\mathrm{a} g \tag{2.24}$$

is the gravitational force with effective airborne mass m_a and gravitational acceleration g. By substituting (2.24) into (2.23), inserting further the nominal roll angle $\psi_\mathrm{w} = \psi_\mathrm{w,n}$, and solving for $F_\mathrm{a} = F_\mathrm{a,min}$, the minimum aerodynamic force is defined by

$$F_\mathrm{a,min} = m_\mathrm{a} g \frac{\cos(\vartheta)}{\sin(\psi_\mathrm{w,n})} \tag{2.25}$$

$$\Rightarrow F_\mathrm{a} \geq F_\mathrm{a,min}. \tag{2.26}$$

Apart from estimating $F_\mathrm{a,min}$, a negligible roll angle is assumed and thus Assumption 2.1 is not relaxed.

2.1.6 Effective Airborne Mass and Mass Contributions

If $\vartheta = 0$, then the two tether attachments kite and ground carry each about half of the tether mass. If the kite is above the ground station anchor, i.e. with $\vartheta \neq 0$, then the kite tether attachment carries a higher portion of the tether mass (and vice-versa), which justifies the following assumption:

Assumption 2.8: *The effective airborne mass can be approximated by*

$$m_\mathrm{a} = m_\mathrm{k} + f_\mathrm{m\text{-}te} m_\mathrm{te} \tag{2.27}$$

where m_k is the kite mass and $f_\mathrm{m\text{-}te}$ is the a-priori estimated tether mass contribution factor, typically with $f_\mathrm{m\text{-}te} \geq 0.5$.

The kite mass can be generally further specified by

$$m_\mathrm{k} = \underbrace{m_\mathrm{m} + m_\mathrm{pe,k}}_{=: m_\mathrm{pt,k}} + m_\mathrm{af\&o} \tag{2.28}$$

where m_m is the mass of electrical machines, $m_\mathrm{pe,k}$ is the mass of onboard power electronics, which both can be summarized as powertrain mass onboard the kite $m_\mathrm{pt,k}$, and $m_\mathrm{af\&o}$ is the mass of airframe and other parts.

The mass of the electrical machines m_m and of the onboard power electronics $m_\mathrm{pe,k}$ are approximately proportional to their nominal power across many system scales for this application, which justifies the following assumption:

Assumption 2.9: *The mass of electrical machines and onboard power electronics are approximately proportional to their installed nominal powers, i.e.*

$$m_{\mathrm{m}} = \gamma_{\mathrm{m}} P_{\mathrm{s,n\text{-}ins}} \tag{2.29}$$

$$m_{\mathrm{pe,k}} = \gamma_{\mathrm{pe,k}} P_{\mathrm{el,m,n\text{-}ins}} \tag{2.30}$$

where γ_{m} and $\gamma_{\mathrm{pe,k}}$ are the specific masses of the electrical machines and of the kite power electronics, and $P_{\mathrm{s,n\text{-}ins}}$ and $P_{\mathrm{el,m,n\text{-}ins}}$ are the installed total nominal shaft power (which is the same as the installed total nominal mechanical power of the electrical machines) and installed total nominal electrical power of the electrical machines (which is the same as the installed total nominal machine-side electrical power of the onboard power electronics).

2.1.7 Upper Bound of Nominal Angular Speed

The kite travels on a sphere with the radius of the tether length L_{te}. The angular speed on this sphere is

$$\tilde{\omega} = \frac{v_{\mathrm{k}}}{L_{\mathrm{te}}}, \tag{2.31}$$

where v_{k} is the kite's speed. The flight direction has to be changed permanently to keep the kite on a figure eight or circular flight path. For a kite *with mass*, this is only possible as long as $\tilde{\omega}$ is small enough. Knowing that the kite's speed v_{k} is related with the kite's airflow speed v_{a}, this implies in view of (2.31) that

$$\omega_{\mathrm{n}} := \frac{v_{\mathrm{a,n}}}{L_{\mathrm{te}}} \leq \overline{\omega}_{\mathrm{n}} \tag{2.32}$$

must hold true, where $v_{\mathrm{a,n}}$ is the nominal airflow speed, and $\overline{\omega}_{\mathrm{n}}$ is some feasible upper bound of the ("airflow speed-related") nominal angular speed.

2.1.8 Hovering and Transitions

During hovering (i.e. launching and landing) the kite stays approximately at a constant position and therefore the dynamics are relatively simple. The transitions between hovering and crosswind flight are complex, but short and therefore not regarded in detail in this steady model. The dominant effect for hovering and transitions is the significant power demand of the rotors. A model for that remains to be specified in the subsequent sections.

2.2 Kite Aerodynamics Model

The contributions to the kite's lift and drag coefficients originate from the main wings and other parts such as fuselage or empennage. Moreover, it is considered that the kite's drag can be steered via an actuation e.g. by air brakes or sideslipping, cf. Sect. 1.5. The kite's total lift coefficient is already given with Assumption 2.7 by (2.15). The kite's total drag coefficient is generally given by

$$C_{\mathrm{D,k}} = C_{\mathrm{D,k,mw}} + C_{\mathrm{D,k,o}} + C_{\mathrm{D,k,a}}, \tag{2.33}$$

where index "mw" is for main wing(s), index "o" is for other parts, and index "a" is for actuation (e.g. through air brakes).

2.2.1 Main Wings

As efficient airfoils are considered, the following assumption is imposed for a (single main) wing:

Assumption 2.10: *The "lifting-line theory" can be applied, hence the lift and drag coefficients of a single main wing are*

$$C_{\mathrm{L,k,mw,s}} = \frac{c_{\mathrm{L,s}}}{1 + \frac{2}{\mathit{A\!R}_{\mathrm{s}}}} \tag{2.34}$$

$$C_{\mathrm{D,k,mw,s}} = C_{\mathrm{D,k,mw,s,p}} + C_{\mathrm{D,k,mw,s,i}} \tag{2.35}$$

with

$$C_{\mathrm{D,k,mw,s,p}} = c_{\mathrm{D,s}} \tag{2.36}$$

$$C_{\mathrm{D,k,mw,s,i}} = \frac{C_{\mathrm{L,k,mw,s}}^2}{\pi e_{\mathrm{s}} \mathit{A\!R}_{\mathrm{s}}} \tag{2.37}$$

$$\mathit{A\!R}_{\mathrm{s}} = \frac{b_{\mathrm{s}}^2}{A_{\mathrm{s}}} \tag{2.38}$$

where $c_{\mathrm{L,s}}$ and $c_{\mathrm{D,s}}$ are the lift and drag coefficients of the wing's airfoil (i.e. 2D), wherein $c_{\mathrm{D,s}}$ is by implication the parasitic drag $C_{\mathrm{D,k,mw,s,p}}$, $C_{\mathrm{D,k,mw,s,i}}$ is the induced drag, $\mathit{A\!R}_{\mathrm{s}}$ is the wing's aspect ratio, b_{s} is the wing's span, A_{s} is the wing's area (and the reference area for the coefficients), and e_{s} is the wing's span efficiency factor, cf. e.g. [113, Chap. 8].

The flow around the kite depends on the complete geometry of the kite. However, with the considered kite design described in Sect. 1.5, the following assumption is imposed:

Assumption 2.11: *Aerodynamic interferences, particularly between wings and rotors, are negligible, or can be modeled with appropriate values for e and $C_{\mathrm{D,k,o}}$.*

This assumption is justified also for a biplane (ultimately with appropriate e and $C_{\mathrm{D,k,o}}$, unequal to baseline values of a monoplane). Moreover, the rotors affect only a fraction of the wings' span (cf. Fig. 1.7), their induction factor is usually low (cf. [16], or below, Chaps. 3 and 5), and therefore have low interference, possibly even if they are placed in front of the main wings.

If the kite has n_{mw} identical main wings (i.e. for a monoplane $n_{\mathrm{mw}} = 1$ and for a biplane $n_{\mathrm{mw}} = 2$) with total area A and each with wing span b (which is also the kite's span), the total lift and drag coefficients of the main wings can be written as follows:

Theorem 2.2 (Multiplane Wing Aerodynamics With Negligible Interference): *If Assumptions 2.10 and 2.11 apply for a multiplane with n_{mw} identical wings, the total lift and drag coefficients of the main wings w.r.t. the total area A are*

$$C_{\mathrm{L,k,mw}} = \frac{c_{\mathrm{L}}}{1 + \frac{2}{\mathit{A\!R}}} \tag{2.39}$$

$$C_{\mathrm{D,k,mw}} = C_{\mathrm{D,k,mw,p}} + C_{\mathrm{D,k,mw,i}} \tag{2.40}$$

with

$$C_{\mathrm{D,k,mw,p}} = c_{\mathrm{D}} \tag{2.41}$$

$$C_{\mathrm{D,k,mw,i}} = \frac{C_{\mathrm{L,k,mw}}^2}{\pi e \mathit{A\!R}} \tag{2.42}$$

$$\mathit{A\!R} = \frac{b^2}{A} n_{\mathrm{mw}} \tag{2.43}$$

where c_L and c_D are the lift and drag coefficients of a wing's airfoil (i.e. 2D), $C_\mathrm{D,k,mw,p}$ and $C_\mathrm{D,k,mw,i}$ are a wing's parasitic and induced drag, $\mathit{Æ}$ is a wing's aspect ratio, and e is a wing's span efficiency.

Proof. By implication of identical main wings, define $c_\mathrm{L} := c_\mathrm{L,s}$, $b := b_\mathrm{s}$, $A = n_\mathrm{mw} A_\mathrm{s}$ and

$$\mathit{Æ} := \mathit{Æ}_\mathrm{s} = \frac{b_\mathrm{s}^2}{A_\mathrm{s}} = \frac{b^2}{A/n_\mathrm{mw}} = \frac{b^2}{A} n_\mathrm{mw}. \tag{2.44}$$

The total lift force of the main wings (2.6) is

$$\begin{aligned} F_\mathrm{L} &= \sum_{i=0}^{n_\mathrm{mw}-1} F_\mathrm{L,s} \\ \frac{1}{2}\rho v_\mathrm{a}^2 A C_\mathrm{L,k,mw} &= n_\mathrm{mw} \frac{1}{2}\rho v_\mathrm{a}^2 A_\mathrm{s} C_\mathrm{L,k,mw,s} \\ &= n_\mathrm{mw} \frac{1}{2}\rho v_\mathrm{a}^2 \frac{A}{n_\mathrm{mw}} C_\mathrm{L,k,mw,s} \\ &= \frac{1}{2}\rho v_\mathrm{a}^2 A C_\mathrm{L,k,mw,s} \\ \Rightarrow C_\mathrm{L,k,mw} &= C_\mathrm{L,k,mw,s}. \end{aligned} \tag{2.45}$$

Similarly, the equivalent can be found for the drag coefficients. ■

Remark 2.1: *If the gap between the biplane wings is small, Assumption 2.11 must be taken with care. This may particularly be the case for multiplanes with $n_\mathrm{mw} \geq 3$ (which is one reason why those are not considered throughout this dissertation, cf. Sect. 1.5). To account for such interferences, $C_\mathrm{D,k,o}$, e, or/and $\mathit{Æ}$ need to be corrected e.g. with correction factors, or effective values are to be used for the considered wing design in the first place (which may also account for effects of winglets or a box wing configuration etc.), cf. e.g. [114] or [115, Chap. VII.3] and references therein. That means, e might be below 1 even if the individual wings have an ideal (elliptical) lift distribution.*

As an alternative view, which is however not employed here, the multiplane wing as whole can be seen as one wing with aspect ratio defined by $\mathit{Æ} := b^2/A$ with wing span b and wing reference area A defined as the sum of the projected areas (see also e.g. [116]) and thus with e possibly above 1.

Finally, the airfoil lift and drag coefficients are related: Apart from stall, the drag coefficient of an airfoil (also called profile drag) increases approximately quadratically with the airfoil's lift coefficient, which justifies the following assumption:

Assumption 2.12: *For $c_\mathrm{L} \in [c_\mathrm{L,min\text{-}op}, c_\mathrm{L,max\text{-}op}]$ with minimum and maximum operationally allowed lift coefficients $c_\mathrm{L,min\text{-}op}$ and $c_\mathrm{L,max\text{-}op}$, which are both before stall including a safety margin, the airfoil's polar can be modeled by*

$$c_\mathrm{D} = c_\mathrm{D,0} + c_\mathrm{D,2} c_\mathrm{L}^2, \tag{2.46}$$

where $c_\mathrm{D,0}$ is the airfoil's drag coefficient at $c_\mathrm{L} = 0$ and $c_\mathrm{D,2}$ is the drag coefficient slope w.r.t. the lift coefficient squared. Changes of c_L may originate from both, changed angle of attack or changed control surface deflections.

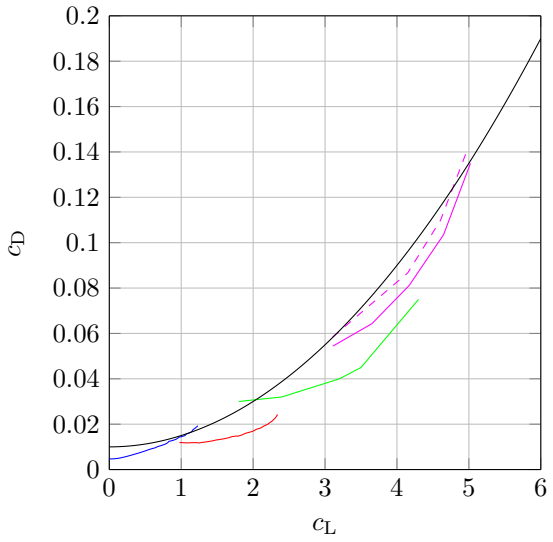

Figure 2.5: Example airfoil polars for varied angles of attack and approximation (2.46): single-element symmetrical airfoil NACA0010 in ——, predicted by XFoil with `Mach = 0.0`, `Re = 1.0e6`, `Ncrit = 9.0`, extracted from [117]; single-element high-lift low-Reynolds number airfoil S1223 in ——, predicted by XFoil with `Mach = 0.0`, `Re = 1.0e6`, `Ncrit = 9.0`, extracted from [117]; three-element airfoil NHLP 2-D L1T2 in ——, measurements extracted from [118, Fig. 5]; novel proposed four-element airfoil in monoplane configuration in —— and in biplane configuration in - - - -, investigated via CFDs in the prior work by the author of this dissertation in [110, Fig. 8] and shown in Fig. 2.6; and approximation (2.46) with $c_{D,0} = 0.010$ and $c_{D,2} = 0.005$ in ——. The airfoil polars are plotted only within reasonable bounds, i.e. with reasonable $c_{L,\text{min-op}}$ and $c_{L,\text{max-op}}$ (e.g. with safety margin from stall and only positive lift coefficients).

Fig. 2.5 plots example airfoil polars and the approximation (2.46) with a good fit for $c_{D,0}$ and $c_{D,2}$. Note that the model (2.46) with the values in Fig. 2.5 is (approximately) valid across many airfoils and that the choice of the airfoil lift coefficient (nominal value or range) dictates the selection of airfoil and design angle of incidence (or vice-versa). Moreover, Fig. 2.6 shows the CFD results of the four element airfoil whose polar is plotted in magenta in Fig. 2.5. This airfoil is proposed in the prior work [110] of the author of this dissertation. Note that both magenta curves in Fig. 2.5, solid for monoplane and dashed for biplane, are almost identical, which (at least in part) justifies Assumption 2.11.

2.2.2 Drag of Other Parts and Actuated Drag

For the drag of other parts and actuated drag, the following assumptions are imposed:

Assumption 2.13: *The drag contribution of other parts $C_{D,k,o}$ is a fixed value.*

Assumption 2.14: *The actuated drag is steerable freely within the range $C_{D,k,a} \in [C_{D,k,a,\min}, C_{D,k,a,\max}]$, where $C_{D,k,a,\min} = 0$ and $C_{D,k,a,\max}$ are the minimum and maximum steerable values.*

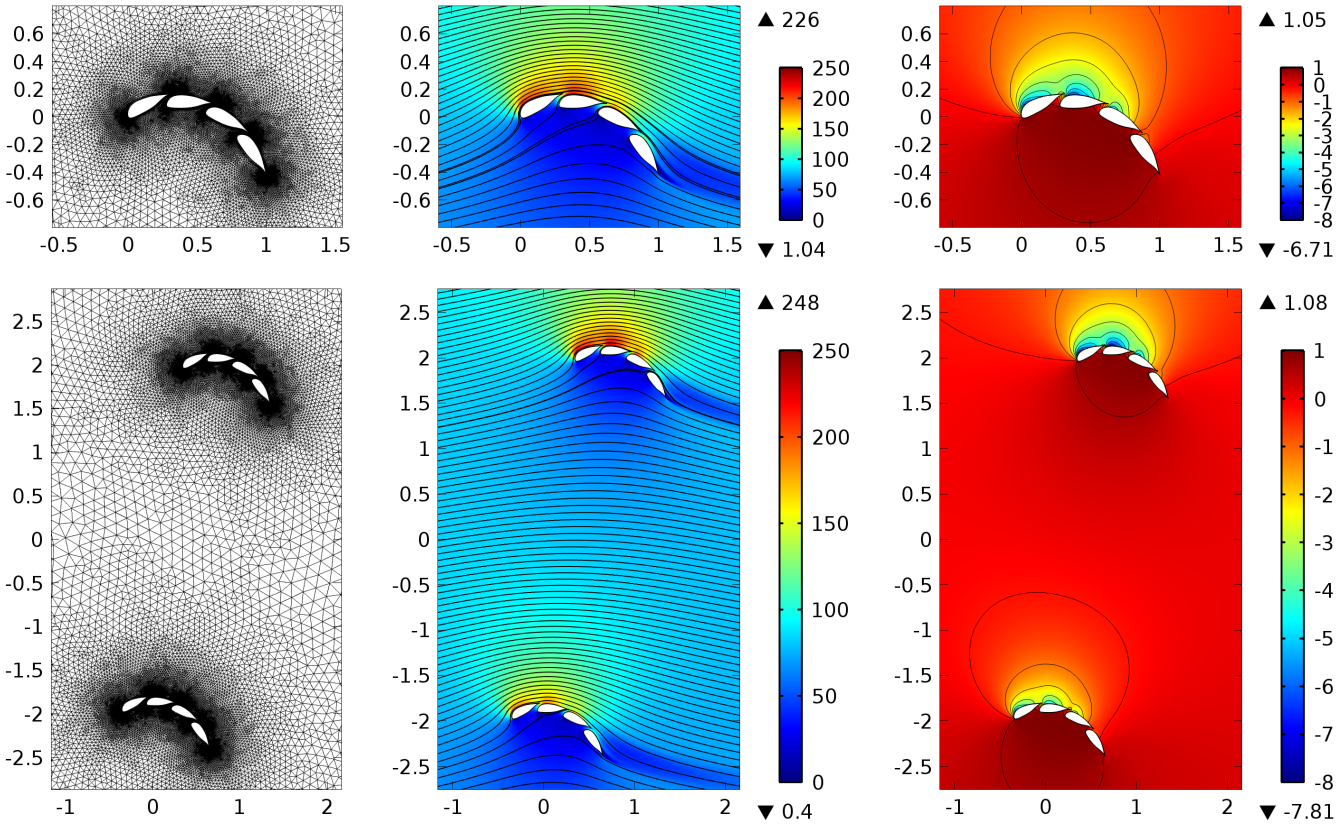

Figure 2.6: CFD results of a four element airfoil with identical elements in monoplane configuration (top) and biplane configuration (bottom), with (reference) chord 1 m and inflow speed 80 m/s: (unstructured) mesh (left), velocity field (middle), and pressure coefficient field (right). All space coordinates are in m and all speed values are in m/s. The CFD was set up in COMSOL Multiphysics 4.4 and solved by a Reynolds-averaged Navier-Stokes (RANS)-solver with the $k\omega$-turbulence model with wall functions for wall boundaries. The monoplane (biplane) airfoil is placed 10 m (15 m) behind the inlet of the virtual wind tunnel with 40 m (60 m) length and 20 m (30 m) height. Image published by the author already in [110, Fig. 7].

2.3 Tether Model

With Assumption 2.3 and 2.4, the tether is already assumed straight and stiff. It remains to quantify the tether drag contribution $C_{\mathrm{D,te}}$ as well as the tether's mechanical, electrical, and thermodynamic characteristics for the considered tether design motivated in Sect. 1.5.

A model of the tether drag lumped on the kite and based on the assumption of a straight and stiff tether is derived by Houska and Diehl [34, 35], refined by Argatov [39, 119], and used by others, cf. e.g. [49, 50] or [120, Chap. 3.4.1, pp. 43]. Such a tether aerodynamics model is also used here. An empiric model (i.e. black-box model) for the electrical characteristics of the tether is introduced by Kolar et al. [81] for a 100 kW kite and for six electrical cables in the tether. Instead of employing that model, a model based on first principles (i.e. white-box model) with obvious advantages (cf. Sect. 1.3) and for an arbitrary number of electrical cables in the tether

is derived. The dielectric strength of an electrical cable is derived analytically. The resulting equation is employed in a similar way in [121–123] to model the cables of another airborne wind energy concept based on blimps. Moreover, the tether's thermodynamics is not neglected. These models are (at least in part) similarly employed by the author of this dissertation in the prior publications [104, 106, 110–112].

2.3.1 Tether Aerodynamics

The following two additional assumptions are made for the tether aerodynamics:

Assumption 2.15: *The airflow speed along the tether is dominated by the contribution of the proper motion and therefore the airflow speed from the kite attachment down to the ground decreases linearly.*

Assumption 2.16: *The tether length is much greater than other tether dimensions.*

Assumption 2.15 is justified, because usually $v_\mathrm{a} \approx v_\mathrm{k} \gg v_\mathrm{w}$ for both, at the kite and for a major portion of the tether. In [119], Argatov shows that the error introduced by this assumption, and of Assumption 2.7, is only a few percent. Assumption 2.16 is obviously justified and, for the aerodynamics, only neglects 3D-flow effects at the tether ends.

With these assumptions, the tether drag contribution is determined:

Theorem 2.3 (Tether Drag Contribution): *If Assumptions 2.3, 2.4, 2.6, 2.7, 2.15, and 2.16 apply, then the tether drag contribution is*

$$C_{\mathrm{D,te}} = \frac{1}{4}\frac{d_\mathrm{te} L_\mathrm{te}}{A} c_{\mathrm{D,te}}, \tag{2.47}$$

where d_te is the tether's frontal width (which is the tether's diameter for the considered tether design), $c_{\mathrm{D,te}}$ is the drag coefficient of the tether's cross section shape (which is a circle for the here considered tether design), L_te is the tether length, and A is the kite's reference area.

Proof. With Assumption 2.7, it is implied that the tether's aerodynamic load is (almost) only drag. In view of (2.7), an infinitesimal segment of the tether generates the infinitesimal drag force at the tether length position l_te

$$\mathrm{d}F_{\mathrm{D,te}} = \frac{1}{2}\rho v_{\mathrm{a},l_\mathrm{te}}^2 c_{\mathrm{D,te}}\,\mathrm{d}A_\mathrm{te} \tag{2.48}$$

where $v_{\mathrm{a},l_\mathrm{te}}$ is the airflow speed at position l_te, and

$$\mathrm{d}A_\mathrm{te} = d_\mathrm{te}\,\mathrm{d}l_\mathrm{te} \tag{2.49}$$

is the infinitesimal tether frontal area with infinitesimal length $\mathrm{d}l_\mathrm{te}$ and tether diameter (or thickness) d_te, which is constant due to Assumption 2.4.

Assumptions 2.15 and 2.16 imply

$$v_{\mathrm{a},l_\mathrm{te}} = \frac{l_\mathrm{te}}{L_\mathrm{te}} v_\mathrm{a}. \tag{2.50}$$

By imposing Assumption 2.3, Fig. 2.7 visualizes the straight tether and the infinitesimal drag forces at the tether (2.48) distributed along the tether, which thus partly act on both, the ground station and the kite. Only the latter contributes to the drag

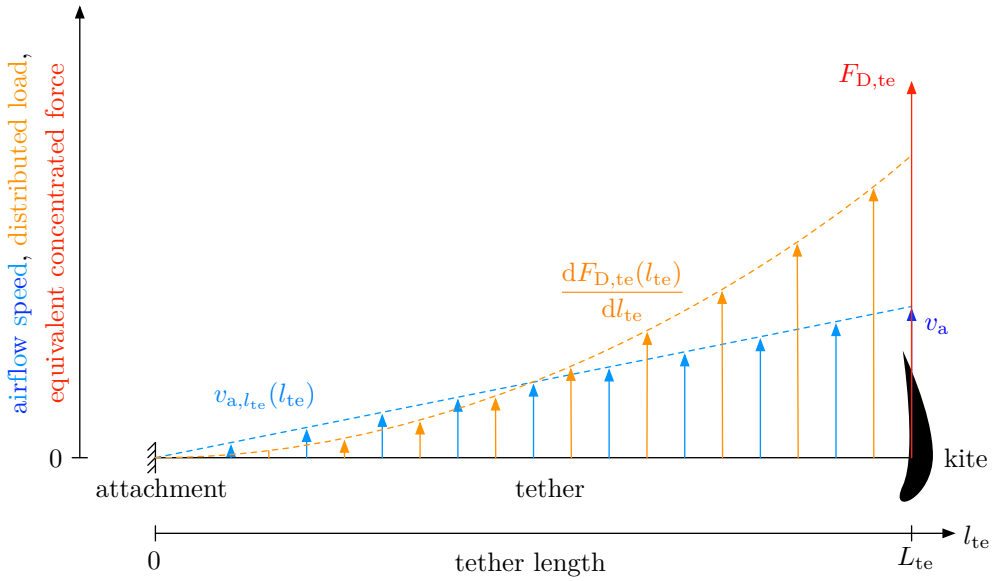

Figure 2.7: Airflow speed and tether drag load distribution along the tether as well as concentrated tether drag force at the kite.

of the kite. To derive that, first the moment of the distributed drag (2.48) w.r.t. the ground station is derived, which is

$$M_{\mathrm{D,te}} = \int_0^{L_{\mathrm{te}}} l_{\mathrm{te}} \times \mathrm{d}F_{\mathrm{D,te}}. \tag{2.51}$$

That same moment can also be expressed by

$$M_{\mathrm{D,te}} = L_{\mathrm{te}} \times F_{\mathrm{D,te}} \tag{2.52}$$

where $F_{\mathrm{D,te}}$ is the tether drag load expressed as concentrated effective force at the kite. In both previous equations, the vectors are orthogonal which is why the cross product of the vectors is the product of the scalar magnitudes, but "$\times$" is left for highlighting purposes.

By equating (2.51) with (2.52), solving for $F_{\mathrm{D,te}}$, inserting (2.48)–(2.50), and integrating over the complete tether length while imposing Assumption 2.6 for $c_{\mathrm{D,te}}$, the concentrated tether drag force acting at the kite is given by

$$\begin{aligned} F_{\mathrm{D,te}} &= \frac{\int_0^{L_{\mathrm{te}}} l_{\mathrm{te}} \mathrm{d}F_{\mathrm{D,te}}}{L_{\mathrm{te}}} \\ &= \frac{\int_0^{L_{\mathrm{te}}} l_{\mathrm{te}} \frac{1}{2}\rho v_{\mathrm{a},l_{\mathrm{te}}}^2 d_{\mathrm{te}} c_{\mathrm{D,te}} \, \mathrm{d}l_{\mathrm{te}}}{L_{\mathrm{te}}} \\ &= \frac{\int_0^{L_{\mathrm{te}}} l_{\mathrm{te}} \frac{1}{2}\rho \left(\frac{l_{\mathrm{te}}}{L_{\mathrm{te}}} v_{\mathrm{a}}\right)^2 d_{\mathrm{te}} c_{\mathrm{D,te}} \, \mathrm{d}l_{\mathrm{te}}}{L_{\mathrm{te}}} \end{aligned}$$

$$
\begin{aligned}
&= \frac{\frac{1}{2}\rho v_\mathrm{a}^2 d_\mathrm{te} c_\mathrm{D,te} \int_0^{L_\mathrm{te}} l_\mathrm{te}^3 \mathrm{d}l_\mathrm{te}}{L_\mathrm{te}^3} \\
&= \frac{\frac{1}{2}\rho v_\mathrm{a}^2 d_\mathrm{te} c_\mathrm{D,te} \left[\frac{1}{4} l_\mathrm{te}^4\right]_0^{L_\mathrm{te}}}{L_\mathrm{te}^3} \\
&= \frac{\frac{1}{2}\rho v_\mathrm{a}^2 d_\mathrm{te} c_\mathrm{D,te} \frac{1}{4} L_\mathrm{te}^4}{L_\mathrm{te}^3} \\
&= \frac{1}{8}\rho v_\mathrm{a}^2 d_\mathrm{te} L_\mathrm{te} c_\mathrm{D,te}. \qquad (2.53)
\end{aligned}
$$

In (2.7) with (2.11), the tether drag force at the kite is given w.r.t. the kite area via tether drag contribution $C_\mathrm{D,te}$, i.e.

$$F_\mathrm{D,te} = \frac{1}{2}\rho v_\mathrm{a}^2 A C_\mathrm{D,te}. \qquad (2.54)$$

Equating both tether drag force expressions, (2.53) with (2.54), and solving for $C_\mathrm{D,te}$ results in (2.47). ■

Remark 2.2: *The airflow speed $v_{\mathrm{a},l_\mathrm{te}}$ does change considerably along the tether and so does the Reynolds number N_Re. This might have an effect on the drag coefficient of the tether cross section shape $c_\mathrm{D,te}$ and thus on $C_\mathrm{D,te}$, i.e. Assumption 2.6 might be too rough for a certain system under investigation. Particularly interesting is the drag coefficient of a cylinder which is $c_\mathrm{D,te} \approx 1$ for $N_\mathrm{Re} > 10^2$, but drops significantly to $c_\mathrm{D,te} \approx 0.3$ at $N_\mathrm{Re} \approx 3 \cdot 10^5$ before it rises for higher N_Re back to $c_\mathrm{D,te} \approx 1$, cf. e.g. [115, Fig. III.12–14]. For a cylinder with a rough surface, that $c_\mathrm{D,te}$-drop is less strong but occurs at lower N_Re, cf. e.g. [115, Fig. III.12–14]. For a multi-megawatt system, N_Re for a major portion of the tether can be right at that $c_\mathrm{D,te}$-drop, which can be used to minimize $C_\mathrm{D,te}$ and thus increase the aerodynamic efficiency. Moreover, if the nominal N_Re is in the $c_\mathrm{D,te}$-drop, the system drag increases for higher airflow speeds which can be used for a simpler airflow speed-, power-, and force limitation control as it can passively limit the kite's speed. Both advantages are apparently used by Makani [105]. To include the Reynolds number dependency of $c_\mathrm{D,te}$ into the model, the integral in (2.53) could be solved analytically or approximately by a sum. Nevertheless, the explicit expression of the kite's airflow speed from (2.1) would likely be lost, as both sides of the equation would then contain v_a, likely without a possibility to solve analytically for v_a. To limit the complexity and to obtain a mostly explicit model, such Reynolds number-effects are not considered here. However, if v_a is known a-priori, with the approach of solving the integral in (2.53) analytically or numerically, a representative or effective $c_\mathrm{D,te}$ could be computed for use in (2.47).*

Remark 2.3: *If the tether cross-section shape is not radial-symmetric, e.g. if it has a fairing with an airfoil-like shape to reduce the drag, then the derived model either requires additional extensions or the additional assumption, that the angle of attack along the tether is constant. However, such a tether design is not considered as it is out of scope of this dissertation, cf. Sect. 1.5.*

2.3.2 Mechanical Strength

The mechanical load carrier absorbs the complete tether force (cf. Sect. 1.5). Its (ideal) design strength is given by

$$F_\mathrm{te,mech,design} = \sigma_\mathrm{te,mech} A_\mathrm{te,mech}, \qquad (2.55)$$

where $\sigma_{\text{te,mech}}$ is the mechanical load carrier's material yield strength, and $A_{\text{te,mech}}$ is its cross-section area. The expected maximum steady strength is the nominal tether force $F_{\text{te,n}}$, i.e.

$$F_{\text{te}} \leq F_{\text{te,n}}. \tag{2.56}$$

However, a real load carrier would usually be a rope constructed from strands of fibers, in which the fibers are loaded in part not only along the tether force vector. Therefore the rope has a lower breaking strength than individual fibers. In addition to that, the load carrier can have manufacturing variances or material defects, and gusts or other dynamic effects over the course of the kite's trajectory may exceed the nominal force. Hence, the design strength $F_{\text{te,mech,design}}$ must be (much) higher then the nominal tether force $F_{\text{te,n}}$:

Assumption 2.17: *The tether design strength and the nominal tether force are related by*

$$F_{\text{te,mech,design}} = S_{\text{te,mech}} F_{\text{te,n}} \tag{2.57}$$

with safety factor $S_{\text{te,mech}} > 1$.[10]

As the mechanical load carrier is round, its diameter $d_{\text{te,mech}}$ is determined by

$$A_{\text{te,mech}} = \pi \frac{d_{\text{te,mech}}^2}{4} \tag{2.58}$$

$$\Leftrightarrow d_{\text{te,mech}} = \sqrt{\frac{4A_{\text{te,mech}}}{\pi}}. \tag{2.59}$$

2.3.3 Electrical Resistance

As identical electrical cables and the same amount of positive $n_{\text{te,c,+}}$ and negative $n_{\text{te,c,-}}$ electrical cables are considered (cf. Sect. 1.5), the amounts are related to the total amount $n_{\text{te,c}}$ by

$$n_{\text{te,c,+}} = n_{\text{te,c,-}} = \frac{n_{\text{te,c}}}{2}. \tag{2.60}$$

The electrical resistance of an ideal litz-wire of a cable is

$$R_{\text{te,c,w,ideal}} = \frac{1}{\kappa_{\text{te,c,w}}} \frac{L_{\text{te}}}{A_{\text{te,c,w}}} \tag{2.61}$$

where $A_{\text{te,c,w}}$ is the litz wire's cross section area, and $\kappa_{\text{te,c,w}}$ is the specific conductivity of the litz wire material. However, a litz wire is usually constructed from a number of strands with which not the complete area $A_{\text{te,c,w}}$ might be filled with the conducting material (i.e. the fill factor is ≤ 1), the temperature varies (through which $\kappa_{\text{te,c,w}}$ varies), it can have manufacturing variances and material defects, and the length of the electrical cables is longer than the length of the tether because of the helical placement of a cable around the core (cf. Sect. 1.5). To account for these effects, a correction is introduced:

Assumption 2.18: *The electrical resistance of a litz wire* $R_{\text{te,c,w}}$ *is related to its ideal value* $R_{\text{te,c,w,ideal}}$ *via the correction factor* $f_{\text{te,c,w}} > 1$ *by*

$$R_{\text{te,c,w}} = f_{\text{te,c,w}} R_{\text{te,c,w,ideal}}. \tag{2.62}$$

[10] Assumption 2.17 and Eq. (2.57) could have also been interpreted as definition of $S_{\text{te,mech}}$ instead of as assumption. However, the value of $S_{\text{te,mech}}$ must be selected a-priori, i.e. an appropriate value must be estimated or assumed, respectively. This is highlighted with a new "assumption" for sake of clarity.

With $f_{\mathrm{te,c,w}}$, also the cabling required onboard and on the ground as well as the resistance of connectors can be accounted for.

As only round wires are considered, a litz wire's cross section area $A_{\mathrm{te,c,w}}$, diameter $d_{\mathrm{te,c,w}}$, and radius $r_{\mathrm{te,c,w}}$ are related by

$$A_{\mathrm{te,c,w}} = \pi \frac{d_{\mathrm{te,c,w}}^2}{4}, \tag{2.63}$$

$$\Leftrightarrow d_{\mathrm{te,c,w}} = \sqrt{\frac{4A_{\mathrm{te,c,w}}}{\pi}}, \tag{2.64}$$

$$r_{\mathrm{te,c,w}} = \frac{d_{\mathrm{te,c,w}}}{2}. \tag{2.65}$$

As $n_{\mathrm{te,c,+}}$ positive cables are connected in parallel and $n_{\mathrm{te,c,-}}$ negative cables are connected in parallel, and, in the circuit, all paralleled positive and all paralleled negative cables are connected in series, the total electrical resistance is with (2.60) given by

$$\begin{aligned} R_{\mathrm{te}} &= \frac{R_{\mathrm{te,c,w}}}{n_{\mathrm{te,c,+}}} + \frac{R_{\mathrm{te,c,w}}}{n_{\mathrm{te,c,-}}} \\ &= \frac{R_{\mathrm{te,c,w}}}{n_{\mathrm{te,c}}/2} + \frac{R_{\mathrm{te,c,w}}}{n_{\mathrm{te,c}}/2} \\ &= \frac{2R_{\mathrm{te,c,w}}}{n_{\mathrm{te,c}}/2} \\ &= 4\frac{R_{\mathrm{te,c,w}}}{n_{\mathrm{te,c}}}. \end{aligned} \tag{2.66}$$

2.3.4 Dielectric Strength

For sake of simplicity, first ideal electrical cables are modeled:

Assumption 2.19: *The electrical cables are "ideal", i.e. (i) there is a homogenous charge distribution in the litz wires, in the shields, and all surroundings through which there is one electric potential across a litz wire and another electric potential across all shields and all surroundings, (ii) the insulation material is homogenous and isotropic, (iii) there are no manufacturing variances, and (iv) an electrical cable is straight, stiff, and long (as extension of Assumptions 2.3, 2.4, and 2.16).*

With that, the dielectric strength and tether voltage are related as follows (cf. e.g. [124, Chap. 24] or [125]):

Theorem 2.4 (Dielectric Strength of a Shielded Ideal Electrical Cable): *If Assumption 2.19 applies, then a shielded electrical cable has the insulation voltage capability*

$$U_{\mathrm{te,ins}} = E_{\mathrm{te,ins}} r_{\mathrm{te,c,w}} \ln\left(\frac{r_{\mathrm{te,c,w}} + w_{\mathrm{te,c,ins}}}{r_{\mathrm{te,c,w}}}\right), \tag{2.67}$$

where $E_{\mathrm{te,ins}}$ is the insulation material's dielectric strength (i.e. maximum electric field strength), $r_{\mathrm{te,c,w}}$ is the wire radius, and $w_{\mathrm{te,c,ins}}$ is the insulation width.

Proof. Gauss's law (Maxwell's equations) in its macroscopic (integral) form is given by

$$\oiint_{\Omega} \boldsymbol{D} \bullet \mathrm{d}\boldsymbol{A}_{\boldsymbol{\Omega}} = \iiint_{\Omega} \rho \mathrm{d}V_{\Omega} \tag{2.68}$$

which means that the flux of the electric displacement field $\boldsymbol{D}$ leaving a volume with its closed surface Ω (where $\mathbf{d}\boldsymbol{A}_{\boldsymbol{\Omega}}$ is the infinitesimal surface area vector, which is area times unity normal vector) is equal to the charge enclosed by that volume (where ρ is the volume charge density in the infinitesimal volume $\mathrm{d}V_\Omega$). In (2.68), the symbol $\bullet$ denotes the dot-product and the volume integral of the volume charge density is the charge enclosed in Ω, i.e.

$$Q_\Omega = \iiint_\Omega \rho \mathrm{d}V_\Omega. \tag{2.69}$$

These equations are valid for any volume Ω.

For a shielded electrical cable, Ω is chosen as a concentric cylinder around the cable's core with the length of the cable L_c and with a radius between the litz wire radius and insulation radius

$$r \in [r_{\mathrm{te,c,w}}, r_{\mathrm{te,c,w}} + w_{\mathrm{te,c,ins}}], \tag{2.70}$$

as visualized in Fig. 2.8.

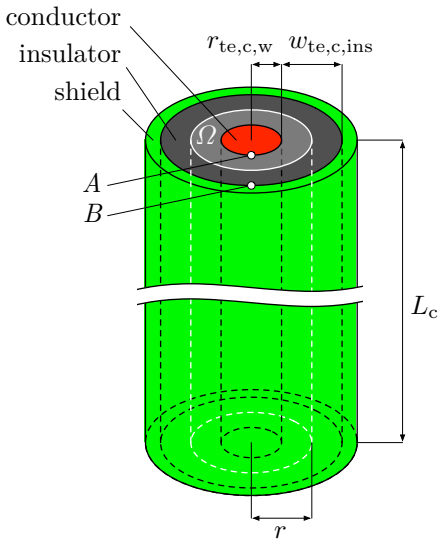

Figure 2.8: Application of Gauss's law to a shielded electrical cable.

Assumption 2.19 implies, that the electric displacement field and the electric field are pure radial inside the insulator,

$$\boldsymbol{D} = D\boldsymbol{e}_\mathrm{r} = \epsilon E \boldsymbol{e}_\mathrm{r}, \tag{2.71}$$

where D is the electric displacement field magnitude, $\epsilon = \varepsilon_0 \epsilon_\mathrm{r}$ is the permittivity with vacuum permittivity ε_0 and relative permittivity of the insulation material ϵ_r, E is the electric field magnitude, and $\boldsymbol{e}_\mathrm{r}$ is the radial unit vector.

With (2.71), the surface integral of the left hand side of (2.68) becomes

$$\begin{aligned}
\oiint_{\Omega} \boldsymbol{D} \bullet \mathrm{d}\boldsymbol{A}_{\boldsymbol{\Omega}} &= \oiint_{\Omega} \epsilon E \boldsymbol{e}_{\mathrm{r}} \bullet \mathrm{d}\boldsymbol{A}_{\boldsymbol{\Omega}} \\
&= \oiint_{\Omega} \epsilon E \mathrm{d}A_{\Omega} \\
&= \epsilon E \underbrace{\int_0^{L_{\mathrm{c}}} \mathrm{d}l \int_0^{2\pi} r \mathrm{d}\phi}_{\oiint_{\Omega} \mathrm{d}A_{\Omega}} \\
&= 2\pi r L_{\mathrm{c}} \epsilon E. \qquad (2.72)
\end{aligned}$$

Substituting (2.69) and (2.72) into (2.68) and solving for E gives

$$\begin{aligned}
2\pi r L_{\mathrm{c}} \epsilon E &= Q_{\Omega} \\
\Leftrightarrow E &= \frac{Q_{\Omega}}{2\pi r L_{\mathrm{c}} \epsilon}. \qquad (2.73)
\end{aligned}$$

The electric voltage between any two points in space A and B is defined by

$$U = \int_A^B \boldsymbol{E} \bullet \mathrm{d}\boldsymbol{l} \qquad (2.74)$$

with infinitesimal length $\mathbf{d}\boldsymbol{l}$ (length times unity tangential vector). Choosing point A on the litz wire's surface and point B radial to A on the insulator's outer surface as in Fig. 2.8, substituting (2.73) into (2.74), and solving the integral gives

$$\begin{aligned}
U &= \int_A^B E \mathrm{d}r \\
&= \int_{r_{\mathrm{te,c,w}}}^{r_{\mathrm{te,c,w}}+w_{\mathrm{te,c,ins}}} \frac{Q_{\Omega}}{2\pi r L_{\mathrm{c}} \epsilon} \mathrm{d}r \\
&= \frac{Q_{\Omega}}{2\pi L_{\mathrm{c}} \epsilon} \int_{r_{\mathrm{te,c,w}}}^{r_{\mathrm{te,c,w}}+w_{\mathrm{te,c,ins}}} \frac{1}{r} \mathrm{d}r \\
&= \frac{Q_{\Omega}}{2\pi L_{\mathrm{c}} \epsilon} [\ln(r)]_{r_{\mathrm{te,c,w}}}^{r_{\mathrm{te,c,w}}+w_{\mathrm{te,c,ins}}} \\
&= \frac{Q_{\Omega}}{2\pi L_{\mathrm{c}} \epsilon} [\ln(r_{\mathrm{te,c,w}} + w_{\mathrm{te,c,ins}}) - \ln(r_{\mathrm{te,c,w}})] \\
&= \frac{Q_{\Omega}}{2\pi L_{\mathrm{c}} \epsilon} \ln\left(\frac{r_{\mathrm{te,c,w}} + w_{\mathrm{te,c,ins}}}{r_{\mathrm{te,c,w}}}\right). \qquad (2.75)
\end{aligned}$$

Solving (2.75) for the charge gives

$$\Leftrightarrow Q_{\Omega} = \frac{2\pi L_{\mathrm{c}} \epsilon U}{\ln\left(\frac{r_{\mathrm{te,c,w}}+w_{\mathrm{te,c,ins}}}{r_{\mathrm{te,c,w}}}\right)}. \qquad (2.76)$$

Substituting that into (2.73) gives

$$E = \frac{\frac{2\pi L_\mathrm{c}\epsilon U}{\ln\left(\frac{r_\mathrm{te,c,w}+w_\mathrm{te,c,ins}}{r_\mathrm{te,c,w}}\right)}}{2\pi r L_\mathrm{c}\epsilon} = \frac{U}{r\ln\left(\frac{r_\mathrm{te,c,w}+w_\mathrm{te,c,ins}}{r_\mathrm{te,c,w}}\right)}. \tag{2.77}$$

With (2.70), the electric field (2.77) has obviously its maximum in the insulator at $r = r_\mathrm{te,c,w}$, which is the electric field to be withstood by the insulation material $E = E_\mathrm{te,ins}$ at the insulation voltage $U = U_\mathrm{te,ins}$. ■

Eq. (2.67) is only valid for an ideal cable. Moreover, the insulation voltage $U_\mathrm{te,ins}$ is not the same as the nominal tether voltage $U_\mathrm{te,n}$, that is the nominal voltage between the positive and negative cables, because the tether voltage is considered to be "centered around ground" (cf. Sect. 1.5), but might experience temporary variations. Therefore a correction is introduced, with which Assumption 2.19 is relaxed:

Assumption 2.20: *The insulation voltage $U_\mathrm{te,ins}$ and the nominal tether voltage $U_\mathrm{te,n}$ are related by*

$$U_\mathrm{te,ins} = S_\mathrm{te,ins} f_\mathrm{te,ins} \frac{U_\mathrm{te,n}}{2}, \tag{2.78}$$

where the division by two accounts for the "centering" of the transmission voltage "around ground", $f_\mathrm{te,ins} > 1$ is a correction factor which accounts e.g. for voltage spikes induced e.g. by the power electronics and parasitic inductances as well as for the $\sqrt{2}$-times voltage difference between peak and effective voltage in case of an AC transmission, and $S_\mathrm{te,ins} > 1$ is a safety factor which accounts e.g. for manufacturing variances, material defects, or geometry and material property changes due to increased temperature or tether loading.

2.3.5 Shield and Jackets

Assumption 2.21: *The withs of the shield $w_\mathrm{te,c,sh}$, electrical cable jacket $w_\mathrm{te,c,j}$, and tether jacket $w_\mathrm{te,j}$ are small values and are based e.g. on empiric data or experience.*

2.3.6 Total Diameter

With the introduced diameters and widths, and in view of Fig. 1.8, the tether diameter is given by

$$d_\mathrm{te} = d_\mathrm{te,mech} + 2d_\mathrm{te,c} + 2w_\mathrm{te,j} \tag{2.79}$$

with electrical cable diameter

$$d_\mathrm{te,c} = d_\mathrm{te,c,w} + 2(w_\mathrm{te,c,ins} + w_\mathrm{te,c,sh} + w_\mathrm{te,c,j}). \tag{2.80}$$

2.3.7 Total Mass

The mass of the tether component i (core, litz wires, insulators, etc.) is determined by

$$m_i = \rho_i V_i, \tag{2.81}$$

where ρ_i is the material density and V_i is the volume, for which the following assumption is made:

Assumption 2.22: *The volume of a tether component is determined by*

$$V_i = A_i L_{\mathrm{te}} f_{\mathrm{V},i}, \tag{2.82}$$

where A_i is the cross section area and $f_{\mathrm{V},i} \geq 1$ is a volume correction factor which accounts e.g. for the helical placement of the electrical cables around the core and manufacturing variances.

As each component generally is an annulus in the 2D cross section (possibly with zero inner radius, i.e. a circle), the cross section area of any component is

$$A_i = \pi \left(r_{\mathrm{out},i}^2 - r_{\mathrm{in},i}^2 \right) \tag{2.83}$$

with outer radius $r_{\mathrm{out},i}$ and inner radius $r_{\mathrm{in},i}$, straightforwardly given in view of Fig. 1.8. The total tether mass is then given by

$$m_{\mathrm{te}} = \sum_i m_i. \tag{2.84}$$

2.3.8 No Overlapping: Feasibility of Electrical Cables Number

All electrical cables are placed in one layer around the core in the considered design, cf. Fig. 1.8. The feasibility of a certain number of electrical cables $n_{\mathrm{te,c}}$, i.e. without overlapping, can be derived as follows: The angle between two electrical cables is

$$\epsilon = \frac{2\pi}{n_{\mathrm{te,c}}}. \tag{2.85}$$

In view of Fig. 2.9, one finds, by employing the law of sines,

$$\frac{\delta}{\sin(\epsilon)} = \frac{d_{\mathrm{te,mech}}/2 + d_{\mathrm{te,c}}/2}{\sin[(\pi - \epsilon)/2]}, \tag{2.86}$$

where δ is the distance between the center of two neighboring electrical cables. For a feasible number of electrical cables, i.e. without overlapping,

$$\delta \geq d_{\mathrm{te,c}} \tag{2.87}$$

must hold true.

2.3.9 Thermodynamic Limits

The heat input into the tether is modeled with the following assumption:

Assumption 2.23: *Power losses in the tether are dominated by conduction losses with negligible skin effect.*

Hence, the electrical losses in the tether are given by

$$P_{\text{te-loss}} = R_{\mathrm{te}} I_{\mathrm{te}}^2, \tag{2.88}$$

which is converted into heat, and which in turn increases the temperature of the litz wires, insulations, shields, jackets, and core. This can reduce the material properties, which is covered in part by the safety and correction factors $S_{\mathrm{te,mech}}$, $f_{\mathrm{te,c,w}}$, $S_{\mathrm{te,ins}}$, $f_{\mathrm{te,ins}}$. However, there is some

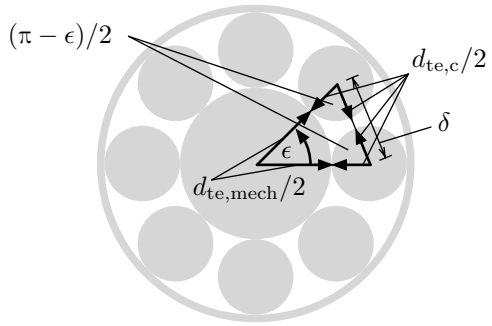

Figure 2.9: Angle and distance between the centers of two neighboring electrical cables. Image published by the author already in [106, Fig. 16].

upper limit of the specific tether power loss for which these safety and correction factors are valid and before the temperatures are so high that parts of the tether would break or even melt, i.e.

$$\frac{P_{\text{te-loss}}}{L_{\text{te}}} =: p_{\text{te-loss,L}} \leq p_{\text{te-loss,L,max}} \tag{2.89}$$

with specific power loss $p_{\text{te-loss,L}}$ w.r.t. length and its feasible maximum $p_{\text{te-loss,L,max}}$, or

$$\frac{P_{\text{te-loss}}}{\pi d_{\text{te}} L_{\text{te}}} =: p_{\text{te-loss,A}} \leq p_{\text{te-loss,A,max}} \tag{2.90}$$

with specific power loss $p_{\text{te-loss,A}}$ w.r.t. surface area and its feasible maximum $p_{\text{te-loss,A,max}}$.

The heat flux is generally nonlinear and not trivial: The heat flux from the litz wires to the tether surface is mostly conduction and depends on the geometry and materials. The heat flux from the tether surface into the ambient consists of free convection (e.g. during hovering with no tether movement and no wind), forced convection (only during crosswind flight with strong tether movement or wind), and radiation, but that latter can be expected to be negligible. A critical case is hovering at no wind, because then there is almost only free convection.—To keep the modeling complexity low, no detailed thermodynamics model is employed here. Instead, the following assumption is imposed:

Assumption 2.24: *The thermodynamic limit of the tether is given by (2.89) or (2.90) with some value of $p_{\text{te-loss,L,max}}$ or $p_{\text{te-loss,A,max}}$, respectively, whose values may depend on the flight mode.*

2.4 Rotor Model

To further specify $C_{\text{D,rot}}$ and losses involved in the power extraction (2.17)–(2.19) by the onboard rotors, a rotor is modeled with the following assumption:

Assumption 2.25: *A rotor can be approximated by an actuator disk.*[11]

This rotor model is commonly used also for conventional wind turbines (Betz' model). Such a model extension for drag power kites is used by the prior work of the author of this dissertation [104] and, for crosswind flight, is sketched by Vander Lind [16]. A rotor model based on Assumption 2.25 is in the following referred to as "ideal rotor". In a later step, this assumption is relaxed for a "real rotor".

[11] The actuator disk model itself is based on a number of assumptions, cf. e.g. [126, Chap. 14.5, pp. 632], therefore Assumption 2.25 is a collection of assumptions.

2.4.1 Ideal Rotors During Crosswind Flight

During crosswind flight the airflow speed at a single rotor is $v_{\mathrm{a,s}} > 0$ for which the common formulation of the thrust and power within the actuator disk model is

$$\text{for } v_{\mathrm{a,s}} > 0: \qquad F_{\mathrm{rot,s}} = 2\rho A_{\mathrm{rot,s}} v_{\mathrm{a,s}}^2 a_{\mathrm{s}}(1 - a_{\mathrm{s}}) \tag{2.91}$$

$$P_{\mathrm{rot,s,ideal}} = 2\rho A_{\mathrm{rot,s}} v_{\mathrm{a,s}}^3 a_{\mathrm{s}}(1 - a_{\mathrm{s}})^2 \tag{2.92}$$

with

$$a_{\mathrm{s}} = \frac{v_{\mathrm{a,s}} - v_{\mathrm{a,s,disk}}}{v_{\mathrm{a,s}}} \tag{2.93}$$

where $A_{\mathrm{rot,s}}$, $v_{\mathrm{a,s}}$, and a_{s} are the disk area, free stream speed, and axial induction factor of the rotor, and $v_{\mathrm{a,s,disk}}$ is the airflow speed at the rotor disk, cf. Fig. 2.10 and e.g. [127, Chap. 3].

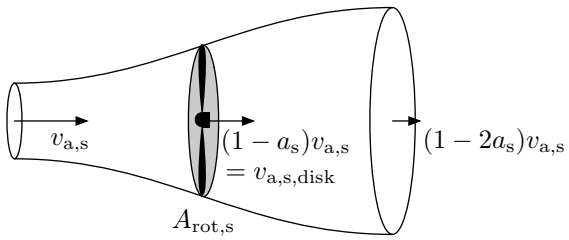

Figure 2.10: Actuator disk rotor model in stream tube.

The kite's rotors are considered to be identical apart from the rotation direction (cf. Sect. 1.5) and, for the steady kite model, the following assumption is made for sake of simplicity:

Assumption 2.26: *All rotors experience the same airflow speed*

$$v_{\mathrm{a,s}} = v_{\mathrm{a}}, \tag{2.94}$$

and all operating rotors are steered with the same induction factor

$$a_{\mathrm{s}} = a. \tag{2.95}$$

This assumption is justified by the close distances of the rotors to the kite's center of rotation (which is the kite's center of mass) and by the steering of the kite mainly by control surfaces instead of by rotors.

With n_{rot} identical rotors, the total rotor area is

$$A_{\mathrm{rot}} = A_{\mathrm{rot,s}} n_{\mathrm{rot}}. \tag{2.96}$$

By defining the ratio of the total rotor area A_{rot} to the kite's main wings total area (the kite's reference area) A by

$$r_{\mathrm{rot}} = \frac{A_{\mathrm{rot}}}{A}, \tag{2.97}$$

the total thrust and total power of all operating rotors $n_{\mathrm{rot,op}}$ are, with (2.91)–(2.97), given by

$$\begin{aligned}
F_{\mathrm{rot}} &= F_{\mathrm{rot,s}} n_{\mathrm{rot,op}} \\
&= 2\rho A_{\mathrm{rot,s}} v_{\mathrm{a,s}}^2 a_{\mathrm{s}} (1 - a_{\mathrm{s}}) n_{\mathrm{rot,op}} \\
&= 2\rho A_{\mathrm{rot,s}} v_{\mathrm{a}}^2 a (1 - a) n_{\mathrm{rot,op}} \\
&= 2\rho \frac{A_{\mathrm{rot}}}{n_{\mathrm{rot}}} v_{\mathrm{a}}^2 a (1 - a) n_{\mathrm{rot,op}} \\
&= 2\rho \frac{r_{\mathrm{rot}} A}{n_{\mathrm{rot}}} v_{\mathrm{a}}^2 a (1 - a) n_{\mathrm{rot,op}} \\
&= 2\rho \frac{n_{\mathrm{rot,op}}}{n_{\mathrm{rot}}} r_{\mathrm{rot}} A v_{\mathrm{a}}^2 a (1 - a) \qquad (2.98) \\
P_{\mathrm{rot,ideal}} &= 2\rho \frac{n_{\mathrm{rot,op}}}{n_{\mathrm{rot}}} r_{\mathrm{rot}} A v_{\mathrm{a}}^3 a (1 - a)^2. \qquad (2.99)
\end{aligned}$$

The rotor drag coefficient $C_{\mathrm{D,rot}}$ as function of the induction factor a is then given by equating (2.16) with (2.98)

$$\begin{aligned}
F_{\mathrm{rot}} = \frac{1}{2} \rho v_{\mathrm{a}}^2 A C_{\mathrm{D,rot}} &= 2\rho \frac{n_{\mathrm{rot,op}}}{n_{\mathrm{rot}}} r_{\mathrm{rot}} A v_{\mathrm{a}}^2 a (1 - a) = F_{\mathrm{rot}} \\
\Leftrightarrow C_{\mathrm{D,rot}} &= 4 \frac{n_{\mathrm{rot,op}}}{n_{\mathrm{rot}}} r_{\mathrm{rot}} a (1 - a), \qquad (2.100)
\end{aligned}$$

or, vice versa, a as function of $C_{\mathrm{D,rot}}$ is given by solving (2.100) for a, which becomes

$$\begin{aligned}
\Leftrightarrow \frac{C_{\mathrm{D,rot}}}{4 \frac{n_{\mathrm{rot,op}}}{n_{\mathrm{rot}}} r_{\mathrm{rot}}} &= a - a^2 \\
\Leftrightarrow 0 &= a^2 - a + \frac{C_{\mathrm{D,rot}}}{4 \frac{n_{\mathrm{rot,op}}}{n_{\mathrm{rot}}} r_{\mathrm{rot}}} \\
\Leftrightarrow a &= \frac{1}{2} \pm \sqrt{\frac{1}{4} - \frac{C_{\mathrm{D,rot}}}{4 \frac{n_{\mathrm{rot,op}}}{n_{\mathrm{rot}}} r_{\mathrm{rot}}}} \\
&= \frac{1}{2} \pm \sqrt{\frac{\frac{n_{\mathrm{rot,op}}}{n_{\mathrm{rot}}} r_{\mathrm{rot}} - C_{\mathrm{D,rot}}}{4 \frac{n_{\mathrm{rot,op}}}{n_{\mathrm{rot}}} r_{\mathrm{rot}}}} \\
\Rightarrow a &= \frac{1}{2} - \sqrt{\frac{\frac{n_{\mathrm{rot,op}}}{n_{\mathrm{rot}}} r_{\mathrm{rot}} - C_{\mathrm{D,rot}}}{4 \frac{n_{\mathrm{rot,op}}}{n_{\mathrm{rot}}} r_{\mathrm{rot}}}}. \qquad (2.101)
\end{aligned}$$

Only the negative solution is physically meaningful, otherwise the solution would always be $a \geq 1/2$ and $a = 1$ for $C_{\mathrm{D,rot}} = 0$ instead of $a = 0$ for $C_{\mathrm{D,rot}} = 0$.

With (2.101) and for a real a (obviously, an a with non-zero imaginary part would not be physically meaningful), the upper limits of a and $C_{\mathrm{D,rot}}$ are given by

$$a \leq \frac{1}{2} \qquad (2.102)$$

$$C_{\mathrm{D,rot}} \leq \frac{n_{\mathrm{rot,op}}}{n_{\mathrm{rot}}} r_{\mathrm{rot}}. \qquad (2.103)$$

However, for a given v_a, the maximum power (2.99) occurs at

$$\begin{aligned}
0 &= \frac{\mathrm{d}P_\mathrm{rot,ideal}(a=a^*)}{\mathrm{d}a^*} \\
&= \frac{\mathrm{d}}{\mathrm{d}a^*} 2\rho \frac{n_\mathrm{rot,op}}{n_\mathrm{rot}} r_\mathrm{rot} A v_\mathrm{a}^3 a^*(1-a^*)^2 \\
&= \frac{\mathrm{d}}{\mathrm{d}a^*} a^*(1-a^*)^2 \\
&= 3a^{*2} - 4a^* + 1 \\
&= a^{*2} - \frac{4}{3}a^* + \frac{1}{3} \\
\Leftrightarrow a^* &= \frac{2}{3} \pm \sqrt{\frac{4}{9} - \frac{1}{3}} \\
&= \frac{2}{3} \pm \frac{1}{3} \\
\Rightarrow a^* &= \frac{2}{3} - \frac{1}{3} = \frac{1}{3}.
\end{aligned} \tag{2.104}$$

Again, only the negative solution is valid to comply with (2.102) (which is also a local maximum, whereas the positive solution is a local minimum), cf. also e.g. [127, Chap. 3]. Hence, $a > a^*$ leads only to higher drag, that is indeed part of the rotor drag coefficient $C_\mathrm{D,rot}$, but with which only aerodynamic losses instead of useful power is generated. Therefore, it is meaningful to limit the induction factor a to a^*, i.e. (2.102) is replaced by

$$a \leq a^* = \frac{1}{3} =: a_\mathrm{max}, \tag{2.105}$$

and, by substituting (2.105) into (2.100), Eq. (2.103) is replaced by

$$\begin{aligned}
C_\mathrm{D,rot} &\leq 4 \frac{n_\mathrm{rot,op}}{n_\mathrm{rot}} r_\mathrm{rot} a^*(1-a^*) \\
&\leq 4 \frac{n_\mathrm{rot,op}}{n_\mathrm{rot}} r_\mathrm{rot} \frac{1}{3}\left(1 - \frac{1}{3}\right) \\
&\leq 4 \frac{n_\mathrm{rot,op}}{n_\mathrm{rot}} r_\mathrm{rot} \frac{1}{3}\frac{2}{3} \\
&\leq \frac{8}{9} \frac{n_\mathrm{rot,op}}{n_\mathrm{rot}} r_\mathrm{rot} =: C_\mathrm{D,rot,max}.
\end{aligned} \tag{2.106}$$

Remark 2.4: *The power must be limited at high wind speeds, e.g. by increasing the drag, for which $a > a^*$ (including even stalling the rotors, which is not resolved by the here presented model) could be useful. However, it is left to future research on the power limitation control of drag power kites, if such an approach is a viable strategy. Throughout this dissertation, (2.105) and (2.106) are considered as maximum rotor steerings.*

With (2.17) and (2.99), the *actuator disk* efficiency for generated power is[12] (cf. [16])

$$\text{for } P_\mathrm{a} > 0\text{: } \eta_\mathrm{a,+} = \frac{P_\mathrm{rot,ideal}}{P_\mathrm{a}} \tag{2.107}$$

[12] Note that, if $P_\mathrm{a} > 0$, then also $C_\mathrm{D,rot}, a, P_\mathrm{rot,ideal} > 0$ and, vice versa, if $P_\mathrm{a} < 0$, then also $C_\mathrm{D,rot}, a, P_\mathrm{rot,ideal} < 0$.

$$
\begin{aligned}
&= \frac{P_{\mathrm{rot,ideal}}}{v_{\mathrm{a}} F_{\mathrm{rot}}} \\
&= \frac{2\rho \frac{n_{\mathrm{rot,op}}}{n_{\mathrm{rot}}} r_{\mathrm{rot}} A v_{\mathrm{a}}^3 a (1-a)^2}{2\rho \frac{n_{\mathrm{rot,op}}}{n_{\mathrm{rot}}} r_{\mathrm{rot}} A v_{\mathrm{a}}^3 a (1-a)} \\
&= 1 - a, \qquad (2.108)
\end{aligned}
$$

and the inverse for consumed power, i.e.

$$
\text{for } P_{\mathrm{a}} < 0\text{: } \eta_{\mathrm{a},-} = \frac{P_{\mathrm{a}}}{P_{\mathrm{rot,ideal}}} = \frac{1}{1-a}, \qquad (2.109)
$$

which can be combined as

$$
\eta_{\mathrm{a}} := \begin{cases} \eta_{\mathrm{a},+} & \text{for } P_{\mathrm{a}} > 0 \text{ (generative)} \\ \eta_{\mathrm{a},-} & \text{for } P_{\mathrm{a}} < 0 \text{ (consumptive).} \end{cases} \qquad (2.110)
$$

Note that, to achieve a given $C_{\mathrm{D,rot}}$, a high r_{rot} enables a low a, cf. (2.100), and thus a high η_{a}, possibly far higher than the Betz power factor of tower based wind turbines of $16/27 \approx 0.59$, cf. e.g. [127, Chap. 3]. In fact, with (2.105) in (2.108), the actuator disk efficiency is always $\eta_{\mathrm{a},+} \geq 2/3 \approx 0.67$.

Remark 2.5: *With the efficiency definition in (2.107), conventional wind turbines have the same high efficiency of at least* $2/3 \approx 0.67$ *if* $a \leq 1/3$*, but with* $v_{\mathrm{a}} = v_{\mathrm{w}}$*. However, the efficiency for conventional wind turbines is usually not defined by the ratio of harvested (usable) power and from the wind field extracted power, but by the ratio of the harvested (usable) power and the in the wind field contained power in the size of the rotor disk area, which is limited by the Betz efficiency* $16/27 \approx 0.59$*, cf. e.g. [127, Chap. 3]. Such an efficiency definition is not meaningful for rotors of drag power kites, because it has no practical relevance as* $v_{\mathrm{a}} \neq v_{\mathrm{w}}$*.*

Without rotor failure, the number of operating rotors is identical to the number rotors, $n_{\mathrm{rot,op}} = n_{\mathrm{rot}}$, with which all terms $n_{\mathrm{rot,op}}/n_{\mathrm{rot}}$ vanish in the above derived equations. However, a high reliability and thus a high fault tolerance is required for this technology [106]. Crosswind flight *must* still work normally if one rotor fails, i.e. with $n_{\mathrm{rot,op}} = n_{\mathrm{rot}} - 1$. As the kite is considered to have enough and also redundant control surfaces (cf. Sect. 1.5), a stable flight is possible also during rotor failures. Nevertheless, if the wind is low, the rotors are used as propellers to maintain crosswind flight (at least for a short time until a landing is scheduled), for which during a rotor failure (i) a reduced maximum power is available, (ii) an increased induction factor is required to maintain the demanded rotor drag coefficient, and (iii) because of that the actuator disk efficiency is reduced. The implications of that are discussed below, in Sect. 2.7.14.

2.4.2 Ideal Rotors During Hovering

During hovering, the power demand can be significant, up to the magnitude of the nominal power. Therefore, hovering has to be considered within the system design.

For hovering, $v_{\mathrm{a,s}} = 0$ with which a_{s} is undefined, cf. (2.93). However, another formulation of the actuator disk model compared to (2.91)–(2.93) for this special case of hovering results in

$$
P_{\mathrm{a,hov,s}} = \sqrt{\frac{F_{\mathrm{rot,hov,s}}^3}{2\rho A_{\mathrm{rot,s}}}}, \qquad (2.111)
$$

where $P_{\mathrm{a,hov,s}}$ is the aerodynamic hovering power of a single rotor to generate the hovering thrust $F_{\mathrm{rot,hov,s}}$ (cf. e.g. [126, Chap. 14]).

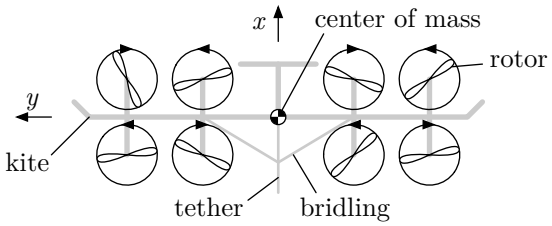

Figure 2.11: Example of a meaningful rotor placement with eight rotors (similar to Makani's design, cf. e.g. [27, 98]). Image published by the author already in [106, Fig. 7].

During hovering, the kite is like a multicopter. Usually, the rotors are placed somewhat symmetrical, e.g. in a circle or in two rows as in Fig. 2.11. One or more rotors are placed in each horizontal axis direction (in Fig. 2.11: $+x$, $-x$, $+y$, $-y$) some distance apart from the center of mass. The placement and rotation direction are usually chosen such that all rotors are equally loaded and that an arbitrary 3D moment can be generated by differential angular speeds of the rotors. A difference to usual multicopters is that the kite is tethered. The kite should always pull slightly on the tether via a small pitch angle such that the tether is always under tension, does not drag on the ground, and tether angle sensors as in [128] are usable. If a "Y"-like bridling as in Fig. 2.11 is chosen to connect the tether to the kite, the movement about the vertical axis is constrained, or more precisely there is a restoring tether bridling moment if the yaw angle does not coincide with the azimuth angle [129], with which the rotor moment about the vertical axis and thus the rotor rotation directions might be irrelevant and all rotors can even rotate in the same direction.

With the discussion of the previous paragraph, the required thrust of a single rotor is determined with the following assumption:

Assumption 2.27: *For $n_{\mathrm{rot,op}}$ operating rotors, each rotor must generate the thrust*

$$F_{\mathrm{rot,hov,s}} = -S_{\mathrm{hov}} \frac{m_{\mathrm{a}} g}{n_{\mathrm{rot,op}}} \tag{2.112}$$

where $S_{\mathrm{hov}} > 1$ is a safety and correction factor which accounts e.g. for (i) thrust imbalances due to unequal rotor placements or manufacturing variances, (ii) a pitch angle during hovering not equal to zero with which the tether is tensioned but which requires a higher thrust due to both, the pitched thrust vector and the downward component of the tether force for an elevation angle $\vartheta \neq 0$, (iii) an accelerating thrust and increased airflow speed (i.e. higher power demand) for the transition to crosswind flight (whereby this particular power excess is required only for a short time in the magnitude of seconds, and thus could also be achieved by a short-time overloading of the powertrain), (iv) to balance aerodynamic forces and moments generated by the kite's surface (including those within the stream tube of rotors), and (v) for control actuations to stabilize the hovering during all reasonable wind conditions. The negative sign is for consistency with the force and power flow direction (cf. also Fig. 2.2; during hovering, power is demanded from the grid).

With (2.96), (2.97), (2.111), and (2.112), the total hovering power is given by

$$\begin{aligned} P_{\mathrm{a,hov}} &= n_{\mathrm{rot,op}} P_{\mathrm{a,hov,s}} \\ &= n_{\mathrm{rot,op}} \sqrt{\frac{\left(-S_{\mathrm{hov}} \frac{m_{\mathrm{a}} g}{n_{\mathrm{rot,op}}}\right)^3}{2\rho A_{\mathrm{rot,s}}}} \end{aligned}$$

$$= -\sqrt{\frac{n_{\mathrm{rot,op}}^2}{n_{\mathrm{rot,op}}^3} \frac{\left(S_{\mathrm{hov}} m_{\mathrm{a}} g\right)^3}{2\rho \frac{A_{\mathrm{rot}}}{n_{\mathrm{rot}}}}}$$

$$= -\sqrt{\frac{1}{n_{\mathrm{rot,op}}} \frac{\left(S_{\mathrm{hov}} m_{\mathrm{a}} g\right)^3}{2\rho \frac{r_{\mathrm{rot}} A}{n_{\mathrm{rot}}}}}$$

$$= -\sqrt{\frac{\left(S_{\mathrm{hov}} m_{\mathrm{a}} g\right)^3}{2\rho \frac{n_{\mathrm{rot,op}}}{n_{\mathrm{rot}}} r_{\mathrm{rot}} A}}. \tag{2.113}$$

Again, a high reliability and thus a high fault tolerance is required for this technology [106]. Hovering and a safe normal landing *must* still be possible if one rotor fails. Fault tolerance is therefore an important design aspect. During hovering, the control surfaces can hardly contribute to the fault tolerance, and instead the rotors are the most important actuators. All fault tolerance measures for fault tolerant multicopters can be applied, cf. e.g. [130] and references therein. For multicopters, the higher the number of rotors is, the higher is the fault tolerance and, depending on the system design, possibly even without special measures in the control algorithm, cf. e.g. [130] and references therein. Moreover, the higher the number of rotors is, the smaller is the percentage of missing thrust and moment, the higher is the rotor efficiency due to lower rotor disk loading excesses, and hence the lower is the power excess to maintain hovering thrust during a rotor failure, cf. (2.113) or e.g. [130]. Many rotor numbers and placements are possible, but with the previous discussions and to obtain a level of fault tolerance with which at least one rotor can fail, a meaningful number of rotors is six, eight or a higher even number which are placed somewhat symmetrical. In such a symmetrical design any rotor has a counterpart rotor which is point-symmetrical w.r.t. the center of mass, cf. Fig. 2.11. This allows for a conservative estimation:

Assumption 2.28: *If one rotor fails, the point-symmetrical counterpart rotor needs also to be turned off to balance the moments.*

The thrusts of the remaining rotors are increased to compensate the missing thrust to maintain hovering.

In normal operation, obviously $n_{\mathrm{rot,op}} = n_{\mathrm{rot}}$, but, with Assumption 2.28, hovering must still work for $n_{\mathrm{rot,op}} = n_{\mathrm{rot}} - 2$. Therefore, the hovering power (2.113) becomes

$$P_{\mathrm{a,hov}} = \begin{cases} P_{\mathrm{a,hov,ok}} & \text{for no rotor failure (i.e. system ok)} \\ P_{\mathrm{a,hov,flt}} & \text{for rotor failure (i.e. system faulty)} \end{cases} \tag{2.114}$$

with the hovering power during normal operation and during rotor failure

$$P_{\mathrm{a,hov,ok}} = -\sqrt{\frac{\left(S_{\mathrm{hov,ok}} m_{\mathrm{a}} g\right)^3}{2\rho r_{\mathrm{rot}} A}}, \tag{2.115}$$

$$P_{\mathrm{a,hov,flt}} = -\sqrt{\frac{\left(S_{\mathrm{hov,flt}} m_{\mathrm{a}} g\right)^3}{2\rho \frac{n_{\mathrm{rot}}-2}{n_{\mathrm{rot}}} r_{\mathrm{rot}} A}}, \tag{2.116}$$

where $S_{\mathrm{hov,ok}}$ is the safety and correction factor for normal operation and $S_{\mathrm{hov,flt}}$ is the one for operation with rotor failure (which could be smaller than $S_{\mathrm{hov,ok}}$, as no extra acceleration thrust for a relaunch is required, if the kite is only launched when all rotors are available). Note again that a high r_{rot} allows for a low $P_{\mathrm{a,hov}}$, and additionally a high n_{rot} allows for a low $P_{\mathrm{a,hov,flt}}$ and a low then missing maximum available power. The implications of the latter are discussed below, in Sect. 2.7.14.

2.4.3 Real Rotors

Real rotors have additional power losses e.g. due to the drag of the rotor blades, which is not resolved by the actuator disk model. To account for that and to relax Assumption 2.25, the following assumption is introduced:

Assumption 2.29: *The shaft power of real rotors is the power of the ideal rotors reduced (for generative) or increased (for consumptive) by a constant efficiency factor, one for generative crosswind flight* $\eta_{\mathrm{rot},+} < 1$*, one for consumptive crosswind flight* $\eta_{\mathrm{rot},-} < 1$*, and one for hovering* $\eta_{\mathrm{rot,hov}} < 1$*.*

With that, the real rotor shaft power during crosswind flight becomes[13]

$$P_{\mathrm{rot}} = \begin{cases} \eta_{\mathrm{rot},+} P_{\mathrm{rot,ideal}} & \text{for } P_{\mathrm{a}} > 0 \\ \frac{1}{\eta_{\mathrm{rot},-}} P_{\mathrm{rot,ideal}} & \text{for } P_{\mathrm{a}} < 0 \end{cases} \tag{2.117}$$

with $P_{\mathrm{rot,ideal}}$ from (2.99), and during hovering

$$P_{\mathrm{rot,hov}} = \frac{1}{\eta_{\mathrm{rot,hov}}} P_{\mathrm{a,hov}} \tag{2.118}$$

with $P_{\mathrm{a,hov}}$ from (2.114).

The rotor efficiencies for the different cases can be combined to the total rotor efficiency (i.e. combination of rotor efficiency and possibly actuator disk efficiency, whereby the latter is only defined for $v_{\mathrm{a}} \neq 0$ and thus during crosswind flight), given by

$$\eta_{\mathrm{rot},\Pi} := \begin{cases} \eta_{\mathrm{rot},\Pi,+} & \text{for } P_{\mathrm{a}} > 0 \\ \eta_{\mathrm{rot},\Pi,-} & \text{for } P_{\mathrm{a}} < 0 \end{cases} \tag{2.119}$$

with

$$\eta_{\mathrm{rot},\Pi,+} := \eta_{\mathrm{rot},+} \eta_{\mathrm{a},+} \tag{2.120}$$

$$\eta_{\mathrm{rot},\Pi,-} := \begin{cases} \eta_{\mathrm{rot},-} \eta_{\mathrm{a},-} & \text{for crosswind flight and } P_{\mathrm{a}} < 0, \\ \eta_{\mathrm{rot,hov}} & \text{for hovering.} \end{cases} \tag{2.121}$$

2.5 Powertrain Model

2.5.1 Powertrain Components

Fig. 2.12 (top) shows a general block diagram of the powertrain of a drag power kite (cf. [106]). From left to right: The aerodynamic power extracted from the wind is converted by rotors into mechanical power, which is possibly further converted by gearboxes to high speed mechanical power. Electrical machines (i.e. motors/generators) convert mechanical power into electrical power. Rotating field electrical machines (hence multiphase AC electrical power), in particular permanent magnet synchronous machines, are preferable, as these machines achieve the highest power-to-mass ratio and efficiency compared to other AC or DC machines. The electrical machines are controlled by power electronic converters (forth block from left) which may include also further converters, such as DC-DC converters (as in [81]) or DC-AC converters (as in [91]) for a higher

[13] Note again that, if $P_{\mathrm{a}} > 0$, then also $C_{\mathrm{D,rot}}, a, P_{\mathrm{rot,ideal}}, P_{\mathrm{rot}} > 0$ and, vice versa, if $P_{\mathrm{a}} < 0$, then also $C_{\mathrm{D,rot}}, a, P_{\mathrm{rot,ideal}}, P_{\mathrm{rot}} < 0$.

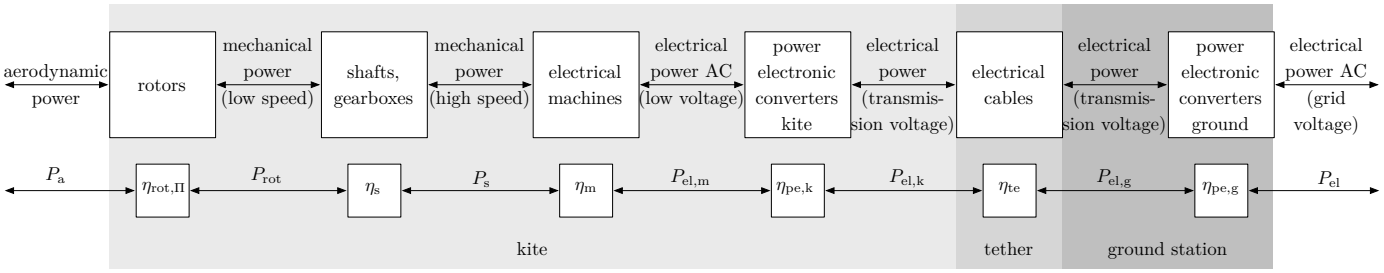

Figure 2.12: Block diagram of the powertrain of a drag power kite (top) with definition of powers and efficiencies (bottom).

transmission voltage than electrical machine voltage. The electrical power from the kite power electronic converters is transmitted via the electrical cables in the tether to the ground station power electronic converters (most right block). They convert the transmission voltage to the grid voltage. This might also include grid transformers (50 Hz or 60 Hz). The power transmission is bi-directional to allow also e.g. for hovering (launching and landing) and powered crosswind flight. Note that possibly further power transmission concepts e.g. with a series connection or with current source DC power transmission (cf. [131] and references therein) are captured by the general block diagram of Fig. 2.12.

Fig. 2.12 (bottom) defines powers and efficiencies according to the powertrain components, where η_s is the efficiency of the shafts and gears (if present, otherwise η_s may be one), P_s is the total shaft power (or mechanical power of the electrical machines), η_m is the efficiency of the electrical machines, $P_{el,m}$ is the total electrical power of the electrical machines, $\eta_{pe,k}$ and $P_{pe,k}$ are the efficiency and total tether-side electrical power of the power electronics onboard the kite, η_{te} is the tether transmission efficiency, $P_{el,g}$ and $\eta_{pe,g}$ are the total tether-side electrical power and efficiency of the power electronics on the ground (including possible transformers), and P_{el} is the total electrical power at the connection to the power grid.

The rotor efficiency was already defined in the previous section. In the following, the remaining efficiency factors are defined.

2.5.2 Tether Efficiency and Tether Voltage Control

In view of Fig. 2.12 (bottom), the tether efficiency factor can be derived as[14]

$$\eta_{te} = \begin{cases} \eta_{te,+} & \text{for } P_a > 0 \\ \eta_{te,-} & \text{for } P_a < 0 \end{cases} \tag{2.122}$$

with

$$\eta_{te,+} = \frac{P_{el,g}}{P_{el,k}} \tag{2.123}$$

$$\eta_{te,-} = \frac{P_{el,k}}{P_{el,g}}, \tag{2.124}$$

wherein

$$P_{el,g} = P_{el,k} - P_{te\text{-}loss} \tag{2.125}$$

[14] Note again that, if $P_a > 0$, then $C_{D,rot}, a, P_{rot,ideal}, P_{rot}, P_s, P_{el,m}, P_{el,k}, P_{el,g}, P_{el} > 0$ and, vice versa, if $P_a < 0$, then $C_{D,rot}, a, P_{rot,ideal}, P_{rot}, P_s, P_{el,m}, P_{el,k}, P_{el,g}, P_{el} < 0$.

with tether power loss from (2.88).

The tether current, required to calculate $P_{\text{te-loss}}$ with (2.88), is determined with the following consideration: The tether voltage is controlled by the ground (grid) power electronics while the kite power electronics simply inject a (positive or negative) current into the tether (and while those may control the voltage of an onboard bus), depending on the demands of the flight controller, i.e. for the here employed model, depending on the actuated rotor drag coefficient, airflow speed, aerodynamic power etc. The tether cables and the power electronics, both on the ground and on the kite, are designed for a certain maximum (insulation) voltage. As the tether cables have a possibly significant resistance and thus voltage drop

$$\Delta U_{\text{te}} = R_{\text{te}} I_{\text{te}}, \tag{2.126}$$

the voltage at both tether ends can differ significantly. The maximum voltage occurs at one tether end, depending on the power flow: for generative power the highest voltage is at the kite and for consumptive power the highest voltage is at the ground. Usually, the ground power electronics would control the tether voltage at the ground tether terminals to the fixed nominal value, cf. e.g. [81]. However, in such a control scheme, the voltage at the kite tether terminals is higher than the nominal tether voltage during power generation. Therefore, here it is considered, that instead the ground power electronics control the highest voltage in the tether to the nominal value, i.e. they control the maximum voltage in the tether to the nominal tether voltage. Hence, for power demand, the voltage at the ground is at the nominal voltage, while, for power generation, the voltage at the kite is at the nominal voltage, and the voltage at the respective other tether end is lower than the nominal voltage. By that, the tether voltage capability is utilized to its maximum. Based on this consideration, the tether current is given by

$$I_{\text{te}} = \begin{cases} \frac{P_{\text{el,k}}}{U_{\text{te,n}}} & \text{for } P_{\text{a}} > 0, \\ \frac{P_{\text{el,g}}}{U_{\text{te,n}}} & \text{for } P_{\text{a}} < 0. \end{cases} \tag{2.127}$$

In a controller implementation, the consumptive case could be realized traditionally as e.g. in [81]. The generative case could be implemented, either with voltage sensing at the kite or with fast real time communication, but also with a ground voltage controller with a voltage set value of the nominal voltage minus the voltage drop induced by the measured injected current of the ground power electronics and the known tether resistance. Note that, if the voltage drop is small, both cases in (2.127) have almost the same result, regardless which tether terminal voltage is controlled. Therefore, also the simpler traditional approach of controlling just the voltage on ground to the nominal value [81] could be used for certain system designs, in which the voltage drop is small and if the tether voltage safety and correction factors and power electronics voltage capabilities are high enough.

Substituting (2.127) into (2.88) and then into (2.125) gives

$$\text{for } P_{\text{a}} > 0\text{: } P_{\text{el,g}} = P_{\text{el,k}} - R_{\text{te}} \frac{P_{\text{el,k}}^2}{U_{\text{te,n}}^2} \tag{2.128}$$

$$\text{for } P_{\text{a}} < 0\text{: } P_{\text{el,g}} = P_{\text{el,k}} - R_{\text{te}} \frac{P_{\text{el,g}}^2}{U_{\text{te,n}}^2} \tag{2.129}$$

The following four cases can be differentiated:

Case 1: $P_{\text{el,k}}$ is known and $P_{\text{a}} > 0$. Then (2.128) gives explicitly the unknown $P_{\text{el,g}}$.

However, the transmittable power over the tether is limited. That limit can be found by maximizing (2.128) w.r.t. $P_{\mathrm{el,k}} = P_{\mathrm{el,k,max}}$, which becomes

$$\begin{aligned} 0 &= \frac{\mathrm{d}}{\mathrm{d}P_{\mathrm{el,k,max}}} \left(P_{\mathrm{el,k,max}} - R_{\mathrm{te}} \frac{P_{\mathrm{el,k,max}}^2}{U_{\mathrm{te,n}}^2} \right) \\ &= 1 - 2R_{\mathrm{te}} \frac{P_{\mathrm{el,k,max}}}{U_{\mathrm{te,n}}^2} \\ \Leftrightarrow 2R_{\mathrm{te}} \frac{P_{\mathrm{el,k,max}}}{U_{\mathrm{te,n}}^2} &= 1 \\ \Leftrightarrow P_{\mathrm{el,k,max}} &= \frac{U_{\mathrm{te,n}}^2}{2R_{\mathrm{te}}}, \end{aligned} \tag{2.130}$$

i.e.

$$\Rightarrow P_{\mathrm{el,k}} \leq \frac{U_{\mathrm{te,n}}^2}{2R_{\mathrm{te}}}. \tag{2.131}$$

Note that, $P_{\mathrm{el,k}} > P_{\mathrm{el,k,max}}$ is possible, but $P_{\mathrm{el,g}}$ is then further reduced, the voltage at the ground becomes below $U_{\mathrm{te,n}}/2$, and power is increasingly converted into heat in the tether. Power and voltage at the ground may even become negative, which might not be feasible for the power electronic system. Therefore, $P_{\mathrm{el,k}} > P_{\mathrm{el,k,max}}$ is not meaningful and can be excluded.

Substituting (2.130) into (2.128) also gives the maximum power at the ground $P_{\mathrm{el,g}} = P_{\mathrm{el,g,max}}$ as

$$\begin{aligned} P_{\mathrm{el,g,max}} &= P_{\mathrm{el,k,max}} - R_{\mathrm{te}} \frac{P_{\mathrm{el,k,max}}^2}{U_{\mathrm{te,n}}^2} \\ &= \frac{U_{\mathrm{te,n}}^2}{2R_{\mathrm{te}}} - R_{\mathrm{te}} \frac{\frac{U_{\mathrm{te,n}}^4}{4R_{\mathrm{te}}^2}}{U_{\mathrm{te,n}}^2} \\ &= \frac{U_{\mathrm{te,n}}^2}{2R_{\mathrm{te}}} - \frac{U_{\mathrm{te,n}}^2}{4R_{\mathrm{te}}} \\ &= \frac{U_{\mathrm{te,n}}^2}{4R_{\mathrm{te}}} \end{aligned} \tag{2.132}$$

i.e.

$$\Rightarrow P_{\mathrm{el,g}} \leq \frac{U_{\mathrm{te,n}}^2}{4R_{\mathrm{te}}}. \tag{2.133}$$

Case 2: $P_{\mathrm{el,k}}$ is known and $P_{\mathrm{a}} < 0$. Then (2.129) must be solved for $P_{\mathrm{el,g}}$, which becomes

$$\begin{aligned} \text{for } P_{\mathrm{a}} < 0\text{:} \qquad P_{\mathrm{el,g}} &= P_{\mathrm{el,k}} - R_{\mathrm{te}} \frac{P_{\mathrm{el,g}}^2}{U_{\mathrm{te,n}}^2} \\ \Leftrightarrow 0 &= P_{\mathrm{el,g}}^2 + \frac{U_{\mathrm{te,n}}^2}{R_{\mathrm{te}}} P_{\mathrm{el,g}} - \frac{P_{\mathrm{el,k}} U_{\mathrm{te,n}}^2}{R_{\mathrm{te}}} \\ \Leftrightarrow P_{\mathrm{el,g}} &= -\frac{U_{\mathrm{te,n}}^2}{2R_{\mathrm{te}}} \pm \sqrt{\frac{U_{\mathrm{te,n}}^4}{4R_{\mathrm{te}}^2} + \frac{P_{\mathrm{el,k}} U_{\mathrm{te,n}}^2}{R_{\mathrm{te}}}} \\ \Rightarrow P_{\mathrm{el,g}} &= -\frac{U_{\mathrm{te,n}}^2}{2R_{\mathrm{te}}} + \sqrt{\frac{U_{\mathrm{te,n}}^4}{4R_{\mathrm{te}}^2} + \frac{P_{\mathrm{el,k}} U_{\mathrm{te,n}}^2}{R_{\mathrm{te}}}}. \end{aligned} \tag{2.134}$$

Only the positive solution needs to be considered, otherwise $P_{\mathrm{el,g}} \neq 0$ for $P_{\mathrm{el,k}} = 0$. Additionally, for a real $P_{\mathrm{el,g}}$, the condition

$$\begin{aligned} \frac{U_{\mathrm{te,n}}^4}{4R_{\mathrm{te}}^2} + \frac{P_{\mathrm{el,k}} U_{\mathrm{te,n}}^2}{R_{\mathrm{te}}} &\geq 0 \\ \Leftrightarrow P_{\mathrm{el,k}} &\geq -\frac{U_{\mathrm{te,n}}^2}{4R_{\mathrm{te}}} =: P_{\mathrm{el,k,min}} \end{aligned} \tag{2.135}$$

must hold. Substituting that into (2.134), also the lower bound for $P_{\mathrm{el,g}}$ is given by

$$P_{\mathrm{el,g}} \geq -\frac{U_{\mathrm{te,n}}^2}{2R_{\mathrm{te}}} =: P_{\mathrm{el,g,min}}. \tag{2.136}$$

Case 3: $P_{\mathrm{el,g}}$ is known and $P_{\mathrm{a}} > 0$. Then (2.128) must be solved for $P_{\mathrm{el,k}}$, which becomes

$$\begin{aligned} \text{for } P_{\mathrm{a}} > 0: \qquad P_{\mathrm{el,g}} &= P_{\mathrm{el,k}} - R_{\mathrm{te}} \frac{P_{\mathrm{el,k}}^2}{U_{\mathrm{te,n}}^2} \\ \Leftrightarrow 0 &= P_{\mathrm{el,k}}^2 - \frac{U_{\mathrm{te,n}}^2}{R_{\mathrm{te}}} P_{\mathrm{el,k}} + \frac{P_{\mathrm{el,g}} U_{\mathrm{te,n}}^2}{R_{\mathrm{te}}} \\ \Leftrightarrow P_{\mathrm{el,k}} &= \frac{U_{\mathrm{te,n}}^2}{2R_{\mathrm{te}}} \pm \sqrt{\frac{U_{\mathrm{te,n}}^4}{4R_{\mathrm{te}}^2} - \frac{P_{\mathrm{el,g}} U_{\mathrm{te,n}}^2}{R_{\mathrm{te}}}} \\ \Rightarrow P_{\mathrm{el,k}} &= \frac{U_{\mathrm{te,n}}^2}{2R_{\mathrm{te}}} - \sqrt{\frac{U_{\mathrm{te,n}}^4}{4R_{\mathrm{te}}^2} - \frac{P_{\mathrm{el,g}} U_{\mathrm{te,n}}^2}{R_{\mathrm{te}}}}. \end{aligned} \tag{2.137}$$

Only the negative solution needs to be considered, otherwise $P_{\mathrm{el,k}} \neq 0$ for $P_{\mathrm{el,g}} = 0$. Additionally, for a real $P_{\mathrm{el,k}}$, the condition

$$\begin{aligned} \frac{U_{\mathrm{te,n}}^4}{4R_{\mathrm{te}}^2} - \frac{P_{\mathrm{el,g}} U_{\mathrm{te,n}}^2}{R_{\mathrm{te}}} &\geq 0 \\ \Leftrightarrow P_{\mathrm{el,g}} &\leq \frac{U_{\mathrm{te,n}}^2}{4R_{\mathrm{te}}} \end{aligned} \tag{2.138}$$

must hold. Substituting that into (2.137), also the lower bound for $P_{\mathrm{el,g}}$ is given by

$$P_{\mathrm{el,k}} \leq \frac{U_{\mathrm{te,n}}^2}{2R_{\mathrm{te}}}. \tag{2.139}$$

Note that (2.139) and (2.138) are identical to (2.131) and (2.133), respectively.

Case 4: $P_{\mathrm{el,g}}$ is known and $P_{\mathrm{a}} < 0$. Then (2.129) must be solved for $P_{\mathrm{el,k}}$, which becomes

$$\begin{aligned} \text{for } P_{\mathrm{a}} < 0: \qquad P_{\mathrm{el,g}} &= P_{\mathrm{el,k}} - R_{\mathrm{te}} \frac{P_{\mathrm{el,g}}^2}{U_{\mathrm{te,n}}^2} \\ \Leftrightarrow P_{\mathrm{el,k}} &= P_{\mathrm{el,g}} + R_{\mathrm{te}} \frac{P_{\mathrm{el,g}}^2}{U_{\mathrm{te,n}}^2}. \end{aligned} \tag{2.140}$$

Similar to Case 1, the transmittable power is limited by

$$\begin{aligned} 0 &= \frac{\mathrm{d}}{\mathrm{d}P_{\mathrm{el,g,min}}} \left(P_{\mathrm{el,g,min}} + R_{\mathrm{te}} \frac{P_{\mathrm{el,g,min}}^2}{U_{\mathrm{te,n}}^2} \right) \\ &= 1 + 2R_{\mathrm{te}} \frac{P_{\mathrm{el,g,min}}}{U_{\mathrm{te,n}}^2} \\ \Leftrightarrow -2R_{\mathrm{te}} \frac{P_{\mathrm{el,g,min}}}{U_{\mathrm{te,n}}^2} &= 1 \\ \Leftrightarrow P_{\mathrm{el,g,min}} &= -\frac{U_{\mathrm{te,n}}^2}{2R_{\mathrm{te}}}, \end{aligned} \tag{2.141}$$

i.e.

$$\Rightarrow P_{\mathrm{el,g}} \geq -\frac{U_{\mathrm{te,n}}^2}{2R_{\mathrm{te}}}. \tag{2.142}$$

Substituting (2.141) into (2.140) gives the minimum power at the kite $P_{\mathrm{el,k}} = P_{\mathrm{el,k,min}}$ as

$$\begin{aligned} P_{\mathrm{el,k,min}} &= P_{\mathrm{el,g,min}} + R_{\mathrm{te}} \frac{P_{\mathrm{el,g,min}}^2}{U_{\mathrm{te,n}}^2} \\ &= -\frac{U_{\mathrm{te,n}}^2}{2R_{\mathrm{te}}} + R_{\mathrm{te}} \frac{\frac{U_{\mathrm{te,n}}^4}{4R_{\mathrm{te}}^2}}{U_{\mathrm{te,n}}^2} \\ &= -\frac{U_{\mathrm{te,n}}^2}{2R_{\mathrm{te}}} + \frac{U_{\mathrm{te,n}}^2}{4R_{\mathrm{te}}} \\ &= -\frac{U_{\mathrm{te,n}}^2}{4R_{\mathrm{te}}} \end{aligned} \tag{2.143}$$

i.e.

$$\Rightarrow P_{\mathrm{el,k}} \geq -\frac{U_{\mathrm{te,n}}^2}{4R_{\mathrm{te}}}. \tag{2.144}$$

Note that (2.144) and (2.142) are identical to (2.135) and (2.136), respectively.

Fig. 2.13 plots results of (2.122)–(2.144) in all the mentioned cases for exemplary systems with high and low tether resistance, to visualize the mentioned effects.

2.5.3 Efficiencies of Shafts/Gears, Machines, and Converters

For all other efficiency factors, a similar assumption as for the real rotors is imposed:

Assumption 2.30: *The efficiencies $\eta_{\mathrm{s}} \leq 1$, $\eta_{\mathrm{m}} < 1$, $\eta_{\mathrm{pe,k}} < 1$ and $\eta_{\mathrm{pe,g}} < 1$ are constant, but may differ for generative (index +) and consumptive operation (index −).*

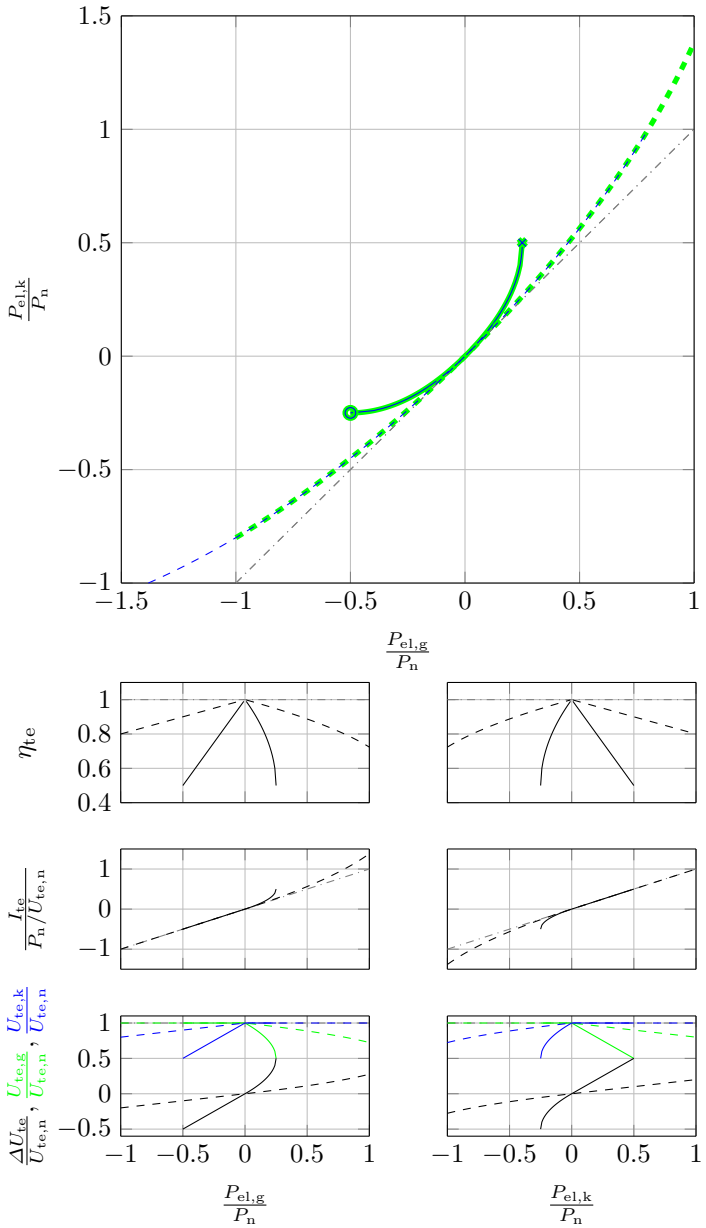

Figure 2.13: Exemplary power transmission across tether: Results of (2.122)–(2.144) with $U_{\mathrm{te,n}} = 1\,\mathrm{kV}$ and a high tether resistance of $R_{\mathrm{te}} = 10\,\Omega$ in solid —— and with a low tether resistance of $R_{\mathrm{te}} = 2\,\Omega$ in dashed - - - -. All values are normalized with the nominal power $P_{\mathrm{n}} := 100\,\mathrm{kW}$. From top to bottom, row 1: powers at ground and at kite with $P_{\mathrm{el,g}}$ known and changed in green and with $P_{\mathrm{el,k}}$ known and changed in blue whereby the minimum and maximum powers are marked by a circle and by a cross, respectively; left column: $P_{\mathrm{el,g}}$ known and changed; right column $P_{\mathrm{el,k}}$ known and changed; row 2: efficiency; row 3: tether current; row 4: voltage drop and tether voltage at ground and at kite. Ideal values, i.e. with $R_{\mathrm{te}} \to 0$, are in gray dash-dotted -·-·-.

2.5.4 Total Power and Total Efficiency

With all efficiency factors defined, with (2.117)–(2.121), and in view of Fig 2.12, the generative powers are given by

$$\begin{aligned}
\text{for } P_\mathrm{a} > 0: \qquad P_\mathrm{rot} &= \eta_{\mathrm{rot},\Pi,+} P_\mathrm{a} && (2.145)\\
P_\mathrm{s} &= \eta_{\mathrm{s},+} P_\mathrm{rot} && (2.146)\\
P_\mathrm{el,m} &= \eta_{\mathrm{m},+} P_\mathrm{s} && (2.147)\\
P_\mathrm{el,k} &= \eta_{\mathrm{pe,k},+} P_\mathrm{el,m} && (2.148)\\
P_\mathrm{el,g} &= \eta_{\mathrm{te},+} P_\mathrm{el,k} && (2.149)\\
P_\mathrm{el} &= \eta_{\mathrm{pe,g},+} P_\mathrm{el,g}, && (2.150)
\end{aligned}$$

the consumptive powers are given by

$$\begin{aligned}
\text{for } P_\mathrm{a} < 0: \qquad P_\mathrm{el,g} &= \eta_{\mathrm{pe,g},-} P_\mathrm{el} && (2.151)\\
P_\mathrm{el,k} &= \eta_{\mathrm{te},-} P_\mathrm{el,g} && (2.152)\\
P_\mathrm{el,m} &= \eta_{\mathrm{pe,k},-} P_\mathrm{el,k} && (2.153)\\
P_\mathrm{s} &= \eta_{\mathrm{m},-} P_\mathrm{el,m} && (2.154)\\
P_\mathrm{rot} &= \eta_{\mathrm{s},-} P_\mathrm{s} && (2.155)\\
P_\mathrm{a} &= \eta_{\mathrm{rot},\Pi,-} P_\mathrm{rot}, && (2.156)
\end{aligned}$$

and a total efficiency factor can be defined by

$$\eta_\Pi := \eta_{\mathrm{rot},\Pi}\eta_\mathrm{s}\eta_\mathrm{m}\eta_{\mathrm{pe,k}}\eta_\mathrm{te}\eta_{\mathrm{pe,g}} = \begin{cases} \frac{P_\mathrm{el}}{P_\mathrm{a}} & \text{for } P_\mathrm{a} > 0, \\ \frac{P_\mathrm{a}}{P_\mathrm{el}} & \text{for } P_\mathrm{a} < 0. \end{cases} \tag{2.157}$$

2.6 Atmosphere Model

The atmosphere model is based on two assumptions, which are justified by their common use also for conventional wind turbines, cf. e.g. [127, Chap. 2], [132, Chap. 6.2] or [133–135]:

Assumption 2.31: *The wind speed at the altitude of the kite above ground h (i.e. at the kite's position) can (on average) be described by*

$$v_\mathrm{w} = f_\mathrm{shear}(h) v_{\mathrm{w},h_\mathrm{ref}}, \tag{2.158}$$

where $v_{\mathrm{w},h_\mathrm{ref}}$ is the wind speed in the reference altitude above ground h_ref, and $f_\mathrm{shear}(h)$ is the wind shear factor defined by

$$f_\mathrm{shear}(h) = \begin{cases} \frac{\ln\left(\frac{h}{z_0}\right)}{\ln\left(\frac{h_\mathrm{ref}}{z_0}\right)} & \textit{for a logarithmic wind shear with roughness length } z_0, \textit{ or} \\ \left(\frac{h}{h_\mathrm{ref}}\right)^{\alpha_\mathrm{H}} & \textit{for an exponential wind shear with Hellmann exponent } \alpha_\mathrm{H}. \end{cases} \tag{2.159}$$

Herein, due to Assumptions 2.3 and 2.4, the (effective or averaged) altitude above ground is composed of

$$h = h_\mathrm{to} + L_\mathrm{te} \sin(\vartheta) \tag{2.160}$$

where h_{to} is the height of the ground station tether connection above ground which is in the following denoted in short as tower height. Note that a tower of at least a few meters is necessary for the considered relatively simple kite design without tiltable tail or similar measures for a simple launch and landing (see also the prior work of the author of this dissertation [14] and references therein). Note also that, with $\alpha_{\mathrm{H}} = 0$, a uniform wind field without shear can be modeled. Fig. 2.14 plots several possible wind shears.

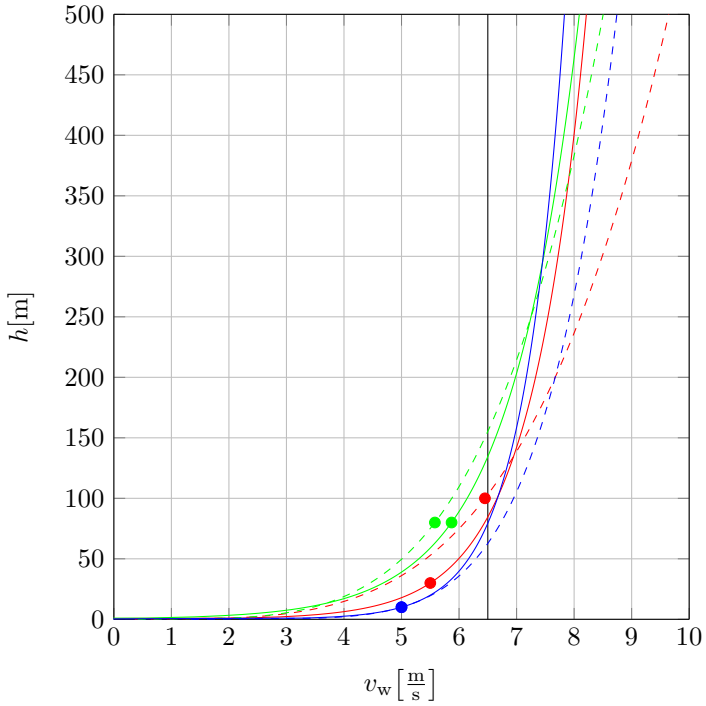

Figure 2.14: Wind shears for different parameters: typical benchmark logarithmic wind shear $h_{\mathrm{ref}} = 10\,\mathrm{m}$, $z_0 = 0.1\,\mathrm{m}$, $v_{\mathrm{w},h_{\mathrm{ref}}} = 5\,\mathrm{m/s}$ in —— and benchmark exponential wind shear $h_{\mathrm{ref}} = 10\,\mathrm{m}$, $\alpha_{\mathrm{H}} = 1/7 \approx 0.14$, $v_{\mathrm{w},h_{\mathrm{ref}}} = 5\,\mathrm{m/s}$ in - - - -, cf. e.g. [133]; fitted wind shears from global measurements by Archer and Jacobson [133] with the logarithmic wind shear $h_{\mathrm{ref}} = 80\,\mathrm{m}$, $z_0 = 0.63\,\mathrm{m}$, $v_{\mathrm{w},h_{\mathrm{ref}}} = 5.87\,\mathrm{m/s}$ in —— and the exponential wind shear $h_{\mathrm{ref}} = 80\,\mathrm{m}$, $\alpha_{\mathrm{H}} = 0.23$, $v_{\mathrm{w},h_{\mathrm{ref}}} = 5.58\,\mathrm{m/s}$ in - - - - [133, Tab. 5]; "reference location" with mean wind speed according to the German renewable energies law (Erneuerbare Energien Gesetz, EEG) editions until 2014 with the logarithmic wind shear $h_{\mathrm{ref}} = 30\,\mathrm{m}$, $z_0 = 0.1\,\mathrm{m}$, $v_{\mathrm{w},h_{\mathrm{ref}}} = 5.5\,\mathrm{m/s}$ [134, Appendix 2, Paragraph 4] in ——; "reference location" with mean wind speed according to the EEG edition from 2017 with the exponential wind shear $h_{\mathrm{ref}} = 100\,\mathrm{m}$, $\alpha_{\mathrm{H}} = 0.25$, $v_{\mathrm{w},h_{\mathrm{ref}}} = 6.45\,\mathrm{m/s}$ [135, Appendix 2, Paragraph 4] in - - - -; and uniform wind field with 6.5 m/s wind speed, realized with the exponential wind shear $h_{\mathrm{ref}} \neq 0$, $\alpha_{\mathrm{H}} = 0$, $v_{\mathrm{w},h_{\mathrm{ref}}} = 6.5\,\mathrm{m/s}$ in ——. The dots in the curves represent the reference wind speed $v_{\mathrm{w},h_{\mathrm{ref}}}$ in the reference altitude h_{ref}.

Assumption 2.32: *The probability of a certain wind speed in the reference altitude can be described by the Weibull distribution*

$$p(v_{\mathrm{w},h_{\mathrm{ref}}}) = \frac{\lambda}{\mu}\left(\frac{v_{\mathrm{w},h_{\mathrm{ref}}}}{\mu}\right)^{\lambda-1}\exp\left[-\left(\frac{v_{\mathrm{w},h_{\mathrm{ref}}}}{\mu}\right)^{\lambda}\right] \tag{2.161}$$

with shape parameter λ and scale parameter μ.

In the special case of $\lambda = 2$, Eq. (2.161) is a Rayleigh distribution

$$p_{\lambda=2}(v_{\mathrm{w},h_{\mathrm{ref}}}) = \frac{2v_{\mathrm{w},h_{\mathrm{ref}}}}{\mu^2}\exp\left[-\left(\frac{v_{\mathrm{w},h_{\mathrm{ref}}}}{\mu}\right)^{2}\right] \tag{2.162}$$

for which mean wind speed $\tilde{v}_{\mathrm{w},h_{\mathrm{ref}}}$ and scale parameter μ are related by

$$\mu_{\lambda=2} = \frac{2}{\sqrt{\pi}}\tilde{v}_{\mathrm{w},h_{\mathrm{ref}}}. \tag{2.163}$$

Fig. 2.15 plots several possible Weibull distributions.

Remark 2.6: *The following points should be noted regarding this atmosphere model:*

- *There are alternatives for both assumptions: Eq. (2.158) could be replaced by other wind shear approximations and (2.161) could be replaced by other probability distribution approximations (cf. e.g. [127, Chap. 2] or [133]), or both could be replaced by actual wind measurements. The here employed simplified equations are black-box models (although they might be motivated from first principles) in which the parameters z_0, h_{ref}, α_{H}, μ, and λ can be fitting parameters from measurements. With the help of weather services, weather maps, or measurements, these parameters can be fitted for an anticipated deployment site, cf. e.g. [136]. Alternatively, "reference parameters" for a "reference location" as e.g. defined in the German renewable energies law [134, 135] can be used.*
- *No gusts, turbulence, or other fluctuations are resolved by these models. This is justified, because the goal is to derive a steady model. With Assumptions 2.31 and 2.32 it is also assumed, that a reasonably long time span (e.g. months or years) is considered, i.e. these assumptions are only on average valid.*
- *No further detailed model for the decrease of the air density with altitude and temperature is considered here. Instead of formulating such a model, which would be based on an assumed or estimated site temperature (or temperature probability distribution) and site altitude above sea level, only the parameter ρ needs to be assumed or estimated as the average site-specific air density. This approach is justified by the usually relatively low optimal flight altitude of the kite of only a few hundred meters above ground, even without considering a decrease of the air density for an increased altitude, cf. below, Chap. 5.*

2.7 Control Model: Power Curve Optimization

A basic power curve of a drag power kite is given by Vander Lind in [16], which is similarly used by the author of this dissertation in [110] and extended in [104]. Here, this extension is presented in detail. Differences to [16] include justifications of the different power curve regions and derivations of equations for each actuation to achieve that power curve.

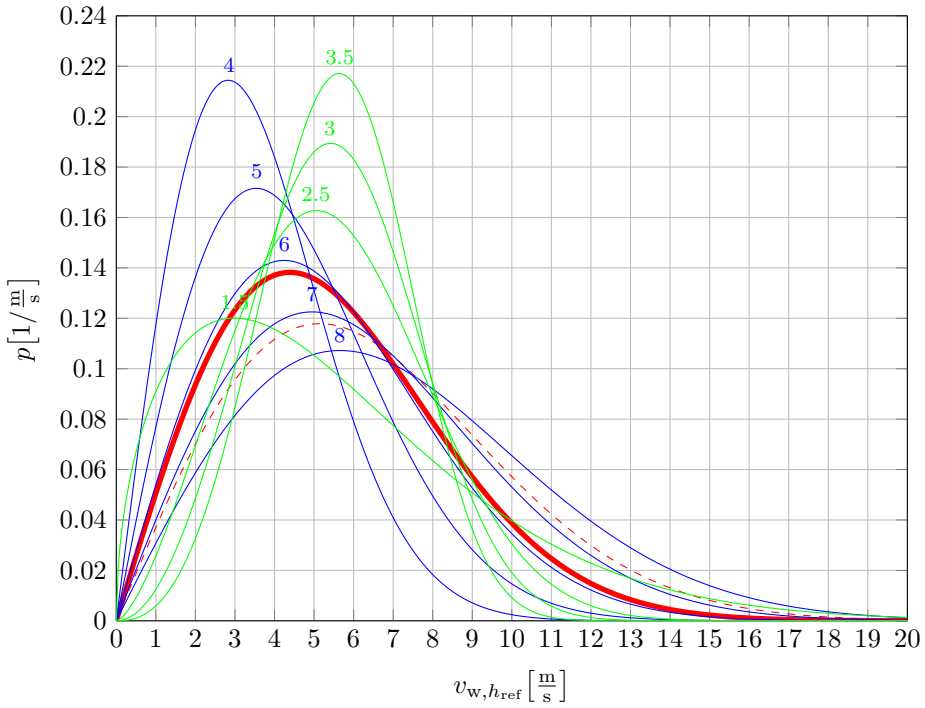

Figure 2.15: Weibull distribution for different parameters: "reference location" according to the EEG edition from 2014 with $\lambda = 2$ and $\tilde{v}_{\mathrm{w},h_{\mathrm{ref}}} = 5.5\,\mathrm{m/s}$ (i.e., according to (2.163), with $\mu = 2/\sqrt{\pi} \cdot \tilde{v}_{\mathrm{w},h_{\mathrm{ref}}} = 2/\sqrt{\pi} \cdot 5.5\,\mathrm{m/s} \approx 6.21\,\mathrm{m/s}$) in ——— [134, Appendix 2, Paragraph 4]; "reference location" according to the EEG edition from 2017 with $\lambda = 2$ and $\tilde{v}_{\mathrm{w},h_{\mathrm{ref}}} = 6.45\,\mathrm{m/s}$ (i.e., according to (2.163), with $\mu = 2/\sqrt{\pi} \cdot \tilde{v}_{\mathrm{w},h_{\mathrm{ref}}} = 2/\sqrt{\pi} \cdot 6.45\,\mathrm{m/s} \approx 7.28\,\mathrm{m/s}$) in - - - - [135, Appendix 2, Paragraph 4]; from the baseline ——— varied μ (values in m/s are printed above the corresponding curve) in ———; and from the baseline ——— varied λ (values are printed above the corresponding curve) in ———.

2.7.1 Problem Formulation

The kite should be controlled optimally such that it is utilized maximally and thus the optimal power curve is flown. The power curve optimization can be formally written as follows: For a given kite power plant design, the maximum possible electrical power shall be generated (or the minimum possible electrical power shall be consumed, respectively) from no wind up to the cut-out wind speed in the reference altitude $v_{\mathrm{w},h_{\mathrm{ref}},\text{cut-out}}$. Hence, the power curve optimization problem can be formulated as maximization problem

$$\forall v_{\mathrm{w},h_{\mathrm{ref}}} \in [0, v_{\mathrm{w},h_{\mathrm{ref}},\text{cut-out}}]: \quad \max_{\boldsymbol{u}} \quad P_{\mathrm{el}} \tag{2.164}$$

$$\text{s.t.} \quad \underline{\boldsymbol{u}} \leq \boldsymbol{u} \leq \overline{\boldsymbol{u}} \tag{2.165}$$

$$\underline{\boldsymbol{x}} \leq \boldsymbol{x} \leq \overline{\boldsymbol{x}} \tag{2.166}$$

where

$$\boldsymbol{u} := \begin{pmatrix} C_{\mathrm{D,rot}} \\ c_{\mathrm{L}} \\ C_{\mathrm{D,k,a}} \\ \Delta\varphi_{\mathrm{a}} \\ \Delta\vartheta_{\mathrm{a}} \end{pmatrix}, \qquad \underline{\boldsymbol{u}} := \begin{pmatrix} C_{\mathrm{D,rot,min}} \\ c_{\mathrm{L,min\text{-}op}} \\ C_{\mathrm{D,k,a,min}} = 0 \\ \Delta\varphi_{\mathrm{a,min}} = 0 \\ \Delta\vartheta_{\mathrm{a,min}} = 0 \end{pmatrix}, \qquad \overline{\boldsymbol{u}} := \begin{pmatrix} C_{\mathrm{D,rot,n}} \\ c_{\mathrm{L,max\text{-}op}} =: c_{\mathrm{L,n}} \\ C_{\mathrm{D,k,a,max}} \\ \Delta\varphi_{\mathrm{a,max}} \leq \pi/2 - \varphi_{\mathrm{n}} \\ \Delta\vartheta_{\mathrm{a,max}} \leq \pi/2 - \vartheta_{\mathrm{n}} \end{pmatrix}, \tag{2.167}$$

are the control actuations and bounds with

$$\varphi =: \varphi_{\mathrm{n}} + \Delta\varphi_{\mathrm{a}} \tag{2.168}$$

$$\vartheta =: \vartheta_{\mathrm{n}} + \Delta\vartheta_{\mathrm{a}} \tag{2.169}$$

in which $\varphi_{\mathrm{n}}, \vartheta_{\mathrm{n}}$ are the nominal effective azimuth and elevation angles and $\Delta\varphi_{\mathrm{a}}, \Delta\vartheta_{\mathrm{a}}$ are their actuated increase (i.e. change of flight path to one with reduced power), and

$$\boldsymbol{x} := \begin{pmatrix} F_{\mathrm{a}} \\ v_{\mathrm{a}} \\ P_{\mathrm{el}} \end{pmatrix}, \qquad \underline{\boldsymbol{x}} := \begin{pmatrix} F_{\mathrm{a,min}} \\ v_{\mathrm{a,min}} \\ P_{\mathrm{el,min}} \end{pmatrix} \qquad \overline{\boldsymbol{x}} := \begin{pmatrix} F_{\mathrm{a,max}} =: F_{\mathrm{a,n}} \\ v_{\mathrm{a,max}} =: v_{\mathrm{a,n}} \\ P_{\mathrm{el,max}} =: P_{\mathrm{el,n}} \end{pmatrix}, \tag{2.170}$$

are the system states[15] and bounds. Herein, underlined and overlined quantities are bounds for the optimization to be satisfied, "min" and "max" are for minimum and maximum[16], index "min-op" and "max-op" are for operational minimum and maximum[16], and index "n" is for nominal.

Remark 2.7: *The nominal airfoil lift coefficient is considered as maximum operational airfoil lift coefficient, $c_{\mathrm{L,max\text{-}op}} =: c_{\mathrm{L,n}}$, which cannot be further increased for safe operation e.g. with enough safety margin to stalling (cf. e.g. Sect. 2.2.1 or [110]). However, the actual maximum airfoil lift coefficient may be higher than $c_{\mathrm{L,max\text{-}op}}$. Similarly, the minimum lift coefficient is equal to or greater than the minimum operational lift coefficient with safety margin to stalling.*

Remark 2.8: *The rotor drag coefficient is chosen over the induction factor as control actuation for sake of simplicity. Both can be used equivalently because they are coupled via (2.100). Ultimately, the rotor speeds might be the actual control actuation with the underlying (usually highly dynamic) torque and current controllers of the electrical machines, which are, however, in steady-state also coupled to the rotor drag coefficient and induction factor for a given rotor design and airflow speed.*

Remark 2.9: *Besides the stated bounds, more variables must actually be kept within bounds:*

- *Besides the aerodynamic force, also the tether force F_{te}, lift force F_{L}, and/or drag force F_{D} need to be kept within bounds. Particularly, the aerodynamic force and the tether force might differ substantially, when the kite flies a turn within the figure eights flight path caused by its roll angle w.r.t. the tether. However, Assumption 2.1 imposes a small roll angle. Additionally, with Remark 2.7, the highest tether force occurs at the nominal/maximum aerodynamic force at zero roll angle, which is therefore argued to be the only case that needs consideration.*

[15] The wording "system states" is used here, although the utilized model is steady. However, in a more detailed model, the here defined $\boldsymbol{x}$ would indeed in part be a member of the system state vector or be depending on it, which motivates the here used wording and symbol.

[16] The nominal minimum (maximum) is meant, i.e. the averaged value (cf. Assumptions 2.5, "averaged crosswind flight"), which is however bounded by the instantaneous minimum (maximum).

- *Besides the electrical power at the grid connection P_{el}, also the powers of each individual powertrain component has to be kept within bounds. Similarly, other values of powertrain components must be limited, e.g. the rotational speeds or torques of the rotors, gears, or electrical machines. However, all of that is considered to be ensured by a proper match of the individual nominal values (nominal/maximum powers) of the powertrain components. Therefore and for sake of simplicity, no further powertrain bounds are stated.*
- *In the here utilized model, thermodynamic bounds of the powertrain components are captured implicitly by the power bounds, because the nominal power of a component is defined by the nominal/maximal temperature. However, it should be noted, that a full utilization of thermodynamic bounds with the use of increasing airflow speed for forced cooling might lead to differences in an optimized power curve, cf. [137]. Moreover, the thermodynamic limit of the tether is considered to be validated through (2.89) or (2.90) a-posteriori, as a to be met feasibility condition for the power plant design.*

For a low computational cost, an analytical solution to the problem (2.164)–(2.170) is preferred, in which reasonable requirements (equalities, inequalities, or relations) for the nominal values (e.g. parts of the bounds of $\boldsymbol{u}$ and $\boldsymbol{x}$ or derived values) are deduced. The optimization of only those nominal values is then left to a superimposed optimization. These values are in the following referred to as *dimensioning parameters*. Moreover, an explicit solution is preferred for sake of simplicity and particularly for low computational costs, and thus to enable fast optimizations and fast studies (e.g. sensitivity analyses) with the dimensioning parameters.

2.7.2 Simplifying Assumptions

To derive an explicit, analytical solution, the following simplifying assumptions are imposed:

Assumption 2.33: *The total lift coefficient is much higher than the total drag coefficient such that*

$$\sqrt{C_{\mathrm{L}}^2 + C_{\mathrm{D}}^2} \approx C_{\mathrm{L}}. \tag{2.171}$$

Assumption 2.34: *The actuation $\boldsymbol{u}^*$ for which the electrical power P_{el} is maximized at a given wind speed $v_{\mathrm{w},h_{\mathrm{ref}}}$ is approximately the same as the actuation which maximizes the aerodynamic power P_{a}, i.e.*

$$\boldsymbol{u}^* = \arg\max_{\boldsymbol{u}} P_{\mathrm{el}} \approx \arg\max_{\boldsymbol{u}} P_{\mathrm{a}} \tag{2.172}$$

and therefore (2.164) can be replaced by

$$\forall v_{\mathrm{w},h_{\mathrm{ref}}} \in [0, v_{\mathrm{w},h_{\mathrm{ref}},\text{cut-out}}] : \quad \max_{\boldsymbol{u}} P_{\mathrm{a}}, \tag{2.173}$$

and, as the powers are coupled by (2.145)–(2.156), Eq. (2.170) can be replaced by

$$\boldsymbol{x} := \begin{pmatrix} F_{\mathrm{a}} \\ v_{\mathrm{a}} \\ P_{\mathrm{a}} \end{pmatrix}, \qquad \underline{\boldsymbol{x}} := \begin{pmatrix} F_{\mathrm{a,min}} \\ v_{\mathrm{a,min}} \\ P_{\mathrm{a,min}} \end{pmatrix} \qquad \overline{\boldsymbol{x}} := \begin{pmatrix} F_{\mathrm{a,max}} =: F_{\mathrm{a,n}} \\ v_{\mathrm{a,max}} =: v_{\mathrm{a,n}} \\ P_{\mathrm{a,max}} =: P_{\mathrm{a,n}} \end{pmatrix}. \tag{2.174}$$

Assumption 2.33 is a usual assumption for crosswind kite power, cf. e.g. [10, 12, 13], and is justified as efficient airfoils are considered. Assumption 2.34 is justified because the efficiencies in η_{Π} (i.e. the difference between P_{a} and P_{el}) can be expected to have a relatively low sensitivity

on the optimized actuations $\boldsymbol{u}^*$ for a meaningful kite design, e.g. with high enough r_{rot}.—Note that Assumption 2.34 does *not* impose $P_{\text{a}} \approx P_{\text{el}}$, it only imposes that the optimal actuation $\boldsymbol{u}^*$ is approximately the same for maximizing P_{a} or P_{el}, cf. (2.172). With the found optimal actuation $\boldsymbol{u}^*$, all power losses in the conversions between P_{a} and P_{el} are then accounted for through (2.145)–(2.156).

With (2.171) and with (2.11), Eqs. (2.1) and (2.19)–(2.21) become

$$v_{\text{a}} = \cos(\varphi)\cos(\vartheta) v_{\text{w}} \frac{C_{\text{L}}}{C_{\text{D}}} \tag{2.175}$$

$$= \cos(\varphi)\cos(\vartheta) v_{\text{w}} \frac{C_{\text{L}}}{C_{\text{D,eq}} + C_{\text{D,rot}}}, \tag{2.176}$$

$$P_{\text{a}} = \frac{1}{2}\rho \cos^3(\varphi)\cos^3(\vartheta) v_{\text{w}}^3 A \frac{C_{\text{L}}^3}{(C_{\text{D,eq}} + C_{\text{D,rot}})^3} C_{\text{D,rot}}, \tag{2.177}$$

$$F_{||} := F_{\text{L}} = F_{\text{te}} = F_{\text{a}} = \frac{1}{2}\rho v_{\text{a}}^2 A C_{\text{L}}, \tag{2.178}$$

$$= \frac{1}{2}\rho \cos^2(\varphi)\cos^2(\vartheta) v_{\text{w}}^2 A \frac{C_{\text{L}}^3}{(C_{\text{D,eq}} + C_{\text{D,rot}})^2}, \tag{2.179}$$

where $F_{||}$ is the force parallel to the tether (cf. also Remark 2.9).

Depending on the flight path, the airflow speed, power, and forces might change significantly around their average values, cf. Sect. 2.1.2. To keep the power curve derivation simple, the following additional assumption is made, which can be seen as an extension of Assumption 2.5:

Assumption 2.35: *Eqs. (2.175)–(2.179) are valid to also compute minimal and maximal values of airflow speed, power, and force for the complete flight path at given effective azimuth and elevation angles. Temporarily lower and higher values over the course of the kite's flight path are either prevented by the flight controller, but with negligible effects on the resulting average power (power curve), or temporary underloading and overloading is not harmful (e.g. the electrical machines can usually be well overloaded for a few seconds) or is covered by safety factors (e.g. S_{te}).*

2.7.3 Power Curve Regions

Similar to a conventional wind turbine, the power curve of a drag power kite can be divided into four main regions, visualized in Fig. 2.16:

Region I: In the first region, at low wind speeds $0 \leq v_{\text{w},h_{\text{ref}}} \leq v_{\text{w},h_{\text{ref}},\text{I}\leftrightarrow\text{II}}$, the wind is insufficient for (optimal) power generation. One or more system states are at their lower bound $\underline{\boldsymbol{x}}$ and some actuations $\boldsymbol{u}$ may be at a bound, or the power plant is turned off (i.e. the kite is landed), because the power would be negative (cf. dashed and solid line in Fig. 2.16).

Region II: In the second region, at medium wind speeds $v_{\text{w},h_{\text{ref}},\text{I}\leftrightarrow\text{II}} \leq v_{\text{w},h_{\text{ref}}} \leq v_{\text{w},h_{\text{ref}},\text{II}\leftrightarrow\text{III}}$, neither a system state $\boldsymbol{x}$ nor an actuation $\boldsymbol{u}$ is at a bound. The power plant is operated without constraints and the power at the given wind speed is at the maximum possible value.

Region III: In the third region, at high wind speeds $v_{\text{w},h_{\text{ref}},\text{II}\leftrightarrow\text{III}} \leq v_{\text{w},h_{\text{ref}}} \leq v_{\text{w},h_{\text{ref}},\text{III}\leftrightarrow\text{IV}}$, one or more system states are at the upper bound $\overline{\boldsymbol{x}}$ and some actuations $\boldsymbol{u}$ may be at a bound. To keep all system states and actuations within their bounds, the efficiency of the power plant is reduced (e.g. by pitching similar to conventional wind turbines). At certain wind speeds in this region (not necessarily in the entire region from $v_{\text{w},h_{\text{ref}},\text{II}\leftrightarrow\text{III}}$ to $v_{\text{w},h_{\text{ref}},\text{III}\leftrightarrow\text{IV}}$), the nominal power is generated.

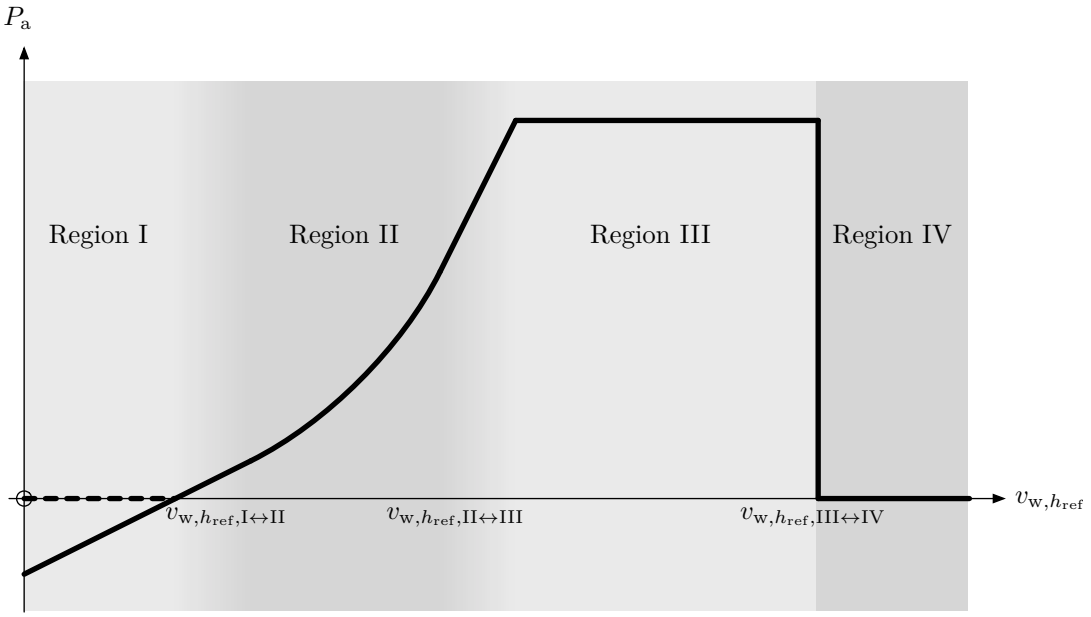

Figure 2.16: Power curve of a drag power kite with four main regions. (The borders between Regions I to III are drawn blurred, because Regions I and III are further subdivided, as derived below.)

Region IV: In the forth region, at storm $v_{\mathrm{w},h_\mathrm{ref},\mathrm{III}\leftrightarrow\mathrm{IV}} \leq v_{\mathrm{w},h_\mathrm{ref}} \leq \infty$, the wind is too strong for safe operation and hence the power plant is turned off (i.e. the kite is landed).

Mathematically, many more (sub-) regions are possible, e.g. a region in which different lower and upper bounds of a state or actuation are active, but here only meaningful (sub-) regions are considered. For that, certain conditions on the minimal, maximal, and nominal values are derived, which is expected for the preferred solution as mentioned in Sect 2.7.1. The equations for each region are derived in the following. The simplest case, Region II, where no bounds are effective, is used as starting point. From thereon, the other regions are derived and, depending at what wind speed which bound becomes active, Regions I and III are further subdivided into meaningful subregions. Finally, feasibility conditions for the minimal, maximal, and nominal values for the states and actuations are formulated to obtain the derived power curve.

In the following, the notation $\#_i$ is used for actuations, system states, and intermediate/derived values for the different regions (e.g. $i = \mathrm{II}$), transitions between regions (e.g. $i = \mathrm{I} \leftrightarrow \mathrm{II}$), or nominal values (e.g. $i = \mathrm{n}$). Only the important or representative results are derived explicitly, i.e. e.g. the total lift coefficient $C_{\mathrm{L},i}$ may be derived for a region i, but the derivation of $c_{\mathrm{L},i}$ from (2.39) and (2.15) solved as $c_{\mathrm{L},i} = (1+2/\mathit{AR})C_{\mathrm{L},i}$ may not be shown explicitly. Similarly, only the derivation of the resulting aerodynamic power P_a is shown, while from thereon the electrical power and all other powers are readily given through (2.145)–(2.156).

2.7.4 Region II

Region II is defined by no activated bounds, for which the result of the optimization is readily given similar to Loyd's result [13]:

Theorem 2.5 (Maximum Power Without Bounds): *If Assumptions 2.1–2.7, 2.10–2.16, 2.33, and 2.34 apply, and if no bounds are effective, then the solution of (2.164)–(2.170) is*

$$\boldsymbol{u}^* =: \boldsymbol{u}_{\mathrm{II}} = \begin{pmatrix} C_{\mathrm{D,rot,II}} \\ c_{\mathrm{L,II}} \\ C_{\mathrm{D,k,a,II}} \\ \Delta\varphi_{\mathrm{a,II}} \\ \Delta\vartheta_{\mathrm{a,II}} \end{pmatrix} = \begin{pmatrix} \frac{1}{2}C_{\mathrm{D,eq,n}} \\ c_{\mathrm{L,n}} \\ 0 \\ 0 \\ 0 \end{pmatrix} \tag{2.180}$$

$$\boldsymbol{x}^* =: \boldsymbol{x}_{\mathrm{II}} = \begin{pmatrix} F_{||,\mathrm{II}} \\ v_{\mathrm{a,II}} \\ P_{\mathrm{a,II}} \end{pmatrix} = \begin{pmatrix} \frac{4}{9}\frac{1}{2}\rho\cos^2(\varphi_{\mathrm{n}})\cos^2(\vartheta_{\mathrm{n}})v_{\mathrm{w}}^2\frac{C_{\mathrm{L,n}}^3}{C_{\mathrm{D,eq,n}}^2} \\ \frac{3}{2}\cos(\varphi_{\mathrm{n}})\cos(\vartheta_{\mathrm{n}})v_{\mathrm{w}}\frac{C_{\mathrm{L,n}}}{C_{\mathrm{D,eq,n}}} \\ \frac{4}{27}\frac{1}{2}\rho\cos^3(\varphi_{\mathrm{n}})\cos^3(\vartheta_{\mathrm{n}})\,v_{\mathrm{w}}^3 A\frac{C_{\mathrm{L,n}}^3}{C_{\mathrm{D,eq,n}}^2} \end{pmatrix}, \tag{2.181}$$

with optimal actuations $\boldsymbol{u}_{\mathrm{II}} := \boldsymbol{u}^*$ and resulting states $\boldsymbol{x}_{\mathrm{II}} := \boldsymbol{x}^*$, where $C_{\mathrm{D,eq,n}}$ and $C_{\mathrm{L,n}}$ are the nominal equivalent drag coefficient and the nominal total lift coefficient, respectively, which occur at $C_{\mathrm{D,k,a}} = 0$ and $c_{\mathrm{L}} = c_{\mathrm{L,n}}$.

Proof. As no bounds are effective, the optimal rotor drag coefficient is determined straightforwardly by maximizing (2.177) w.r.t. the rotor drag coefficient

$$\begin{aligned}
0 &= \frac{\mathrm{d}P_{\mathrm{a}}(C_{\mathrm{D,rot}} = C_{\mathrm{D,rot}}^*)}{\mathrm{d}C_{\mathrm{D,rot}}^*} \\
&= \frac{\mathrm{d}}{\mathrm{d}C_{\mathrm{D,rot}}^*}\frac{1}{2}\rho\cos^3(\varphi)\cos^3(\vartheta)v_{\mathrm{w}}^3 A\frac{C_{\mathrm{L}}^3}{(C_{\mathrm{D,eq}} + C_{\mathrm{D,rot}}^*)^3}C_{\mathrm{D,rot}}^* \\
&= \frac{\mathrm{d}}{\mathrm{d}C_{\mathrm{D,rot}}^*}C_{\mathrm{D,rot}}^*(C_{\mathrm{D,eq}} + C_{\mathrm{D,rot}}^*)^{-3} \\
&= 1(C_{\mathrm{D,eq}} + C_{\mathrm{D,rot}}^*)^{-3} + C_{\mathrm{D,rot}}^*(-3)(C_{\mathrm{D,eq}} + C_{\mathrm{D,rot}}^*)^{-4} \\
&= \frac{1}{(C_{\mathrm{D,eq}} + C_{\mathrm{D,rot}}^*)^3} - \frac{3C_{\mathrm{D,rot}}^*}{(C_{\mathrm{D,eq}} + C_{\mathrm{D,rot}}^*)^4} \\
&= \frac{C_{\mathrm{D,eq}} + C_{\mathrm{D,rot}}^*}{(C_{\mathrm{D,eq}} + C_{\mathrm{D,rot}}^*)^4} - \frac{3C_{\mathrm{D,rot}}^*}{(C_{\mathrm{D,eq}} + C_{\mathrm{D,rot}}^*)^4} \\
&= \frac{C_{\mathrm{D,eq}} - 2C_{\mathrm{D,rot}}^*}{(C_{\mathrm{D,eq}} + C_{\mathrm{D,rot}}^*)^4} \\
&= C_{\mathrm{D,eq}} - 2C_{\mathrm{D,rot}}^* \\
\Leftrightarrow C_{\mathrm{D,rot}}^* &= \frac{1}{2}C_{\mathrm{D,eq}}
\end{aligned} \tag{2.182}$$

for which the aerodynamic power (2.177) becomes

$$\begin{aligned}
P_{\mathrm{a}}^* &= \frac{1}{2}\rho\cos^3(\varphi)\cos^3(\vartheta)v_{\mathrm{w}}^3 A\frac{C_{\mathrm{L}}^3}{(C_{\mathrm{D,eq}} + C_{\mathrm{D,rot}}^*)^3}C_{\mathrm{D,rot}}^* \\
&= \frac{1}{2}\rho\cos^3(\varphi)\cos^3(\vartheta)v_{\mathrm{w}}^3 A\frac{C_{\mathrm{L}}^3}{\left(C_{\mathrm{D,eq}} + \frac{1}{2}C_{\mathrm{D,eq}}\right)^3}\frac{1}{2}C_{\mathrm{D,eq}} \\
&= \frac{1}{2}\rho\cos^3(\varphi)\cos^3(\vartheta)v_{\mathrm{w}}^3 A\frac{C_{\mathrm{L}}^3}{\frac{3^3}{2^3}C_{\mathrm{D,eq}}^3}\frac{1}{2}C_{\mathrm{D,eq}} \\
&= \frac{4}{27}\frac{1}{2}\rho\cos^3(\varphi)\cos^3(\vartheta)\,v_{\mathrm{w}}^3 A\frac{C_{\mathrm{L}}^3}{C_{\mathrm{D,eq}}^2}.
\end{aligned} \tag{2.183}$$

Eq. (2.183) is maximized w.r.t. the actuated drag coefficient and increase of the effective azimuth and elevation angles, in view of (2.11) and (2.33) as well as (2.168) and (2.169), by

$$C_{\mathrm{D,k,a,II}} := C^*_{\mathrm{D,k,a}} = 0 \tag{2.184}$$

$$\Delta\varphi_{\mathrm{a,II}} := \Delta\varphi^*_{\mathrm{a}} = 0 \tag{2.185}$$

$$\Delta\vartheta_{\mathrm{a,II}} := \Delta\vartheta^*_{\mathrm{a}} = 0. \tag{2.186}$$

The remaining actuation, the optimal airfoil lift coefficient, is considered to be defined as the nominal airfoil lift coefficient,

$$c_{\mathrm{L,II}} := c^*_{\mathrm{L}} =: c_{\mathrm{L,n}}. \tag{2.187}$$

Finding the *optimal* value of $c_{\mathrm{L,n}}$ is not trivial and likely impossible analytically. The nominal airfoil lift coefficient $c_{\mathrm{L,n}}$ is not considered as an actuation that is to be further optimized within the power curve optimization, but is considered as a power plant *dimensioning parameter*. As mentioned in Sect. 2.7.1, finding the optimal dimensioning parameters is left to a superimposed parameter optimization, which therefore includes e.g. the actual choice of the airfoil. Similarly, further dimensioning parameters include the nominal effective elevation ϑ_{n} which may be optimized within a superimposed optimization.

With the in Region II constant airfoil lift coefficient (2.187) and constant actuated drag coefficient (2.184), a nominal total lift coefficient and a nominal equivalent drag coefficient as well as a (first) nominal rotor drag coefficient (a second nominal rotor drag coefficient is introduced later) with (2.182) can be defined by

$$C_{\mathrm{L,n}} := C_{\mathrm{L,II}}, \tag{2.188}$$

$$C_{\mathrm{D,eq,n}} := C_{\mathrm{D,eq,II}}, \tag{2.189}$$

$$C_{\mathrm{D,rot,n(1)}} := C_{\mathrm{D,rot,II}} = \frac{1}{2} C_{\mathrm{D,eq,II}} = \frac{1}{2} C_{\mathrm{D,eq,n}}. \tag{2.190}$$

Substituting the obtained optimal actuations (2.184)–(2.187) and (2.190) into the optimal power equation (2.183), airflow speed equation (2.176), and the parallel force equation (2.179) gives

$$P_{\mathrm{a,II}} = \frac{4}{27}\frac{1}{2}\rho \cos^3(\varphi_{\mathrm{n}}) \cos^3(\vartheta_{\mathrm{n}})\, v_{\mathrm{w}}^3 A \frac{C_{\mathrm{L,n}}^3}{C_{\mathrm{D,eq,n}}^2}, \tag{2.191}$$

$$\begin{aligned} v_{\mathrm{a,II}} &= \cos(\varphi_{\mathrm{n}}) \cos(\vartheta_{\mathrm{n}}) v_{\mathrm{w}} \frac{C_{\mathrm{L,n}}}{C_{\mathrm{D,eq,n}} + C_{\mathrm{D,rot,n(1)}}} \\ &= \cos(\varphi_{\mathrm{n}}) \cos(\vartheta_{\mathrm{n}}) v_{\mathrm{w}} \frac{C_{\mathrm{L,n}}}{C_{\mathrm{D,eq,n}} + \frac{1}{2} C_{\mathrm{D,eq,n}}} \\ &= \frac{2}{3} \cos(\varphi_{\mathrm{n}}) \cos(\vartheta_{\mathrm{n}}) v_{\mathrm{w}} \frac{C_{\mathrm{L,n}}}{C_{\mathrm{D,eq,n}}}, \end{aligned} \tag{2.192}$$

$$\begin{aligned} F_{||,\mathrm{II}} &= \frac{1}{2}\rho \cos^2(\varphi_{\mathrm{n}}) \cos^2(\vartheta_{\mathrm{n}}) v_{\mathrm{w}}^2 A \frac{C_{\mathrm{L,n}}^3}{(C_{\mathrm{D,eq,n}} + C_{\mathrm{D,rot,n(1)}})^2} \\ &= \frac{1}{2}\rho \cos^2(\varphi_{\mathrm{n}}) \cos^2(\vartheta_{\mathrm{n}}) v_{\mathrm{w}}^2 A \frac{C_{\mathrm{L,n}}^3}{(C_{\mathrm{D,eq,n}} + \frac{1}{2} C_{\mathrm{D,eq,n}})^2} \\ &= \frac{1}{2}\rho \cos^2(\varphi_{\mathrm{n}}) \cos^2(\vartheta_{\mathrm{n}}) v_{\mathrm{w}}^2 A \frac{C_{\mathrm{L,n}}^3}{\frac{3^2}{2^2} C_{\mathrm{D,eq,n}}^2} \end{aligned}$$

$$= \frac{4}{9}\frac{1}{2}\rho\cos^2(\varphi_\mathrm{n})\cos^2(\vartheta_\mathrm{n})v_\mathrm{w}^2 A\frac{C_\mathrm{L,n}^3}{C_\mathrm{D,eq,n}^2}. \tag{2.193}$$

■

The expression

$$\zeta_{\mathrm{n}(1)} := \frac{4}{27}\cos^3(\varphi_\mathrm{n})\cos^3(\vartheta_\mathrm{n})\frac{C_\mathrm{L,n}^3}{C_\mathrm{D,eq,n}^2} \tag{2.194}$$

in (2.191) can be defined as (first nominal) power harvesting factor and can be used as a figure of merit for a kite design [18].

Note also that the equations are given in the form $\# = \mathrm{f}(v_\mathrm{w})$ instead of $\# = \mathrm{f}(v_{\mathrm{w},h_\mathrm{ref}})$. However, the kite's altitude h is constant because tether length L_te and effective elevation ϑ (and obviously also the tower height h_to) are constant, with which also f_shear in (2.158) and (2.159) is constant. Therefore, conversions from $\# = \mathrm{f}(v_\mathrm{w})$ to $\# = \mathrm{f}(v_{\mathrm{w},h_\mathrm{ref}})$ are trivial and, for sake of brevity, are neither written here nor for the equations of the other regions derived in the following, unless the altitude h changes.

2.7.5 Region I

Derivation of the Optimal Result

For low wind speeds, the parallel force (2.193) is low and possibly the condition (2.26) is not fulfilled unless the actuations are altered. Therefore, Region I is defined by the force constraint (2.25). Inserting that constraint $F_{||} = F_{||,\mathrm{min}}$ into (2.179) with $\varphi = \varphi_\mathrm{I}$, $\vartheta = \vartheta_\mathrm{I}$, $C_\mathrm{L} = C_\mathrm{L,I}$, $C_\mathrm{D,eq} = C_\mathrm{D,eq,I}$, and $C_\mathrm{D,rot} = C_\mathrm{D,rot,I}$, one obtains

$$F_{||,\mathrm{min}} =: F_{||,\mathrm{I}} = \frac{1}{2}\rho\cos^2(\varphi_\mathrm{I})\cos^2(\vartheta_\mathrm{I})v_\mathrm{w}^2 A\frac{C_\mathrm{L,I}^3}{(C_\mathrm{D,eq,I}+C_\mathrm{D,rot,I})^2}. \tag{2.195}$$

As the wind speed decreases $v_\mathrm{w} \to 0$, factors which include actuations on the right hand side of (2.195) must be increased and/or divisors must be decreased, because the left hand side of (2.195) is a constant.

Obviously, φ_I and ϑ_I as well as $C_\mathrm{D,k,a,I}$ as part of $C_\mathrm{D,eq,I}$ cannot further be decreased compared to what is set in Region II, cf. (2.184)–(2.186). Therefore it is left at

$$C_\mathrm{D,k,a,I} = 0 \tag{2.196}$$
$$\Delta\varphi_\mathrm{a,I} = 0 \tag{2.197}$$
$$\Delta\vartheta_\mathrm{a,I} = 0 \tag{2.198}$$

and the effective azimuth and elevation stay at their nominal values, cf. (2.168) and (2.169). Moreover, the equivalent drag $C_\mathrm{D,eq,I}$ could only be decreased, if the induced drag is decreased via decreasing $c_\mathrm{L,I}$ and thus decreasing $C_\mathrm{L,I}$, cf. Sect. 2.2.1. However, as $C_\mathrm{L,I}^3$ is also a factor in (2.195), this approach is relatively ineffective in decreasing the term $C_\mathrm{L,I}^3/(C_\mathrm{D,eq,I}+C_\mathrm{D,rot,I})^2$. The most effective actuation to fulfill (2.195) is $C_\mathrm{D,rot,I}$, which particularly can also be negative

(propeller/motor mode). The required $C_{\mathrm{D,rot,I}}$ is given by solving (2.195) for $C_{\mathrm{D,rot,I}}$,

$$\begin{aligned}
(C_{\mathrm{D,eq,I}} + C_{\mathrm{D,rot,I}})^2 &= \frac{1}{2}\rho \cos^2(\varphi_\mathrm{n}) \cos^2(\vartheta_\mathrm{n}) v_\mathrm{w}^2 A \frac{C_{\mathrm{L,I}}^3}{F_{||,\mathrm{min}}} \\
C_{\mathrm{D,eq,I}} + C_{\mathrm{D,rot,I}} &= \sqrt{\frac{1}{2}\rho \cos^2(\varphi_\mathrm{n}) \cos^2(\vartheta_\mathrm{n}) v_\mathrm{w}^2 A \frac{C_{\mathrm{L,I}}^3}{F_{||,\mathrm{min}}}} \\
\Leftrightarrow C_{\mathrm{D,rot,I}} &= \sqrt{\frac{1}{2}\rho \cos^2(\varphi_\mathrm{n}) \cos^2(\vartheta_\mathrm{n}) v_\mathrm{w}^2 A \frac{C_{\mathrm{L,I}}^3}{F_{||,\mathrm{min}}}} - C_{\mathrm{D,eq,I}}.
\end{aligned} \tag{2.199}$$

With $F_\mathrm{a} = F_{||,\mathrm{min}}$ and the above derived actuations for Region I inserted into (2.22), the power $P_\mathrm{a} = P_{\mathrm{a,I}}$ then becomes

$$\begin{aligned}
P_{\mathrm{a,I}} &= F_{||,\mathrm{min}} \cos(\varphi_\mathrm{n}) \cos(\vartheta_\mathrm{n}) v_\mathrm{w} \frac{C_{\mathrm{D,rot,I}}}{C_{\mathrm{D,eq,I}} + C_{\mathrm{D,rot,I}}} \\
&= F_{||,\mathrm{min}} \cos(\varphi_\mathrm{n}) \cos(\vartheta_\mathrm{n}) v_\mathrm{w} \frac{\sqrt{\frac{1}{2}\rho \cos^2(\varphi_\mathrm{n}) \cos^2(\vartheta_\mathrm{n}) v_\mathrm{w}^2 A \frac{C_{\mathrm{L,I}}^3}{F_{||,\mathrm{min}}}} - C_{\mathrm{D,eq,I}}}{\sqrt{\frac{1}{2}\rho \cos^2(\varphi_\mathrm{n}) \cos^2(\vartheta_\mathrm{n}) v_\mathrm{w}^2 A \frac{C_{\mathrm{L,I}}^3}{F_{||,\mathrm{min}}}}} \\
&= F_{||,\mathrm{min}} \cos(\varphi_\mathrm{n}) \cos(\vartheta_\mathrm{n}) v_\mathrm{w} \left(1 - \frac{C_{\mathrm{D,eq,I}}}{\sqrt{\frac{1}{2}\rho \cos^2(\varphi_\mathrm{n}) \cos^2(\vartheta_\mathrm{n}) v_\mathrm{w}^2 A \frac{C_{\mathrm{L,I}}^3}{F_{||,\mathrm{min}}}}} \right).
\end{aligned} \tag{2.200}$$

For the remaining unknown actuation, which is the optimal airfoil lift coefficient in Region I, the following assumption is imposed in view of (2.200):

Assumption 2.36: *With a certain defined parallel force $F_{||} = \mathrm{const.}$, the aerodynamic power with nominal airfoil lift coefficient $c_\mathrm{L} = c_{\mathrm{L,n}}$ is approximately the same as the aerodynamic power with the optimal airfoil lift coefficient, i.e.*

$$c_{\mathrm{L,n}} \approx c_\mathrm{L}^* = \arg\max_{c_\mathrm{L}} P_\mathrm{a} \quad \text{s.t.} \quad F_{||} = \mathrm{const.} \tag{2.201}$$

This assumption is justified by the following rationale: (i) To maximize $P_{\mathrm{a,I}}$ (2.200) w.r.t. $c_{\mathrm{L,I}}$, the term $C_{\mathrm{D,eq,I}}/\sqrt{\frac{1}{2}\rho \cos^2(\varphi_\mathrm{n}) \cos^2(\vartheta_\mathrm{n}) v_\mathrm{w}^2 A C_{\mathrm{L,I}}^3 / F_{||,\mathrm{min}}}$ must be minimized. However, similarly as above, that term's sensitivity on $c_{\mathrm{L,I}}$ is rather low, because, with all coefficients written out (cf. Sect. 2.2.1), the denominator has the structure $c_{\mathrm{L,I}}^2 + \mathrm{const.}$ due to the induced drag while the numerator has the structure ${c_{\mathrm{L,I}}}^{3/2}$. (ii) Turns in the figure eight or circular flight path are enabled by rolling the kite which generates a sideward force component proportional to c_L and the sine of the roll angle. To hold the nominal azimuth φ_n and the nominal elevation ϑ_n, i.e. to hold (2.197) and (2.198), while c_L is reduced, the roll angle would need to be increased. This might not be possible for safety reasons (there is some maximum allowed or nominal roll angle) and it reduces the in (2.176) effective lift and thereby reduces the power, cf. Sect. 2.1.1. Therefore, a reduction of c_L can lead to a significantly lower power than expected from the here presented simplified model (2.200). (iii) Not least, Assumption 2.36 allows a simple power curve analysis and control implementation. Otherwise, first the lift coefficient might be altered, but sooner or later, at some wind speed relatively close to the wind speed of the border of Region I and II, also the rotor drag coefficient would need to be reduced anyways once the minimum airfoil lift coefficient is reached.

With Assumption 2.36, the airfoil lift coefficient in Region I is the same as in Region II and constant at

$$c_{\mathrm{L,I}} = c_{\mathrm{L,n}}, \tag{2.202}$$

hence, the equivalent drag coefficient stays at

$$C_{\mathrm{D,eq,I}} = C_{\mathrm{D,eq,n}} \tag{2.203}$$

and (2.199) becomes

$$C_{\mathrm{D,rot,I}} = \sqrt{\frac{1}{2}\rho \cos^2(\varphi_{\mathrm{n}}) \cos^2(\vartheta_{\mathrm{n}}) v_{\mathrm{w}}^2 A \frac{C_{\mathrm{L,n}}^3}{F_{||,\mathrm{min}}}} - C_{\mathrm{D,eq,n}}. \tag{2.204}$$

Inserting $C_{\mathrm{L}} = C_{\mathrm{L,n}}$ and $F_{||} = F_{||,\mathrm{min}}$ into (2.178) and solving for $v_{\mathrm{a}} = v_{\mathrm{a,I}}$, the airflow speed in Region I is given by

$$F_{||,\mathrm{min}} = \frac{1}{2}\rho v_{\mathrm{a,I}}^2 A C_{\mathrm{L,n}} \tag{2.205}$$

$$\Leftrightarrow v_{\mathrm{a,min}} =: v_{\mathrm{a,I}} = \sqrt{\frac{F_{||,\mathrm{min}}}{\frac{1}{2}\rho A C_{\mathrm{L,n}}}}, \tag{2.206}$$

which also defines the minimum airflow speed.

Alternative Expression of the Rotor Drag and Aerodynamic Power Equations of Region I

The rotor drag coefficient and the power in Region I can also be expressed via $v_{\mathrm{a,min}}$: Substituting (2.205) with $v_{\mathrm{a,I}} = v_{\mathrm{a,min}}$ into (2.204) yields

$$\begin{aligned} C_{\mathrm{D,rot,I}} &= \sqrt{\frac{1}{2}\rho \cos^2(\varphi_{\mathrm{n}}) \cos^2(\vartheta_{\mathrm{n}}) v_{\mathrm{w}}^2 A \frac{C_{\mathrm{L,n}}^3}{\frac{1}{2}\rho v_{\mathrm{a,min}}^2 A C_{\mathrm{L,n}}}} - C_{\mathrm{D,eq,n}} \\ &= \sqrt{\cos^2(\varphi_{\mathrm{n}}) \cos^2(\vartheta_{\mathrm{n}}) v_{\mathrm{w}}^2 \frac{C_{\mathrm{L,n}}^2}{v_{\mathrm{a,min}}^2}} - C_{\mathrm{D,eq,n}} \\ &= \frac{\cos(\varphi_{\mathrm{n}}) \cos(\vartheta_{\mathrm{n}}) v_{\mathrm{w}}}{v_{\mathrm{a,min}}} C_{\mathrm{L,n}} - C_{\mathrm{D,eq,n}}, \end{aligned} \tag{2.207}$$

and substituting (2.207) into (2.18) with $C_{\mathrm{D,rot}} = C_{\mathrm{D,rot,I}}$, $P_{\mathrm{a}} = P_{\mathrm{a,I}}$, and $v_{\mathrm{a}} = v_{\mathrm{a,min}}$ yields

$$\begin{aligned} P_{\mathrm{a,I}} &= \frac{1}{2}\rho v_{\mathrm{a,min}}^3 A C_{\mathrm{D,rot,I}} \\ &= \frac{1}{2}\rho v_{\mathrm{a,min}}^3 A \left(\frac{\cos(\varphi_{\mathrm{n}}) \cos(\vartheta_{\mathrm{n}})\, v_{\mathrm{w}}}{v_{\mathrm{a,min}}} C_{\mathrm{L,n}} - C_{\mathrm{D,eq,n}} \right). \end{aligned} \tag{2.208}$$

Subdivision of Region I

Region I can be divided into Region I(a), where the kite is propelled by the rotors or grounded (i.e. the power is negative or zero), and Region I(b), where a lower than optimal rotor drag coefficient (2.190), but still above zero and thus with positive power, is applied. Nevertheless, the equations for both, Region I(a) and (b), are identical, because the starting point of the derivation (2.195) holds for the entire Region I.

Note on Bounds/Feasibility

So far, the lower bounds of force and airflow speed are derived, and thus, apart from the power, all lower bounds of the state variables are known. Moreover, actuated drag and actuated increase of azimuth and elevation angles are at their lower bound, while the airfoil lift coefficient is at its upper bound, and thus, apart from the rotor drag coefficient, all actuations are at a known bound. The two remaining lower bounds of power (i.e. upper bound of demanded power) and rotor drag coefficient occur at $v_\mathrm{w} = 0$ and for hovering. It is ensured that those bounds are reachable by a-posteriori feasibility conditions, defined below in Sect. 2.7.14. With that, all (meaningful) possibilities of low-bound conditions $\underline{\boldsymbol{x}}$ are covered.

2.7.6 Transition between Region I and II

The wind speed of the border between Region I and Region II, $v_{\mathrm{w,I}\leftrightarrow\mathrm{II}}$, can be derived by determining at what wind speed the minimum airflow speed within Region II is achieved, i.e. inserting $v_\mathrm{a,II} = v_\mathrm{a,min}$ into (2.192) and solving for $v_\mathrm{w} = v_{\mathrm{w,I}\leftrightarrow\mathrm{II}}$, which is

$$\begin{aligned} v_\mathrm{a,min} &= \frac{2}{3}\cos(\varphi_\mathrm{n})\cos(\vartheta_\mathrm{n}) v_{\mathrm{w,I}\leftrightarrow\mathrm{II}} \frac{C_\mathrm{L,n}}{C_\mathrm{D,eq,n}} \\ \Leftrightarrow v_{\mathrm{w,I}\leftrightarrow\mathrm{II}} &= \frac{3}{2}\frac{v_\mathrm{a,min}}{\cos(\varphi_\mathrm{n})\cos(\vartheta_\mathrm{n})}\frac{C_\mathrm{D,eq,n}}{C_\mathrm{L,n}}. \end{aligned} \tag{2.209}$$

Note again, as mentioned at the end of Sect. 2.7.4, the wind speed in the reference altitude at the border between Region I and Region II, $v_{\mathrm{w},h_\mathrm{ref},\mathrm{I}\leftrightarrow\mathrm{II}}$, can be readily derived with the known shear factor f_shear. The same holds true for all other transition wind speeds derived in the following, unless the altitude h changes.

2.7.7 Transition between Region I(a) and I(b)

Moreover, the cut-in wind speed, which is the wind speed at which the power becomes positive and divides Region I(a) and I(b), $v_\mathrm{w,cut\text{-}in} := v_{\mathrm{w,I(a)}\leftrightarrow\mathrm{I(b)}}$, can be derived by setting $P_\mathrm{a,I} = 0$ in (2.208) and solving for $v_\mathrm{w} = v_{\mathrm{w,I(a)}\leftrightarrow\mathrm{I(b)}} =: v_\mathrm{w,cut\text{-}in}$, which becomes

$$\begin{aligned} 0 &= \frac{1}{2}\rho v_\mathrm{a,min}^3 A \left(\frac{\cos(\varphi_\mathrm{n})\cos(\vartheta_\mathrm{n})\, v_{\mathrm{w,I(a)}\leftrightarrow\mathrm{I(b)}}}{v_\mathrm{a,min}} C_\mathrm{L,n} - C_\mathrm{D,eq,n} \right) \\ &= \cos(\varphi_\mathrm{n})\cos(\vartheta_\mathrm{n})\, v_{\mathrm{w,I(a)}\leftrightarrow\mathrm{I(b)}} C_\mathrm{L,n} - v_\mathrm{a,min} C_\mathrm{D,eq,n} \\ \Leftrightarrow v_\mathrm{w,cut\text{-}in} := v_{\mathrm{w,I(a)}\leftrightarrow\mathrm{I(b)}} &= \frac{v_\mathrm{a,min}}{\cos(\varphi_\mathrm{n})\cos(\vartheta_\mathrm{n})}\frac{C_\mathrm{D,eq,n}}{C_\mathrm{L,n}}. \end{aligned} \tag{2.210}$$

Note that

$$v_\mathrm{w,cut\text{-}in} := v_{\mathrm{w,I(a)}\leftrightarrow\mathrm{I(b)}} = \frac{2}{3} v_{\mathrm{w,I}\leftrightarrow\mathrm{II}}. \tag{2.211}$$

2.7.8 Identification of Main Subregions of Region III

In Region III, some upper bounds of states $\overline{\boldsymbol{x}}$ and some bounds of actuations $\boldsymbol{u}$ are reached. To identify the meaningful order at what wind speed which bound becomes active and thus meaningful subregions, firstly, the bounds of the control actuations $\boldsymbol{u}$ are considered to define the nominal values of the actuators with which the state bounds (i.e. the nominal states) are achievable. It is again ensured that those bounds are reachable in a later step, e.g. by a-posteriori feasibility

conditions, defined below in Sect. 2.7.14, and therefore the actuations $\boldsymbol{u}$ can be considered to be always within their bounds. Secondly, any order of the constraints of $\boldsymbol{x}$ w.r.t. the wind speed is possible with a large number of total possibilities for subregions from a mathematical standpoint, including that two or more bounds become active at the same wind speed or that some bounds become active at a wind speed but become inactive again at a higher wind speed. However, meaningful main subregions of Region III can be derived with the following rationale:

- For increasing wind speeds, $P_{\mathrm{a,max}} =: P_{\mathrm{a,n}}$ is reached last, because when $P_{\mathrm{a,max}} =: P_{\mathrm{a,n}}$ there would be no benefit (e.g. no higher yield) if v_{a} or $F_{||}$ are further increased. On the contrary, if v_{a} was further increased, the noise emissions would be increased or faster control actions would be required, and if $F_{||}$ was further increased, the kite and the tether would need to sustain a higher force, i.e. the tether would need to be thicker, leading to a higher tether drag which in turn would reduce the power in Region II. For the same reason, the power stays at $P_{\mathrm{a,max}} =: P_{\mathrm{a,n}}$ at high wind speeds, while airflow speed v_{a} and force $F_{||}$ are constant or may decrease.

  Therefore, for increasing wind speeds starting from Region II with no constraints up to the wind speed at which $P_{\mathrm{a,max}} =: P_{\mathrm{a,n}}$ is reached, the meaningful possibilities are limited to:

  A: force bound wind speed $<$ airflow speed bound wind speed $<$ power bound wind speed
  B: force bound wind speed $=$ airflow speed bound wind speed $<$ power bound wind speed
  C: force bound wind speed $<$ airflow speed bound wind speed $=$ power bound wind speed
  D: force bound wind speed $=$ airflow speed bound wind speed $=$ power bound wind speed
  E: airflow speed bound wind speed $<$ force bound wind speed $<$ power bound wind speed
  F: airflow speed bound wind speed $=$ force bound wind speed $<$ power bound wind speed
  G: airflow speed bound wind speed $<$ force bound wind speed $=$ power bound wind speed
  H: airflow speed bound wind speed $=$ force bound wind speed $=$ power bound wind speed

  Cases F and H are only written for sake of completeness, but can be dropped as they are identical to Cases B and D, respectively.
- A region, in which only the airflow speed limit is reached, but the force is further increased with increasing wind speeds is not possible, because the maximum lift coefficient is already achieved in Region II and therefore all terms in (2.178) would then be constant. This excludes Cases E and G.
- A region, in which the force limit is reached, but the airflow speed and power are further increased with increasing wind speeds, would require that the lift coefficient is reduced, cf. (2.178). This is already evaluated as not meaningful or hardly possible through Assumption 2.36 and its justification. Therefore, Cases A and C can also be excluded, and the airflow speed limit $v_{\mathrm{a,max}} =: v_{\mathrm{a,n}}$ and the force limit $F_{||,\mathrm{max}} =: F_{||,\mathrm{n}}$ are reached at the same wind speed.
- The two remaining Cases B and D can be combined to the only left possible case:

  B/D: force bound wind speed $=$ airflow speed bound wind speed $\leq$ power bound wind speed

Based on that, Region III is divided into two main subregions:

Region III(a): In the first part of Region III, airflow speed and force are at the upper bound, while the power increases with the wind speed.

Region III(b): In the second part of Region III, the power is at the upper bound, while airflow speed and force are constant, possibly at a bound, or are decreasing.

However, Region III(a) may also have zero width (Case D).

2.7.9 Region III(a)

Region III(a) is defined by the force constraint $F_{||,\mathrm{III(a)}} = F_{||,\max} =: F_{||,\mathrm{n}}$ and simultaneously the airflow speed constraint $v_{\mathrm{a,III(a)}} = v_{\mathrm{a,max}} =: v_{\mathrm{a,n}}$. This combination of force and airflow speed constraint is exactly the same as in Region I. As additionally the region next to Region I and Region III(a) is Region II, all derived equations for Region I from Sect. 2.7.5 can be transferred to Region III(a), i.e. for the actuations

$$C_{\mathrm{D,k,a,III(a)}} = 0 \tag{2.212}$$

$$\Delta\varphi_{\mathrm{a,III(a)}} = 0 \tag{2.213}$$

$$\Delta\vartheta_{\mathrm{a,III(a)}} = 0 \tag{2.214}$$

$$c_{\mathrm{L,III(a)}} = c_{\mathrm{L,n}} \tag{2.215}$$

$$C_{\mathrm{D,rot,III(a)}} = \frac{\cos(\varphi_{\mathrm{n}})\cos(\vartheta_{\mathrm{n}})v_{\mathrm{w}}}{v_{\mathrm{a,n}}} C_{\mathrm{L,n}} - C_{\mathrm{D,eq,n}} \tag{2.216}$$

and for the states

$$F_{||,\mathrm{n}} := F_{||,\max} = F_{||,\mathrm{III(a)}} = \frac{1}{2}\rho v_{\mathrm{a,n}}^2 A C_{\mathrm{L,n}} \tag{2.217}$$

$$v_{\mathrm{a,n}} := v_{\mathrm{a,max}} = v_{\mathrm{a,III(a)}} = \frac{F_{\mathrm{a,n}}}{\frac{1}{2}\rho A C_{\mathrm{L,n}}} \tag{2.218}$$

$$P_{\mathrm{a,III(a)}} = \frac{1}{2}\rho v_{\mathrm{a,n}}^3 A \left(\frac{\cos(\varphi_{\mathrm{n}})\cos(\vartheta_{\mathrm{n}})\, v_{\mathrm{w}}}{v_{\mathrm{a,n}}} C_{\mathrm{L,n}} - C_{\mathrm{D,eq,n}} \right). \tag{2.219}$$

Identical to Region I, all actuations and states are constant w.r.t. v_{w}, except for the rotor drag coefficient and the power which both increase linearly with v_{w}.

2.7.10 Transition between Region II and III(a)

Similarly, the equations for the transition between Region I and Region II from Sect. 2.7.6 can be transferred to the transition between Region II and Region III(a) as

$$v_{\mathrm{w,n(1)}} := v_{\mathrm{w,II\leftrightarrow III(a)}} = \frac{3}{2} \frac{v_{\mathrm{a,n}}}{\cos(\varphi_{\mathrm{n}})\cos(\vartheta_{\mathrm{n}})} \frac{C_{\mathrm{D,eq,n}}}{C_{\mathrm{L,n}}}. \tag{2.220}$$

As this transition can also be called “first power point”, the corresponding wind speed and power can also be called “first nominal wind speed” (defined by $v_{\mathrm{w,n(1)}}$) and “first nominal power”. The latter is determined by inserting $v_{\mathrm{a}} = v_{\mathrm{a,n}}$ and the first nominal rotor drag coefficient (2.190) into (2.18), which becomes

$$\begin{aligned} P_{\mathrm{a,n(1)}} := P_{\mathrm{a,II\leftrightarrow III(a)}} &= \frac{1}{2}\rho v_{\mathrm{a,n}}^3 A C_{\mathrm{D,rot,n(1)}} \\ &= \frac{1}{2}\rho v_{\mathrm{a,n}}^3 A \frac{1}{2} C_{\mathrm{D,eq,n}}. \end{aligned} \tag{2.221}$$

2.7.11 Transition between Region III(a) and III(b)

The transition between Region III(a) and III(b) can similarly be called “second power point”. This transition is defined by all state constraints

$$F_{||,\mathrm{III(a)\leftrightarrow III(b)}} = F_{||,\max} =: F_{||,\mathrm{n}} \tag{2.222}$$

$$v_{\mathrm{a,III(a)\leftrightarrow III(b)}} = v_{\mathrm{a,max}} =: v_{\mathrm{a,n}} \tag{2.223}$$

$$P_{\mathrm{a,III(a)\leftrightarrow III(b)}} = P_{\mathrm{a,max}} =: P_{\mathrm{a,n}} = P_{\mathrm{a,n(2)}} = r_{\mathrm{P}} P_{\mathrm{a,n(1)}}, \tag{2.224}$$

where $P_{\mathrm{a,n(2)}}$ is the "second nominal power", or just *the* nominal power $P_{\mathrm{a,n}}$, and $r_{\mathrm{P}} \geq 1$ is the ratio of the "second" and "the first nominal power".

The wind speed of this transition can be called accordingly "second nominal wind speed" and is given by inserting $P_{\mathrm{a,III(a)}} = P_{\mathrm{a,n(2)}}$ into (2.219) and solving for $v_{\mathrm{w}} = v_{\mathrm{w,n(2)}}$ which is

$$\begin{aligned}
P_{\mathrm{a,n(2)}} &= \frac{1}{2}\rho v_{\mathrm{a,n}}^3 A \left(\cos(\varphi_{\mathrm{n}}) \cos(\vartheta_{\mathrm{n}}) \frac{v_{\mathrm{w,n(2)}}}{v_{\mathrm{a,n}}} C_{\mathrm{L,n}} - C_{\mathrm{D,eq,n}} \right) \\
\Leftrightarrow \frac{P_{\mathrm{a,n(2)}}}{\frac{1}{2}\rho v_{\mathrm{a,n}}^3 A} &= \cos(\varphi_{\mathrm{n}}) \cos(\vartheta_{\mathrm{n}}) \frac{v_{\mathrm{w,n(2)}}}{v_{\mathrm{a,n}}} C_{\mathrm{L,n}} - C_{\mathrm{D,eq,n}} \\
\Leftrightarrow \frac{P_{\mathrm{a,n(2)}}}{\frac{1}{2}\rho v_{\mathrm{a,n}}^3 A} + C_{\mathrm{D,eq,n}} &= \cos(\varphi_{\mathrm{n}}) \cos(\vartheta_{\mathrm{n}}) \frac{v_{\mathrm{w,n(2)}}}{v_{\mathrm{a,n}}} C_{\mathrm{L,n}} \\
\Leftrightarrow v_{\mathrm{w,III(a)\leftrightarrow III(b)}} =: v_{\mathrm{w,n(2)}} &= \frac{\frac{P_{\mathrm{a,n(2)}}}{\frac{1}{2}\rho v_{\mathrm{a,n}}^3 A} + C_{\mathrm{D,eq,n}}}{\cos(\varphi_{\mathrm{n}}) \cos(\vartheta_{\mathrm{n}}) C_{\mathrm{L,n}}} v_{\mathrm{a,n}}.
\end{aligned} \tag{2.225}$$

2.7.12 Region III(b)

Region III(b) is defined by the power constraint

$$P_{\mathrm{a,III(b)}} = P_{\mathrm{a,n(2)}}. \tag{2.226}$$

Airflow speed and force are arbitrary, but within their bounds, and do not necessarily need to stay at their upper bounds. However, it is meaningful to let the airflow speed at its upper bound (nominal airflow speed) for several reasons: (i) If otherwise the airflow speed was reduced, the rotor drag coefficient $C_{\mathrm{D,rot}}$ would need to be increased to maintain the power (2.226), cf. (2.18), which leads to an increased induction factor a (2.100), which in turn leads to a reduced actuator disk efficiency η_{a} (2.108), and thus leads to a reduced electrical power. (ii) Fixed pitch rotors are considered (cf. Sect. 1.5) and thus an increased $C_{\mathrm{D,rot}}$ can only be achieved with increased rotor torques and decreased rotor speeds. However, the size, mass, and costs of an electrical machine are in principle defined by its nominal torque. Thus, a power limitation strategy with reducing airflow speed would require also larger, heavier, and more costly electrical machines (or gearboxes).

Therefore, the airflow speed in Region III(b) is left constant at

$$v_{\mathrm{a,III(b)}} = v_{\mathrm{a,max}} =: v_{\mathrm{a,n}}. \tag{2.227}$$

With $v_{\mathrm{a}} = v_{\mathrm{a,n}}$ in (2.18), the power in Region III(b), $P_{\mathrm{a}} = P_{\mathrm{a,III(b)}} = P_{\mathrm{a,n(2)}}$, can be expressed by

$$P_{\mathrm{a,III(b)}} = P_{\mathrm{a,n(2)}} = \frac{1}{2}\rho v_{\mathrm{a,n}}^3 A C_{\mathrm{D,rot,n(2)}} \tag{2.228}$$

where $C_{\mathrm{D,rot,n(2)}}$ is the second nominal rotor drag coefficient, or *the* nominal rotor drag coefficient $C_{\mathrm{D,rot,n}}$. This is the definition of $C_{\mathrm{D,rot,n(2)}}$, because $P_{\mathrm{a,n(2)}}$ is defined by (2.224), i.e.

$$\Leftrightarrow C_{\mathrm{D,rot,III(b)}} =: C_{\mathrm{D,rot,n(2)}} =: C_{\mathrm{D,rot,n}} = \frac{P_{\mathrm{a,n(2)}}}{\frac{1}{2}\rho v_{\mathrm{a,n}}^3 A}. \tag{2.229}$$

To maintain the power (2.226) and the airflow speed (2.227) for increasing wind speeds above $v_{\mathrm{w,n(2)}}$, the kite's efficiency has to be reduced with the actuations. As the power and all its factors are constant in (2.228) due to the constant actuation of the rotor drag coefficient (2.229), the

remaining actuations must be set only such that the airflow speed is maintained (while respecting the force bounds and possibly other bounds e.g. for actuations or altitude), i.e. substituting (2.168), (2.169), (2.15), (2.11), (2.33), (2.40)–(2.43), (2.46) with the values for Region III(b) (i.e. with the indices "III(b)" or "n(2)", respectively) into (2.176) yields

$$v_{\mathrm{a,n}} =: v_{\mathrm{a,III(b)}} = \cos(\varphi_{\mathrm{n}} + \Delta\varphi_{\mathrm{a,III(b)}}) \cos(\vartheta_{\mathrm{n}} + \Delta\vartheta_{\mathrm{a,III(b)}}) v_{\mathrm{w}} \frac{c_{\mathrm{L,III(b)}} / \left(1 + \frac{2}{AR}\right)}{c_{\mathrm{D},0} + \left[c_{\mathrm{D},2} + \frac{1/\left(1+\frac{2}{AR}\right)^2}{\pi e AR}\right] c_{\mathrm{L,III(b)}}^2 + C_{\mathrm{D,k,o}} + C_{\mathrm{D,k,a,III(b)}} + C_{\mathrm{D,te}} + C_{\mathrm{D,rot,n(2)}}} \tag{2.230}$$

that must hold true. This is only one equation with the four free actuation variables $c_{\mathrm{L,III(b)}}$, $C_{\mathrm{D,k,a,III(b)}}$, $\Delta\varphi_{\mathrm{a}}$, and $\Delta\vartheta_{\mathrm{a}}$. Therefore, an infinite number of valid actuations can be found, but a meaningful solution for increasing wind speeds is the following strategy:

1. First reduce c_{L}, i.e. e.g. pitch the kite or retract flaps/flaperons, until the minimum feasible lift coefficient is achieved, whereby the following must be considered:
   - The minimum feasible lift coefficient is not necessarily zero (or even negative). Instead, multi-element airfoils with a very high (nominal) lift coefficient tend to be optimal [110] for which the minimum operationally safe lift coefficient can be considerable, e.g. well above two, cf. e.g. Fig. 2.5 and [110]. Moreover, as the force has also the lower bound $F_{||,\min}$ (2.26), another lower bound for the airfoil lift coefficient is given (at that constant airflow speed (2.227)) by inserting $F_{||} = F_{||,\min}$, $v_{\mathrm{a}} = v_{\mathrm{a,n}}$, and (2.15) with (2.39) into (2.178) and solving for $c_{\mathrm{L}} = c_{\mathrm{L,min\text{-}F}}$ which is
   $$\begin{aligned} F_{||,\min} &= \frac{1}{2}\rho v_{\mathrm{a,n}}^2 A \frac{c_{\mathrm{L,min\text{-}F}}}{1 + \frac{2}{AR}} \\ \Leftrightarrow c_{\mathrm{L,min\text{-}F}} &= \frac{F_{||,\min}\left(1 + \frac{2}{AR}\right)}{\frac{1}{2}\rho v_{\mathrm{a,n}}^2 A} \end{aligned} \tag{2.231}$$
   which, with (2.205), $v_{\mathrm{a,I}} = v_{\mathrm{a,min}}$, and (2.39), can also be expressed by
   $$\begin{aligned} c_{\mathrm{L,min\text{-}F}} &= \frac{\frac{1}{2}\rho v_{\mathrm{a,min}}^2 A c_{\mathrm{L,n}}}{\frac{1}{2}\rho v_{\mathrm{a,n}}^2 A} \\ &= \frac{v_{\mathrm{a,min}}^2}{v_{\mathrm{a,n}}^2} c_{\mathrm{L,n}}. \end{aligned} \tag{2.232}$$
   Therefore, the condition
   $$c_{\mathrm{L,III(b)}} \geq c_{\mathrm{L,min}} := \max\{c_{\mathrm{L,min\text{-}F}}, c_{\mathrm{L,min\text{-}op}}\} \tag{2.233}$$
   must hold true.
   - A reduced c_{L} (at the constant airflow speed (2.227)) also reduces the tether force, which is beneficial, because at high wind speeds also stronger gusts can be expected. As the tether force decreases with increasing wind speed, gusts become less and less harmful. This effect is not existent for another actuation, as the tether force at a constant airflow speed depends only on c_{L}.
   - As mentioned in the justification of Assumption 2.36, a reduced lift coefficient can lead to an increased φ and ϑ. However, this is even beneficial in Region III(b) because it increases the effectiveness of reducing the efficiency.

2. Second, when the lower bound of c_L is reached, increase $C_\mathrm{D,k,a}$, i.e. increase the kite's drag via air brakes or sideslipping.
3. Third, when the upper bound of $C_\mathrm{D,k,a}$ is also reached, increase $\Delta\varphi_\mathrm{a}$ and/or $\Delta\vartheta_\mathrm{a}$. Note that an increase of $\Delta\vartheta_\mathrm{a}$ increases also the flight altitude with possibly higher wind speeds. However, if ϑ_n is optimized in a superimposed optimization, it is at the optimum with maximized power in the other regions, and thus an increase of $\Delta\vartheta_\mathrm{a}$ yields a reduced airflow speed and thus limited power and force. Otherwise, a small increase of $\Delta\vartheta_\mathrm{a}$ might first yield an increase of power, airflow speed, or force before they are decreased or limited, respectively.

Note, however, that $\Delta\varphi_\mathrm{a}$ and $\Delta\vartheta_\mathrm{a}$ can be actuated much slower than c_L and $C_\mathrm{D,k,a}$ (in the order of several seconds compared to a few tens or hundreds of milliseconds). Therefore, it might be infeasible to use the presented strategy, but a possible modification is to increase the low-dynamic $\Delta\varphi_\mathrm{a}$ and/or $\Delta\vartheta_\mathrm{a}$ w.r.t. the also on average low-dynamic (and additionally filtered) wind speed already before c_L or $C_\mathrm{D,k,a}$ are at a bound. Those high-dynamic actuations are then also available to compensate for dynamic gusts and dynamics caused by the flight path.—As the exact actuations in Region III(b) are of less importance here, and as the airflow speed and power limitation strategy might be subject to effects not covered in the here utilized steady model, the derivation of the equations for the remaining actuations and states for the above strategy is moved to Appendix B.

2.7.13 Region IV and Transition between Region III(b) and IV

In the forth region at storm wind speeds $v_\mathrm{w,cut\text{-}out} := v_\mathrm{w,III\leftrightarrow IV} \leq v_\mathrm{w} \leq \infty$, the wind is too strong for safe operation, so the kite is grounded and no power is generated. The desired cut-out wind speed defines requirements for the actuator constraints, or vice-versa the chosen actuators and their constraints define the cut-out wind speed, cf. Appendix B.

Note that it might be also possible to reduce the power for higher wind speeds less abruptly to further harvest energy, similar to a conventional wind turbine [138]. However, if the power is reduced at high wind speeds, the actuations must be much stronger than in Region III(b). This might not be only impractical, but it is also not optimal in the sense of solving (2.164)–(2.170) with the here utilized model: The optimal solution is to generate the maximum power as long as possible and thus with an abrupt cut-out. Additionally, a less abrupt cut-out is more complex and wind speeds at and above the usually high cut-out wind speed are so rare (cf. Fig. 2.15 with a usual $v_{\mathrm{w},h_\mathrm{ref},\mathrm{cut\text{-}out}} = 25\,\mathrm{m/s}$), that the effect on the energy yield would be negligible anyways. Therefore, a strategy with a non-abrupt cut-out is not considered here.

2.7.14 Nominal Values and Feasibility Conditions

For the power curve, only the aerodynamic power P_a is derived. The other powers and further power dependent values (e.g. tether efficiency η_te) down to the electrical power at the grid P_el are readily given by (2.145)–(2.156). In the following, several nominal values (e.g. nominal powers and nominal efficiencies) are defined. Herein, "nominal" denotes the continuous duty "S1", cf. also Assumption 2.35. Moreover, feasibility conditions are stated which have to be met for the derived power curve equations.

2.7.14.1 Nominal Generative Powers (During Crosswind Flight)

The nominal generative aerodynamic power $P_\mathrm{a,n} = P_\mathrm{a,n(2)}$ defines the nominal generative powers of the powertrain components, i.e. of the shafts/gears, electrical machines, and power electronics.

With (2.145)–(2.150) and with (2.119)–(2.121), the nominal generative powers (indices + and n) are

$$P_{\mathrm{a},+,\mathrm{n}} =: P_{\mathrm{a},\mathrm{n}(2)} =: P_{\mathrm{a},\mathrm{n}} \tag{2.234}$$
$$P_{\mathrm{rot},+,\mathrm{n}} = \eta_{\mathrm{rot},+}\eta_{\mathrm{a},+,\mathrm{n}}P_{\mathrm{a},+,\mathrm{n}} \tag{2.235}$$
$$P_{\mathrm{s},+,\mathrm{n}} = \eta_{\mathrm{s},+}P_{\mathrm{rot},+,\mathrm{n}} \tag{2.236}$$
$$P_{\mathrm{el},\mathrm{m},+,\mathrm{n}} = \eta_{\mathrm{m},+}P_{\mathrm{s},+,\mathrm{n}} \tag{2.237}$$
$$P_{\mathrm{el},\mathrm{k},+,\mathrm{n}} = \eta_{\mathrm{pe},\mathrm{k},+}P_{\mathrm{el},\mathrm{m},+,\mathrm{n}} \tag{2.238}$$
$$P_{\mathrm{el},\mathrm{g},+,\mathrm{n}} = \eta_{\mathrm{te},+,\mathrm{n}}P_{\mathrm{el},\mathrm{k},+,\mathrm{n}} \tag{2.239}$$
$$P_{\mathrm{el},+,\mathrm{n}} = \eta_{\mathrm{pe},\mathrm{g},+}P_{\mathrm{el},\mathrm{g},+,\mathrm{n}}, \tag{2.240}$$

where $\eta_{\mathrm{a},+,\mathrm{n}}$ is the nominal generative actuator disk efficiency and $\eta_{\mathrm{te},+,\mathrm{n}}$ is the nominal generative tether transmission efficiency, which both are derived as follows: With $C_{\mathrm{D,rot}} = C_{\mathrm{D,rot,n}(2)}$ and with all $n_{\mathrm{rot,op}} = n_{\mathrm{rot}}$ operating rotors in (2.101), the (second) nominal induction factor is

$$a_{\mathrm{n}(2)} := a_{+,\mathrm{n}} = \frac{1}{2} - \sqrt{\frac{r_{\mathrm{rot}} - C_{\mathrm{D,rot,n}(2)}}{4r_{\mathrm{rot}}}}. \tag{2.241}$$

Substituting that into (2.108), the (second) nominal (generative) actuator disk efficiency is determined by

$$\eta_{\mathrm{a},\mathrm{n}(2)} := \eta_{\mathrm{a},+,\mathrm{n}} = 1 - a_{\mathrm{n}(2)}. \tag{2.242}$$

With the nominal generative powers in (2.123), (2.88), and (2.127), the nominal generative tether transmission efficiency with nominal generative tether power loss and nominal generative tether current are

$$\eta_{\mathrm{te},+,\mathrm{n}} = \frac{P_{\mathrm{el},\mathrm{g},+,\mathrm{n}}}{P_{\mathrm{el},\mathrm{k},+,\mathrm{n}}}, \tag{2.243}$$
$$P_{\text{te-loss},+,\mathrm{n}} = R_{\mathrm{te}}I^2_{\mathrm{te},+,\mathrm{n}}, \tag{2.244}$$
$$I_{\mathrm{te},+,\mathrm{n}} = \frac{P_{\mathrm{el},\mathrm{k},+,\mathrm{n}}}{U_{\mathrm{te,n}}}. \tag{2.245}$$

Note that the nominal generative power of each next subsystem from the kite down to the ground station is lower than or equal to that of the previous subsystem, because $\eta_{\#} \leq 1$.

The condition (2.131) must be satisfied, such that these equations are valid and thus for feasibility.

2.7.14.2 Installed Nominal Powers

The above derived nominal powers are the minimum values which each powertrain subsystem must be able to process, i.e. the *installed* nominal power of each subsystem must be at least as high as (2.234)–(2.240), i.e. generally

$$P_{\#,\text{n-ins}} \geq |P_{\#}|. \tag{2.246}$$

As the instantaneous powers might exceed the above defined nominal powers over the course of the flight path, the installed powers may need to be higher. However, through Assumption 2.35, enough overloading capability is assumed for each powertrain subsystem. Nevertheless, it should be noted, that the absolute value of the nominal power during generative crosswind flight,

consumptive crosswind flight, and hovering may differ significantly. Particularly, the power required for hovering might be significant.

For the bidirectional power capability of a powertrain subsystem, i.e. for the installed nominal power, the following assumption is imposed:

Assumption 2.37: *For each bidirectional powertrain subsystem #, the absolute values of the installed nominal powers in both power flow directions (index + for generative, index − for consumptive, for both crosswind flight and hovering) are (approximately) equal, i.e.*

$$P_{\#,\text{n-ins}} := |P_{\#,+,\text{n-ins}}| = |P_{\#,-,\text{n-ins}}|. \tag{2.247}$$

Ideally, the nominal generative powers define the installed powers, or, vice versa, crosswind flight at low wind and hovering do not dictate the powertrain size, and thus the powertrain is as small and as cost-effective as possible. In this case, the installed powers are defined by the nominal generative powers (2.234)–(2.240). As each efficiency factor is ≤ 1, the electrical power has the lowest value defined by

$$P_{\text{el,n-ins}} := |P_{\text{el},+,\text{n}}| = P_{\text{el},+,\text{n}} \quad \text{i.e., if power generation defines powertrain size.} \tag{2.248}$$

Unless denoted otherwise, this case is considered throughout this dissertation.

2.7.14.3 Nominal or Maximum Available Consumptive Powers

With (2.247) and (2.248), the installed nominal electrical power defines the nominal or maximum available (indicated in the following by $\hat{}$) consumptive electrical power by

$$\hat{P}_{\text{el},-} = -|P_{\text{el,n-ins}}| \tag{2.249}$$

and the other available consumptive powers are then given via (2.151)–(2.156) while respecting (2.136)[17] by

$$\hat{P}_{\text{el,g},-} = \begin{cases} \eta_{\text{pe,g},-}\hat{P}_{\text{el},-} & \text{if } \eta_{\text{pe,g},-}\hat{P}_{\text{el},-} \geq P_{\text{el,g,min}} \\ P_{\text{el,g,min}} & \text{otherwise} \end{cases} \tag{2.250}$$

$$\hat{P}_{\text{el,k},-} = \hat{\eta}_{\text{te},-}\hat{P}_{\text{el,g},-} \tag{2.251}$$

$$\hat{P}_{\text{el,m},-} = \eta_{\text{pe,k},-}\hat{P}_{\text{el,k},-} \tag{2.252}$$

$$\hat{P}_{\text{s},-} = \eta_{\text{m},-}\hat{P}_{\text{el,m},-} \tag{2.253}$$

$$\hat{P}_{\text{rot},-} = \eta_{\text{s},-}\hat{P}_{\text{s},-} \tag{2.254}$$

$$\hat{P}_{\text{a},-} = \hat{\eta}_{\text{rot},\Pi,-}\hat{P}_{\text{rot},-}, \tag{2.255}$$

which are all smaller than the respective installed nominal power because each efficiency factor is ≤ 1. Herein, analogously to (2.243)–(2.245), the tether efficiency, tether power loss, and tether current at the maximum available consumptive power are given by

$$\hat{\eta}_{\text{te},-} = \frac{\hat{P}_{\text{el,k},-}}{\hat{P}_{\text{el,g},-}}, \tag{2.256}$$

$$\hat{P}_{\text{te-loss},-} = R_{\text{te}}\hat{I}^2_{\text{te},-}, \tag{2.257}$$

$$\hat{I}_{\text{te},-} = \frac{\hat{P}_{\text{el,g},-}}{U_{\text{te,n}}}. \tag{2.258}$$

[17] Note that (2.135) is automatically fulfilled if (2.136) is fulfilled.

Note that, through (2.249)–(2.255) and (2.247), each installed nominal power can also be written as

$$P_{\#,\text{n-ins}} = \max\{|P_{\#,+,\text{n}}|, |\hat{P}_{\#,-}|\}. \tag{2.259}$$

The maximum available aerodynamic power and the total rotor efficiency depend on the flight modes, discussed in the following.

2.7.14.4 Nominal Consumptive Rotor Power in Crosswind Flight

For consumptive crosswind flight, Eq. (2.255) becomes with (2.121)

$$\hat{P}_{\text{a},-} = \eta_{\text{rot},-}\hat{\eta}_{\text{a},-}\hat{P}_{\text{rot},-}. \tag{2.260}$$

Herein, $\hat{P}_{\text{a},-}$ and $\hat{\eta}_{\text{a},-}$ depend (nonlinearly) on the same rotor drag coefficient, for which (2.260) cannot be solved easily. However, the minimal required rotor drag coefficient, which can also be referred to as nominal consumptive rotor drag coefficient, can be derived by inserting $v_\text{w} = 0$ into (2.207) which becomes

$$C_{\text{D,rot},-,\text{n}} := C_{\text{D,rot,I}}(v_\text{w} = 0) = -C_{\text{D,eq,I}} = -C_{\text{D,eq,n}} \tag{2.261}$$

with which further, analogously to (2.241) and (2.242), the nominal consumptive induction factor and corresponding actuator disk efficiency become

$$a_{-,\text{n}} = \frac{1}{2} - \sqrt{\frac{r_\text{rot} - C_{\text{D,rot},-,\text{n}}}{4r_\text{rot}}} \tag{2.262}$$

$$\eta_{\text{a},-,\text{n}} = \frac{1}{1 - a_{-,\text{n}}}. \tag{2.263}$$

With $C_{\text{D,rot},-,\text{n}}$ and $v_{\text{a,min}}$ in (2.18), the minimum required or nominal consumptive aerodynamic power is given by

$$P_{\text{a},-,\text{n}} = \frac{1}{2}\rho v_{\text{a,min}}^3 A C_{\text{D,rot},-,\text{n}}. \tag{2.264}$$

With that and (2.260)–(2.263), the minimum required or nominal consumptive rotor shaft power is given by

$$P_{\text{rot},-,\text{n}} = \frac{1}{\eta_{\text{rot},-}\eta_{\text{a},-,\text{n}}} P_{\text{a},-,\text{n}} \tag{2.265}$$

Clearly, for feasibility,

$$|P_{\text{rot},-,\text{n}}| \leq |\hat{P}_{\text{rot},-}| \tag{2.266}$$

must be satisfied[18].

2.7.14.5 Nominal Consumptive Rotor Power in Crosswind Flight with Rotor Failure

If there is a rotor failure, then only $n_{\text{rot,op}} = n_\text{rot} - 1$ rotors are available, but still the same rotor drag coefficient (2.261) and aerodynamic power (2.264) are effective. This leads to the altered available rotor power (2.254) of (cf. also (2.99))

$$\hat{P}_{\text{rot},-,\text{flt}} = \frac{n_\text{rot} - 1}{n_\text{rot}} \hat{P}_{\text{rot},-}. \tag{2.267}$$

[18] The absolute values are written only for better perception.

Moreover, with $n_{\mathrm{rot,op}} = n_{\mathrm{rot}} - 1$ and (2.261) substituted into (2.101), the induction factor (2.262) is replaced by

$$a_{-,\mathrm{n,flt}} = \frac{1}{2} - \sqrt{\frac{\frac{n_{\mathrm{rot}}-1}{n_{\mathrm{rot}}} r_{\mathrm{rot}} - C_{\mathrm{D,rot,-,n}}}{4\frac{n_{\mathrm{rot}}-1}{n_{\mathrm{rot}}} r_{\mathrm{rot}}}} \tag{2.268}$$

with which actuator disk efficiency (2.109) becomes

$$\eta_{\mathrm{a,-,n,flt}} = \frac{1}{1 - a_{-,\mathrm{n,flt}}} \tag{2.269}$$

and the required rotor power (2.265) is altered to

$$P_{\mathrm{rot,-,n,flt}} = \frac{1}{\eta_{\mathrm{rot,-}}\eta_{\mathrm{a,-,n,flt}}} P_{\mathrm{a,-,n,flt}}. \tag{2.270}$$

The feasibility condition, Eq. (2.266), then becomes

$$|P_{\mathrm{rot,-,n,flt}}| \leq |\hat{P}_{\mathrm{rot,-,flt}}|. \tag{2.271}$$

2.7.14.6 Maximum Available Consumptive Aerodynamic Power in Hovering

For hovering, Eq. (2.255) becomes with (2.121) simply

$$\hat{P}_{\mathrm{a,hov}} = \eta_{\mathrm{rot,hov}} \hat{P}_{\mathrm{rot,-}}, \tag{2.272}$$

and, clearly, the absolute value of the actual hovering power (2.114), or (2.115) respectively, must be smaller than absolute value of the maximum available one,

$$|P_{\mathrm{a,hov,ok}}| \leq |\hat{P}_{\mathrm{a,hov}}|. \tag{2.273}$$

2.7.14.7 Maximum Available Consumptive Aerodynamic Power in Hovering with Rotor Failure

If there is a rotor failure, according to Assumption 2.28 two rotors and their powertrain components become unavailable, hence (2.272) is replaced by

$$\hat{P}_{\mathrm{a,hov,flt}} = \frac{n_{\mathrm{rot}} - 2}{n_{\mathrm{rot}}} \hat{P}_{\mathrm{a,hov}}, \tag{2.274}$$

and, clearly, the absolute value of the actual hovering power (2.116) must be smaller than the absolute value of the maximum available one,

$$|P_{\mathrm{a,hov,flt}}| \leq |\hat{P}_{\mathrm{a,hov,flt}}|. \tag{2.275}$$

2.7.14.8 Further Feasibility Conditions

In addition to the feasibility conditions derived previously for the nominal and maximum available powers, the presented power curve and equations are only valid if the conditions

$$F_{||,\mathrm{min}} \leq F_{||,\mathrm{max}} =: F_{||,\mathrm{n}} = F_{\mathrm{te,n}} \quad \text{or equivalently} \quad v_{\mathrm{a,min}} \leq v_{\mathrm{a,max}} = v_{\mathrm{a,n}} \tag{2.276}$$

$$c_{\mathrm{L,min\text{-}op}} \leq c_{\mathrm{L,n}} \tag{2.277}$$
$$r_{\mathrm{P}} \geq 1 \tag{2.278}$$
$$v_{\mathrm{w},h_{\mathrm{ref}},\mathrm{n}(2)} \leq v_{\mathrm{w},h_{\mathrm{ref}},\mathrm{cut\text{-}out}} \tag{2.279}$$

hold true. Note that these conditions also allow for a zero width of any region, apart from Region IV which always "fills" the remaining wind speeds from $v_{\mathrm{w},h_{\mathrm{ref}},\mathrm{cut\text{-}out}}$ to ∞.

In addition to that, Eq. (2.106), or equivalently (2.105), must hold true in all regions. It should be noted, that also the instantaneous $C_{\mathrm{D,rot}}$ over the course of the flight path must satisfy (2.106) or ultimately (2.103), regardless of Assumption 2.35.

Similarly, Eqs. (2.131) and (2.135) or equivalently (2.133) and (2.136) must hold true, not only for the nominal and maximum available values of $P_{\mathrm{el,k}}$ and $P_{\mathrm{el,g}}$, but also through all regions as well as the instantaneous values over the course of the flight regardless of Assumption 2.35.

Also, Eq. (2.246) must be satisfied for the nominal values and all regions.

The thermodynamic bound (2.89) or (2.90), respectively, must be satisfied in all regions, cf. Assumption 2.24.

Finally, the radicand in Eq. (B.9) must not be below zero, to avoid non-physical complex values.

2.8 Economics Model

Once the power curve is known, i.e. once the electrical power as function of the wind speed in the reference altitude $P_{\mathrm{el}}(v_{\mathrm{w},h_{\mathrm{ref}}})$ is known, the same economic models as for conventional wind turbines can be used to compute the plant's economic performance. Such models are similarly used by the prior works of the author of this dissertation in [104, 110].

2.8.1 Energy Yield

For a drag power kite, the power curve can contain a region wherein the power is significantly negative (consumptive) to maintain a powered crosswind flight at low winds or for launching and landing (hovering). However, such maneuvers are comparatively rare and, if the wind is insufficient, the kite would usually be grounded. Therefore, the following assumption can be made:

Assumption 2.38: *To compute the energy yield, only the generative power of the power curve*

$$P_{\mathrm{el},+}(v_{\mathrm{w},h_{\mathrm{ref}}}) = \max\{0, P_{\mathrm{el}}(v_{\mathrm{w},h_{\mathrm{ref}}})\} \tag{2.280}$$

needs to be considered.

With (2.161) and (2.280), the (ideal) annual energy yield $E_{\mathrm{el,yr,ideal}}$ in Wh/yr is determined by (cf. e.g. [127, Chap. 3.16], [132, Chap. 6.7.1])

$$E_{\mathrm{el,yr,ideal}} = \frac{8,760\,\mathrm{h}}{1\,\mathrm{yr}} \int_0^\infty p(v_{\mathrm{w},h_{\mathrm{ref}}}) P_{\mathrm{el},+}(v_{\mathrm{w},h_{\mathrm{ref}}}) \mathrm{d}v_{\mathrm{w},h_{\mathrm{ref}}}, \tag{2.281}$$

where the factor $8,760\,\mathrm{h}/1\,\mathrm{yr}$ is for the unit conversion from Ws/s in Wh/yr for convenience.

A power plant might have a fault, needs inspection at certain times, needs to be cut-off by the grid operator to ensure grid stability, and the like, such that it is not available at all times at which it could generate power. To account for that, the ideal energy yield (2.281) is corrected:

Assumption 2.39: *A non* 100 % *availability of a power plant e.g. caused by inspections and similar can be modeled with the reduction of the ideal energy yield by*

$$E_{\mathrm{el,yr}} = f_{\mathrm{avail}} E_{\mathrm{el,yr,ideal}} \tag{2.282}$$

where $E_{\mathrm{el,yr}}$ *is the real energy yield and* $f_{\mathrm{avail}} \in [0, 1]$ *is the availability (correction) factor.*

2.8.2 Capacity Factor

An important figure of merit of a power plant is also its capacity factor, which is defined by (cf. e.g. [108, Chap. 1.6], [139])

$$H = \frac{E_{\mathrm{el,yr}} / \frac{8{,}760\,\mathrm{h}}{1\,\mathrm{yr}}}{P_{\mathrm{el},+,\mathrm{n}}}, \tag{2.283}$$

where $P_{\mathrm{el},+,\mathrm{n}}$ is the nominal generative electrical power from (2.240), which can also be expressed by

$$P_{\mathrm{el},+,\mathrm{n}} = \max_{v_{\mathrm{w}}, h_{\mathrm{ref}}} P_{\mathrm{el}}(v_{\mathrm{w}}, h_{\mathrm{ref}}), \tag{2.284}$$

and the factor $8{,}760\,\mathrm{h}/1\,\mathrm{yr}$ is again for unit conversion.

Remark 2.10: *The installed nominal electrical power* $P_{\mathrm{el,n\text{-}ins}}$ *might differ from the nominal generative electrical power, e.g. if a higher power is required for hovering. If this is not the case, then* $P_{\mathrm{el},+,\mathrm{n}} = P_{\mathrm{el,n\text{-}ins}}$.

2.8.3 Costs

Generally, the annual costs of the power plant k (e.g. in EUR/yr or USD/yr) are

$$k = k_{\mathrm{inv}} + k_{\mathrm{op}} \tag{2.285}$$

with investment costs k_{inv} (i.e. the cash flow with which the initial total investment of the power plant is refinanced) and operational costs k_{op}. Both costs are (at least) to be balanced by the revenue of the power plant.

For the investment cost, the following assumption is made, which is usual for simple economic performance estimations of power plants (cf. e.g. [108, Chap. 1.6], [140], [141, Chap. 12.5]):

Assumption 2.40: *The total costs of the power plant* K_{inv}*, which include taxes, transportation costs, deployment costs, permit costs etc., are to be payed to the power plant manufacturer when the power plant is deployed. The investor, e.g. a utility company, who invests* K_{inv}*, expects annual constant paybacks* k_{inv} *with a compound interest rate p.a.* I *over the (minimum) life time of the power plant* T *(which is also the dynamic amortization time). There is no financing, i.e. the investor alone pays the complete* K_{inv}*, there are no subsidies and taxes (apart from the ones covered in* K_{inv}*), no inflation/deflation and no other price increases or decreases at any time (i.e. those are neglected). After the lifetime (dynamic amortization time)* T*, the power plant has to be demolished, but the scrap price is equal to the demolition costs.*

The annual investment costs are then determined as follows (cf. e.g. [108, Chap. 1.6], [140], [141, Chap. 12.5]):

Theorem 2.6: *If Assumption 2.40 applies, then the annual investment costs are*

$$k_{\text{inv}} = f_{\text{an}} K_{\text{inv}} \tag{2.286}$$

with total investment price of the power plant K_{inv} *and annuity factor*

$$f_{\text{an}} = \begin{cases} \frac{1}{T} & \text{for } I = 0 \\ \frac{I(1+I)^{T/\text{yr}}}{(1+I)^{T/\text{yr}}-1} & \text{for } I \neq 0, \end{cases} \tag{2.287}$$

where I *is the interest rate p.a. (which is expected by the investor of the power plant) and* T *is the (minimum) life time of the power plant and the dynamic amortization time of the investment in years.*

Proof. The derivation of (2.286) and (2.287) can be found similarly cf. e.g. [141, Chap. 12.5]: With compound interest p.a. I, a capital now K_{now} (present value) has a future value K_{fut} of

$$K_{\text{fut}} = K_{\text{now}}(1+I)^{T/\text{yr}}, \tag{2.288}$$

i.e. if K_{now} is invested with compound interest p.a. I, it will have the value K_{fut} in the future year T.

Vice versa, the present value of a future capital (e.g. an income in the future) is (2.288) converted to

$$K_{\text{now}} = K_{\text{fut}} \frac{1}{(1+I)^{T/\text{yr}}}. \tag{2.289}$$

Similarly, the present value of several equal future capitals (equal incomes/payments) k_{fut} in each year from 1 until T is

$$\begin{aligned} K_{\text{now}} &= \underbrace{k_{\text{fut}} \frac{1}{(1+I)^1}}_{\text{for } t = 1\,\text{yr}} + \underbrace{k_{\text{fut}} \frac{1}{(1+I)^2}}_{\text{for } t = 2\,\text{yr}} + \cdots + \underbrace{k_{\text{fut}} \frac{1}{(1+I)^{T/\text{yr}}}}_{\text{for } t = T} \\ &= k_{\text{fut}} \sum_{t=1\,\text{yr}}^{T} \frac{1}{(1+I)^{t/\text{yr}}}. \end{aligned} \tag{2.290}$$

If K_{now}, T, and I are given, then the equal payments are determined by solving (2.290) for k_{fut}, i.e.

$$\Leftrightarrow k_{\text{fut}} = K_{\text{now}} \underbrace{\frac{1}{\sum_{t=1\,\text{yr}}^{T} \frac{1}{(1+I)^{t/\text{yr}}}}}_{=: f_{\text{an}}}, \tag{2.291}$$

where f_{an} is defined as annuity factor.

Obviously, for $I = 0$ one obtains

$$f_{\text{an}} = \frac{1}{T}. \tag{2.292}$$

Otherwise, for $I \neq 0$, the annuity factor f_{an} from (2.291) can be further solved by (i) writing out again the sum,

$$\begin{aligned} f_{\text{an}}^{-1} &= \sum_{t=1\,\text{yr}}^{T} \frac{1}{(1+I)^{t/\text{yr}}} \\ &= \frac{1}{(1+I)^1} + \frac{1}{(1+I)^2} + \cdots + \frac{1}{(1+I)^{T/\text{yr}}}, \end{aligned} \tag{2.293}$$

(ii) multiplying that by $(1+I)$,

$$(1+I) f_{\text{an}}^{-1} = 1 + \frac{1}{(1+I)^1} + \cdots + \frac{1}{(1+I)^{T/\text{yr}-1}}, \tag{2.294}$$

and (iii) subtracting (2.294) from (2.293),

$$\begin{aligned} f_{\text{an}}^{-1} - (1+I) f_{\text{an}}^{-1} &= \left[\frac{1}{(1+I)^1} + \frac{1}{(1+I)^2} + \cdots + \frac{1}{(1+I)^{T/\text{yr}}}\right] \\ &\quad - \left[1 + \frac{1}{(1+I)^1} + \cdots + \frac{1}{(1+I)^{T/\text{yr}-1}}\right] \\ [1-(1+I)] f_{\text{an}}^{-1} &= \frac{1}{(1+I)^{T/\text{yr}}} - 1 \\ -I f_{\text{an}}^{-1} &= \frac{1}{(1+I)^{T/\text{yr}}} - \frac{(1+I)^{T/\text{yr}}}{(1+I)^{T/\text{yr}}} \\ &= \frac{1-(1+I)^{T/\text{yr}}}{(1+I)^{T/\text{yr}}} \qquad \big| : -I \\ f_{\text{an}}^{-1} &= \frac{1-(1+I)^{T/\text{yr}}}{-I(1+I)^{T/\text{yr}}} \\ &= \frac{(1+I)^{T/\text{yr}}-1}{I(1+I)^{T/\text{yr}}}. \end{aligned} \tag{2.295}$$

Substituting (2.292) or respectively (2.295) into (2.291), and considering $K_{\text{now}} = K_{\text{inv}}$ as present value of an investment and $k_{\text{fut}} = k_{\text{inv}}$ as the future paybacks, results in (2.286) with (2.287). ■

A kite power plant does not require fuel. Moreover, a fully autonomous plant is considered, so no pilots or other permanent operators are required. Therefore, the operational costs per year narrow down e.g. to small costs for checkup services, for communications for remote maintenance/servicing, possibly for small repairs or replacements (e.g. power electronics, batteries, or tether), possibly for land lease, or possibly for a farm operator when considering a kite power plant farm. This justifies the following assumption:

Assumption 2.41: *The yearly operational costs can be formulated as a (small) percentage I_{op} of the total investment costs, i.e.*[19]

$$k_{\text{op}} = I_{\text{op}} K_{\text{inv}}. \tag{2.296}$$

[19] It can be argued, that k_{op} should be discounted for the present value with the same argument as in the proof of Theorem 2.6. This is here not applied for sake of simplicity.

Substituting (2.286) and (2.296) into (2.285) yields

$$k = K_{\text{inv}}(I_{\text{op}} + f_{\text{an}}). \tag{2.297}$$

The investment costs can generally be further specified by

$$K_{\text{inv}} = K_{\text{inv,pt}} + K_{\text{inv,o\&p}} \tag{2.298}$$

where $K_{\text{inv,pt}}$ is the cost of the powertrain, and $K_{\text{inv,o\&p}}$ is the cost of the airframe, tether, ground station, and other parts, includes also development costs, as well as the profit margin of the power plant manufacturer. As the costs of the powertrain are approximately proportional to the installed power, the following assumption is justified:

Assumption 2.42: *The powertrain costs can be modeled by*

$$K_{\text{inv,pt}} = k_{\text{pt}} P_{\text{el,n-ins}}, \tag{2.299}$$

where k_{pt} is the specific cost of the powertrain (e.g. in EUR/W *or* USD/W*), and $P_{\text{el,n-ins}}$ is the installed electrical power.*

Finally, the levelized cost of electricity (LCOE) is given by (cf. e.g. [108, Chap. 1.6], [140])

$$k_{\text{LCOE}} = \frac{k}{E_{\text{el,yr}}}. \tag{2.300}$$

Remark 2.11: *The LCOE is the (minimum) price at which the generated electricity must be sold on average. This must also hold true in an island grid or in a public grid with high wind power penetration in which the stock exchange price of electricity might be very volatile and possibly low during high winds. Therefore, the to be achieved LCOE might need to be lower than the average price of electricity in the for deployment anticipated market. Alternatively, the economics model is extended with a market model with fluctuating energy prices, which is, however, not considered here for sake of simplicity.*

2.8.4 Static Amortization

If energy is sold at k_{LCOE} (on average) and if K_{inv} is payed off by k_{inv} from (2.286) every year (on average), then the static amortization time is given by

$$\begin{aligned} T_{\text{am}} &= \frac{K_{\text{inv}}}{k_{\text{inv}}} \\ &= \frac{K_{\text{inv}}}{K_{\text{inv}} f_{\text{an}}} \\ &= f_{\text{an}}^{-1} \end{aligned} \tag{2.301}$$

2.9 Coupling of Submodels

The in the previous sections derived equations for each submodel of the drag power kite plant are in the following coupled, such that a fast kite power plant performance computation for a set of parameters is possible. Specifically, the equations are arranged analytically (i.e. "by hand") into an order which is as explicit as possible (i.e. ideally solely a sequence of explicit analytical equations), instead of e.g. simply implementing all equations in an algebra tool and letting it

solve the system of equations and constraints numerically with the obvious disadvantage of the high computational costs for iteratively finding the solution. The resulting algorithm particularly includes the tether sizing such that a feasible system is likely for a given set of parameters. This submodel coupling also serves to summarize the complete drag power kite plant systems engineering model. Similar ideas were introduced by the author of this dissertation in the prior publications [104, 106, 110].

2.9.1 Key Ideas

The basic idea is to start with somewhat fixed parameters for a drag power kite plant prototype or product development, whose (optimal) values are also relatively easily estimated. With those parameters, all other values, including the figures of merit, are "inversely" computed. For example, one would usually first fix the kite's size, i.e. the wing span. It suggests itself to fix or limit the nominal airflow speed to a narrow range and thus also the tether length, or vice versa, because the maximum angular speed on the tether sphere is a somewhat fixed value. Effective azimuth and elevation are also fixed or only variable in narrow limits. With these values, the nominal tether force, tether size, tether drag contribution, and so on can be computed, until the relevant figures of merit are available. Note that this approach incorporates explicitly the tether sizing. Possibly, the performance is then optimized in iterative steps by changing the parameters like the nominal airflow speed, until the desired plant performance is achieved.

A further key idea is that serious estimates or elaborate submodels for the airframe mass m_{af} and for the investment costs "of other parts" and profit margin $K_{\mathrm{inv,o\&p}}$ are considered not meaningful, i.e. with too many too rough assumptions, or are too hard at an early development stage without (known) economy of scale. Instead, parameters which are closely related to those values and are easily estimated, are used as starting point, from which the "maximum allowed" mass $\hat{m}_{\mathrm{af}}$ and the "maximum allowed" costs $\hat{K}_{\mathrm{inv,o\&p}}$ (all "maximum allowed" values are indicated by $\hat{}$ in the following) are computed "inversely" as requirements for a detailed design of the drag power kite plant. For example, the power for hovering is bounded by the installed nominal power, which in turn may be defined by the nominal generative power, cf. (2.248). From that, a maximum allowed effective airborne mass $\hat{m}_{\mathrm{a}}$ can be derived by solving (2.113) for $m_{\mathrm{a}} = \hat{m}_{\mathrm{a}}$ and from which further the maximum allowed airframe mass $\hat{m}_{\mathrm{af}}$ can be derived with (2.27)–(2.30). Similarly, instead of computing k_{LCOE} for different design parameter choices and possibly treat the design with the lowest k_{LCOE} as the best, k_{LCOE} is used as starting point that is to be achieved in order to reach competitiveness in the targeted market (whereby k_{LCOE} might be artificially lower than the average sale price of electricity in the targeted market to overcome limitations of the economics model, as mentioned in Remark 2.11). From there on, the maximum allowed $\hat{K}_{\mathrm{inv,o\&p}}$ is "inversely" computed by solving (2.285)–(2.287) and (2.296)–(2.300) for $K_{\mathrm{inv,o\&p}} = \hat{K}_{\mathrm{inv,o\&p}}$. Note that $K_{\mathrm{inv,o\&p}}$ includes the development budget and the profit margin. For both a kite power plant manufacturer has a strong interest to be (very) high. Further discussions on that are below, in Chap. 4.

Within the performance computation, the derived feasibility conditions from Sect. 2.7.14 and possibly additional to be defined constraints, e.g. a maximum wing loading which may be required for a (possibly easier) realizable drag power kite plant design, are only checked against validity. Unfeasible designs are considered to be discarded.

2.9.2 Algorithm

The previously stated ideas are implemented in detail with the following algorithm:

1. Determine design parameters:

1.1. Estimate/select/choose values for the "fixed parameters"[20] for a projected kite power plant installation site:
   - Environmental parameters for considered installation site: g, ρ, h_{ref}, z_0, α_{H}[21], λ, μ.
   - Economic parameters for targeted market: k_{LCOE}, I, T, I_{op}, f_{avail}.
   - Kite aerodynamics parameters: b, n_{mw}, $c_{\text{D},0}$, $c_{\text{D},2}$, $c_{\text{L,min-op}}$, e, $C_{\text{D,k,o}}$, $C_{\text{D,k,a,max}}$.
   - Rotor parameters: n_{rot}, r_{rot}, $\eta_{\text{rot},+}$, $\eta_{\text{rot},-}$, $\eta_{\text{rot,hov}}$.
   - Tether parameters: $c_{\text{D,te}}$, $f_{\text{m-te}}$, $n_{\text{te,c}}$[22], $\rho_{\text{te,mech}}$, $\sigma_{\text{te,mech}}$, $\rho_{\text{te,c,w}}$, $\kappa_{\text{te,c,w}}$, $\rho_{\text{te,ins}}$, $E_{\text{te,ins}}$, $\rho_{\text{te,c,sh}}$, $\rho_{\text{te,c,j}}$, $\rho_{\text{te,j}}$, $w_{\text{te,c,sh}}$, $w_{\text{te,c,j}}$, $w_{\text{te,j}}$, $S_{\text{te,mech}}$, $S_{\text{te,ins}}$, $f_{\text{te,c,w}}$, $f_{\text{te,ins}}$, $\forall i \neq \text{mech} : f_{\text{te,m},i}$.
   - Powertrain subsystems parameters: $\eta_{\text{s},+}$, $\eta_{\text{s},-}$, $\eta_{\text{m},+}$, $\eta_{\text{m},-}$, $\eta_{\text{pe,k},+}$, $\eta_{\text{pe,k},-}$, $\eta_{\text{pe,g},+}$, $\eta_{\text{pe,g},-}$, γ_{m}, $\gamma_{\text{pe,k}}$, k_{pt}, $S_{\text{hov,ok}}$, $S_{\text{hov,flt}}$, $P_{\text{el,n-ins}}$[23].
   - Ground station parameters and flight trajectory parameters: h_{to}, φ_{n}, $\psi_{\text{w,n}}$.
   - Power curve "shaping" parameters: $v_{\text{a,min}}$[24], $v_{\text{w},h_{\text{ref}},\text{cut-out}}$.

1.2. Choose (initial) values for the "dimensioning parameters"[20]:
   - Kite aerodynamics parameters: AR, $c_{\text{L,n}}$.
   - Tether parameters: L_{te}, $U_{\text{te,n}}$, R_{te}[25].
   - Ground station parameters and flight trajectory parameters: ϑ_{n}.
   - Power curve "shaping" parameters: $v_{\text{a,n}}$, r_{P}.

2. Initialize infeasibility variable $f_{\text{infeas}} = 0$.[26]

3. Check feasibility of design parameters:

3.1. Check if (2.276) is true, otherwise increase f_{infeas} by $(v_{\text{a,min}} - v_{\text{a,n}})^2$.

3.2. Check if (2.277) is true, otherwise increase f_{infeas} by $(c_{\text{L,min-op}} - c_{\text{L,n}})^2$.

3.3. Check if (2.278) is true, otherwise increase f_{infeas} by $(r_{\text{P}} - 1)^2$.

4. Compute dependent design parameters:

[20] The parameters are separated into the two classes "fixed parameters" and "dimensioning parameters" for superimposed optimization purposes, as mentioned in Sect. 2.7. Details on these superimposed optimizations are given below, in Chap. 4.

[21] Depending on the considered wind shear, only either z_0 or α_{H} must be specified.

[22] If the number of electrical cables is not specified here, it is maximized below, in Step 6.2.9.

[23] If the installed nominal electrical power is not specified here, Eq. (2.248) is considered below, in Step 13.

[24] The minimum airflow speed is chosen as input parameter, because $v_{\text{a,min}}$ is somewhat constant across many system sizes. With that, the maximum allowed airborne mass during crosswind flight is computed below, in Step 15.3.1.

[25] The tether resistance is chosen as input parameter over e.g. the wire cross section area or the (targeted) tether efficiency as in the prior work of the author of this dissertation [106]. The reasons for this approach include that R_{te} is in a narrow range across many system sizes with an optimal value usually the order of $1\,\Omega$ (cf. below, Chaps. 3 and 5), and, most importantly, it allows a sequence of explicit analytical equations.

[26] If the parameter set from Step 1 is detected as infeasible at any later step, the computation could be simply aborted (possibly with an error message) right there for minimal computation time. However, in the here used implementation, the computation is continued as follows: First, the infeasibility variable f_{infeas} is increased by a value proportional to the square of the distance from the next feasible value of the infeasible variable. With that, a continuous value of the infeasibility is known, instead of just a boolean condition, although clearly a boolean condition can be derived from that by checking if f_{infeas} is equal to zero. With that continuous infeasibility, a superimposed optimizer can easier find a feasible set of parameters by minimizing the continuous f_{infeas}. Second, either the computation is then aborted, or the variable causing the infeasibility is set to the next feasible value. This ensures that complex and `nan` values are avoided in later steps. Finally, the computation is continued normally in order to detect further conditions for infeasibility, which might be independent of previously discovered infeasibilities, to further increase f_{infeas}. This may help an optimizer to find feasible designs quicker. However, the computed results of the power curve etc. are likely nonsense which is indicated if $f_{\text{infeas}} \neq 0$.

4.1. Compute A with (2.43) converted to

$$A = \frac{b^2}{\mathcal{R}} n_{\mathrm{mw}}. \tag{2.302}$$

4.2. Compute nominal effective altitude h_{n} with $h = h_{\mathrm{n}}$ and $\vartheta = \vartheta_{\mathrm{n}}$ in (2.160).

4.3. Compute ω_{n} with (2.32).

5. Compute $d_{\mathrm{te,mech}}$ (first set of computations for first power point, II↔III(a)):

5.1. Compute $C_{\mathrm{L,n}}$ with $C_{\mathrm{L,n}} = C_{\mathrm{L}}$, $c_{\mathrm{L}} = c_{\mathrm{L,n}}$ in (2.39) and (2.15).

5.2. Compute $F_{||,\mathrm{n}}$ with (2.217).

5.3. Compute $A_{\mathrm{te,mech}}$ and $d_{\mathrm{te,mech}}$ with (2.55)–(2.59).

6. Compute d_{te} and m_{te} (second set of computations for first power point, II↔III(a)):

6.1. If no $n_{\mathrm{te,c}}$ was specified in Step 1.2, initialize it with $n_{\mathrm{te,c}} = 2$.

6.2. Compute $d_{\mathrm{te,c}}$ and its feasibility, and possibly maximize $n_{\mathrm{te,c}}$ for the given $d_{\mathrm{te,mech}}$:

6.2.1. Compute $R_{\mathrm{te,c,w}}$ with (2.66) converted to

$$R_{\mathrm{te,c,w}} = \frac{R_{\mathrm{te}} n_{\mathrm{te,c}}}{4}. \tag{2.303}$$

6.2.2. Compute $A_{\mathrm{te,c,w}}$ with (2.61) in (2.62) converted to

$$A_{\mathrm{te,c,w}} = f_{\mathrm{te,c,w}} \frac{1}{\kappa_{\mathrm{te,c,w}}} L_{\mathrm{te}} \frac{1}{R_{\mathrm{te,c,w}}} \tag{2.304}$$

6.2.3. Compute $d_{\mathrm{te,c,w}}$ with (2.64) and $r_{\mathrm{te,c,w}}$ with (2.65).

6.2.4. Compute $w_{\mathrm{te,c,ins}}$ by substituting (2.78) into (2.67) and solved for $w_{\mathrm{te,c,ins}}$ which is

$$\begin{aligned}
S_{\mathrm{te,ins}} f_{\mathrm{te,ins}} \frac{U_{\mathrm{te,n}}}{2} &= E_{\mathrm{te,ins}} r_{\mathrm{te,c,w}} \ln\left(\frac{r_{\mathrm{te,c,w}} + w_{\mathrm{te,c,ins}}}{r_{\mathrm{te,c,w}}}\right) \\
\Leftrightarrow \frac{S_{\mathrm{te,ins}} f_{\mathrm{te,ins}} U_{\mathrm{te,n}}}{2E_{\mathrm{te,ins}} r_{\mathrm{te,c,w}}} &= \ln\left(\frac{r_{\mathrm{te,c,w}} + w_{\mathrm{te,c,ins}}}{r_{\mathrm{te,c,w}}}\right) \qquad | \exp() \\
\exp\left(\frac{S_{\mathrm{te,ins}} f_{\mathrm{te,ins}} U_{\mathrm{te,n}}}{2E_{\mathrm{te,ins}} r_{\mathrm{te,c,w}}}\right) &= \frac{r_{\mathrm{te,c,w}} + w_{\mathrm{te,c,ins}}}{r_{\mathrm{te,c,w}}} \\
\Leftrightarrow r_{\mathrm{te,c,w}} \exp\left(\frac{S_{\mathrm{te,ins}} f_{\mathrm{te,ins}} U_{\mathrm{te,n}}}{2E_{\mathrm{te,ins}} r_{\mathrm{te,c,w}}}\right) &= r_{\mathrm{te,c,w}} + w_{\mathrm{te,c,ins}} \\
\Leftrightarrow w_{\mathrm{te,c,ins}} &= r_{\mathrm{te,c,w}} \left[\exp\left(\frac{S_{\mathrm{te,ins}} f_{\mathrm{te,ins}} U_{\mathrm{te,n}}}{2E_{\mathrm{te,ins}} r_{\mathrm{te,c,w}}}\right) - 1\right].
\end{aligned} \tag{2.305}$$

6.2.5. Compute $d_{\mathrm{te,c}}$ with (2.80).

6.2.6. Compute ϵ with (2.85).

6.2.7. Compute δ with (2.86) converted to

$$\delta = \frac{\sin(\epsilon)}{\sin[(\pi - \epsilon)/2]} (d_{\mathrm{te,mech}}/2 + d_{\mathrm{te,c}}/2). \tag{2.306}$$

6.2.8. If $n_{\mathrm{te,c}}$ was set in Step 1.1: Check if (2.87) is true, otherwise increase f_{infeas} by $(\delta - d_{\mathrm{te,c}})^2$.

6.2.9. If no $n_{\mathrm{te,c}}$ was specified in Step 1.2, and if the maximum $n_{\mathrm{te,c}}$, in which the condition (2.87) is just fulfilled is not yet obtained, increase $n_{\mathrm{te,c}}$ by two (or another even number, cf. [106]) and continue at Step 6.2.1.[27]

6.3. Compute d_{te} with (2.79).

6.4. Compute radii, cross section areas, volumes, masses, and total tether mass with (2.81)–(2.84).

6.5. Compute tether core increase factor

$$f_{\mathrm{te}} := \frac{d_{\mathrm{te}}}{d_{\mathrm{te,mech}}}, \tag{2.307}$$

i.e. the factor by which the tether diameter is increased due to the electrical cables and jacket, which was only estimated as fixed value in the prior work of the author of this dissertation [110].[28]

7. Remaining set of computations for the first power point/the transition II↔III(a):

7.1. Compute $c_{\mathrm{D,n}}$ with $c_{\mathrm{L}} = c_{\mathrm{L,n}}$ in (2.46) as well as $C_{\mathrm{D,k,mw,p,n}}$ with $c_{\mathrm{D}} = c_{\mathrm{D,n}}$ in (2.41).

7.2. Compute $C_{\mathrm{D,k,mw,i,n}}$ with $C_{\mathrm{L,k,mw}} = C_{\mathrm{L,n}}$ in (2.42).

7.3. Compute $C_{\mathrm{D,k,n}}$ with $C_{\mathrm{D,k,mw,p,n}}$ and $C_{\mathrm{D,k,mw,i,n}}$ in (2.40) and (2.33) with $C_{\mathrm{D,k,a}} = C_{\mathrm{D,k,a,min}} = 0$.

7.4. Compute $C_{\mathrm{D,te}}$ with (2.47).

7.5. Compute $C_{\mathrm{D,eq,n}}$ with $C_{\mathrm{D,k,n}}$ and $C_{\mathrm{D,te}}$ in (2.12).

7.6. Compute $C_{\mathrm{D,rot,n(1)}}$ with (2.190).

7.7. Compute $P_{\mathrm{a,n(1)}}$ with (2.221).

7.8. Compute $\zeta_{\mathrm{n(1)}}$ with (2.194).[28]

7.9. Compute $v_{\mathrm{w,n(1)}}$ with (2.220).

7.10. Compute $f_{\mathrm{shear,n}}$ with $h = h_{\mathrm{n}}$ in (2.159).

7.11. Compute $v_{\mathrm{w},h_{\mathrm{ref}}} = v_{\mathrm{w},h_{\mathrm{ref}},\mathrm{n(1)}}$ with $v_{\mathrm{w}} = v_{\mathrm{w,n(1)}}$ and $f_{\mathrm{shear}} = f_{\mathrm{shear,n}}$ in (2.158) converted to

$$v_{\mathrm{w},h_{\mathrm{ref}},\mathrm{n(1)}} = \frac{v_{\mathrm{w,n(1)}}}{f_{\mathrm{shear,n}}}. \tag{2.308}$$

8. Set of computations for the transition I(b)↔II and for the cut-in point/the transition I(a)↔I(b):

8.1. Compute $v_{\mathrm{w,I\leftrightarrow II}}$ with (2.209).

8.2. Compute $v_{\mathrm{w},h_{\mathrm{ref}}} = v_{\mathrm{w},h_{\mathrm{ref}},\mathrm{I\leftrightarrow II}}$ with $v_{\mathrm{w}} = v_{\mathrm{w,I\leftrightarrow II}}$ and $f_{\mathrm{shear}} = f_{\mathrm{shear,n}}$ in (2.158) converted to

$$v_{\mathrm{w},h_{\mathrm{ref}},\mathrm{I\leftrightarrow II}} = \frac{v_{\mathrm{w,I\leftrightarrow II}}}{f_{\mathrm{shear,n}}}. \tag{2.309}$$

8.3. Compute $v_{\mathrm{w,cut\text{-}in}}$ with (2.211).

8.4. Compute $v_{\mathrm{w},h_{\mathrm{ref}}} = v_{\mathrm{w},h_{\mathrm{ref}},\mathrm{cut\text{-}in}}$ with $v_{\mathrm{w}} = v_{\mathrm{w,cut\text{-}in}}$, (2.211), and with $f_{\mathrm{shear}} = f_{\mathrm{shear,n}}$ in (2.158) converted to

$$v_{\mathrm{w},h_{\mathrm{ref}},\mathrm{cut\text{-}in}} = \frac{v_{\mathrm{w,cut\text{-}in}}}{f_{\mathrm{shear,n}}} = \frac{2}{3}\frac{v_{\mathrm{w,I\leftrightarrow II}}}{f_{\mathrm{shear,n}}} = \frac{2}{3}v_{\mathrm{w},h_{\mathrm{ref}},\mathrm{I\leftrightarrow II}}. \tag{2.310}$$

[27] This step is also interpreted as "explicit", because it is optional (only executed if no $n_{\mathrm{te,c}}$ was specified in Step 1.2) and because the search for the optimal $n_{\mathrm{te,c}}$ requires only a few iterations with low computational load of the few explicit analytical equations.

[28] This step is optional, as the result is not needed in later steps.

9. Set of computations for the second power point/the transition III(a)↔III(b):
   9.1. Compute $P_{\mathrm{a,n(2)}}$ with (2.224).
   9.2. Compute $C_{\mathrm{D,rot,n(2)}}$ with (2.229).
   9.3. Compute $v_{\mathrm{w,n(2)}}$ with (2.225), whereby inserting (2.229) leads to the simpler expression

$$v_{\mathrm{w,n(2)}} = \frac{C_{\mathrm{D,rot,n(2)}} + C_{\mathrm{D,eq,n}}}{\cos(\varphi_{\mathrm{n}})\cos(\vartheta_{\mathrm{n}})C_{\mathrm{L,n}}} v_{\mathrm{a,n}}. \tag{2.311}$$

   9.4. Compute $v_{\mathrm{w},h_{\mathrm{ref}}} = v_{\mathrm{w},h_{\mathrm{ref}},\mathrm{n(2)}}$ with $v_{\mathrm{w}} = v_{\mathrm{w,n(2)}}$ and $f_{\mathrm{shear}} = f_{\mathrm{shear,n}}$ in (2.158) converted to

$$v_{\mathrm{w},h_{\mathrm{ref}},\mathrm{n(2)}} = \frac{v_{\mathrm{w,n(2)}}}{f_{\mathrm{shear,n}}}. \tag{2.312}$$

   9.5. Check if (2.279) is true, otherwise increase f_{infeas} by $(v_{\mathrm{w},h_{\mathrm{ref}},\mathrm{n(2)}} - v_{\mathrm{w},h_{\mathrm{ref}},\mathrm{cut\text{-}out}})^2$.
10. Set of computations for transitions inside Region III(b):[29]
   10.1. Determine minimum lift coefficient:
      10.1.1. Compute $c_{\mathrm{L,min\text{-}F}}$ with (2.232).
      10.1.2. Compute $c_{\mathrm{L,min}}$ with (2.233).
   10.2. Set of computations for the transition III(b)-1↔III(b)-2:
      10.2.1. Compute k_1 to k_4 with (B.1)–(B.3) in (B.4)–(B.7).
      10.2.2. Compute $v_{\mathrm{w,III(b)\text{-}1\leftrightarrow III(b)\text{-}2}}$ with (B.12).
      10.2.3. Compute $v_{\mathrm{w},h_{\mathrm{ref}},\mathrm{III(b)\text{-}1\leftrightarrow III(b)\text{-}2}}$ with $f_{\mathrm{shear}} = f_{\mathrm{shear,n}}$ in (B.13).
   10.3. Set of computations for the transition III(b)-2↔III(b)-3:
      10.3.1. Compute $v_{\mathrm{w,III(b)\text{-}2,end}}$ with (B.21).
      10.3.2. Compute $v_{\mathrm{w},h_{\mathrm{ref}},\mathrm{III(b)\text{-}2\leftrightarrow III(b)\text{-}3}}$ with $f_{\mathrm{shear}} = f_{\mathrm{shear,n}}$ in (B.22).
11. At this point, all transition wind speeds of the power curve regions are known and the complete power curve with all actuations and further derived results can be computed. For a $v_{\mathrm{w},h_{\mathrm{ref}}} \in [0, \infty)$:
   11.1. Compute v_{w} with $f_{\mathrm{shear}} = f_{\mathrm{shear,n}}$ in (2.159) and further in (2.158).[30]
   11.2. Compute actuations ...
      11.2.1. ... for Region I, i.e. if $0 \leq v_{\mathrm{w},h_{\mathrm{ref}}} < v_{\mathrm{w},h_{\mathrm{ref}},\mathrm{I}\leftrightarrow\mathrm{II}}$:
         11.2.1.1. Compute $C_{\mathrm{D,rot}} = C_{\mathrm{D,rot,I}}$ with (2.207).
         11.2.1.2. Set $c_{\mathrm{L}} = c_{\mathrm{L,I}} = c_{\mathrm{L,n}}$ according to (2.202).
         11.2.1.3. Set $C_{\mathrm{D,k,a}} = C_{\mathrm{D,k,a,I}} = 0$ according to (2.196).
         11.2.1.4. Set $\Delta\varphi_{\mathrm{a}} = \Delta\varphi_{\mathrm{a,I}} = 0$ according to (2.197).
         11.2.1.5. Set $\Delta\vartheta_{\mathrm{a}} = \Delta\vartheta_{\mathrm{a,I}} = 0$ according to (2.198).
      11.2.2. ... for Region II, i.e. if $v_{\mathrm{w},h_{\mathrm{ref}},\mathrm{I}\leftrightarrow\mathrm{II}} \leq v_{\mathrm{w},h_{\mathrm{ref}}} < v_{\mathrm{w},h_{\mathrm{ref}},\mathrm{II}\leftrightarrow\mathrm{III(a)}}$:
         11.2.2.1. Set $C_{\mathrm{D,rot}} = C_{\mathrm{D,rot,II}} = C_{\mathrm{D,rot,n(1)}}$ according to (2.190).
         11.2.2.2. Set $c_{\mathrm{L}} = c_{\mathrm{L,II}} = c_{\mathrm{L,n}}$ according to (2.187).
         11.2.2.3. Set $C_{\mathrm{D,k,a}} = C_{\mathrm{D,k,a,II}} = 0$ according to (2.184).
         11.2.2.4. Set $\Delta\varphi_{\mathrm{a}} = \Delta\varphi_{\mathrm{a,II}} = 0$ according to (2.185).

[29] These steps are optional, if the exact actuations in Region III(b) are not of interest. (The important power and from that derived values are unaffected, if it is simply computed by $P_{\mathrm{a}} = P_{\mathrm{a,n(2)}}$ instead of from the actuations in Step 11.3.)

[30] This value of v_{w} is corrected in a later step, if the altitude h is changed from the nominal h_{n}.

11.2.2.5. Set $\Delta\vartheta_\mathrm{a} = \Delta\vartheta_\mathrm{a,II} = 0$ according to (2.186).

11.2.3. ... for Region III(a), i.e. if $v_\mathrm{w,}h_\mathrm{ref,II\leftrightarrow III(a)} \leq v_\mathrm{w,}h_\mathrm{ref} < v_\mathrm{w,}h_\mathrm{ref,III(a)\leftrightarrow III(b)}$:

11.2.3.1. Compute $C_\mathrm{D,rot} = C_\mathrm{D,rot,III(a)}$ with (2.216).

11.2.3.2. Set $c_\mathrm{L} = c_\mathrm{L,III(a)} = c_\mathrm{L,n}$ according to (2.215).

11.2.3.3. Set $C_\mathrm{D,k,a} = C_\mathrm{D,k,a,III(a)} = 0$ according to (2.212).

11.2.3.4. Set $\Delta\varphi_\mathrm{a} = \Delta\varphi_\mathrm{a,III(a)} = 0$ according to (2.213).

11.2.3.5. Set $\Delta\vartheta_\mathrm{a} = \Delta\vartheta_\mathrm{a,III(a)} = 0$ according to (2.214).

11.2.4. ... for Region III(b)-1, i.e. if $v_\mathrm{w,}h_\mathrm{ref,III(a)\leftrightarrow III(b)} \leq v_\mathrm{w,}h_\mathrm{ref} < v_\mathrm{w,}h_\mathrm{ref,III(b)\text{-}1\leftrightarrow III(b)\text{-}2}$:

11.2.4.1. Set $C_\mathrm{D,rot} = C_\mathrm{D,rot,III(b)} = C_\mathrm{D,rot,n(2)}$ according to (2.229).

11.2.4.2. Check if the radicand in (B.9) is greater or equal to zero, otherwise first increase f_infeas by the square of the radicand, second set the radicand to zero, third compute $c_\mathrm{L} = c_\mathrm{L,III(b)\text{-}1}$ with the possibly altered radicand and (B.9).

11.2.4.3. Set $C_\mathrm{D,k,a} = C_\mathrm{D,k,a,III(b)\text{-}1} = 0$ according to (B.1).

11.2.4.4. Set $\Delta\varphi_\mathrm{a} = \Delta\varphi_\mathrm{a,III(b)\text{-}1} = 0$ according to (B.2).

11.2.4.5. Set $\Delta\vartheta_\mathrm{a} = \Delta\vartheta_\mathrm{a,III(b)\text{-}1} = 0$ according to (B.3).

11.2.5. ... for Region III(b)-2, i.e. if $v_\mathrm{w,}h_\mathrm{ref,III(b)\text{-}1\leftrightarrow III(b)\text{-}2} \leq v_\mathrm{w,}h_\mathrm{ref} < v_\mathrm{w,}h_\mathrm{ref,III(b)\text{-}2\leftrightarrow III(b)\text{-}3}$:

11.2.5.1. Set $C_\mathrm{D,rot} = C_\mathrm{D,rot,III(b)} = C_\mathrm{D,rot,n(2)}$ according to (2.229).

11.2.5.2. Set $c_\mathrm{L} = c_\mathrm{L,III(b)\text{-}2} = c_\mathrm{L,min}$ with (B.16).

11.2.5.3. Compute $C_\mathrm{D,k,a} = C_\mathrm{D,k,a,III(b)\text{-}2}$ with (B.20).

11.2.5.4. Set $\Delta\varphi_\mathrm{a} = \Delta\varphi_\mathrm{a,III(b)\text{-}2} = 0$ according to (B.14).

11.2.5.5. Set $\Delta\vartheta_\mathrm{a} = \Delta\vartheta_\mathrm{a,III(b)\text{-}2} = 0$ according to (B.15).

11.2.6. ... for Region III(b)-3, i.e. if $v_\mathrm{w,}h_\mathrm{ref,III(b)\text{-}2\leftrightarrow III(b)\text{-}3} \leq v_\mathrm{w,}h_\mathrm{ref} \leq v_\mathrm{w,}h_\mathrm{ref,cut\text{-}out}$:

11.2.6.1. Set $C_\mathrm{D,rot} = C_\mathrm{D,rot,III(b)} = C_\mathrm{D,rot,n(2)}$ according to (2.229).

11.2.6.2. Set $c_\mathrm{L} = c_\mathrm{L,III(b)\text{-}3} = c_\mathrm{L,min}$ according to (B.23).

11.2.6.3. Set $C_\mathrm{D,k,a} = C_\mathrm{D,k,a,III(b)\text{-}3} = C_\mathrm{D,k,a,max}$ according to (B.24).

11.2.6.4. Set $\Delta\varphi_\mathrm{a} = \Delta\varphi_\mathrm{a,III(b)\text{-}3} = 0$.[31]

11.2.6.5. Compute $\Delta\vartheta_\mathrm{a} = \Delta\vartheta_\mathrm{a,III(b)\text{-}3}$ by solving (B.31).[32] Correct v_w with the new altitude h (2.160) in (2.159) and (2.158).

11.3. If $v_\mathrm{w,}h_\mathrm{ref} \in [0, v_\mathrm{w,}h_\mathrm{ref,cut\text{-}out}]$, then compute derived values ...

11.3.1. ... for aerodynamic coefficients:

11.3.1.1. Compute C_L with (2.39) and (2.15).

11.3.1.2. Compute c_D with (2.46) as well as $C_\mathrm{D,k,mw,p}$ with (2.41).

11.3.1.3. Compute $C_\mathrm{D,k,mw,i}$ with $C_\mathrm{L,k,mw} = C_\mathrm{L}$ in (2.42).

11.3.1.4. Compute $C_\mathrm{D,k}$ with (2.40) and (2.33).

11.3.1.5. Compute $C_\mathrm{D,eq}$ with (2.12).

11.3.1.6. Compute C_D with (2.11).

11.3.2. ... for azimuth, elevation, and altitude:

11.3.2.1. Compute φ with (2.168).

[31] In this variant, the azimuth is not utilized for the power limitation, cf. Sect. 2.7.12 and Appendix B.5.

[32] In the here utilized implementation, Eq. (B.31) is solved numerically with a grid search and a good initial guess. This is implemented as for-loop in which only a few computations are made with a guaranteed convergence. Overall, the computational load of a single iteration is low and the number of iterations is low resulting overall in a low computational load. Moreover, this computation is optional and could be skipped, because the power is constant and known for Region III(b). Therefore, also this step can be considered as analytical and explicit.

11.3.2.2. Compute ϑ with (2.169).

11.3.2.3. Compute h with (2.160).

11.3.3. ... for airflow speed, parallel force, and aerodynamic power:

11.3.3.1. Compute v_a with (2.175).

11.3.3.2. Compute $F_{||}$ with (2.178).

11.3.3.3. Compute P_a with (2.18).

11.3.4. ... for induction factor:

11.3.4.1. Check if (2.106) is true, otherwise first increase f_infeas by $(C_\mathrm{D,rot} - C_\mathrm{D,rot,max})^2$ with $C_\mathrm{D,rot,max}$ from (2.106), second set $C_\mathrm{D,rot} = C_\mathrm{D,rot,max}$.

11.3.4.2. Compute a with (2.101).

11.3.5. ... other powers, efficiencies, and tether current for $P_\mathrm{a} \geq 0$:[33]

11.3.5.1. Compute $\eta_\mathrm{a} = \eta_{\mathrm{a},+}$ with (2.108).

11.3.5.2. Compute $\eta_\mathrm{rot,\Pi} = \eta_{\mathrm{rot},\Pi,+}$ with (2.120).

11.3.5.3. Compute P_rot with (2.145).

11.3.5.4. Compute P_s with (2.146).

11.3.5.5. Compute $P_\mathrm{el,m}$ with (2.147).

11.3.5.6. Compute $P_\mathrm{el,k}$ with (2.148).

11.3.5.7. Check if (2.131) is true, otherwise first increase f_infeas by $(P_\mathrm{el,k} - P_\mathrm{el,k,max})^2$ with $P_\mathrm{el,k,max}$ from (2.130), second set $P_\mathrm{el,k} = P_\mathrm{el,k,max}$.

11.3.5.8. Compute I_te with (2.127).

11.3.5.9. Compute $P_\mathrm{te\text{-}loss}$ with (2.88).

11.3.5.10. Compute $P_\mathrm{el,g}$ with (2.125).

11.3.5.11. If $P_\mathrm{a} > 0$, compute $\eta_\mathrm{te} = \eta_{\mathrm{te},+}$ through (2.122) and (2.123). Otherwise, set $\eta_\mathrm{te} = 1$.

11.3.5.12. Compute P_el with (2.150).

11.3.5.13. Compute η_Π with (2.157).[28]

11.3.6. ... other powers, efficiencies, and tether current for $P_\mathrm{a} < 0$:

11.3.6.1. Compute $\eta_\mathrm{a} = \eta_{\mathrm{a},-}$ with (2.109).

11.3.6.2. Compute $\eta_\mathrm{rot,\Pi} = \eta_{\mathrm{rot},\Pi,-}$ with (2.121).

11.3.6.3. Compute P_rot with (2.156) converted to

$$P_\mathrm{rot} = \frac{1}{\eta_{\mathrm{rot},\Pi,-}} P_\mathrm{a}. \tag{2.313}$$

11.3.6.4. Compute P_s with (2.155) converted to

$$P_\mathrm{s} = \frac{1}{\eta_{\mathrm{s},-}} P_\mathrm{rot}. \tag{2.314}$$

11.3.6.5. Compute $P_\mathrm{el,m}$ with (2.154) converted to

$$P_\mathrm{el,m} = \frac{1}{\eta_{\mathrm{el,m},-}} P_\mathrm{s}. \tag{2.315}$$

[33] Both cases, $P_\mathrm{a} > 0$ and $P_\mathrm{a} = 0$, are covered in the following steps, because the important equations also cover the result for $\lim_{P_\mathrm{a} \to +0}$.

11.3.6.6. Compute $P_{\mathrm{el,k}}$ with (2.153) converted to

$$P_{\mathrm{el,k}} = \frac{1}{\eta_{\mathrm{pe,k,-}}} P_{\mathrm{el,m}}. \tag{2.316}$$

11.3.6.7. Check if (2.135) is true, otherwise first increase f_{infeas} by $(P_{\mathrm{el,k}} - P_{\mathrm{el,k,min}})^2$ with $P_{\mathrm{el,k,min}}$ from (2.135), second set $P_{\mathrm{el,k}} = P_{\mathrm{el,k,min}}$.

11.3.6.8. Compute $P_{\mathrm{el,g}}$ with (2.134).

11.3.6.9. Compute I_{te} with (2.127).

11.3.6.10. Compute $P_{\mathrm{te\text{-}loss}}$ with (2.88).

11.3.6.11. Compute $\eta_{\mathrm{te}} = \eta_{\mathrm{te,-}}$ with (2.122) and (2.124).

11.3.6.12. Compute P_{el} with (2.151) converted to

$$P_{\mathrm{el}} = \frac{1}{\eta_{\mathrm{pe,g,-}}} P_{\mathrm{el,g}}. \tag{2.317}$$

11.3.6.13. Compute η_{Π} with (2.157).[28]

11.4. If not enough $v_{\mathrm{w},h_{\mathrm{ref}}} \in [0, \infty)$ have been computed, continue at Step 11.1 with the next $v_{\mathrm{w},h_{\mathrm{ref}}} \in [0, \infty)$.

12. Compute remaining nominal generative values:[34]

12.1. Check if (2.106) is true for $C_{\mathrm{D,rot}} = C_{\mathrm{D,rot,n(2)}}$, otherwise first increase f_{infeas} by $(C_{\mathrm{D,rot,n(2)}} - C_{\mathrm{D,rot,max}})^2$ with $C_{\mathrm{D,rot,max}}$ from (2.106), second set $C_{\mathrm{D,rot,n(2)}} = C_{\mathrm{D,rot,max}}$, third compute $a_{\mathrm{n(2)}}$ with (2.241).

12.2. Compute $\eta_{\mathrm{a,n(2)}}$ with (2.242).

12.3. Compute $P_{\mathrm{a,+,n}}$, $P_{\mathrm{rot,+,n}}$, $P_{\mathrm{s,+,n}}$, $P_{\mathrm{el,m,+,n}}$, and $P_{\mathrm{el,k,+,n}}$ with (2.234)–(2.238).

12.4. Check if (2.131) is true for $P_{\mathrm{el,k}} = P_{\mathrm{el,k,+,n}}$, otherwise first increase f_{infeas} by $(P_{\mathrm{el,k,+,n}} - P_{\mathrm{el,k,max}})^2$ with $P_{\mathrm{el,k,max}}$ from (2.130), second set $P_{\mathrm{el,k,+,n}} = P_{\mathrm{el,k,max}}$.

12.5. Compute $I_{\mathrm{te,+,n}}$ with (2.245).

12.6. Compute $P_{\mathrm{te\text{-}loss,+,n}}$ with (2.244).

12.7. Compute $P_{\mathrm{el,g,+,n}}$ with $P_{\mathrm{el,k,+,n}}$ and $P_{\mathrm{te\text{-}loss,+,n}}$ in (2.125).

12.8. Compute $\eta_{\mathrm{te,+,n}}$ with (2.243).

12.9. Compute $P_{\mathrm{el,g,+,n}}$ with (2.239).

12.10. Compute $P_{\mathrm{el,+,n}}$ with (2.240).

12.11. Compute nominal (generative) total efficiency $\eta_{\Pi,\mathrm{n}} = \eta_{\Pi,\mathrm{n},+}$ with nominal values in (2.157).[28]

13. If $P_{\mathrm{el,n\text{-}ins}}$ was not specified in Step 1.1, define $P_{\mathrm{el,n\text{-}ins}}$ with (2.248). If $P_{\mathrm{el,n\text{-}ins}} < P_{\mathrm{el,+,n}}$, i.e. if (2.246) is not fulfilled, abord computation with error message.

14. Compute maximum available consumptive powers:

14.1. Compute $\hat{P}_{\mathrm{el,-}}$ with (2.249).

14.2. Compute $\hat{P}_{\mathrm{el,g,-}}$ with (2.250).

14.3. Compute $\hat{I}_{\mathrm{te,-}}$ with (2.258).

14.4. Compute $\hat{P}_{\mathrm{te\text{-}loss,-}}$ with (2.257).

[34] The following computations could also be simplified by taking simply the maximum value from the power curve computations of Step 11.

14.5. Compute $\hat{P}_{\mathrm{el,k},-}$ with $\hat{P}_{\mathrm{el,g},-}$ and $\hat{P}_{\mathrm{te\text{-}loss},-}$ in (2.125) converted to

$$\hat{P}_{\mathrm{el,k},-} = \hat{P}_{\mathrm{el,g},-} + \hat{P}_{\mathrm{te\text{-}loss},-}. \tag{2.318}$$

14.6. Compute $\hat{\eta}_{\mathrm{te},-}$ with (2.256).

14.7. Compute $\hat{P}_{\mathrm{el,m},-}$ with (2.252).

14.8. Compute $\hat{P}_{\mathrm{s},-}$ with (2.253).

14.9. Compute $\hat{P}_{\mathrm{rot},-}$ with (2.254).

14.10. Compute nominal consumptive aerodynamic power during crosswind flight:

14.10.1. Compute $C_{\mathrm{D,rot},-,\mathrm{n}}$ with (2.261).

14.10.2. Compute $P_{\mathrm{a},-,\mathrm{n}}$ with (2.264).

14.11. Compute nominal consumptive rotor power during crosswind flight (without rotor failure) and check for feasibility:

14.11.1. Compute $a_{-,\mathrm{n}}$ with (2.262).

14.11.2. Compute $\eta_{\mathrm{a},-,\mathrm{n}}$ with (2.263).

14.11.3. Compute $P_{\mathrm{rot},-,\mathrm{n}}$ with (2.265).

14.11.4. Check if (2.266) is true, otherwise increase f_{infeas} by $(P_{\mathrm{rot},-,\mathrm{n}} - \hat{P}_{\mathrm{rot},-})^2$.

14.12. Compute nominal consumptive rotor power during crosswind flight with rotor failure and check for feasibility:

14.12.1. Compute $\hat{P}_{\mathrm{rot},-,\mathrm{flt}}$ with (2.267).

14.12.2. Compute $a_{-,\mathrm{n,flt}}$ with (2.268).

14.12.3. Compute $\eta_{\mathrm{a},-,\mathrm{n,flt}}$ with (2.269).

14.12.4. Compute $P_{\mathrm{rot},-,\mathrm{n,flt}}$ with (2.270).

14.12.5. Check if (2.271) is true, otherwise increase f_{infeas} by $(P_{\mathrm{rot},-,\mathrm{n,flt}} - \hat{P}_{\mathrm{rot},-,\mathrm{flt}})^2$.

14.13. Compute $\hat{P}_{\mathrm{a,hov}}$ with (2.272).

14.14. Compute $\hat{P}_{\mathrm{a,hov,flt}}$ with (2.274).

15. Compute (maximum allowed) masses (other than tether mass):[35]

15.1. Compute $P_{\mathrm{s,n\text{-}ins}}$ and $P_{\mathrm{el,m,n\text{-}ins}}$ with (2.259).

15.2. Compute m_{m} and $m_{\mathrm{pe,k}}$ with (2.29) and (2.30).

15.3. For crosswind flight (i.e. Region I(a) with $v_{\mathrm{w}} = 0$):

15.3.1. Compute maximum allowed airborne mass for crosswind flight $\hat{m}_{\mathrm{a,flight}}$ with (2.205) equated with (2.25) with $\vartheta = \vartheta_{\mathrm{n}}$ and solved for $m_{\mathrm{a}} = \hat{m}_{\mathrm{a,flight}}$, which is

$$\begin{aligned} \frac{1}{2}\rho v_{\mathrm{a,min}}^2 A C_{\mathrm{L,n}} &= \hat{m}_{\mathrm{a,flight}} g \frac{\cos(\vartheta_{\mathrm{n}})}{\sin(\psi_{\mathrm{w,n}})} \\ \Leftrightarrow \hat{m}_{\mathrm{a,flight}} &= \frac{\frac{1}{2}\rho v_{\mathrm{a,min}}^2 A C_{\mathrm{L,n}}}{g} \frac{\sin(\psi_{\mathrm{w,n}})}{\cos(\vartheta_{\mathrm{n}})}. \end{aligned} \tag{2.319}$$

15.3.2. Compute maximum allowed kite mass for crosswind flight $\hat{m}_{\mathrm{k,flight}}$ with $m_{\mathrm{a}} = \hat{m}_{\mathrm{a,flight}}$ and $m_{\mathrm{k}} = \hat{m}_{\mathrm{k,flight}}$ in (2.27) and converted to

$$\hat{m}_{\mathrm{k,flight}} = \hat{m}_{\mathrm{a,flight}} - f_{\mathrm{m\text{-}te}} m_{\mathrm{te}}. \tag{2.320}$$

[35] Note that (2.273) and (2.275) are automatically satisfied with that approach.

15.3.3. Compute maximum allowed mass of airframe and other for crosswind flight $\hat{m}_{\text{af\&o,flight}}$ with $m_{\text{k}} = \hat{m}_{\text{k,flight}}$ and $m_{\text{af\&o}} = \hat{m}_{\text{af\&o,flight}}$ in (2.28) and converted to

$$\hat{m}_{\text{af\&o,flight}} = \hat{m}_{\text{k,flight}} - m_{\text{m}} - m_{\text{pe,k}}. \tag{2.321}$$

15.4. For hovering during normal operation:

15.4.1. Compute maximum allowed airborne mass for hovering during normal operation $\hat{m}_{\text{a,hov,ok}}$ with $P_{\text{a,hov,ok}} = \hat{P}_{\text{a,hov}}$ in (2.115) solved for $m_{\text{a}} = \hat{m}_{\text{a,hov,ok}}$, which is

$$\begin{aligned}
\hat{P}_{\text{a,hov}} &= -\sqrt{\frac{\left(S_{\text{hov,ok}}\hat{m}_{\text{a,hov,ok}}g\right)^3}{2\rho r_{\text{rot}}A}} \\
\hat{P}^2_{\text{a,hov}} &= \frac{\left(S_{\text{hov,ok}}\hat{m}_{\text{a,hov,ok}}g\right)^3}{2\rho r_{\text{rot}}A} \\
\Leftrightarrow \sqrt[3]{2\rho r_{\text{rot}}A\hat{P}^2_{\text{a,hov}}} &= S_{\text{hov,ok}}\hat{m}_{\text{a,hov,ok}}g \\
\Leftrightarrow \hat{m}_{\text{a,hov,ok}} &= \frac{\sqrt[3]{2\rho r_{\text{rot}}A\hat{P}^2_{\text{a,hov}}}}{S_{\text{hov,ok}}g}
\end{aligned} \tag{2.322}$$

15.4.2. Analogous to (2.320) and (2.321), compute maximum allowed kite mass and maximum allowed mass of airframe and other for hovering during normal operation, i.e.

$$\hat{m}_{\text{k,hov,ok}} = \hat{m}_{\text{a,hov,ok}} - f_{\text{m-te}}m_{\text{te}} \tag{2.323}$$

$$\hat{m}_{\text{af\&o,hov,ok}} = \hat{m}_{\text{k,hov,ok}} - m_{\text{m}} - m_{\text{pe,k}}. \tag{2.324}$$

15.5. For hovering with rotor failure:

15.5.1. Compute maximum allowed airborne mass for hovering with rotor failure $\hat{m}_{\text{a,hov,flt}}$ with $P_{\text{a,hov,flt}} = \hat{P}_{\text{a,hov,flt}}$ in (2.116) solved for $m_{\text{a}} = \hat{m}_{\text{a,hov,flt}}$, which is

$$\begin{aligned}
\hat{P}_{\text{a,hov,flt}} &= -\sqrt{\frac{\left(S_{\text{hov,flt}}\hat{m}_{\text{a,hov,flt}}g\right)^3}{2\rho\frac{n_{\text{rot}}-2}{n_{\text{rot}}}r_{\text{rot}}A}} \\
\hat{P}^2_{\text{a,hov,flt}} &= \frac{\left(S_{\text{hov,flt}}\hat{m}_{\text{a,hov,flt}}g\right)^3}{2\rho\frac{n_{\text{rot}}-2}{n_{\text{rot}}}r_{\text{rot}}A} \\
\Leftrightarrow \sqrt[3]{2\rho\frac{n_{\text{rot}}-2}{n_{\text{rot}}}r_{\text{rot}}A\hat{P}^2_{\text{a,hov,flt}}} &= S_{\text{hov,flt}}\hat{m}_{\text{a,hov,flt}}g \\
\Leftrightarrow \hat{m}_{\text{a,hov,flt}} &= \frac{\sqrt[3]{2\rho\frac{n_{\text{rot}}-2}{n_{\text{rot}}}r_{\text{rot}}A\hat{P}^2_{\text{a,hov,flt}}}}{S_{\text{hov,flt}}g}.
\end{aligned} \tag{2.325}$$

15.5.2. Analogous to (2.320) and (2.321), compute maximum allowed kite mass and maximum allowed mass of airframe and other for hovering during rotor failure, i.e.

$$\hat{m}_{\text{k,hov,flt}} = \hat{m}_{\text{a,hov,flt}} - f_{\text{m-te}}m_{\text{te}} \tag{2.326}$$

$$\hat{m}_{\text{af\&o,hov,flt}} = \hat{m}_{\text{k,hov,flt}} - m_{\text{m}} - m_{\text{pe,k}}. \tag{2.327}$$

15.6. Compute overall maximum allowed airborne mass, maximum allowed kite mass, and maximum allowed mass of airframe and other with

$$\hat{m}_\mathrm{a} = \min\{\hat{m}_\mathrm{a,flight}, \hat{m}_\mathrm{a,hov,ok}, \hat{m}_\mathrm{a,hov,flt}\} \tag{2.328}$$

$$\hat{m}_\mathrm{k} = \min\{\hat{m}_\mathrm{k,flight}, \hat{m}_\mathrm{k,hov,ok}, \hat{m}_\mathrm{k,hov,flt}\} \tag{2.329}$$

$$\hat{m}_\mathrm{af\&o} = \min\{\hat{m}_\mathrm{af\&o,flight}, \hat{m}_\mathrm{af\&o,hov,ok}, \hat{m}_\mathrm{af\&o,hov,flt}\}. \tag{2.330}$$

16. Compute economic performance:

16.1. Compute $p(v_{\mathrm{w},h_\mathrm{ref}})$ with (2.161) for all $v_{\mathrm{w},h_\mathrm{ref}}$.

16.2. Compute $P_{\mathrm{el},+}(v_{\mathrm{w},h_\mathrm{ref}})$ with (2.280) for all $v_{\mathrm{w},h_\mathrm{ref}}$.

16.3. Compute $E_\mathrm{el,yr}$ with (2.281) in (2.282).

16.4. Compute H with (2.283).

16.5. Compute $K_\mathrm{inv,pt}$ with (2.299).

16.6. Compute f_an with (2.287).

16.7. Compute maximum allowed investment costs $\hat{K}_\mathrm{inv}$ by solving (2.300) for k, inserting that into (2.297), and solving for $K_\mathrm{inv} = \hat{K}_\mathrm{inv}$, which is

$$\begin{aligned} k_\mathrm{LCOE} E_\mathrm{el,yr} &= \hat{K}_\mathrm{inv}(I_\mathrm{op} + f_\mathrm{an}) \\ \Leftrightarrow \hat{K}_\mathrm{inv} &= \frac{k_\mathrm{LCOE} E_\mathrm{el,yr}}{I_\mathrm{op} + f_\mathrm{an}}. \end{aligned} \tag{2.331}$$

16.8. Compute maximum allowed investment costs of airframe etc., development costs, and profit margin $\hat{K}_\mathrm{inv,o\&p}$ with $K_\mathrm{inv} = \hat{K}_\mathrm{inv}$ in (2.298) solved for $K_\mathrm{inv,o\&p} = \hat{K}_\mathrm{inv,o\&p}$, which is

$$\hat{K}_\mathrm{inv,o\&p} = \hat{K}_\mathrm{inv} - K_\mathrm{inv,pt}. \tag{2.332}$$

16.9. Compute T_am with (2.301).

17. Compute further derived results, if required, e.g.:

- Informative relations of the nominal power, such as power density w.r.t. kite area $P_\mathrm{el,n}/A$, power density w.r.t. maximum allowed total airborne mass $P_\mathrm{el,n}/(\hat{m}_\mathrm{k} + m_\mathrm{te})$, maximum allowed specific investment costs $\hat{K}_\mathrm{inv}/P_\mathrm{el,n}$.
- Turnover per year $E_\mathrm{el,yr} k_\mathrm{LCOE}$.
- Maximum allowed operational costs per year $\hat{K}_\mathrm{inv} I_\mathrm{op}$.
- Percentage-wise voltage drop over tether at nominal generative power $R_\mathrm{te} I_\mathrm{te,+,n}/U_\mathrm{te,n}$.
- Nominal wing loading $F_{||,\mathrm{n}}/(Ag)$.
- Specific tether power loss at maximum available consumptive power, which with (2.89) and (2.90) are

$$\hat{p}_\mathrm{te\text{-}loss,L,-} = \hat{P}_\mathrm{te\text{-}loss,-}/L_\mathrm{te} \tag{2.333}$$

and

$$\hat{p}_\mathrm{te\text{-}loss,A,-} = \hat{P}_\mathrm{te\text{-}loss,-}/(\pi d_\mathrm{te} L_\mathrm{te}), \tag{2.334}$$

which may occur during hovering if the actual airborne mass is equal to the maximum allowed airborne mass.

Moreover, check if constraints on these further derived values are met, e.g. if the wing loading $F_{||,\mathrm{n}}/(Ag)$ is not too high, otherwise increase f_infeas accordingly.

18. If performance is not satisfactory or if design parameters are infeasible (i.e. if $f_{\text{infeas}} \neq 0$), restart at Step 1.2 with a different set of parameters.

Step 18 is for an iterative optimization of the "dimensioning parameters". Note that Steps 1–17 are (mostly) explicit, particularly it includes explicitly the tether sizing, and thus allows a quick evaluation of a power plant design.

2.9.3 Implementation

The above stated algorithm can be straightforwardly implemented as computer program. Here, this task was completed with MATLAB together with result visualizations. Within the implementation, the power curve is computed for a discrete set of wind speeds in the reference altitude. The samples are chosen with small distances such that the results are quasi-continuous. The integral in (2.281) is then solved numerically with the trapezoidal rule. The implementation includes measures to increase computation speed, avoid numerical noise, avoid divisions by zero, and avoid complex and `nan` values. Steps 1–17 are implemented as a single MATLAB function. The core source is only a few hundred lines of code. For sake of compactness, further implementation details are omitted.

Chapter 3

Validation of the Systems Engineering Model

In this chapter the multidisciplinary steady drag power kite model (systems engineering model) derived in the previous chapter is validated by means of comparing the model predictions to (i) measured power curve data of Makani's Wing 7 in Sect. 3.1, (ii) expected data of Makani's M600 and M5 in Sect. 3.2, and (iii) simulations with a higher fidelity model in Sect. 3.3. Sect. 3.4 closes with concluding remarks. Within this chapter, some pages are intentionally left partly blank, such that text and corresponding tables and figures are close to each other.

3.1 Comparison to Power Curve Measurements of Makani's Wing 7

First, the model is validated against power curve measurements by Makani reported in [16] as well as data reported in [16, 102]. Only the aerodynamic power P_a as function of the wind speed and a few properties of the system like the mass of the tether m_te and of the kite m_k were found publicly. Therefore, only the model predictions of P_a, m_te, and maximum allowed kite mass $\hat{m}_\mathrm{k}$ can be used for this validation. In the following subsections, the model parameters required for this task are listed, the obtained results are presented, and the results as well as the in part uncertainly estimated parameters are discussed.

A preview of the here presented results was already given in the prior work of the author of this dissertation [104].

3.1.1 Parameters

Tab. 3.1 lists the parameters for the simulation of Makani's Wing 7. The main sources of the data are Refs. [16, 102]. Tab. 3.2 lists properties for a number of materials used in Tab. 3.1 and in later parts of this dissertation.

Table 3.1: Parameters for the Makani Wing 7 simulation.

Color-coding: green = reliable value available, e.g. from literature; yellow = no exact value known but good estimate available; red = neither exact value nor good estimate available, instead value had to be guessed ("scientific guess") or in part fitted to obtain reasonable results; light gray = irrelevant for power curve, but relevant for maximum allowed mass; dark gray = neither relevant for power curve nor for maximum allowed mass.

Parameter	Value	Comment/Justification
Environmental parameters for considered installation site.		
g	$= 9.81\,\mathrm{m/s^2}$	≈ Standard Gravity; but actual value of [16] and during tests could differ slightly
ρ	$= 1.255\,\mathrm{kg/m^3}$	≈ International Standard Atmosphere; but actual value of [16] and during tests could differ slightly
h_{ref}	$=$ *anything* $\neq 0$	no wind shear considered in [16]
α_{H}	$= 0$	no wind shear considered in [16]
λ	$=$ *anything*	has no effect on power curve or maximum allowed mass
μ	$=$ *anything*	has no effect on power curve or maximum allowed mass
Economic parameters for targeted market.		
k_{LCOE}	$=$ *anything*	has no effect on power curve or maximum allowed mass
I	$=$ *anything*	has no effect on power curve or maximum allowed mass
T	$=$ *anything*	has no effect on power curve or maximum allowed mass
I_{op}	$=$ *anything*	has no effect on power curve or maximum allowed mass
f_{avial}	$=$ *anything*	has no effect on power curve or maximum allowed mass
Kite aerodynamics parameters.		
b	$= 8\,\mathrm{m}$	Ref. [16, Fig. 28.7]
$\mathit{Æ}$	$= 16.1616$	$= b^2/A$ with $A = 3.96\,\mathrm{m^2}$ from [16, Fig. 28.7]
n_{mw}	$= 1$	Wing 7 is a monoplane, cf. e.g. [16]
$c_{\mathrm{D},0}$	$= 0.010$	based on data fitting for different airfoils, cf. Fig. 2.5
$c_{\mathrm{D},2}$	$= 0.005$	based on data fitting for different airfoils, cf. Fig. 2.5
$c_{\mathrm{L,n}}$	$= 2.2475$	$= C_{\mathrm{L,n}}(1 + 2/\mathit{Æ})$ with $C_{\mathrm{L,n}} = 2$ from [16, Fig. 28.7]
$c_{\mathrm{L,min\text{-}op}}$	$= 0.5$	estimated, but has no effect on the power curve w.r.t. the aerodynamic power or maximum allowed mass
e	$= 0.8$	estimated, slightly higher than $e \approx 0.7$ for rectangular wings to account for the winglets of Wing 7 [16, Fig. 28.7]; but actual value could differ
$C_{\mathrm{D,k,o}}$	$= 0.025$	$= (C_{\mathrm{D,k}} - C_{\mathrm{D,k,mw,i}})_{\mathrm{n}} - (c_{\mathrm{D},0} + c_{\mathrm{D},0} c_{\mathrm{L,n}}^2)$ with $(C_{\mathrm{D,k}} - C_{\mathrm{D,k,mw,i}})_{\mathrm{n}} = 0.06$ from [16, Tab. 28.1], cf. Chap. 2
$C_{\mathrm{D,k,a,max}}$	$= 0.1$	estimated, but has no effect on the power curve w.r.t. the aerodynamic power or maximum allowed mass

Table 3.1: Parameters for the Makani Wing 7 simulation. (continued)

Parameter	Value	Comment/Justification
Rotor parameters.		
n_{rot}	$= 4$	Wing 7 has four rotors, cf. e.g. [16]
r_{rot}	$= 0.52$	Ref. [16, p. 483]
$\eta_{\text{rot},+} = \eta_{\text{rot},-}$	$= 0.9$	estimated, but has no effect on the power curve w.r.t. the aerodynamic power
$\eta_{\text{rot,hov}}$	$= 0.9$	estimated, but has no effect on the power curve w.r.t. the aerodynamic power
Tether parameters.		
L_{te}	$= 144\,\text{m}$	Ref. [102]
$U_{\text{te,n}}$	$= 1,100\,\text{V}$	Ref. [102]
R_{te}	$= 5\,\Omega$	estimated based on model results; actual value could be very different
$c_{\text{D,te}}$	$= 1$	estimated, $\approx c_{\text{D}}$ of cylinder at reasonable N_{Re}
$f_{\text{m-te}}$	$= 0.5$	estimated, but has no effect on the power curve
$n_{\text{te,c}}$	$= 6$	same as in [81]; based on model results: enough room for communication cables; but actual value could differ, though the effect on results is marginal
$\rho_{\text{te,mech}}$	$= \rho_{\text{Dyn}}$	Ref. [102]; value in Tab. 3.2
$\sigma_{\text{te,mech}}$	$= \sigma_{\text{Dyn}}$	Ref. [102]; value in Tab. 3.2
$\rho_{\text{te,c,w}}$	$= \rho_{\text{Cu}}$	Ref. [102]; value in Tab. 3.2
$\kappa_{\text{te,c,w}}$	$= \kappa_{\text{Cu}}$	Ref. [102]; value in Tab. 3.2
$\rho_{\text{te,ins}}$	$= \rho_{\text{PE}}$	assumed used material, same as in [81]; value in Tab. 3.2; but value of actually used material could differ slightly
$E_{\text{te,ins}}$	$= E_{\text{PE}}$	assumed used material, same as in [81]; value in Tab. 3.2; but value of actually used material could differ slightly
$\rho_{\text{te,c,sh}}$	$= \rho_{\text{Al}}$	assumed used material; value in Tab. 3.2; but value of actually used material could differ slightly (or no shield at all could have been used)
$\rho_{\text{te,c,j}} = \rho_{\text{te,j}}$	$= \rho_{\text{PE}}$	assumed used material, similar as in [81]; value in Tab. 3.2; but value of actually used material could differ slightly
$w_{\text{te,c,sh}}$	$= 0.1\,\text{mm}$	estimated, but corresponds approximately to usual value for cable shields
$w_{\text{te,c,j}}$	$= 0.5\,\text{mm}$	estimated, e.g. thin coating or tape; but value driven partly by model results, so actual value could be very different
$w_{\text{te,j}}$	$= 0.5\,\text{mm}$	estimated, e.g. thin coating or tape; but value driven partly by model results, so actual value could be very different
$S_{\text{te,mech}}$	$= 9$	estimated: factor 3 for fiber-rope derating (cf. e.g. [142]) multiplied by factor 3 for dynamic excesses (gusts etc.); but actual value could differ
$S_{\text{te,ins}}$	$= 3$	estimated; but actual value could differ
$f_{\text{te,ins}}$	$= 3$	estimated, cf. also the prior work of the author of this dissertation [106]; but actual value could differ

Table 3.1: Parameters for the Makani Wing 7 simulation. (continued)

Parameter	Value	Comment/Justification
$f_{\mathrm{te,c,w}}$	$= 1.5$	estimated; but actual value could differ
$f_{\mathrm{te,m,mech}}$	$= 1.0$	estimated; but actual value could differ
$\forall i \neq \mathrm{mech} : f_{\mathrm{te,m},i}$	$= 1.5$	estimated; but actual value could differ
Powertrain subsystems parameters.		
$\eta_{\mathrm{s},+} = \eta_{\mathrm{s},-}$	$= 1$	direct drive used, cf. e.g. [16, Fig. 28.11]
$\eta_{\mathrm{m},+} = \eta_{\mathrm{m},-}$	$= 0.96$	estimated based on [81] (low-voltage machine); but actual value could differ slightly, though no effect on the power curve w.r.t. the aerodynamic power
$\eta_{\mathrm{pe,k},+} = \eta_{\mathrm{pe,k},-}$	$= 0.98$	estimated based on [81] (machine converter); but actual value could differ slightly, though no effect on the power curve w.r.t. the aerodynamic power
$\eta_{\mathrm{pe,g},+} = \eta_{\mathrm{pe,g},-}$	$= 0.98$	estimated; but actual value could differ slightly, though no effect on the power curve w.r.t. the aerodynamic power
γ_{m}	$= 0.333\,\mathrm{kg/kW}$	estimated based on [81] (low-voltage machine); but actual value could differ slightly, though no effect on the power curve w.r.t. the aerodynamic power
$\gamma_{\mathrm{pe,k}}$	$= 0.056\,\mathrm{kg/kW}$	estimated based on [81] (machine converter); but actual value could differ slightly, though no effect on the power curve w.r.t. the aerodynamic power
k_{pt}	$=$ *anything*	has neither an effect on power curve nor on maximum allowed mass
$S_{\mathrm{hov,ok}}$	$= 1.5$	estimated; but has no effect on power curve
$S_{\mathrm{hov,flt}}$	$= 0$	no rotor failures considered as reliable hover with less than four rotors not (or only hardly) possible
$P_{\mathrm{el,ins}}$	$= 30\,\mathrm{kW}$	estimated, based on model results for maximum allowed mass during hovering; also justified by temporary higher powers over the course of the flight trajectory, cf. [16, Fig. 28.10]; but has no effect on power curve
Ground station parameters and flight trajectory parameters.		
h_{to}	$= 15\,\mathrm{m}$	estimated from [16, Fig. 28.8], but has neither an effect on power curve nor on maximum allowed mass as no wind shear considered in [16]
φ_{n}	$= 0$	same consideration as in [16], justified as Wing 7 flew relatively tight circles instead of wide figure eights [16, Fig. 28.8]
ϑ_{n}	$= 40\,^\circ$	Ref. [16, Fig. 28.7]
$\psi_{\mathrm{w,n}}$	$= 20\,^\circ$	estimated based on [102, Fig. 6]; but has no effect on the power curve

Table 3.1: Parameters for the Makani Wing 7 simulation. (continued)

Parameter	Value	Comment/Justification
Power curve "shaping" parameters.		
$v_{\mathrm{a,min}}$	$= 30.5\,\mathrm{m/s}$	Ref. [16, p. 487]
$v_{\mathrm{a,n}}$	$= 37\,\mathrm{m/s}$	estimated based on model results; actual value could be very different
r_{P}	$= 1.2$	extracted from [16, Fig. 28.12]
$v_{\mathrm{w},h_{\mathrm{ref}},\mathrm{cut\text{-}out}}$	$= 12\,\mathrm{m/s}$	based on [16, Fig. 28.12]; but has neither an effect on the power curve w.r.t. the aerodynamic power apart from cut-off point nor on the maximum allowed mass

Table 3.2: Material properties. Some values are similar to the prior work of the author of this dissertation [104, 106, 110]. The symbol Y is the Young's modulus (elastic modulus). Values shaded in gray are primarily for reference (partly for other chapters).

Parameter & Value	Comment/Justification
Dyneema – as core only.	
$\rho_{\mathrm{Dyn}} = 980\,\mathrm{kg/m^3}$	Ref. [143, Dyneema DM20]
$\sigma_{\mathrm{Dyn}} = 3,100\,\mathrm{MPa}$	Ref. [143, Dyneema DM20]
$Y_{\mathrm{Dyn}} = 94\,\mathrm{GPa}$	Ref. [143, Dyneema DM20]
	Remark: Dyneema DM20 has very low creep compared to other Dyneema fibers and thus makes it suitable for airborne wind energy applications [142], but all Dyneema fibers lose strength significantly for increased temperature (about half of the tensile strength at 100 °C compared to room temperature) [142, 143].
Kevlar (Aramid) – as core only.	
$\rho_{\mathrm{Kev}} = 1,440\,\mathrm{kg/m^3}$	Ref. [144, "DuPont™ Kevlar® 49 Aramid Fiber"]
$\sigma_{\mathrm{Kev}} = 3,620\,\mathrm{MPa}$	Ref. [144, "DuPont™ Kevlar® 49 Aramid Fiber", Epoxy-impregnated strands, ASTM D2343]
$Y_{\mathrm{Kev}} = 112\,\mathrm{GPa}$	Ref. [144, "DuPont™ Kevlar® 49 Aramid Fiber"]
	Remark: Maximum service temperature for long-term use is given at 149 . . . 177 °C with little loss of strength [145].
Carbon fiber (CF) – as core, and possibly as wire.	
$\rho_{\mathrm{CF}} = 1,760\,\mathrm{kg/m^3}$	Ref. [144, "Hexcel® HexTow™ IM6 Carbon Fiber"]
$\sigma_{\mathrm{CF}} = 5,700\,\mathrm{MPa}$	Ref. [144, "Hexcel® HexTow™ IM6 Carbon Fiber"]
$Y_{\mathrm{CF}} = 279\,\mathrm{GPa}$	Ref. [144, "Hexcel® HexTow™ IM6 Carbon Fiber"]
$\kappa_{\mathrm{CF}} = (5.2 \cdot 10^{-3})^{-1}\,\mathrm{S/m}$	Ref. [144, "Hexcel® HexTow™ IM6 Carbon Fiber"]
	Remark: An epoxy composite might be required (e.g. the material is then in the form of pultruded carbon fiber as considered by Makani in [102]) which results in significantly lower σ_{CF} and Y_{CF} [144, "Hexcel® HexTow™ IM6 Carbon Fiber"].
Steel – as core, and possibly as wire.	
$\rho_{\mathrm{St}} = 7,850\,\mathrm{kg/m^3}$	Ref. [146]
$\sigma_{\mathrm{St}} = 1,770\,\mathrm{MPa}$	Ref. [146]
$Y_{\mathrm{St}} = 200\,\mathrm{GPa}$	Ref. [146]
$\kappa_{\mathrm{St}} = (1.42 \cdot 10^{-7})^{-1}\,\mathrm{S/m}$	Ref. [144, "Overview of materials for Low Carbon Steel"]

Table 3.2: Material properties. (continued)

Parameter & Value	Comment/Justification
Carbon nanotubes (CNT) – as core, and possibly as wire.	
$\rho_{\mathrm{CNT}} = 1,090\,\mathrm{kg/m^3}$	Ref. [147]
$\sigma_{\mathrm{CNT}} = 110,000\,\mathrm{MPa}$	Ref. [148, sample 2 in Tab. 1, highest value]
$Y_{\mathrm{CNT}} = 1,049\,\mathrm{GPa}$	Ref. [148, sample 2 in Tab. 1]
$\kappa_{\mathrm{CNT}} = (5.1 \cdot 10^{-8})^{-1}\,\mathrm{S/m}$	Ref. [149, lowest resistivity value in Tab. 1] Remark: Each value corresponds to one of the best ever measured. The values are recorded by different groups with different synthesis methods or conditions. The values given here are therefore for hypothetic CNT fibers only.
Aluminum – as wire and shield, and possibly as core.	
$\rho_{\mathrm{Al}} = 2,699\,\mathrm{kg/m^3}$	Ref. [144, "Aluminum, Al"]
$\sigma_{\mathrm{Al}} \lesssim 503\,\mathrm{MPa}$	for high-strength alloy [144, "Aluminum 7075-T6, 7075-T651"]
$Y_{\mathrm{Al}} \lesssim 71.7\,\mathrm{GPa}$	for high-strength alloy [144, "Aluminum 7075-T6, 7075-T651"]
$\kappa_{\mathrm{Al}} = (2.70 \cdot 10^{-8})^{-1}\,\mathrm{S/m}$	Ref. [144, "Aluminum, Al"]
Copper – as wire, and possibly as shield and core.	
$\rho_{\mathrm{Cu}} = 8,930\,\mathrm{kg/m^3}$	Ref. [144, "Copper, Cu, Annealed", at 20 °C]
$\sigma_{\mathrm{Cu}} \lesssim 965\,\mathrm{MPa}$	for high-strength alloy [144, "Phosphor bronze 8% Sn, UNS C52100, H06 Temper wire"]
$Y_{\mathrm{Cu}} \lesssim 110\,\mathrm{GPa}$	for high-strength alloy [144, "Phosphor bronze 8% Sn, UNS C52100, H06 Temper wire"]
$\kappa_{\mathrm{Cu}} = (1.70 \cdot 10^{-8})^{-1}\,\mathrm{S/m}$	Ref. [144, "Copper, Cu, Annealed"]
Teflon – as insulator.	
$\rho_{\mathrm{Tef}} = 2,145\,\mathrm{kg/m^3}$	Ref. [144, "Chemours Teflon® PFA Grade 345T Extrusion and Molding Resin for High Temperature Applications", average of given range]
$E_{\mathrm{Tef}} = 52\,\mathrm{kV/mm}$	Ref. [144, "Chemours Teflon® PFA Grade 345T Extrusion and Molding Resin for High Temperature Applications"]
Polyethylene (PE) – as insulator and jacket.	
$\rho_{\mathrm{PE}} = 0,922\,\mathrm{kg/m^3}$	Ref. [144, "Borealis LE4201R Polyethylene Insulation Compound, Crosslinkable"]
$E_{\mathrm{PE}} = 22\,\mathrm{kV/mm}$	Ref. [144, "Borealis LE4201R Polyethylene Insulation Compound, Crosslinkable"]

3.1.2 Results

Tab. 3.3 lists relevant results, Fig. 3.1 shows the power curve and other values as function of the wind speed, Fig. 3.2 shows the tether cross section, and Fig. 3.3 visualizes drag- and mass distributions. The most important results are the values highlighted in green in Tab. 3.3 and the first row of Fig. 3.1, because those results can be compared to real values or measurements. In the following sections, only those results are discussed while all other results are provided for sake of completeness.

Table 3.3: Results for the Makani Wing 7.

Parameter	Value		
Nominal power and nominal wind speeds.			
$P_{\mathrm{a,n}}$	=	19,681.85	W
$P_{\mathrm{el,n}}$	=	14,046.42	W
$P_{\mathrm{el,n}}/A$	=	3,547.07	W/m^2
$P_{\mathrm{el,n}}/(\hat{m}_{\mathrm{k}} + m_{\mathrm{te}})$	=	138.80	W/kg
$v_{\mathrm{w},h_{\mathrm{ref}},\text{cut-in}}$	=	5.19	m/s
$v_{\mathrm{w},h_{\mathrm{ref}},\mathrm{n}(1)}$	=	9.44	m/s
$v_{\mathrm{w},h_{\mathrm{ref}},\mathrm{n}(2)}$	=	10.07	m/s

(continued)

Parameter	Value		
Other nominal values.			
ω_{n}	=	14.72	°/s
h_{n}	=	107.56	m
$F_{\vert\vert,\mathrm{n}}$	=	6,803.66	N
$F_{\vert\vert,\mathrm{n}}/(Ag)$	=	175.14	kg/m^2
$C_{\mathrm{D,te}}$	=	0.10	
$C_{\mathrm{D,k,p,n}} + C_{\mathrm{D,k,o}}$	=	0.06	
$C_{\mathrm{D,k,i,n}}$	=	0.10	
$C_{\mathrm{D,eq,n}}$	=	0.26	
$C_{\mathrm{D,rot,n}(1)}$	=	0.13	
$C_{\mathrm{D,rot,n}(2)}$	=	0.16	
$a_{\mathrm{n}(1)}$	=	0.07	
$a_{\mathrm{n}(2)}$	=	0.08	
$\eta_{\Pi,\mathrm{n}}$	=	71.37	%
$\zeta_{\mathrm{n}(1)}$	=	7.84	
$R_{\mathrm{te}} I_{\mathrm{te},+,\mathrm{n}}/U_{\mathrm{te,n}}$	=	6.32	%
$\hat{p}_{\text{te-loss,L},-}$	=	24.80	W/m
$\hat{p}_{\text{te-loss,A},-}$	=	704.49	W/m^2
Dimensions and masses.			
A	=	3.96	m^2
$\hat{m}_{\mathrm{a,flight}}$	=	210.41	kg
$\hat{m}_{\mathrm{a,hov,ok}}$	=	91.89	kg
$\hat{m}_{\mathrm{a}}$	=	91.89	kg
$\hat{m}_{\mathrm{k}}$	=	82.57	kg
$\hat{m}_{\mathrm{k}}/A$	=	20.85	kg/m^2
$\hat{m}_{\mathrm{af\&o}}$	=	73.07	kg
$\hat{m}_{\mathrm{af\&o}}/A$	=	18.45	kg/m^2
$m_{\mathrm{pt,k}}$	=	9.51	kg
m_{te}	=	18.63	kg
$m_{\mathrm{te,mech}}$	=	2.79	kg
$m_{\mathrm{te,c}}$	=	12.49	kg
$n_{\mathrm{te,c}}$	=	6	
d_{te}	=	11.21	mm
f_{te}	=	2.23	

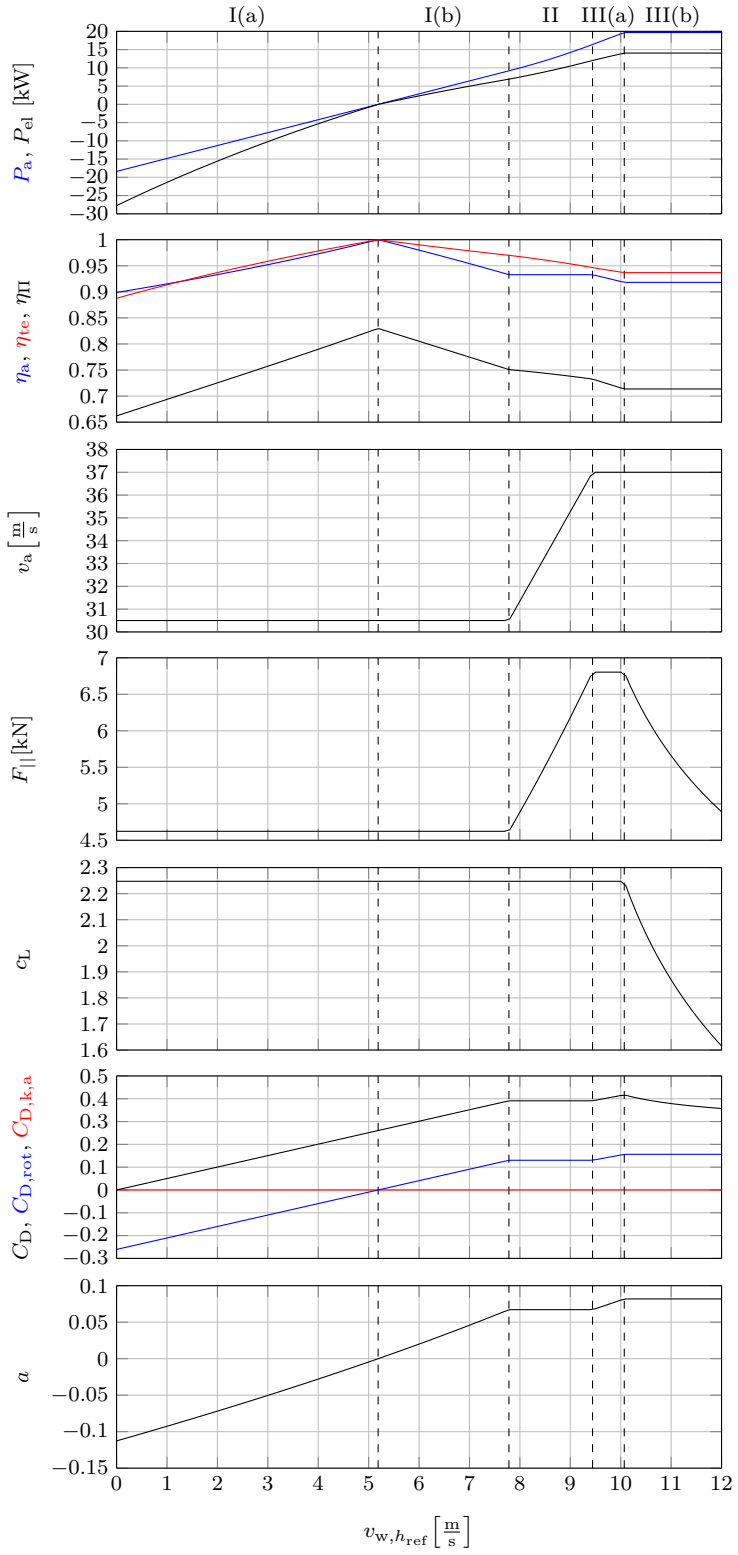

Figure 3.1: Power curve results for the Makani Wing 7.

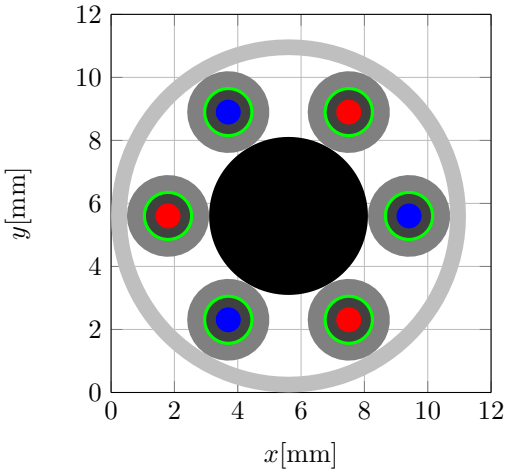

Figure 3.2: Visualization of the tether cross section for the Makani Wing 7 with color coding as in Fig. 1.8.

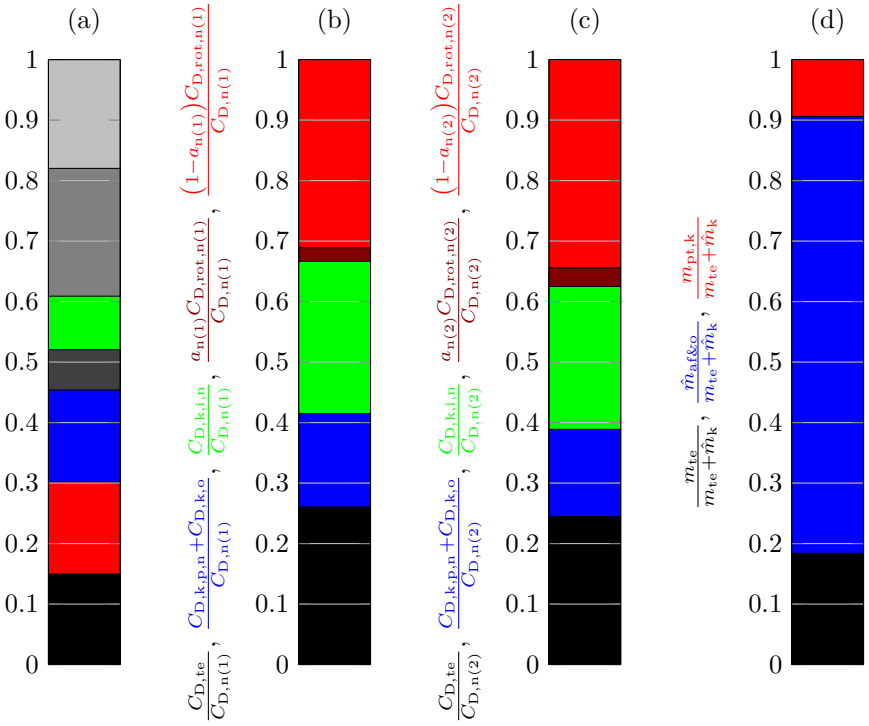

Figure 3.3: Visualization of distributions of some results for the Makani Wing 7: (a) tether mass distribution with color coding as in Fig. 1.8, (b) distribution of drag portions in Region II and at first power point, (c) distribution of drag portions at second power point, (d) distribution of total (maximum allowed) airborne masses.

3.1.3 Power Curve: Model vs. Reality

Fig. 3.4 shows an overlay of [16, Fig. 28.12], which contains measured powers and simulation results of Makani/Vander Lind, and the computed power curve for the aerodynamic power P_a from Fig. 3.1 with the size, axes, and line thickness altered for better perception.

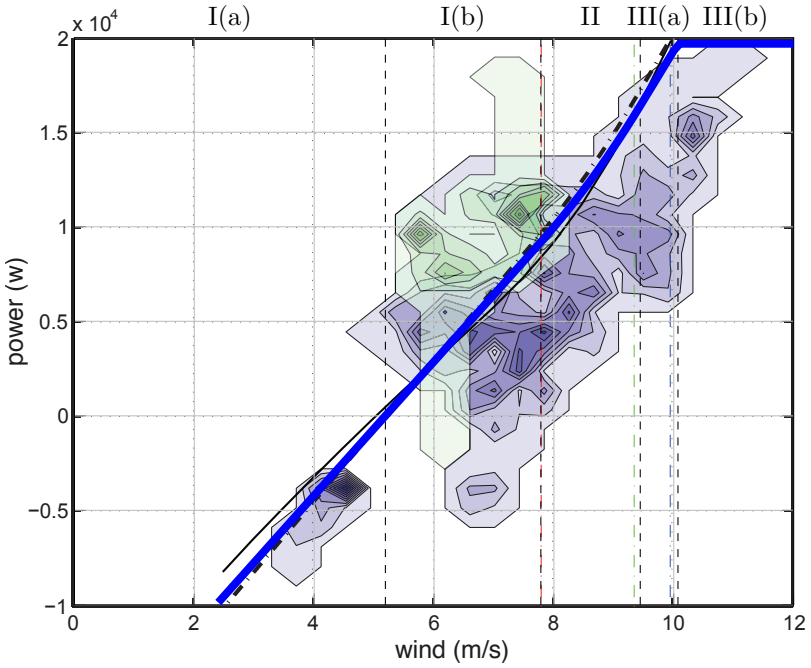

Figure 3.4: Overlay of [16, Fig. 28.12] and Fig. 3.1 (row 1) with size, axes, and line thickness altered: Purple areas show the density of measurements for an early version of Wing 7 and green areas for a later version. The black solid —— and dash-dotted lines -·-·-· are Makani's/Vander Lind's simulation results from a simpler steady model [16] and from a dynamic model, respectively. The thick blue line ▬ is the power curve computed with the in this dissertation derived model. All quantities are the aerodynamic power P_a.

The results of the in this dissertation derived model are almost identical to the measurements as well as static and dynamic simulation results by Makani/Vander Lind.

3.1.4 Tether Mass: Model vs. Reality

Tab. 3.3 lists the tether mass with $m_{te} = 18.63\,\text{kg}$ which is only slightly higher than the real value $m_{te} = 16\,\text{kg}$ given in [102]. The discrepancy can be explained with the not available tether construction parameters and materials, which had to be estimated or guessed, cf. Tab. 3.1. Specifically, Makani could be using other safety and correction factors, electrical cables without shields, or other materials. Nevertheless, this error can be evaluated as negligibly small.

3.1.5 Maximum Allowed Kite Mass: Model vs. Reality

In [16, 102] the kite mass is given with $m_\mathrm{k} = 60\,\mathrm{kg}$. Tab. 3.3 lists the maximum allowed kite mass as $\hat{m}_\mathrm{k} = 82.57\,\mathrm{kg}$. Obviously, also this computed value matches with the real value.

3.1.6 Some Other Values: Model vs. Reality

Tab. 3.3 lists the tether drag coefficient with $C_{\mathrm{D,te}} = 0.10$, which is in good accordance to [16, Tab. 28.1] wherein the value $C_{\mathrm{D,te}} = 0.11$ is stated. Moreover, Tab. 3.3 lists the (nominal) equivalent drag coefficient with $C_{\mathrm{D,eq,n}} = 0.26$, which is also in good accordance to [16, Fig. 28.7] wherein the value $C_{\mathrm{D,eq,n}} = 1/4$ is stated.

3.1.7 Sensitivity Analysis of Most Uncertain Model Parameters

As highlighted by the colors yellow and red in Tab. 3.1, some values were unknown and thus needed to be estimated. Particularly critical are the four values in red, namely tether resistance R_te, tether cable jacket width $w_\mathrm{te,c,j}$, tether jacket width $w_\mathrm{te,j}$, and nominal airflow speed $v_\mathrm{a,n}$. For those, neither the exact value nor a good estimate were available. Instead the values had to be guessed ("scientific guess") or in part fitted to obtain reasonable results. Fig. 3.5 shows how the model results change for changes of these four uncertain values.

Clearly, the sensitivity for all four uncertain parameters is low on virtually all relevant results. Only $v_\mathrm{a,n}$ has a rather significant effect on the nominal power $P_\mathrm{a,n}$, visible in the first two rows in the last column of Fig. 3.5, but there is almost no change of the power curve shape below the nominal wind speed. The values for R_te, $w_\mathrm{te,c,j}$, and $w_\mathrm{te,j}$ may be quite different from the assumed values as their effects on the results are rather small.

3.1.8 Discussion on Nominal Airflow Speed Uncertainty

It should be noted that particularly the nominal airflow speed was indeed found by trial-and-error to obtain a reasonably good match to [16, Fig. 28.12]. However, this value does not coincide with [16, Fig. 28.10] which records the time course of the measured kite speed (which is approximately the same as the airflow speed) during a flight of Wing 7: While the recorded relatively high mean power of $\approx 11\,\mathrm{kW}$ at only $\approx 6\,\mathrm{m/s}$ wind speed was explained by Vander Lind [16, Chap. 28.12] with a wind shear between the ground wind sensor and the kite, the kite also flies very fast with a mean airflow speed of $\approx 41.5\,\mathrm{m/s}$ and generates a high mean tension of $\approx 7.5\,\mathrm{kN}$. These values exceed the above considered nominal airflow speed of $v_\mathrm{a,n} = 37\,\mathrm{m/s}$ and the computed nominal parallel force (tether force) of $F_{||,\mathrm{n}} \approx 6.8\,\mathrm{kN}$ which are actually expected to be reached at the higher wind speed of $\gtrsim 9.4\,\mathrm{m/s}$ and with $\gtrsim 16\,\mathrm{kW}$ power. In the following, an attempt to explain that discrepancy is carried out.

Simple Power Curve with Specified Values

If no constraints apply, the power, the airflow speed, and the tether tension are given by (2.191)–(2.193) which are essentially the same equations as derived by Vander Lind [16] as extension of Loyd [13]. Fig. 3.6 plots these three equations, once with the values provided by [16, Fig. 28.7] in ——, and once with the resulting equivalent drag coefficient of the here derived model from Tab. 3.3 in - - - -. Those plots are compared to the quantities resulting from the complete model derived in this dissertation in ——.

As expectable, the curves - - - - and —— are identical in Region II. The curves —— and - - - - are also almost identical. The small discrepancy is caused by the slightly lower equivalent drag coefficient of [16, Fig. 28.7] compared to Tab. 3.3. Most importantly, the airflow speed

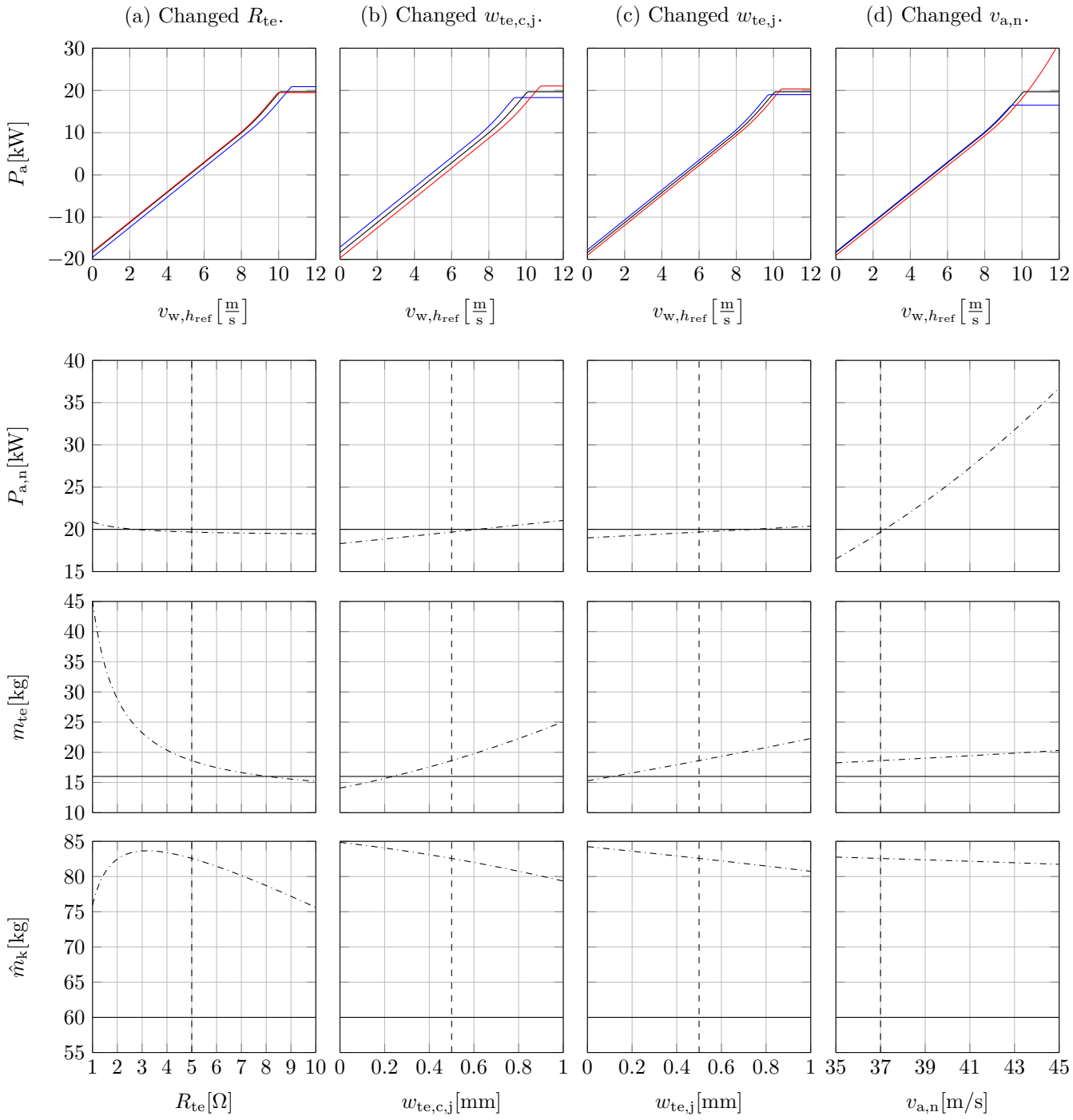

Figure 3.5: Results for changes of the four most uncertain model parameters. First row: power curve with baseline value in —— (which is almost identical to the real power curve, cf. Fig 3.4), lowest investigated uncertain parameter value in ——, and highest investigated uncertain parameter value in ——. Second to last row: nominal aerodynamic power, tether mass, and (maximum allowed) kite mass, each with baseline value in - - - -, uncertain parameter changed in -·-·-, and real resulting value in ——.

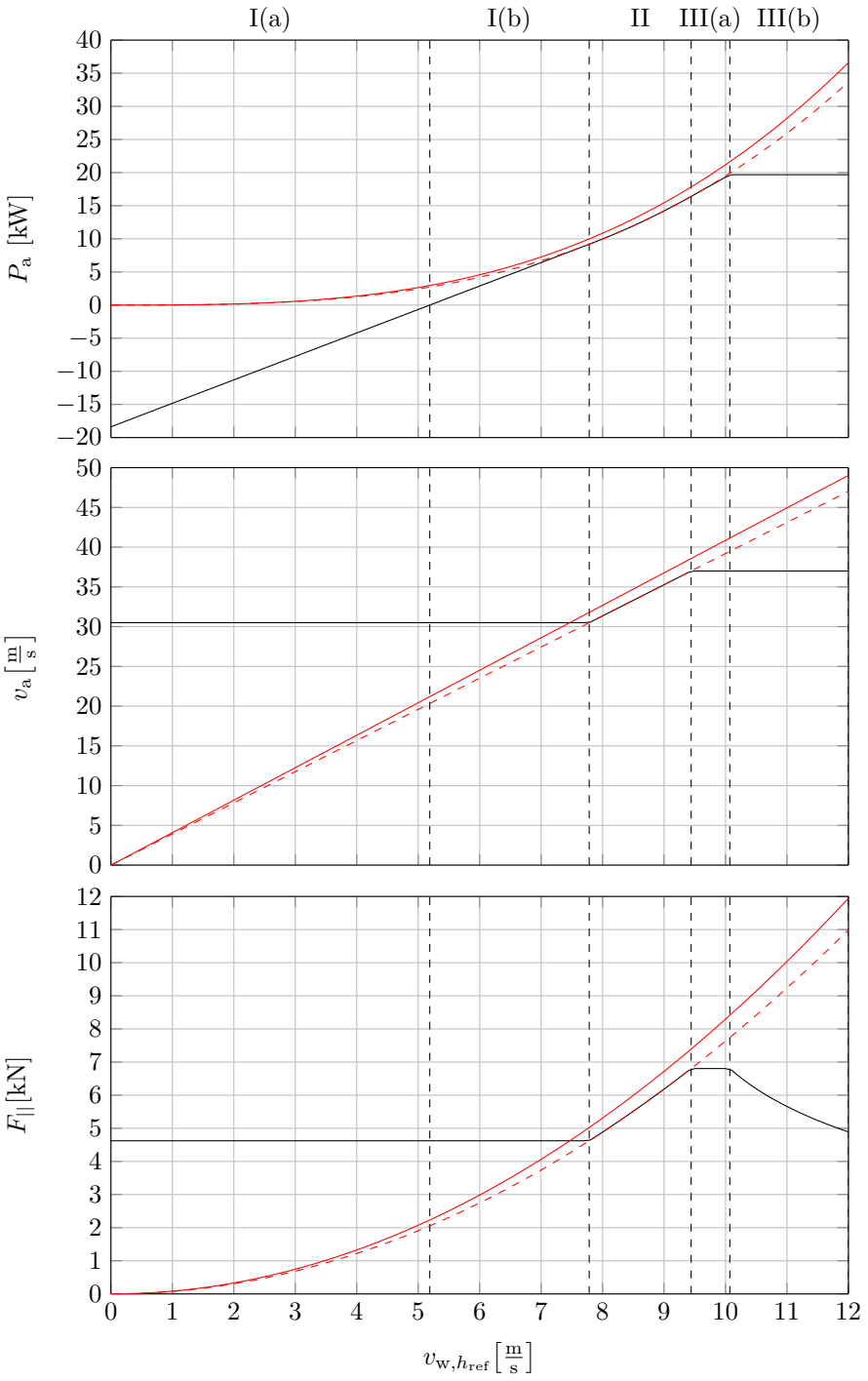

Figure 3.6: Power curve computed with the multidisciplinary model in —— compared to (2.191)–(2.193) with the values given by [16, Fig. 28.7], i.e. with $\rho = 1.255$, $\varphi_\mathrm{n} = 0$, $\vartheta_\mathrm{n} = 40\,^\circ$, $A = 3.96\,\mathrm{m}^2$, $C_{\mathrm{L,n}} = 2$, $C_{\mathrm{D,eq,n}} = 0.25$ in ——. For reference, the latter is also plotted for the system parameters computed by the multidisciplinary model, i.e. with the different nominal equivalent drag of $C_{\mathrm{D,eq,n}} = 0.26$ in - - - -.

and the parallel force (tether force) at $v_{\mathrm{w},h_{\mathrm{ref}}} \approx 9.4\,\mathrm{m/s}$—which are the nominal airflow speed and the nominal parallel force—are in all cases $v_{\mathrm{a,n}} = 37.0 \ldots 38.4\,\mathrm{m/s}$ and $F_{||} = 6.8 \ldots 7.3\,\mathrm{kN}$, respectively, which are both in good agreement with the values computed in the here derived model. Concluding, the lower airflow speed and tether tension in the model results compared to the measurement [16, Fig. 28.10] can so far not be explained by errors in the parameters or errors in the derived model.

Aerodynamic Coefficients Derived from Measurements

Tab. 3.4 lists three representative values for quantities recorded in [16, Fig. 28.10] and aerodynamic coefficients calculated from that. The lift coefficient is calculated from (2.178) solved for C_{L} which becomes

$$\begin{aligned} F_{||} := F_{\mathrm{L}} = F_{\mathrm{te}} = F_{\mathrm{a}} &= \frac{1}{2}\rho v_{\mathrm{a}}^2 A C_{\mathrm{L}} \\ \Leftrightarrow C_{\mathrm{L}} &= \frac{F_{\mathrm{te}}}{\frac{1}{2}\rho v_{\mathrm{a}}^2 A}, \end{aligned} \tag{3.1}$$

the rotor drag coefficient is calculated from (2.18) solved for $C_{\mathrm{D,rot}}$ which becomes

$$\begin{aligned} P_{\mathrm{a}} &= \frac{1}{2}\rho v_{\mathrm{a}}^3 A C_{\mathrm{D,rot}} \\ \Leftrightarrow C_{\mathrm{D,rot}} &= \frac{P_{\mathrm{a}}}{\frac{1}{2}\rho v_{\mathrm{a}}^3 A}, \end{aligned} \tag{3.2}$$

and the equivalent drag coefficient is calculated from (2.176) solved for $C_{\mathrm{D,eq}}$ which becomes

$$\begin{aligned} v_{\mathrm{a}} &= \cos(\varphi)\cos(\vartheta) v_{\mathrm{w}} \frac{C_{\mathrm{L}}}{C_{\mathrm{D,eq}} + C_{\mathrm{D,rot}}} \\ \Leftrightarrow C_{\mathrm{D,eq}} &= \frac{\cos(\varphi)\cos(\vartheta) v_{\mathrm{w}}}{v_{\mathrm{a}}} C_{\mathrm{L}} - C_{\mathrm{D,rot}}. \end{aligned} \tag{3.3}$$

The calculated results indicate that in the recorded measurements from [16, Fig. 28.10] the lift coefficient is slightly lower and the drag coefficient is significantly lower than expected. These discrepancies can have a number of reasons:

- Makani improved the aerodynamics of Wing 7 [16, Fig. 28.11], visible also in Fig. 3.4 in the difference of the purple and green areas. The lift and drag coefficients given in [16, Fig. 28.7] might be the ones for the earlier version (purple areas in Fig. 3.4) while the measurements [16, Fig. 28.10] might be from the newer version (green areas in Fig. 3.4). The lift and drag coefficients of [16, Fig. 28.7] could also be rounded or mean values. In fact, also the value $C_{\mathrm{L}} = 1.7$ is given in [16, Tab. 28.1]. Similarly, other values of the real demonstrator can differ from those given in [16] and [102].
- A lower (effective) lift coefficient can be explained by a non-zero roll angle of the kite, necessary to fly the circular flight path, cf. Sect. 2.1.1. On the other hand, an increased tension (and also increased lift coefficient calculated with (3.1)) can be caused by inertial forces which are not covered by any of the above equations. Other dynamic effects like the influence of the gravitation are also not covered by any of the above equations.
- The recorded measurements [16, Fig. 28.10] could have offsets and drifts. Moreover, at least some of the quantities must have been estimated, e.g. a direct measurement of P_{a}

Table 3.4: Calculation of aerodynamic coefficients from [16, Fig. 28.10] at three time points with a low power (value 1), mean power (value 2), and high power (value 3).

#	Value 1	Value 2	Value 3	Comment
Recorded values in [16, Fig. 28.10].				
P_a[kW]	4	11	18	
v_a[m/s]	35	41.5	48	Assumption: $v_\mathrm{a} \approx v_\mathrm{k}$
$F_{\vert\vert}$[kN]	5	7.75	10.5	
ϑ[°]	56	35.5	15	
$v_{\mathrm{w},h_\mathrm{ref}}$[m/s]	6	6	6	
Derived values.				
C_L	1.64	1.81	1.83	from (3.1) with $\rho = 1.255\,\mathrm{kg/m^3}$, $A = 3.96\,\mathrm{m^2}$
$C_\mathrm{D,rot}$	0.038	0.062	0.065	from (3.2) with $\rho = 1.255\,\mathrm{kg/m^3}$, $A = 3.96\,\mathrm{m^2}$
$C_\mathrm{D,eq}$	0.119	0.151	0.156	from (3.3) with $\rho = 1.255\,\mathrm{kg/m^3}$, $\varphi = 0$ (however, caution: $v_{\mathrm{w},h_\mathrm{ref}}$ is likely higher due to wind shear according to [16, p. 28.12] and so $C_\mathrm{D,eq}$ is likely higher)

is not possible. (A straightforward estimation is to measure v_a and estimate $C_\mathrm{D,rot}$ from CFD-simulated or in the wind tunnel measured rotor characteristic, i.e. thrust as function of airflow speed and rotor speed.)

- The controllers could have been altering the lift coefficient (with flaperons, as α was constant [16, Fig. 28.10]), the rotor drag coefficient, and the (actuated) drag coefficient e.g. to keep tether tension limits and airflow speed limits satisfied or to achieve other goals. For example, Value 1 in Tab. 3.4 is close to the lower tether tension limit (2.205) which is with $\rho = 1.255\,\mathrm{kg/m^3}$, $v_\mathrm{a,I} = v_\mathrm{a,min} = 30.5\,\mathrm{m/s}$, $A = 3.96\,\mathrm{m^2}$, and $C_\mathrm{L,n} = 2$ given by

$$F_\mathrm{te,min} = F_{\vert\vert,\mathrm{min}} = \frac{1}{2}\rho v_\mathrm{a,I}^2 A C_\mathrm{L,n} = \frac{1}{2}\cdot 1.255\,\mathrm{kg/m^3}\cdot(30.5\,\mathrm{m/s})^2\cdot 3.96\,\mathrm{m^2}\cdot 2 = 4,623\,\mathrm{N}. \tag{3.4}$$

  Because of safety reasons, the controller could have been commanded to limit the tension to a higher value. Moreover, some controller-, stability-, or other tests might have been carried out during that particular measurement [16, Fig. 28.10], which could explain discrepancies.

Concluding Remarks

Concluding, this investigation indicates that the simulation results for the Wing 7 should be treated with some care. Nevertheless, as visible in Fig. 3.4, the measurements, the static simulations, and the dynamic simulations of the important value of the aerodynamic power by Makani/Vander Lind [16, Fig. 28.12] as well as the results of the model derived in this dissertation agree very well. Therefore, the discrepancies discussed above can be also evaluated as insignificant.

3.1.9 Discussion on Model Fitting

The derived model employs a number of correction factors and similar (safety factors, efficiency factors, or also effective azimuth, and drag coefficient for other parts). It even could be enhanced with further correction factors e.g. for the effect of the mass during crosswind flight to relax the corresponding assumptions. If no measured data is available, these values have to be estimated

a-priori. If measured data is available, these values can be fitted so that the model results match the measurements. This is the usual approach for black-box model parts. If the model results have a good agreement to the measurements, then, by implication, the model is already validated at least for that particular case. This is in part the model validation approach discussed here.

However, there is a grain of salt: Some parameters or results of an experiment might be unknown. Referring to the previous sections, e.g. Makani neither published details on the tether dimensions such as the jacket width or the resistance, nor is the power curve for the electrical power at the ground published. Moreover, if the model employs enough such fitting factors, it is likely adaptable to almost any measured data (this is the principle of a neural network or "artificial intelligence/AI").

One approach to overcome those weaknesses is to record enough measured data and separate it into the two parts "training data" and "generality validation data". First, the model is parametrized such that it reproduces the training data, i.e. the data fitting is performed only with the training data. Afterwards the fitted parameters are kept constant. Second, if the model can then also reproduce the generality validation data, its generality is validated.

However, the available measured data (e.g. published measured power curves) is currently very limited, so that such a data separation is currently not possible. Therefore, so far the model's agreement to measurements is proven, but the model's generality could not yet be proven.

Nevertheless, the model can be expected to be general, because (i) it is based on first principles or (ii) on black-box submodels which are (at least in part) validated on its own, cf. e.g. the airfoil model validation in Fig. 2.5. Moreover, (iii) the fitting of parameters is minimized as much as possible, particularly all correction factors etc. were based a-priori on realistic values from experience and were not fitted, cf. Tab. 3.1. Once those correction factors etc. are validated against measured data, they should be kept constant, which is done for the remainder of this dissertation (unless stated otherwise with a justification).—Validating the model's generality is one aspect for the following sections.

As a conclusion so far, the derived model was successfully validated against measured data of the Makani Wing 7. However, these investigations have to be treated with care, because the model's generality could not be proven with the limited available measured data.

3.2 Comparison to Expectations of Larger Makani Kites

To validate at least in part the model's generality, the model results are also computed for Makani's anticipated utility-scale systems M600 and M5. For those systems, even less data compared to Wing 7 is available, such that for many more values a "scientific guess" has to be made. Therefore, even if the model predictions match well with the data provided by Makani, it can only serve as validation that the derived model might not be wrong. Nevertheless, such a study is a fast and simple plausibility check.

3.2.1 Simulation of the Makani M600

3.2.1.1 Parameters and Results

Similar to the previous section with the simulation of Wing 7, Tab. 3.5 lists the from literature extracted and assumed parameters for the Makani M600, Tab. 3.6 lists relevant simulation results, Fig. 3.7 shows the power curve and other values as function of the wind speed, Fig. 3.8 shows the tether cross section, and Fig. 3.9 visualizes drag-, mass-, and cost distributions. The most important results are the values highlighted in green in Tab. 3.6 and the first row of Fig. 3.7.

Table 3.5: Parameters for the Makani M600 simulation.
Color-coding: green = reliable value available, e.g. from literature; yellow = no exact value known but good estimate available; red = neither exact value nor good estimate available, instead value had to be guessed ("scientific guess") or in part fitted to obtain reasonable results.

Parameter	Value	Comment/Justification
Environmental parameters for considered installation site.		
g	$= 9.81\,\mathrm{m/s^2}$	$\approx$ Standard Gravity
ρ	$= 1.255\,\mathrm{kg/m^3}$	$\approx$ International Standard Atmosphere
h_{ref}	$= 30\,\mathrm{m}$	guessed, same as "reference location" of EEG [134]
z_0	$= 0.1\,\mathrm{m}$	guessed, same as "reference location" of EEG [134] (logarithmic wind shear)
λ	$= 2$	guessed, same as "reference location" of EEG [134] (Rayleigh distribution)
μ	$= 2/\sqrt{\pi} \cdot 5.5\,\mathrm{m/s}$	guessed, same as "reference location" of EEG [134] (5.5 m/s mean wind speed, cf. (2.163))
Economic parameters for targeted market.		
k_{LCOE}	$= 0.05\,\mathrm{EUR/kWh}$	assumed
I	$= 10\,\%/\mathrm{yr}$	assumed
T	$= 20\,\mathrm{yr}$	assumed
I_{op}	$= 5\,\%/\mathrm{yr}$	assumed
f_{avail}	$= 98\,\%$	estimated, similar to conventional wind turbines, cf. e.g. [150]
Kite aerodynamics parameters.		
b	$= 28\,\mathrm{m}$	Ref. [102]
$\mathit{Æ}$	$= 32.6667$	$= b^2/A$ with $A = 24\,\mathrm{m^2}$ extracted from [102]
n_{mw}	$= 1$	M600 is a monoplane, cf. e.g. [102]
$c_{\mathrm{L,n}}$	$= 3$	assumed; value is in accordance with [97, 103]
$c_{\mathrm{L,min\text{-}op}}$	$= 2$	assumed, but has only an effect on the actuations in Region III(b)
e	$= 0.9$	almost elliptical lift distribution estimated, as a tapered wing is visible in photographs, cf. e.g. [19]
$C_{\mathrm{D,k,o}}$	$= 0.01$	assumed
$C_{\mathrm{D,k,a,max}}$	$= 0.1$	assumed, but has only an effect on the actuations in Region III(b)
Rotor parameters.		
n_{rot}	$= 8$	M600 has eight rotors, cf. e.g. [102]
r_{rot}	$= 1.3849$	$= \pi(d_{\mathrm{rot}}/2)^2 n_{\mathrm{rot}}/A$ with rotor diameter $d_{\mathrm{rot}} = 2.3\,\mathrm{m}$ from [19] and other values from this table here
$\eta_{\mathrm{rot},+} = \eta_{\mathrm{rot},-}$	$= 0.9$	estimated
$\eta_{\mathrm{rot,hov}}$	$= 0.9$	estimated

Table 3.5: Parameters for the Makani M600 simulation. (continued)

Parameter	Value	Comment/Justification
Tether parameters.		
L_{te}	$= 440\,\mathrm{m}$	Ref. [102]
$U_{\mathrm{te,n}}$	$= 4\,\mathrm{kV}$	from face-to-face conversation with Fort Felker (Makani) at the AWEC2017 [19] (note that this is different from the earlier publication [102] which states $U_{\mathrm{te,n}} = 8\,\mathrm{kV}$)
R_{te}	$= 1\,\Omega$	estimated based on model results
$c_{\mathrm{D,te}}$	$= 1$	estimated, $\approx c_{\mathrm{D}}$ of cylinder at reasonable N_{Re}
$f_{\text{m-te}}$	$= 0.5$	estimated
$n_{\mathrm{te,c}}$	$= 14$	Nick Tucker (Makani) showed photographs of the cut tether of the M600 in his AWEC2017 presentation [78], in which 14 electrical cables around the core are visible.
$\rho_{\mathrm{te,mech}}$	$= \rho_{\mathrm{CF}}$	Ref. [102]; value in Tab. 3.2
$\sigma_{\mathrm{te,mech}}$	$= \sigma_{\mathrm{CF}}$	Ref. [102]; value in Tab. 3.2
$\rho_{\mathrm{te,c,w}}$	$= \rho_{\mathrm{Al}}$	Ref. [102]; value in Tab. 3.2
$\kappa_{\mathrm{te,c,w}}$	$= \kappa_{\mathrm{Al}}$	Ref. [102]; value in Tab. 3.2
$\rho_{\mathrm{te,ins}}$	$= \rho_{\mathrm{Tef}}$	assumed used material; with PE as assumed for Wing 7 and in [81], $n_{\mathrm{te,c}}$ would have been < 14 according to the model results; value in Tab. 3.2
$E_{\mathrm{te,ins}}$	$= E_{\mathrm{Tef}}$	assumed used material; with PE as assumed for Wing 7 and in [81], $n_{\mathrm{te,c}}$ would have been < 14 according to the model results; value in Tab. 3.2
$\rho_{\mathrm{te,c,sh}}$	$= \rho_{\mathrm{Al}}$	assumed used material; value in Tab. 3.2; but usual material for shields
$\rho_{\mathrm{te,c,j}} = \rho_{\mathrm{te,j}}$	$= \rho_{\mathrm{PE}}$	assumed used material, similar as in [81]; value in Tab. 3.2
$w_{\mathrm{te,c,sh}}$	$= 0.1\,\mathrm{mm}$	estimated, but corresponds approximately to usual value for cable shields
$w_{\mathrm{te,c,j}}$	$= 0.5\,\mathrm{mm}$	estimated
$w_{\mathrm{te,j}}$	$= 1.0\,\mathrm{mm}$	estimated
$S_{\mathrm{te,mech}}$	$= 9$	estimated: factor 3 for fiber-rope derating (cf. e.g. [142]) multiplied by factor 3 for dynamic excesses (gusts etc.)
$S_{\mathrm{te,ins}}$	$= 3$	estimated
$f_{\mathrm{te,ins}}$	$= 3$	estimated, cf. also the prior work of the author of this dissertation [106]
$f_{\mathrm{te,c,w}}$	$= 1.5$	estimated
$f_{\mathrm{te,m,mech}}$	$= 1.0$	estimated
$\forall i \neq \mathrm{mech} : f_{\mathrm{te,m},i}$	$= 1.5$	estimated

Table 3.5: Parameters for the Makani M600 simulation. (continued)

Parameter	Value	Comment/Justification
Powertrain subsystems parameters.		
$\eta_{\mathrm{s},+} = \eta_{\mathrm{s},-}$	$= 1$	direct drive expected
$\eta_{\mathrm{m},+} = \eta_{\mathrm{m},-}$	$= 0.96$	estimated based on [81] (low-voltage machine)
$\eta_{\mathrm{pe,k},+} = \eta_{\mathrm{pe,k},-}$	$= 0.95$	estimated based on [81] (machine converter and low-voltage to high-voltage DC-DC converter)
$\eta_{\mathrm{pe,g},+} = \eta_{\mathrm{pe,g},-}$	$= 0.98$	estimated
γ_{m}	$= 0.333\,\mathrm{kg/kW}$	estimated based on [81] (low-voltage machine)
$\gamma_{\mathrm{pe,k}}$	$= 0.278\,\mathrm{kg/kW}$	estimated based on [81] (machine converter and low-voltage to high-voltage DC-DC converter)
k_{pt}	$= 0.15\,\mathrm{EUR/W}$	assumed
$S_{\mathrm{hov,ok}}$	$= 1.5$	estimated
$S_{\mathrm{hov,flt}}$	$= 1.2$	estimated
$P_{\mathrm{el,ins}}$	$=$ *optimal*	assumed; i.e. $P_{\mathrm{el,ins}}$ is optimized "internally" within the algorithm in Sect. 2.9.2, such that the powertrain is as small as possible, cf. (2.248)
Ground station parameters and flight trajectory parameters.		
h_{to}	$= 15\,\mathrm{m}$	Ref. [19, presentation slides]
φ_{n}	$= 0$	same consideration as in [16], justified as M600 flies relatively tight circles instead of wide figure eights cf. [20]
ϑ_{n}	$= 30\,^\circ$	estimated, in accordance to [20, 78]
$\psi_{\mathrm{w,n}}$	$= 20\,^\circ$	estimated
Power curve "shaping" parameters.		
$v_{\mathrm{a,min}}$	$= 35\,\mathrm{m/s}$	estimated
$v_{\mathrm{a,n}}$	$= 60\,\mathrm{m/s}$	estimated, based on a video shown in Fort Felker's AWEC2017 presentation [19] in which an airflow speed indicator was visible whose range was from 0 to 60 m/s
r_{P}	1.8	fitted to reach $P_{\mathrm{el,n}} \approx 600\,\mathrm{kW}$
$v_{\mathrm{w},h_{\mathrm{ref}},\text{cut-out}}$	$= 20\,\mathrm{m/s}$	Ref. [151]

Table 3.6: Results for the Makani M600.

Parameter		Value	
Economic values.			
$E_{\mathrm{el,yr}}$	=	1,626,286.88	kWh/yr
H	=	30.53	%
$\hat{K}_{\mathrm{inv}}$	=	485,575.82	EUR
$K_{\mathrm{inv,pt}}$	=	91,224.31	EUR
$\hat{K}_{\mathrm{inv,o\&p}}$	=	394,351.51	EUR
$\hat{K}_{\mathrm{inv}}/P_{\mathrm{el,n}}$	=	0.80	EUR/W
$E_{\mathrm{el,yr}}k_{\mathrm{LCOE}}$	=	81,314.34	EUR/yr
$\hat{K}_{\mathrm{inv}}I_{\mathrm{op}}$	=	24,278.79	EUR/yr
T_{am}	=	8.51	yr
Nominal power and nominal wind speeds.			
$P_{\mathrm{a,n}}$	=	827,868.06	W
$P_{\mathrm{el,n}}$	=	608,162.04	W
$P_{\mathrm{el,n}}/A$	=	25,340.08	W/m^2
$P_{\mathrm{el,n}}/(\hat{m}_{\mathrm{k}}+m_{\mathrm{te}})$	=	312.56	W/kg
$v_{\mathrm{w},h_{\mathrm{ref}},\mathrm{cut\text{-}in}}$	=	2.97	m/s
$v_{\mathrm{w},h_{\mathrm{ref}},\mathrm{n}(1)}$	=	7.64	m/s
$v_{\mathrm{w},h_{\mathrm{ref}},\mathrm{n}(2)}$	=	9.68	m/s

(continued)

Parameter		Value	
Other nominal values.			
ω_{n}	=	7.81	°/s
h_{n}	=	235.00	m
$F_{\vert\vert,\mathrm{n}}$	=	153,264.46	N
$F_{\vert\vert,\mathrm{n}}/(Ag)$	=	650.97	kg/m^2
$C_{\mathrm{D,te}}$	=	0.13	
$C_{\mathrm{D,k,p,n}}+C_{\mathrm{D,k,o}}$	=	0.06	
$C_{\mathrm{D,k,i,n}}$	=	0.09	
$C_{\mathrm{D,eq,n}}$	=	0.28	
$C_{\mathrm{D,rot,n}(1)}$	=	0.14	
$C_{\mathrm{D,rot,n}(2)}$	=	0.25	
$a_{\mathrm{n}(1)}$	=	0.03	
$a_{\mathrm{n}(2)}$	=	0.05	
$\eta_{\Pi,\mathrm{n}}$	=	73.46	%
$\zeta_{\mathrm{n}(1)}$	=	27.19	
$R_{\mathrm{te}}I_{\mathrm{te},+,\mathrm{n}}/U_{\mathrm{te,n}}$	=	4.04	%
$\hat{p}_{\mathrm{te\text{-}loss,L},-}$	=	50.46	W/m
$\hat{p}_{\mathrm{te\text{-}loss,A},-}$	=	560.85	W/m^2
Dimensions and masses.			
A	=	24.00	m^2
$\hat{m}_{\mathrm{a,flight}}$	=	2,099.55	kg
$\hat{m}_{\mathrm{a,hov,ok}}$	=	1,797.52	kg
$\hat{m}_{\mathrm{a,hov,flt}}$	=	1,685.17	kg
$\hat{m}_{\mathrm{a}}$	=	1,685.17	kg
$\hat{m}_{\mathrm{k}}$	=	1,424.59	kg
$\hat{m}_{\mathrm{k}}/A$	=	59.36	kg/m^2
$\hat{m}_{\mathrm{af\&o}}$	=	999.20	kg
$\hat{m}_{\mathrm{af\&o}}/A$	=	41.63	kg/m^2
$m_{\mathrm{pt,k}}$	=	425.38	kg
m_{te}	=	521.18	kg
$m_{\mathrm{te,mech}}$	=	187.40	kg
$m_{\mathrm{te,c}}$	=	280.94	kg
$n_{\mathrm{te,c}}$	=	14	
d_{te}	=	28.64	mm
f_{te}	=	1.63	

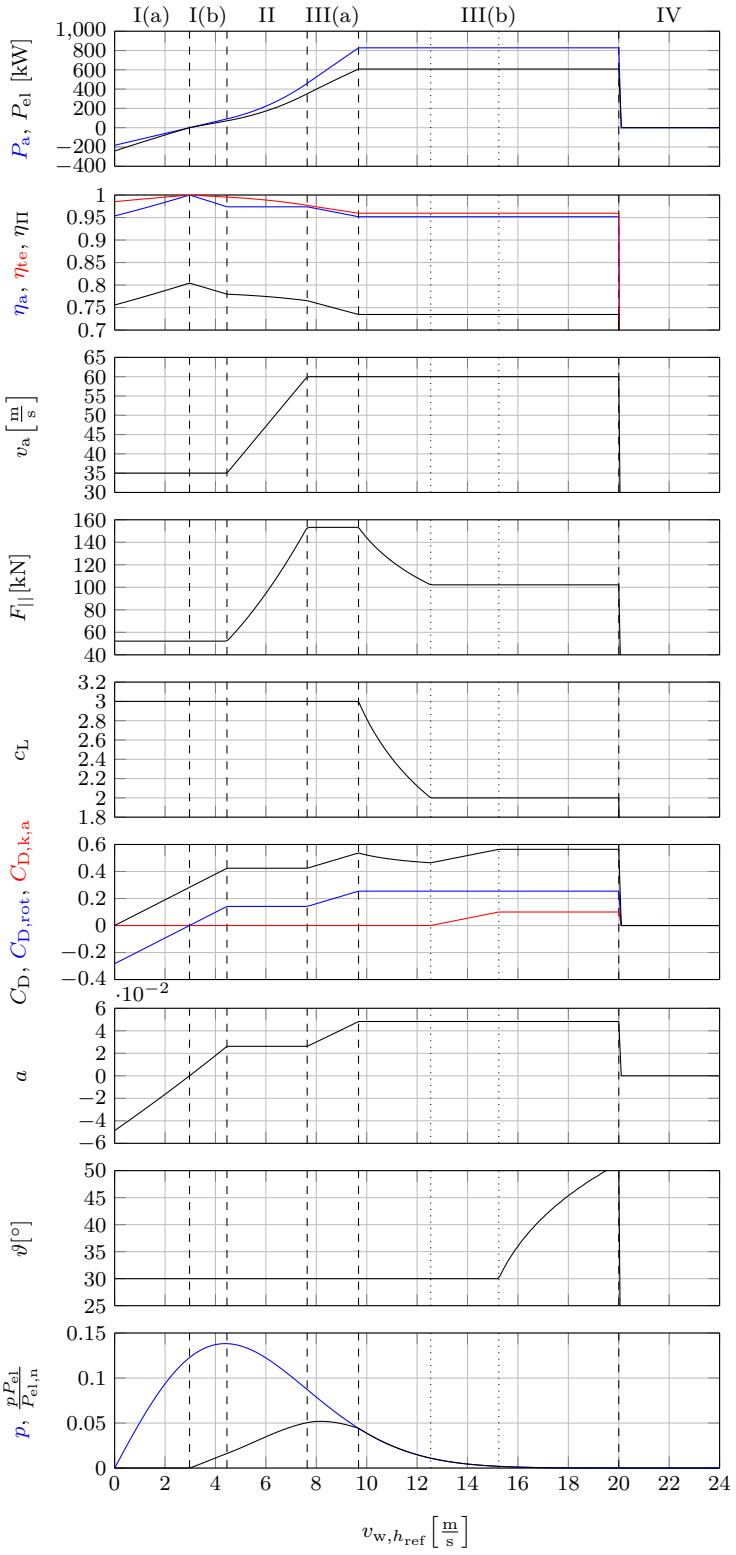

Figure 3.7: Power curve results for the Makani M600.

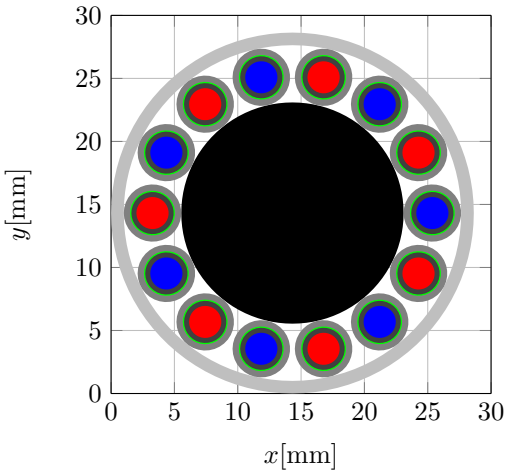

Figure 3.8: Visualization of the tether cross section for the Makani M600 with color coding as in Fig. 1.8.

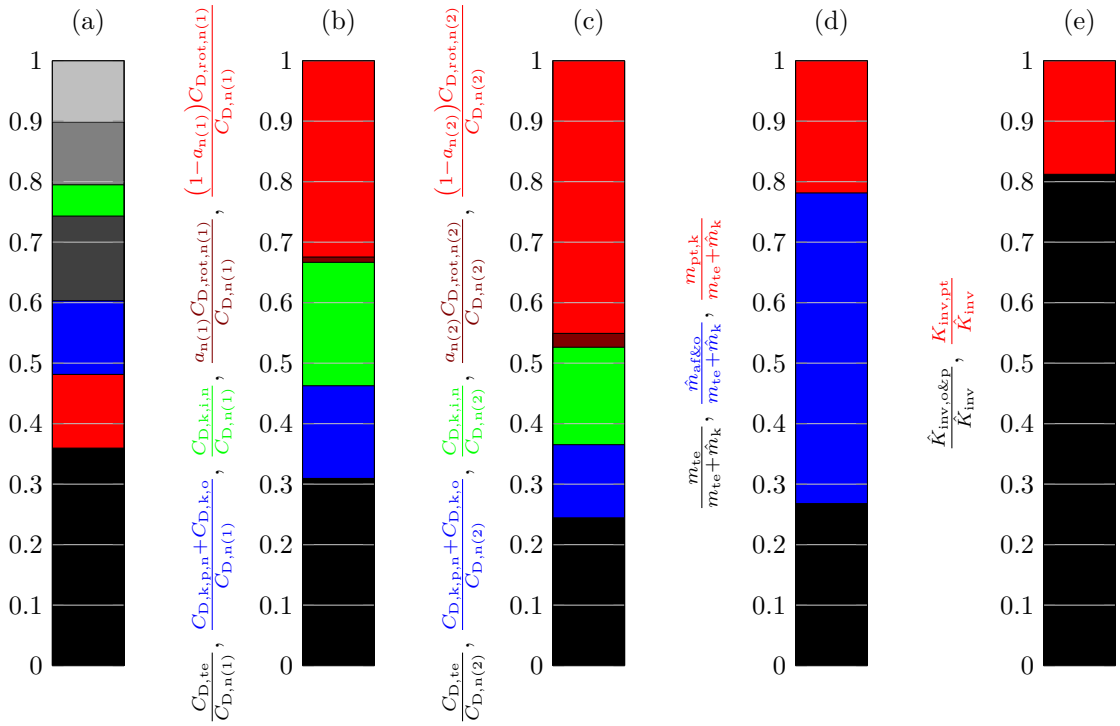

Figure 3.9: Visualization of distributions of some results for the Makani M600: (a) tether mass distribution with color coding as in Fig. 1.8, (b) distribution of drag portions in Region II and at first power point, (c) distribution of drag portions at second power point, (d) distribution of total (maximum allowed) airborne masses, (e) distribution of costs.

3.2.1.2 Power Curve: Model vs. Makani's Expectations

Fig. 3.10 shows the power curve of the Makani M600 taken from [151], which is likely the result of a simulation conducted by Makani (i.e. it is an expectation), but it is for sure no measurement because the M600 was still under construction at the time this power curve was published. It is assumed that this "power" is the electrical power at the grid connection. Makani's power curve is overlaid by the computed electrical power curve from Fig. 3.7 with size, axes, and line thickness altered for better perception.

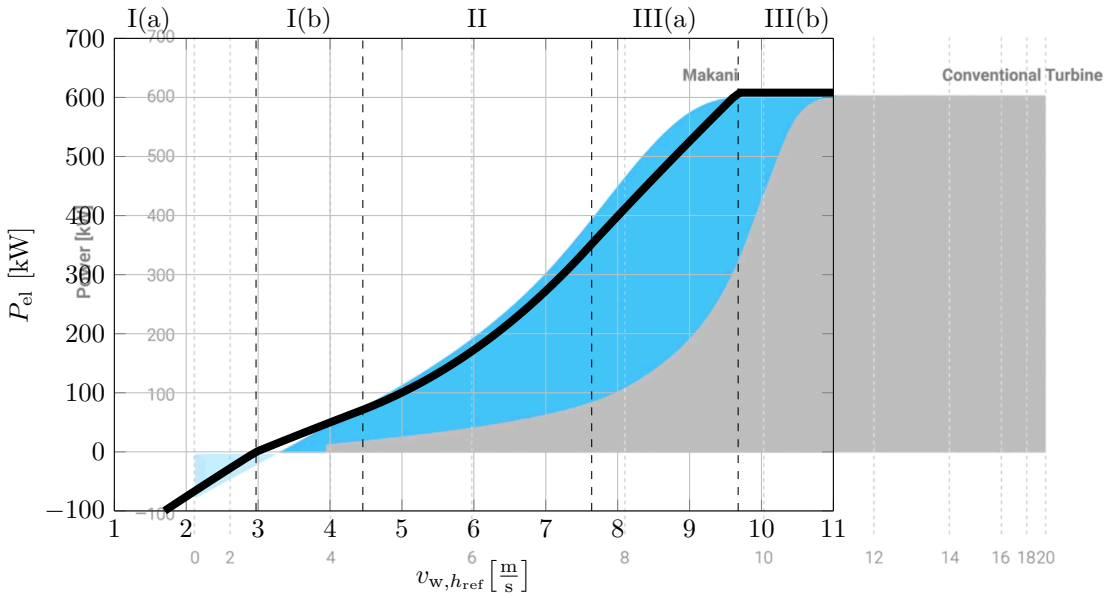

Figure 3.10: Overlay of [151] and Fig. 3.7 (row 1) with size, axes, and line thickness altered: Blue areas show the by Makani expected power curve for the M600, gray areas show the power curve of a conventional wind turbine with the same nominal power, and the thick black line ━ is the power curve computed with the in this dissertation derived model. All quantities are the electrical power P_{el}.

Obviously, the results of the in this dissertation derived model match well with the expectations of Makani.

3.2.1.3 Maximum Allowed Kite Mass: Model vs. Makani's Expectation

In [102] the kite mass is given with $m_{\mathrm{k}} = 1,050\,\mathrm{kg}$. Tab. 3.6 lists the maximum allowed kite mass as $\hat{m}_{\mathrm{k}} \approx 1,425\,\mathrm{kg}$. Obviously, also this computed value matches with the real value.

3.2.1.4 Tether Mass: Model vs. Makani's Expectation

Tab. 3.6 lists the tether mass with $m_{\mathrm{te}} \approx 521\,\mathrm{kg}$ which is twice as much than $m_{\mathrm{te}} = 250\,\mathrm{kg}$ stated in [102]. However, in [102] the tether voltage is given with $U_{\mathrm{te,n}} = 8\,\mathrm{kV}$ instead of the here used $U_{\mathrm{te,n}} = 4\,\mathrm{kV}$ provided by Fort Felker (Makani) in a face-to-face conversation at the AWEC2017 [19]. The lower voltage is probably chosen to simplify the powertrain design at the cost of a heavier tether.

3.2.1.5 Power Curve: Other Results

Besides the aerodynamic and electrical power, Fig. 3.7 plots further results as function of the wind speed which are both, plausible and interesting:

- Region III(a), in which force and airflow speed are at the upper bound but the power still increases, is relatively wide. This is in accordance with [78] in which Nick Tucker (Makani) concludes that a relatively low nominal tether force and a significant Region III(a) (in the terminology of this dissertation) are meaningful.
- The majority of the energy is generated in Region III(a). This is plausible as the power is high and the probability for the wind speeds in this region is also still high.
- In Region III(b) the complete power limitation scheme motivated in Sect. 2.7.12 and derived in Appendix B is utilized: For increasing wind speeds, first the lift coefficient is reduced which also reduces the force and the (induced) drag, than the actuated drag is increased, and finally the elevation is increased.
- The efficiencies reduce for increasing wind speeds, mainly due to increased induction factor and tether transmission loss.
- The consumptive power at zero wind during crosswind flight is much lower than the nominal power.
- The cut-in wind speed is significantly lower than that of Wing 7 and the specific power (e.g. power per area) is significantly higher than that of Wing 7. Both can be explained by the efficiency increase due to the relatively thinner tether (the tether core diameter increases only with $\sqrt{F_{||,\mathrm{n}}} \sim \sqrt{P_\mathrm{n}}$, cf. (2.55)–(2.59) and (2.22)) as well as through a higher Reynolds number, as already concluded in the prior work of the author of this dissertation [110].
- The other actuations and results also in the other regions are as expected from the derivation of the power curve equations.

3.2.1.6 Tether Cross Section: Model vs. Reality

The tether cross section shown in Fig. 3.8 looks almost identical to the photographs of the cut tether shown by Nick Tucker (Makani) in his AWEC2017 presentation [78]. It should be noted that $n_{\mathrm{te,c}} = 14$ is also the optimal number of electrical cables in the tether to obtain the minimal tether diameter.

3.2.1.7 Mass Distribution: Model vs. Makani's Expectation/Reality

In his AWEC2017 presentation, Nick Tucker (Makani) also showed a diagram of the mass distribution of the kite [78], in which the airframe is about one half and the powertrain about one third of the total kite mass. This is in well accordance with Fig. 3.9 (d). Though, note that this figure shows in part the maximum allowed mass which is not the same as the actual mass, and it shows the mass distribution w.r.t. kite mass plus tether mass (maximum allowed total airborne mass).

3.2.1.8 Other Results

Other results shown in Tab. 3.6 and Figs. 3.7–3.9 are also plausible, but are not further elaborated.

3.2.2 Simulation of the Makani M5

Similar to the previous sections, Tab. 3.7 lists the from literature extracted and assumed parameters for the Makani M5, but for sake of compactness only those which are different from Tab. 3.5 from the Makani M600. Tab. 3.8 lists relevant simulation results, Fig. 3.11 shows the power curve and other values as function of the wind speed, Fig. 3.12 shows the tether cross section, and Fig. 3.13 visualizes drag-, mass-, and cost distributions. The most important results are the values highlighted in green in Tab. 3.8 and the first row of Fig. 3.11.

Table 3.7: Parameters for the Makani M5 simulation which are different from Tab. 3.5.
Color-coding: green = reliable value available, e.g. from literature; yellow = no exact value known but good estimate available; red = neither exact value nor good estimate available, instead value had to be guessed ("scientific guess") or in part fitted to obtain reasonable results.

Parameter	Value	Comment/Justification
Kite aerodynamics parameters.		
b	$= 65\,\mathrm{m}$	Ref. [102]
AR	$= 37.3894$	$= b^2/A$ with $A = 113\,\mathrm{m}^2$ extracted from [102]
Tether parameters.		
L_{te}	$= 1,060\,\mathrm{m}$	Ref. [102]
$U_{\mathrm{te,n}}$	$= 8\,\mathrm{kV}$	Ref. [102]
$n_{\mathrm{te,c}}$	$=$ *optimal*	assumed design decision; i.e. $n_{\mathrm{te,c}}$ is optimized "internally" within Step 6 of the algorithm in Sect. 2.9.2
Ground station parameters and flight trajectory parameters.		
h_{to}	$= 25\,\mathrm{m}$	estimated 10 m higher than in [19, presentation slides], because of longer tail cf. [102]
Power curve "shaping" parameters.		
$v_{\mathrm{a,min}}$	$= 40\,\mathrm{m/s}$	estimated
$v_{\mathrm{a,n}}$	$= 73\,\mathrm{m/s}$	fitted to reach $P_{\mathrm{el,n}} \approx 5\,\mathrm{MW}$

Table 3.8: Results for the Makani M5.

Parameter	Value		
Economic values.			
$E_{\mathrm{el,yr}}$	=	11,309,344.10	kWh/yr
H	=	26.29	%
$\hat{K}_{\mathrm{inv}}$	=	3,376,737.56	EUR
$K_{\mathrm{inv,pt}}$	=	736,702.98	EUR
$\hat{K}_{\mathrm{inv,o\&p}}$	=	2,640,034.58	EUR
$\hat{K}_{\mathrm{inv}}/P_{\mathrm{el,n}}$	=	0.69	EUR/W
$E_{\mathrm{el,yr}}k_{\mathrm{LCOE}}$	=	565,467.20	EUR/yr
$\hat{K}_{\mathrm{inv}}I_{\mathrm{op}}$	=	168,836.88	EUR/yr
T_{am}	=	8.51	yr
Nominal power and nominal wind speeds.			
$P_{\mathrm{a,n}}$	=	7,016,070.80	W
$P_{\mathrm{el,n}}$	=	4,911,353.21	W
$P_{\mathrm{el,n}}/A$	=	43,463.30	W/m^2
$P_{\mathrm{el,n}}/(\hat{m}_{\mathrm{k}}+m_{\mathrm{te}})$	=	353.02	W/kg
$v_{\mathrm{w},h_{\mathrm{ref}},\mathrm{cut\text{-}in}}$	=	3.03	m/s
$v_{\mathrm{w},h_{\mathrm{ref}},\mathrm{n}(1)}$	=	8.30	m/s
$v_{\mathrm{w},h_{\mathrm{ref}},\mathrm{n}(2)}$	=	10.52	m/s

(continued)

Parameter	Value		
Other nominal values.			
ω_{n}	=	3.95	°/s
h_{n}	=	555.00	m
$F_{\mid\mid,\mathrm{n}}$	=	1,076,039.63	N
$F_{\mid\mid,\mathrm{n}}/(Ag)$	=	970.69	kg/m^2
$C_{\mathrm{D,te}}$	=	0.14	
$C_{\mathrm{D,k,p,n}}+C_{\mathrm{D,k,o}}$	=	0.06	
$C_{\mathrm{D,k,i,n}}$	=	0.08	
$C_{\mathrm{D,eq,n}}$	=	0.28	
$C_{\mathrm{D,rot,n}(1)}$	=	0.14	
$C_{\mathrm{D,rot,n}(2)}$	=	0.25	
$a_{\mathrm{n}(1)}$	=	0.03	
$a_{\mathrm{n}(2)}$	=	0.05	
$\eta_{\Pi,\mathrm{n}}$	=	70.00	%
$\zeta_{\mathrm{n}(1)}$	=	27.82	
$R_{\mathrm{te}}I_{\mathrm{te},+,\mathrm{n}}/U_{\mathrm{te,n}}$	=	8.56	%
$\hat{p}_{\mathrm{te\text{-}loss,L},-}$	=	341.48	W/m
$\hat{p}_{\mathrm{te\text{-}loss,A},-}$	=	1,809.10	W/m^2
Dimensions and masses.			
A	=	113.00	m^2
$\hat{m}_{\mathrm{a,flight}}$	=	13,006.32	kg
$\hat{m}_{\mathrm{a,hov,ok}}$	=	11,806.07	kg
$\hat{m}_{\mathrm{a,hov,flt}}$	=	11,068.19	kg
$\hat{m}_{\mathrm{a}}$	=	11,068.19	kg
$\hat{m}_{\mathrm{k}}$	=	8,223.92	kg
$\hat{m}_{\mathrm{k}}/A$	=	72.78	kg/m^2
$\hat{m}_{\mathrm{af\&o}}$	=	4,618.74	kg
$\hat{m}_{\mathrm{af\&o}}/A$	=	40.87	kg/m^2
$m_{\mathrm{pt,k}}$	=	3,605.18	kg
m_{te}	=	5,688.53	kg
$m_{\mathrm{te,mech}}$	=	3,169.67	kg
$m_{\mathrm{te,c}}$	=	2,246.75	kg
$n_{\mathrm{te,c}}$	=	28	
d_{te}	=	60.08	mm
f_{te}	=	1.29	

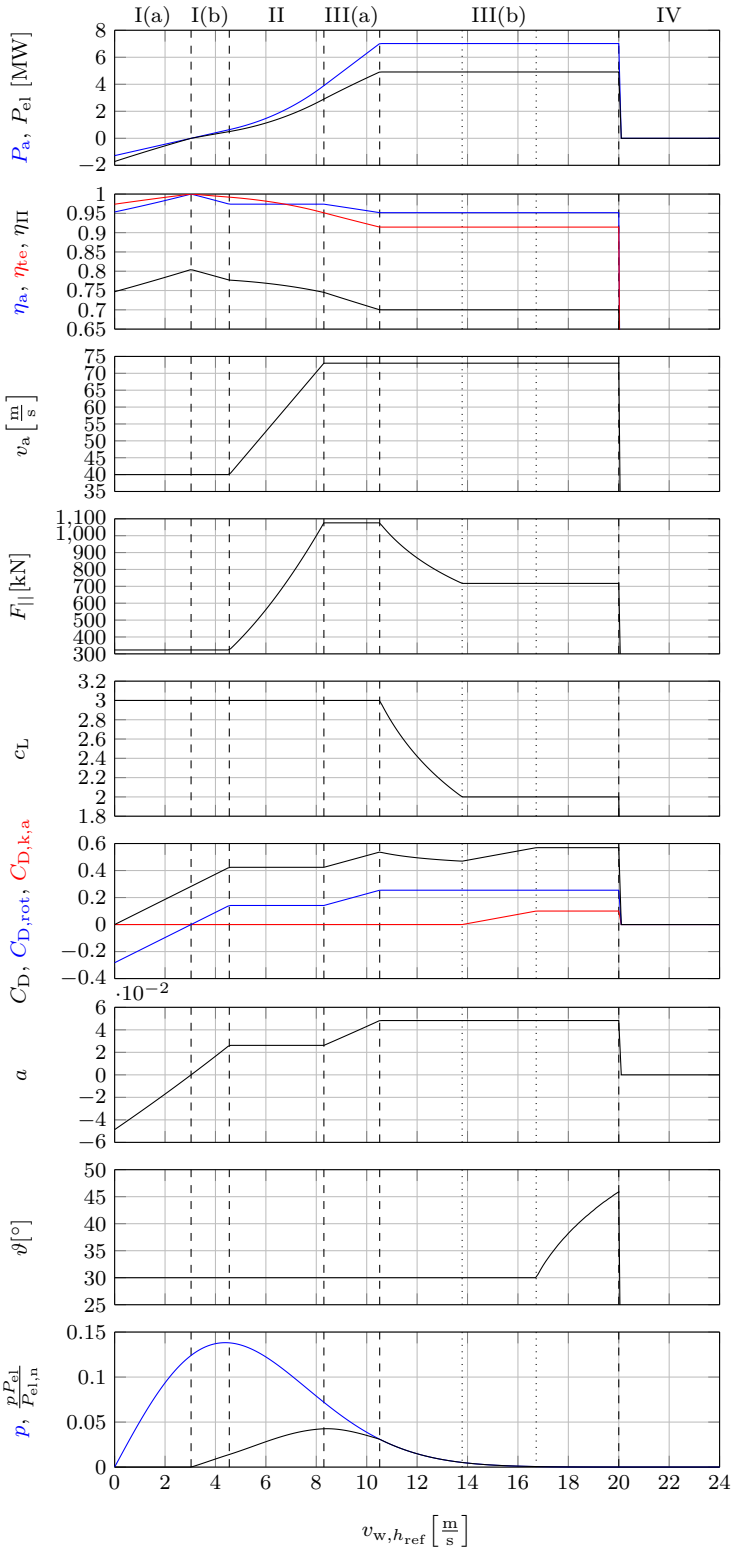

Figure 3.11: Power curve results for the Makani M5.

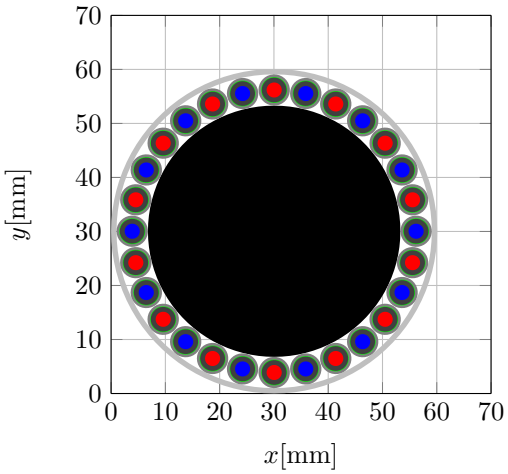

Figure 3.12: Visualization of the tether cross section for the Makani M5 with color coding as in Fig. 1.8.

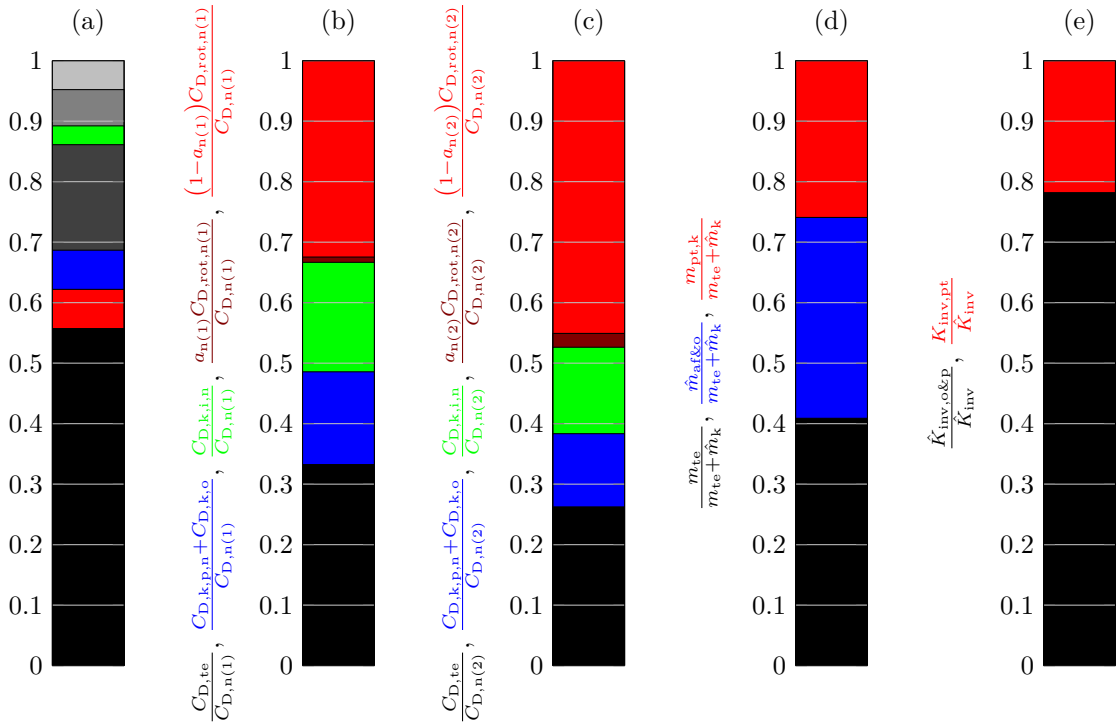

Figure 3.13: Visualization of distributions of some results for the Makani M5: (a) tether mass distribution with color coding as in Fig. 1.8, (b) distribution of drag portions in Region II and at first power point, (c) distribution of drag portions at second power point, (d) distribution of total (maximum allowed) airborne masses, (e) distribution of costs.

The power curve data in Tab. 3.8 and Fig. 3.11, i.e. the cut-in and second nominal wind speed as well as the nominal electrical power, match again with what is expected, cf. [102]. The other results are also plausible.

Only the tether mass in Tab. 3.8 is about two tons higher than what is given in [102]. Reasons may include that lower safety- and correction factors were assumed by Makani. For example, for $S_{\mathrm{te}} = 3 \cdot 1.5 = 4.5$, the tether mass is almost identical to the value in [102]. Lower safety factors for later developed systems seem reasonable, because the maturity of the technology can be expected to increase and allow for reduced safety factors. Possibly due to the same reason, the maximum allowed kite mass in Tab. 3.8 is about two tons lower than in [102].

3.2.3 Discussion on Model Generality

Based on the successful simulation studies for the Makani M600 and M5, the generality in this dissertation derived model could not be falsified. Quite the contrary, the results are plausible. It should be noted, that no safety and correction factors were changed. Nevertheless, the model should still be treated with care due to the many values for which only a "scientific guess" is available, visible by the many red rows in Tabs. 3.5 and 3.7.

3.3 Comparison to Simulations with a Higher Fidelity Model

Some submodels and parameters are already validated against higher fidelity models and measurements, e.g. the airfoil polar model, cf. Fig. 2.5. For further validations of the generality of the complete systems engineering model and of the applicability of some of its most rough assumptions, simulation results are also compared to simulation results of a higher fidelity model. Here, the point-mass model is chosen which replaces in part or entirely Assumptions 2.1, 2.4, 2.5, 2.33, and 2.35 with less rough ones, and hence particularly the kite dynamics submodel is of higher fidelity. As the derivation of the point-mass model is not the main focus of this dissertation, it is moved to Appendix C. In Appendix C.4, it is also validated successfully against the measured power curve of the Makani Wing 7 (similarly to Fig. 3.4) with a very good match.

In the following, the validated point-mass model is used to validate the simulation results of the steady model of the Makani M600 and M5 from the previous section, and thus also validate the generality of both models.—The wording of this sentence already implies that care should be taken, because a model (even if it is of high fidelity) cannot in general validate another model. Ultimately, only measurements can provide a full validation. Nevertheless, if the steady model cannot be falsified by such a comparison, it is an indication that it might be a good representation of reality.

For sake of brevity, only the power curves of the point-mass model with its comparison to the steady model and only the kite's trajectory computed from the point-mass model at $v_{\mathrm{w},h_{\mathrm{ref}}} = 10\,\mathrm{m/s}$ are shown.

3.3.1 Parameters

Tab. 3.9 shows the target point list utilized for the Makani M600 and M5 system, which differs slightly from Wing 7 and Tab. C.3 due to the 10 ° lower (absolute) mean elevation angle. For the Makani M600 simulation, the effective airborne mass is computed from (2.27) with $f_{\text{m-te}}$ and m_{te} from the steady model parameters and results, and with the kite mass from [102], i.e.

$$\text{for Makani M600:} \quad m_{\mathrm{k}} = 1,050\,\mathrm{kg}. \tag{3.5}$$

Table 3.9: Target point list for the Makani M600 and M5.

Note	φ_{set}	ϑ_{set}	Threshold Type	x_{th}	Turn Dir.
Clockwise circle with four points.					
top right	$-10\,^\circ$	$-40\,^\circ$	AzimuthBelowThreshold	0	Shortest
bottom right	$-10\,^\circ$	$-20\,^\circ$	ElevationAboveThreshold	$-30\,^\circ$	Shortest
bottom left	$10\,^\circ$	$-20\,^\circ$	AzimuthAboveThreshold	0	Shortest
top left	$10\,^\circ$	$-40\,^\circ$	ElevationBelowThreshold	$-30\,^\circ$	Shortest

For the Makani M5, the maximum allowed airborne mass is used as effective airborne mass for the point-mass model due to the discrepancy of $\hat{m}_{\text{k}}$ and m_{k} given in [102], i.e.

$$\text{for Makani M5:} \quad m_{\text{a}} = \hat{m}_{\text{a}}. \tag{3.6}$$

All other parameters for the Makani M600 and M5 simulations are as in Tabs. 3.5, 3.7, and C.2.

3.3.2 Simulation of the Makani M600

3.3.2.1 Power Curve Results

Fig. 3.14 reports the power curve results.

It can be seen that the majority of the mean values over a flight path loop match well with those of the steady model. However, the mean powers from the point-mass model are a bit lower (or shifted to higher wind speeds) compared to those of the steady model. As indicated in Appendix C.4.3, there are two plausible explanations for that: (i) The effective azimuth of the steady model is $\varphi_{\text{n}} = 0$, see Tab. 3.5, while in fact the mean absolute value recorded with the point-mass model is $\approx 10\,^\circ$, see second last row in Fig. 3.14. (ii) The flight path is suboptimal, because no maximum power point (MPP) tracking is utilized and because the switching flight path controller is arguably not a good choice for a circular flight path (cf. also Appendix C.4).

One further discrepancy, already observed for the Wing 7 simulation in Fig. C.6, is that the mean efficiencies of the point-mass model are lower around the cut-in wind speed compared to those of the steady model, while at higher wind speeds there is a very good match. Because of that, the electrical power and energy harvested at lower wind speeds is also lower for the point-mass model. The explanation for that is simple: While an individual efficiency (like η_{a} and η_{te}) can oscillate around a mean value $\ll 100\,\%$, it cannot exceed $100\,\%$. Therefore, at a high efficiency in the steady model, the dynamic point-mass model has a significantly lower mean efficiency.[36]

[36] An idea to overcome that weakness of the steady model, which is however not implemented here for sake of simplicity, is to limit the efficiencies to some values below $100\,\%$.

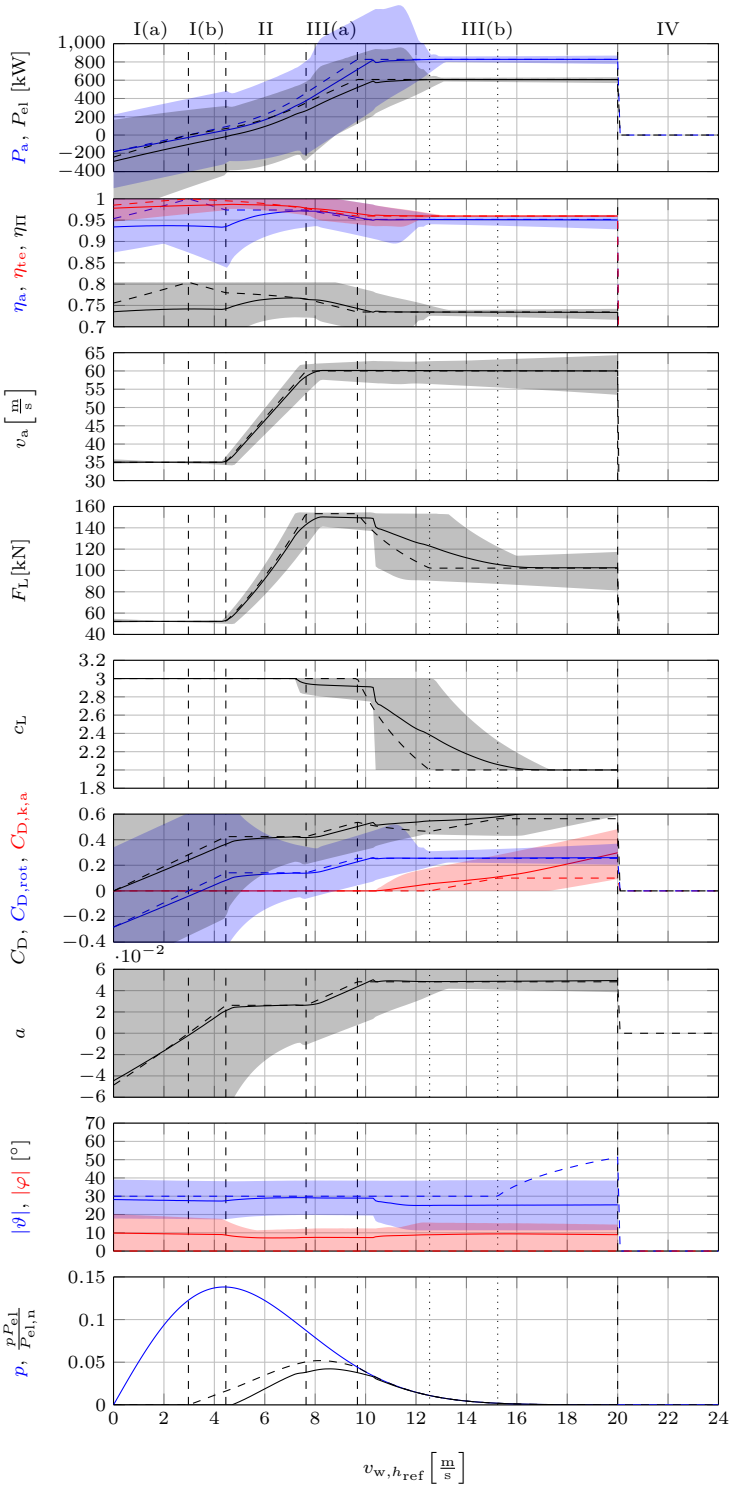

Figure 3.14: Power curve results for the Makani M600: steady model in dashed vs. point-mass model with mean values over flight path loop in solid and range of minimum and maximum values over flight path loop as area.

3.3.2.2 Power Curve: Point-Mass Model vs. Steady Model vs. Makani's Expectations

To further visualize the results, the electrical power from the point-mass model is additionally overlaid onto [151], similar to Fig. 3.10. That overlay is shown in Fig. 3.15.

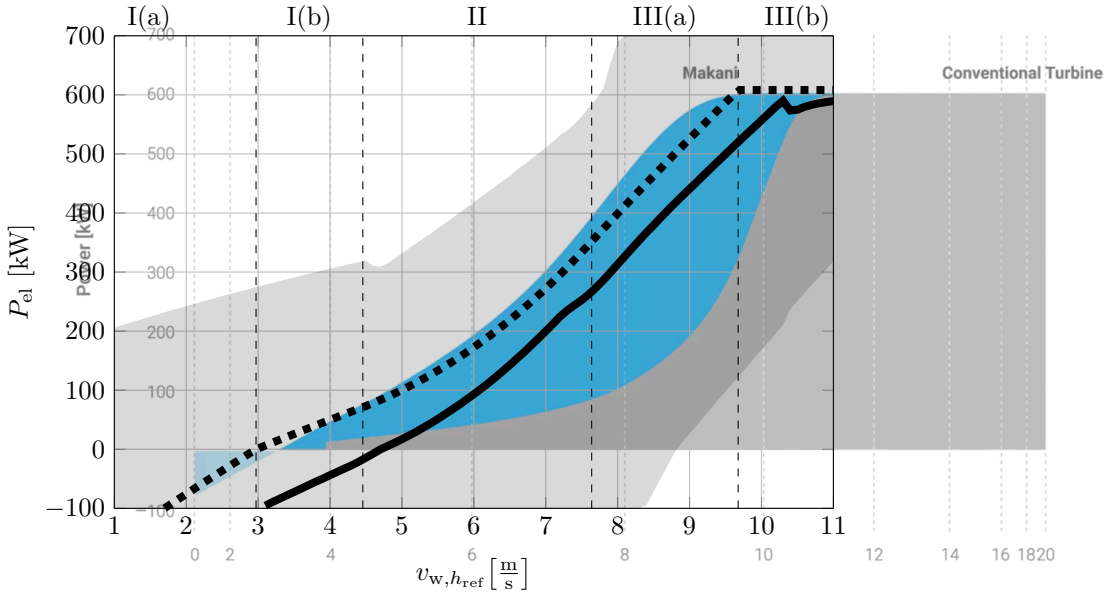

Figure 3.15: Overlay of [151] and Fig. 3.14 (row 1) with size, axes, and line thickness altered: Blue areas show the by Makani expected power curve for the M600 and gray areas show the power curve of a conventional wind turbine with the same nominal power. The thick dashed black line ▪▪▪▪ is the power curve computed with the in this dissertation derived steady model. The thick black solid line ━━ is the mean power over the flight path loop computed with the point-mass model and the light gray areas indicate the range of the minimum and maximum values over a flight path loop. All quantities are the electrical power P_{el}.

The previously noticed discrepancy of the power recorded with the point-mass model compared to the steady model is highlighted.

3.3.2.3 Trajectory

Fig. 3.16 visualizes M600's trajectory at $v_{\mathrm{w},h_{\mathrm{ref}}} = 10\,\mathrm{m/s}$. As already known from Appendix C.4.4, the flight trajectory is not a smooth circle due to the switching behavior of the chosen flight path controller. Again, this indicates potentials for optimizations and a higher mean power output, once improvements are implemented.

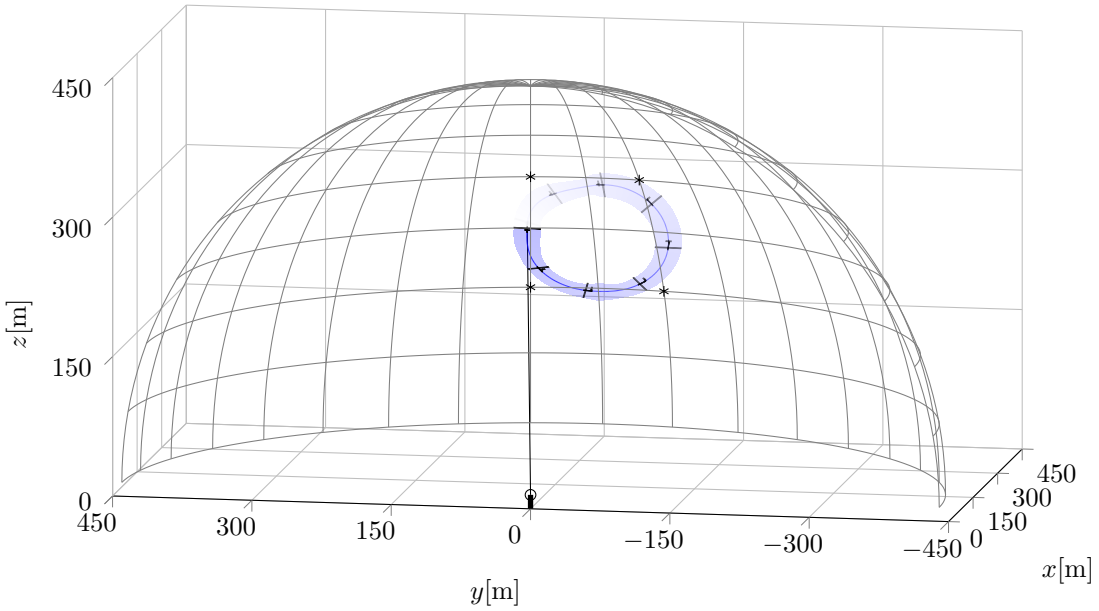

Figure 3.16: Flight trajectory of the Makani M600 at $v_{\mathrm{w},h_{\mathrm{ref}}} = 10\,\mathrm{m/s}$ with the flight path target points in * and with the kite's orientation every 1 s before the path loop ends.

3.3.3 Simulation of the Makani M5

Figs. 3.17 and 3.18 report the M5's power curve results and trajectory at $v_{\mathrm{w},h_{\mathrm{ref}}} = 10\,\mathrm{m/s}$.

Again, most mean values of the point-mass model are close to the values of the steady model, but the mean powers of the point-mass model are slightly lower. For the latter, the same explanation as for the Wing 7 and M600 can be given. In particular, the M5 flies a rather cornered circle with frequent steps of the roll angle, visible in Fig. 3.18, indicating a great potential for optimizations. Indeed, reducing the maximum roll angle to $\psi_{\max} = -\psi_{\min} = 20\,^\circ$ allows a smoother (although larger) trajectory with by several percents increased power (not shown here for sake of brevity).

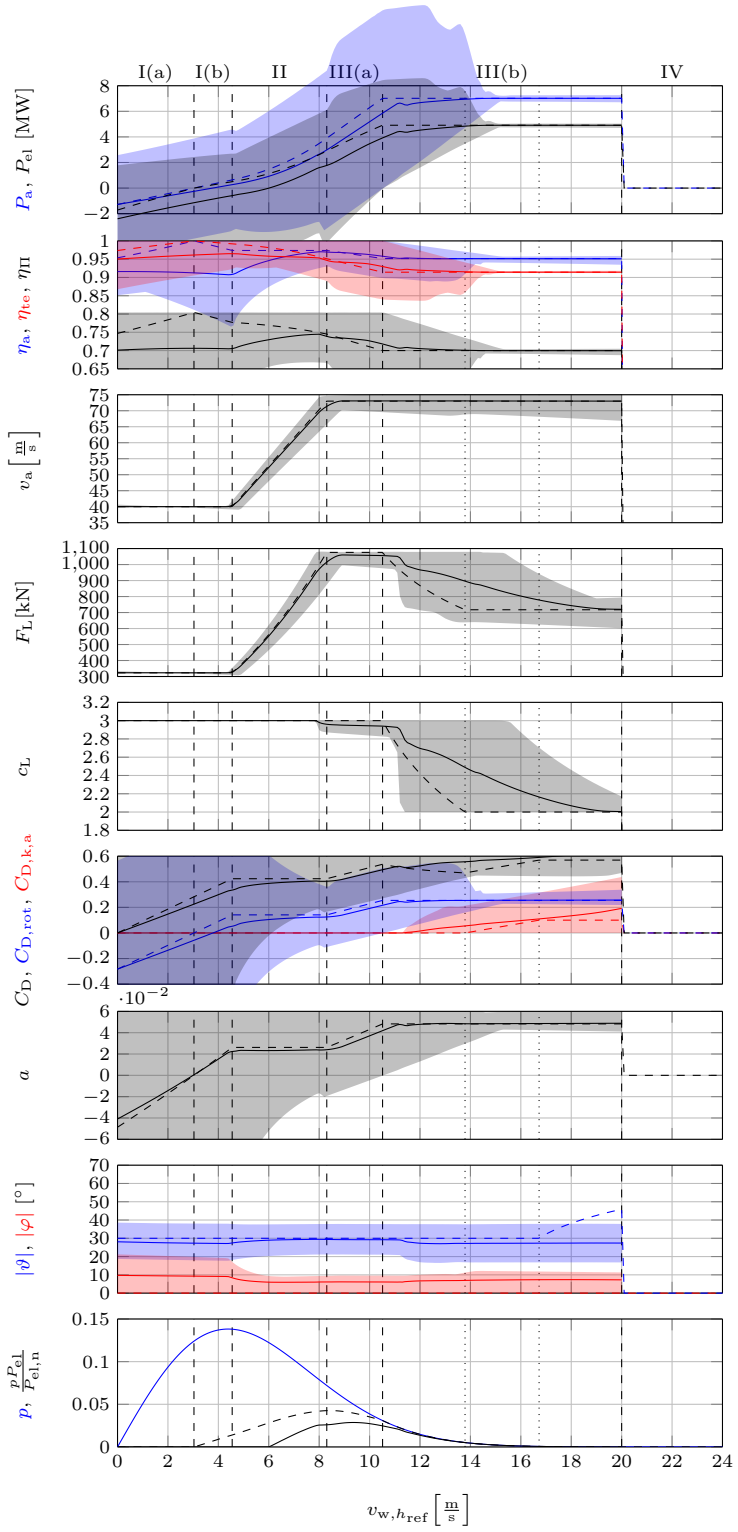

Figure 3.17: Power curve results for the Makani M5: steady model in dashed vs. point-mass model with mean values over flight path loop in solid and range of minimum and maximum values over flight path loop as area.

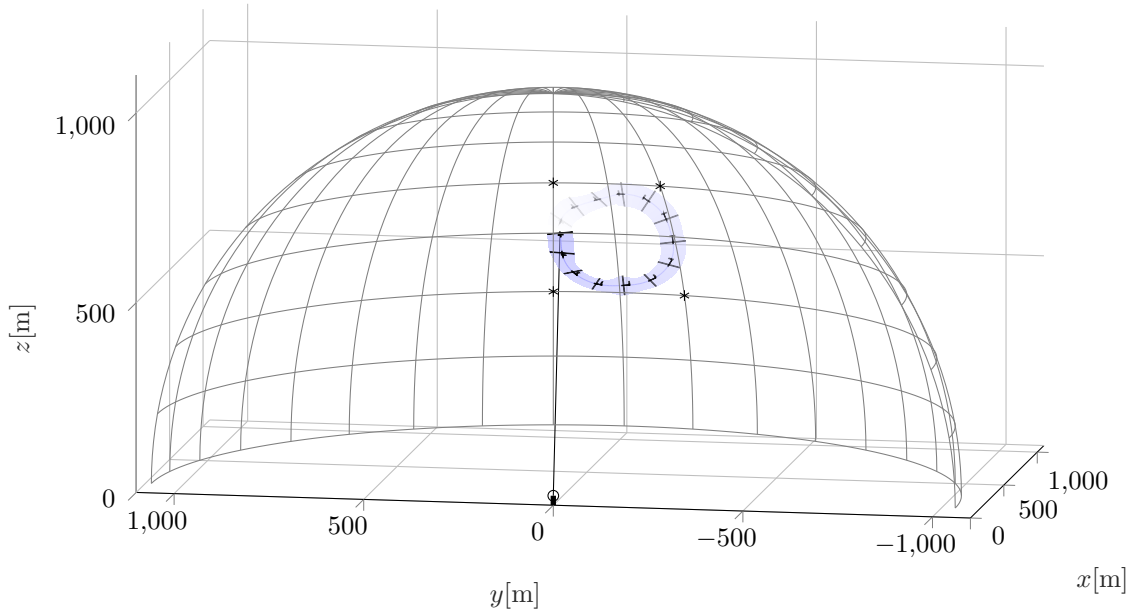

Figure 3.18: Flight trajectory of the Makani M5 at $v_{\mathrm{w},h_{\mathrm{ref}}} = 10\,\mathrm{m/s}$ with the flight path target points in * and with the kite's orientation every 1 s before the path loop ends.

3.3.4 Discussion

The steady model's results compare well with the point-mass model's results for all Makani systems, but with a noticeable difference in the power. Given that a zero effective azimuth was assumed for the steady model, that no MPP-tracking was utilized, and that a for circular paths likely suboptimal flight path controller was considered, it is plausible that the point-mass model's mean power is lower. Nevertheless, the effect of an MPP-tracker and better flight path controller are unknown. Therefore, two conclusions can be drawn: (i) Even for circular paths a non-zero effective azimuth must be considered. (ii) The steady model might overestimate the power (mainly for low to medium wind speeds).

3.4 Concluding Remarks

The validation of the steady systems engineering model can be evaluated as successful: It complies well with measurements of the Makani Wing 7 and its generality could not be falsified neither with the expectations of the utility-scale Makani M600 and M5 nor with the higher fidelity point-mass model. The steady model was seen to overestimate the power compared to the point-mass model, which however could in part be explained by a false parameter assumption (zero effective azimuth) and missing flight controller optimizations. Concluding, the steady systems engineering model can well be used for optimization studies. Nevertheless, some care should be taken, e.g. it should be expected that the power (and all dependent values such as energy yield and maximum allowed costs) might be a bit overestimated. In order to evaluate the trustability of the steady model's

result (at least in part), it should be checked also against the higher fidelity point-mass model's results.[37]

It should be admitted again, that a full validation of the systems engineering model, or generally of the kite system designs computed or optimized with it, can only be provided with significant man-power and budget by building actual kite power plant demonstrators.

[37] Note that the point-mass model cannot directly be used for optimizations and sensitivity analyses, particularly because of the *much* higher computational load, cf. Appendix C.5.

Chapter 4

Optimization Procedure

In this chapter, an optimization procedure is developed, for use with the derived and validated drag power kite systems engineering model. The general requirements for the optimization procedure are as follows:

1. The optimization shall be a single objective optimization, because within the alternative of a multi-objective optimization it would be unclear which Pareto-optimal solution is "truly" optimal.
2. The optimization algorithm shall find the global optimum, because the optimization problem itself may be highly nonlinear and may have several local optima.
3. The setup effort for the optimization shall be low. In particular, the algorithm shall not require a Jacobian. This is important to allow for fast refinements of submodels and later inclusion of possibly highly complex submodels. As an example, if the model is refined with a dynamic simulation of the kite as point-mass or even as rigid body together with a sophisticated aerodynamics model, it would be hard to derive the analytical Jacobian for such a submodel.
4. An "off-the-shelf" and simple to use optimization algorithm shall be used. The focus of this dissertation and of a drag power kite research and development team in general is the modeling and design of the kite power plant, not the development of an optimization algorithm.

This chapter is structured as follows: Sect. 4.1 formulates the optimization problem as a nonlinear constraint maximization problem. Sect. 4.2 selects a solution algorithm. Finally, Sect. 4.3 gives some details on the implementation.

The here employed optimization procedure is similar to the prior works of the author of this dissertation [104, 110].

4.1 Optimization Problem Formulation

The kite power plant optimization problem can be generally formulated as follows:

> *Find the optimal drag power kite plant parameters which minimize (maximize) a cost function (fitness function) subject to constraints. Parts of that problem are finding parameters to optimize with, finding a suitable cost function (fitness function) to optimize for, and finding suitable constraints.*

In the following, this problem is formulated mathematically after selecting optimization parameters, the cost function (fitness function), and constraints.

4.1.1 Choice of Parameters to Optimize With

The derived steady drag power kite plant model employs a number of parameters. Some of these parameters can be considered as "fixed (design) parameters" and others as "(free) dimensioning parameters" (or "free design parameters" or "optimization parameters").

Fixed parameters are those parameters which cannot be optimized because they are environmental parameters (e.g. g) or for which an optimization is not meaningful because their optimum for the employed model is zero or infinitive (e.g. the optimal r_{rot} is ∞ in the model, which is clearly not true in reality or with more elaborate submodels) or they are material constants (e.g. $\sigma_{\mathrm{te,mech}}$). For the latter, a finite number of values for different materials could be used for an optimization. However, this would lead to a mixed-integer optimization, which may be harder to solve. As reasonable close-to-optimal materials are known and their amount is relatively low, different material selections are not included in the parameters to optimize with, but handled in superimposed parameter studies.

Dimensioning parameters are those parameters for which an optimal value is obscure (e.g. L_{te} or nominal values of the power curve). Many of these values were already referred to as "dimensioning parameters" in Chap. 2. These are the parameters selected to optimize with.—In Step 1 of the presented algorithm in Sect. 2.9.2, the parameters of the steady model were already separated in fixed parameters (Step 1.1) and dimensioning parameters (Step 1.2).

4.1.2 Choice of Cost Function or Fitness Function to Optimize For

A real difficulty is to find a suitable cost function, fitness function, or figure of merit to optimize for. As derived by the prior work of the author of this dissertation [110], the rated power alone is not a good figure of merit, as it can be very high for high drag coefficients but at the cost of a high rated wind speed. The rated power might be a good figure of merit with the constraint of a certain rated wind speed, which however has to be chosen to some obscure value. Also the capacity factor ("capacity factor paradox" [152]) or maximum allowed costs per rated power alone do not seem to be suitable figures of merit, as higher energy yields, with which revenue is generated, can be achieved off their maxima [110]. A suitable optimization goal for the electricity customer might be the minimization of k_{LCOE}. For the kite power plant manufacturer, a suitable optimization target might be the maximization of the profit margin. However, for both previous variants a detailed model for the actual $K_{\mathrm{inv,o\&p}}$ has to be found, which is out of scope of this dissertation (see also Sect. 2.9.1). For an environmental activist, a suitable optimization goal could be the maximization of $E_{\mathrm{el,yr}}$ as this is the actual contribution for the energy shift with more renewable energy generation. For an energy utility company or the kite power plant investor it might be interesting to maximize the revenue, i.e. $k_{\mathrm{LCOE}}E_{\mathrm{el,yr}}$ (which is the same as maximizing $E_{\mathrm{el,yr}}$ for a fixed k_{LCOE}—note that k_{LCOE} is a market demand), as this generates the return on investment. Other values such as the land use might also be objectives, but also require model refinements or extensions which are not in the scope of this dissertation.

Here, as a compromise, and in accordance with the ideas from Sect. 2.9.1, the maximum allowed investment costs of airframe etc., development costs, and profit margin $\hat{K}_{\mathrm{inv,o\&p}}$ w.r.t. the kite area A is selected as fitness function to be maximized with reasonable constraints on the optimization parameters, because (i) the kite power plant manufacturer decides how to design its kite, (ii) the kite power plant manufacturer is interested in having a high budget for the power plant development as well as a high profit margin, (iii) it can be assumed that the costs of a kite power plant product are dominated by the development costs, particularly in view of today's low technology readiness level, and (iv) the power plant costs can be expected to be somewhat proportional to the kite area, at least increasing with the kite area. Note that this is a single

objective optimization problem which is in accordance with the first goal stated at the beginning of this chapter.

It should be highlighted, that a kite power plant manufacturer does not want to minimize the price of electricity, which corresponds in the here employed model to k_{LCOE}. On the contrary, in his perspective, the energy costs should be high, because it allows for high development budgets, high revenues, and high profits. However, as stated in Sect. 2.9.1, k_{LCOE} is more like a fixed value for the targeted market which is why it is an input to the optimization and not an output (to optimize for). It should also be highlighted that the difference of the actual selling price of energy to a minimized k_{LCOE} for sure is a profit, but first it is the profit of both energy-utility and power-plant manufacturer, and second given the nonlinearity of the model or of the optimization problem as a whole, it is not the same as maximizing $\hat{K}_{\mathrm{inv,o\&p}}$. Therefore, minimizing k_{LCOE} likely leads to off-optimal resulting optimization parameters and figures of merit w.r.t. $\hat{K}_{\mathrm{inv,o\&p}}$ or respectively $\hat{K}_{\mathrm{inv,o\&p}}/A$.

4.1.3 Choice of Constraints

The constraints are straightforward: First, the optimization variables must be within reasonable bounds, e.g. the airfoil lift coefficient c_{L} has some upper realizable limit. Second, the feasibility constraints formulated in Chap. 2 have to be met, i.e. the infeasibility variable defined in Sect. 2.9.2 must be zero. Third, some resulting values, e.g. the wing loading, may be forced to stay within some bounds.

4.1.4 Mathematical Formulation as Nonlinear Constraint Maximization Problem

With the discussion and choices in the previous three subsections, the selected optimization problem can be written as the nonlinear constraint maximization problem

$$\max_{\boldsymbol{y}} \quad \frac{\hat{K}_{\mathrm{inv,o\&p}}}{A} \tag{4.1}$$

$$\text{s.t.} \quad \underline{\boldsymbol{y}} \leq \boldsymbol{y} \leq \overline{\boldsymbol{y}} \tag{4.2}$$

$$f_{\mathrm{infeas}} = 0 \tag{4.3}$$

$$\underline{\boldsymbol{z}} \leq \boldsymbol{z} \leq \overline{\boldsymbol{z}} \tag{4.4}$$

where $\underline{\#}$ and $\overline{\#}$ denote the bounds of the according variable $\#$,

$$\boldsymbol{y} = \begin{pmatrix} \text{Æ}R \\ c_{\mathrm{L,n}} \\ L_{\mathrm{te}} \\ U_{\mathrm{te,n}} \\ R_{\mathrm{te}} \\ \vartheta_{\mathrm{n}} \\ v_{\mathrm{a,n}} \\ r_{\mathrm{P}} \end{pmatrix}, \qquad \underline{\boldsymbol{y}} = \begin{pmatrix} \underline{\text{Æ}R} \\ \underline{c}_{\mathrm{L,n}} \\ \underline{L}_{\mathrm{te}} \\ \underline{U}_{\mathrm{te,n}} \\ \underline{R}_{\mathrm{te}} \\ \underline{\vartheta}_{\mathrm{n}} \\ \underline{v}_{\mathrm{a,n}} \\ \underline{r}_{\mathrm{P}} \end{pmatrix}, \qquad \overline{\boldsymbol{y}} = \begin{pmatrix} \overline{\text{Æ}R} \\ \overline{c}_{\mathrm{L,n}} \\ \overline{L}_{\mathrm{te}} \\ \overline{U}_{\mathrm{te,n}} \\ \overline{R}_{\mathrm{te}} \\ \overline{\vartheta}_{\mathrm{n}} \\ \overline{v}_{\mathrm{a,n}} \\ \overline{r}_{\mathrm{P}} \end{pmatrix} \tag{4.5}$$

are the optimization parameters (dimensioning parameters) and -bounds, and

$$\boldsymbol{z} = \begin{pmatrix} \omega_{\mathrm{n}} \\ h_{\mathrm{n}} \\ \vdots \end{pmatrix}, \qquad \underline{\boldsymbol{z}} = \begin{pmatrix} 0 \\ \underline{h}_{\mathrm{n}} \\ \vdots \end{pmatrix}, \qquad \overline{\boldsymbol{z}} = \begin{pmatrix} \overline{\omega}_{\mathrm{n}} \\ \overline{h}_{\mathrm{n}} \\ \vdots \end{pmatrix} \tag{4.6}$$

are other resulting properties and their bounds (here, nominal angular speed on tether sphere and nominal kite altitude above ground, but further values may be added, e.g. a bound on the nominal wing loading).

4.2 Selection of Solution Algorithm and Reformulation

Similar to the prior work of the author of this dissertation [110], the Covariance Matrix Adaptation Evolution Strategy (CMA-ES) is used to solve (4.1)–(4.4), because the cost function evaluation with the explicit analytical equations of the algorithm of Sect. 2.9.2 can be computed rather fast, CMA-ES does not require a Jacobian, it likely finds the global optimum (cf. e.g. [153] and references therein), and the algorithm is implemented in various programming languages, including MATLAB which is the variant used here, and can be downloaded for free from [154]. This choice is in well accordance with the second to forth goal stated at the beginning of this chapter.

The implementation of CMA-ES in MATLAB cannot directly solve (4.1)–(4.4). The problem has to be slightly reformulated: First, the CMA-ES implementation in MATLAB can only minimize a cost function and not maximize a fitness function, hence Eq. (4.1) is replaced by

$$\min_{\boldsymbol{y}} \quad -\frac{\hat{K}_{\mathrm{inv,o\&p}}}{A}. \tag{4.7}$$

Second, the CMA-ES implementation can only handle bounds to optimization variables. However, this functionality is not used here and instead the following general constraint handling via penalties to the cost function for any parameter or result is employed: Let $\#_i$, $\underline{\#}_i$, and $\overline{\#}_i$ be the ith component of $(\boldsymbol{y}^\top, f_{\mathrm{infeas}}, \boldsymbol{z}^\top)$, $(\underline{\boldsymbol{y}}^\top, 0, \underline{\boldsymbol{z}}^\top)$, and $(\overline{\boldsymbol{y}}^\top, 0, \overline{\boldsymbol{z}}^\top)$, respectively (note that the constraint $f_{\mathrm{infeas}} = 0$ from (4.3) is the same as $0 \leq f_{\mathrm{infeas}} \leq 0$). Let ϱ_i be a "penalty" cost contribution, defined by

$$\varrho_i := \begin{cases} \varrho_\mathrm{o} + \varrho_\mathrm{s} ||\overline{\#}_i - \#_i||^2 & \text{for } \#_i > \overline{\#}_i \\ \varrho_\mathrm{o} + \varrho_\mathrm{s} ||\#_i - \underline{\#}_i||^2 & \text{for } \#_i < \underline{\#}_i \\ 0 & \text{otherwise,} \end{cases} \tag{4.8}$$

where $\varrho_\mathrm{o}, \varrho_\mathrm{s} > 0$ are positive values (offset and slope). Let ϱ_Σ be the total penalty cost

$$\varrho_\Sigma := \sum_i \varrho_i. \tag{4.9}$$

With (4.7)–(4.9), the nonlinear constrained maximization problem (4.1)–(4.4) is finally replaced by the nonlinear unconstrained minimization problem

$$\min_{\boldsymbol{y}} \quad \begin{cases} \varrho_\Sigma & \text{if } \varrho_\Sigma \neq 0, \\ -\frac{\hat{K}_{\mathrm{inv,o\&p}}}{A} & \text{otherwise,} \end{cases} \tag{4.10}$$

which can be solved directly by the CMA-ES implementation in MATLAB.

Note that, with this strategy, CMA-ES likely finds the optimum quickly, because the cost is negative if no constraint (4.2)–(4.4) is violated, while the cost is positive if a constraint is violated, and therefore new generations (iterations) likely move away from the constraints towards valid results (offsprings). Moreover, the penalty costs increase with the square (or even with the power of four for infeasibility penalty costs, cf. Sect. 2.9.2) of the distance from constraints, and therefore the further offsprings are away from a constraint, the faster new generations likely move towards valid results (offsprings). If (4.1)–(4.4) is solvable, it is likely that at least one offspring has a negative cost (4.10), which would be much lower than any invalid offspring. This valid solution likely improves more and more in every next generation (iteration).

4.3 Implementation

Fig. 4.1 visualizes the general implementation of an optimization study. In the study computation

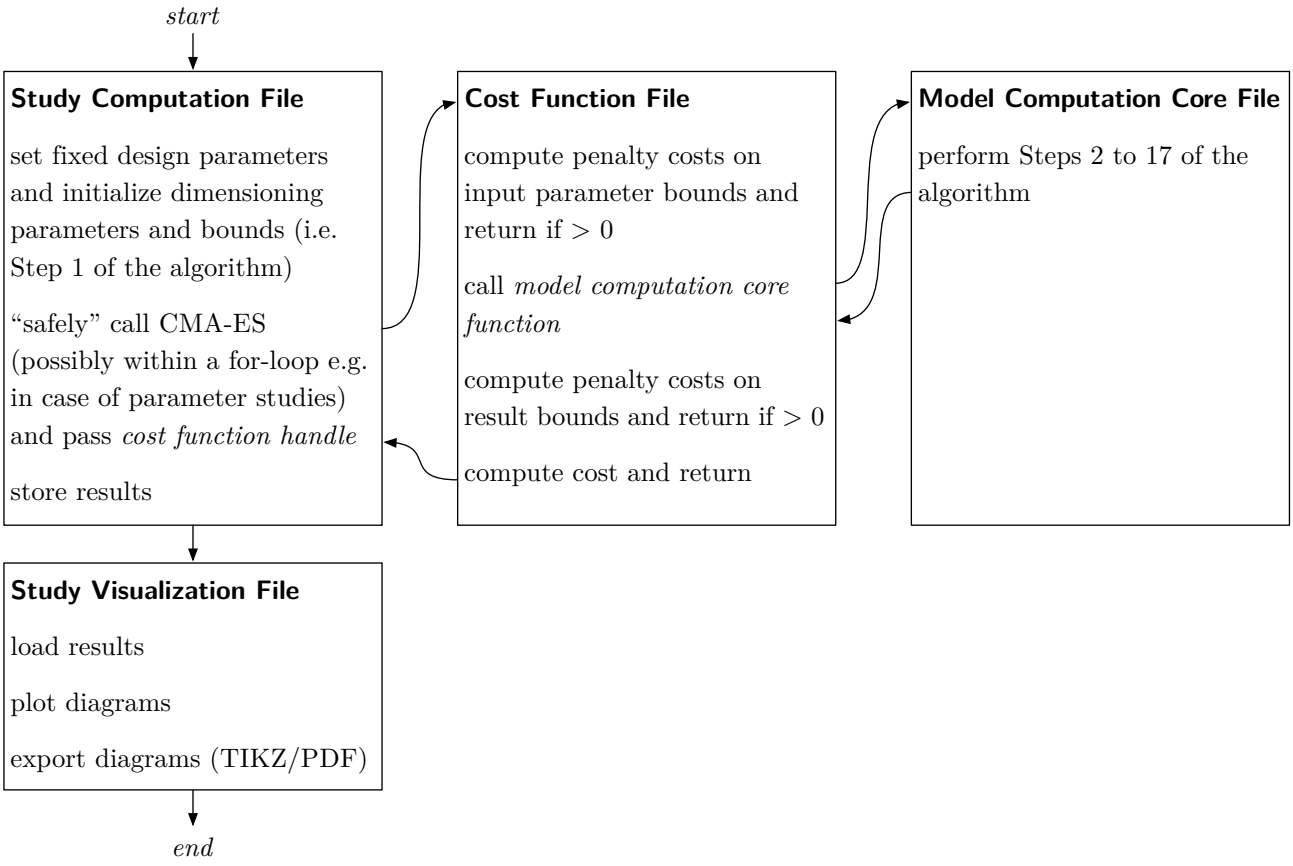

Figure 4.1: Block diagram of the implementation of an optimization study.

file (which can be referred to as main file) the (initial) parameters are set, CMA-ES is called, and the results are stored. To avoid convergence into a local minimum, appropriate initial values, initial covariances, population size, and stop conditions are configured. CMA-ES is called "safely", which means that an invalid result or a local minimum is assumed, if the cost is positive or only a few iterations are performed. In such a case the optimization is restarted. Only if several restarts are without success, the maximization problem is assumed unsolvable. In the cost function file, costs are computed essentially through Eq. (4.10), but also with premature return in case of early indication of a violation of parameter bounds. It calls the model computation core file, which is essentially Steps 2–17 of the performance computation algorithm from Sect. 2.9.2. Within the study computation file, the results are only stored on the hard drive and not visualized, apart from simple visualizations for debugging purposes. Fine visualizations and export of diagrams are done within a separate study visualization file. This allows iterating fast the look of visualizations without relatively costly re-computations of results.

Chapter 5

Conducted Optimizations and Parameter Studies

In this chapter, the derived multidisciplinary steady drag power kite plant systems engineering model is applied for optimizations and parameter studies with the procedure visualized in Fig. 4.1. This might be the most interesting part of this dissertation, as it shows what an optimal drag power kite plant looks like, what performance values are expectable, and how sensitive a parameter is on a figure of merit. It therefore gives indications on the importance of the detail design of a subsystem or component of the kite power plant.

This chapter is structured as follows: In Sect. 5.1, a utility-scale biplane kite is optimized. Such a system was also proposed and analyzed in the prior work of the author of this dissertation [110]. The results are validated against the higher fidelity point-mass model mentioned in Sect. 3.3 and derived in Appendix C. That utility-scale biplane is used as reference scenario (or baseline) in the subsequent sections: In Sect. 5.2, some further interesting specific systems are investigated, e.g. the monoplane variant of the utility-scale reference system. In Sects. 5.3 through 5.11, numerous parameter sensitivity analyses are conducted w.r.t. the reference scenario (unless stated otherwise) for almost all parameters, in the order as in the parameter tables, Tab. 3.1, 3.5, or also below, Tab. 5.1. Only a few of those parameters are omitted or summarized if meaningful. Those sensitivity analyses include also sensitivities of optimization bounds and, in the final section, Sect. 5.11, also sensitivities of bounds on possibly critical result values, e.g. a bound on the nominal wing loading. To investigate the full nonlinearities, a parameter sensitivity is analyzed for vast changes of its value, instead of only modest relative changes as in the prior work of the author of this dissertation [110]. Unless stated otherwise, only the respective parameter itself and possibly its bounds are varied within such an analysis, i.e. the parameter value is varied within Step 1 of the algorithm in Sect. 2.9.2, then the complete optimization procedure, Steps 2–18, is executed again, and, therefore, always the optimal solution is computed, see also Fig. 4.1.

The results of each study are discussed and possible implications are drawn right after the presentation of results. Many result tables and figures are shown, but for sake of brevity only the most important results are elaborated in the according discussion text. Within this chapter, some pages are intentionally left partly blank, such that text and corresponding tables and figures are close to each other.

A preview of preliminary results was given by the author of this dissertation in the prior works [104, 111].

5.1 Reference Scenario: Optimized Utility-Scale Biplane

First, a utility-scale biplane kite is optimized, similar to the prior work of the author of this dissertation [110]. In the following, the considered fixed parameters, the optimization bounds, and the results are listed, similar to the studies of the Makani systems in Chap. 3.

5.1.1 Parameters and Bounds

Tab. 5.1 lists the considered fixed parameters (used in Step 1.1 of the algorithm in Sect. 2.9.2), Tab. 5.2 lists the employed bounds for the optimization parameters (dimensioning parameters) $\boldsymbol{y}$ (required for the dimensioning parameters in Step 1.2 of the algorithm in Sect. 2.9.2, cf. Chap. 4), and Tab 5.3 lists the employed bounds on the results $\boldsymbol{z}$ (cf. Chap. 4). All values in Tabs. 5.1–5.3 are used for the remainder of this chapter as reference scenario and are only changed if stated so.

Table 5.1: Fixed parameters for the utility-scale biplane at the EEG "reference location" (reference scenario). Many values are similar to Chap. 3, particularly the correction and safety factors are identical. Many values are also similar to the prior works of the author of this dissertation [104, 106, 110]. Rows in gray are parameters which are optimized either "internally" or "externally".

Parameter	Value	Comment/Justification
Environmental parameters for considered installation site.		
g	$= 9.81\,\mathrm{m/s^2}$	$\approx$ Standard Gravity
ρ	$= 1.255\,\mathrm{kg/m^3}$	$\approx$ International Standard Atmosphere
h_{ref}	$= 30\,\mathrm{m}$	"reference location" of EEG [134]
z_0	$= 0.1\,\mathrm{m}$	"reference location" of EEG [134] (logarithmic wind shear)
λ	$= 2$	"reference location" of EEG [134] (Rayleigh distribution)
μ	$= 2/\sqrt{\pi} \cdot 5.5\,\mathrm{m/s}$	"reference location" of EEG [134] (5.5 m/s mean wind speed, cf. (2.163))
Economic parameters for targeted market.		
k_{LCOE}	$= 0.05\,\mathrm{EUR/kWh}$	estimated requirement
I	$= 10\,\%/\mathrm{yr}$	estimated requirement
T	$= 20\,\mathrm{yr}$	estimated requirement, usual for wind energy
I_{op}	$= 5\,\%/\mathrm{yr}$	estimated requirement, corresponds to complete investment costs again as operational costs over T
f_{avail}	$= 98\,\%$	estimated achievable, similar to conventional wind turbines, cf. e.g. [150]
Kite aerodynamics parameters.		
b	$= 40\,\mathrm{m}$	design consideration
$\mathit{Æ}$	$=$ *optimal*	*is optimized "externally" with CMA-ES*
n_{mw}	$= 2$	design consideration (biplane)
$c_{\mathrm{D,0}}$	$= 0.010$	based on data fitting for different airfoils, cf. Fig. 2.5
$c_{\mathrm{D,2}}$	$= 0.005$	based on data fitting for different airfoils, cf. Fig. 2.5
$c_{\mathrm{L,n}}$	$=$ *optimal*	*is optimized "externally" with CMA-ES*
$c_{\mathrm{L,min\text{-}op}}$	$= 2.5$	estimated for high lift airfoil, cf. Fig. 2.5
e	$= 0.7$	estimated, $\approx e$ for considered rectangular wings
$C_{\mathrm{D,k,o}}$	$= 0.01$	estimated
$C_{\mathrm{D,k,a,max}}$	$= 0.1$	estimated

Table 5.1: Fixed parameters and initial optimization parameters for the utility-scale biplane at EEG "reference location" (reference scenario). (continued)

Parameter	Value	Comment/Justification
Rotor parameters.		
n_{rot}	$= 8$	design consideration, cf. Sect. 1.5
r_{rot}	$= 1$	design consideration, cf. Sect. 1.5
$\eta_{\mathrm{rot},+} = \eta_{\mathrm{rot},-}$	$= 0.9$	estimated
$\eta_{\mathrm{rot,hov}}$	$= 0.9$	estimated
Tether parameters.		
L_{te}	$=$ *optimal*	*is optimized "externally" with CMA-ES*
$U_{\mathrm{te,n}}$	$=$ *optimal*	*is optimized "externally" with CMA-ES*
R_{te}	$=$ *optimal*	*is optimized "externally" with CMA-ES*
$c_{\mathrm{D,te}}$	$= 1$	estimated, $\approx c_{\mathrm{D}}$ of cylinder at reasonable N_{Re}
$f_{\mathrm{m\text{-}te}}$	$= 0.5$	estimated
$n_{\mathrm{te,c}}$	$=$ *optimal*	*is optimized "internally" within Step 6 of the algorithm in Sect. 2.9.2*
$\rho_{\mathrm{te,mech}}$	$= \rho_{\mathrm{Kev}}$	design consideration[38], value from Tab. 3.2
$\sigma_{\mathrm{te,mech}}$	$= \sigma_{\mathrm{Kev}}$	design consideration[38], value from Tab. 3.2
$\rho_{\mathrm{te,c,w}}$	$= \rho_{\mathrm{Al}}$	design consideration, value from Tab. 3.2
$\kappa_{\mathrm{te,c,w}}$	$= \kappa_{\mathrm{Al}}$	design consideration, value from Tab. 3.2
$\rho_{\mathrm{te,ins}}$	$= \rho_{\mathrm{Tef}}$	design consideration, value from Tab. 3.2
$E_{\mathrm{te,ins}}$	$= E_{\mathrm{Tef}}$	design consideration, value from Tab. 3.2
$\rho_{\mathrm{te,c,sh}}$	$= \rho_{\mathrm{Al}}$	design consideration, value from Tab. 3.2
$\rho_{\mathrm{te,c,j}} = \rho_{\mathrm{te,j}}$	$= \rho_{\mathrm{PE}}$	design consideration, value from Tab. 3.2
$w_{\mathrm{te,c,sh}}$	$= 0.1\,\mathrm{mm}$	estimated requirement
$w_{\mathrm{te,c,j}}$	$= 0.5\,\mathrm{mm}$	estimated requirement
$w_{\mathrm{te,j}}$	$= 1\,\mathrm{mm}$	estimated requirement
$S_{\mathrm{te,mech}}$	$= 9$	estimated requirement: factor 3 for fiber-rope derating (cf. e.g. [142]) multiplied by factor 3 for dynamic excesses (gusts etc.)[39]
$S_{\mathrm{te,ins}}$	$= 3$	estimated requirement
$f_{\mathrm{te,ins}}$	$= 3$	estimated (requirement), cf. the prior work of the author of this dissertation [106]
$f_{\mathrm{te,c,w}}$	$= 1.5$	estimated requirement
$f_{\mathrm{te,m,mech}}$	$= 1.0$	estimated
$\forall i \neq \mathrm{mech} : f_{\mathrm{te,m},i}$	$= 1.5$	estimated

[38] Kevlar is chosen over Dyneema because of its higher yield strength and much better temperature resilience, which can be considered important because of the heating up of electrical cables due to ohmic losses. Kevlar is also chosen over carbon fiber because of its higher maturity and availability for ropes.

[39] It should be noted, that the first factor 3 is missing in the prior works of the author of this dissertation [104, 106, 110].

Table 5.1: Fixed parameters and initial optimization parameters for the utility-scale biplane at EEG "reference location" (reference scenario). (continued)

Parameter	Value	Comment/Justification
Powertrain subsystems parameters.		
$\eta_{\mathrm{s},+} = \eta_{\mathrm{s},-}$	$= 1$	direct drive considered
$\eta_{\mathrm{m},+} = \eta_{\mathrm{m},-}$	$= 0.96$	estimated, based on [81] (low-voltage machine)
$\eta_{\mathrm{pe,k},+} = \eta_{\mathrm{pe,k},-}$	$= 0.95$	estimated, based on [81] (machine converter and low-voltage to high-voltage DC-DC converter)
$\eta_{\mathrm{pe,g},+} = \eta_{\mathrm{pe,g},-}$	$= 0.98$	estimated
γ_{m}	$= 0.333\,\mathrm{kg/kW}$	estimated, based on [81] (low-voltage machine)
$\gamma_{\mathrm{pe,k}}$	$= 0.278\,\mathrm{kg/kW}$	estimated, based on [81] (machine converter and low-voltage to high-voltage DC-DC converter)
k_{pt}	$= 0.15\,\mathrm{EUR/W}$	estimated
$S_{\mathrm{hov,ok}}$	$= 1.5$	estimated requirement
$S_{\mathrm{hov,flt}}$	$= 1.2$	estimated requirement
$P_{\mathrm{el,ins}}$	$=$ *optimal*	*is optimized "internally" within the algorithm in Sect. 2.9.2, such that the powertrain is as small as possible, cf. (2.248)*
Ground station parameters and flight trajectory parameters.		
h_{to}	$= 15\,\mathrm{m}$	estimated requirement for kite tail with $\approx b/4$ length
φ_{n}	$= 15\,^\circ$	estimated for feasible figure eight flight path
ϑ_{n}	$=$ *optimal*	*is optimized "externally" with CMA-ES*
$\psi_{\mathrm{w,n}}$	$= 20\,^\circ$	estimated requirement
Power curve "shaping" parameters.		
$v_{\mathrm{a,min}}$	$= 40\,\mathrm{m/s}$	estimated requirement for realistic airborne mass
$v_{\mathrm{a,n}}$	$=$ *optimal*	*is optimized "externally" with CMA-ES*
r_{P}	$=$ *optimal*	*is optimized "externally" with CMA-ES*
$v_{\mathrm{w},h_{\mathrm{ref}},\mathrm{cut\text{-}out}}$	$= 25\,\mathrm{m/s}$	estimated requirement

Table 5.2: Bounds on the optimization parameters $\boldsymbol{y}$ for the utility-scale biplane (reference scenario). Many values are similar to the prior works of the author of this dissertation [104, 110].

Bound & Value	Comment/Justification
$\overline{AR} = 40$	estimated realizable maximum
$\underline{AR} = 10$	estimated meaningful minimum
$\overline{c}_{\mathrm{L,n}} = 6$	estimated realizable maximum
$\underline{c}_{\mathrm{L,n}} = 1$	estimated meaningful minimum
$\overline{L}_{\mathrm{te}} = 2,000\,\mathrm{m}$	estimated meaningful to limit occupied air volume
$\underline{L}_{\mathrm{te}} = 50\,\mathrm{m}$	estimated meaningful minimum
$\overline{U}_{\mathrm{te,n}} = 20\,\mathrm{kV}$	estimated realizable maximum
$\underline{U}_{\mathrm{te,n}} = 500\,\mathrm{V}$	estimated meaningful minimum
$\overline{R}_{\mathrm{te}} = 10\,\Omega$	estimated meaningful maximum
$\underline{R}_{\mathrm{te}} = 0.01\,\Omega$	estimated meaningful minimum
$\overline{\vartheta}_{\mathrm{n}} = 90\,^\circ$	feasible maximum
$\underline{\vartheta}_{\mathrm{n}} = 0\,^\circ$	lowest feasible minimum and meaningful minimum with tower
$\overline{v}_{\mathrm{a,n}} = 80\,\mathrm{m/s}$	estimated required maximum ($\approx$ maximum tip speed of conventional wind turbine rotor)
$\underline{v}_{\mathrm{a,n}} = 20\,\mathrm{m/s}$	estimated meaningful minimum[40]
$\overline{r}_{\mathrm{P}} = 4$	estimated meaningful maximum
$\underline{r}_{\mathrm{P}} = 1$	required minimum for feasibility

Table 5.3: Bounds on results $\boldsymbol{z}$ for the utility-scale biplane (reference scenario). Some values are similar to the prior works of the author of this dissertation [104, 110].

Bound & Value	Comment/Justification
$\overline{\omega}_{\mathrm{n}} = 20\,^\circ/\mathrm{s}$	estimated feasible maximum
$\underline{h}_{\mathrm{n}} = 50\,\mathrm{m}$	estimated required minimum for safe operation
$\overline{h}_{\mathrm{n}} = 1,000\,\mathrm{m}$	estimated required maximum to avoid interference with general aviation

5.1.2 Results

Tab. 5.4 lists relevant results, Fig. 5.1 shows the power curve and other values as function of the wind speed, Fig. 5.2 shows the tether cross section, and Fig. 5.3 visualizes drag-, mass-, and cost distributions.

[40] It should be noted, that this low value of $\underline{v}_{\mathrm{a,n}}$ does not comply with $v_{\mathrm{a,min}}$ from Tab. 5.1 such that (2.276) might be violated. Nevertheless, this is automatically caught by the algorithm through f_{infeas}, and $\underline{v}_{\mathrm{a,n}}$ does not need to be changed when optimizing a small-scale system with a lower $v_{\mathrm{a,min}}$.

Table 5.4: Results for the utility-scale biplane (reference scenario).

Parameter	Value		
Optimized dimensioning parameters.			
$\mathit{Æ}$	=	40.00	
$c_{\mathrm{L,n}}$	=	3.40	
L_{te}	=	221.62	m
$U_{\mathrm{te,n}}$	=	6,660.92	V
R_{te}	=	0.23	Ω
ϑ_{n}	=	19.25	°
$v_{\mathrm{a,n}}$	=	77.36	m/s
r_{P}	=	1.90	
Cost function.			
$\hat{K}_{\mathrm{inv,o\&p}}/A$	=	26,888.58	EUR/m^2
Economic values.			
$E_{\mathrm{el,yr}}$	=	9,204,580.48	kWh/yr
H	=	26.39	%
$\hat{K}_{\mathrm{inv}}$	=	2,748,298.43	EUR
$K_{\mathrm{inv,pt}}$	=	597,212.02	EUR
$\hat{K}_{\mathrm{inv,o\&p}}$	=	2,151,086.41	EUR
$\hat{K}_{\mathrm{inv}}/P_{\mathrm{el,n}}$	=	0.69	EUR/W
$E_{\mathrm{el,yr}}k_{\mathrm{LCOE}}$	=	460,229.02	EUR/yr
$\hat{K}_{\mathrm{inv}}I_{\mathrm{op}}$	=	137,414.92	EUR/yr
T_{am}	=	8.51	yr
Nominal power and nominal wind speeds.			
$P_{\mathrm{a,n}}$	=	5,390,466.00	W
$P_{\mathrm{el,n}}$	=	3,981,413.49	W
$P_{\mathrm{el,n}}/A$	=	49,767.67	W/m^2
$P_{\mathrm{el,n}}/(\hat{m}_{\mathrm{k}}+m_{\mathrm{te}})$	=	460.53	W/kg
$v_{\mathrm{w},h_{\mathrm{ref}},\mathrm{cut\text{-}in}}$	=	2.78	m/s
$v_{\mathrm{w},h_{\mathrm{ref}},\mathrm{n(1)}}$	=	8.06	m/s
$v_{\mathrm{w},h_{\mathrm{ref}},\mathrm{n(2)}}$	=	10.48	m/s

(continued)

Parameter	Value		
Other nominal values.			
ω_{n}	=	20.00	°/s
h_{n}	=	88.08	m
$F_{\mid\mid,\mathrm{n}}$	=	973,255.59	N
$F_{\mid\mid,\mathrm{n}}/(Ag)$	=	1,240.13	kg/m^2
$C_{\mathrm{D,te}}$	=	0.05	
$C_{\mathrm{D,k,p,n}}+C_{\mathrm{D,k,o}}$	=	0.08	
$C_{\mathrm{D,k,i,n}}$	=	0.12	
$C_{\mathrm{D,eq,n}}$	=	0.24	
$C_{\mathrm{D,rot,n(1)}}$	=	0.12	
$C_{\mathrm{D,rot,n(2)}}$	=	0.23	
$a_{\mathrm{n(1)}}$	=	0.03	
$a_{\mathrm{n(2)}}$	=	0.06	
$\eta_{\Pi,\mathrm{n}}$	=	73.86	%
$\zeta_{\mathrm{n(1)}}$	=	64.20	
$R_{\mathrm{te}}I_{\mathrm{te,+,n}}/U_{\mathrm{te,n}}$	=	2.13	%
$\hat{p}_{\mathrm{te\text{-}loss,L,-}}$	=	352.30	W/m
$\hat{p}_{\mathrm{te\text{-}loss,A,-}}$	=	1,661.40	W/m^2
Dimensions and masses.			
A	=	80.00	m^2
$\hat{m}_{\mathrm{a,flight}}$	=	9,609.45	kg
$\hat{m}_{\mathrm{a,hov,ok}}$	=	8,530.52	kg
$\hat{m}_{\mathrm{a,hov,flt}}$	=	7,997.37	kg
$\hat{m}_{\mathrm{a}}$	=	7,997.37	kg
$\hat{m}_{\mathrm{k}}$	=	7,349.38	kg
$\hat{m}_{\mathrm{k}}/A$	=	91.87	kg/m^2
$\hat{m}_{\mathrm{af\&o}}$	=	4,618.98	kg
$\hat{m}_{\mathrm{af\&o}}/A$	=	57.74	kg/m^2
$m_{\mathrm{pt,k}}$	=	2,730.40	kg
m_{te}	=	1,295.97	kg
$m_{\mathrm{te,mech}}$	=	772.21	kg
$m_{\mathrm{te,c}}$	=	459.74	kg
$n_{\mathrm{te,c}}$	=	38	
d_{te}	=	67.50	mm
f_{te}	=	1.22	

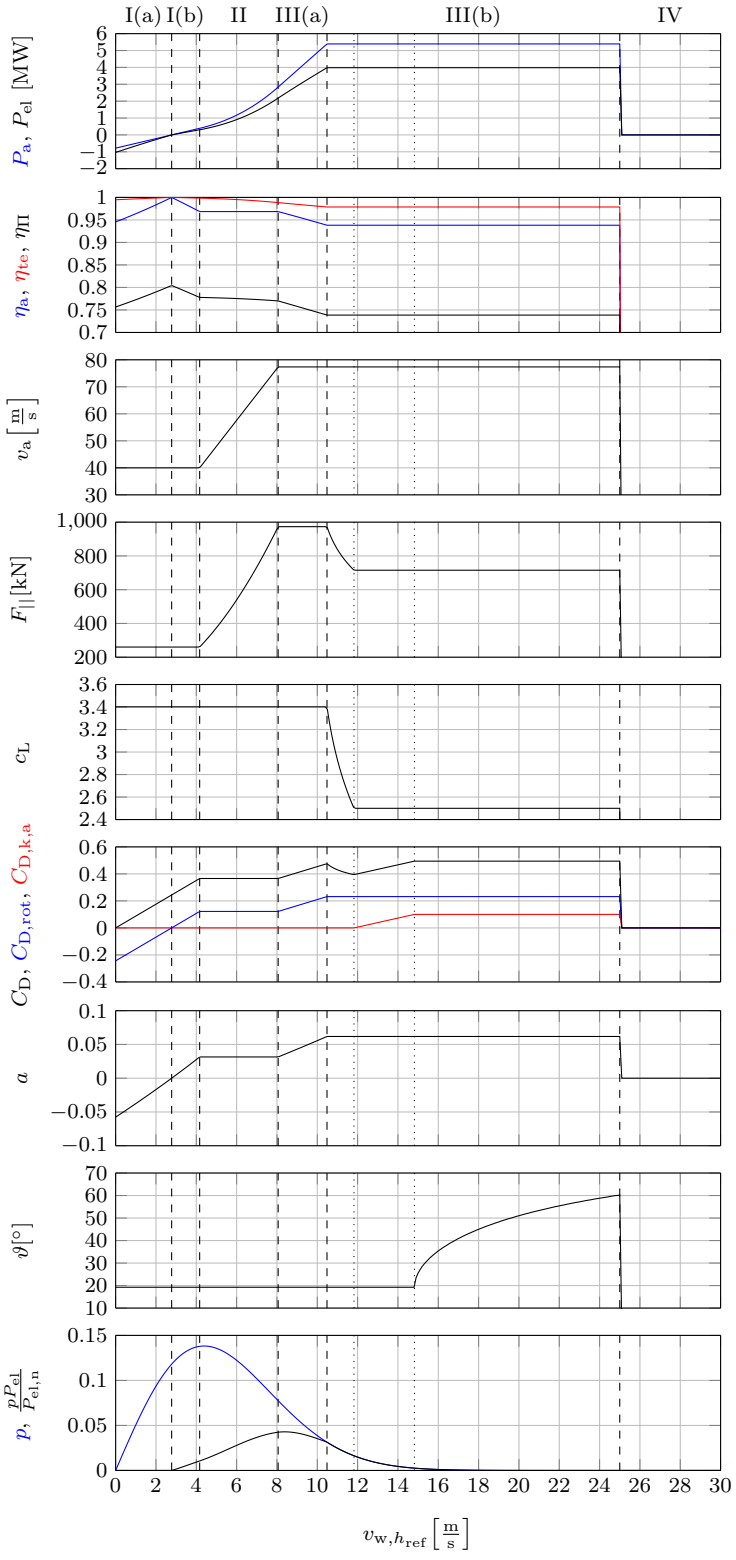

Figure 5.1: Power curve results for the utility-scale biplane (reference scenario).

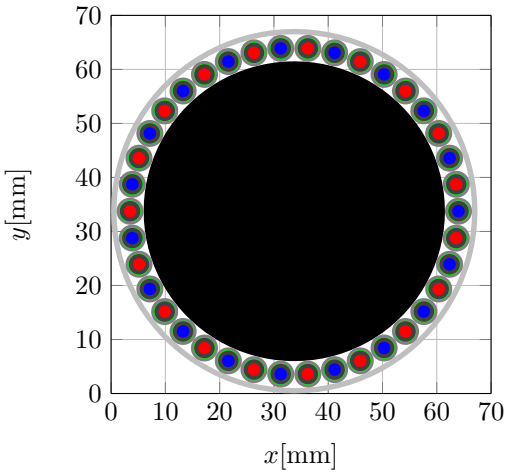

Figure 5.2: Visualization of the tether cross section for the utility-scale biplane (reference scenario) with color coding as in Fig. 1.8.

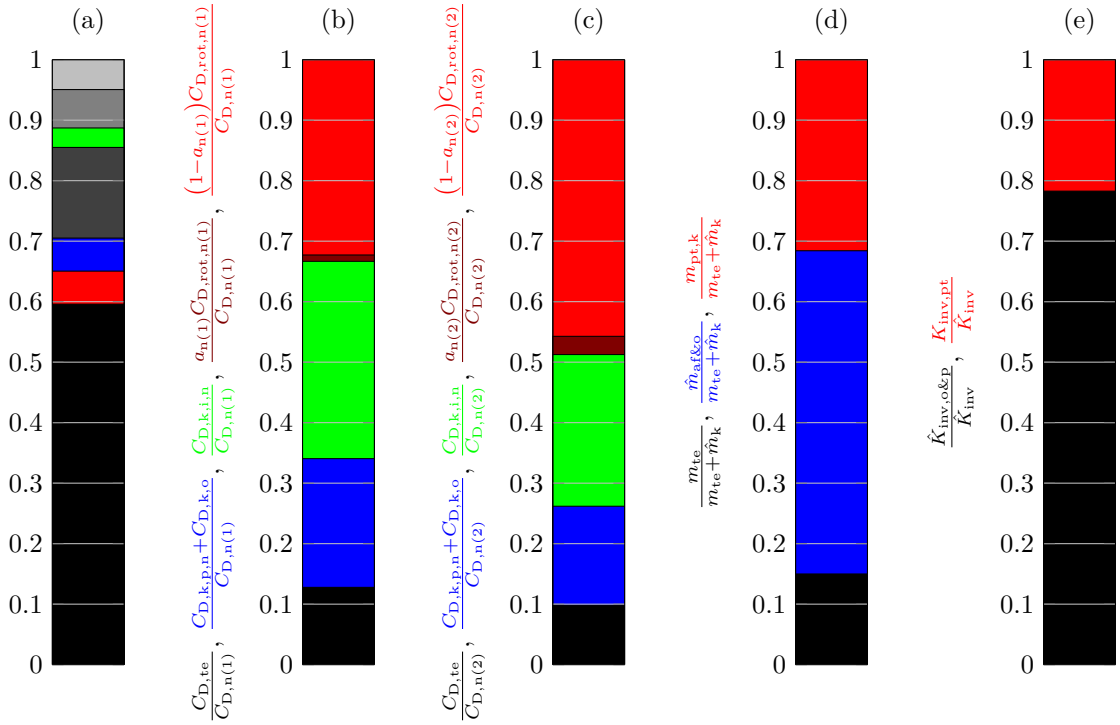

Figure 5.3: Visualization of distributions of some results for the utility-scale biplane (reference scenario): (a) tether mass distribution with color coding as in Fig. 1.8, (b) distribution of drag portions in Region II and at first power point, (c) distribution of drag portions at second power point, (d) distribution of total (maximum allowed) airborne masses, (e) distribution of costs.

5.1.3 Discussions

Optimal Dimensioning Parameters

Tab. 5.4 lists the optimal dimensioning parameters and important resulting properties of the optimized utility-scale system: Similar as found in the author's prior work with a simpler steady model [110], the optimal $\mathcal{AR}$ is at the upper bound, $c_{\mathrm{L,n}}$ is with over three relatively high, but considerably lower than in [110], the tether is relatively short, even much shorter than in [110], ϑ_{n} is only $\approx 20\,^{\circ}$, and $v_{\mathrm{a,n}}$ is close to the upper bound $\approx 80\,\mathrm{m/s}$. The lower airfoil lift coefficient allows the use of the airfoil proposed in [110] and shown in Fig. 2.6, at least w.r.t. the maximum lift coefficient. The optimal $U_{\mathrm{te,n}}$ is with $\approx 7\,\mathrm{kV}$ similar to what was found optimal by Kolar et al. [81]. The optimal R_{te} is in the order of $1\,\Omega$. With the short tether and low elevation, the nominal flight altitude is with $\approx 90\,\mathrm{m}$ relatively low and similar to a conventional wind turbine's hub height.

Important Resulting Figures of Merit

Generally, many resulting properties are similar to [110] with a simpler model and without a power curve Region III(a), although e.g. the overall efficiency was overestimated: Here, the overall nominal efficiency is only $\approx 74\,\%$, which is however optimal w.r.t. the employed model and cost function of the optimization, yet the nominal power absolute and per wing area are almost $4\,\mathrm{MW}$ and $50\,\mathrm{kW/m^2}$, respectively—this is several orders of magnitude higher than photovoltaics with only about $0.2\,\mathrm{kW/m^2}$. Similar to [110], the cut-in wind speed is quite low, despite the rather high maximum allowed kite mass of over $7\,\mathrm{t}$ or $90\,\mathrm{kg/m^2}$, which seems realizable (cf. also e.g. [102]), maybe even for a kite made from aluminum. The nominal wind speed and the capacity factor are $\approx 11\,\mathrm{m/s}$ and $\approx 26\,\%$, respectively, similar to [110] and similar to a conventional wind turbine. Due to the usage of a wide Region III(a) and a lower nominal lift coefficient, the drag coefficients are also lower than in [110]. The maximum allowed cost requirements seem realizable, in view that a conventional wind turbine has to fulfill approximately the same cost requirement, but has about one order of magnitude higher overall construction mass. The specific tether power losses are in the same order as expected for the Makani M5, cf. Tab. 3.8.

Only the nominal wing loading is rather high: Wing loadings of commercial airliners are typically $\lesssim 800\,\mathrm{kg/m^2}$, and additionally have a much lower aspect ratio. However, a biplane kite is considered here, designed similar to a truss structure, cf. Fig. 1.7, for which a higher wing loading seems realizable. Though, the actual achievable wing load is not (yet) known, which is why a parameter study below examines the results for lower wing loads.

Power Curve

Fig. 5.1 plots the power curve with additional results as function of the wind speed. The general form of the curves are similar to the Makani M600 and M5 results from Chap. 3 and from what is expected from the derivation of Chap. 2. As mentioned above, Region III(a) is relatively wide. The absolute consumptive power at zero wind during crosswind flight is much lower than the absolute nominal power. The efficiencies reduce for increasing wind speeds due to the increased induction factor and tether transmission loss. In view of the last row in Fig. 5.1, the majority of the energy is generated in Regions II and III(a).

It should be highlighted that significant power, in the magnitude of the nominal power, is likely required for hovering. For a drag power kite, this does not seem to be a big challenge, because it requires only modest measures. In particular, the powertrain and rotors are present already and only need to enable a bidirectional power flow. This is contrary to a lift power kite concept with multicopter launch and landing, which likely becomes unfeasible for a scaled up kite already for a

relatively low airborne mass, if batteries are carried within the kite. A few more details on this discussion are given in Appendix A.

Tether Cross Section

Fig. 5.2 visualizes the tether cross section. Obviously, the electrical cables increase the tether diameter only by a relatively small amount. Moreover, a relatively high number of electrical cables is utilized.

Distributions

Finally, the in Fig. 5.3 visualized distributions of some results from Tab. 5.4 are interesting: (a) Most of the tether mass, about 60 %, is the core, the second largest portion is the insulation, and the conductors make only about 10 % of the tether mass. (b) The drag of the tether is significant, but the induced drag is the dominant factor in Region II. The rotor drag is only a third of the total drag, as expected from (2.190). (c) At the second power point, the rotor drag becomes the dominant drag. (d) More than half of the (maximum allowed) mass is the airframe, the onboard powertrain is about a third, and the tether mass is rather low with only about 15 %. (e) Only about 20 % of the (maximum allowed) costs are for the powertrain while about 80 % is for everything else.

5.1.4 Validation with the Higher Fidelity Model

As motivated in Chap. 3, the steady model results for the utility-scale biplane are validated against the higher fidelity point-mass model. For that, the parameters and results of Tabs. 5.1, 5.4, and C.2 are used. Only the value of the maximum roll angle in Tab. C.2 is increased to

$$\psi_{\max} = -\psi_{\min} = 45\,^\circ, \tag{5.1}$$

justified by considering a single tether connection point at the kite without bridle, cf. Fig. 1.7, which seems particularly possible for a biplane due to its high-strength truss-like structure. Apart from that, the flight path target point list of Tab. C.3 is replaced by Tab. 5.5 to comply with the optimal nominal elevation angle of Tab. 5.4 and to obtain a realistic figure eight. As the actual

Table 5.5: Target point list for the utility-scale biplane (reference scenario).

Note	φ_{set}	ϑ_{set}	Threshold Type	x_{th}	Turn Dir.
Inside-down figure eight with four points.					
bottom right	$-20\,^\circ$	$-5\,^\circ$	AzimuthBelowThreshold	$-10\,^\circ$	Shortest
top right	$-20\,^\circ$	$-25\,^\circ$	CourseAngleBelowThreshold	0	Negative
bottom left	$20\,^\circ$	$-5\,^\circ$	AzimuthAboveThreshold	$10\,^\circ$	Shortest
top left	$20\,^\circ$	$-25\,^\circ$	CourseAngleAboveThreshold	0	Positive

airborne mass is not known, the two values

$$m_{\text{a}} = 0.50\hat{m}_{\text{a}} \tag{5.2}$$

and

$$m_{\text{a}} = 0.75\hat{m}_{\text{a}} \tag{5.3}$$

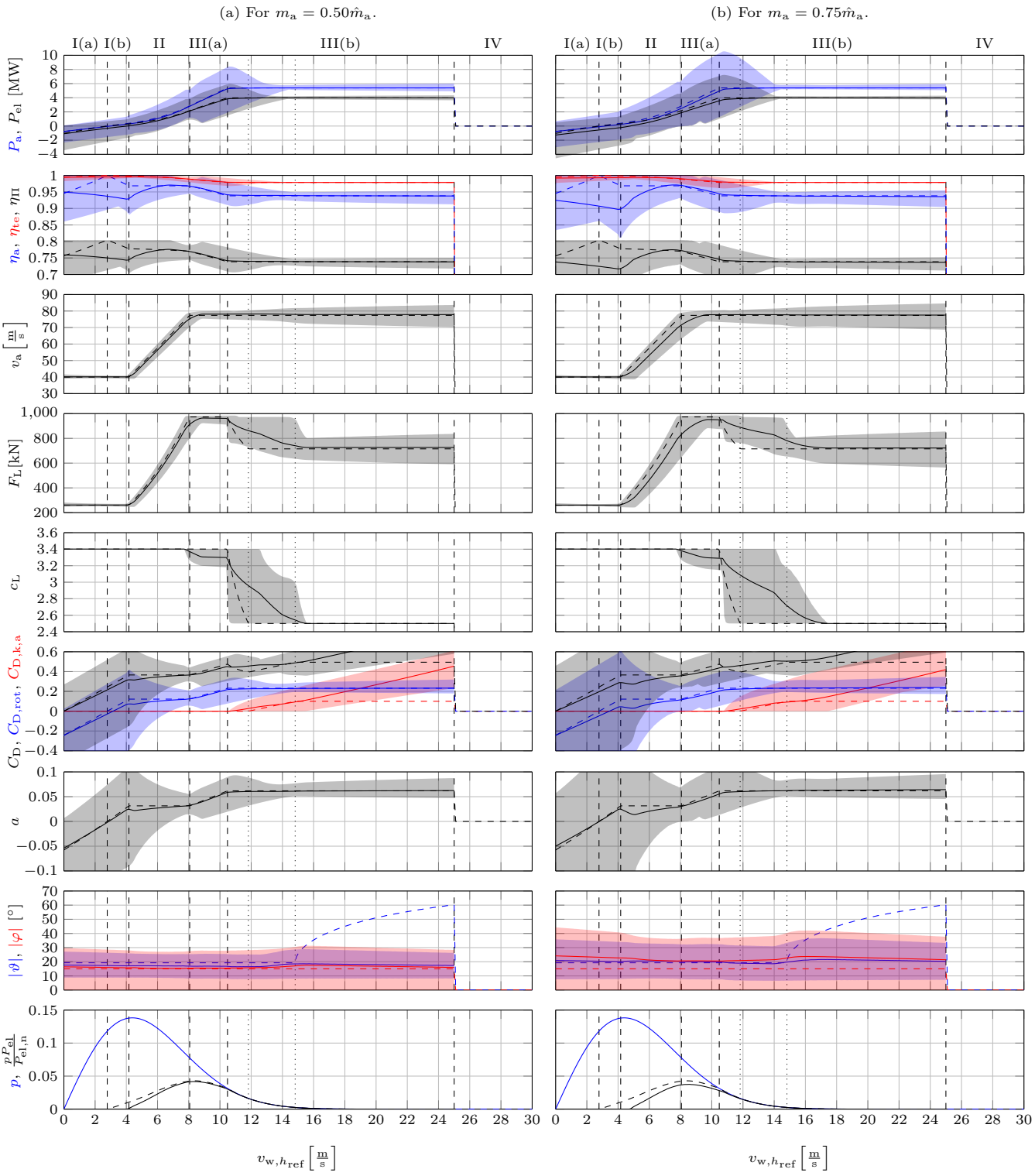

Figure 5.4: Power curve results for the utility-scale biplane (reference scenario) for two different effective airborne masses: steady model in dashed vs. point-mass model with mean values over flight path loop in solid and range of minimum and maximum values over flight path loop as area.

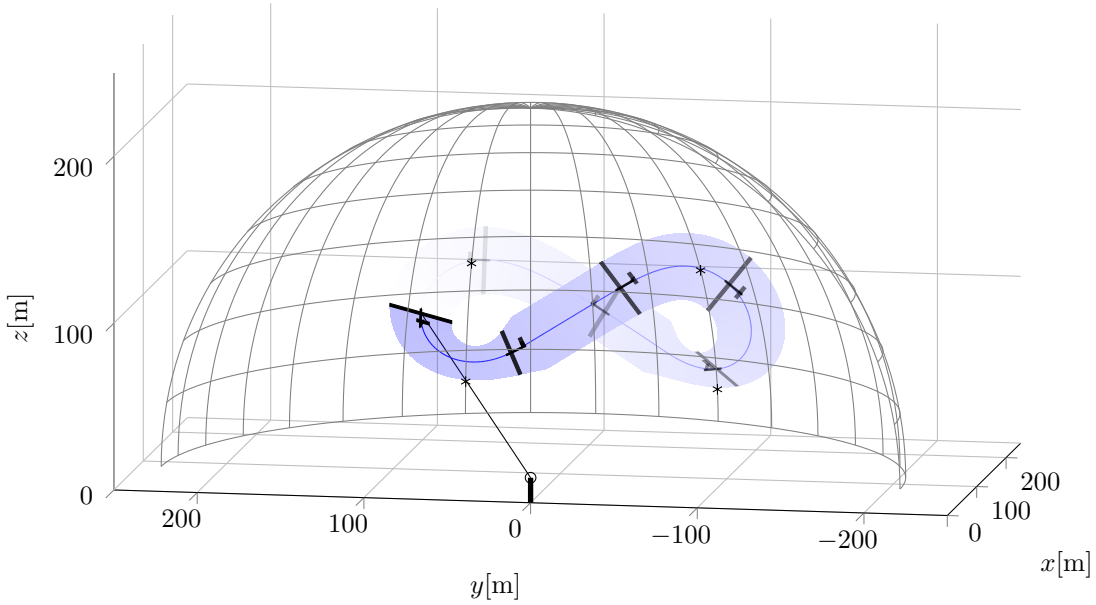

Figure 5.5: Flight trajectory of the utility-scale biplane (reference scenario) with $m_a = 0.50\hat{m}_a$ at $v_{w,h_{ref}} = 10\,\mathrm{m/s}$ with the flight path target points in * and with the kite's orientation every 1 s before the path loop ends.

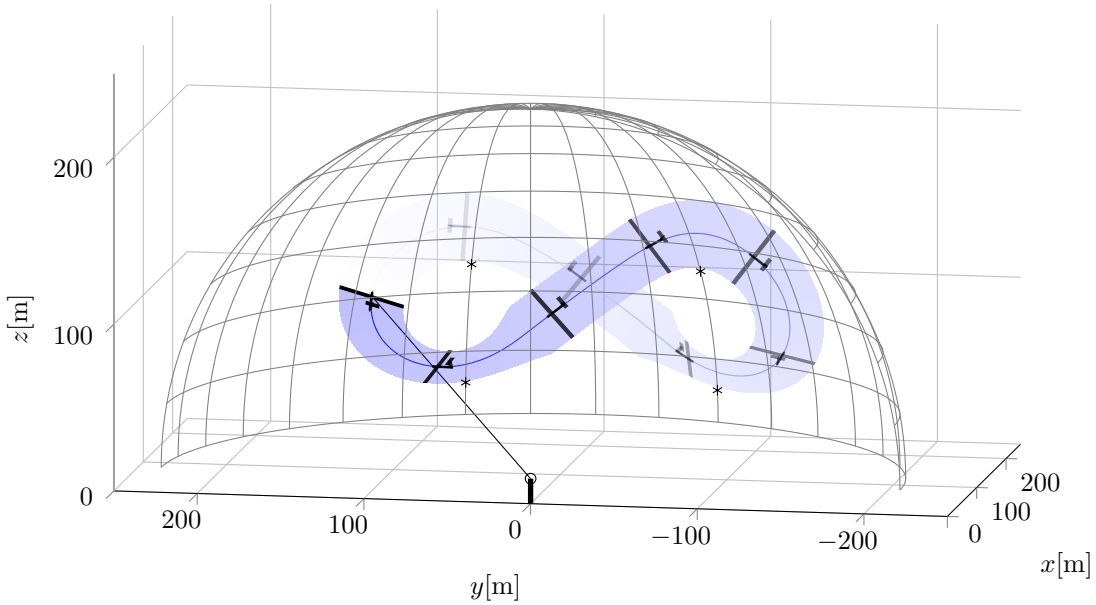

Figure 5.6: Flight trajectory of the utility-scale biplane (reference scenario) with $m_a = 0.75\hat{m}_a$ at $v_{w,h_{ref}} = 10\,\mathrm{m/s}$ with the flight path target points in * and with the kite's orientation every 1 s before the path loop ends.

are tested. Figs. 5.4–5.6 report the power curve and the kite's trajectory at $v_{\mathrm{w},h_{\mathrm{ref}}} = 10\,\mathrm{m/s}$ for the two airborne mass values. Those figures were in part shown in the prior works by the author of this dissertation in [111, Poster, Figs. 2 and 3].

The results match very well, in particular the powers for the case $m_{\mathrm{a}} = 0.50\hat{m}_{\mathrm{a}}$ in Fig. 5.4 (a) are almost identical. The correlation of the results of the steady model and the point-mass model is significantly better than for the Makani M500 and M6000 from Sect. 3.3. Reasons for that include that a non-zero effective azimuth angle is considered for the steady model of the utility-scale biplane and that the switching flight path controller is better suitable for figure eights than for circles. A discrepancy between steady model and point-mass model in Fig. 5.4 is a slightly lower power for the higher mass variant $m_{\mathrm{a}} = 0.75\hat{m}_{\mathrm{a}}$. The main reason for that can be concluded from the second last row of Fig. 5.4 and from comparing Figs. 5.5 and 5.6: The flight path is larger for $m_{\mathrm{a}} = 0.75\hat{m}_{\mathrm{a}}$, i.e. particularly the mean absolute azimuth is increased, which was not expected within the parameters of the steady model. A further discrepancy in Fig. 5.4 is that the point-mass model has a lower efficiency and thus lower electrical power etc. at low wind speeds at which the steady model expects $\eta_{\mathrm{a}} = \eta_{\mathrm{te}} \approx 100\,\%$. That was already observed in the simulation results for the Makani systems and is explained e.g. in Sect. 3.3.2.1.

In view of Figs. 5.5 and 5.6, the kite's altitude is rather low in some parts of the trajectory which might be evaluated as dangerous. Therefore, the minimum nominal altitude bound $\underline{h}_{\mathrm{n}}$ might need to be increased for the optimization (with the steady model), which is why a sensitivity analysis on that constraint is conducted below. If the minimum nominal altitude bound is increased, the optimizer likely increases not only the elevation angle (due to a then decreased cosine efficiency, cf. [14]), but also increases the tether length. Due to the latter, the kite version with the higher mass might fly a smaller path in degrees of azimuth and elevation and thus might harvest almost the same power as the one with lower mass. Further noticeable facts from Figs. 5.5 and 5.6 include that the area swept by the kite is a significant area of the wind window, which raises the question on the validity of Assumption 2.2. Moreover, the kite's turns are rather tight compared to its wing span such that the rotors might experience significantly different airflow speeds, particularly if they are mounted on the wing tips as in Fig. 1.7. Even though the rotor powers are on average very similar, the minimum and maximum feasible values (e.g. maximum rotor drag coefficient or rotor stalling, or maximum instantaneous overloading power of powertrain components) might be violated for some rotors in a part of the kite's trajectory. This immediately suggests to improve the fidelity of the model by not introducing Assumption 2.26. In addition to that, the accelerations and g-forces are with up to $\approx 18g$, according to the point-mass model simulation results (not shown), rather high. Nevertheless, if tether is longer, due to an increase of $\underline{h}_{\mathrm{n}}$, all those concerns might be less of an issue.

5.2 Other Interesting Specific Systems

In this section, a few specific systems deduced from the utility-scale biplane reference scenario are investigated. In particular, monoplane variants, offshore variants, and smaller system sizes are the focus.

Monoplanes are worth to investigate, because they do not suffer from aerodynamic interferences like biplane wings, and the center of mass can almost coincide with the tether connection point and thus monoplanes may not suffer from large tether moments. For all the monoplane variants, only the parameter of the number of main wings is altered to

$$n_{\mathrm{mw}} = 1. \tag{5.4}$$

Offshore deployments are of particular interest for kite power, because the ground station does not need to consist of a large underwater platform extending from the sea floor as for conventional wind turbines, but instead can be a relatively small buoy-like floating platform only moored to the sea floor. Moreover, the noise emissions of the rotors of a drag power kite might be considerable, which, however, is not an issue at an offshore site. All in the following investigated offshore variants have the altered wind field parameters in Tab. 5.6 in common.

Table 5.6: Wind field parameters for offshore systems different from the reference scenario.

Parameter & Value		Comment/Justification
Environmental parameters for considered installation site.		
h_{ref}	$= 103\,\mathrm{m}$	from Ref. [155] in combination with the μ-value below
z_0	$= 0.0002\,\mathrm{m}$	Ref. [136, Tab. 3, "See" (Engl.: "lake/open ocean")]
μ	$= 2/\sqrt{\pi} \cdot 9.9\,\mathrm{m/s}$	9.9 m/s mean wind speed, from Ref. [155] in combination with the h_{ref}-value above

Investigating smaller system sizes is motivated due to the much lower development costs and risks. Moreover, small-scale systems may be already competitive in some markets allowing a validation which includes also economics and other effects e.g. the technology's environmental impact on flora and fauna.

All further parameter changes from the reference scenario are detailed within the respective specific system study.

5.2.1 Optimized Utility-Scale Monoplane

The most important results for the utility-scale monoplane are summarized without reporting all result tables and figures for sake of brevity: With similar optimal dimensioning parameters compared to the utility-scale biplane (reference scenario)—including a high optimal lift coefficient $c_{\mathrm{L,n}} = 3.66$, but only half the wing area A due to the same optimal $\mathit{Æ} = 40$ and fixed b—, the resulting specific maximum allowed costs are with $\hat{K}_{\mathrm{inv,o\&p}}/A = 23,312.98\,\mathrm{EUR/m^2}$ more than a tenth lower. Due to the by half lower area, also the nominal power is with $P_{\mathrm{el,n}} = 1.7\,\mathrm{MW}$ less than half of the nominal power for the biplane. As concluded in [110], the biplane outperforms the monoplane.

5.2.2 Onshore-Optimized Utility-Scale Biplane at an Offshore Site

The first investigated offshore system is only applying the offshore wind field parameters of Tab. 5.6 to the reference scenario of the biplane kite system from Sect. 5.1, which was actually

optimized with the wind field parameters of an onshore site ("onshore-optimized"). Neither design parameters nor the power curve are changed. The new wind field parameters only have an effect on the year energy yield, capacity factor, and (maximum allowed) costs. This means that the onshore-optimized utility-scale biplane is simply deployed at an offshore site.

Again, the most important results are summarized without reporting all result tables and figures for sake of brevity: With $\hat{K}_{\mathrm{inv,o\&p}}/A = 58,460.22\,\mathrm{EUR/m^2}$, the maximum allowed costs are about 2.5 times higher than that for the onshore site. The energy yield and capacity factor almost doubled to $E_{\mathrm{el,yr}} \approx 18\,\mathrm{Mio.\ kWh}$ and $H \approx 50\,\%$.

5.2.3 Offshore-Optimized Utility-Scale Biplane

Now it is interesting to investigate, how an offshore-optimized system would look like. With the new wind field parameters of Tab. 5.6, the optimization of the dimensioning parameters is repeated. Tab. 5.7 and Figs. 5.7–5.9 report the results.

Discussion on Important Performance Figures of Merit

The maximum allowed costs, nominal power, power density, and maximum allowed mass increase significantly compared to the onshore version and compared to the onshore-optimized version placed offshore. In particular, $\hat{K}_{\mathrm{inv,o\&p}}/A$ is almost three times the value of the onshore-optimized system on an onshore site and $> 25\,\%$ higher than that of the onshore-optimized system at an offshore site. The nominal power and the power density increase to well above 8 MW and almost $110\,\mathrm{kW/m^2}$. The dimensioning parameters of elevation and altitude are even lower, which can be explained by the weak wind shear. The nominal airfoil lift coefficient is significantly higher than for the onshore-optimized system at $c_{\mathrm{L,n}} \approx 4.4$. This still allows the use of the airfoil proposed in [110] and shown in Fig. 2.6 without design changes w.r.t. the maximum lift coefficient.

Capacity Factor Paradox: Discussion on the Arguably Low Capacity Factor

The power curve in Fig. 5.7 visualizes another interesting result: Region III(a) of the offshore-optimized system is much wider than that of the onshore-optimized system and the second nominal wind speed is much higher at $\approx 18\,\mathrm{m/s}$. Therefore the capacity factor is $\approx 32\,\%$ which is significantly lower than that of the onshore-optimized system at an offshore site and only slightly higher than that of the onshore-optimized system at an onshore site. This is an example of the so called *capacity factor paradox* [152]: The onshore-optimized system at an offshore site has a much higher capacity factor, but it also has a much lower nominal power, which is significantly off-optimal. Obviously, it is better to have a higher nominal power at the cost of a higher nominal wind speed and a lower capacity factor. This can be explained by the fact that still a significant energy is harvested at high wind speeds, even though those high wind speeds are not as probable as low wind speeds. Moreover, it must be acknowledged that the energy yield and dependent economic values are proportional to the product of capacity factor and nominal power. From these results, one can conclude that the capacity factor of a site-optimized system remains at around 30 % for kite power, which is a similar value as for a conventional wind turbine.

Discussion on Other Interesting Figures of Merit

A few more results are interesting to be discussed:

- The total nominal efficiency is below 70 %, mainly caused by the much higher induction factor in Region III(b). This implies that even higher performance figures of merit can be

Table 5.7: Results for the offshore-optimized utility-scale biplane.

Parameter	Value		
Optimized dimensioning parameters.			
$Æ$	=	40.00	
$c_{\mathrm{L,n}}$	=	4.42	
L_{te}	=	229.18	m
$U_{\mathrm{te,n}}$	=	7,820.56	V
R_{te}	=	0.14	Ω
ϑ_{n}	=	14.26	°
$v_{\mathrm{a,n}}$	=	80.00	m/s
r_{P}	=	2.67	
Cost function.			
$\hat{K}_{\mathrm{inv,o\&p}}/A$	=	73,677.98	EUR/m^2
Economic values.			
$E_{\mathrm{el,yr}}$	=	24,087,911.25	kWh/yr
H	=	31.78	%
$\hat{K}_{\mathrm{inv}}$	=	7,192,154.91	EUR
$K_{\mathrm{inv,pt}}$	=	1,297,913.52	EUR
$\hat{K}_{\mathrm{inv,o\&p}}$	=	5,894,241.38	EUR
$\hat{K}_{\mathrm{inv}}/P_{\mathrm{el,n}}$	=	0.83	EUR/W
$E_{\mathrm{el,yr}}k_{\mathrm{LCOE}}$	=	1,204,395.56	EUR/yr
$\hat{K}_{\mathrm{inv}}I_{\mathrm{op}}$	=	359,607.75	EUR/yr
T_{am}	=	8.51	yr
Nominal power and nominal wind speeds.			
$P_{\mathrm{a,n}}$	=	12,874,361.83	W
$P_{\mathrm{el,n}}$	=	8,652,756.82	W
$P_{\mathrm{el,n}}/A$	=	108,159.41	W/m^2
$P_{\mathrm{el,n}}/(\hat{m}_{\mathrm{k}}+m_{\mathrm{te}})$	=	660.86	W/kg
$v_{\mathrm{w},h_{\mathrm{ref}},\mathrm{cut\text{-}in}}$	=	3.92	m/s
$v_{\mathrm{w},h_{\mathrm{ref}},\mathrm{n(1)}}$	=	11.77	m/s
$v_{\mathrm{w},h_{\mathrm{ref}},\mathrm{n(2)}}$	=	18.31	m/s

(continued)

Parameter	Value		
Other nominal values.			
ω_{n}	=	20.00	°/s
h_{n}	=	71.47	m
$F_{\mathrm{\|\|,n}}$	=	1,351,591.37	N
$F_{\mathrm{\|\|,n}}/(Ag)$	=	1,722.21	kg/m^2
$C_{\mathrm{D,te}}$	=	0.06	
$C_{\mathrm{D,k,p,n}}+C_{\mathrm{D,k,o}}$	=	0.12	
$C_{\mathrm{D,k,i,n}}$	=	0.20	
$C_{\mathrm{D,eq,n}}$	=	0.38	
$C_{\mathrm{D,rot,n(1)}}$	=	0.19	
$C_{\mathrm{D,rot,n(2)}}$	=	0.50	
$a_{\mathrm{n(1)}}$	=	0.05	
$a_{\mathrm{n(2)}}$	=	0.15	
$\eta_{\mathrm{\Pi,n}}$	=	67.21	%
$\zeta_{\mathrm{n(1)}}$	=	64.19	
$R_{\mathrm{te}}I_{\mathrm{te,+,n}}/U_{\mathrm{te,n}}$	=	2.07	%
$\hat{p}_{\mathrm{te\text{-}loss,L,-}}$	=	721.78	W/m
$\hat{p}_{\mathrm{te\text{-}loss,A,-}}$	=	2,901.41	W/m^2
Dimensions and masses.			
A	=	80.00	m^2
$\hat{m}_{\mathrm{a,flight}}$	=	12,155.32	kg
$\hat{m}_{\mathrm{a,hov,ok}}$	=	14,317.56	kg
$\hat{m}_{\mathrm{a,hov,flt}}$	=	13,422.71	kg
$\hat{m}_{\mathrm{a}}$	=	12,155.32	kg
$\hat{m}_{\mathrm{k}}$	=	11,217.49	kg
$\hat{m}_{\mathrm{k}}/A$	=	140.22	kg/m^2
$\hat{m}_{\mathrm{af\&o}}$	=	5,286.86	kg
$\hat{m}_{\mathrm{af\&o}}/A$	=	66.09	kg/m^2
$m_{\mathrm{pt,k}}$	=	5,930.63	kg
m_{te}	=	1,875.67	kg
$m_{\mathrm{te,mech}}$	=	1,108.99	kg
$m_{\mathrm{te,c}}$	=	688.83	kg
$n_{\mathrm{te,c}}$	=	38	
d_{te}	=	79.19	mm
f_{te}	=	1.21	

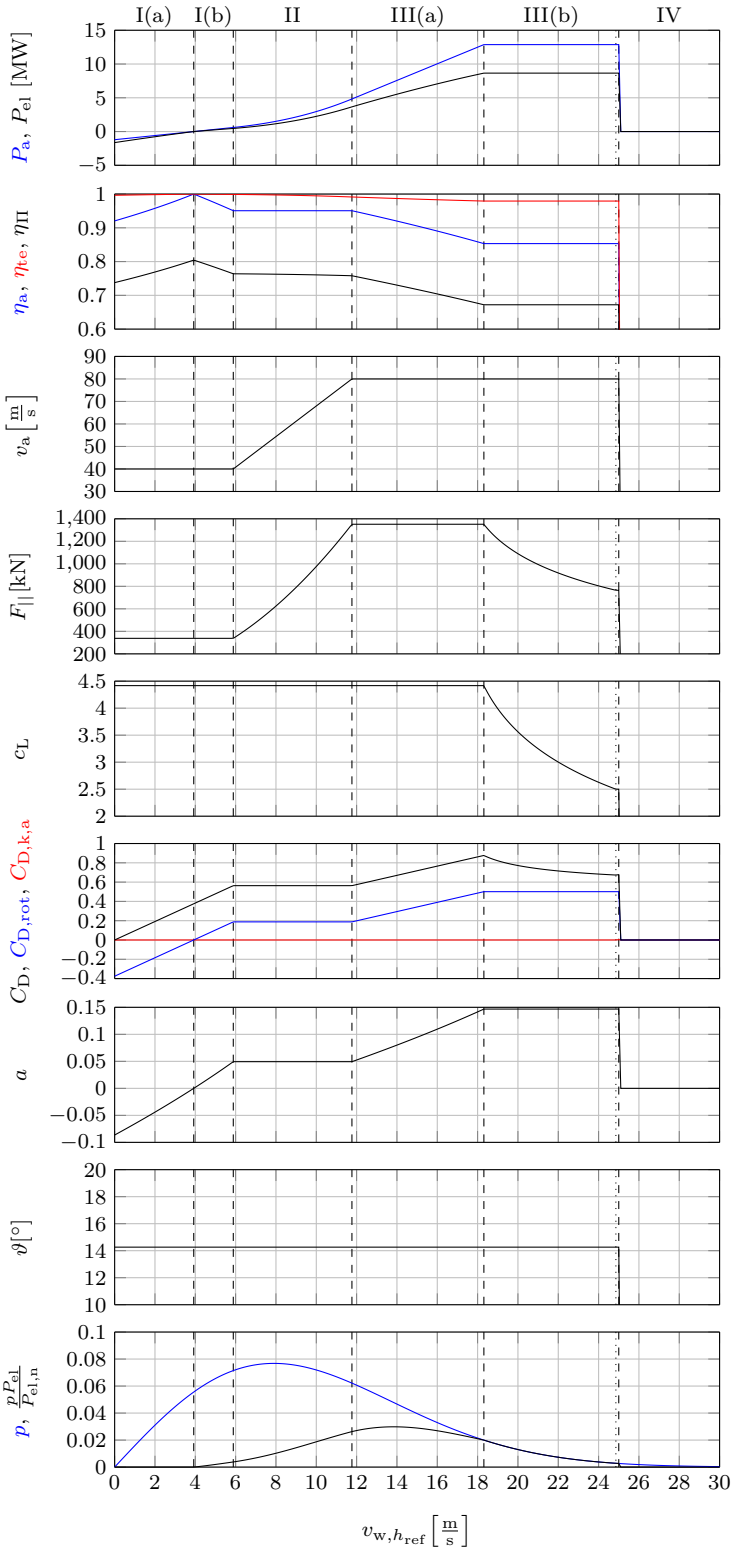

Figure 5.7: Power curve results for the offshore-optimized utility-scale biplane.

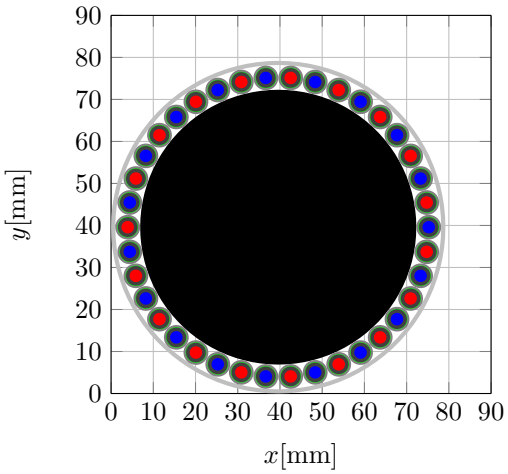

Figure 5.8: Visualization of the tether cross section for the offshore-optimized utility-scale biplane with color coding as in Fig. 1.8.

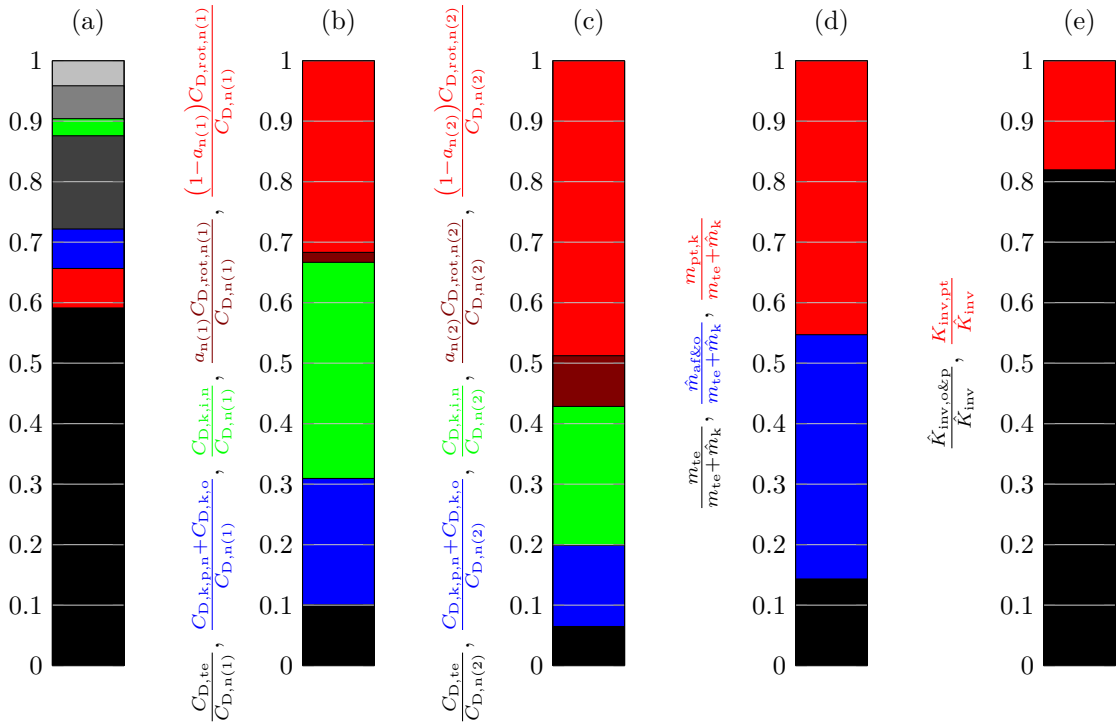

Figure 5.9: Visualization of distributions of some results for the offshore-optimized utility-scale biplane: (a) tether mass distribution with color coding as in Fig. 1.8, (b) distribution of drag portions in Region II and at first power point, (c) distribution of drag portions at second power point, (d) distribution of total (maximum allowed) airborne masses, (e) distribution of costs.

expected, if the rotor area (ratio) is increased. Note again, this arguably low efficiency is the optimal result w.r.t. the employed model and cost function.

- Region III(b) is so short and the rotor drag becomes so high, that the power limitation scheme needs to reduce the airfoil lift coefficient only.
- The maximum allowed mass is limited by the maximum allowed mass during crosswind flight. If the minimum airflow speed is increased, then the maximum allowed mass can be increased by another about two tons, until the maximum allowed mass is defined by hovering with rotor failure. An increase of the minimum airflow speed comes at the cost of a higher cut-in wind speed and thus a reduced energy yield at low wind speeds. However, in the prior work of the author of this dissertation [110] it was shown that the impact on the overall energy yield for changed minimum airflow speeds is negligible, because only a very low energy is anyways harvested at low wind speeds. Nevertheless, a sensitivity analysis is conducted below with the here employed higher fidelity (steady) model compared to [110].
- The wing loading is increased significantly to $\approx 1.7\,\mathrm{tons/m^2}$, which is about twice as much as today's highest wing loading commercial aircraft have. Again, this is one motivation to use a biplane kite, which can be expected to withstand much higher wing loadings compared to a monoplane, because of its truss-like structure and high structural depth.

Results for an Increase of the Nominal Airflow Speed Bound

The airflow speed is at its upper bound. It was interesting to execute the optimization also with a higher upper bound, which seems to be realizable for an offshore site, e.g. because higher noise emissions due to a higher airflow speed hardly matter: With

$$\overline{v}_{\mathrm{a,n}} = 100\,\mathrm{m/s}, \tag{5.5}$$

the performance is even better: The optimal nominal airflow speed is then $\approx 91\,\mathrm{m/s}$, the nominal electrical power slightly exceeds 10 MW or $125\,\mathrm{kW/m^2}$, and the maximum allowed specific costs become $K_{\mathrm{inv,o\&p}}/A = 76,112.58\,\mathrm{EUR/m^2}$.

5.2.4 Offshore-Optimized Utility-Scale Monoplane

It was also interesting to execute the optimization for the monoplane configuration at an offshore site: With similar optimal parameters—including optimal $c_{\mathrm{L,n}} \approx 4.5$, but area only $A = 40\,\mathrm{m^2}$ due to the same optimal $\mathit{AR} = 40$ and fixed b—, the resulting maximum allowed costs are with $\hat{K}_{\mathrm{inv,o\&p}}/A = 66,363.85\,\mathrm{EUR/m^2}$ more than a tenth lower than that of the biplane. The nominal power is only $P_{\mathrm{el,n}} \approx 4.2\,\mathrm{MW}$, which is less than half of the nominal power of the biplane. Thus, the biplane again outperforms the monoplane, approximately with the same difference as found in Sect. 5.2.1.

5.2.5 Optimized Small-Scale Biplane

For a novel power plant technology such as crosswind kite power and the here investigated drag power kite biplane, first small-scale prototypes, demonstrators, or niche-market products have to be developed and built, in order to verify and validate the technology with low budgets, low costs of failures—which are inevitable to learn, develop, and improve the technology—, and thus low risks [156, 157], cf. also Appendix A. A first niche market is one that can be accessed relatively easily, has high mean wind speeds, and thus allows for high LCOEs. A suitable example is therefore a windy onshore site, i.e. e.g. farm fields on an island, but also near the coast of Germany with self-consumption, which allows for a much higher LCOE compared to the stock exchange market price of electricity.

5.2.5.1 Parameters and Results

Tabs. 5.8 and 5.9 list the considered fixed parameters and bounds of the optimization parameters which are different from the reference scenario. Tab. 5.10 and Figs. 5.10–5.12 report the results.

Table 5.8: Fixed parameters for the small-scale biplane which are different from the reference scenario of Tab. 5.1.

Parameter	Value	Comment/Justification
Environmental parameters for considered installation site.		
h_{ref}	$= 80\,\mathrm{m}$	reference altitude for considered mean wind speed [158]
z_0	$= 0.03\,\mathrm{m}$	Ref. [136, Tab. 3, "offen"]
μ	$= 2/\sqrt{\pi} \cdot 7.5\,\mathrm{m/s}$	7.5 m/s mean wind speed at nearshore site [158]
Economic parameters for targeted market.		
k_{LCOE}	$= 0.30\,\mathrm{EUR/kWh}$	corresponds approximately to house hold electricity price in Germany in 2018 [159]
I	$= 3\,\%/\mathrm{yr}$	lower interest rate for early adopters willing to accept a high risk (in 2018, this seems still competitive to alternative investment offers e.g. by banks)
T	$= 15\,\mathrm{yr}$	it might be hard to convince that 20 yr lifetime is achievable, so lifetime expectancy is reduced by 25 %
I_{op}	$= 2\,\%/\mathrm{yr}$	assuming that the majority of the investment price is profit margin (to re-finance the development) and only a relatively small portion (about one third) is material and manufacturing costs, I_{op} can be smaller; this value is similar to conventional small wind turbines
Kite aerodynamics parameters.		
b	$= 4\,\mathrm{m}$	design consideration
$c_{\mathrm{D},0}$	$= 0.0167$	estimated two thirds higher because of rather low N_{Re}, also based on CFDs similar to Fig. 2.6
$c_{\mathrm{D},2}$	$= 0.0083$	estimated two thirds higher because of rather low N_{Re}, also based on CFDs similar to Fig. 2.6
Rotor parameters.		
r_{rot}	$= 1.5$	a bit larger, because wide Region III(a) expectable
Tether parameters.		
$n_{\mathrm{te,c}}$	$= 6$	same as in [81] and as for the Makani Wing 7; based on model results: enough room for communication cables
$w_{\mathrm{te,j}}$	$= 0.5\,\mathrm{mm}$	estimated requirement, same as for the Makani Wing 7
Powertrain subsystems parameters.		
$\eta_{\mathrm{pe,k},+} = \eta_{\mathrm{pe,k},-}$	$= 0.98$	estimated, based on [81] (machine converter only)
$\gamma_{\mathrm{pe,k}}$	$= 0.056\,\mathrm{kg/kW}$	estimated, based on [81] (machine converter only)
Ground station parameters and flight trajectory parameters.		
h_{to}	$= 3\,\mathrm{m}$	ISO container-based ground station
Power curve "shaping" parameters.		
$v_{\mathrm{a,min}}$	$= 25\,\mathrm{m/s}$	estimated requirement for realistic airborne mass

Table 5.9: Bounds on the optimization parameters $\boldsymbol{y}$ for the small-scale biplane which are different from the reference scenario Tab. 5.2.

Bound & Value	Comment/Justification
$\overline{\text{Æ}} = 32$	estimated realizable maximum with shorter development time
$\overline{c}_{\mathrm{L,n}} = 4$	estimated realizable maximum with shorter development time, also based on CFDs similar to Fig. 2.6
$\overline{U}_{\mathrm{te,n}} = 800\,\mathrm{V}$	estimated realizable maximum with shorter development time, enables usage of $1,200\,\mathrm{V}$ power electronic switches

Table 5.10: Results for the small-scale biplane.

Parameter	Value		
Optimized dimensioning parameters.			
Æ	=	32.00	
$c_{\mathrm{L,n}}$	=	4.00	
L_{te}	=	111.41	m
$U_{\mathrm{te,n}}$	=	799.99	V
R_{te}	=	4.14	Ω
ϑ_{n}	=	24.95	°
$v_{\mathrm{a,n}}$	=	38.89	m/s
r_{P}	=	3.02	
Cost function.			
$\hat{K}_{\mathrm{inv,o\&p}}/A$	=	88,718.38	EUR/m^2
Economic values.			
$E_{\mathrm{el,yr}}$	=	31,695.68	kWh/yr
H	=	18.61	%
$\hat{K}_{\mathrm{inv}}$	=	91,635.50	EUR
$K_{\mathrm{inv,pt}}$	=	2,917.00	EUR
$\hat{K}_{\mathrm{inv,o\&p}}$	=	88,718.50	EUR
$\hat{K}_{\mathrm{inv}}/P_{\mathrm{el,n}}$	=	4.71	EUR/W
$E_{\mathrm{el,yr}}k_{\mathrm{LCOE}}$	=	9,508.70	EUR/yr
$\hat{K}_{\mathrm{inv}}I_{\mathrm{op}}$	=	1,832.71	EUR/yr
T_{am}	=	11.94	yr
Nominal power and nominal wind speeds.			
$P_{\mathrm{a,n}}$	=	34,096.12	W
$P_{\mathrm{el,n}}$	=	19,446.67	W
$P_{\mathrm{el,n}}/A$	=	19,446.64	W/m^2
$P_{\mathrm{el,n}}/(\hat{m}_{\mathrm{k}} + m_{\mathrm{te}})$	=	315.76	W/kg
$v_{\mathrm{w},h_{\mathrm{ref}},\mathrm{cut\text{-}in}}$	=	4.93	m/s
$v_{\mathrm{w},h_{\mathrm{ref}},\mathrm{n}(1)}$	=	11.50	m/s
$v_{\mathrm{w},h_{\mathrm{ref}},\mathrm{n}(2)}$	=	19.25	m/s

(continued)

Parameter	Value		
Other nominal values.			
ω_{n}	=	20.00	°/s
h_{n}	=	50.00	m
$F_{\mid\mid,\mathrm{n}}$	=	3,572.92	N
$F_{\mid\mid,\mathrm{n}}/(Ag)$	=	364.21	kg/m^2
$C_{\mathrm{D,te}}$	=	0.25	
$C_{\mathrm{D,k,p,n}} + C_{\mathrm{D,k,o}}$	=	0.16	
$C_{\mathrm{D,k,i,n}}$	=	0.20	
$C_{\mathrm{D,eq,n}}$	=	0.61	
$C_{\mathrm{D,rot,n}(1)}$	=	0.31	
$C_{\mathrm{D,rot,n}(2)}$	=	0.92	
$a_{\mathrm{n}(1)}$	=	0.05	
$a_{\mathrm{n}(2)}$	=	0.19	
$\eta_{\Pi,\mathrm{n}}$	=	57.03	%
$\zeta_{\mathrm{n}(1)}$	=	14.22	
$R_{\mathrm{te}}I_{\mathrm{te},+,\mathrm{n}}/U_{\mathrm{te,n}}$	=	15.13	%
$\hat{p}_{\text{te-loss,L,}-}$	=	21.10	W/m
$\hat{p}_{\text{te-loss,A,}-}$	=	747.47	W/m^2
Dimensions and masses.			
A	=	1.00	m^2
$\hat{m}_{\mathrm{a,flight}}$	=	56.78	kg
$\hat{m}_{\mathrm{a,hov,ok}}$	=	61.84	kg
$\hat{m}_{\mathrm{a,hov,flt}}$	=	57.97	kg
$\hat{m}_{\mathrm{a}}$	=	56.78	kg
$\hat{m}_{\mathrm{k}}$	=	51.96	kg
$\hat{m}_{\mathrm{k}}/A$	=	51.96	kg/m^2
$\hat{m}_{\mathrm{af\&o}}$	=	42.35	kg
$\hat{m}_{\mathrm{af\&o}}/A$	=	42.35	kg/m^2
$m_{\mathrm{pt,k}}$	=	9.61	kg
m_{te}	=	9.62	kg
$m_{\mathrm{te,mech}}$	=	1.43	kg
$m_{\mathrm{te,c}}$	=	6.15	kg
$n_{\mathrm{te,c}}$	=	6	
d_{te}	=	8.98	mm
f_{te}	=	2.67	

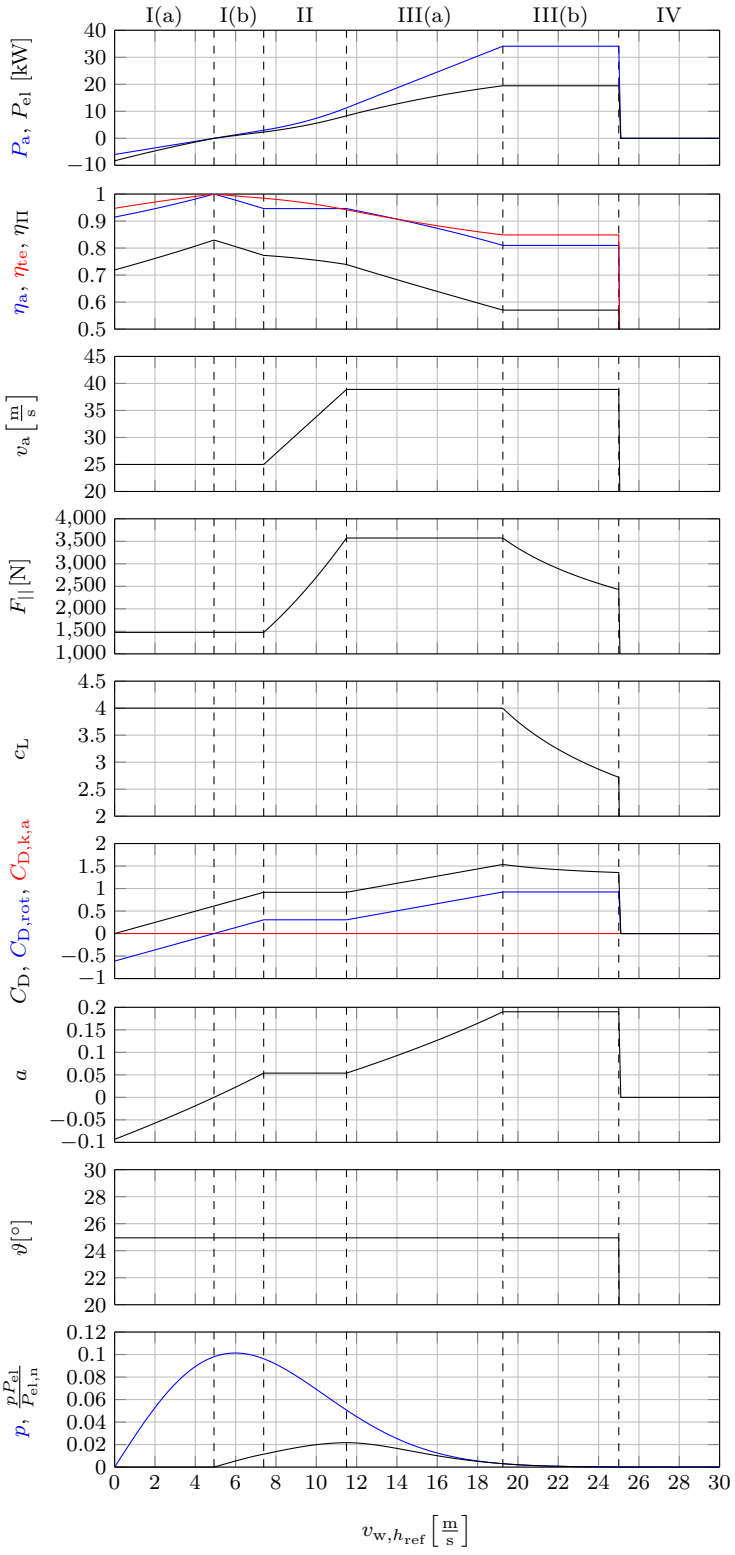

Figure 5.10: Power curve results for the small-scale biplane.

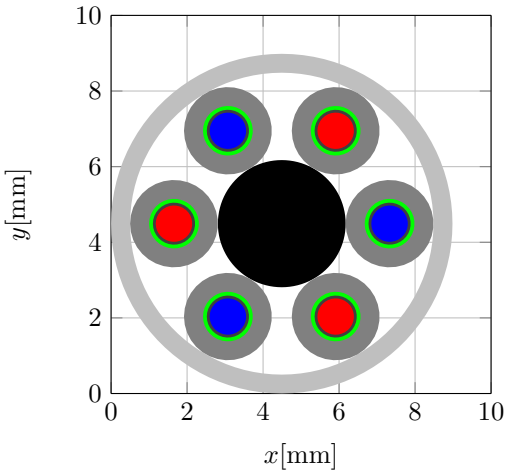

Figure 5.11: Visualization of the tether cross section for the small-scale biplane with color coding as in Fig. 1.8.

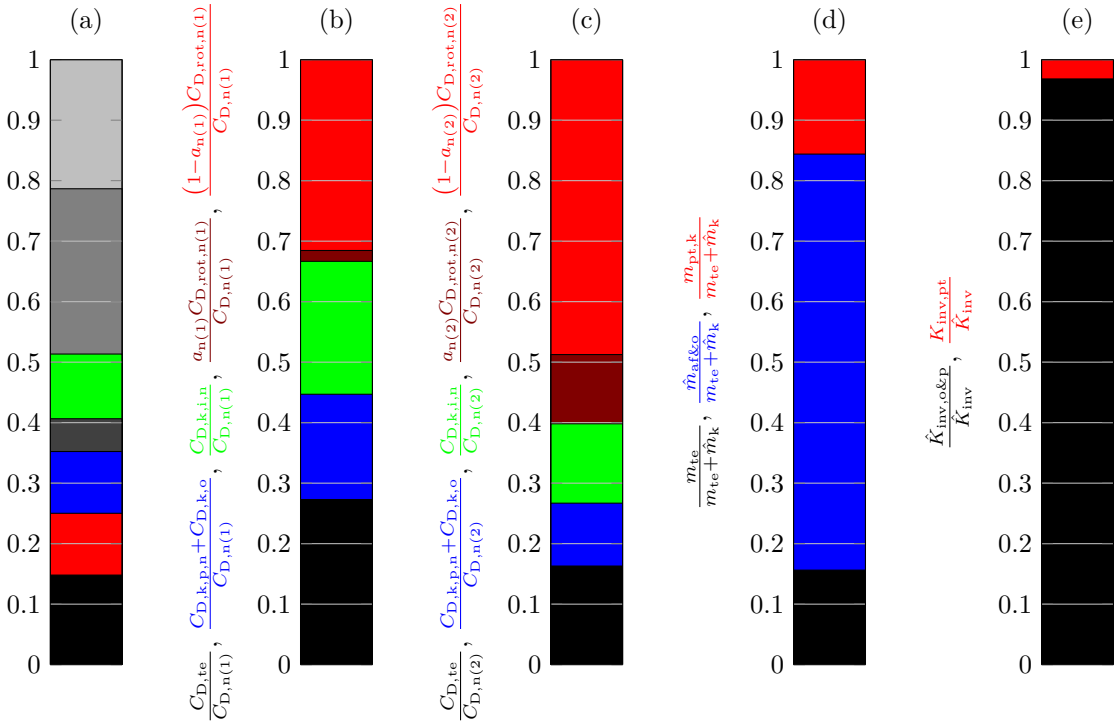

Figure 5.12: Visualization of distributions of some results for the small-scale biplane: (a) tether mass distribution with color coding as in Fig. 1.8, (b) distribution of drag portions in Region II and at first power point, (c) distribution of drag portions at second power point, (d) distribution of total (maximum allowed) airborne masses, (e) distribution of costs.

5.2.5.2 Discussions

The total maximum allowed cost of $\approx 90\,\mathrm{kEUR}$ seems realizable, in fact a rough cost estimate (not shown here) concluded a total material and manufacturing cost of about 30 kEUR. Hence, developing and selling even such small systems can be a viable business case.

The other resulting values are also interesting: The electrical power and power density are already at $\approx 20\,\mathrm{kW}$ and $\approx 20\,\mathrm{kW/m^2}$. The power curve is qualitatively similar to the offshore-optimized utility-scale system, which is not surprising due to a similarly high mean wind speed. The nominal wind speed is rather high at $\approx 19\,\mathrm{m/s}$, Region III(a) is rather wide, the capacity factor is rather low, and the total nominal efficiency is even only at $\approx 60\,\%$, which however is optimal w.r.t. the employed model and cost function. For the power limitation, almost only a reduction of the lift coefficient is required. The wing loading of $< 400\,\mathrm{kg/m^2}$ and the maximum allowed kite mass of $> 50\,\mathrm{kg/m^2}$ seem realizable.

It is interesting to compare the results of the optimized biplane with the results of the Makani Wing 7: That achieved a nominal aerodynamic power and aerodynamic power densities (electrical powers were not published) of $P_{\mathrm{a,n}} = 20\,\mathrm{kW}$, $P_{\mathrm{a,n}}/A = 5\,\mathrm{kW/m^2}$, and $P_{\mathrm{a,n}}/m_{\mathrm{k}} = 333\,\mathrm{W/kg}$ (cf. Sect. 3.1) which are significantly lower than the values of the proposed biplane kite with $P_{\mathrm{a,n}} \approx 34\,\mathrm{kW}$, $P_{\mathrm{a,n}}/A \approx 34\,\mathrm{kW/m^2}$, and $P_{\mathrm{a,n}}/\hat{m}_{\mathrm{k}} \approx 650\,\mathrm{W/kg}$ (cf. Tab. 5.10), whereby the latter is the power density with the maximum allowed mass, but the actual mass might be lower. Note also, that Wing 7 has twice the wing span of the small-scale biplane kite. (Though Wing 7 has a lower nominal wind speed and it was already built and flown in reality, while the proposed biplane kite is yet to be demonstrated.)

5.2.5.3 Result for Higher Tether Voltages

The optimal tether voltage is at its upper bound $U_{\mathrm{te,n}} = \overline{U}_{\mathrm{te,n}} = 800\,\mathrm{V}$. It was interesting to execute the optimization with the altered voltage bound of $\overline{U}_{\mathrm{te,n}} = 1,300\,\mathrm{V}$ with which e.g. $1,700\,\mathrm{V}$ power electronic switches would be used: The results change only slightly in the magnitude of a few percent. If the nominal voltage was not bounded, the optimum is $U_{\mathrm{te,n}} = 1,710.93\,\mathrm{V}$, but again with hardly changed results, e.g. the cost function increased only to $\hat{K}_{\mathrm{inv,o\&p}}/A = 93,329.85\,\mathrm{EUR/m^2}$. Therefore, it seems not worth to increase the nominal tether voltage to above 800 V for such a technology demonstrator.

5.2.5.4 Result for Monoplane

It was also interesting to execute the optimization for the monoplane configuration: With similar optimal parameters—including optimal $c_{\mathrm{L,n}} \approx 4$, but area only $A = 0.5\,\mathrm{m^2}$ due to the same optimal $\mathit{AR} = 32$ and fixed b—, the resulting maximum allowed costs are with $\hat{K}_{\mathrm{inv,o\&p}}/A = 58,398.88\,\mathrm{EUR/m^2}$ more than a third lower than that of the biplane. The nominal power is only $P_{\mathrm{el,n}} \approx 9.5\,\mathrm{kW}$, which is less than half of the nominal power of the biplane. Thus, the biplane again outperforms the monoplane, approximately with the same difference as found in Sects. 5.2.1 and 5.2.4.

5.2.5.5 Result for Off-Grid Market with High Penetration from diesel Generators

Moreover, it was interesting to execute the optimization for another possible entry market, namely off-grid mines, remote communities, or geographical islands, for which the LCOE is allowed be in the order of $k_{\mathrm{LCOE}} \approx 0.50\,\mathrm{EUR/kWh}$ to be competitive with the there usually used diesel generators, cf. e.g. [160]. In the result, the maximum allowed costs almost double to $K_{\mathrm{inv,o\&p}}/A = 149,759.84\,\mathrm{EUR/m^2}$. In view of such a small kite with only 4 m wing span, this figure and this market is very interesting.

5.2.5.6 Validation with the Higher Fidelity Model

Because such a small-scale system constitutes an interesting business case, because such a system can be used as proof-of-concept and thus for further validations of the in this dissertation presented models, concepts, and results, and because such a small-scale system seems to be realizable with a manageable amount of time and budget in the near-term to medium-term, it is interesting to also validate the results of the steady model against the higher fidelity point-mass model. The same procedure as in Sect. 5.1.4 is used for that, only with the altered flight path target point list of Tab. 5.11 to comply with the different optimal nominal elevation angle of Tab. 5.10.

Table 5.11: Target point list for the small-scale biplane.

Note	φ_{set}	ϑ_{set}	Threshold Type	x_{th}	Turn Dir.
Inside-down figure eight with four points.					
bottom right	$-20\,^\circ$	$-10\,^\circ$	AzimuthBelowThreshold	$-10\,^\circ$	Shortest
top right	$-20\,^\circ$	$-30\,^\circ$	CourseAngleBelowThreshold	0	Negative
bottom left	$20\,^\circ$	$-10\,^\circ$	AzimuthAboveThreshold	$10\,^\circ$	Shortest
top left	$20\,^\circ$	$-30\,^\circ$	CourseAngleAboveThreshold	0	Positive

Figs. 5.13–5.15 report the power curve and the kite's trajectory at $v_{\text{w},h_{\text{ref}}} = 10\,\text{m/s}$ for the two investigated airborne mass values $m_{\text{a}} = 0.50\hat{m}_{\text{a}}$ and $m_{\text{a}} = 0.75\hat{m}_{\text{a}}$.

The results are similar as in the utility-scale reference scenario from Sect. 5.1.4: The results of the steady model and of the point-mass model match very well. A slightly lower power is visible for the higher mass $m_{\text{a}} = 0.75\hat{m}_{\text{a}}$ which can at least in part again be explained by the larger flight path and thus larger absolute mean azimuth. Unlike the utility-scale system, the kite does not seem to fly dangerously low, the area swept by the kite is not a significant portion of the wind window, and the turns are by far not that tight. It is reasonable to assume that MPP-tracking improves the electrical power closer to what is expected from the steady model.

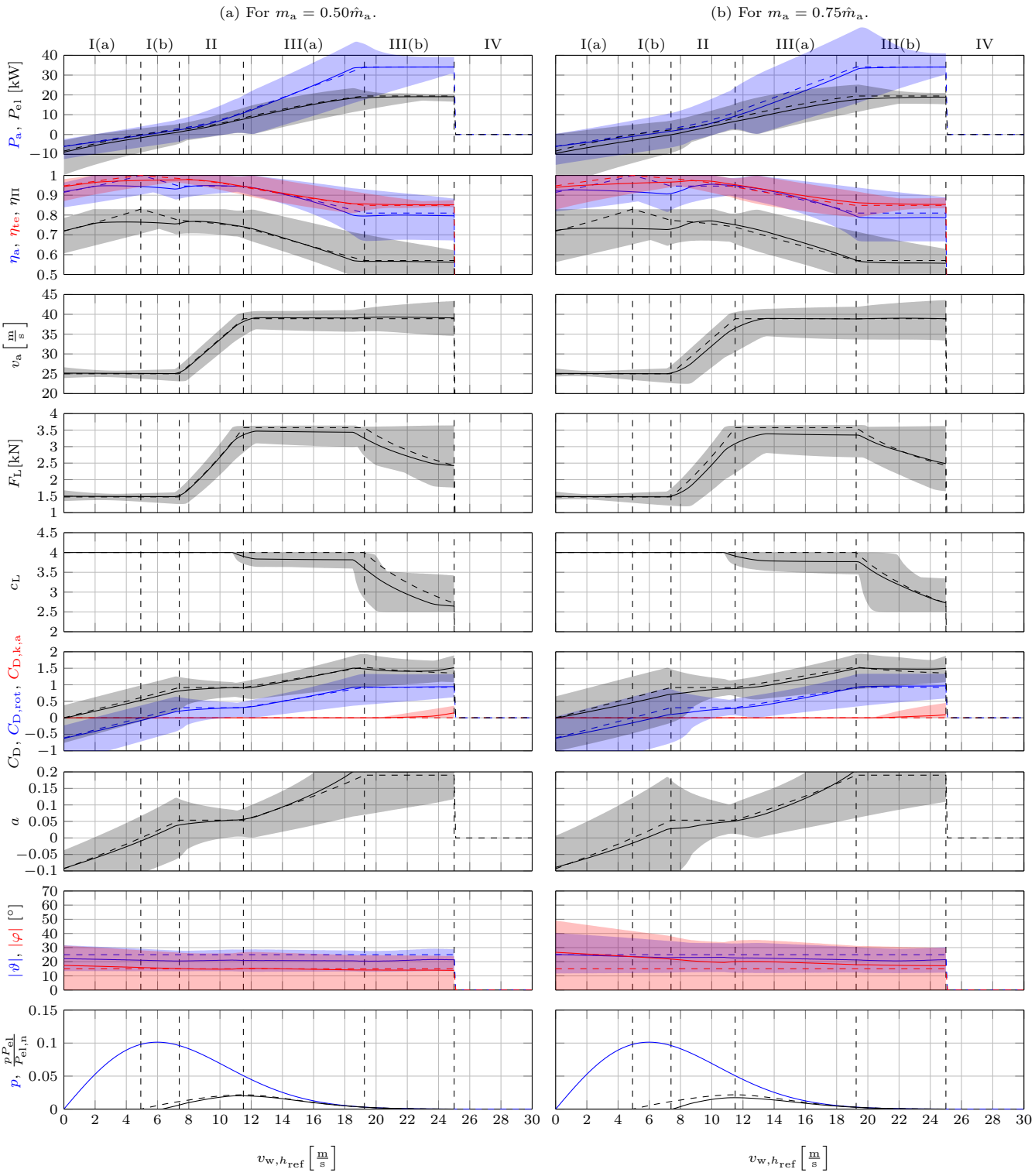

Figure 5.13: Power curve results for the small-scale biplane for two different effective airborne masses: steady model in dashed vs. point-mass model with mean values over flight path loop in solid and range of minimum and maximum values over flight path loop as area.

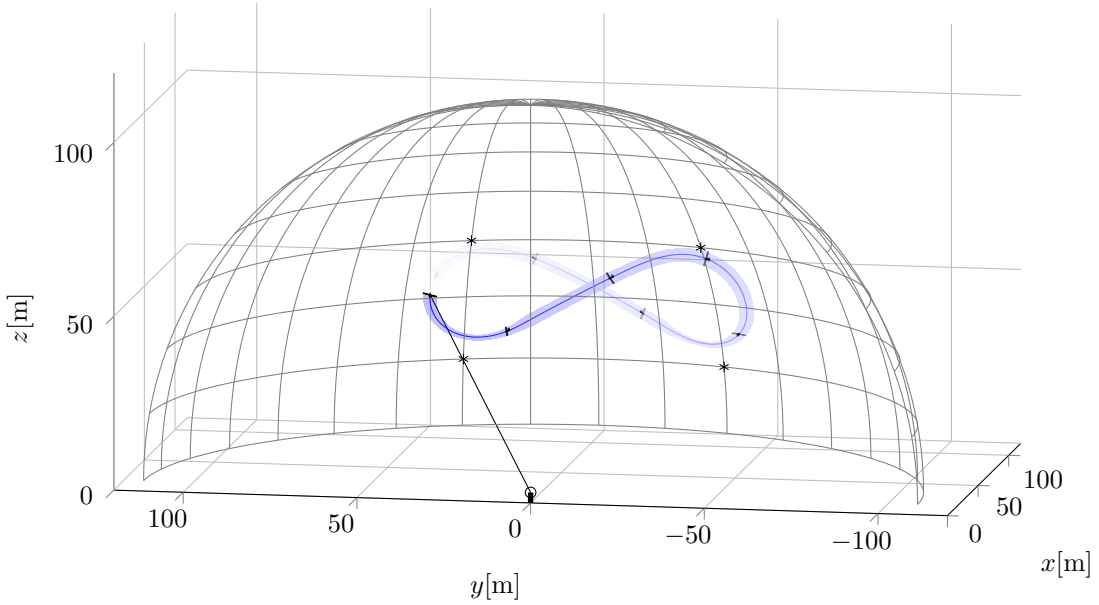

Figure 5.14: Flight trajectory of the small-scale biplane with $m_\mathrm{a} = 0.50\hat{m}_\mathrm{a}$ at $v_{\mathrm{w},h_\mathrm{ref}} = 10\,\mathrm{m/s}$ with the flight path target points in * and with the kite's orientation every 1 s before the path loop ends.

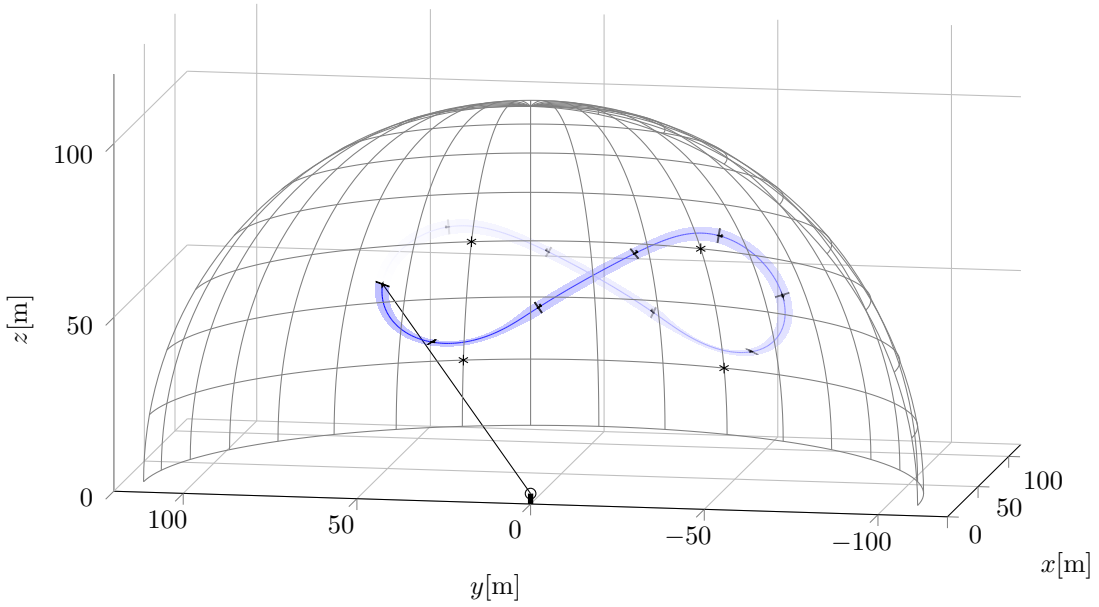

Figure 5.15: Flight trajectory of the small-scale biplane with $m_\mathrm{a} = 0.75\hat{m}_\mathrm{a}$ at $v_{\mathrm{w},h_\mathrm{ref}} = 10\,\mathrm{m/s}$ with the flight path target points in * and with the kite's orientation every 1 s before the path loop ends.

5.2.6 Tiny-Scale Biplane

The small-scale demonstrator already has a quite high voltage, wing loading, and power. Therefore, its development requires diverse engineering, prototyping, and testing competencies as well as considerable funding. It might be desirable to validate the biplane drag power kite concept at least in part with a very low-cost demonstrator, made with a low-voltage powertrain, low wing loading, and low power. For that, a tiny-scale technology demonstrator constructed e.g. with low-cost foam wings similar to remote controlled (RC) airplanes is conceptualized with the developed steady systems engineering model. Tab. 5.12 lists the considered fixed parameters which are different from the reference scenario. The parameters are not optimized, but chosen for a simple demonstrator design. To enable a low voltage $\leq 60\,\mathrm{V}$ with standard RC motors, no electrical power transmission between kite and ground is considered. Instead, onboard lithium-type batteries as power source and sink are considered. The corresponding tether parameters are assigned such that the system can be simulated without changes in the developed model and code. As the only goal for the demonstrator would be to show the feasibility of the biplane kite, the economic parameters are of no interest. Due to the considered low-cost foam wings, only a low achievable lift coefficient is expected.

Tab. 5.13 and Figs. 5.16–5.18 report the results.

The wing loading is relatively low, but already exceeds $100\,\mathrm{kg/m^2}$, and the resulting power density and other figures of merit are by far not as good as for the small-scale or utility-scale system. Nevertheless, already a multitude of the power density of photovoltaics is expected. The maximum allowed mass seems realizable with foam wings.

It should be noted, that such a demonstrator can only validate the concept in part, because a main aspect is the usage of an airfoil with a very high lift coefficient, with which however high wing loadings will occur. High wing loadings are likely impossible to be realized with foam wings and instead require a strong airframe entirely made from carbon fiber or light metals. Therefore, a realized tiny-scale demonstrator can only be considered as a first proof-of-principle, while the in Sect. 5.2.5 optimized small-scale demonstrator can be considered as full validation of the concept and thus as proof-of-concept.

Table 5.12: Fixed parameters for the tiny-scale biplane which are different from the reference scenario of Tab. 5.1. Rows in gray are parameter values set such that no power transmission over the tether is simulated without changing the actual model equations and model code.

Parameter	Value	Comment/Justification
Kite aerodynamics parameters.		
b	$= 1.8\,\mathrm{m}$	design consideration
AR	$= 18$	design consideration
$c_{\mathrm{D},0}$	$= 0.02$	estimated two times higher because of rather low N_{Re}, based on CFDs similar to Fig. 2.6
$c_{\mathrm{D},2}$	$= 0.01$	estimated two times higher because of rather low N_{Re}, based on CFDs similar to Fig. 2.6
$c_{\mathrm{L,n}}$	$= 2.5$	estimated realizable for rather low N_{Re}, also based on CFDs similar to Fig. 2.6
$c_{\mathrm{L,min\text{-}op}}$	$= 1.0$	estimated
$C_{\mathrm{D,k,o}}$	$= 0.1$	estimated higher, because of bulky electronics
$C_{\mathrm{D,k,a,max}}$	$= 0$	no brakes, no vertical wings for sideslipping, no rudders
Rotor parameters.		
r_{rot}	$= 1.1438$	$= \pi \cdot (d_{\mathrm{rot}}/2)^2 \cdot n_{\mathrm{rot}}/A$ with $d_{\mathrm{rot}} = 10\,\mathrm{in} \approx 0.256\,\mathrm{m}$ RC propeller
$\eta_{\mathrm{rot},+} = \eta_{\mathrm{rot},-}$	$= 0.8$	assumed for RC propeller, but might be optimistic
$\eta_{\mathrm{rot,hov}}$	$= 0.8$	assumed for RC propeller, but might be optimistic
Tether parameters.		
L_{te}	$= 150\,\mathrm{m}$	design consideration
$U_{\mathrm{te,n}}$	$= 10^3\,\mathrm{V}$	*to simulate no power transmission over tether*
R_{te}	$= 10^{-3}\,\Omega$	*to simulate no power transmission over tether*
$n_{\mathrm{te,c}}$	$= 2$	*as no power transmission over the tether is simulated, $n_{\mathrm{te,c}}$ does not need to be optimized "internally" within Step 6 of the algorithm in Sect. 2.9.2 and can instead be set to some (valid) value*
$w_{\mathrm{te,c,sh}}$	$= 0$	*to simulate no power transmission over tether*
$w_{\mathrm{te,c,j}}$	$= 0$	*to simulate no power transmission over tether*
$w_{\mathrm{te,j}}$	$= 0$	*to simulate no power transmission over tether*
$S_{\mathrm{te,mech}}$	$= 10^{-9}$	*to simulate no power transmission over tether*
$S_{\mathrm{te,ins}}$	$= 10^{-9}$	*to simulate no power transmission over tether*
Powertrain subsystems parameters.		
$\eta_{\mathrm{m},+} = \eta_{\mathrm{m},-}$	$= 0.9$	estimated for RC machine, but might be optimistic
$\eta_{\mathrm{pe,g},+} = \eta_{\mathrm{pe,g},-}$	$= 1$	*to simulate no power transmission over tether*
γ_{m}	$= 0.40\,\mathrm{kg/kW}$	measured from RC propeller plus machine
$\gamma_{\mathrm{pe,k}}$	$= 0.26\,\mathrm{kg/kW}$	measured from RC motor controller
$P_{\mathrm{el,ins}}$	$= 2,000\,\mathrm{W}$	estimated for selected RC propellers, machines, and power electronics
Ground station parameters and flight trajectory parameters.		
h_{to}	$= 0\,\mathrm{m}$	ground anchor
ϑ_{n}	$= 40\,^\circ$	higher for safety/higher ground clearance

Table 5.12: Fixed parameters for the tiny-scale biplane. (continued)

Parameter	Value	Comment/Justification
Power curve "shaping" parameters.		
$v_{\mathrm{a,min}}$	$= 20\,\mathrm{m/s}$	design consideration
$v_{\mathrm{a,n}}$	$= 30\,\mathrm{m/s}$	design consideration
r_{P}	$= 1.2$	design consideration, same as Makani Wing 7
$v_{\mathrm{w},h_{\mathrm{ref}},\mathrm{cut\text{-}out}}$	$= 12\,\mathrm{m/s}$	design consideration and estimated requirement for small power limitation actuations, but a high cut-out wind speed is not required for a first technology demonstrator

Table 5.13: Results for the tiny-scale biplane.

Parameter	Value		
Nominal power and nominal wind speeds.			
$P_{\mathrm{a,n}}$	$=$	$1,597.08$	W
$P_{\mathrm{el,n}}$	$=$	$1,025.82$	W
$P_{\mathrm{el,n}}/A$	$=$	$2,849.51$	$\mathrm{W/m^2}$
$P_{\mathrm{el,n}}/(\hat{m}_{\mathrm{k}} + m_{\mathrm{te}})$	$=$	127.26	W/kg
$v_{\mathrm{w},h_{\mathrm{ref}},\mathrm{cut\text{-}in}}$	$=$	4.35	m/s
$v_{\mathrm{w},h_{\mathrm{ref}},\mathrm{n(1)}}$	$=$	9.79	m/s
$v_{\mathrm{w},h_{\mathrm{ref}},\mathrm{n(2)}}$	$=$	10.44	m/s

(continued)

Parameter	Value		
Other nominal values.			
ω_{n}	$=$	11.46	°/s
h_{n}	$=$	96.42	m
$F_{\mid\mid,\mathrm{n}}$	$=$	457.45	N
$F_{\mid\mid,\mathrm{n}}/(Ag)$	$=$	129.53	$\mathrm{kg/m^2}$
$C_{\mathrm{D,te}}$	$=$	0.13	
$C_{\mathrm{D,k,p,n}} + C_{\mathrm{D,k,o}}$	$=$	0.18	
$C_{\mathrm{D,k,i,n}}$	$=$	0.13	
$C_{\mathrm{D,eq,n}}$	$=$	0.44	
$C_{\mathrm{D,rot,n(1)}}$	$=$	0.22	
$C_{\mathrm{D,rot,n(2)}}$	$=$	0.26	
$a_{\mathrm{n(1)}}$	$=$	0.05	
$a_{\mathrm{n(2)}}$	$=$	0.06	
$\zeta_{\mathrm{n(1)}}$	$=$	3.59	
Dimensions and masses.			
A	$=$	0.36	$\mathrm{m^2}$
$\hat{m}_{\mathrm{a,flight}}$	$=$	9.25	kg
$\hat{m}_{\mathrm{a,hov,ok}}$	$=$	8.47	kg
$\hat{m}_{\mathrm{a,hov,flt}}$	$=$	7.94	kg
$\hat{m}_{\mathrm{a}}$	$=$	7.94	kg
$\hat{m}_{\mathrm{k}}$	$=$	7.82	kg
$\hat{m}_{\mathrm{k}}/A$	$=$	21.71	$\mathrm{kg/m^2}$
$\hat{m}_{\mathrm{af\&o}}$	$=$	6.64	kg
$\hat{m}_{\mathrm{af\&o}}/A$	$=$	18.44	$\mathrm{kg/m^2}$
$m_{\mathrm{pt,k}}$	$=$	1.18	kg
m_{te}	$=$	0.25	kg
d_{te}	$=$	1.21	mm

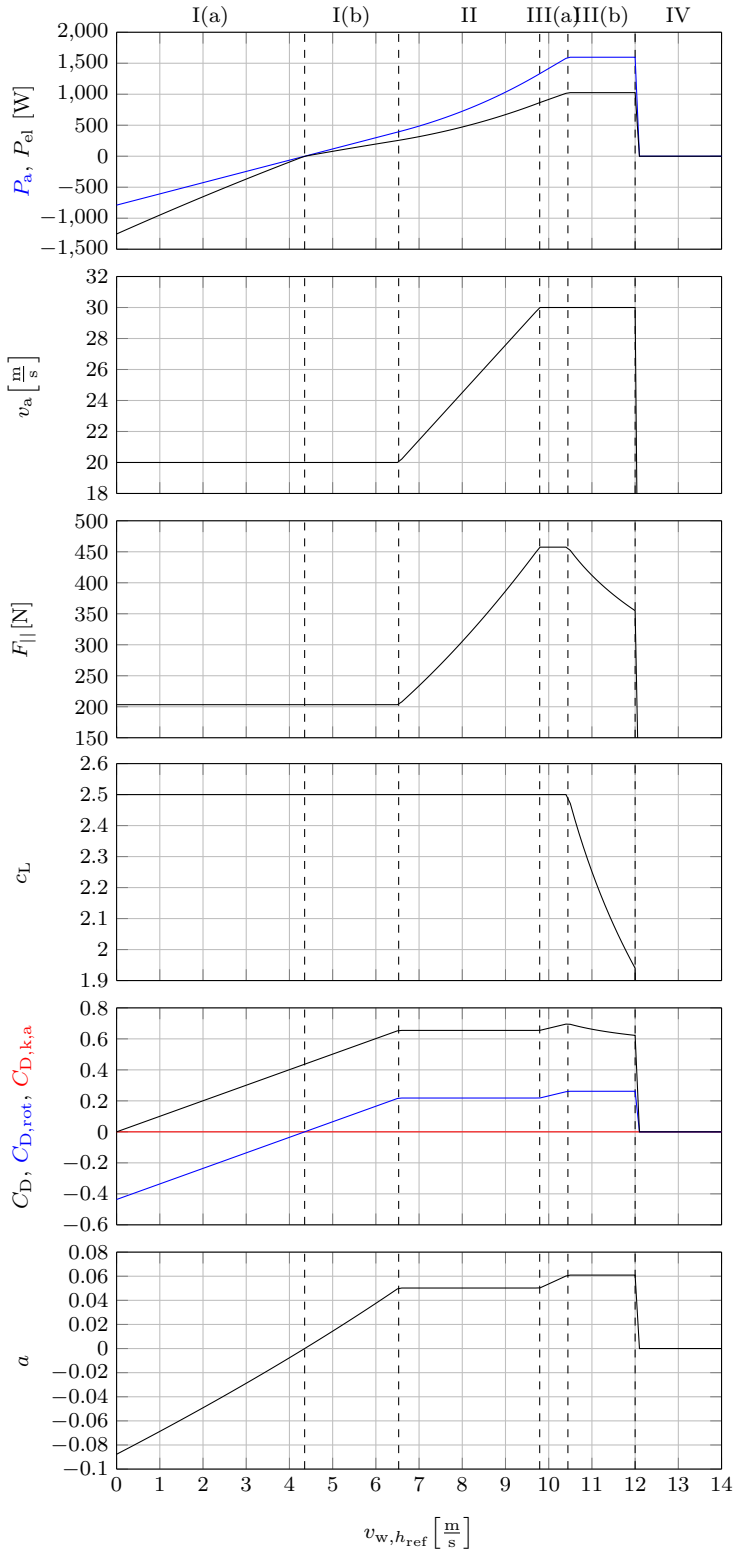

Figure 5.16: Power curve results for the tiny-scale biplane.

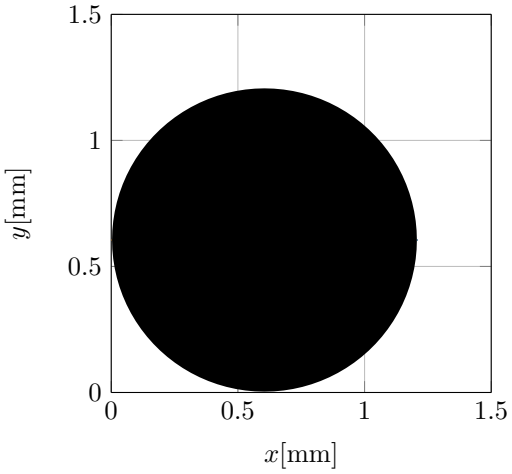

Figure 5.17: Visualization of the tether cross section for the tiny-scale biplane with color coding as in Fig. 1.8.

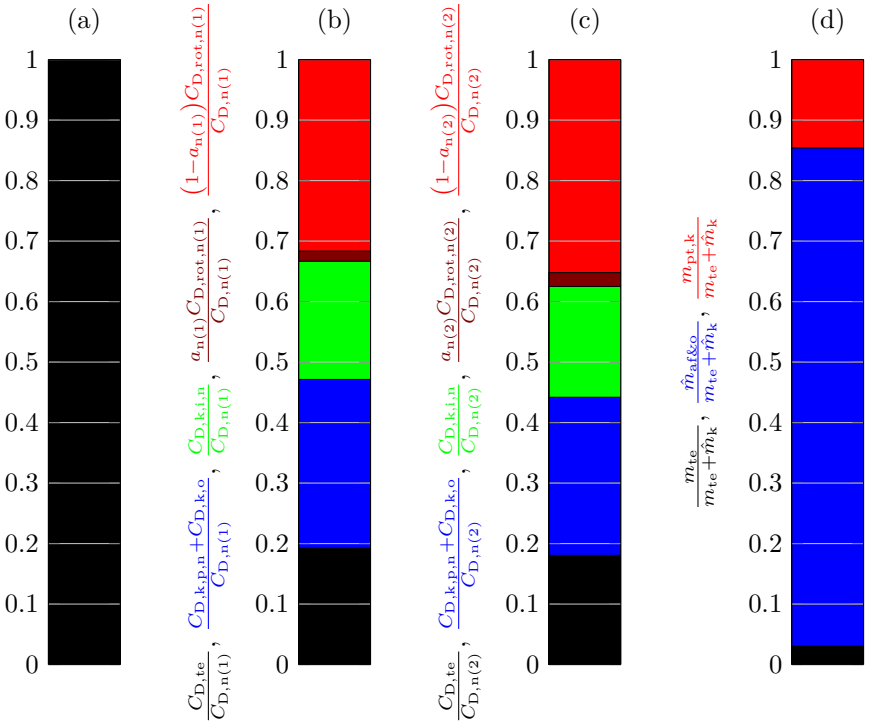

Figure 5.18: Visualization of distributions of some results for the tiny-scale biplane: (a) tether mass distribution with color coding as in Fig. 1.8, (b) distribution of drag portions in Region II and at first power point, (c) distribution of drag portions at second power point, (d) distribution of total (maximum allowed) airborne masses.

5.3 Sensitivities of the Environmental Parameters for the Considered Installation Site

With the utility-scale biplane from Sect. 5.1 as reference scenario, in the following a sensitivity analysis of each environmental parameter for the considered installation site (cf. Tab. 5.1) is conducted, with the following exceptions:

- The gravitational acceleration g is almost identical everywhere on planet earth. Investigating different values of g is therefore not meaningful.
- Changing the reference altitude h_{ref} is essentially identical to changing the mean wind speed or the scale parameter of the Weibull distribution μ, respectively (see also below, Sect. 5.3.2). Therefore, a sensitivity analysis of h_{ref} is not meaningful.

5.3.1 Air Density

The air density ρ varies for different places and atmospheric conditions on planet earth. The largest air density of up to about $1.6\,\mathrm{kg/m^3}$ may be expected in an arctic region at sea level altitude and at very low negative degrees Celsius temperatures, and the lowest one down to about $0.8\,\mathrm{kg/m^3}$ may be expected in high deserts at high temperatures. Fig. 5.19 shows important results of optimizations for different ρ within that range.

Important figures such as $P_{\mathrm{a,n}}$ and dependent values such as $\hat{K}_{\mathrm{inv,o\&p}}/A$ change linearly with ρ. This is expectable because the power equation (2.19) has ρ as a factor. The optimum of many design parameters and particularly the (installed) nominal powers, maximum allowed masses, nominal wing loading, and similar quantities change quite significantly. This indicates that a good choice for the design air density of the power plant or/and according safety factors are required.

The tether voltage and tether resistance as well as closely related values (e.g. voltage drop) appear a bit noisy. This is likely caused by the stochastic nature of the CMA-ES algorithm, which terminates when the cost function value hardly changes anymore. That noise is therefore an indication that the optimization parameters $U_{\mathrm{te,n}}$ and R_{te} might have a relatively low sensitivity on the cost function $\hat{K}_{\mathrm{inv,o\&p}}/A$. Fig. 5.20 plots the cost function at the optimal parameters from the reference scenario from Sect. 5.1, but with varied $U_{\mathrm{te,n}}$ and R_{te}, showing that indeed the cost function is very flat around the optimum.

The other reported results in Fig. 5.19 are of less interest and are therefore not further discussed. This is similarly made for all following parameter sensitivity analyses and the very same diagrams, y-axis ranges, and colors as in Fig. 5.19 are used to allow for quick comparisons of the different parameter sensitivity studies. Note that the most important figure of merit, the cost function $\hat{K}_{\mathrm{inv,o\&p}}/A$, is highlighted by a light-gray background.

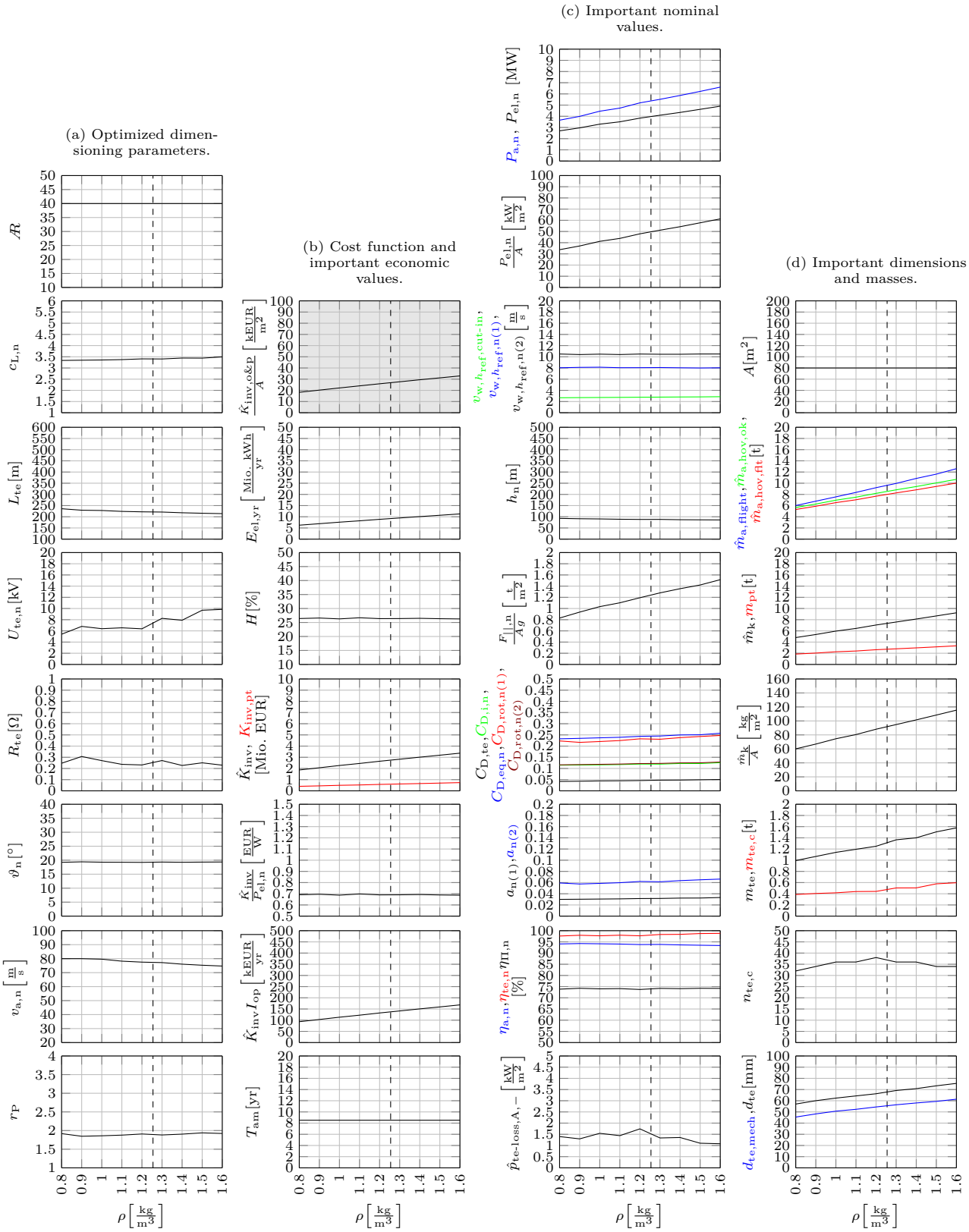

Figure 5.19: Results for different ρ (solid) compared to the reference scenario (dashed).

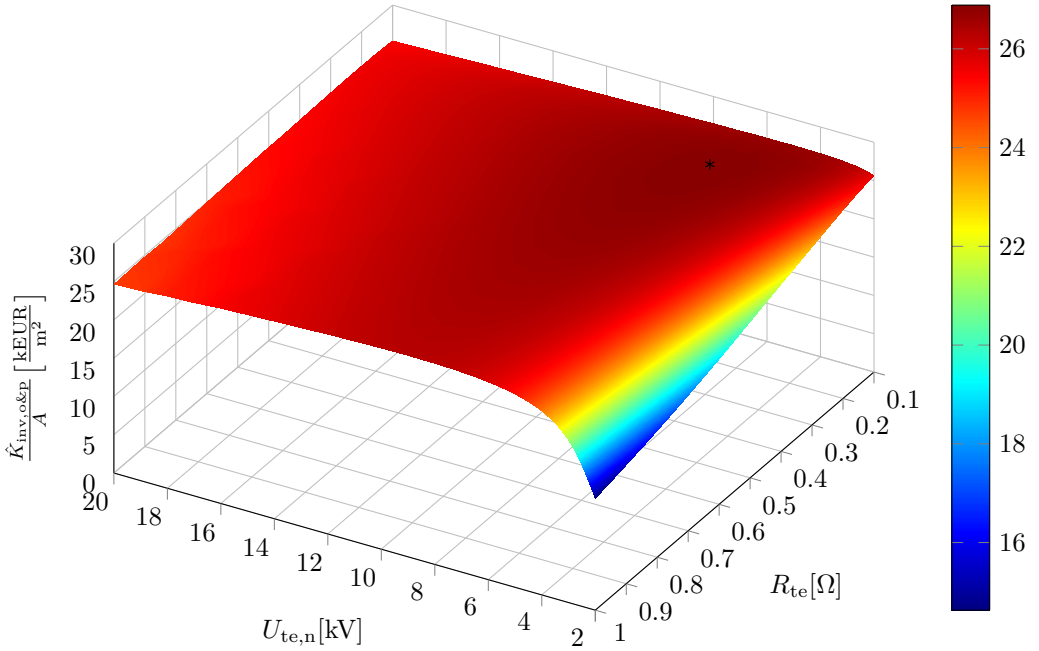

Figure 5.20: Cost function $\hat{K}_{\mathrm{inv,o\&p}}/A$ at the optimal parameters from the reference scenario of Sect. 5.1, but with varied $U_{\mathrm{te,n}}$ and R_{te}. The found optimum from the reference scenario of Sect. 5.1 is indicated by *. This figure was shown in the prior work by the author of this dissertation in [111, Poster, Fig. 4].

5.3.2 Wind Shear

Tab. 5.14 shows definitions of roughness length values z_0 for different terrains and Fig. 5.21 plots logarithmic wind shears for different parameters.

Table 5.14: Roughness length definitions taken and translated from [136, Tab. 3]. The gray row is the value of the reference scenario and of the "reference location" of the EEG [134].

Terrain Class	Description	z_0 [m]
1 – sea, lake	open sea for at least 1 km	0.0002
2 – smooth	tideland, snow-covered areas without vegetation and without obstacles	0.005
3 – open	open, flat terrain, grassland, runways, only few isolated obstacles	0.03
4 – open but rough	agriculturally used terrain with low stock, occasionally larger obstacles with distance $\geq 20 \cdot$ height	0.1
5 – rough	agriculturally used terrain with high stock, individual larger obstacles with distance $15 \ldots 20 \cdot$ height	0.25
6 – very rough	park landscape with bushes and trees, numerous obstacles with mutual distance $10 \cdot$ height	0.5
7 – closed	regular obstacles, e.g. villages, suburbs, forests	1.0
8 – city cores	centers of big cities with high and low buildings	2.0

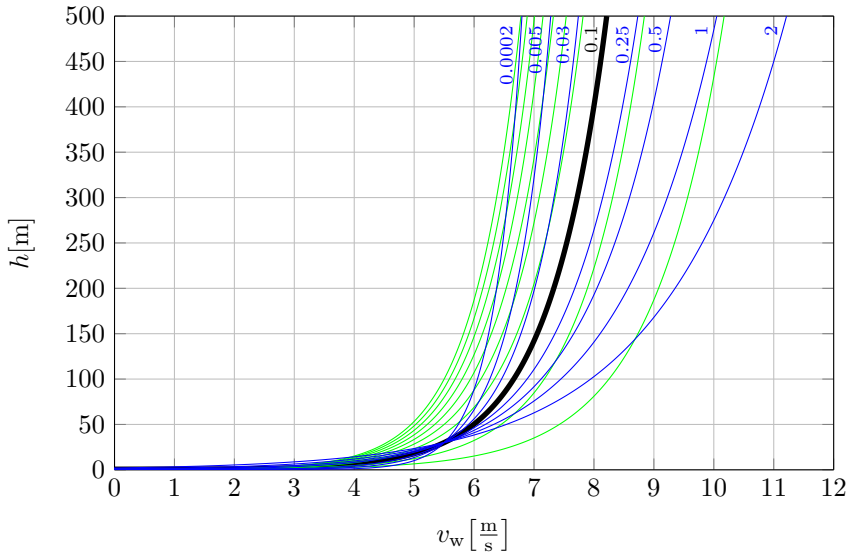

Figure 5.21: Logarithmic wind shear for different parameters: reference scenario with $z_0 = 0.1\,\mathrm{m}$ and $h_{\mathrm{ref}} = 30\,\mathrm{m}$ in ——; from the reference scenario varied z_0 (values in m are printed next to the corresponding curve) in ——; and from the reference scenario varied $h_{\mathrm{ref}}/\mathrm{m} \in [10, 20, \ldots, 100]$ in ——.

In view of Fig. 5.21, a change of h_{ref} is essentially the same as a change of the wind speed. This is also obvious from the equation, logarithmic wind shear factor (2.159) substituted into (2.158),

$$v_{\mathrm{w}} = \frac{\ln\left(\frac{h}{z_0}\right)}{\ln\left(\frac{h_{\mathrm{ref}}}{z_0}\right)} v_{\mathrm{w},h_{\mathrm{ref}}}, \tag{5.6}$$

in which both, $v_{\mathrm{w},h_{\mathrm{ref}}}$ and $1/\ln(h_{\mathrm{ref}}/z_0)$, are factors. Hence, investigating the sensitivity of h_{ref} is omitted or, respectively, embedded into investigating the sensitivity of the mean wind speed or μ, below, in Sect. 5.3.4.

In view of Fig. 5.21, investigating the sensitivity of z_0 directly is not very meaningful either: The baseline h_{ref} is rather low such that a higher z_0 results in much higher wind speeds at typical operating altitudes of the kite leading directly to much higher energy and likely to different optimal dimensioning parameters. As mentioned, changes of the (mean) wind speed are subject of another parameter study. Instead, the interesting question to be investigated here is if the optimal operation altitude (and correspondingly the optimal power plant design) changes for a higher wind speed above or below the reference scenario's operation altitude (i.e. for stronger or weaker wind shears). This translates as follows: First, because the wind speed at the nominal altitude of the reference scenario h_{n}^0 from Tab. 5.4 (the superscript 0 stands for reference scenario, not for "to the power of 0") shall not change for different z_0, the reference altitude is altered to

$$h_{\mathrm{ref}} = h_{\mathrm{n}}^0. \tag{5.7}$$

Second, because the wind speed in that altitude shall remain as in the reference scenario, a correction factor is introduced, given by

$$\begin{aligned}
\begin{pmatrix}\text{new wind shear at}\\ h = h_{\mathrm{n}}^0, h_{\mathrm{ref}} = h_{\mathrm{n}}^0, z_0 = z_0^0\end{pmatrix} \cdot f_{\mathrm{shear,cor}} &= \begin{pmatrix}\text{baseline wind shear at}\\ h = h_{\mathrm{n}}^0, h_{\mathrm{ref}} = h_{\mathrm{ref}}^0, z_0 = z_0^0\end{pmatrix} \\
v_{\mathrm{w}}(h = h_{\mathrm{n}}^0, h_{\mathrm{ref}} = h_{\mathrm{n}}^0, z_0 = z_0^0) f_{\mathrm{shear,cor}} &= v_{\mathrm{w}}(h = h_{\mathrm{n}}^0, h_{\mathrm{ref}} = h_{\mathrm{ref}}^0, z_0 = z_0^0) \\
\frac{\ln\left(\frac{h_{\mathrm{n}}^0}{z_0^0}\right)}{\ln\left(\frac{h_{\mathrm{n}}^0}{z_0^0}\right)} v_{\mathrm{w},h_{\mathrm{ref}}} f_{\mathrm{shear,cor}} &= \frac{\ln\left(\frac{h_{\mathrm{n}}^0}{z_0^0}\right)}{\ln\left(\frac{h_{\mathrm{ref}}^0}{z_0^0}\right)} v_{\mathrm{w},h_{\mathrm{ref}}} \\
f_{\mathrm{shear,cor}} &= \frac{\ln\left(\frac{h_{\mathrm{n}}^0}{z_0^0}\right)}{\ln\left(\frac{h_{\mathrm{ref}}^0}{z_0^0}\right)}
\end{aligned} \tag{5.8}$$

with reference altitude and roughness length from the reference scenario, h_{ref}^0 and z_0^0. This correction factor $f_{\mathrm{shear,cor}}$ is multiplied with $v_{\mathrm{w},h_{\mathrm{ref}}}$. Fig. 5.22 plots the new wind shear in ━━ which is identical to the one in Fig. 5.21, and it plots the new wind shear for the different investigated z_0 in ——.

For the computation of the complete multidisciplinary model in which $v_{\mathrm{w},h_{\mathrm{ref}}}$ is a probability distribution, the correction factor is applied for the scale parameter

$$\mu = f_{\mathrm{shear,cor}} \mu^0 \tag{5.9}$$

with the scale parameter from the reference scenario μ^0.

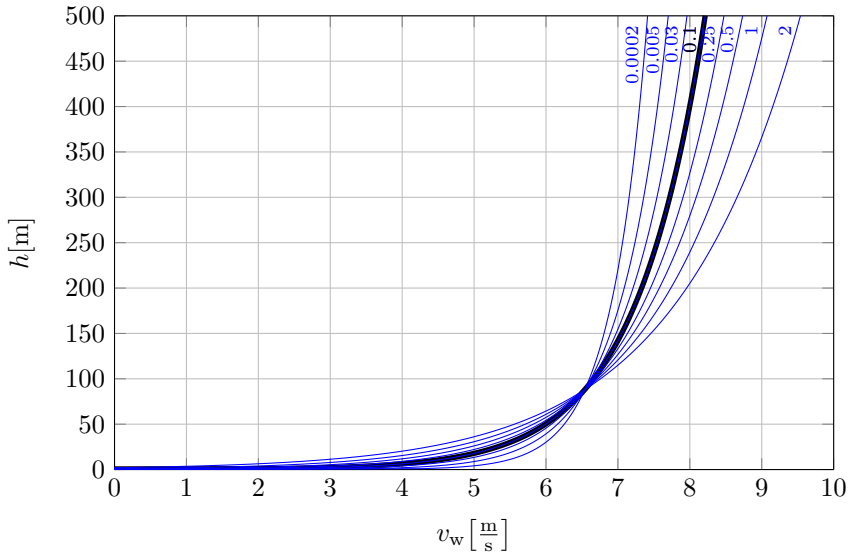

Figure 5.22: Investigated logarithmic wind shears with $h_\mathrm{ref} = h_\mathrm{n}^0$ and correction factor $f_\mathrm{shear,cor}$ from (5.8) for different z_0: reference scenario wind shear in ━━ with $z_0 = z_0^0$ and from the reference scenario varied z_0 (values in m are next to the corresponding curve) in ——.

Fig. 5.23 shows important results of optimizations with the wind shears of Fig. 5.22.

For weaker wind shears than in the reference scenario the parameters and results change only slightly. Indeed, the altitude is reduced slightly via a lower elevation angle and thus a higher cosine efficiency leading overall to slightly better figures of merit. For stronger wind shears, the optimal nominal altitude increases, mainly driven by a longer tether (instead of a much higher elevation angle). The optimal nominal power increases, but the efficiencies decrease and thus the economic performance increases not significantly. Given that a kite power plant would not be deployed in city cores ($z_0 = 2$), one can conclude that the sensitivity of the wind shear on the economic performance is low or even almost negligible.

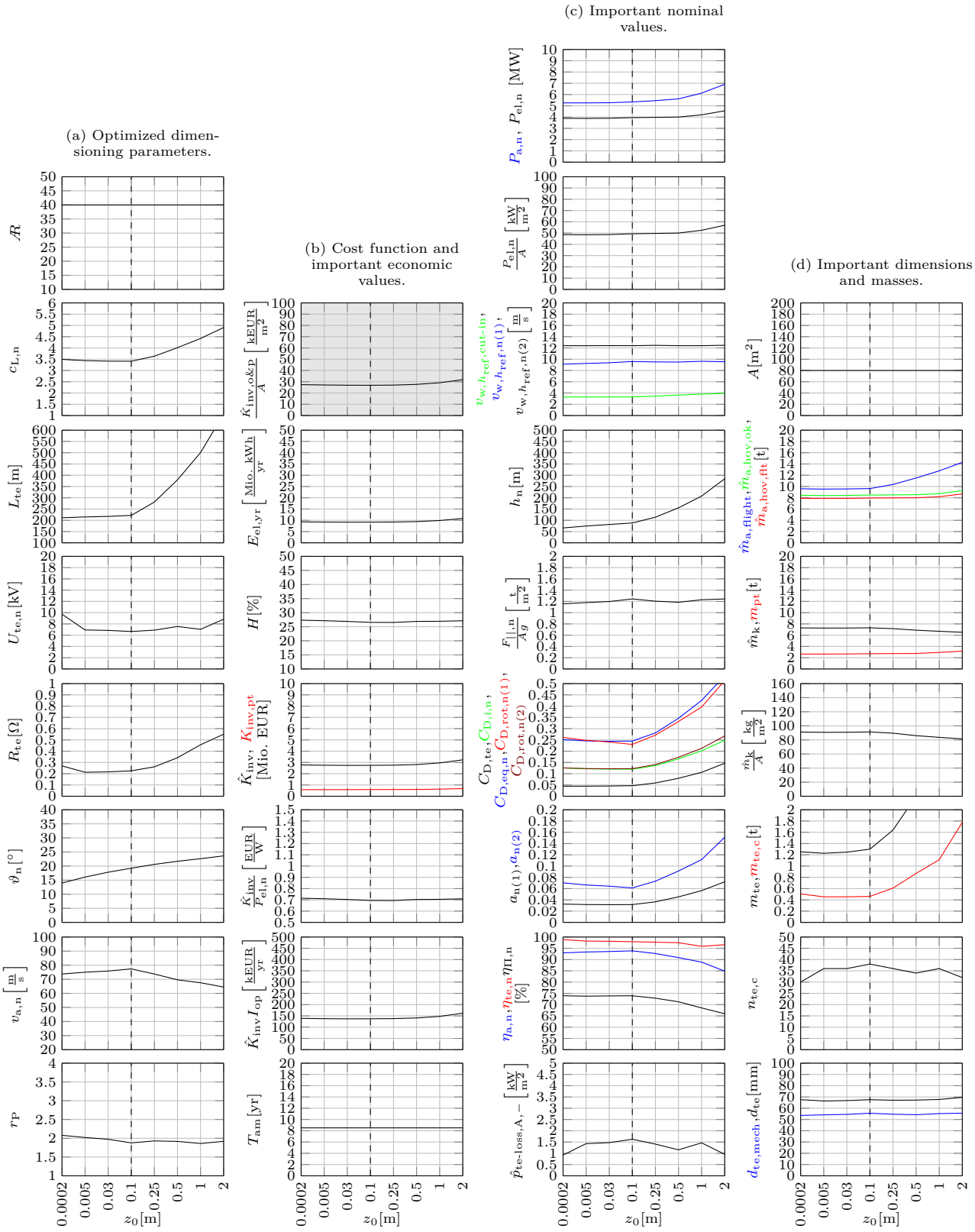

Figure 5.23: Results for the different wind shears of Fig. 5.22 (solid) compared to the reference scenario (dashed).

5.3.3 Weibull Distribution Shape Parameter

Depending on the deployment site, the Weibull distribution shape parameter may vary significantly, even though $\lambda = 2$ (i.e. a Rayleigh distribution) is a usual value. In [136, Tab. 9], the Weibull parameters are fitted to measurements at different locations in Germany. The shape parameter varies between $\lambda = 0.9$ to $\lambda = 2.36$. Therefore, it is interesting to investigate the effect for other λ.

Here, the investigated minimum value is $\lambda = 1$, with which valid results are obtained without changing the model code, because there would be a singularity for $\lambda < 1$. The investigated maximum value is $\lambda = 3.5$ to investigate also the results for such extremely high values, in which the Weibull distribution is more like a Gauss distribution.

Similar to the investigation of the wind shear, it is meaningful to not simply re-compute the results for changed λ, because the wind speed mean value varies with λ by a few percent, which could have a significant effect on the results. Instead, it is interesting to isolate the effect of a changing wind speed probability distribution shape without a change in the mean wind speed. The mean wind speed of the Weibull distribution is given by

$$\tilde{v}_{\mathrm{w},h_{\mathrm{ref}}} = \mu \, \Gamma\left(1 + \frac{1}{\lambda}\right), \tag{5.10}$$

where $\Gamma(\#)$ is the gamma function, cf. e.g. [127, Chap. 2.4]. In order to keep the mean wind speed constant at the value of the reference scenario $\tilde{v}^0_{\mathrm{w},h_{\mathrm{ref}}}$, the scale parameter μ must be altered for changed λ by

$$\mu = \frac{\tilde{v}^0_{\mathrm{w},h_{\mathrm{ref}}}}{\Gamma\left(1 + \frac{1}{\lambda}\right)}. \tag{5.11}$$

Fig. 5.24 plots (5.10), (5.11), and the altered and here investigated Weibull distributions.

Fig. 5.25 reports the results of the optimizations of the utility-scale biplane with the Weibull distributions from Fig. 5.24 (c).

The results are quite affected. The maximum allowed costs decrease moderately with λ. This can be explained by the very low probability of higher wind speeds for high λ, with which a significant portion of the energy can be harvested due to the cubic relationship between wind speed and power. The optimal nominal power is reduced significantly for high λ due to the same reason. Therefore, also the maximum allowed masses reduce with λ. On the other hand, the capacity factor increases significantly with λ. This is because of the reduced nominal power and reduced nominal wind speed for increasing λ. This is again caused by the very rare high wind speeds due to the tighter probability distribution for high λ. These results indicate that a good λ (and μ) value should be used for the kite power plant design optimization of a to be realized system.

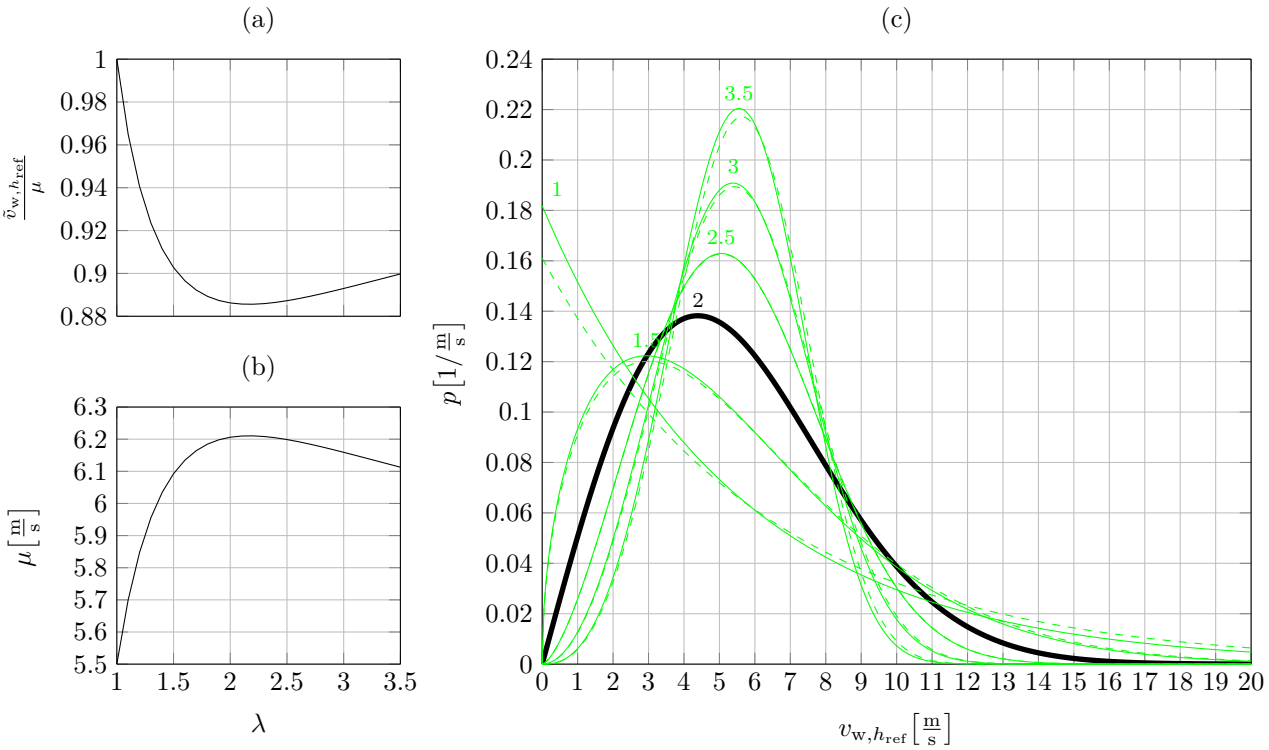

Figure 5.24: Investigated Weibull distributions: (a) Eq. (5.10) relative to μ (i.e. the Gamma function), (b) Eq. (5.11), and (c) Weibull distributions of the reference scenario in ——— and for altered λ and through Eq. (5.11) altered μ (values are above the corresponding curve) in ———. In the latter, also the Weibull distributions for altered λ with unaltered μ are plotted in - - - - for reference.

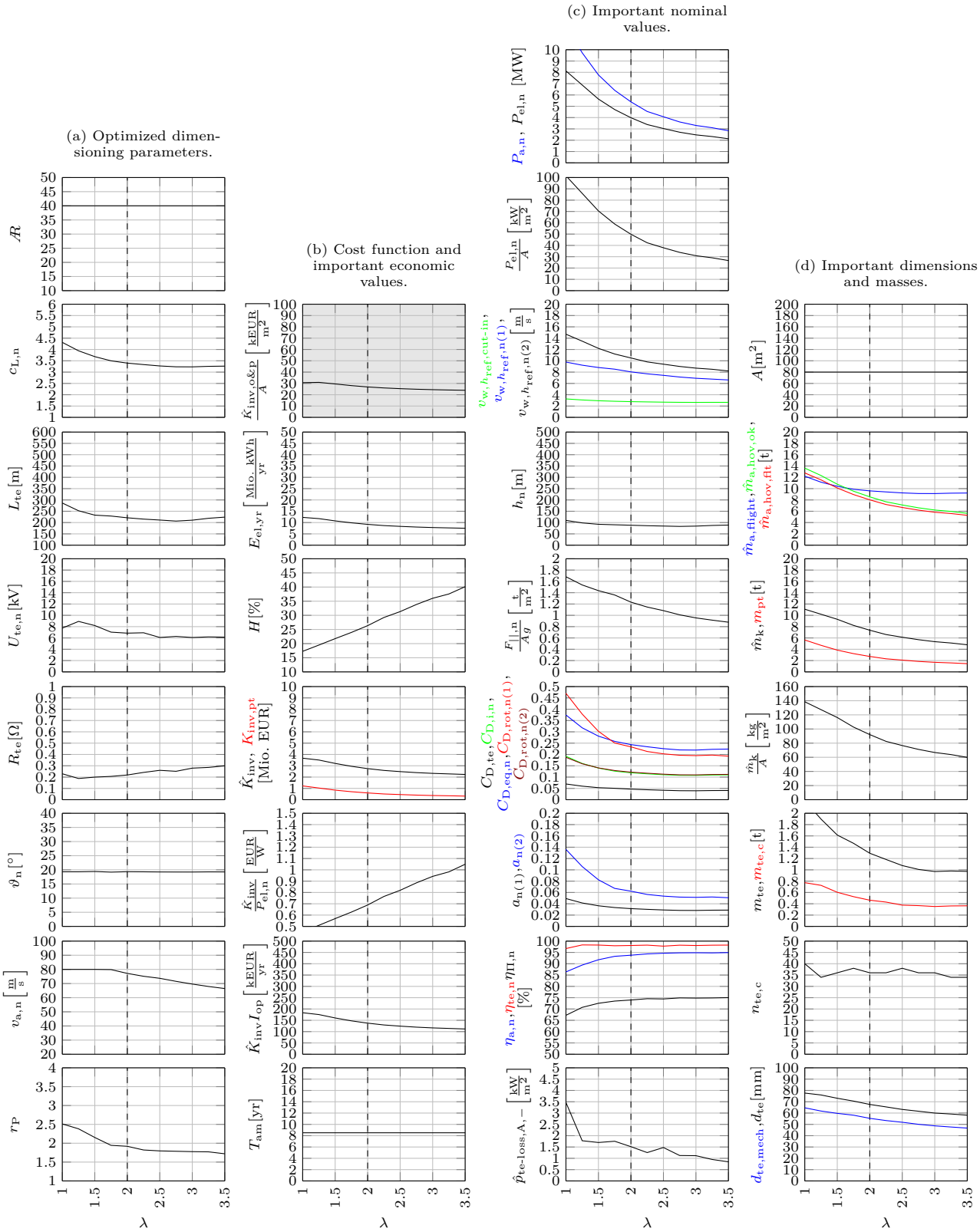

Figure 5.25: Results for different λ (solid) compared to the reference scenario (dashed).

5.3.4 Weibull Distribution Scale Parameter

The mean wind speed, or the Weibull distribution scale parameter μ, is probably the most important parameter of a power plant deployment site due to the cubic relationship between wind speed and power. The mean wind speed may range from 4 m/s on a low wind site to 10 m/s at a high-wind near-shore or offshore site. Hence, the range $\mu \in [2/\sqrt{\pi} \cdot 4\,\mathrm{m/s}, 2/\sqrt{\pi} \cdot 10\,\mathrm{m/s}]$ is investigated, cf. (2.163). Fig. 5.26 shows the results.

As expected, the most important figures have a very high sensitivity on μ. A slight increase from 5.5 m/s mean wind speed from the reference scenario (EEG reference location) to 7.0 m/s already doubles the maximum allowed costs per area. Moreover, the nominal power and maximum allowed masses increase significantly with μ. These very high sensitivities imply that it might be worth to optimize and built different kite power plants for low-wind and high-wind sites.

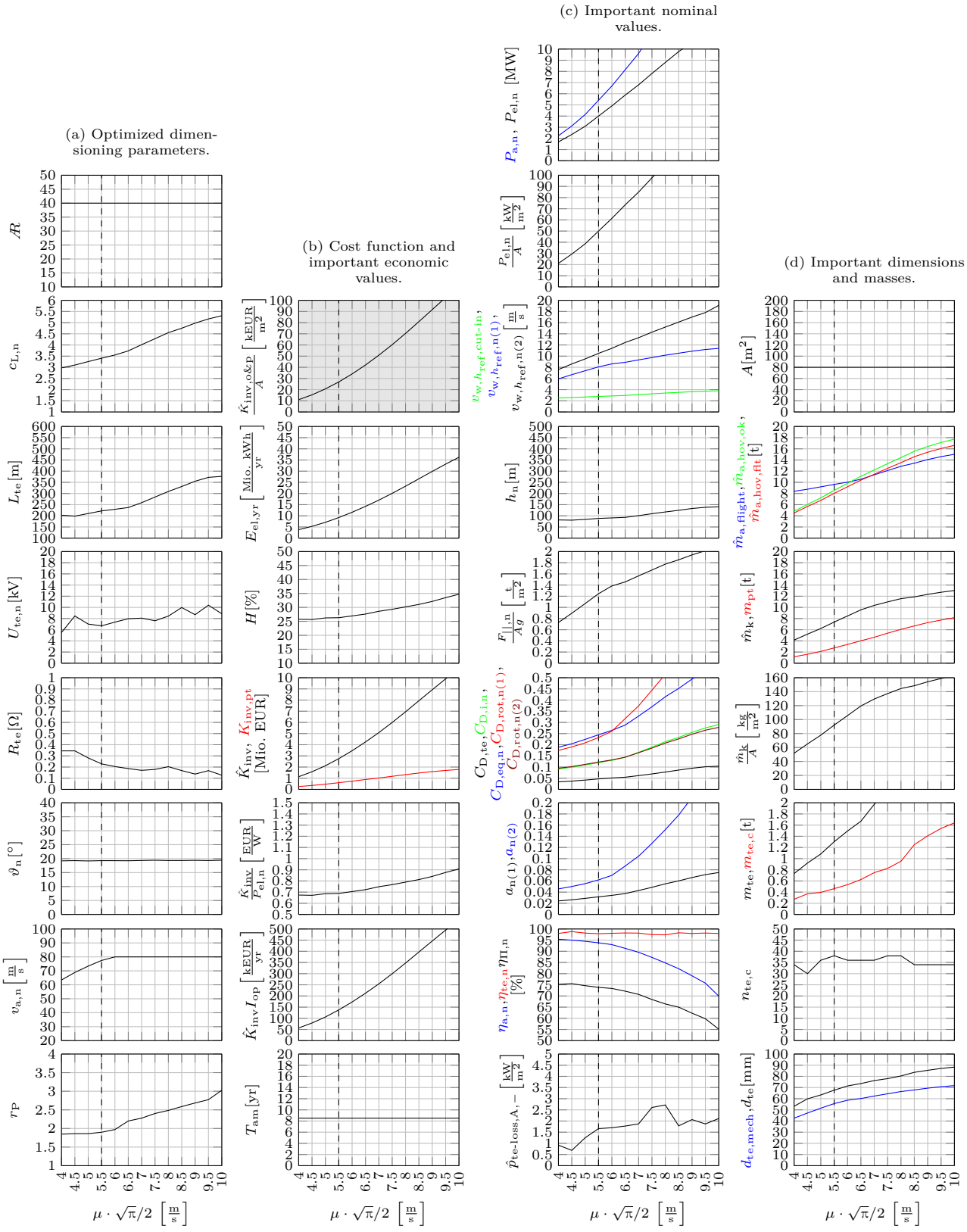

Figure 5.26: Results for different μ (solid) compared to the reference scenario (dashed).

5.4 Sensitivities of the Economic Parameters for the Targeted Market

In the following, a sensitivity analysis of each economic parameter for the targeted market (cf. Tab. 5.1) is conducted, with the following exception: The availability factor f_{avail} has no direct impact on the power curve and it has a linear impact on the energy yield and further thereof dependent values. Therefore, an almost exactly linear sensitivity can well be expected which is why a detailed sensitivity analysis on f_{avail} is omitted.

5.4.1 Levelized Cost of Electricity (LCOE)

The LCOE depends on the targeted market and can vary significantly. For example, the stock-exchange price in Europe is in the range of about $0.03 \ldots 0.05\,\text{EUR/kWh}$ in 2018, cf. [161]. If there is a high wind power penetration in the future, then the prices can drop significantly and the average achieved selling price might drop maybe to around $0.02\,\text{EUR/kWh}$. In case the power plant is used for self-consumption, it competes with the costs payed by the electricity customer, which is in 2018 in Germany around $0.15\,\text{EUR/kWh}$ for industrial customers and around $0.30\,\text{EUR/kWh}$ for households, cf. [159]. If the power plant's electricity is in part used for self-consumption and in part fed into the public grid, then the LCOE depends on that ratio of self-consumption and fed-in energy and may thus be somewhere in the range of $0.03 \ldots 0.30\,\text{EUR/kWh}$. If the power plant is used in an island grid, also about $0.20 \ldots 0.30\,\text{EUR/kWh}$ could be expected, cf. e.g. [160]. If the power plant is used in an island grid with significant diesel power penetration, even up to about $0.50\,\text{EUR/kWh}$ can be expected, cf. e.g. [160]. Therefore it is interesting to investigate the sensitivity of k_{LCOE}. However, here only the range of $0.02 \ldots 0.20\,\text{EUR/kWh}$ is investigated in detail, because one motivation of this dissertation is to contribute to the research and development for a high number of large-scale kite power plants, for which the majority will feed the public grid with an expected price in that range. Fig. 5.27 plots the results.

The maximum allowed costs are very sensitive on k_{LCOE}: Doubling k_{LCOE} well more than doubles $\hat{K}_{\text{inv,o\&p}}/A$. Also the other figures and power plant parameters have quite a significant sensitivity for $k_{\text{LCOE}} \lesssim 0.10\,\text{EUR/kWh}$. In particular, the nominal powers and wind speed reduce, through which the capacity factor increases, but not above 40 % for the investigated parameters, proving again the capacity factor paradox. Note also that the optimal nominal airfoil lift coefficient hardly changes from its high value. From these results, it can be concluded, that the first markets should be those with a high average selling price of electricity, and markets just with a few cents higher electricity prices should be preferred.

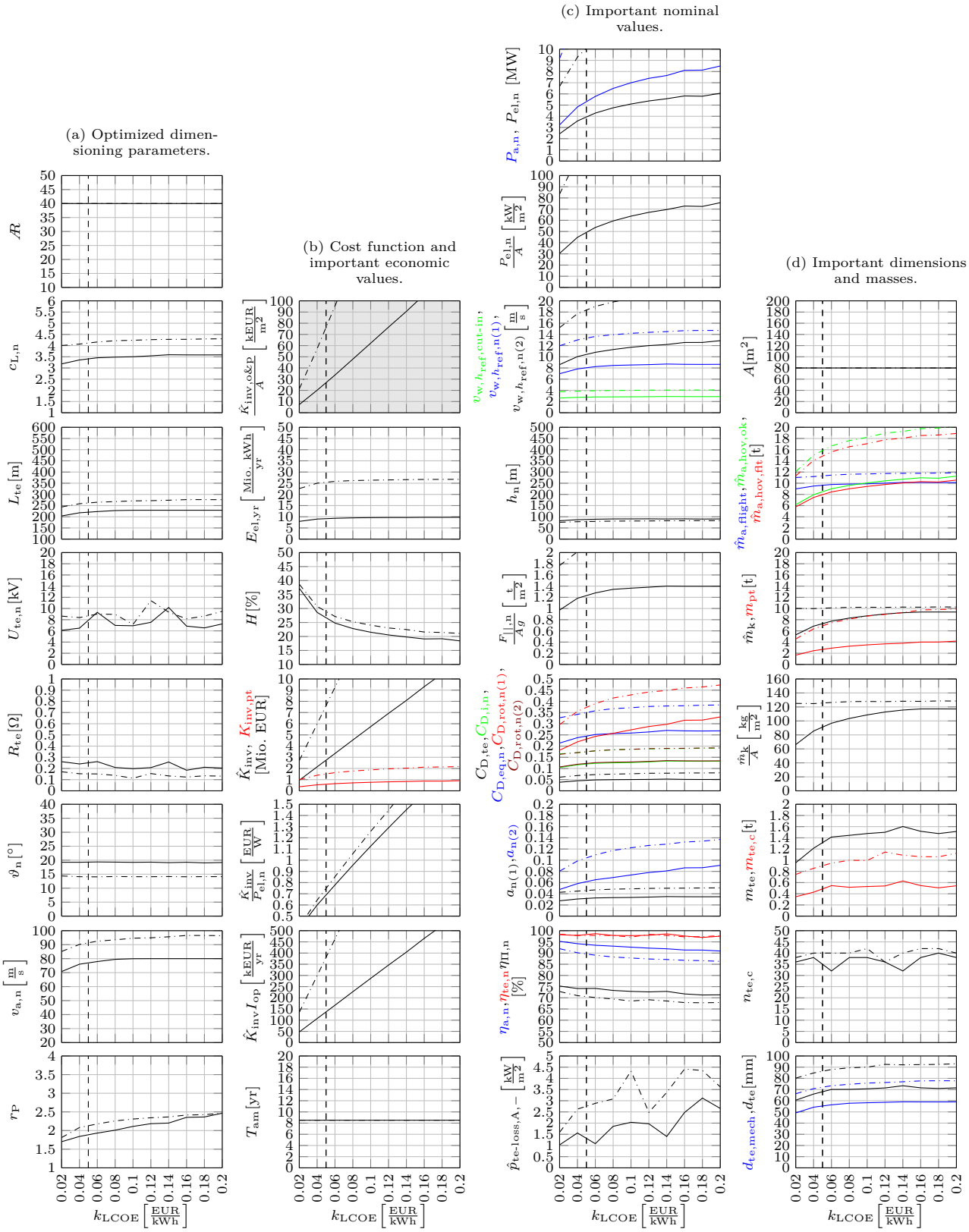

Figure 5.27: Results for different k_{LCOE} (solid), also for the offshore variant (dash-dotted), compared to the reference scenario (dashed).

5.4.2 Interest Rate

A certain interest rate is expected by an investor for both, to make profit and to compensate the investment risk. Usual expected profits may range from 5 %/yr to 10 %/yr. However, particularly the first kite power plants and kite farms will have a very high investment risk, because the technology is not proven. For example, no statistics will be available if the claimed power curve values and energy yields are reached in reality, if the availability and lifetime figures are reached, if the maintenance budget is sufficient, and if the kites do not crash. In addition to that, the wind predictions over the operational life of the power plants has some error and thus imposes a further risk. Therefore, a significant risk surcharge must be expected, particularly for the first kite power plants. Here, interest rates in the range of $I \in [0, 30\,\%]$ are investigated. Fig. 5.28 shows the results.

While the nominal powers, maximum allowed mass, and other design parameters and results have only a moderate sensitivity, the maximum allowed costs are very sensitive on I. An increase of I from 10 % to 15 % already reduces the maximum allowed costs by about one third. This highlights how important it is for a kite power company, to have a convincing verification and validation, i.e. particularly a number of working prototypes and demonstrators or ideally already sold and still running smaller-scale systems, as well as to have a very fault tolerant system. One promising example for the latter is the powertrain concept [106] published by the author of this dissertation, which has no single point of failure and guarantees (w.r.t. the powertrain) that the kite can always be landed in multicopter hovering mode, even if there is a short circuit in the tether. The lower the risk for the investors is, the higher may be the research and development budget as well as the profit margin for the kite power plant manufacturer.

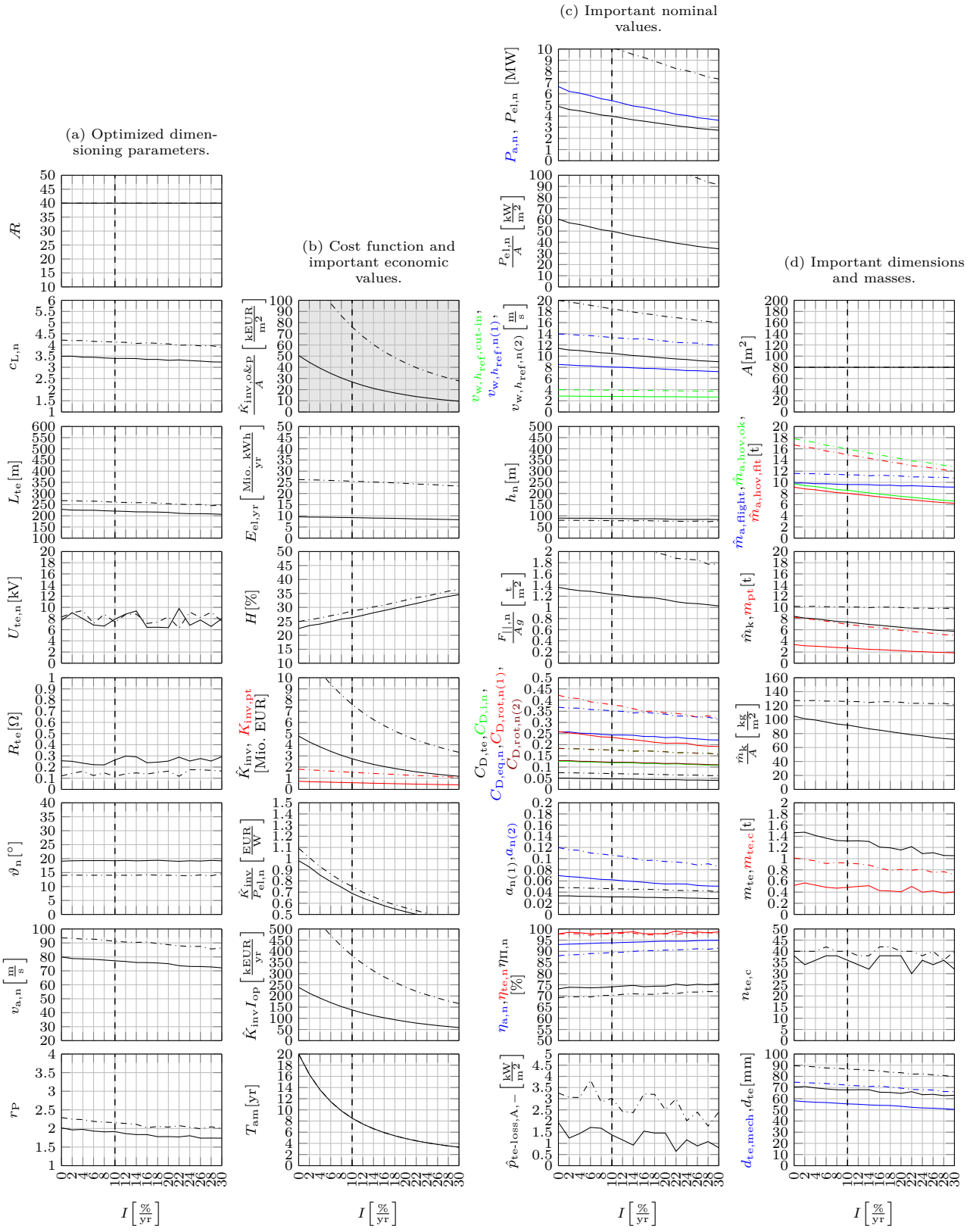

Figure 5.28: Results for different I (solid), also for the offshore variant (dash-dotted), compared to the reference scenario (dashed).

5.4.3 Power Plant Lifetime

Fossil power plants have lifetimes of up to about 50 years. Conventional wind turbines have lifetimes of 20 to 30 years. Commercial airliners reach lifetimes of up to about 40 years with a total flight time in the order of 100,000 h to 200,000 h or several thousand flight cycles, cf. e.g. [162]. In the reference scenario, a lifetime of $T = 20\,\mathrm{yr}$ was assumed, as this number is similar to conventional wind turbines. Assuming that the kite is in flight 80 % of the time (i.e. it is grounded for only 20 % of the time due to insufficient or too high wind, or due to maintenance/overhaul), the total flight hours add up to $80\,\% \cdot 20\,\mathrm{yr} \cdot 8760\,\mathrm{h/yr} = 140,160\,\mathrm{h}$. This is in the range of commercial airliners. However, a kite must be much cheaper than a commercial airliner to be economic. On the other hand, the kite flies much slower, flies always at low altitudes with no or much smaller pressure and temperature fluctuations, the kite is not pressurized, and the kite is landed vertically by hovering with low speeds, low forces, and almost entirely without shocks (note that this is contrary to other kite power concepts or launch and landing concepts, see also Appendix A). Moreover, the kite is considered to have a tailplane with which the kite is automatically and passively pitched into a gust (contrary to lift power flexible kites). Additionally, the loads reduce at high wind speeds due to the decrease of the airfoil lift coefficient in Region III(b). Therefore, the maximum loads of such a kite might not be very high. Nevertheless, the actual reachable lifetimes are unknown to date. Moreover, the reachable lifetime is a function of the kite design and concept, e.g. whether carbon fiber or aluminum or which safety factors are chosen. The lifetime is likely also dependent on the deployment site (harsh climate vs. moderate climate). Therefore, the sensitivity on the lifetime is investigated here. Fig. 5.29 plots the results.

The most important figures, maximum allowed costs, nominal power, and maximum allowed masses have a low to moderate sensitivity around the reference $T = 20\,\mathrm{yr}$. Not very much is gained above that value. However, below about $T = 15\,\mathrm{yr}$, the sensitivity on important figures is significant. These results imply that a lifetime around that of the reference scenario should be targeted.

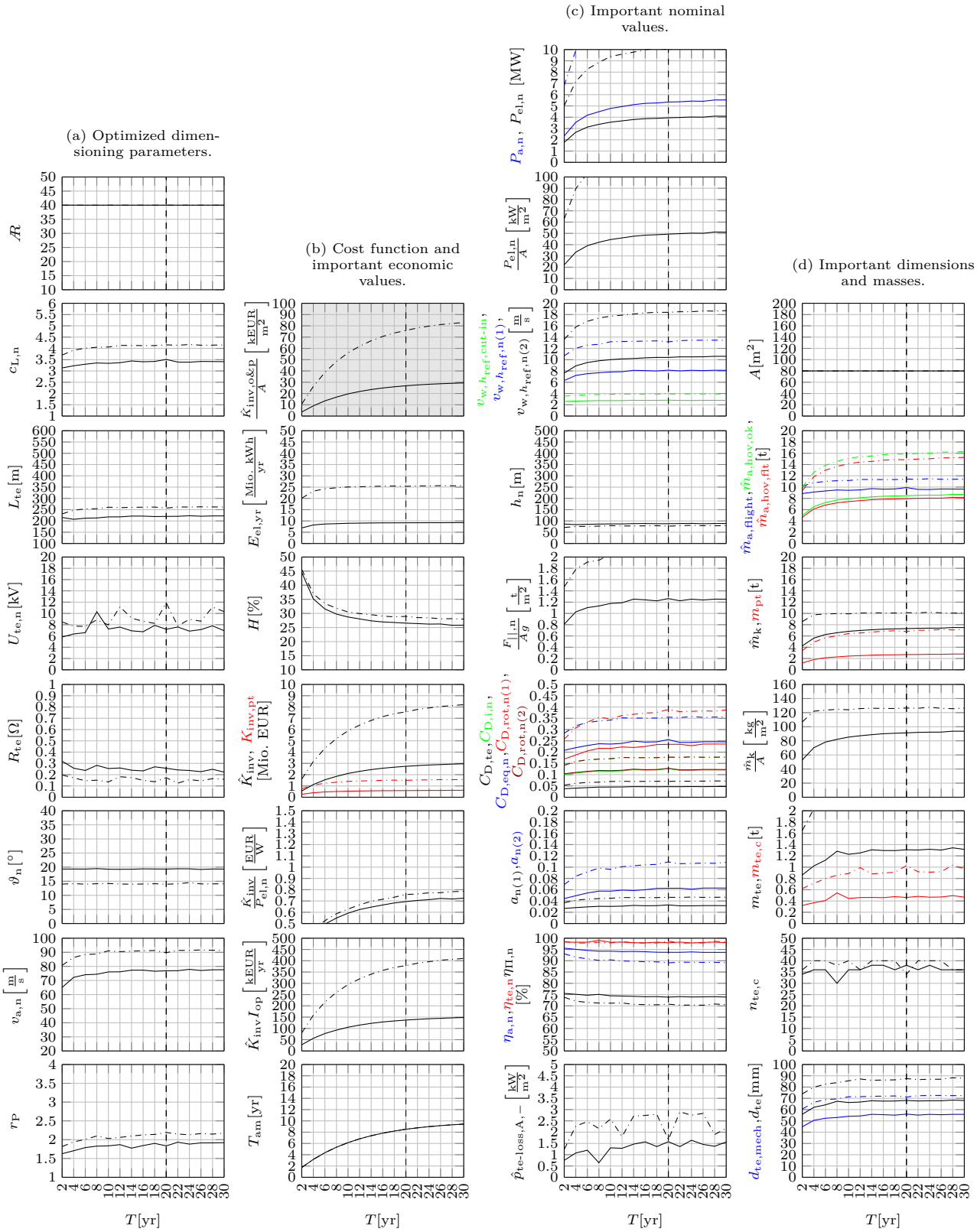

Figure 5.29: Results for different T (solid), also for the offshore variant (dash-dotted), compared to the reference scenario (dashed).

5.4.4 Operational Cost Rate

In order to reach the targeted lifetime with the many load cycles (cf. previous section), regular maintenance and overhauls might be unavoidable. In particular, the power electronics might need to be replaced every five years or so, or highly loaded parts need to be replaced due to material fatigue. How often parts need to be replaced is hard to estimate without statistics from actual for many years operating systems. Conventional wind turbines have operational cost rates around 3 %/yr, cf. [5, Tab. ES1, OpEx divided by CapEx]. In the reference scenario, $I_{\mathrm{op}} = 5\,\%/\mathrm{yr}$ was assumed, which means that the full investment price is used a second time for maintenance over a 20 year lifetime. This already sounds high, but particularly the first systems are likely not very reliable and might therefore well exceed that value. Once experience is gained and the kite power plant design is improved, the operational costs may decrease. Therefore, it is interesting to investigate the sensitivity of I_{op} on the figures of merit. Fig. 5.30 shows the results.

While the nominal powers and maximum allowed masses have only a moderate sensitivity, the maximum allowed costs have a rather high sensitivity, particularly for low operational cost rate values. This implies, that small improvements even at already low I_{op} are highly rewarded.

A further conclusion can be drawn regarding the lifetime of the kite: While in the previous study the lifetime of the power plant as a whole was investigated, one may consider a low lifetime of the kite and its regular replacement as operational costs. As it can be expected that the kite's costs are a significant portion of the total power plant investment costs, a regular kite replacement would mean a high I_{op}. Therefore, the kite should have a long life time, ideally as long as the power plant as a whole, maybe only by replacing highly loaded fatigue-prone parts. Due to the same reason, a flexible kite lift power system may be unfavorable, because such a kite lasts only a few months, see also Appendix A.

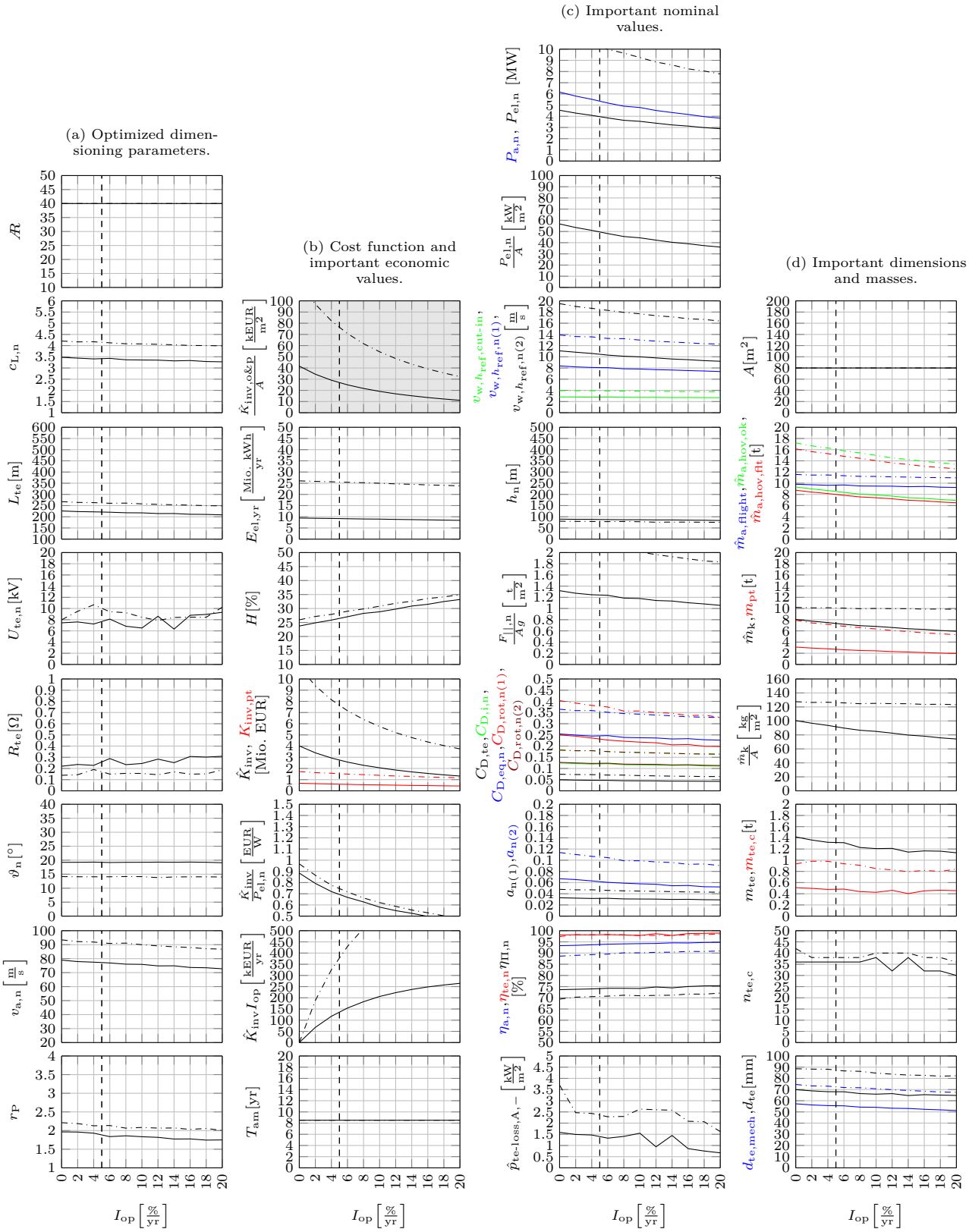

Figure 5.30: Results for different I_{op} (solid), also for the offshore variant (dash-dotted), compared to the reference scenario (dashed).

5.5 Sensitivities of Kite Aerodynamics Parameters

In the following, a sensitivity analysis of each kite aerodynamics parameter (cf. Tab. 5.1) is conducted, with the following exceptions:

- Monoplane configurations, i.e. a different number of main wings n_{mw}, were already investigated in Sect. 5.2. Other values of n_{mw} are not in scope of this dissertation (cf. Sect. 1.5).
- The sensitivity of the airfoil zero lift drag $c_{\mathrm{D},0}$ is not investigated, because it has the same effect as the drag coefficient of the remaining kite parts $C_{\mathrm{D,k,o}}$, whose sensitivity is investigated within this section.
- The minimum airfoil lift coefficient $c_{\mathrm{L,min\text{-}op}}$ and the maximum actuated drag coefficient $C_{\mathrm{D,k,a,max}}$ have only an effect on the power limitation scheme in Region III(b). In the here employed steady model, those values have neither an impact on the power plant design, nor on the energy yield and thereof dependent economic values, which is why a sensitivity analysis on those two variables is not meaningful.

5.5.1 System Scale (Wing Span)

For a novel power plant technology such as crosswind kite power and the in this study investigated drag power, the scalability of the technology is crucial, in order to first develop small power plants to validate and demonstrate the technology with low budgets and low costs of failures—which are inevitable to learn, develop, and improve the technology—, and to later scale up step-by-step to (very) large power plants, see also Appendix A. Therefore, the optimization is repeated with altered wing spans b.

To ensure a feasible maximum allowed airborne mass for a large range of b, the minimum airflow speed is set to

$$v_{\mathrm{a,min}} = \frac{v_{\mathrm{a,n}}}{2}, \tag{5.12}$$

the tower hight is set to

$$h_{\mathrm{to}} = \frac{b}{4} + 5\,\mathrm{m}, \tag{5.13}$$

with which a tailplane with a length of about a quarter of the wing span (as in Fig. 1.7) and an additional safety distance of 5 m is considered, and the minimum effective kite altitude is set to

$$\underline{h} = \max\{50\,\mathrm{m}, 1.25b\}. \tag{5.14}$$

The sensitivity is analyzed for both, the onshore utility-scale biplane and its offshore variant, because large-scale systems are predestinated for offshore sites. For the offshore variant, the same wind field parameters as in Tab. 5.6 and the higher nominal airflow speed upper bound as in (5.5) are used.

Fig. 5.31 reports the results.

The results indicate a good scalability: The maximum allowed costs per wing area, the power density, and the maximum allowed mass increase (mostly) with the system scale. This can be explained by the increase of the tether diameter and thus tether drag contribution with only the square of the nominal tether force, cf. Eqs. (2.55)–(2.59), while the power scales linearly with the force, cf. Eq. (2.22). For smaller scale systems, the wing loading decreases significantly. The airfoil lift coefficient stays almost constant at the rather high values around 3.5 to 4.0, except for

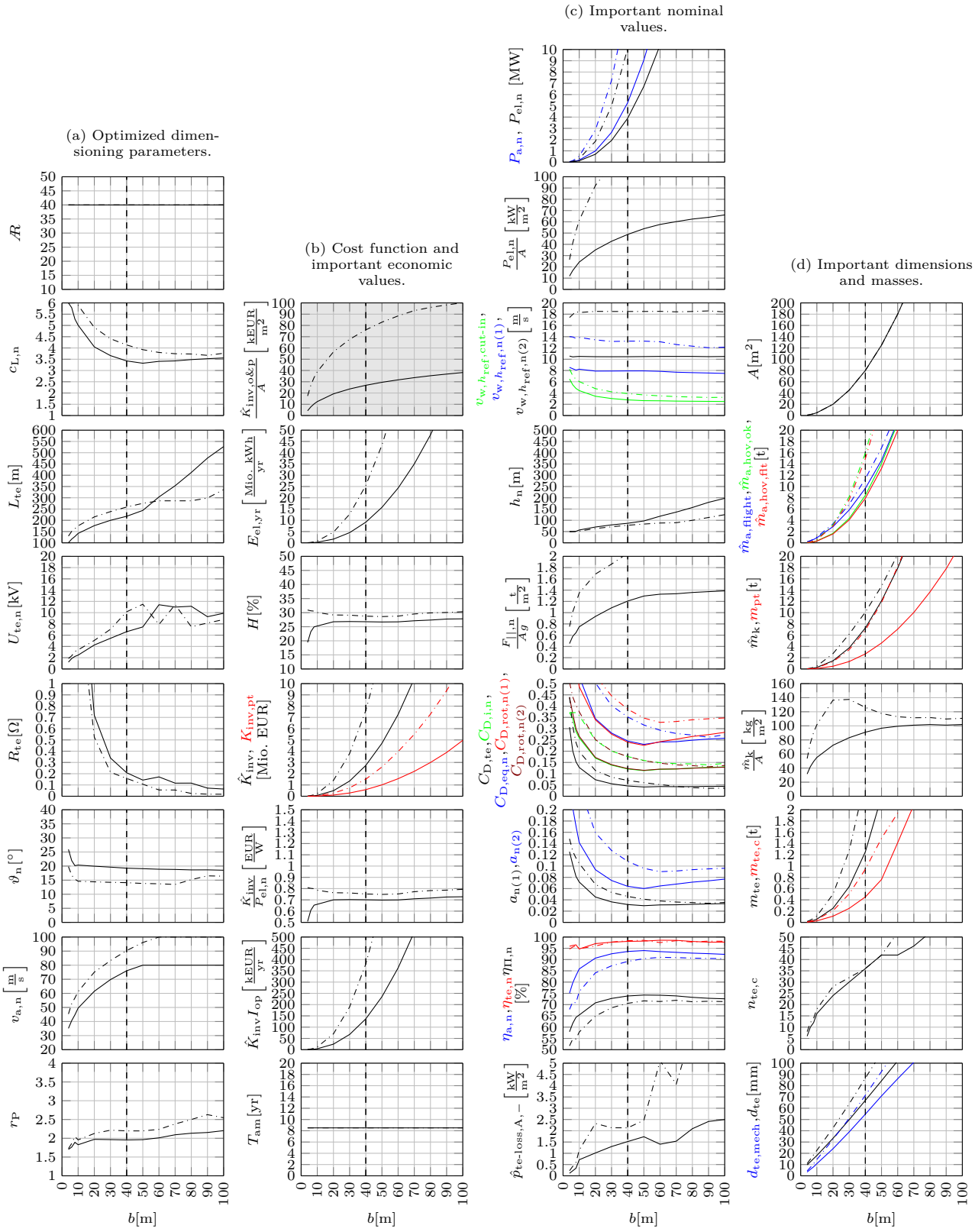

Figure 5.31: Results for different b (solid), also for the offshore variant (dash-dotted), compared to the (offshore) reference scenario (dashed).

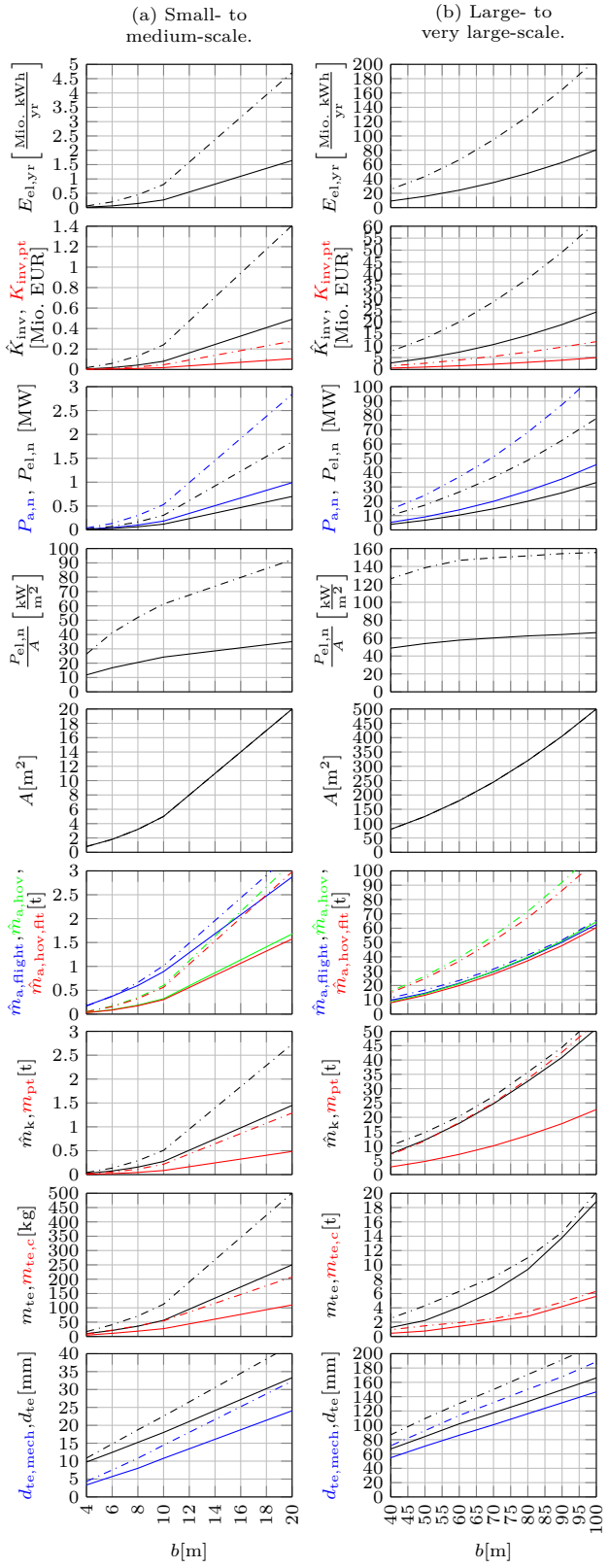

Figure 5.32: Altered axis ranges of important diagrams of Fig. 5.31 for better readability.

small-scale systems, for which it reaches the upper bound of six. The tether length remains at about five times the wing span. The effective elevation hardly changes. The optimal nominal tether voltage increases almost linearly with the wing span until $\approx 10\,\mathrm{kV}$ is reached at $\approx 50\,\mathrm{m}$ wing span.

Fig. 5.32 (a) plots again some of the most important results, but for small- to medium-scale systems, i.e. with altered axis ranges for better readability: A ten-meter wing span offshore system already has a nominal electrical power of $\approx 250\,\mathrm{kW}$. A $20\,\mathrm{m}$ wing span-version, i.e. a similar wing span as the Makani M600, already generates almost $2\,\mathrm{MW}$.

As noted above in Sect. 5.2, a $40\,\mathrm{m}$ wing span kite achieves already about 4 to $10\,\mathrm{MW}$ nominal electrical power (depending if onshore or offshore version) which clearly can already be considered as large-scale or utility-scale, because this is in the power range of large utility-scale conventional wind turbines. The larger investigated wing spans achieve even much higher nominal powers, which are literally off the charts in Fig. 5.31. Therefore, Fig. 5.32 (b) plots again some of the important results for $b \geq 40\,\mathrm{m}$ with altered axis ranges. It should, however, be noted, that $b = 80\,\mathrm{m}$ is the wing span of an Airbus A380. There are even much larger aircraft in terms of wing span: Just recently, on April 13, 2019, the Stratolaunch took off for the first time, which, with $b = 117\,\mathrm{m}$, is the largest aircraft ever flown [163, 164]. With the wing span of $b = 100\,\mathrm{m}$, the offshore system has a nominal electrical power of $\approx 80\,\mathrm{MW}$. Although such a huge kite seems unrealistic in the near future (and might be also a suboptimal size considering much more details such as manufacturing, transportation, testing, etc.), the numbers indicate a great potential of the technology. A more realistic very large-scale wing span can be estimated in the magnitude of about $60\,\mathrm{m}$, which is similar to the wing span of a blade of the largest today commercially available conventional wind turbine, the Enercon E126 with $7.5\,\mathrm{MW}$, and which is also similar to Makani's M5 system with $5\,\mathrm{MW}$ (cf. Tab. 3.7 or [102]). However, with the here proposed biplane drag power kite and the here conducted optimizations (with the accuracy of the employed model), a kite with $60\,\mathrm{m}$ wing span reaches the much higher nominal power of $\approx 10\,\mathrm{MW}$ for the onshore system and well over $20\,\mathrm{MW}$ for the offshore variant.

5.5.2 Aspect Ratio

In virtually all previous parameter studies, the aspect ratio was at its upper bound. In the reference scenario, $\overline{\text{Æ}} = 40$ was estimated realizable. High-efficient gliders reach up to about $\text{Æ} = 50$ [165], while Makani's M600 has a little more than $\text{Æ} = 30$ [102]. Considering that high wing loadings have to be sustained, but a biplane is considered, $\text{Æ} = 40$ seems not unreasonable, and maybe even a higher value is reachable. The actual reachable value, or the optimum in a higher fidelity model which resolves the kite's structure, is not known. Therefore, a sensitivity analysis for a vast range of $\overline{\text{Æ}}$ is conducted. Here, only the upper bound $\overline{\text{Æ}}$ is changed, to see if there is an optimal Æ below that upper bound for high $\overline{\text{Æ}}$. For this study, the minimum operational airfoil lift coefficient is set to

$$c_{\mathrm{L,min\text{-}op}} = 0 \tag{5.15}$$

to always ensure feasibility (2.277), because it can be expected, that a low $c_{\mathrm{L,n}}$ is optimal for low Æ. Note that this only has an effect on the actuations of the power limitation in power curve Region III(b). Fig. 5.33 shows the results.

The optimal aspect ratio is always at the upper bound, $\text{Æ} = \overline{\text{Æ}}$. The important figure of merit $\hat{K}_{\mathrm{inv,o\&p}}/A$ is rather sensitive on Æ. The nominal powers have only a moderate sensitivity, which however increases for lower Æ. This is because the kite area A increases with decreasing Æ and therefore $P_{\mathrm{el,n}}/A$ decreases significantly for low Æ. Similarly, the maximum allowed masses increase for low Æ, but w.r.t. to the area decrease significantly, cf. e.g. $\hat{m}_{\mathrm{k}}/A$. All these results imply that Æ should be rather high.

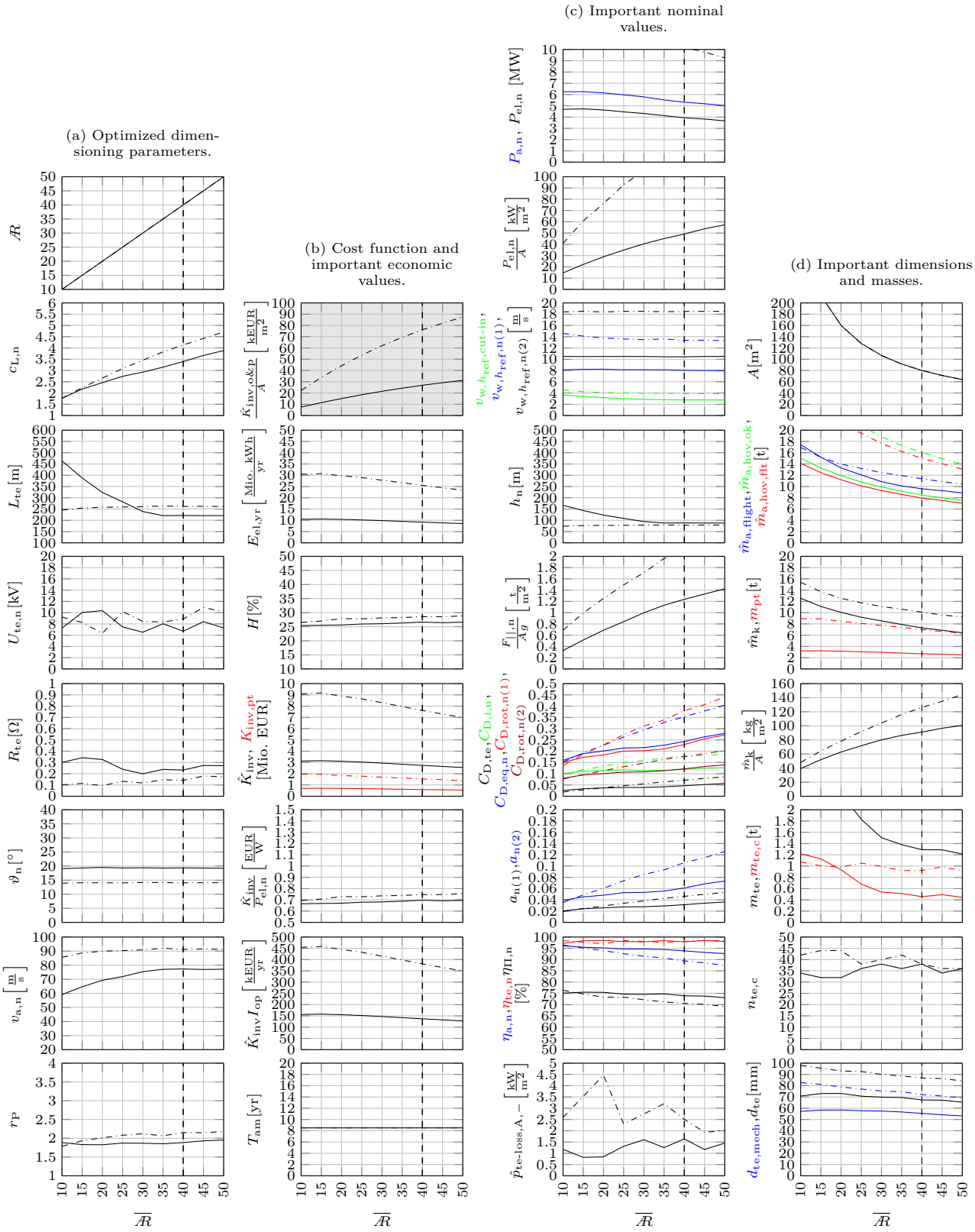

Figure 5.33: Results for different $\mathcal{AR}$ (solid), also for the offshore variant (dash-dotted), compared to the reference scenario (dashed).

5.5.3 Airfoil Quadratic Drag Slope

For the airfoil's quadratic drag slope, $c_{\mathrm{D},2} = 0.005$ was estimated in the reference scenario, which is in good accordance to actual airfoils as visible in Fig. 2.5. In fact, with optimizations and higher Reynolds numbers, even lower values could be expected, cf. Fig. 2.5. However, for lower Reynolds numbers or deteriorated wings e.g. due to dirt accumulation over time, the value can get worse. Therefore, it is interesting to investigate the figures of merits for other $c_{\mathrm{D},2}$. Fig. 5.34 visualizes the results.

A rather high sensitivity of $c_{\mathrm{D},2}$ on the important figures of merit of maximum allowed costs, nominal power, and maximum allowed mass is visible. This implies that airfoil optimizations are meaningful and very rewarding.

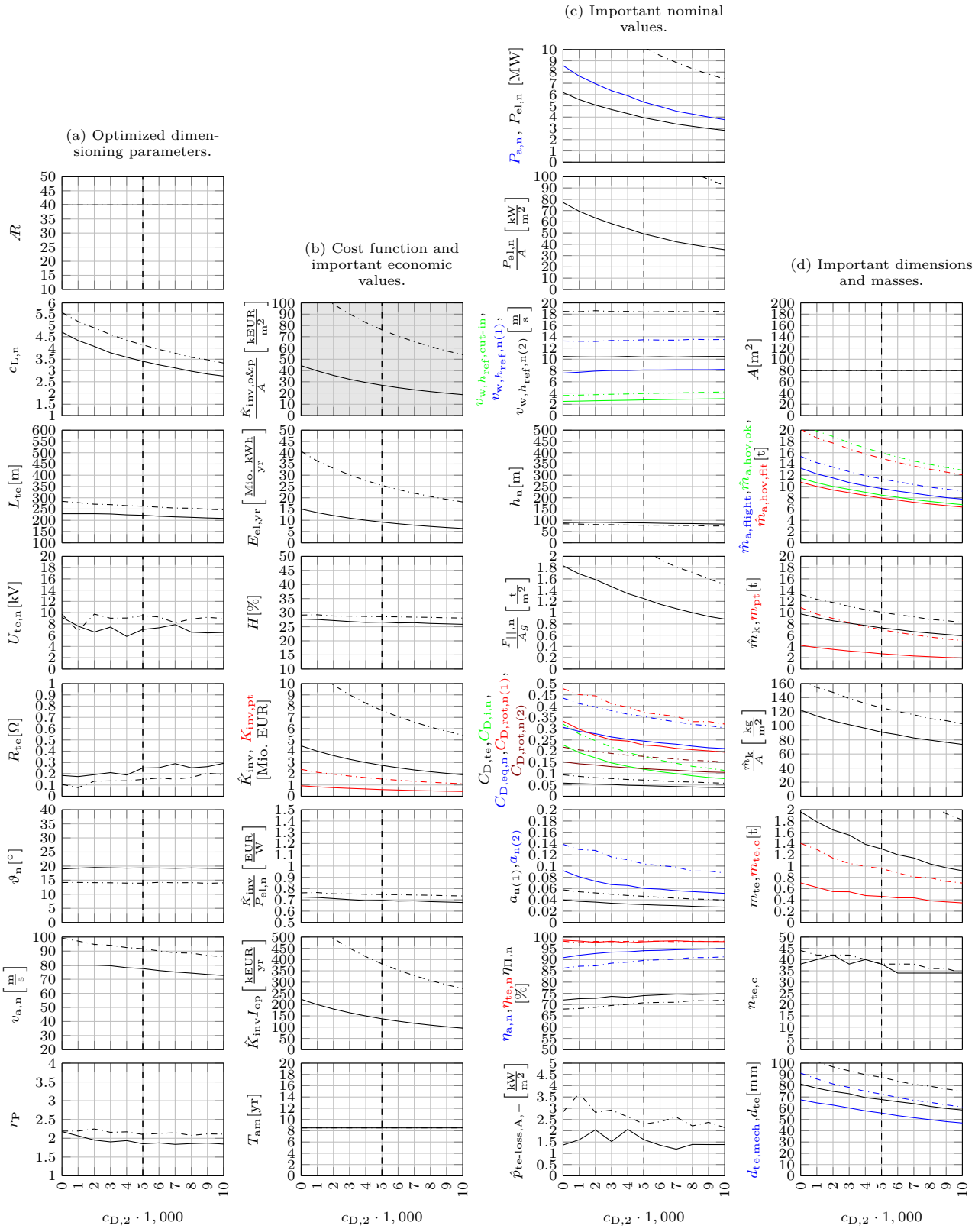

Figure 5.34: Results for different $c_{\mathrm{D},2}$ (solid), also for the offshore variant (dash-dotted), compared to the reference scenario (dashed).

5.5.4 Nominal Airfoil Lift Coefficient

In [110], it was shown that the optimal airfoil lift coefficient of a drag power kite tends to be close to the maximum physically achievable airfoil lift coefficient. The reference scenario biplane kite also has a very high airfoil lift coefficient of ≈ 3.4 as optimum and its offshore variant has even ≈ 4.4 as optimum. Yet, many kite power researchers and developers consider single element airfoils with rather low airfoil lift coefficients, although some conclude, that the maximum airfoil lift coefficient is an important parameter to design for (cf. Sect. 1.2). To investigate the effects of suboptimal airfoil lift coefficients, the optimization is repeated, but with altered bounds for the airfoil lift coefficient $c_{\mathrm{L,n}} = \underline{c}_{\mathrm{L,n}} = \overline{c}_{\mathrm{L,n}}$. Moreover, the minimum operational airfoil lift coefficient is set to

$$c_{\mathrm{L,min\text{-}op}} = 0 \tag{5.16}$$

to ensure feasibility (2.277) also for low $c_{\mathrm{L,n}}$. Note that this only has an effect on the actuations of the power limitation in power curve Region III(b). Fig. 5.35 plots the results.

In the range of $c_{\mathrm{L,n}} \approx 3 \ldots 5$, the maximum allowed costs, nominal power, and maximum allowed kite mass change only by a few percent. However, for $c_{\mathrm{L,n}} < 3$, these figures of merit decrease dramatically, and at $c_{\mathrm{L,n}} = 1.5$, which is the typical maximum lift coefficient for a single element airfoil, those figures of merit are only about half of the value compared to the (optimal) reference scenario. The only benefits of smaller lift coefficients are (i) the reduced wing loading, which simplifies the airframe design and may allow also high aspect ratio monoplane kites, and (ii) a reduced drag, with which also the first nominal wind speed is low. However, as motivated in [110], the research and development costs can be expected to increase with the size of the kite. If the kite is small and yet already has a high nominal power and thus high power density, the return on investment, in particular also for the research and development, is also high.

It should be noted that the tether length was not reduced below $\approx 200 \ldots 250\,\mathrm{m}$ for low lift coefficients, because of the maximum angular speed constraint (not shown).

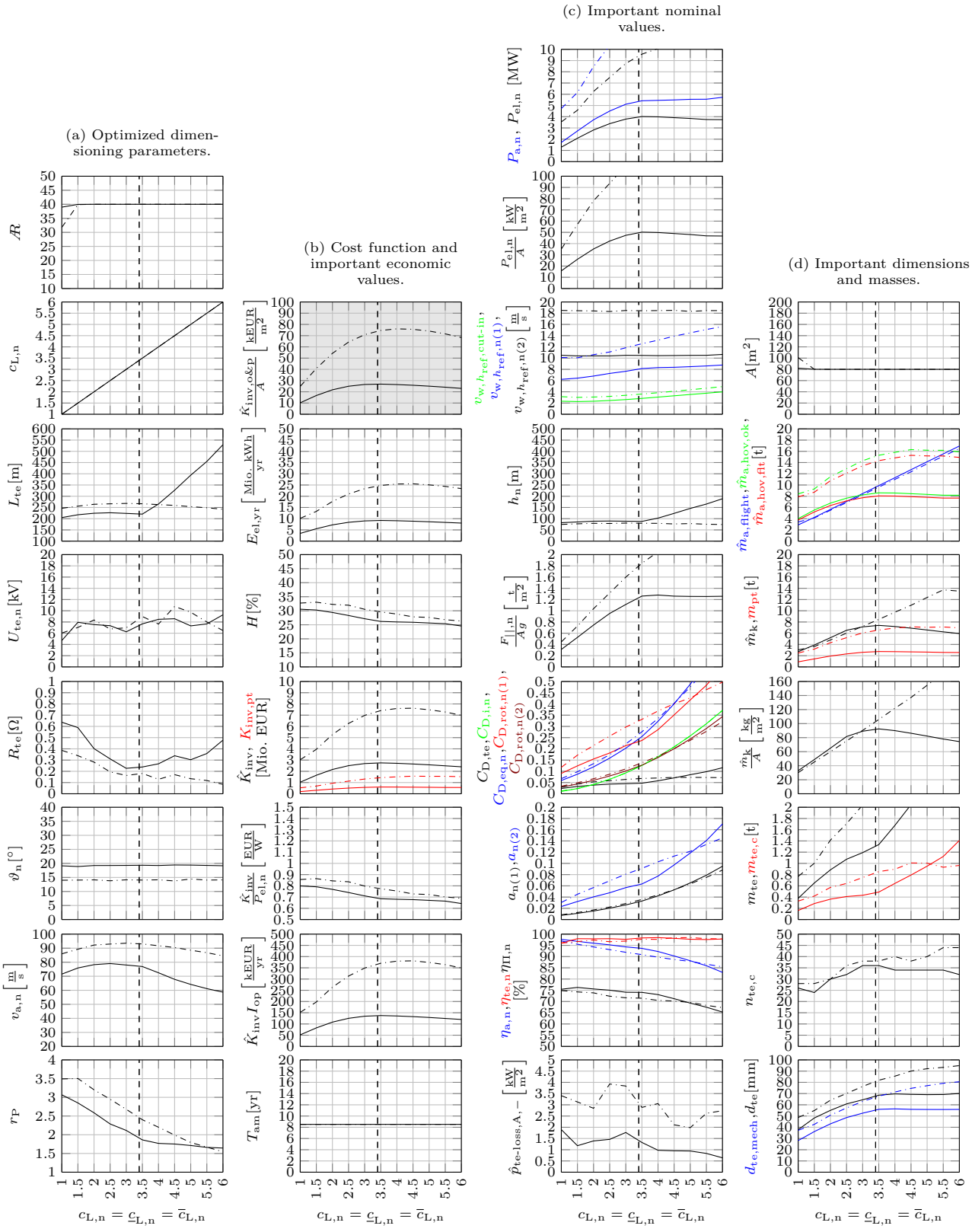

Figure 5.35: Results for different $c_{\mathrm{L,n}}$ (solid), also for the offshore variant (dash-dotted), compared to the reference scenario (dashed). This figure was shown in the prior work by the author of this dissertation in [111, Poster, Fig. 5].

5.5.5 Span Efficiency Factor

Assumption 2.11, without an adaptation of the span efficiency factor e compared to a monoplane wing, might be an over-simplification as stated in Remark 2.1, i.e. the wings of the biplane as well as vertical wings and the tailplane (and also struts, bracing, fuselage, etc.) might interfere aerodynamically. This can lead to a reduced lift (already investigated in the previous section), a reduced span efficiency factor e (investigated here), and/or an increased drag (investigated below, in the next section). In addition to that, it is hard to estimate e and there exist many competing approximations, cf. [116, 166] and references therein. Therefore, Fig. 5.36 shows the optimization results for altered e.

Virtually all figures of merit are very sensitive on e. For the offshore variant, the sensitivity (dash-dotted) is even higher due to the higher nominal lift coefficient. This implies that an airframe design and optimization towards a very high e can be expected to be very rewarding. This particularly includes to use a large enough gap between biplane wings, a box-wing (i.e. vertical wings to connect the two wing tips of the biplane wings), an elliptical lift distribution, winglets, or/and rotors at the wing tips to reduce the wing tip vortexes.

It should be noted that even for the very bad $e = 0.4$, the optimal nominal airfoil lift coefficient remains above 2.5 for the onshore variant and above three for the offshore variant, both not reachable by single element airfoils, cf. e.g. [61, 167].

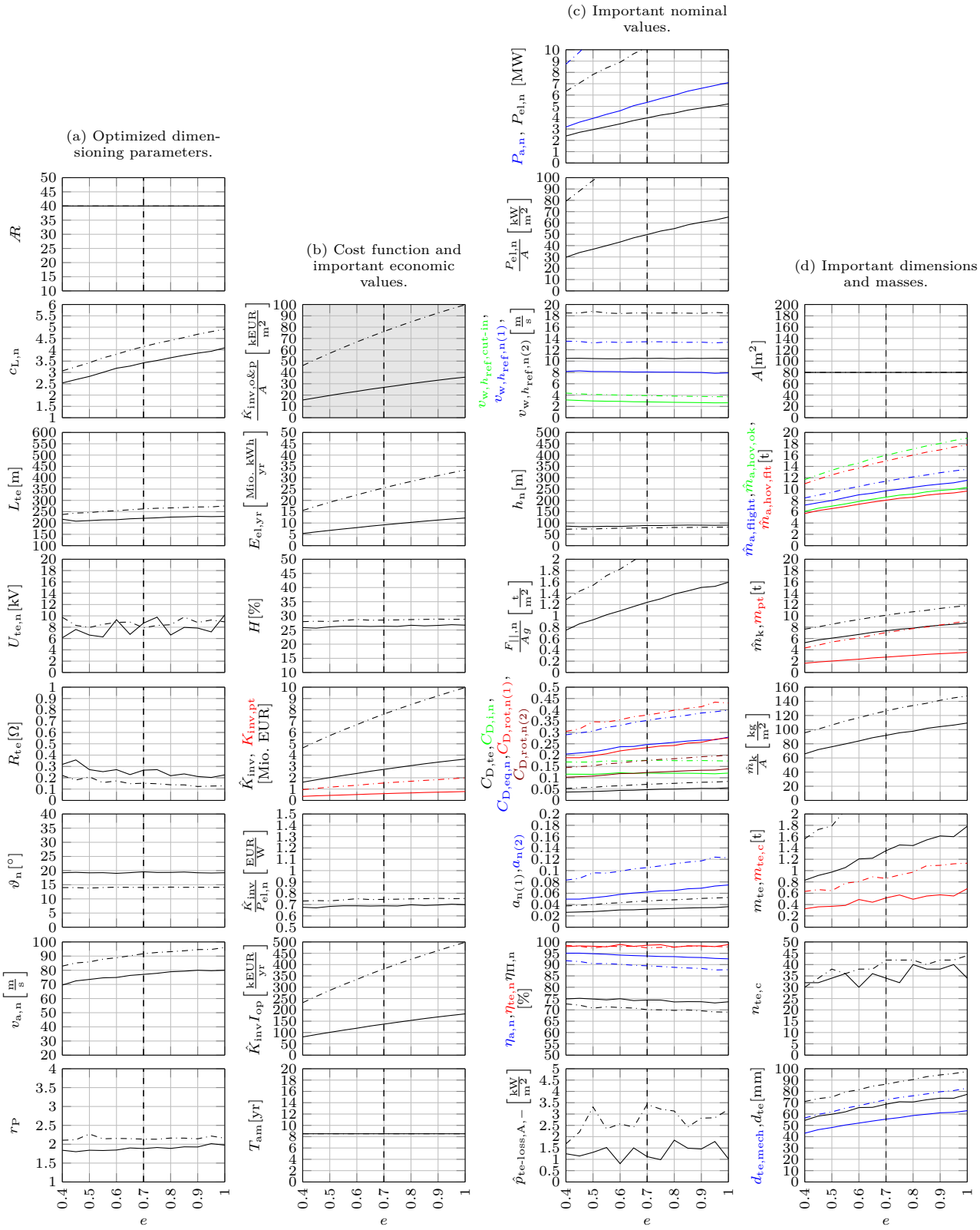

Figure 5.36: Results for different e (solid), also for the offshore variant (dash-dotted), compared to the reference scenario (dashed).

5.5.6 Drag of Other Parts

As stated in the previous section, the aerodynamic interference of the kite's components (particularly biplane wings, struts, bracing, vertical wings) might not be negligible, which can also lead to a higher drag. Therefore, Fig. 5.37 shows the optimization results for altered $C_{\mathrm{D,k,o}}$.

The sensitivity on virtually all figures of merit is again very high. This implies that an airframe design and optimization towards a very low $C_{\mathrm{D,k,o}}$ can be expected to be very rewarding. This includes again to obtain a low aerodynamic interference between the kite parts as well as aerodynamically shaped (i.e. with a low drag) struts, vertical wings (to connect the biplane wings), bracing wires, and fuselage.

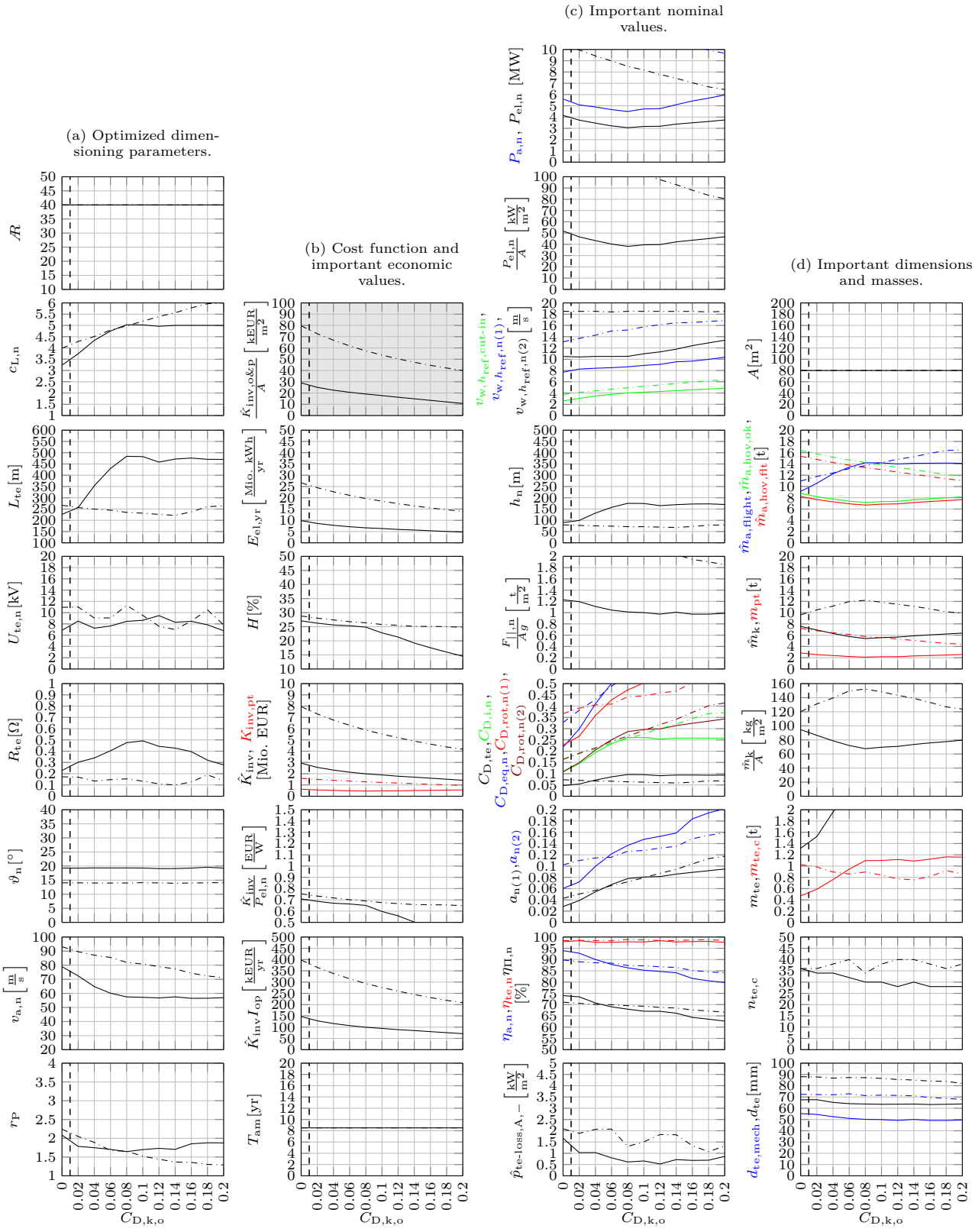

Figure 5.37: Results for different $C_{\mathrm{D,k,o}}$ (solid), also for the offshore variant (dash-dotted), compared to the reference scenario (dashed).

5.6 Sensitivities of Rotor Parameters

In the following, a sensitivity analysis of each rotor parameter (cf. Tab. 5.1) is conducted, with the following exceptions:

- The consumptive rotor efficiency $\eta_{\mathrm{rot},-}$ applies only for Region I(a) in which the kite would be grounded. Therefore, $\eta_{\mathrm{rot},-}$ has neither an impact on the energy yield and thereof dependent economic values, nor on the power plant design.
- The hovering rotor efficiency $\eta_{\mathrm{rot,hov}}$ applies only to hovering and therefore has also no impact on the energy yield and thereof dependent economic values. It only has an impact on the maximum allowed hovering masses, which scales with $\hat{m}_{\mathrm{a,hov}} \sim \eta_{\mathrm{rot,hov}}^{3/2}$, cf. Eqs. (2.322) and (2.325) (and their derivations).

5.6.1 Number of Rotors

As introduced in Sect. 2.4.2, a certain number of rotors is required to ensure some level of fault tolerance, and the higher the number is, the lower is the required hovering power during a rotor failure or, vice versa, the higher is the maximum allowed hovering mass during a rotor failure. Fig. 5.38 shows the results for different n_{rot} highlighting this effect: With $n_{\mathrm{rot}} = 6$, the maximum allowed airborne mass during hovering with rotor failure is reduced to $\hat{m}_{\mathrm{a,hov,flt}} \approx 7\,\mathrm{t}$ compared to $\hat{m}_{\mathrm{a,hov,flt}} \approx 8\,\mathrm{t}$ in the reference scenario. For the offshore system, the drop is even more significant from $\hat{m}_{\mathrm{a,hov,flt}} \approx 15\,\mathrm{t}$ to $\hat{m}_{\mathrm{a,hov,flt}} \approx 13.5\,\mathrm{t}$. In the here employed model, the number of rotors has no effect on any other result. However, in a higher fidelity model which resolves the machine torques, a similar sensitivity can be expected (cf. Appendix D), because the lower the number of rotors is, the larger is their diameter to achieve the same total rotor area. The larger the diameter, the slower must the rotational speed be in order to limit the rotor blade tip speed. Both effects, larger diameter and lower rotational speed, increase the nominal machine torque required to maintain the same nominal power. As the size and mass of electrical machines scale with their nominal torque (not their nominal power), a higher number of rotors tend to decrease the overall machine mass. Nevertheless, the higher the number of rotors, the higher is the system complexity and one can expect that the maintenance costs increase with n_{rot}. In future studies with higher fidelity kite power plant systems engineering models, n_{rot} may be an optimization parameter. From the results of Fig. 5.38, one can expect an optimal number of rotors around $n_{\mathrm{rot}} = 8$ to $n_{\mathrm{rot}} = 12$.

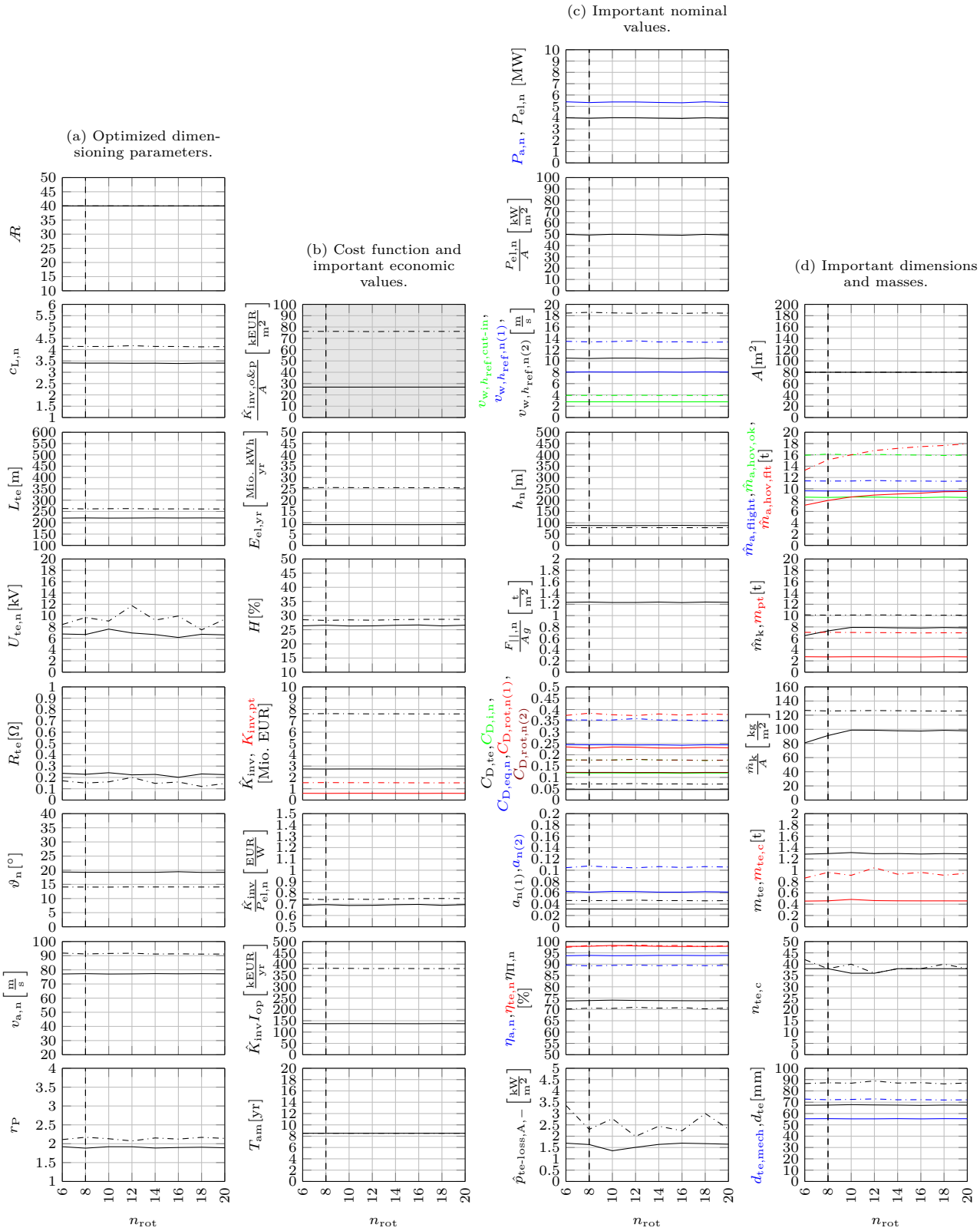

Figure 5.38: Results for different n_{rot} (solid), also for the offshore variant (dash-dotted), compared to the reference scenario (dashed).

5.6.2 Rotor Area Ratio

In Fig. 1.7 and for the parameters of the utility-scale biplane kite reference scenario, the total rotor disk area is identical to the total wing area, i.e. the rotor area ratio is $r_{\mathrm{rot}} = 1$. However, it is interesting to investigate how the results change for changed r_{rot}, particularly for the offshore variant which suffers from high actuator disc efficiency losses. Therefore, the optimization is repeated with altered r_{rot}. Fig. 5.39 plots the results.

For increased r_{rot}, the results do not change that significantly, however for reduced r_{rot}, the performance becomes significantly worse. The baseline value $r_{\mathrm{rot}} = 1$ might already be a good trade-off (when considering that a larger rotor area requires a higher nominal torque and thus larger electrical machines). The maximum allowed mass decreases significantly for $r_{\mathrm{rot}} < 1$ due to the high disc loading during hovering, but does not increase much further for $r_{\mathrm{rot}} > 1$, because the minimum airflow speed is left constant, which in turn defines the maximum allowed mass during crosswind flight. The difference between the onshore and offshore variants is mainly that those effects are more significant for the latter.

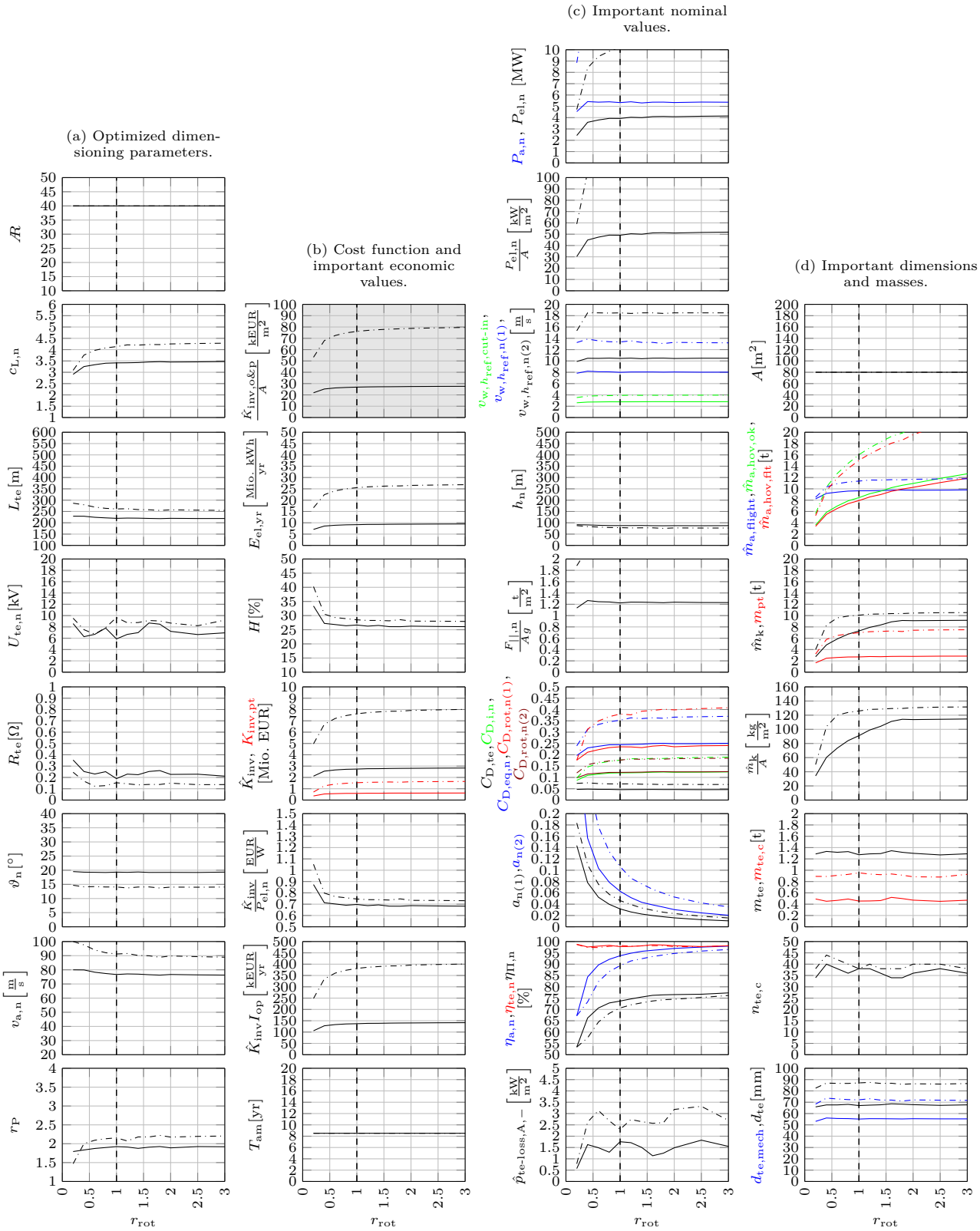

Figure 5.39: Results for different r_{rot} (solid), also for the offshore variant (dash-dotted), compared to the reference scenario (dashed).

5.6.3 Generative Rotor Efficiency

The generative rotor efficiency was estimated with $\eta_{\mathrm{rot},+} = 90\,\%$ in the reference scenario. Moreover, further efficiency factors were estimated to some value. In a realized system, those values might be different. Particularly a good $\eta_{\mathrm{rot},+}$ does not seem too easy to obtain, because the rotors must not only function as wind turbines, but also as propellers for hovering. This is why it is interesting to investigate the sensitivities of the figures of merit on $\eta_{\mathrm{rot},+}$. Fig. 5.40 reports the results.

The important values, maximum allowed costs, nominal electrical power, and maximum allowed kite mass, depend linearly on $\eta_{\mathrm{rot},+}$ with a significant but moderate sensitivity, while the nominal aerodynamic power has almost no sensitivity on $\eta_{\mathrm{rot},+}$. This corresponds with the expectations from the equations, because

$$P_{\mathrm{el,n}}, E_{\mathrm{el,yr}}, \hat{K}_{\mathrm{inv,o\&p}}/A, ... \sim \eta_{\mathrm{rot},+} P_{\mathrm{a,n}}. \tag{5.17}$$

Every percent increase of a generative efficiency factor, roughly gives a percent increase for the important figures of merit, including $\hat{K}_{\mathrm{inv,o\&p}}/A$.

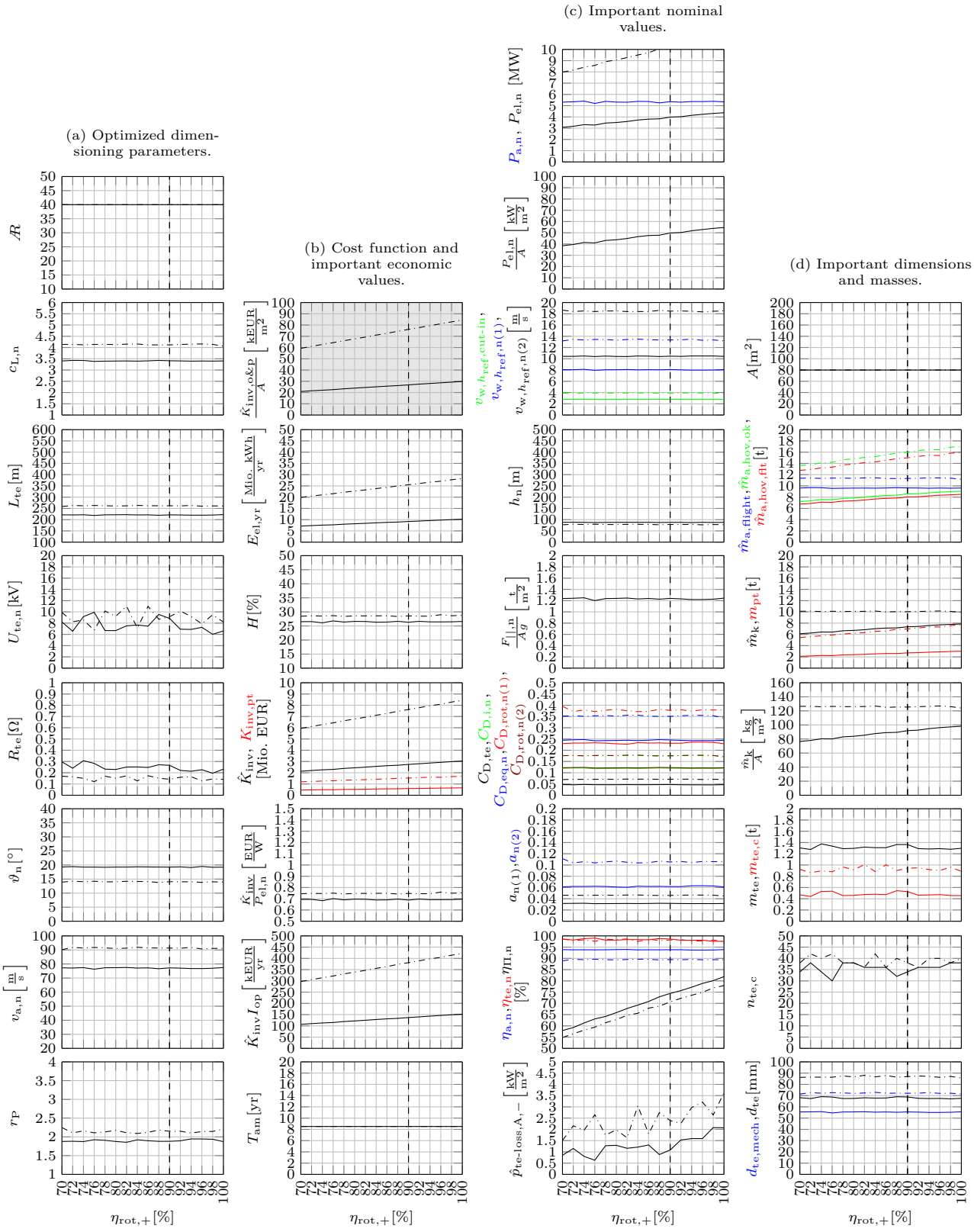

Figure 5.40: Results for different $\eta_{\mathrm{rot},+}$ (solid), also for the offshore variant (dash-dotted), compared to the reference scenario (dashed).

5.7 Sensitivities of Tether Parameters

In the following, a sensitivity analysis of each tether parameter (cf. Tab. 5.1) is conducted, with the following exceptions:

- Changing directly the tether length L_{te} from its optimum is not meaningful. It is only meaningful to investigate the sensitivity of L_{te}-dependent values such as changes of the nominal altitude bound $\underline{h}_{\mathrm{n}}$ or of the nominal angular speed bound $\overline{\omega}_{\mathrm{n}}$. Those are investigated elsewhere, below in Sect. 5.11.
- Similarly, changing directly the tether resistance R_{te} from its optimum is not meaningful. It is only meaningful to investigate the sensitivity of R_{te}-dependent values such as the specific tether power loss bound. Also that is investigated elsewhere, e.g. below in Sect. 5.11.
- A sensitivity analysis of the tether mass contribution factor $f_{\text{m-te}}$ is not interesting, as it has only a linear impact on the maximum allowed kite mass $\hat{m}_{\mathrm{k}}$ in the here employed model.
- The tether material properties can hardly be altered. Only the materials themselves can be altered. Therefore, only a number of different tether materials and there combinations are investigated, instead of varying the values $\rho_{\mathrm{te,mech}}$, $\sigma_{\mathrm{te,mech}}$, $\rho_{\mathrm{te,c,w}}$, $\kappa_{\mathrm{te,c,w}}$, $\rho_{\mathrm{te,ins}}$, and $E_{\mathrm{te,ins}}$ individually.
- For a similar reason, the sensitivities of the values $\rho_{\mathrm{te,c,sh}}$, $\rho_{\mathrm{te,c,j}}$, and $\rho_{\mathrm{te,j}}$, respectively the corresponding materials, are also not investigated.
- Likely no other shield width than the standard value $w_{\mathrm{te,c,sh}} = 0.1\,\mathrm{mm}$ will be chosen. Moreover, the impact of changes of the shield width and jacket widths, $w_{\mathrm{te,c,j}}$ and $w_{\mathrm{te,j}}$, can be expected to have a similar impact. Therefore, a sensitivity analysis only for $w_{\mathrm{te,c,j}}$ is conducted.
- As the tether dielectric strength (or insulation) safety factor $S_{\mathrm{te,ins}}$ and the insulation correction factor $f_{\mathrm{te,ins}}$ are both factors in the design insulation voltage equation (2.78), the sensitivity of only one of them needs to be investigated. Here, $S_{\mathrm{te,ins}}$ is chosen.
- The tether mass correction factors $f_{\mathrm{te,m},i}$ have only a linear impact on the tether mass, but not on the power curve or economic performance (in the here employed steady model). Therefore, sensitivity analyses of $f_{\mathrm{te,m},i}$ are not meaningful.

5.7.1 Nominal Tether Voltage

The optimal nominal tether voltage is relatively high in the order of 8 kV as already found by Kolar et al. [81]. The development of the powertrain can be complex and costly, and a high voltage is generally dangerous. Therefore, it is interesting to investigate how much the performance changes if another nominal tether voltage is chosen. Fig. 5.41 plots the results in solid.

The most important figures of merit, like costs, nominal powers, or maximum allowed kite mass, are very insensitive to the changes of the voltage. Even a nominal tether voltage of only 2 kV has almost no negative effects. The most significant effect at this low voltage is the more than doubled specific tether power loss, which might lead to infeasible temperatures of the tether.

Therefore, changed nominal voltages are also investigated with the additional constraint that the maximum specific tether power loss is limited to the value of the reference scenario. The results are also plotted in Fig. 5.41 in dash-dotted.

Obviously, to keep the tether power loss limited, the optimizer increases the conductors' cross section area. Yet the sensitivity is still low and almost identical as without a specific tether power loss constraint, and still even a nominal tether voltage of only 2 kV has almost no negative effects.

This is an unexpected and astonishing result: A transmission voltage in the order of 2 kV or a bit higher is relatively easily and economically possible with today's available power electronic components. There may also be no need for complex, costly, and heavy DC-DC converters (with their additional efficiency losses) as developed by Kolar et al. [81–83, 85, 86]. Instead, machines and machine converters designed for this voltage seem to be the better option. Concluding, a good trade-off between system figures of merit and low complexity and costs of the powertrain might be at $U_{\mathrm{te,n}} = 2 \ldots 4\,\mathrm{kV}$, which is also used for the Makani M600, cf. Tab. 3.5.

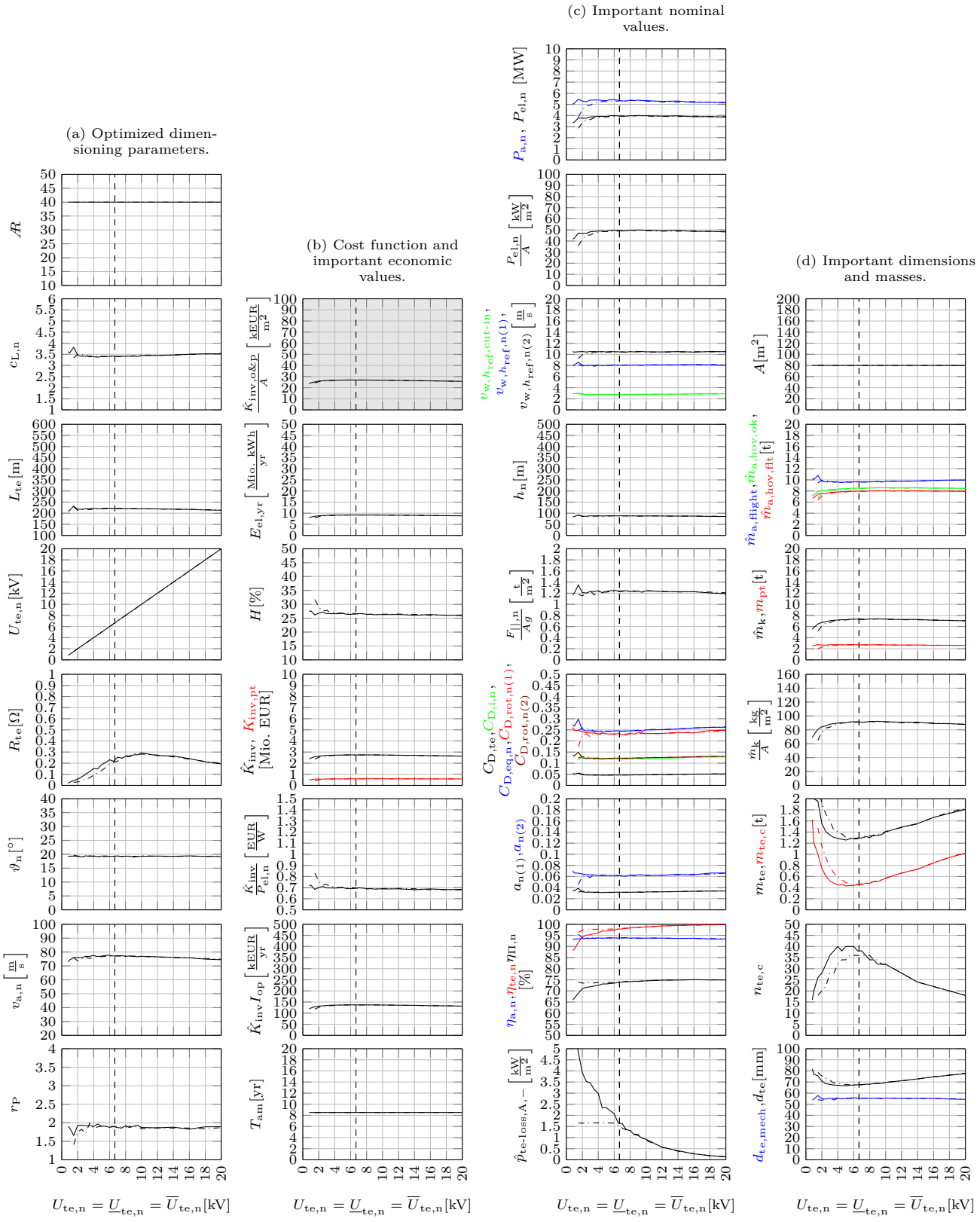

Figure 5.41: Results for different $U_{\mathrm{te,n}}$ (solid), also with constraint of $\hat{p}_{\mathrm{te\text{-}loss,A,-}}$ at the value of the reference scenario (dash-dotted), compared to the reference scenario (dashed).

5.7.2 Tether Shape Drag Coefficient

In Remark 2.2 it was highlighted that the drag coefficient of the tether's cross section shape $c_{\mathrm{D,te}}$ actually is a function of the Reynolds number N_{Re} and has a drop around $N_{\mathrm{Re}} = 3 \cdot 10^5$ down to $c_{\mathrm{D,te}} \approx 0.1$. With a rough tether surface, this drop is shifted to lower N_{Re}. Therefore, a significant part of the tether might have a very low drag coefficient, which reduces the effective $c_{\mathrm{D,te}}$ used in the tether drag model (see also Remark 2.2). Moreover, $c_{\mathrm{D,te}}$ could be improved with a more aerodynamically shaped tether cross section or with a fairing. Therefore, it is interesting to investigate the results for altered $c_{\mathrm{D,te}}$. Fig. 5.42 visualizes the results for the onshore variant (solid) and for the offshore variant (dash-dotted).

Many values and the important figures of merit such as maximum allowed costs and nominal power are quite sensitive on $c_{\mathrm{D,te}}$. Interestingly, for the onshore variant, the (total) tether drag coefficient $C_{\mathrm{D,te}}$ hardly changes, because the optimizer increases the tether length for lower $c_{\mathrm{D,te}}$ to tap stronger winds in higher altitudes. Only for the offshore system (dash-dotted), the tether length is hardly increased until $c_{\mathrm{D,te}} \lesssim 0.2$. This is explainable by the low offshore wind shear, with which the wind speed hardly increases with the altitude. Another interesting result is that the optimal airfoil lift coefficient remains at its rather high value, even for very low $c_{\mathrm{D,te}}$.

From these results, it can be concluded that improvements of $c_{\mathrm{D,te}}$ can be rewarding, in particular if the tether surface just needs to be made a bit rougher.

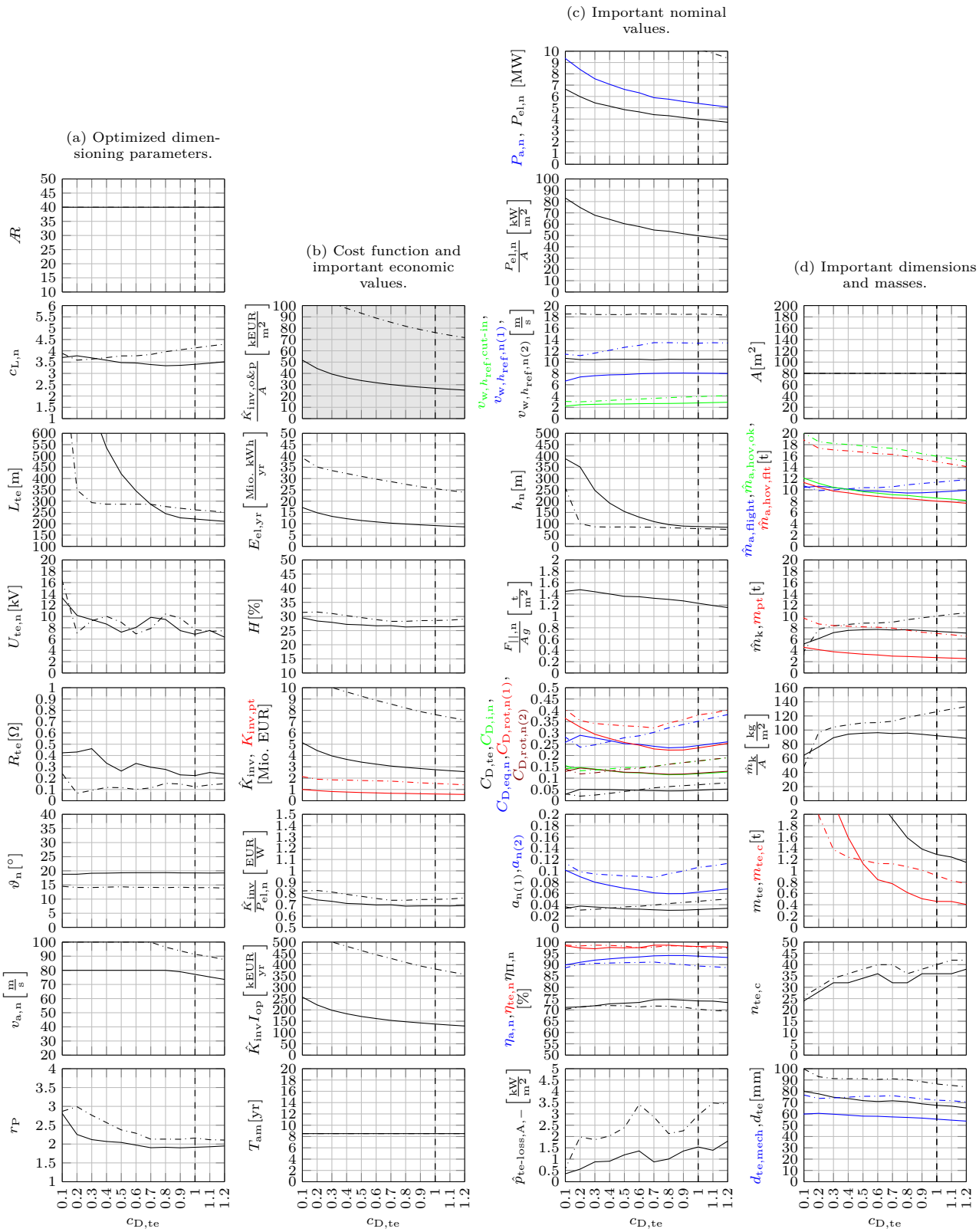

Figure 5.42: Results for different $c_{\mathrm{D,te}}$ (solid), also for the offshore variant (dash-dotted), compared to the reference scenario (dashed).

5.7.3 Number of Electrical Cables in Tether

In all previous optimizations, the number of electrical cables was maximized "internally" for a given $d_{\mathrm{te,mech}}$, R_{te}, and $U_{\mathrm{te,n}}$, such that the total tether diameter was minimized. However, there is only little room for communication cables, see e.g. Fig. 5.2. Moreover, to increase the thermal conductivity of the tether and thus the heat transfer from the wires (ohmic power losses) towards the ambience, it might be meaningful to increase the tether's surface area by having a smaller number of electrical cables in the tether, i.e. possibly large gaps between electrical cables, and to shrink the tether jacket into those gaps towards the core. Such a concept would also increase the roughness of the tether and might shift the $c_{\mathrm{D,te}}$-drop to operation Reynolds numbers (cf. Remark 2.2 and previous section). Another motivation to select or constrain the number of electrical cables is the fault tolerance concept proposed in the prior work [106] by the author of this dissertation. Therefore, the optimization is repeated for different forced numbers of electrical cables in the tether $n_{\mathrm{te,c}}$. Fig. 5.43 plots the results.

All important figures are very insensitive for a reduced $n_{\mathrm{te,c}}$. From these results, it can particularly be confirmed that only a negligible impact on the system performance is expectable if the fault tolerance concept [106] is used.[41]

[41] Note that the fault tolerance concept of [106] provides a powertrain with no single point of failure and can therefore guarantee that at least $n_{\mathrm{rot}} - 2$ rotors stay available in motor mode with which a normal multicopter landing is always possible, even if there is a short circuit in the tether. As such a high fault tolerance is a paramount requirement for a commercial system and therefore highly desirable, at least slight deteriorated performance figures could actually have been tolerated.

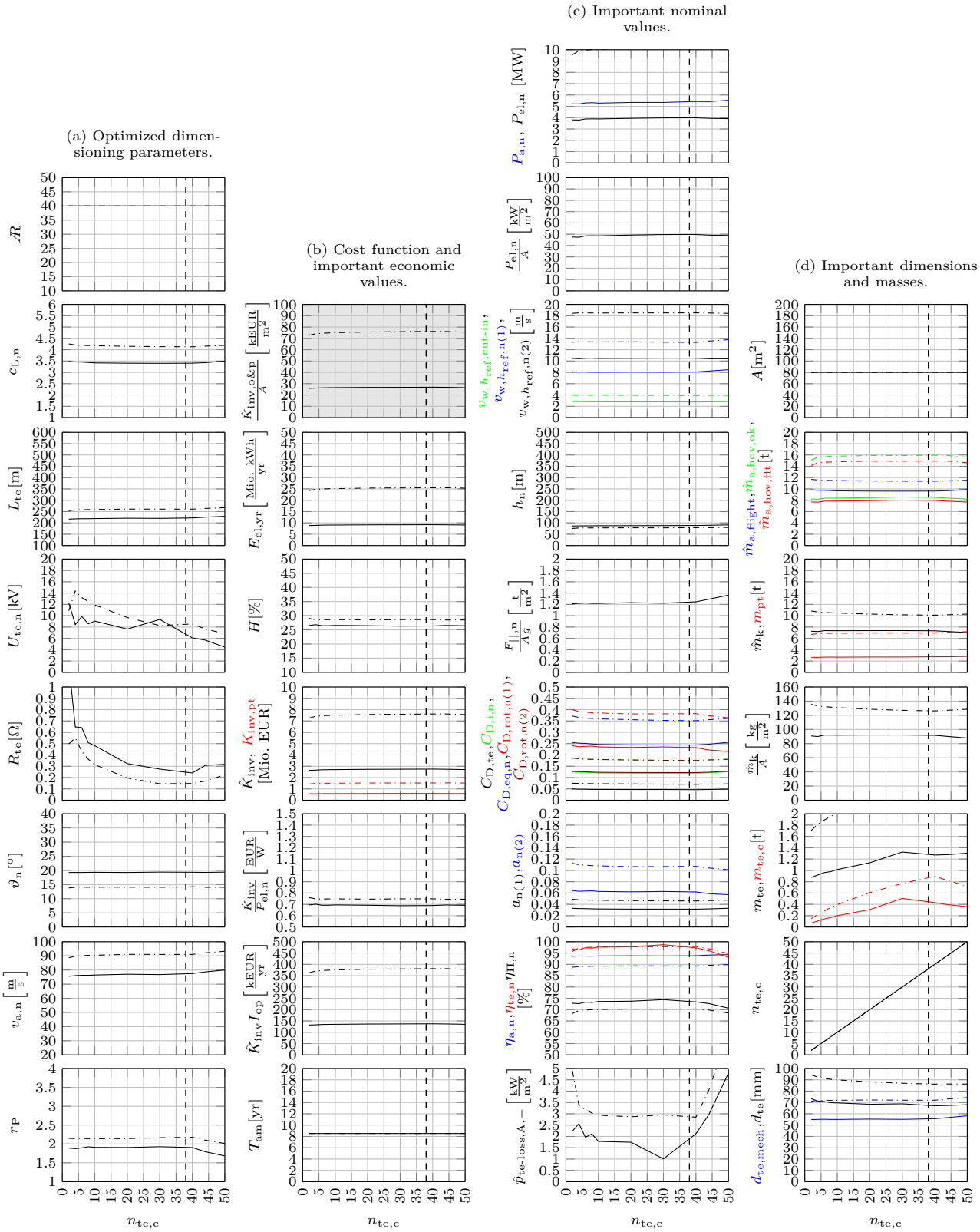

Figure 5.43: Results for different $n_{\mathrm{te,c}}$ (solid), also for the offshore variant (dash-dotted), compared to the reference scenario (dashed).

5.7.4 Tether Materials

The Makani Wing 7 has Dyneema as tether core material while the M600 and M5 have carbon fiber (cf. Chap. 3), and the reference scenario (cf. Tab. 5.1) and Kolar et al. [81] consider Kevlar. Moreover, different conductors and insulators are considered. It is interesting to investigate the effect of such different tether material selections. Here the tether material variants (V#) listed in Tab. 5.15 are investigated. Herein, V0 is the reference scenario, V1–V4 are to compare different

Table 5.15: Investigated tether material combination variants.

Variant	Core Material	Conductor Material	Insulator Material
Reference scenario.			
V0	Kevlar	aluminum	Teflon
Different core.			
V1	Dyneema	aluminum	Teflon
V2	carbon fiber	aluminum	Teflon
V3	carbon nanotubes	aluminum	Teflon
V4	steel	aluminum	Teflon
Different conductor.			
V5	Kevlar	copper	Teflon
V6	Kevlar	carbon nanotubes	Teflon
Different insulator.			
V7	Kevlar	aluminum	PE
Identical core and conductors.			
V8	aluminum	aluminum	Teflon
V9	carbon nanotubes	carbon nanotubes	Teflon

core materials, V5 and V6 are to compare with a different conductor material, V7 is to compare with a different insulator material, and V8 and V9 are to compare with single-material core and conductors. The variants with metal core, V4 and V8, are to investigate if a high-strength low-weight material is really necessary for the core. The variants with carbon nanotubes, V3, V6, and V9, are to get to know how much the performance changes if such a high-tech material becomes available in the future. Note that a conductive core, V2, V3, V4, V8, and V9, can potentially be used electrically for (i) grounding the kite, (ii) as lightning current conductor (but may require further measures such as an insulation layer around the core), or (iii) to conduct the electrical power. For the latter a different tether design might be meaningful, which is however out of scope of this dissertation (cf. Sect. 1.5). According to the material variants, the parameters $\rho_{\mathrm{te,mech}}$, $\sigma_{\mathrm{te,mech}}$, $\rho_{\mathrm{te,c,w}}$, $\kappa_{\mathrm{te,c,w}}$, $\rho_{\mathrm{te,ins}}$, and $E_{\mathrm{te,ins}}$ are altered with the values in Tab. 3.2.

Fig. 5.44 visualizes the tether cross sections for the different variants: The differences are not very significant, except for carbon nanotubes as core (V3 and V9) with a much smaller tether diameter and fewer electrical cables due to the comparatively high yield strength, and for aluminum as core (V8) with a much bigger tether diameter and more electrical cables due to the comparatively low yield strength. Another difference is visible for PE as insulator (V7), which requires a thicker insulation width than Teflon because of its much lower dielectric strength.

Fig. 5.45 plots the resulting figures of merit: Again, differences are not very significant between most variants. The variants with carbon nanotubes as core (V3 and V9) increase $\hat{K}_{\mathrm{inv,o\&p}}/A$ only by about ten percent despite the several times smaller tether diameter and two times higher operation altitude. The variants with metal cores (V4 and V8) are still feasible (w.r.t. the here employed model). For the steel core (V4) even most figures do not change. However, the

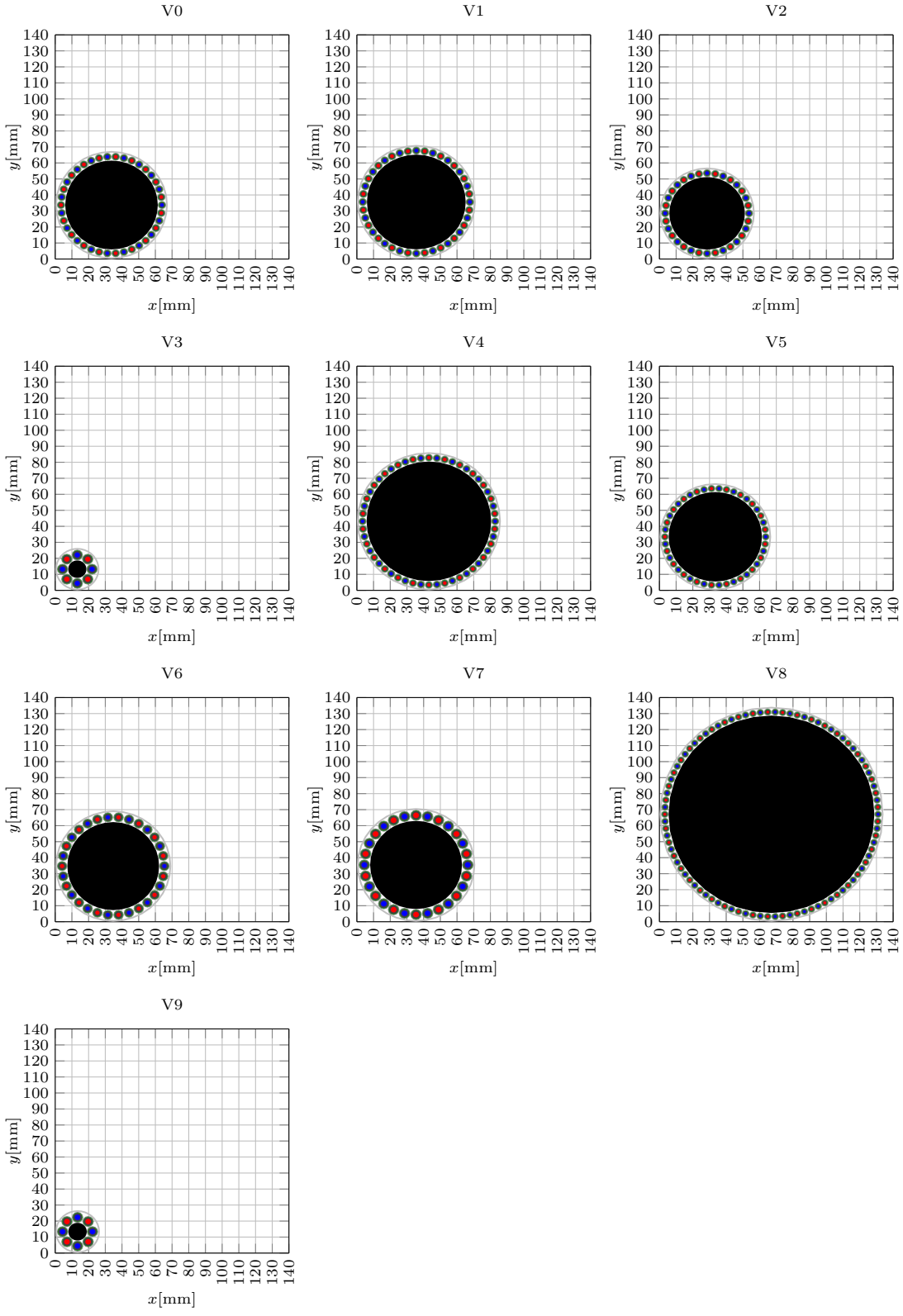

Figure 5.44: Visualization of the tether cross section results for the different tether material variants of Tab. 5.15 with color coding as in Fig. 1.8.

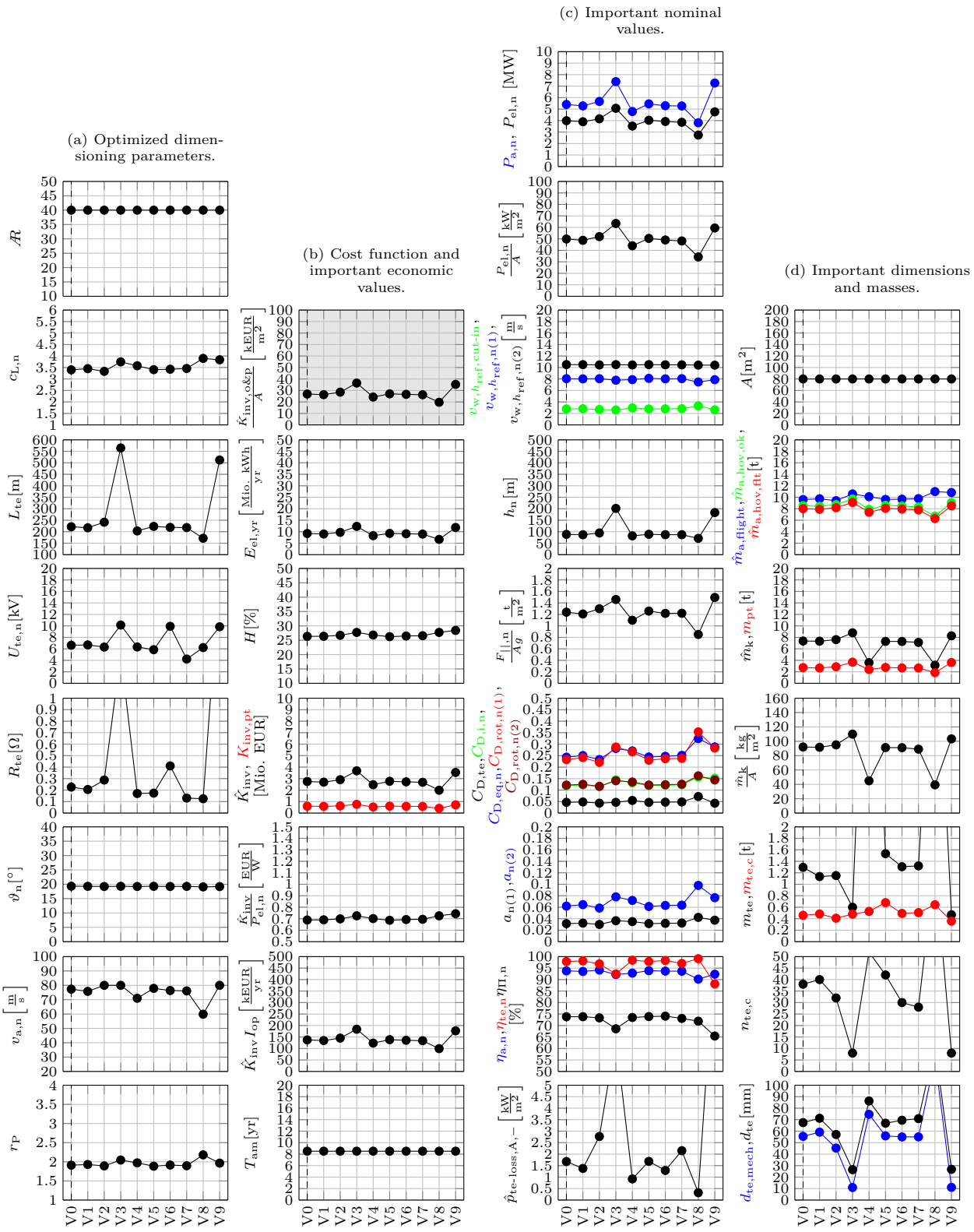

Figure 5.45: Results for the different tether material variants of Tab. 5.15.

metal cores increase the tether mass by several times ($\approx 7.5\,\mathrm{t}$ for V4 and $\approx 6\,\mathrm{t}$ for V8) and thus significantly reduce $\hat{m}_\mathrm{k}/A$, which in turn might not be realizable.

It is interesting to further discuss the different variants: Besides the reduced maximum allowed kite mass, another reason against a metal core is the much lower elastic modulus and thus high elongation under load compared to Kevlar, Dyneema, and carbon nanotubes, cf. Tab. 3.2, by which the electrical cables and the tether jacket are more strained/stressed. However, as discussed above, a metal core is conductive which might serve as lightning conductor when surrounded with a high-voltage insulation (which may also serve as a strain relief layer as suggested in [105]). Although this would further increase the tether diameter, it might help to solve this general kite power problem of lightning protection. If in the future carbon nanotubes become available, such an approach might be more interesting, because this material is much lighter than the metals, because the core diameter is already quite low for carbon nanotubes, and because a high lightning-voltage insulation around the core might still result in an overall smaller tether diameter compared to the baseline variant. Hence, for carbon nanotubes, it might be meaningful to use the same (or similar) tether cross section design as considered here, although in principle further optimizations might be possible in which the electrical conductors also carry a significant mechanical load and in an extreme case there would be only two carbon nanotube-based cables to carry the mechanical load and serve as positive and negative conductors (though with single point of failure, cf. [106]).

With today available materials, the best choice seems to be V0 or V5, i.e. with Kevlar as core, aluminum or copper as conductor, and Teflon as insulator, because Kevlar is light and can be bought as ropes by different vendors, and Kevlar and Teflon have a high temperature resilience (unlike e.g. Dyneema, cf. Tab. 3.2 and references therein) with which the specific power loss in the tether is allowed to be comparatively high.

5.7.5 Tether Cable Jacket Thickness

In the reference scenario a tether cable jacket thickness of $w_{\mathrm{te,c,j}} = 0.5\,\mathrm{mm}$ was utilized. In the model validation with Makani's Wing 7 in Sect. 3.1, this parameter was already only a "scientific guess", but with little influence on the resulting figures of merit. It is unknown what value is required for a long lasting real system. It might be relatively small because the tether might be already robust due to the thick insulation layer, shield, and tether jacket, but it might also be relatively thick due to stresses caused by winding the tether regularly on and off the ground station drum. However, it should be noted that within the drag power principle the tether is wound on the drum only during launching and landing with low speeds and low forces, unlike the lift power principle. For these reasons, a sensitivity analysis for $w_{\mathrm{te,c,j}}$ is interesting. Fig. 5.46 plots the results.

Almost all results are insensitive on $w_{\mathrm{te,c,j}}$, which is in well accordance to the earlier found results in Sect. 3.1.7. Only the number of electrical cables in the tether $n_{\mathrm{te,c}}$ is rather sensitive, which is not surprising because fewer electrical cables fit (in one layer) around the core if they are thicker. For the same reason, the tether diameter increases a bit with $w_{\mathrm{te,c,j}}$. These results imply, that the jackets may be relatively thick, particularly if it helps to increase the tether life time or reduce the maintenance costs, respectively.

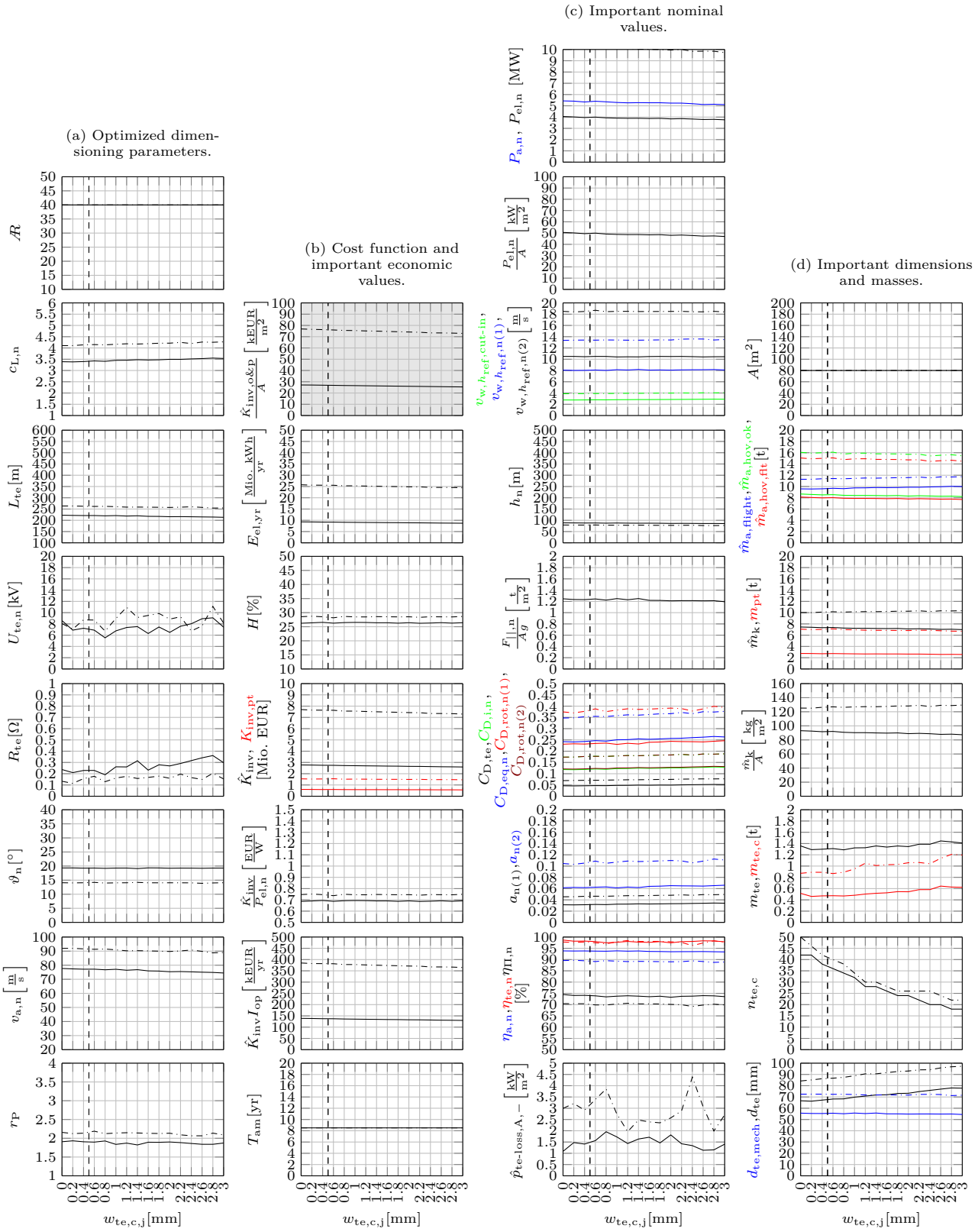

Figure 5.46: Results for different $w_{\mathrm{te,c,j}}$ (solid), also for the offshore variant (dash-dotted), compared to the reference scenario (dashed).

5.7.6 Tether Mechanical Strength Safety Factor

A value of nine was estimated to be required for the tether mechanical strength safety factor $S_{\text{te,mech}}$, composed of factor three for fiber-rope derating (cf. e.g. [142]) multiplied by factor three for dynamic excesses e.g. due to gusts or due to oscillations caused by the flight trajectory. The first portion is a function of the rope braiding and tether attachment designs, the latter depends on the kite concept (e.g. kite with or without tail, actuators and actuation speeds) and on the flight controller's performance. Another important point is the lifetime of the tether core: Every material can withstand only a limited number of load cycles before it fails due to fatigue. The lower the load stresses are, the more cycles can be withstood before fatigue. As $S_{\text{te,mech}}$ is the yield strength safety factor, this means that the higher $S_{\text{te,mech}}$ is, the higher is the tether core lifetime. For these reasons it is interesting to investigate the sensitivity on $S_{\text{te,mech}}$. Fig. 5.47 reports the results.

The most important values, maximum allowed costs, nominal power, and maximum allowed masses, are not very sensitive on $S_{\text{te,mech}}$. It should be noted that $S_{\text{te,mech}}$ could be optimized in a more elaborate model which resolves the lifetime of the tether and its replacement or maintenance costs as function of $S_{\text{te,mech}}$. This is left to future model improvements.

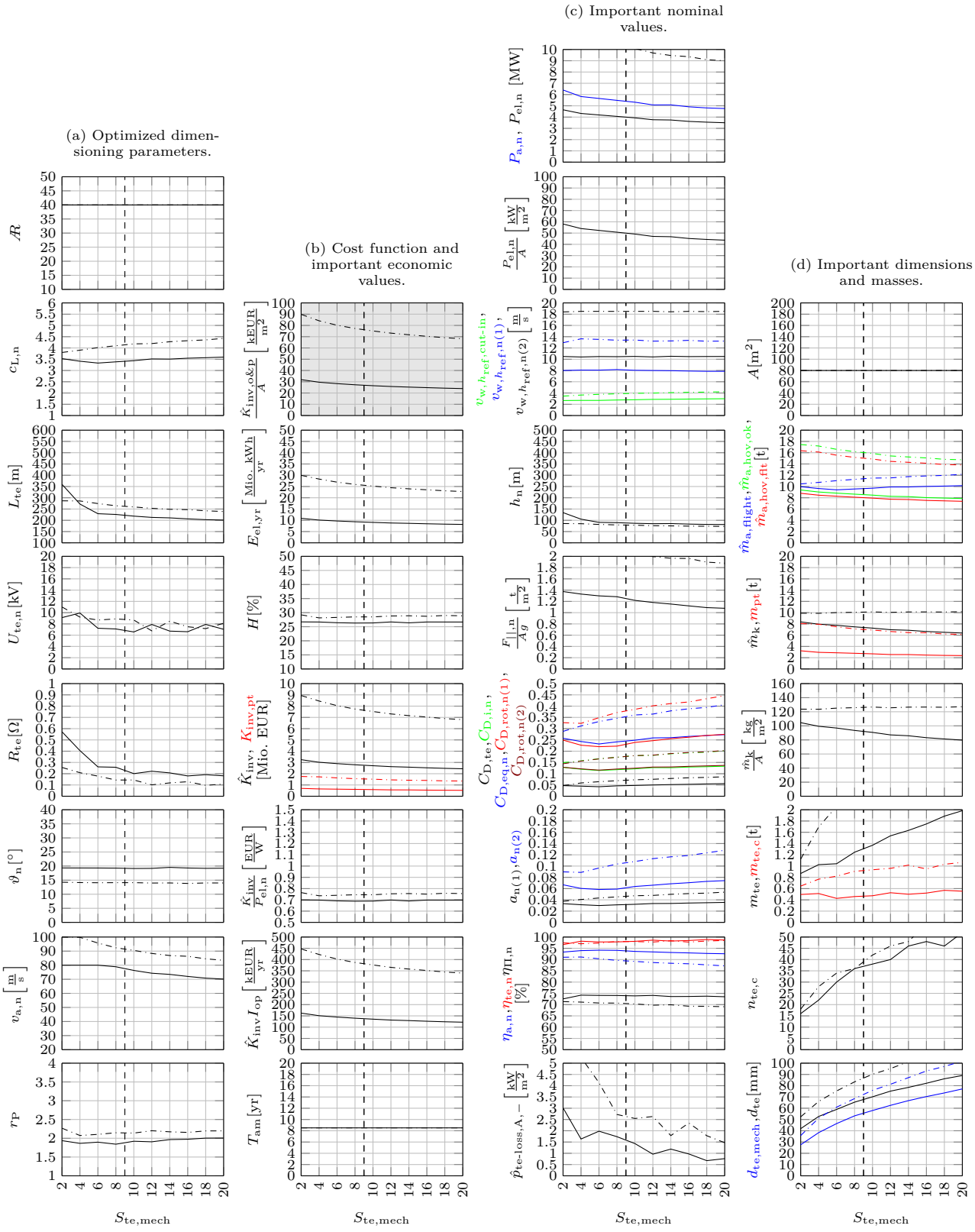

Figure 5.47: Results for different $S_{\mathrm{te,mech}}$ (solid), also for the offshore variant (dash-dotted), compared to the reference scenario (dashed).

5.7.7 Tether Dielectric (Insulation) Strength Safety Factor

Similar to $S_{\text{te,mech}}$, the tether dielectric (insulation) strength safety factor $S_{\text{te,ins}}$ was a "scientific guess" for the reference scenario and might need to be different in a realization. Also here, a high $S_{\text{te,ins}}$ increases the lifetime of the insulation layer and some safety is required due to manufacturing variances, material defects, or unusual or unexpected voltage excesses. Fig. 5.48 reports the sensitivities on $S_{\text{te,ins}}$.

Almost all values are even less sensitive on $S_{\text{te,ins}}$ then on $S_{\text{te,mech}}$, or can be claimed to be entirely insensitive on $S_{\text{te,ins}}$. This result is not very surprising in view of the already found very low sensitivity of the results with the nominal tether voltage.

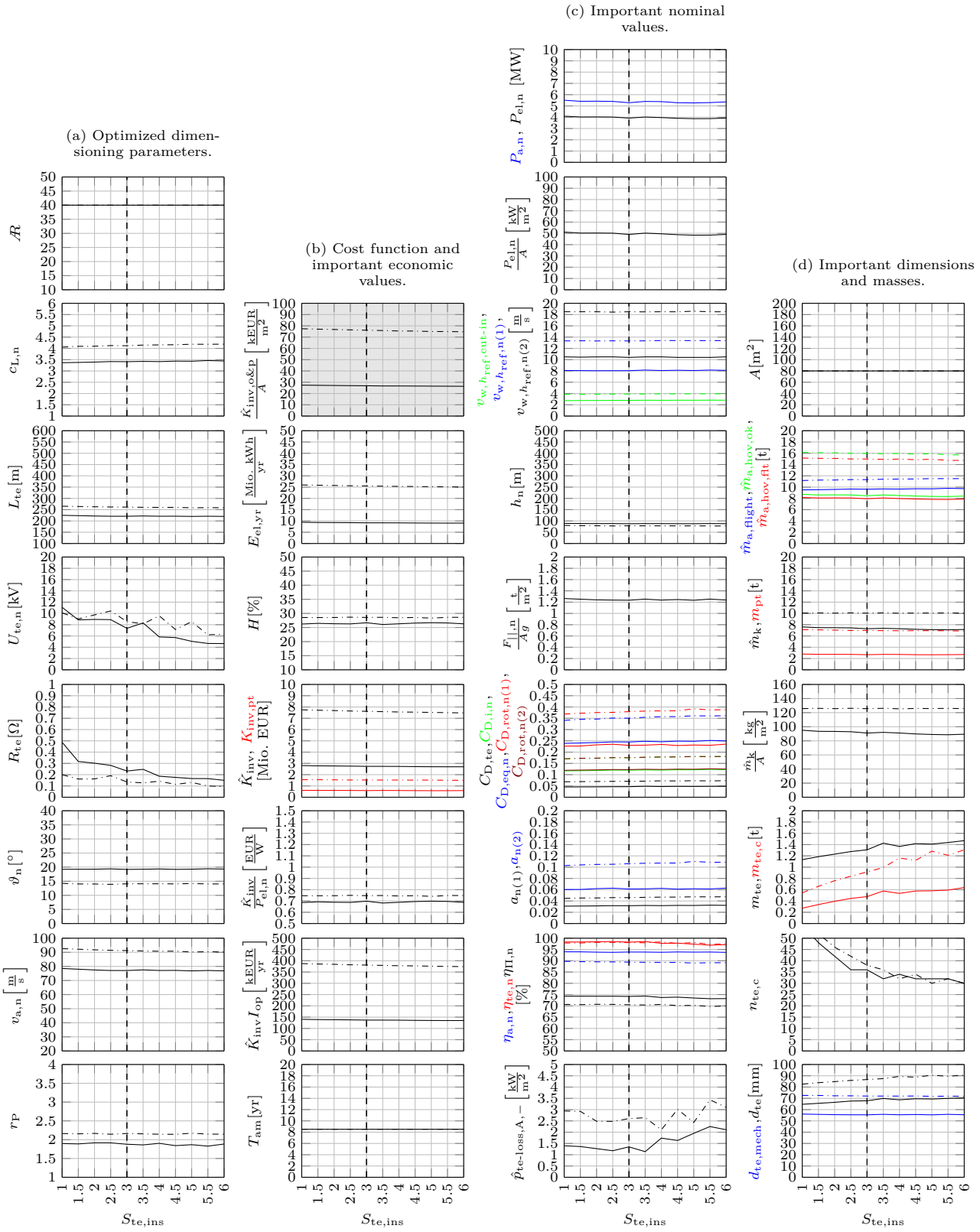

Figure 5.48: Results for different $S_{\mathrm{te,ins}}$ (solid), also for the offshore variant (dash-dotted), compared to the reference scenario (dashed).

5.7.8 Tether Wire Resistance Correction Factor

As stated in the introduction of the tether wire resistance correction factor $f_{\mathrm{te,c,w}}$, its value ≥ 1 accounts for a realistic copper fill factor ≤ 1, temperature variations, manufacturing variances, material defects, the increased cable length due to the helical placement of a cable around the core, as well as connectors and also finite cable lengths onboard the kite and on the ground. Even for more elaborate models, it might be hard to estimate $f_{\mathrm{te,c,w}}$, although once a system is realized it is easy to measure $f_{\mathrm{te,c,w}}$. Therefore it is interesting to investigate the effect of changed $f_{\mathrm{te,c,w}}$. Fig. 5.49 reports the results.

Also for this parameter a negligible sensitivity is found. This implies that e.g. tether cable temperature changes have almost no effect and that the helix of the tether cables around the core may be rather tight.

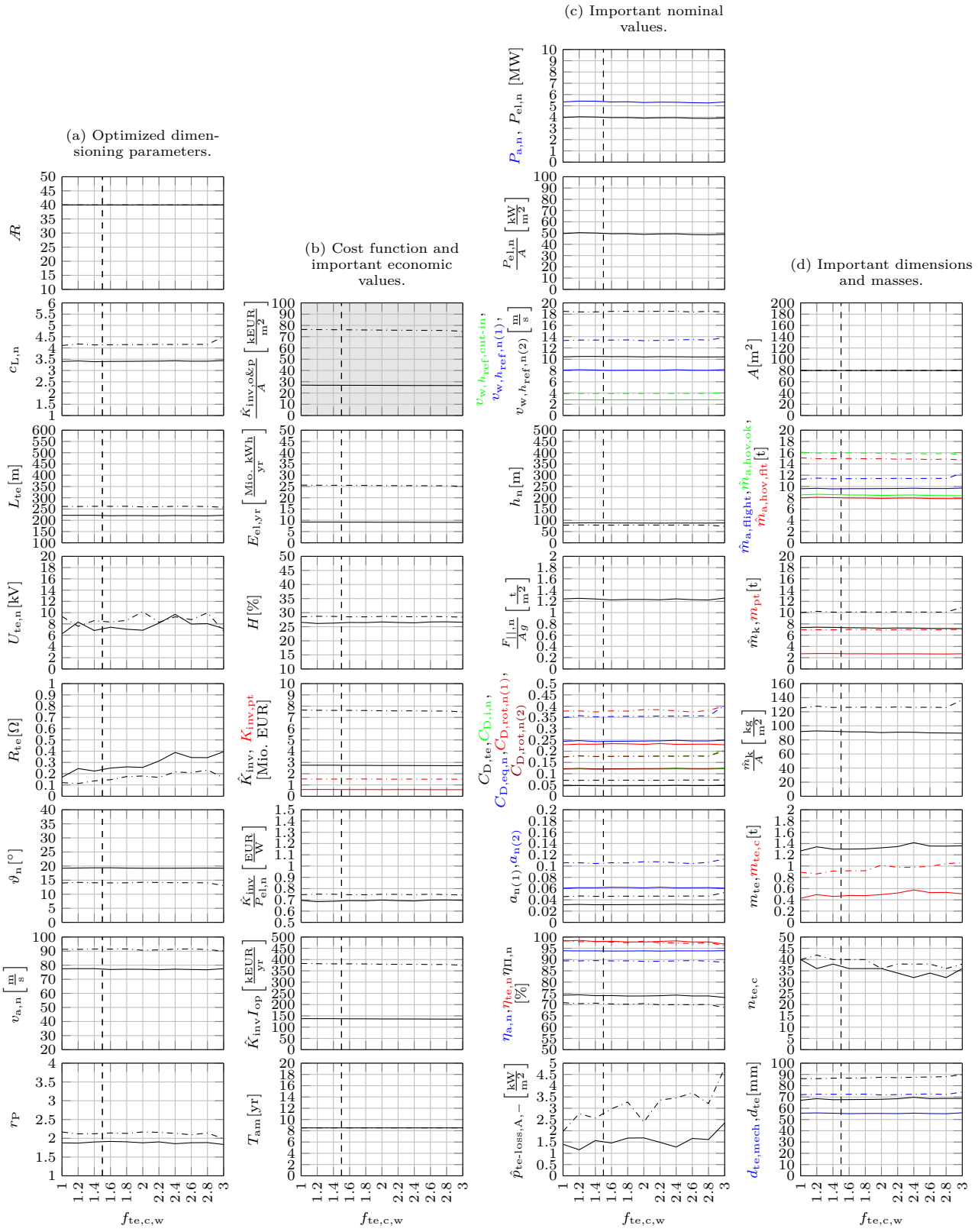

Figure 5.49: Results for different $f_{\mathrm{te,c,w}}$ (solid), also for the offshore variant (dash-dotted), compared to the reference scenario (dashed).

5.8 Sensitivities of Powertrain Subsystems Parameters

In the following, a sensitivity analysis of each powertrain subsystem parameter (cf. Tab. 5.1) is conducted, with the following exceptions:

- The generative efficiency factors $\eta_{\mathrm{s},+}$, $\eta_{\mathrm{m},+}$, $\eta_{\mathrm{pe,k},+}$, and $\eta_{\mathrm{pe,g},+}$ all have a very similar impact, and have a similar impact as $\eta_{\mathrm{rot},+}$ already investigated above in Sect. 5.6.3, because the electrical power is proportional to the product of the efficiency factors. Therefore, no further sensitivities on efficiency factors need to be investigated.
- As also motivated at the beginning of Sect. 5.6, the consumptive efficiency factors $\eta_{\mathrm{s},-}$, $\eta_{\mathrm{m},-}$, $\eta_{\mathrm{pe,k},-}$, and $\eta_{\mathrm{pe,g},-}$ apply only for Region I(a) in which the kite is grounded. Therefore, those parameters have neither an impact on the energy yield and thereof dependent economic values, nor on the power plant design.
- The specific machine mass and kite power electronics mass, γ_{m} and $\gamma_{\mathrm{pe,k}}$, have only an impact on the maximum allowed kite mass $\hat{m}_{\mathrm{k}}$, but not on the maximum allowed airborne mass $\hat{m}_{\mathrm{a}}$ or other important results, which is why a detailed sensitivity analysis is not meaningful.
- The maximum allowed mass during hovering is dictated by the fault case, $\hat{m}_{\mathrm{a,hov,flt}}$, cf. Tab. 5.4. Therefore, investigating the sensitivity of the hovering safety factor without fault $S_{\mathrm{hov,ok}}$ is not very meaningful. Instead, only the sensitivity of the hovering safety factor with rotor failure $S_{\mathrm{hov,flt}}$ is investigated. Note that both safety factors have a similar impact.
- Forcing the installed nominal electrical power $P_{\mathrm{el,ins}}$ to an off-optimal value is not meaningful (at least as long as the consideration of Eq. (2.248) applies) and is therefore not investigated.

5.8.1 Powertrain Specific Costs

In the reference scenario, specific costs for the powertrain are estimated as $k_{\mathrm{pt}} = 0.15\,\mathrm{EUR/W}$. This value originates from the following rationale: Photovoltaic inverters have specific costs at around $0.05\,\mathrm{EUR/W}$ [168]. Assuming that the kite's ground station converters have that same costs, that the drive converters (and possible DC-DC converters) have also the same costs, that also the machines have that costs, and that a possible battery system on the ground has negligible costs, the above value $0.15\,\mathrm{EUR/W}$ is the result. However, the actual value of k_{pt} can be very different and is a function of many design choices. To name a few, it depends on the chosen nominal tether voltage, which powertrain components are bought off-the-shelf or designed and built in-house, and how mature in-house built components are. Moreover, a low weight and high quality is required which is a good argument that $0.15\,\mathrm{EUR/W}$ might be underestimated, particularly for the first systems deployed. Fig. 5.50 reports the results for changed k_{pt}.

All important values, maximum allowed costs, nominal power, and maximum allowed masses, are quite sensitive on k_{pt}. This implies that good choices have to made on the powertrain, because these decisions tend to have a high economic impact.

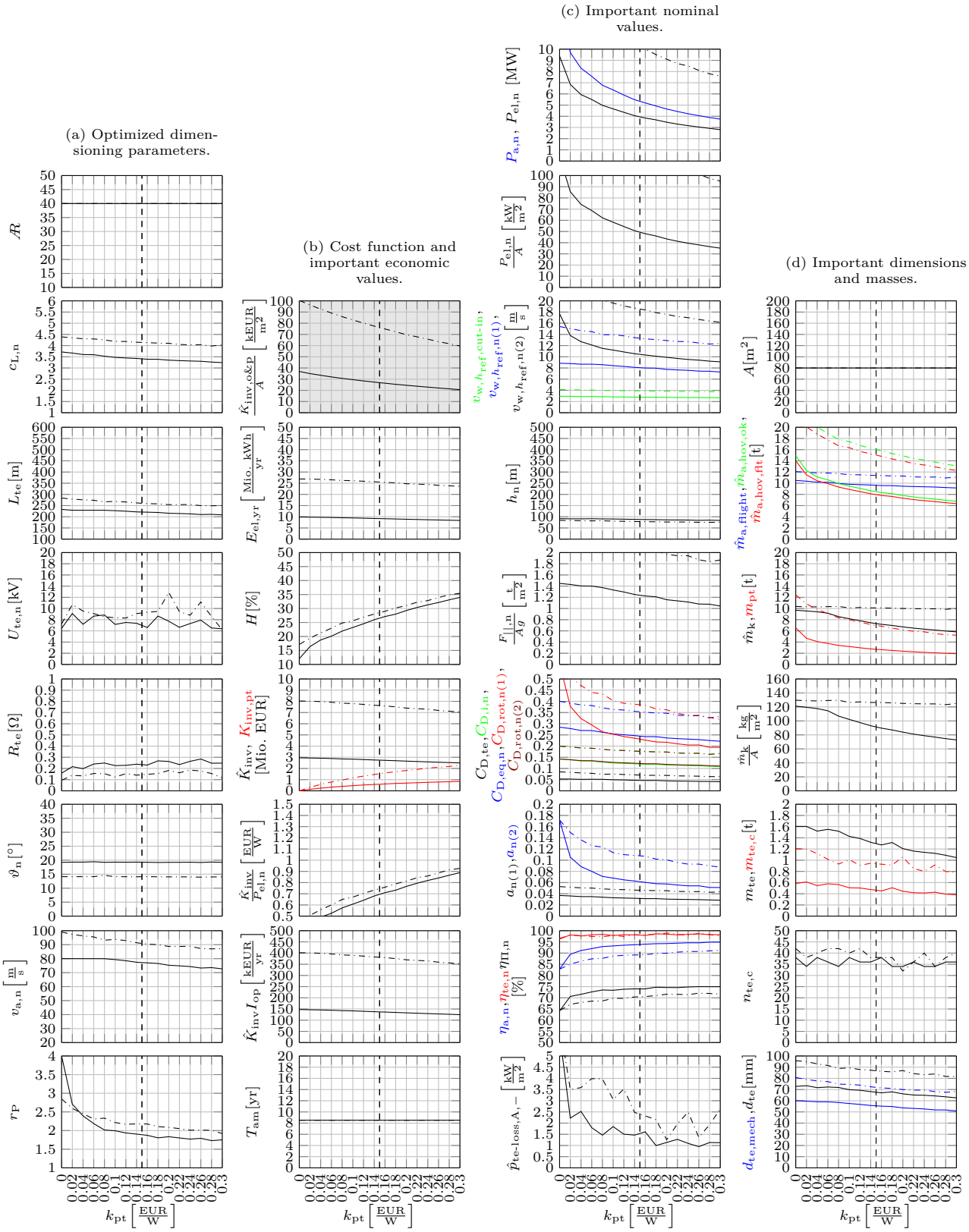

Figure 5.50: Results for different k_{pt} (solid), also for the offshore variant (dash-dotted), compared to the reference scenario (dashed).

5.8.2 Safety Factor for Hovering During Rotor Failure

The safety factor for hovering during rotor failure $S_{\mathrm{hov,flt}}$ was estimated to some value, which might be a bit optimistic. Hence, investigating the effect for changed $S_{\mathrm{hov,flt}}$ is interesting. Fig. 5.51 shows the results.

As expected, $S_{\mathrm{hov,flt}}$ has only an impact on the maximum allowed airborne mass during hovering with rotor failure $\hat{m}_{\mathrm{a,hov,flt}}$ and thereon dependent values. However, the sensitivity is rather high. The baseline value $S_{\mathrm{hov,flt}} = 1.2$ results in $\hat{m}_{\mathrm{a,hov,flt}} \approx 8\,\mathrm{t}$, while an increase to $S_{\mathrm{hov,flt}} = 2$ reduces the maximum allowed mass to $\hat{m}_{\mathrm{a,hov,flt}} \approx 5\,\mathrm{t}$. This implies that measures to achieve a low $S_{\mathrm{hov,flt}}$ are rather important. This seems to be particularly a challenge for the biplane kite, because the tether connection at the kite and the kite's center of mass do not coincide, leading to moments caused by the tether which need to be balanced by the rotors (cf. Assumption 2.27).

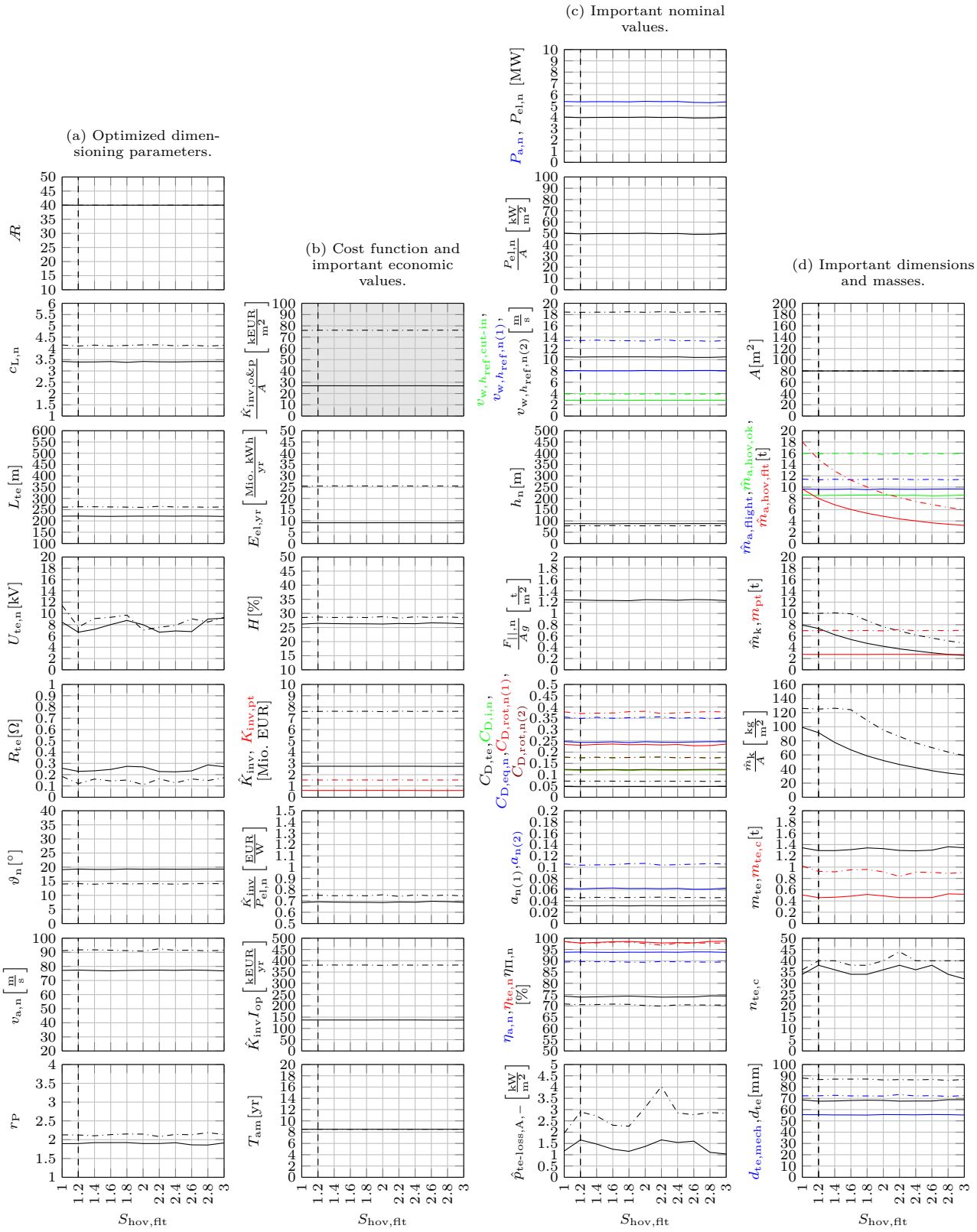

Figure 5.51: Results for different $S_{\mathrm{hov,flt}}$ (solid), also for the offshore variant (dash-dotted), compared to the reference scenario (dashed).

5.9 Sensitivities of Ground Station and Flight Trajectory Parameters

In the following, a sensitivity analysis of each ground station and flight trajectory parameter (cf. Tab. 5.1) is conducted, with the following exceptions:

- Changing directly the elevation ϑ_n from its optimum is not meaningful (similar to changing L_te from its optimum, as stated in Sect. 5.7). It is only meaningful to investigate the sensitivity from on ϑ_n dependent values such as changes of the nominal altitude bound $\underline{h}_\mathrm{n}$. This is investigated elsewhere, below in Sect. 5.11.2.
- The nominal roll angle to balance weight is likely not chosen much different from the reference scenario value $\psi_\mathrm{w,n} = 20\,^\circ$. Instead, in order to obtain changes of the maximum allowed airborne mass for crosswind flight, only the sensitivity of the minimum airflow speed $v_\mathrm{a,min}$ is investigated, but elsewhere, below in Sect. 5.10.1.

5.9.1 Tower Height

In the reference scenario, a small tower is considered to simplify the kite's launching and landing without a tiltable tail or similar (see also [14]). A tower is also considered by Makani for the same reason (cf. Chap. 3 and references therein). A further motivation to consider a tower, is that the cosine efficiency can be increased, without increasing the tether length (and thus increasing the tether drag and mass) and without reducing the kite's operating altitude. Using a possibly high tower was already motivated by the author of this dissertation in [14]. However, only a rather simple kite model was utilized and it was left open if a high tower can be economical. Therefore, the optimization is repeated with the here utilized model and optimization with altered h_to. Fig. 5.52 plots the results.

The costs, power, and energy yield increase significantly and almost linearly with the tower height. As expected, the elevation decreases with the tower height to increase the cosine efficiency. The tether length decreases with the tower height (until the minimum angular speed is reached), because higher altitudes with the strong wind speeds are reached with an increased tower height also with a shorter tether. Up to a tower height of $\approx 20\,\mathrm{m}$, the flight altitude decreases approximately linearly and then increases approximately linearly.

If the tower shall be economical, it must at least bear its own costs. The maximum allowed investment costs of the tower can be introduced as

$$\hat{K}_\mathrm{inv,to} := \hat{K}_{\mathrm{inv,o\&p},h_\mathrm{to}} - \hat{K}_{\mathrm{inv,o\&p},h_\mathrm{to}=0}, \tag{5.18}$$

where $\hat{K}_{\mathrm{inv,o\&p},h_\mathrm{to}=0}$ is the maximum allowed investment costs of other parts (other than the powertrain of the kite power plant) without tower ($h_\mathrm{to} = 0$), and $\hat{K}_{\mathrm{inv,o\&p},h_\mathrm{to}}$ are those with tower of height h_to. Fig. 5.53 plots that maximum allowed tower investment costs absolute and relative to the tower height, revealing interesting results: First, if the initially considered 15 m high tower (with its foundation) costs a little under 200 kEUR or 11.5 kEUR/m, then it bears its own cost. If it costs less, then the difference between the actual tower costs and the maximum allowed ones is added to the profit margin of the kite power plant manufacturer. In fact, this seems to be the case in view that a tower of a 2 MW conventional wind turbine with a 86 m high tower—and thus much higher turnover moment—costs only about 5 kEUR/m [5, Tab. 4 with Tab. 2] (assuming 1 EUR $\approx$ 1 USD). As the maximum allowed costs of the tower increase almost linearly with the tower height and considering that the tower and foundation of a kite power plant can be simpler and less costly compared to a tower of a conventional wind turbine (cf. [14]), even a considerably higher tower might be economically meaningful. For example, a 80 m high tower is allowed to

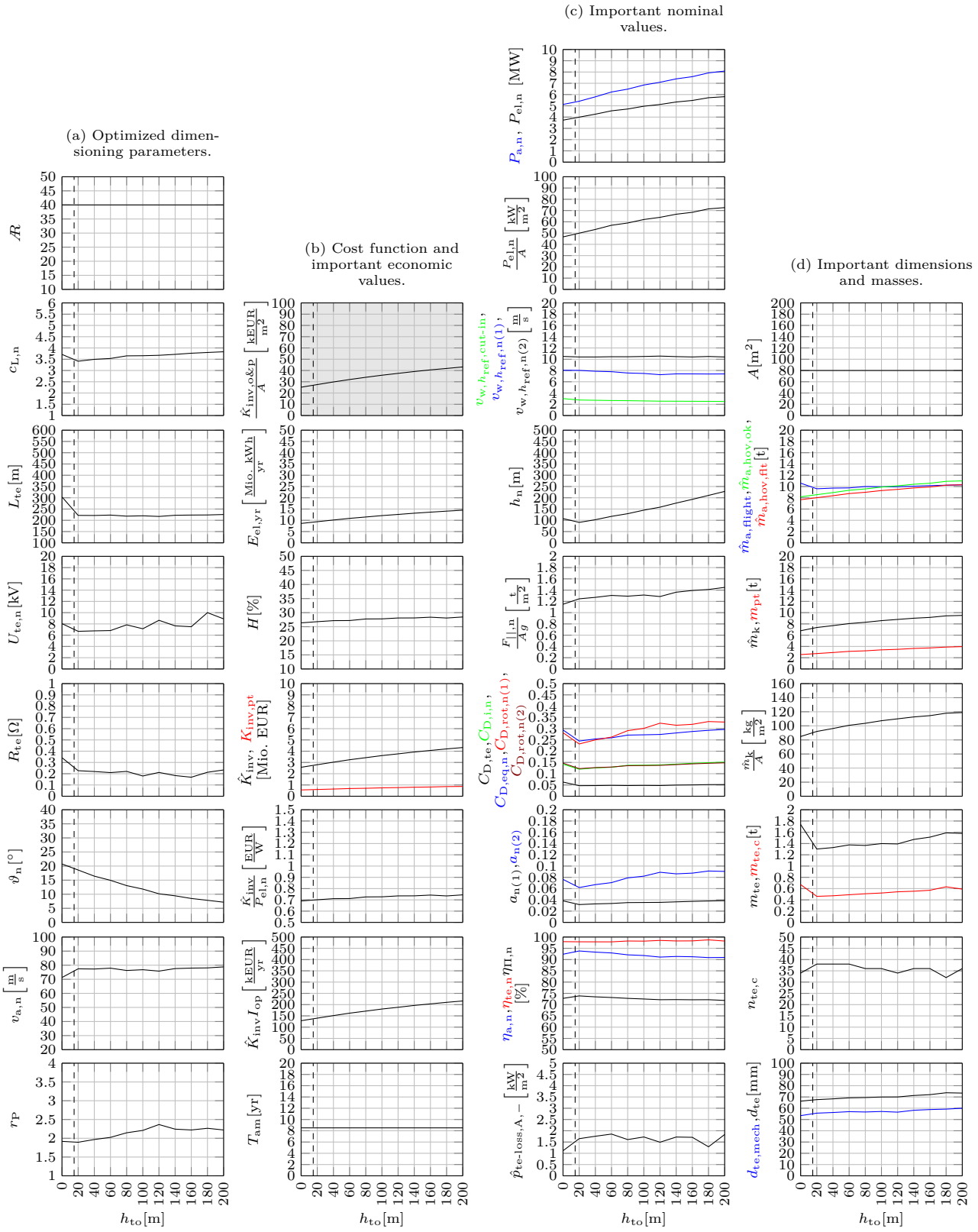

Figure 5.52: Results for different h_{to} (solid) compared to the reference scenario (dashed).

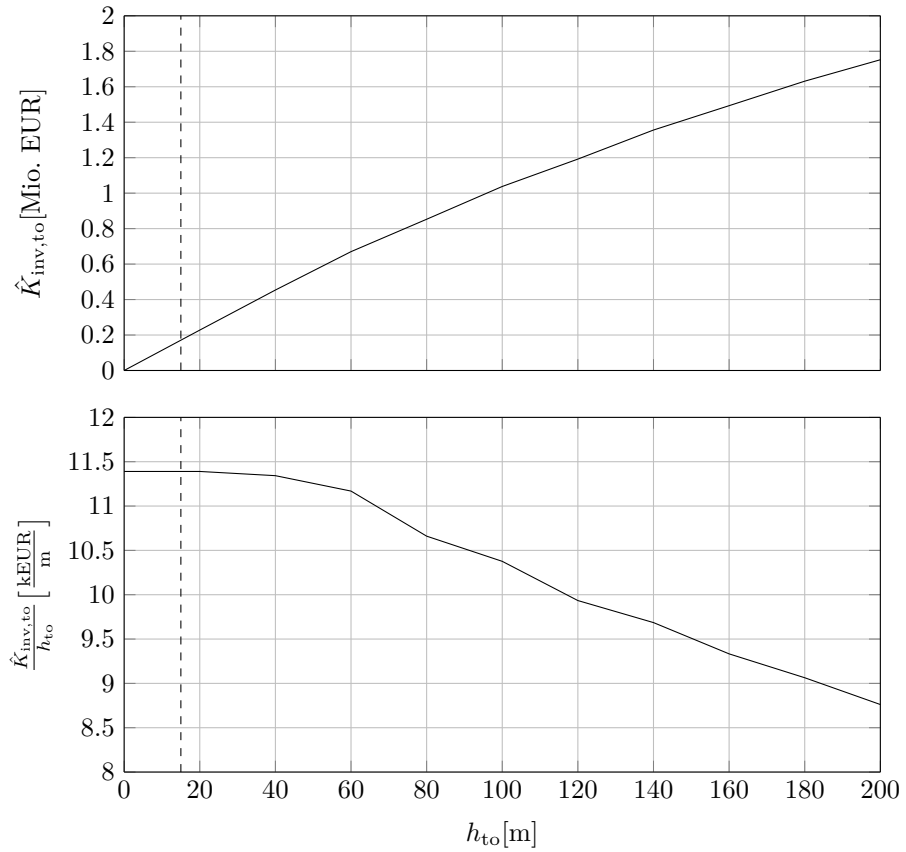

Figure 5.53: Maximum allowed tower costs for different h_{to} (solid) compared to the reference scenario (dashed).

cost over 800 kEUR (or $\approx$ 10.5 kEUR/m) while the above cited actual value of a conventional wind turbine is about 430 kEUR, though the forces of the then 5 MW kite are larger than those of a 2 MW conventional wind turbine, but as stated above, a tower for crosswind kite power can be simpler and less costly [14]. Nevertheless, with the here utilized model, no statement for the actual optimal tower height can be made. For that, a cost model of the tower would need to be included (e.g. costs as function of height and nominal tether force), with which overall the additional increase of maximum allowed development costs and profit margin caused by the tower can be maximized.

5.9.2 Nominal Effective Azimuth

The nominal effective azimuth φ_n depends on the flight path. Ideally, it is zero which is a more or less valid assumption if tight circles are flown. However, the model validations with the higher fidelity point-mass model, which resolves the kite's flight trajectory, found, that this is an over-simplification, cf. Chap. 3. Moreover, it was found that the flight trajectory's width and hence the mean absolute azimuth (which can be referred to as nominal effective azimuth) depends on the effective airborne mass and was made in part responsible for reduced powers, cf. e.g. Sect. 5.1.4. Hence, it is interesting to re-compute the optimizations for varied φ_n. Fig. 5.54 reports the results.

The sensitivity of the maximum allowed costs, nominal power, and maximum allowed masses is low or moderate for low φ_n and increases for high φ_n. In fact, these important result values appear to be proportional to $\cos^3(\varphi_\mathrm{n})$ as expected from Eq. (2.19). This implies that the flight path should not be too wide and instead be relatively tight maybe with a nominal azimuth at $\varphi_\mathrm{n} \lesssim 15\,^\circ$.

It should be noted that φ_n would be implicitly optimized if a higher fidelity dynamics model is utilized in the optimizations, e.g. the point-mass model (see also Appendix C.5).

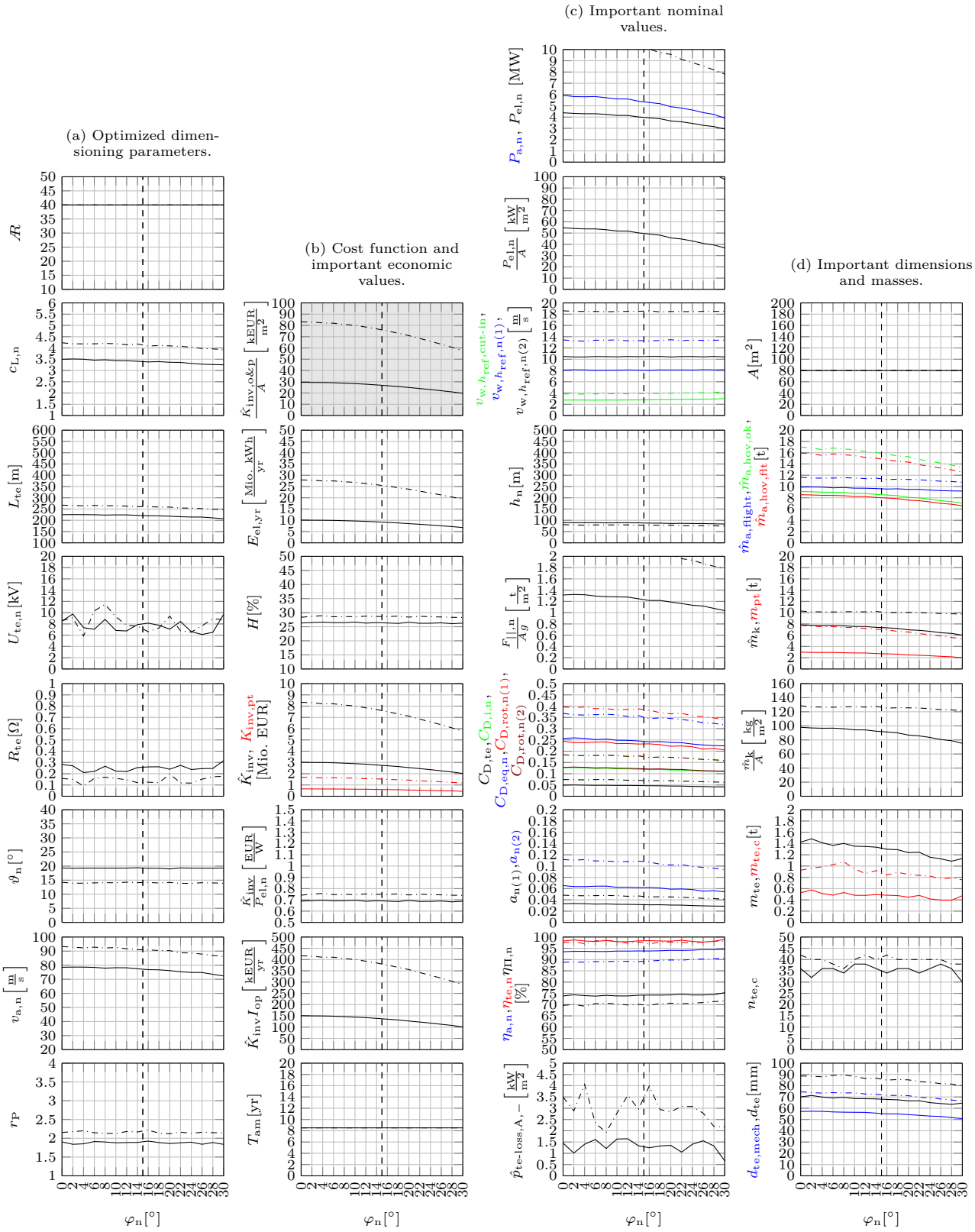

Figure 5.54: Results for different φ_n (solid), also for the offshore variant (dash-dotted), compared to the reference scenario (dashed).

5.10 Sensitivities of Power Curve "Shaping" Parameters

In the following, a sensitivity analysis of each power curve "shaping" parameter (cf. Tab. 5.1) is conducted.

5.10.1 Minimum Airflow Speed

A changed minimum airflow speed $v_{\mathrm{a,min}}$ can significantly increase the maximum allowed airborne mass during crosswind flight at the cost of an increased cut-in wind speed and thus reduced energy yield at low winds. It is interesting to quantify this effect. Therefore, Fig. 5.55 reports the optimization results for changed $v_{\mathrm{a,min}}$.

The important figure of the maximum allowed costs is very insensitive on $v_{\mathrm{a,min}}$, even at $v_{\mathrm{a,min}} = 60\,\mathrm{m/s}$. Also the nominal power and most other results do not change much for that value. Only the cut-in wind speed and the maximum allowed mass during crosswind flight increase significantly. For example, at $v_{\mathrm{a,min}} = 60\,\mathrm{m/s}$, it is doubled from $\hat{m}_{\mathrm{a,flight}} \approx 10\,\mathrm{t}$ to $\hat{m}_{\mathrm{a,flight}} \approx 20\,\mathrm{t}$ for the onshore system. The total maximum allowed airborne mass and kite mass do not increase that much, because those values are also limited by the available power during hovering. That the maximum allowed costs are relatively insensitive for $v_{\mathrm{a,min}}$ (or $v_{\mathrm{w},h_{\mathrm{ref}},\text{cut-in}}$) can be explained by the anyways low generated power at low wind speeds. These results imply that the actual airborne mass has not a high impact on the overall system performance.

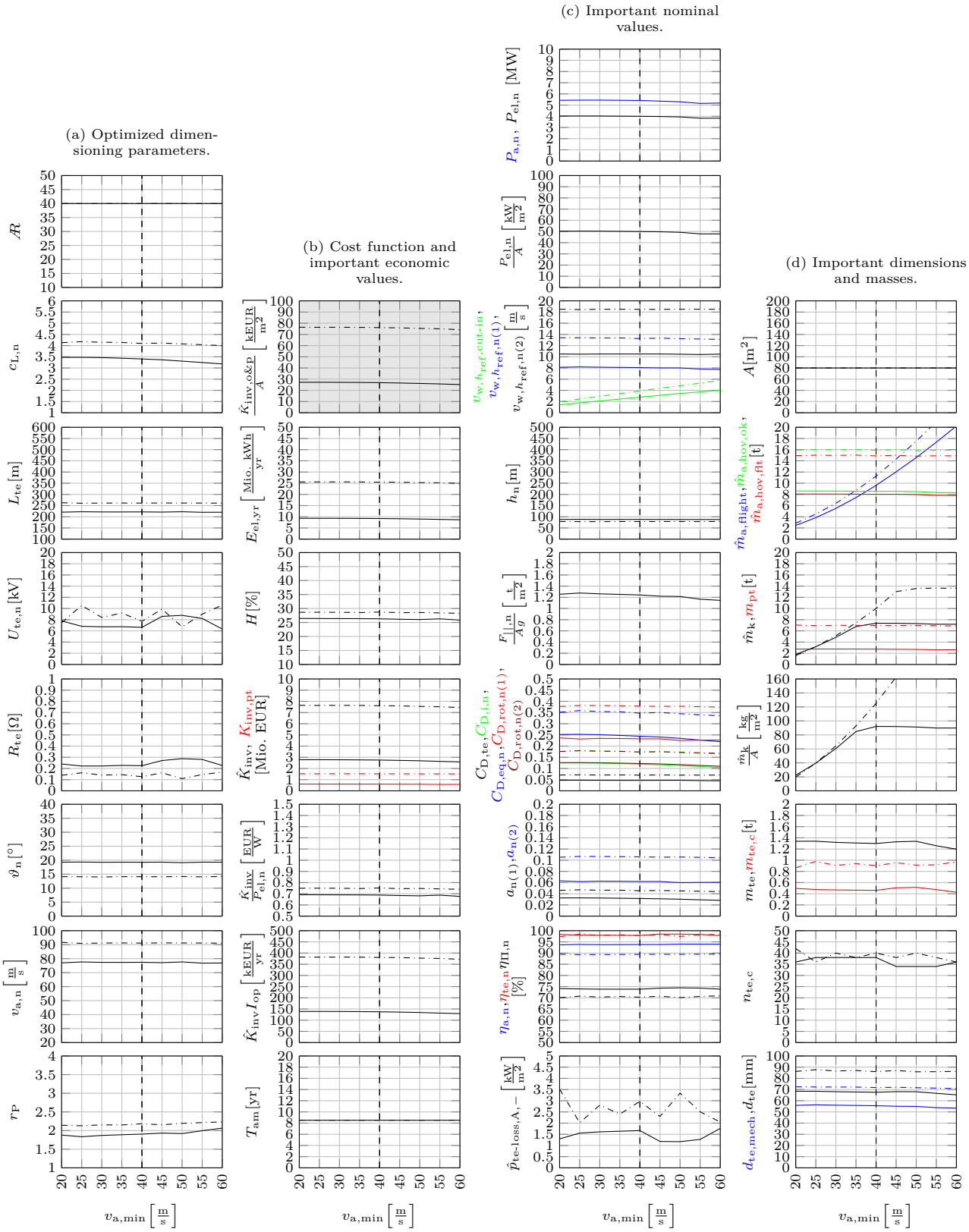

Figure 5.55: Results for different $v_{\mathrm{a,min}}$ (solid), also for the offshore variant (dash-dotted), compared to the reference scenario (dashed).

5.10.2 Nominal Airflow Speed

In the reference scenario, the nominal airflow speed was limited to $\overline{v}_{\mathrm{a,n}} = 80\,\mathrm{m/s}$, which is similar to the tip speed of conventional wind turbines. However, for several reasons other values might be more beneficial. For example, to reduce noise emissions, a much lower upper bound might be helpful. Therefore, a range for the airflow speed and its bounds $v_{\mathrm{a,n}} = \underline{v}_{\mathrm{a,n}} = \overline{v}_{\mathrm{a,n}}$ are investigated. Fig. 5.56 shows the results.

The maximum allowed costs hardly change around the optimum nominal airflow speed, but the further $v_{\mathrm{a,n}}$ is off the optimum, the higher is the sensitivity. The nominal powers and maximum allowed airborne masses change only moderately.

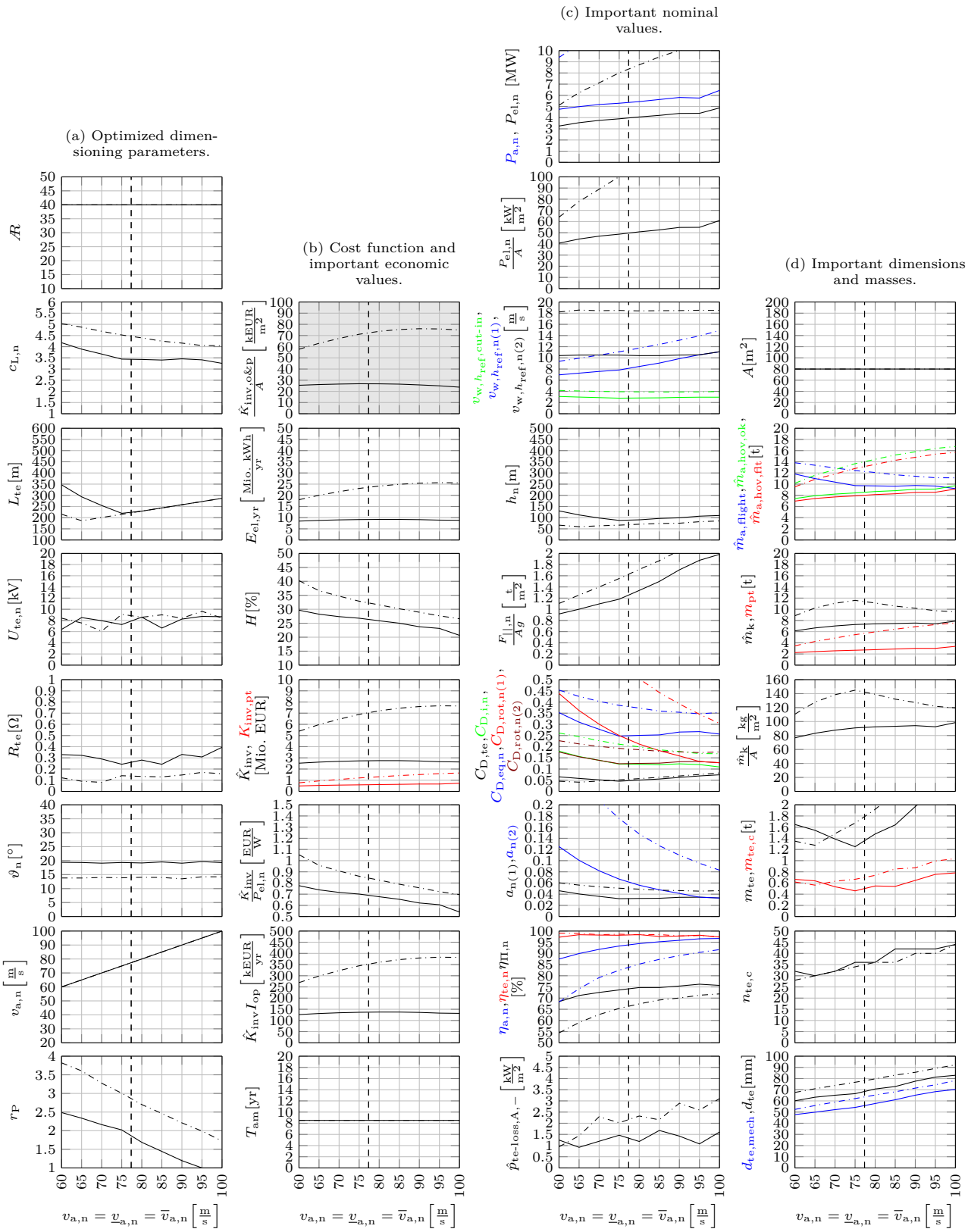

Figure 5.56: Results for different $v_{a,n}$ (solid), also for the offshore variant (dash-dotted), compared to the reference scenario (dashed).

5.10.3 Width of Region III(a)

In the prior work of the author of this dissertation [110], a drag power kite power curve model without Region III(a) (in which only parallel force and airflow speed are limited but power still increases) was considered. To evaluate the importance of such a region, the optimization is repeated with altered bounds for the power ratio $r_\mathrm{P} = \underline{r}_\mathrm{P} = \overline{r}_\mathrm{P}$.

Fig. 5.57 shows the power curves for the optimal r_P (solid) and for $r_\mathrm{P} = 1$ (dashed), which was implicitly used in [110]: The nominal wind speed of the curve with $r_\mathrm{P} = 1$ (dashed) is

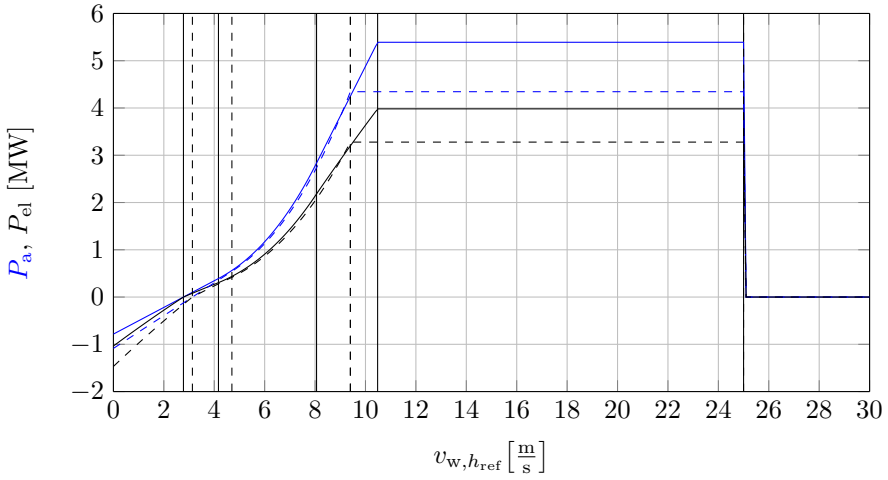

Figure 5.57: Power curve for the biplane kite of the reference scenario with optimal r_P in solid and with $r_\mathrm{P} = 1$ in dashed. Similarly, the transition between the regions are drawn in solid or dashed, respectively.

between the first and second nominal wind speed of the curve with optimal r_P (solid). Until about 9 m/s, the power curves are similar, but the one with $r_\mathrm{P} = 1$ (dashed) has a slightly lower power due to the higher nominal force and thus higher tether drag contribution. For the optimal r_P (solid), the nominal force is significantly lower, and therefore the tether drag contribution and cut-in wind speed are lower. At 9 m/s, the power for the curve with $r_\mathrm{P} = 1$ (dashed) does not increase anymore as this is the nominal wind speed, while the other with optimal r_P still increases significantly by several hundred kilowatts.

Fig. 5.58 reports further resulting power plant figures for further changes of r_P: The maximum allowed costs do not change that much for an off-optimal r_P, but the nominal power decreases notably for lower r_P, as already noticed in Fig. 5.57. The first and second nominal wind speeds diverge for increasing r_P, as expected. The tether length and mass decrease for higher r_P and therefore the maximum allowed kite mass beneficially increases for higher r_P. As already concluded from Fig. 5.57, the drag coefficients are significantly lower for higher r_P. Besides a reduced tether drag, also the induced drag reduces for higher r_P, because of a reduced $c_\mathrm{L,n}$, which is beneficial also for the airfoil design challenge. Moreover, the reduced $c_\mathrm{L,n}$ leads to significantly reduced wing loadings, simplifying the airframe design challenge. The difference between the onshore variant (solid) and offshore variant (dash-dotted) in Fig. 5.58 is mainly that the absolute values are higher for the latter. As a conclusion, the existence of a Region III(a) increases the nominal power and economic performance, but more significantly simplifies the design challenge e.g. due to a reduced force and lift coefficient, and increased maximum allowed kite mass.

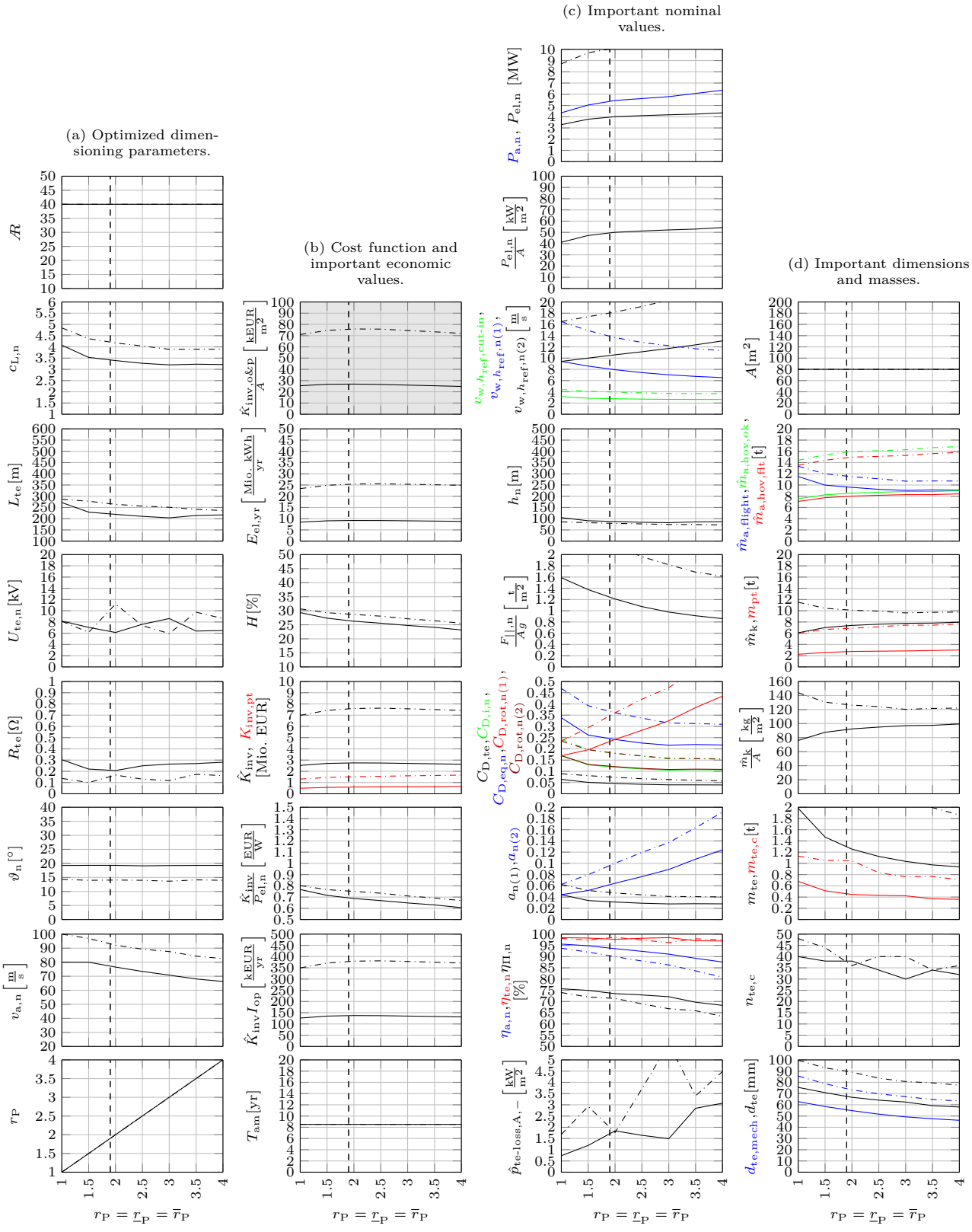

Figure 5.58: Results for different r_P (solid), also for the offshore variant (dash-dotted), compared to the reference scenario (dashed).

5.10.4 Cut-Out Wind Speed

A high cut-out wind speed requires correspondingly capable actuators on the kite, e.g. air brakes. If the cut-out wind speed is reduced, these efforts may be reduced. Moreover, the loads on the overall system might be reduced. Another important point, not resolved by the here employed model, is that the landing in hover mode and the transition from crosswind flight to hover must be reliably possible until the cut-out wind speed is reached plus some safety margin. One can expect that this becomes more challenging for increasing wind speeds. Therefore, it is interesting to investigate the effect for changed $v_{\mathrm{w},h_{\mathrm{ref}},\text{cut-out}}$. Fig. 5.59 reports the results.

The onshore system (solid) is almost completely insensitive on $v_{\mathrm{w},h_{\mathrm{ref}},\text{cut-out}}$, even at the rather low value $v_{\mathrm{w},h_{\mathrm{ref}},\text{cut-out}} = 15\,\mathrm{m/s}$. This implies that the efforts for such a system might be greatly reducible. The results for the offshore system (dash-dotted) are not or only moderately sensitive on $v_{\mathrm{w},h_{\mathrm{ref}},\text{cut-out}}$ around the baseline value $v_{\mathrm{w},h_{\mathrm{ref}},\text{cut-out}} = 25\,\mathrm{m/s}$, but the maximum allowed costs, nominal power, and maximum allowed airborne mass decrease significantly for low $v_{\mathrm{w},h_{\mathrm{ref}},\text{cut-out}}$. The difference between the onshore and offshore systems can be explained by the much higher wind speeds at the offshore site. Note, however, that the offshore-optimized system does not even utilize actuated drag for the power limitation, cf. Fig. 5.7, implying that the power limitation for an offshore system is not much more challenging than for an onshore system with a much lower cut-out wind speed.

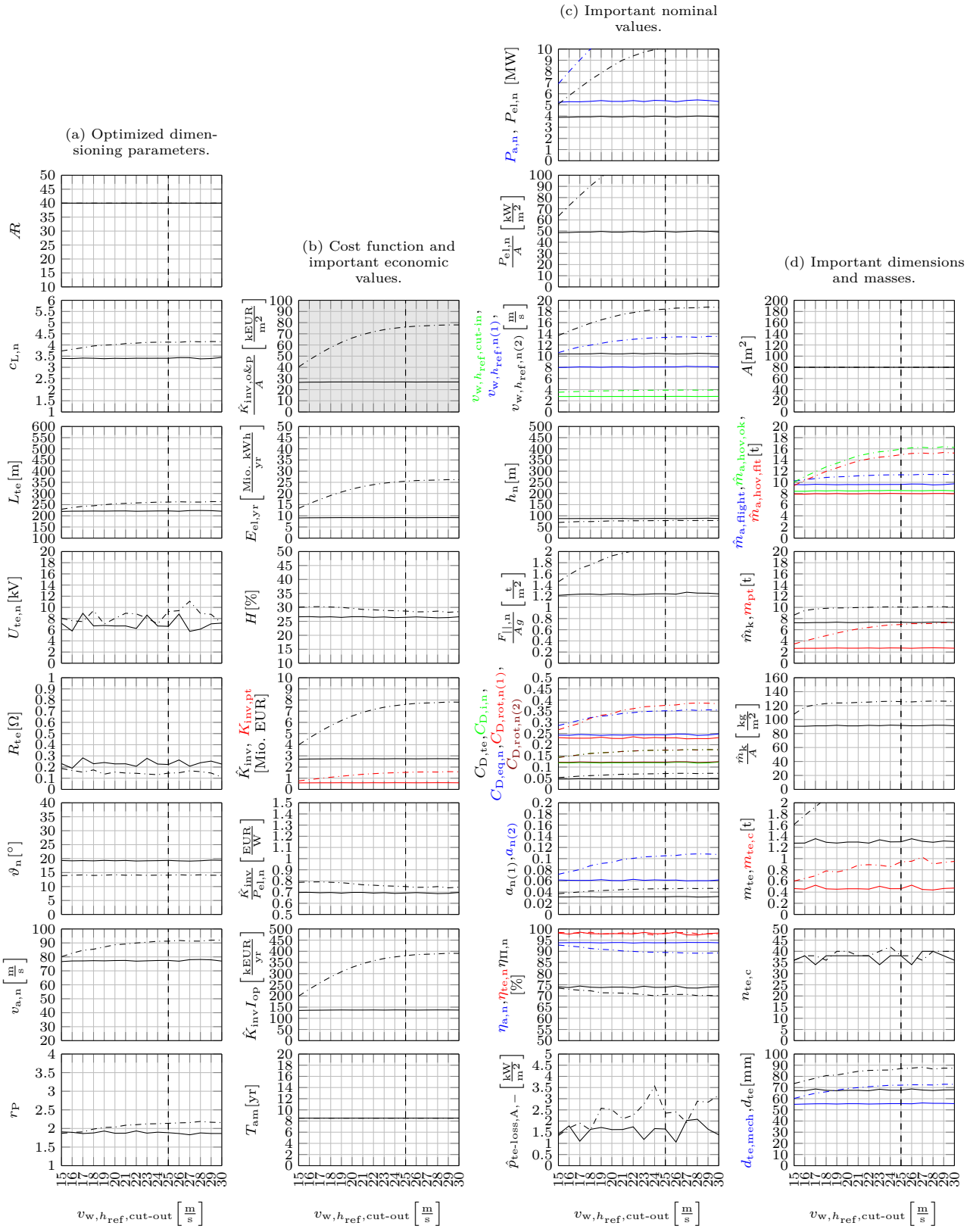

Figure 5.59: Results for different $v_{\mathrm{w},h_{\mathrm{ref}},\mathrm{cut\text{-}out}}$ (solid), also for the offshore variant (dash-dotted), compared to the reference scenario (dashed).

5.11 Sensitivities of Result Bounds

In the following, sensitivity analyses of the result bounds of Tab. 5.3, apart from $\overline{h}_\mathrm{n}$ because the optimal h_n is far away from $\overline{h}_\mathrm{n}$, and of two additional bounds of results from Tab. 5.4 are conducted.

5.11.1 Nominal Angular Speed Upper Bound

In the steady model, the kite does not really fly on a crosswind path such as circles or figure eights and instead stays at the nominal effective azimuth φ_n and elevation ϑ_n. In reality, the kite flies with a significant speed and the flight direction has to be changed permanently. In order to model this fact, an upper bound for the nominal angular speed $\overline{\omega}_\mathrm{n}$ of the kite's flight on the sphere defined by the tether length was introduced. However, depending on the actual airborne mass, its value might be underestimated, which might be the case here, cf. Sect. 5.1.4 or 5.2.5.6. Therefore it is interesting to repeat the optimization with changed $\overline{\omega}_\mathrm{n}$. Fig. 5.60 plots the results.

The maximum allowed costs, nominal powers, and maximum allowed masses have a low sensitivity for the onshore system (solid) and a moderate sensitivity for the offshore system (dash-dotted). For reduced $\overline{\omega}_\mathrm{n}$, the optimizer increases the tether length more than it reduces the nominal airflow speed. In order to compensate the then-increased tether drag, it also increases the nominal airfoil lift coefficient. Nevertheless, these results imply that changes of $\overline{\omega}_\mathrm{n}$ have only a limited impact.

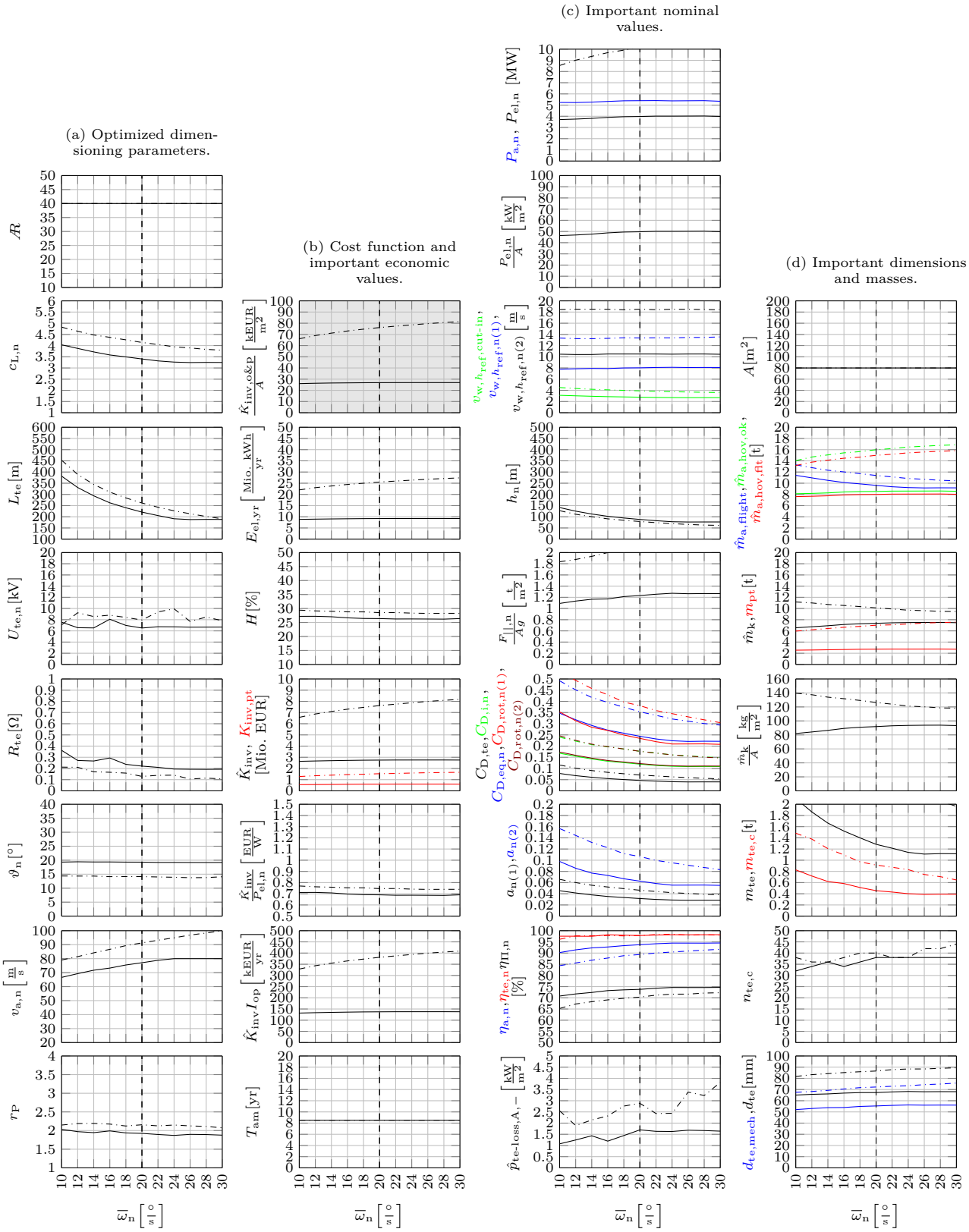

Figure 5.60: Results for different $\overline{\omega}_\mathrm{n}$ (solid), also for the offshore variant (dash-dotted), compared to the reference scenario (dashed).

5.11.2 Nominal Altitude Lower Bound

In the optimization, a lower bound for the nominal altitude $\underline{h}_\mathrm{n}$ was introduced in order to enable a safe operation distance of the kite from the ground. However, this is the *nominal* altitude which is not the same as the minimum altitude that occurs within the circular or figure eight trajectory. In view of the validation with the higher fidelity point-mass model in Sect. 5.1.4, the chosen value for $\underline{h}_\mathrm{n}$ seems to be underestimated, which is why a sensitivity analysis on that parameter is interesting. Fig. 5.61 reports the results.

The maximum allowed costs, nominal powers, and maximum allowed masses are rather insensitive. The nominal airflow speed is reduced for increased $\underline{h}_\mathrm{n}$, which also leads to decreased ω_n (not plotted). These results imply that changes of $\underline{h}_\mathrm{n}$ have only a low impact.

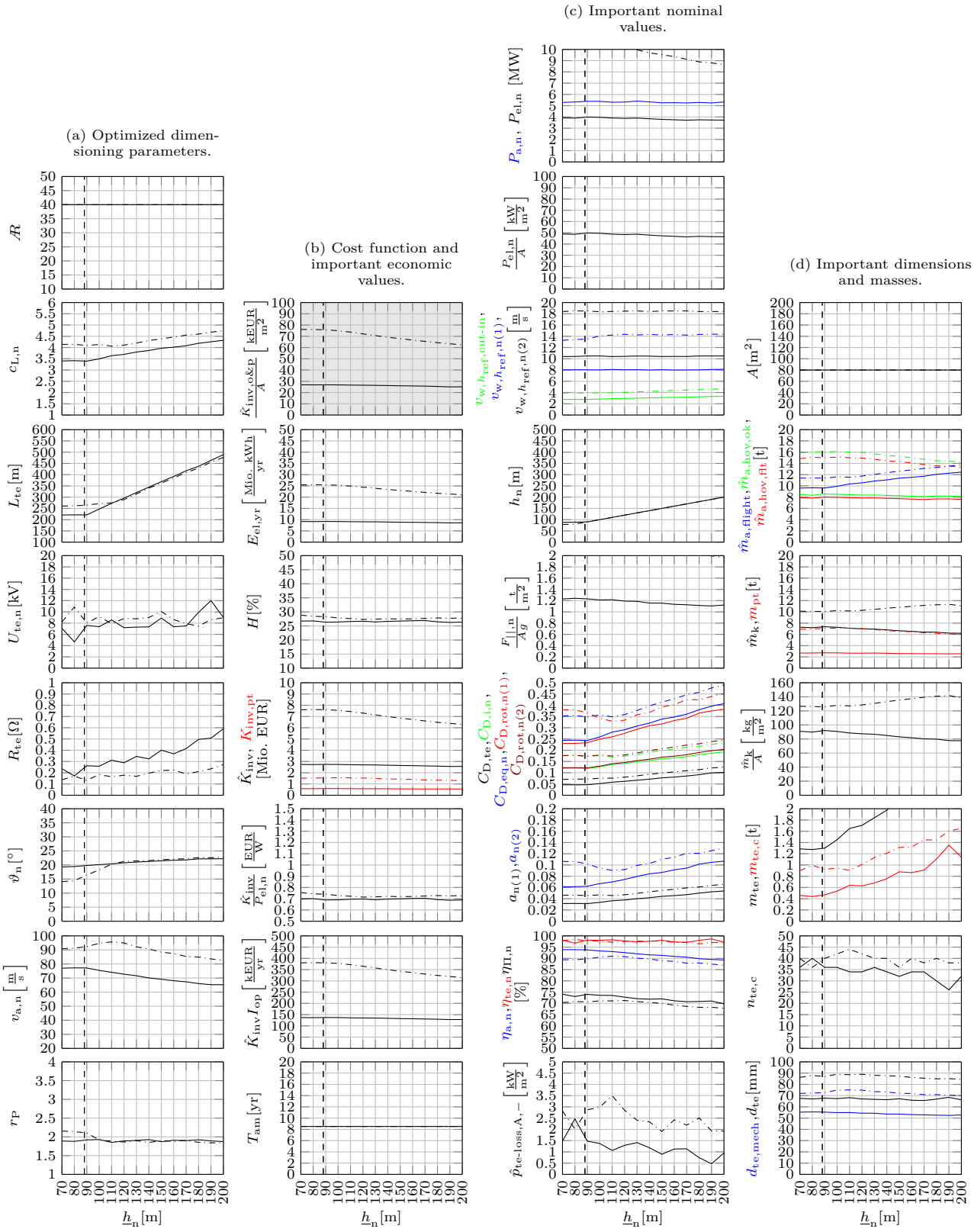

Figure 5.61: Results for different $\underline{h}_\mathrm{n}$ (solid), also for the offshore variant (dash-dotted), compared to the reference scenario (dashed).

5.11.3 Wing Loading Upper Bound

As mentioned in Sect. 5.1.3, the wing loading of the reference scenario is rather high, and it is even higher for the offshore-optimized variant from Sect. 5.2.3. Although the biplane is considered to be designed similar to a truss structure and thus with a low weight and high strength to potentially achieve a high wing loading also for a high aspect ratio, the actual achievable wing loading is not yet known. Therefore, the optimization is repeated with an upper bound on the wing loading $\overline{F_{||,\mathrm{n}}/(Ag)} < \infty$. From the previous parameter study on the nominal airfoil lift coefficient $c_{\mathrm{L,n}}$ in Sect. 5.5.4, it can be expected, that the optimizer reduces $c_{\mathrm{L,n}}$. Therefore, the minimum operational airfoil lift coefficient is again set to

$$c_{\mathrm{L,min\text{-}op}} = 0 \tag{5.19}$$

to ensure feasibility (2.277) also for low $c_{\mathrm{L,n}}$. Note again that this only has an effect on the actuations of the power limitation in power curve Region III(b). Fig. 5.62 reports the results.

For relatively slight reductions of the wing loading, the maximum allowed costs reduce also only slightly, but the nominal powers reduce already quite significantly. For significant reductions of the wing loading, all figures become dramatically worse. To reduce the wing loading, the optimizer reduces both, the nominal airfoil lift coefficient and the nominal airflow speed.

It is not too surprising that a high wing loading is required to achieve high maximum allowed costs per wing area, i.e. a high energy and power density w.r.t. the wing area: For a high power per wing area at a given wind speed, the force and thus wing loading must be high, which is visible from the power and force equations, e.g. (2.183) and (2.193), and which is obvious from conservation of energy, because the usable power of any wind harnessing device is limited by the wind speed multiplied by the force (in the direction of the wind speed). Note however, that a high kite- and airframe mass are allowed for high wing loadings, i.e. it can be expected that the difficulty of the airframe design challenge depends not that much on the wing loading.

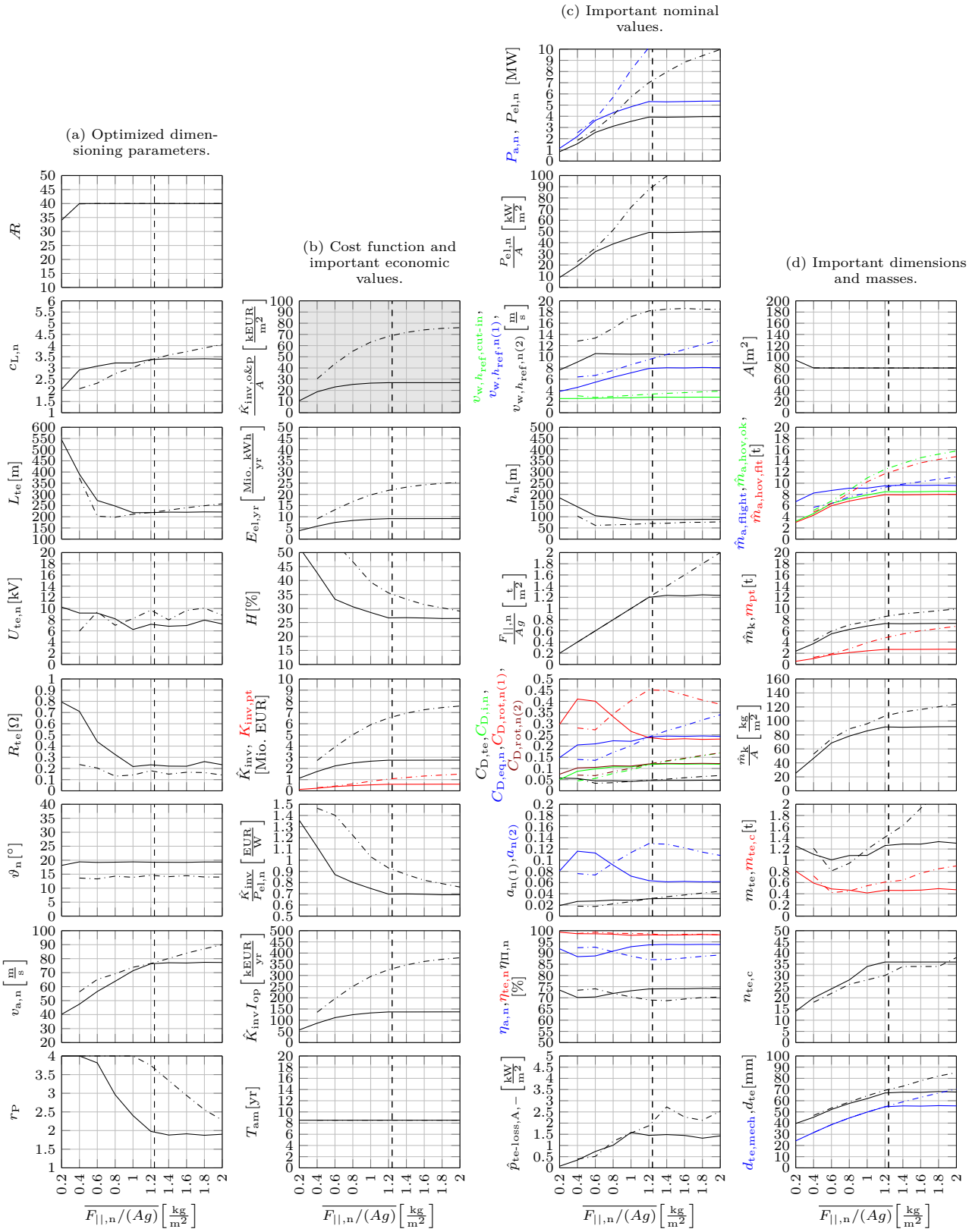

Figure 5.62: Results for different $\overline{F_{||,\mathrm{n}}/(Ag)}$ (solid), also for the offshore variant (dash-dotted), compared to the reference scenario (dashed).

5.11.4 Specific Tether Power Loss Upper Bound

The specific tether power loss of the reference scenario seems with $\hat{p}_{\text{te-loss,A,}-} \approx 1.6\,\text{kW/m}^2$ rather high. To investigate the effects of a reduced value, the optimization is repeated, but with a bound for the specific tether power loss $\overline{\hat{p}}_{\text{te-loss,A,}-} < \infty$. Fig. 5.63 plots the results for a range of $\overline{\hat{p}}_{\text{te-loss,A,}-}$ in solid.

All important figures of merit are very insensitive. Even at $100\,\text{W/m}^2$, the maximum allowed costs reduce by only a few percent.

However, the optimizer increases significantly the tether voltage to reduce the specific tether power loss, which might increase complexity and costs of the development of the power electronics too much. Therefore, the same optimization is repeated once more with the additional constraint, that the tether transmission voltage $U_{\text{te,n}} = \underline{U}_{\text{te,n}} = \overline{U}_{\text{te,n}}$ stays at the value of the reference scenario. The results are also plotted in Fig. 5.63 in dash-dotted.

Now the optimizer increases the conductors' cross section area stronger to keep the specific tether power loss low, but the important figures of merit like maximum allowed costs and nominal power are still very insensitive. Only for very low values around $100\,\text{W/m}^2$, a notable deterioration is visible. These results imply, that thermodynamic problems regarding the tether should not arise in a detailed tether design and power plant realization, or should be solvable relatively easily.

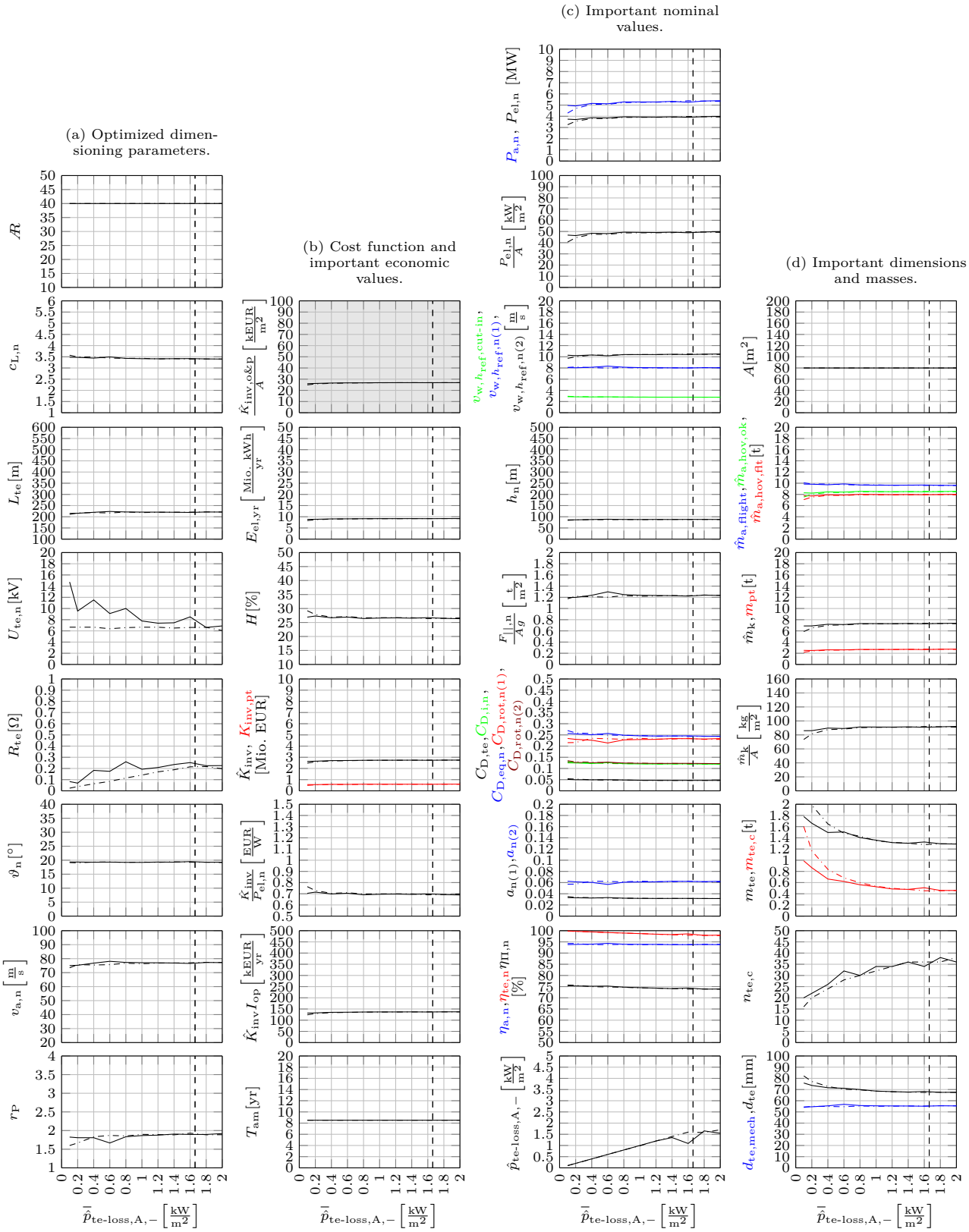

Figure 5.63: Results for different $\overline{\hat{p}}_{\text{te-loss,A,-}}$ (solid), also with constraint of $\overline{U}_{\text{te,n}}$ at the value of the reference scenario (dash-dotted), compared to the reference scenario (dashed).

Chapter 6

Conclusions

6.1 Summary

The *multidisciplinary optimization of drag power kites* is the focus of this dissertation. To allow for fast optimizations and parameter studies, but simultaneously obtain reasonable results by considering all important domains and dominant effects, a multidisciplinary steady systems engineering model of the kite power plant is derived. It consists of a number of submodels which are in part taken from literature, in part extended from literature, and in part derived from scratch. In particular,

- the kite dynamics model is based on an extension of Loyd's crosswind kite power model,
- the kite's aerodynamics model is based on a solution from lifting-line theory,
- the tether is modeled as straight for a simplified aerodynamics model and is dimensioned in accordance with the nominal mechanical and electrical loads together with an electrical cables model,
- the rotors are modeled with Betz' model as actuator disks,
- the powertrain is modeled with efficiency losses, costs, and component masses,
- the atmosphere is modeled with a wind shear and wind probability distribution,
- the kite's control is modeled by an analytically optimized complete power curve, and
- the economics is modeled with interest rate and important capital expenditure and operational expenditure contributions.

Therefore, important characteristics of all involved disciplines are represented: mechanical engineering (flight dynamics, aerodynamics, materials, structure, and thermodynamics), electrical engineering (power conversions through electrical drives and power electronics, and electricity transmission through tether), control engineering (power curve with actuator limitations, as well as reliability and safety issues due to rotor failures), meteorology (wind resource), and business administration (power plant economics). The submodel equations are coupled into a sequence of (mostly) explicit analytical equations, and the kite power plant parameters are divided into a set of "fixed parameters" (e.g. gravitational acceleration) and "dimensioning parameters" (e.g. tether length). A key idea for that is to not estimate the total costs and the total mass, but instead to derive the maximum allowed total costs and the maximum allowed total mass. Therefore, no further and likely rather rough assumptions on cost factors and mass factors have to be introduced, but instead requirements for a detailed power plant design are computed. The system's engineering model equations are implemented in MATLAB. The computation of a complete power curve and all figures of merit for a parameter set takes only a fraction of a second on a modern computer.

The derived model is validated successfully against the measured power curve of Makani's Wing 7, expected power curves for the Makani M600 and M5 systems, and against simulations

with the higher fidelity point-mass model. For the latter, a novel control scheme is derived, which in particular includes the limitation of the kite's speed, forces, and power, such that the complete power curve can be recorded.

With the genetic algorithm CMA-ES, all "dimensioning parameters" can be optimized. The chosen fitness function to be maximized is the maximum allowed investment costs of airframe etc., development costs, and profit margin w.r.t. the kite area with reasonable constraints on parameters and results. This means that the research and development budget as well as the profit margin for the kite power plant manufacturer per square meter kite area are maximized for the given targeted market and power plant deployment site.

Numerous optimizations and parameter studies are conducted. One result is that a 40 m wing span biplane kite with a wing area of $80\,\mathrm{m}^2$, a lift coefficient of ≈ 3.4, and a tether length of $\approx 220\,\mathrm{m}$ is expected to achieve a nominal electrical power of $\approx 4\,\mathrm{MW}$ with a power density of $\approx 50\,\mathrm{kW/m^2}$. The maximum allowed specific kite mass of $\approx 90\,\mathrm{kg/m^2}$ seems realizable. Further possible specific systems are computed, e.g. monoplane-, offshore-, and small-scale variants, with the results that a biplane is always expected to outperform a monoplane, offshore sites improve important figures of merit in part by several times compared to the "EEG reference location" from the German Renewable Energy Law, and small-scale systems are already economically interesting for niche markets. With the 40 m wing span biplane kite as reference scenario, parameter studies for vast changes of almost every parameter are conducted. Tab. 6.1 gives a qualitative summary of the found sensitivities on the important resulting figures of merit of the fitness function $\hat{K}_{\mathrm{inv,o\&p}}/A$, nominal electrical power $P_{\mathrm{el,n}}$, maximum allowed effective airborne mass for crosswind flight $\hat{m}_{\mathrm{a,flight}}$, and maximum allowed effective airborne mass for hovering with rotor failure $\hat{m}_{\mathrm{a,hov,flt}}$. Most important is the $\hat{K}_{\mathrm{inv,o\&p}}/A$-column, for which a further short summary can be given: On the one hand, the mean wind speed is the most important parameter of a deployment site. Moreover, all economic parameters and all kite aerodynamics parameters have a high sensitivity on the overall power plant economics. In particular, a high nominal airfoil lift coefficient and thus a high wing loading, and a high span efficiency enable high maximum allowed costs and a high power density. Those are the reasons why a biplane with its truss-like structure and thus high strength-to-weight ratio as well as a possibly very high aspect ratio is an interesting concept for a drag power kite. On the other hand, different tether materials and the majority of the tether parameters, even the nominal tether voltage, hardly affect any of the important figures of merit.

It can be concluded, that all goals stated at the beginning, in Sect. 1.3, are achieved.

6.2 Assessment of Hypotheses Stated at the Beginning

Based on the assumptions made for the derived systems engineering model, the hypotheses stated in Sect. 1.6 can now be assessed with the results found in this dissertation:

Hypothesis 1: *Confirmed. A multidisciplinary model covering all relevant effects is derived, the model is validated successfully, and the execution of optimizations takes only a few seconds to a few minutes on a modern computer.*

Hypothesis 2: *This hypothesis can neither be confirmed nor disconfirmed with the here utilized systems engineering model.*

Hypothesis 3: *Disconfirmed. For an optimized system, the capacity factor tends to stay around 30 %, similar to a conventional wind turbine. This is due to the capacity factor paradox and due to the fact that for realistic wind shears not much is gained for increased altitudes because of the then increased cosine loss, tether drag loss, and tether transmission loss.*

Table 6.1: Determined sensitivities on important results for the utility-scale biplane kite (reference scenario) from Chap. 5 expressed qualitatively. This table was shown in the prior work by the author of this dissertation in [111, Poster, Tab. 1].

Parameter	Sensitivity on $\hat{K}_{\mathrm{inv,o\&p}}/A$	Sensitivity on $P_{\mathrm{el,n}}$	Sensitivity on $\hat{m}_{\mathrm{a,flight}}$	Sensitivity on $\hat{m}_{\mathrm{a,hov,flt}}$
Environmental parameters for considered installation site.				
ρ	moderate	moderate	moderate	moderate
z_0	low	low	moderate	low
λ	low	high	moderate	high
μ	high	high	high	high
Economic parameters for targeted market.				
k_{LCOE}	high	moderate	moderate	moderate
I	high	moderate	low	moderate
T	high	moderate	low	low
I_{op}	high	moderate	low	low
Kite aerodynamics parameters.				
b	high	high	high	high
$\mathit{Æ}$	high	moderate	high	high
n_{mw} (cf. Sect. 5.2)	high	high	high	high
$c_{\mathrm{D,2}}$	high	high	high	high
$c_{\mathrm{L,n}} = \underline{c}_{\mathrm{L,n}} = \overline{c}_{\mathrm{L,n}}$	high	high	high	high
e	high	high	high	high
$C_{\mathrm{D,k,o}}$	high	moderate	moderate	moderate
Rotor parameters.				
n_{rot}	low	low	low	moderate
r_{rot}	moderate	moderate	low	high
$\eta_{\mathrm{rot,+}}$	moderate	moderate	low	low
Tether parameters.				
$U_{\mathrm{te,n}} = \underline{U}_{\mathrm{te,n}} = \overline{U}_{\mathrm{te,n}}$	low	low	low	low
$c_{\mathrm{D,te}}$	high	high	low	moderate
$n_{\mathrm{te,c}}$	low	low	low	low
tether materials	low	low	low	low
$w_{\mathrm{te,c,j}}$	low	low	low	low
$S_{\mathrm{te,mech}}$	low	low	low	low
$S_{\mathrm{te,ins}}$	low	low	low	low
$f_{\mathrm{te,c,w}}$	low	low	low	low
Powertrain subsystems parameters.				
k_{pt}	high	high	low	moderate
$S_{\mathrm{hov,flt}}$	low	low	low	high
Ground station parameters and flight trajectory parameters.				
h_{to}	moderate	moderate	low	moderate
φ_{n}	moderate	moderate	low	low
Power curve "shaping" parameters.				
$v_{\mathrm{a,min}}$	low	low	high	low
$v_{\mathrm{a,n}}$	moderate	high	moderate	moderate
$r_{\mathrm{P}} = \underline{r}_{\mathrm{P}} = \overline{r}_{\mathrm{P}}$	low	moderate	moderate	low
$v_{\mathrm{w},h_{\mathrm{ref}},\mathrm{cut\text{-}out}}$ (onshore)	low	low	low	low
Result bounds.				
$\overline{\omega}_{\mathrm{n}}$	low	low	moderate	low
$\overline{h}_{\mathrm{n}}$	low	low	moderate	low
$\overline{F_{\mathrm{\|,n}}/(Ag)}$	high	high	high	high
$\hat{\overline{p}}_{\mathrm{te\text{-}loss,A,-}}$	low	low	low	low

Hypothesis 4: *Disconfirmed. The optimal airfoil lift coefficient tends to be at least around three which can be achieved only with a multi-element airfoil.*

Hypothesis 5: *Confirmed. The optimal tether transmission voltage for utility-scale systems is in the order of* $8\,\mathrm{kV}$*, but with a very low sensitivity also for much lower voltages.*

Hypothesis 6: *Confirmed. The optimal tether inclination is around* $20\,^\circ$*, the optimal tether length is only a few hundred meters, and the optimal altitude above ground is not necessarily higher than the height of large conventional wind turbines.*

Hypothesis 7: *Disconfirmed. At least for a simplified launch and landing without tilting rotors or a tilting tail, a tower is vital. Moreover, a small to medium height tower likely bears its own costs and makes additional profit due to the increased cosine efficiency.*

Hypothesis 8: *Disconfirmed. The achievable power density can well exceed* $100\,\mathrm{kW/m^2}$ *for a large-scale biplane kite at an offshore site.*

Hypothesis 9: *Disconfirmed. Even if the aerodynamic interference between biplane wings deteriorates* e*,* $C_{\mathrm{D,k,o}}$*, and/or* $c_{\mathrm{L,n}}$*, a biplane has advantages, e.g. it has twice the area for a given wing span and wing aspect ratio compared to a monoplane and is expected to better withstand the necessary high wing loadings due its truss-like structure while being comparatively light.*

Hypothesis 10: *This hypothesis can neither be conclusively confirmed nor disconfirmed with the here utilized systems engineering model. However, the maximum allowed specific kite mass for a utility-scale system may well exceed* $100\,\mathrm{kg/m^2}$*, with which a kite made from a light metal such as aluminum (and hence possibly lower design and manufacturing efforts and costs as well as better recyclability than carbon fiber) may be realizable.*

Hypothesis 11: *Disconfirmed (at least in part). Again, the maximum allowed specific kite mass for a utility-scale system may well exceed* $100\,\mathrm{kg/m^2}$*. Moreover, the electrical drives are high-speed and low-torque. As the mass of an electrical drive depends in principle on the nominal torque instead of the nominal power, the electrical drives of a drag power kite are much lighter than those of a lift power kite, whose drive is low-speed and high-torque. The tether with the integrated electrical cables is not that much thicker and heavier, the Betz limit does not apply, and the power conversion and transmission losses are significant but not that bad (a lift power kite should have about the same efficiency due to the significant reel-in phase time and its power consumption). Finally, the tether transmission voltage may be only a few kilovolts, which may allow also for some off-the-shelf components (note that it is questionable, if off-the-shelf components are also possible for lift power, cf. Appendix A).*

Hypothesis 12: *Confirmed. Even though a steel tether does not reduce the nominal power and economics much, the tether mass is much higher compared to a Kevlar- or Dyneema-tether core. Apart from that, steel has further disadvantages such as a much lower elastic modulus.*

Hypothesis 13: *Disconfirmed. Carbon nanotubes increase the system performance, but only moderately.*

Hypothesis 14: *Confirmed. A high aspect ratio is very vital for a kite, in particular with the high optimal lift coefficient. In almost all optimization results, the aspect ratio is at its upper bound* $AR = \overline{AR} = 40$*.*

Hypothesis 15: *Confirmed (at least in part). Small-scale systems are already economically interesting in niche markets such as island grids with high diesel generator penetration, and large offshore kites may generate several tens of megawatts of electrical power. The larger the system, the higher the power density.*

Hypothesis 16: *Confirmed. A wide Region III(a) in the power curve, in which the force is constant and the power increases, reduces significantly the optimal airfoil lift coefficient and wing loading.*

Hypothesis 17: *Confirmed. The maximum allowed costs for an offshore system may be well more than twice as much as for an onshore system.*

Hypothesis 18: *Disconfirmed. A powertrain approach without single point of failure was published by the author of this dissertation in [106]. The main constraint for that solution of a certain number of electrical cables is very insensitive on the power plant figures of merit, and thus no negative effects such as reduced performance are expected.*

6.3 Critical Assessment of Approach and Results

A multidisciplinary steady drag power kite plant model is derived with the aim to cover all dominant effects (systems engineering model). The model is then validated particularly against published data from measurements and against a higher fidelity model. Finally, it is applied through conducting optimizations and parameter studies. This whole approach of (i) model derivation, (ii) model validation, and (iii) model application can be assessed as vital and scientific, with which a number of interesting results can be obtained and a number of interesting conclusions can be drawn. To repeat just one interesting conclusion, it is found that the chosen nominal tether voltage hardly has an effect on the system efficiency.

However, one can claim that the model validation could be extended further, and the drawn conclusions must be taken with care, because they are dependent on the level of accuracy of the derived steady model. In particular, the model is well validated only against the measurements of the small-scale Makani Wing 7, and then the model is used to compute a utility-scale biplane, which is an extrapolation. It cannot be excluded that some conclusions have to be retracted, once results of increased fidelity models or measurements from technology demonstrations are available. Therefore, one of the next steps must be the validation of the optimization results with increased fidelity models (e.g. 3D CFDs and FEMs of the kite) and the setup and flying of demonstrators. However, this requires substantial man-power, and significant funding, and can therefore not be part of a single doctoral research project. Moreover, as the model validations found no evidence that the derived steady model is false, this model is deemed particularly useful for a first or preliminary kite design and its parameter optimization, as well as to determine sensitivities of different design choices (e.g. the nominal tether voltage level). This can be seen as the most important practical contribution of this dissertation.

6.4 Recommendations

The method developed in this dissertation can become a viable tool to support decision making within a kite power company as visualized in Fig. 6.1: Decision makers want to know the impact of certain decisions, e.g. a power electronics engineer may think that a lower tether voltage is easier and faster realizable. She asks the systems engineer if the impact on the other subsystems or on the system as a whole is tolerable. The systems engineer then uses the framework of

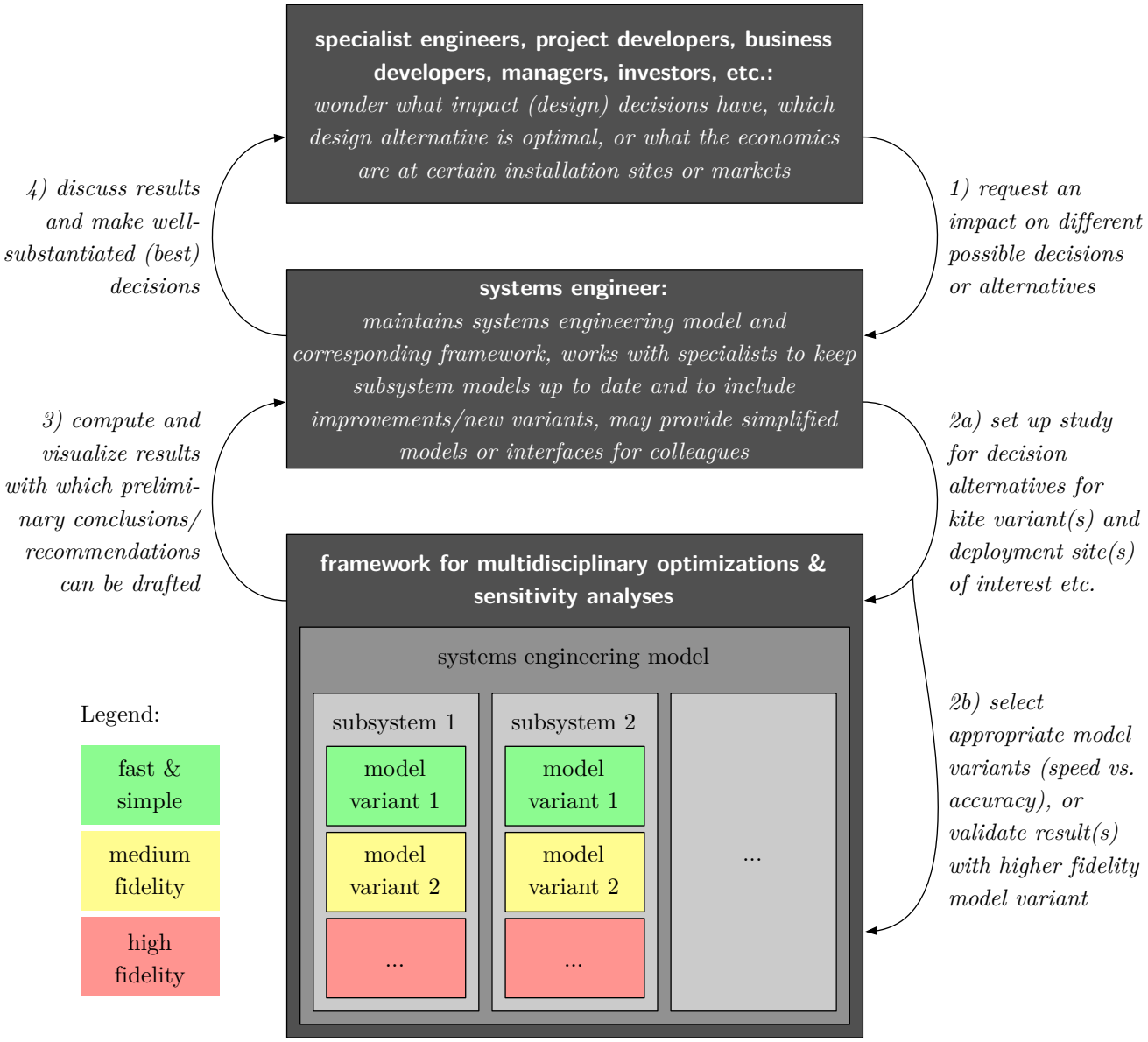

Figure 6.1: Multidisciplinary optimizations as a tool for decision making at a kite power plant research and development company.

systems engineering models and optimizations. He sets up the framework for this particular study, possibly also for different kite variants and deployment sites, and selects appropriate model variants for the speed-vs.-accuracy trade-off. He may also first use the fast and simple models and make only one run of the higher fidelity models at the end to validate the results. If the results do not match well, the parameter optimization studies have to be repeated e.g. with higher fidelity models. Once sound results are obtained, the systems engineer visualizes them, drafts conclusions and recommendations, and discusses the results with the power electronics engineer and possibly others. Finally, the best decisions are made, which are then well-substantiated

because of the systems engineering framework. Again, for this particular example, the interesting and astonishing result is that the power electronics engineer may select a much lower voltage than she might have thought initially.

A further example of a systems engineer's work is already applied in this dissertation: The utility-scale biplane is optimized with the steady systems engineering model, and then, for the sake of validation, the steady kite dynamics subsystem model (fast & simple, green in Fig. 6.1) is replaced by the higher fidelity point-mass model (medium fidelity, yellow in Fig. 6.1). One can directly imagine a further enhancement of the framework through further subsystem model variants for that, e.g. a rigid body model or a multibody kite model might then be the highest fidelity version (red in Fig. 6.1).

Further examples of questions that a systems engineer can answer include the following:

- What is the impact of other design (parameter) alternatives which are arguably easier for a specialist engineer? For instance, an aerodynamics engineer may wonder about the impact of a lower and easier realizable nominal airfoil lift coefficient, a structural engineer may wonder about the impact of a lower aspect ratio, or business developers and investors may wonder about the impact of different interest rates.
- Vice versa, e.g. an aerodynamics engineer designing the rotor wants to have a requirement specification such as rotor operating points.
- Project developers may wonder, what the economics of the current system are for another deployment site and if certain values can be optimized at low costs. For instance, the current system design may be optimized for a low-wind site in Europe and a customer wants to deploy it at a high-wind arctic site. The systems engineer could simply evaluate the new performance, similar to Sect. 5.2.2. However, some optimizations to the power plant without changing the system much and thus at low costs could be introduced: The nominal elevation angle could be optimized without changing a single component, or the tether length could be optimized while retaining all cross-section geometries and thus only introduce small or negligible costs.

To answer all these questions, the systems engineering framework needs to be consistently advanced and maintained, and specialist engineers should contribute further subsystem model variants or refinements. The systems engineer may be responsible for implementing the mathematical equations provided by a specialist engineer into the framework, or he provides an access, e.g. a *git*-repository, such that specialist engineers can contribute directly. All engineers validate and refine the models from measured data once new systems are built and flown.

The systems engineer may also provide simplified models or simple interfaces to the framework for regular tasks of project developers, business developers, and other less-technical persons, who need to evaluate regularly e.g. the economics for different deployment sites. A further alternative is to introduce model-based systems engineering as a primary methodology of decision making and information exchange within the company [169], and to include methods and models from this dissertation into such an approach.

It should be noted, that these tasks and a systems engineer's work and advice are likely vital at every stage of a kite power company: At the beginning, the systems engineer can identify basic sensitivities and basic optimal design parameters (e.g. the nominal tether voltage), and at a later stage the systems engineering model's fidelity has to be high to identify new and the most sensitive improvement opportunities which give the best return on investment.

Very similar approaches can also be used in other energy technologies. For instance, with the same method wave power plants could be modeled. For established technologies, there may be software products already available, e.g. the software "Bladed" [170] is popular at conventional wind turbine manufacturers.

6.5 Outlook

In future works, higher fidelity subsystem model variants should be introduced. Appendix D lists a few ideas on model refinements. However, a drawback of higher fidelity models is a significant increase of the computational load and higher efforts for the model setup (e.g. reasonable parameter estimations). A challenge seems to be the complexity of a versatile systems engineering framework with many subsystem model variants, to identify which subsystem model variant is compatible with other subsystem model variants, and to collaborate with specialist engineers. For example, the here developed submodel coupling algorithm cannot be used directly to study the performance changes of the reference scenario with the utility-scale biplane for an arctic site with a different air density, because then the tether cross section, nominal forces, nominal powers, and so forth change, which in turn means that the power plant design is changed. A proper model implementation approach for the required level of versatility and computational efficiency, a proper programming language and programming framework (e.g. software libraries), and a proper collaboration environment (for specialist engineers etc.) has to be chosen. Therefore, the here utilized MATLAB software might not be the best choice. In addition to that, optimizations with higher fidelity models likely need to be executed on clusters. For example, the exchange of the steady dynamics model with the point-mass model already increased the computational load dramatically from a fraction of a second to about one hour to compute the performance of a single parameter set. However, that computation is highly parallelizable, because the power curve results for different wind speeds are independent from each other.

Another idea is to use the developed model and code, possibly only with refinements which retain the steady and mostly explicit nature of the systems engineering model, for a preliminary kite power plant design and to define requirements for a detailed design. For example, the results of the presented studies give requirements for the maximum allowed costs, the maximum allowed mass, the required wing loading capability, and nominal airfoil lift coefficient. During the development process, the "fixed parameters" (e.g. efficiency factors) should become more certain. With that, the here presented optimizations can be redone, to refine the design requirements for the kite power plant. With a few such iterations, a suitable and close to optimal drag power kite plant design could be found.

Finally, further validations with high fidelity simulations (e.g. 3D CFDs and FEMs) and demonstrators are very important and should become a high priority in future works. In particular, the optimized small-scale biplane kite should be built as demonstrator, possibly with a later commercialization in a niche market. In fact, at the time of finalizing this dissertation, research proposals applying for funding for this goal were submitted. Moreover, the design and construction of the tiny-scale biplane kite together with further increased fidelity simulations has been approached, in order to try to validate experimentally at least parts of the biplane concept. The photograph shown in the preface on p. viii gives an impression on the status of these works at the time of finalizing this dissertation.

A further interesting research would be to apply the findings and methods of this dissertation also to other airborne wind energy concepts, in particular to lift power kites or multiple kite systems.

Appendix A

An Assessment of Airborne Wind Energy Concepts

This chapter further motivates, why the drag power concept with rigid kites from the concept family of crosswind kite power or generally from airborne wind energy is so interesting and became the focus of this doctoral research and dissertation. Some findings presented here were published in the prior work of the author of this dissertation [171].

A.1 Requirements of a Power Plant

Electricity is a commodity, it is indistinguishable from the generation source and can be used arbitrarily by any electric load. Therefore, within the global capitalistic economic system (which is meant impartial), one can state clearly a fundamental requirement of *any* power plant:

(R_0) The fundamental and quantitative requirement of any power plant is to achieve a low levelized cost of electricity (LCOE), which is competitive in the target market.

If this requirement is not fulfilled, there is no business case and thus hardly a chance to deploy a significant amount of systems, maybe apart from a chance of a small niche market in which the costs do not matter much (e.g. military).

There might be economically very interesting niche markets for many different types of airborne wind energy concepts. For instance, flexible kites have the disadvantage of a low life time but are very light, hence they might have an advantage if a market requires a high mobility. Other systems with heavier e.g. rigid kites might be harder to transport, i.e. more costly to transport, which can be included overall in the LCOE. A direct comparison of the LCOE of a flexible kite system and of a rigid kite system might than be in favor of the first.

The fundamental motivation of this research and dissertation is to make as significant a contribution as possible against anthropogenic global warming and for the energy shift towards 100 % clean, renewable primary energy, worldwide. Therefore, only the mass markets of the public electricity grids are focused, i.e. airborne wind energy systems which can potentially reach multiple megawatts of power and LCOEs competitive with all other energy technologies, including the cheapest ones, coal power plants. Note that even if a kite with 10 MW can be built and commercially deployed—which is a few megawatts larger than todays biggest commercially available wind turbines—, then still 300 of such kites are required to replace energy-wise only a single block of a coal power plant, when assuming 33 % capacity factor for the kite and 1 GW power with 99 % capacity factor for the coal power plant block.

It is challenging if not impossible to check if the fundamental requirement (R_0) can be fulfilled for the whole concept space of airborne wind energy systems. Therefore, this requirement has to be translated into derived requirements to simplify comparisons. The following six requirements were identified for an airborne wind energy plant:

(R_1) Simplicity.

(R_2) Autonomous Operation.

(R_3) High Reliability.

(R_4) Long Life Time.

(R_5) High Power- and Energy Density.

(R_6) Scalability.

Many of these derived requirements in part depend on each other. In the following subsections, further details are given.

A.1.1 Requirement (R_1): Simplicity

Conventional wind power plants are very simple compared to airborne wind energy systems: It is basically a rotor mounted to a tower, with relatively simple and established control methods. Fail-safe methods are available and relatively simple. Already in the 1970ies many companies started developing systems similar to the ones of today and commercialized them within months or only a few years after start of development [172]. Today, these machines achieve more operating hours than most other machines, and supply chains and series production are all established [172]. Wind turbines are a proven technology and are *bankable*, i.e. risks and capital costs are low.

In contrast, today not a single airborne wind energy company has a product to sell despite years of development up to more than a decade. Most airborne wind energy systems are inherently unstable without the possibility of a simple emergency shutoff. Supply chains and series production are yet to be established. The technology is unproven and the risk for an investor is very high.

Alone from these facts, it is clear that an airborne wind energy system must be simple, ideally as simple as possible (KISS-principle: keep it simple and stupid). Simplicity refers to the flight patterns or control of the power plant, the design and engineering efforts, as well as the manufacturability. Simplicity also helps to achieve the other derived requirements, particularly (R_2) and (R_3).

A.1.2 Requirement (R_2): Autonomous Operation

An airborne wind power plant must be operating fully autonomous without any human intervention in all flight phases: launch, power generation, landing, relaunch. If a pilot was required to fly the system, actually many pilots in shifts plus holiday and sick day backup pilots are needed for a single power plant which must be ready to operate 24-7. Consequently, profitability would be impossible (unless maybe for very large systems with many megawatts power, which are unlikely system sizes anytime soon). Moreover, human pilots may not be in favor of (R_3).

A.1.3 Requirement (R_3): High Reliability

A reliable power plant, i.e. with a very high fault tolerance, is a paramount requirement, not only for economic viability, but also for general permissions and certifications as well as for acceptance by the general public. In particular, a crash of the airborne system is the maximum credible accident, which *must* have only a negligibly low probability of occurrence. People could die if the airborne system crashes above their heads. Additionally, significant capital is lost [173, 174]. Both is also true for flexible kites, because people can get killed by large enough kites or by the tensioned tethers, damages cannot be excluded, and technicians would have to catch and reset the kite. Moreover, to be profitable, a high availability with rare inspections, revisions, and maintenance are required.

A.1.4 Requirement (R_4): Long Life Time

A renewable energy power plant is capital intensive with little to no operational expenses. The investment price can therefore be distributed over the life time (with compound interest). If the life time is short, then fewer years for this distribution are available, or the operational expenses are more significant, and the availability is reduced if e.g. the kite has to be replaced regularly. Conventional wind turbines and photovoltaic modules reach life times of 20 years and over. Fossil power plants can reach even more than twice this value. Therefore, an airborne wind energy power plant should achieve a life time in the same magnitude, at least tens of years.

A.1.5 Requirement (R_5): High Power- and Energy Density

If e.g. a kite in the size of an Airbus A380 would only generate a few kilowatts, it is apparent that profitability is likely impossible. Instead, also very small and light kites should be able to generate significant amounts of power and energy. Hence, the airborne wind energy concept should enable a high power and energy density referred to the size (e.g. referred to the kite size in W/m^2) and referred to the construction mass (e.g. referred to the kite mass or overall power plant construction mass in W/kg). In addition to that, the occupied ground area should not be much larger than that of a conventional wind turbine, to limit the land lease costs or offshore construction costs to a similar amount as for a conventional wind turbine.

A.1.6 Requirement (R_6): Scalability

The development of a new technology is almost only possible in small steps, because of the high risk of concept and design flaws. Therefore, with limited budget, and thus with limited risk of an investor, an airborne wind energy concept must be able to prove in all key aspects in small-scale first. Ideally, such small-scale systems can already be sold on markets, which may be niche markets, to also prove the economic viability and acceptance. Second, the same small-scale-proven technology must be scalable to (much) larger scales (utility-scale), in order to tap the mass markets of the public grids and contribute significant amounts of energy.

A.2 Comparison and Assessment of Airborne Wind Energy Concepts

In the following, airborne wind energy concepts are compared and assessed against the stated requirements. This assessment lead to the choice of the focus of this dissertation: drag power.

A.2.1 Narrowing the Airborne Wind Energy Concept Space

Fig A.1 shows one of the first airborne wind energy experiments conducted within this doctoral research project: As most teams, also here the lift power concept with a flexible kite was the first choice because of the cheap off-the-shelf kite and because all expensive and complex hardware parts can be kept on ground. A ground station from standard components was designed and built. It was possible to let the kite fly autonomously and contributions were published [171, 175–177]. However, it was much harder than expected to get to the point shown in Fig. A.1. It took about one year of work and three attempts in the field. The kite did not fly very reliably. To this point, the challenging autonomous launch and landing as proposed in [175, 176], which was the original goal, were not even considered. This work made clear that airborne wind energy systems are complex, complicated, and hard to implement. Every actuator and every sensor

Figure A.1: Successful automatic flight of a simple kite conducted by the author of this dissertation in summer 2015 with the former project partner University of California, Irvine, Power Electronics Lab (Prof. Smedley).

need to be thoroughly designed and tested and may require several iterations. It seems very challenging to design and built a marketable flexible kite lift power system. This rationale lead to a complete rethinking if this airborne wind energy concept is really a good choice, or more generally if any airborne wind energy concept can be a good choice at all to fulfill all requirements of a power plant. This was the time when the above requirements were derived. Based on these requirements, many airborne wind energy concepts can be assessed as likely not viable.

Airborne wind energy concepts based on flexible materials will likely not fulfill at least some requirements: For instance, the life time (R_4) of a flexible kite (like a surf kite) is with today's materials limited to a few thousand hours, cf. e.g. [178]. The kite would need to be replaced every few months (a year has 8,760 hours). Another reason is the low aerodynamic efficiency of such flexible kites and particularly that the maximum lift coefficient is limited to around one. Therefore, large kites are required to generate significant power which likely does not fulfill (R_5) and is also not in favor of (R_6).

Airborne wind energy concepts, in which the flying object is not flown crosswind, will likely also not fulfill at least (R_5) and (R_6), cf. e.g. [13]. Moreover, airborne wind energy concepts with "rotating tethers" such as in [179] can also be excluded, as they likely do not fulfill (R_1) and (R_3)–(R_6). Finally, also multiple kite systems, i.e. at least two kites on a possibly long shared tether, are likely too complex and thus do not fulfill (R_1).

What is left is crosswind kite power with single rigid kites, i.e. lift power and drag power wherein the kite is made from light metals such as aluminum or compound materials such as carbon fiber. This assessment is expected to hold for both, the short term and the foreseeable medium to long term. For instance, even if a new high-tech material for flexible kites can be developed which lasts for 20 years, other requirements are likely still not fulfilled. In contrast, crosswind kite power concepts with rigid kites are comparatively simple (R_1), fully autonomous operation has even in part been demonstrated experimentally (R_2), a high reliability (R_3) can be expected with good design and engineering, a long life time (R_4) of these materials is proven by the conventional wind- and aviation industry for decades, a high power- and energy density (R_5) can be achieved

with efficient airfoils, particularly with high-lift multi-element airfoils, and scalability (R_6) is even already in part demonstrated experimentally by Makani.

A.2.2 Comparison of Crosswind Kite Power Concepts with Rigid Kite

Tab. A.1 shows a comparison between crosswind kite power concepts with rigid kites w.r.t. the requirements (R_1)–(R_6), i.e. drag power and lift power are compared, wherein lift power is divided according to the launch and landing concept because its choice has serious consequences on the overall system design.

The following should be added:

- Row 8, 13, and 14 refer particularly to the complexity of the powertrain of a drag power kite with the required high voltage in the tether. However, it can be evaluated that the development of simple solutions are only a matter of time, particularly with new technologies such as silicon carbide power-MOSFETs, cf. e.g. [180]. In addition to that, as shown in Chap. 5, the choice of a lower and off-optimal nominal tether voltage is not very sensitive to the figures of merit.
- The harm from the tether, addressed in rows 23 and 24, is very high for all systems. The high voltage of the integrated electrical cables for drag power add to the danger but hardly increase the already high danger.
- The emergency batteries for drag power, addressed in row 25, are on the ground without weight restrictions. Even though a relatively high power is required for a few minutes, the overall costs for these batteries are likely only a small fraction of the overall system costs.
- In row 31, it is claimed that the airborne mass of drag power is moderate. For sure, it is higher than for lift power and e.g. the rotating arm launching and landing principle. For instance, EnerKite claims to achieve a specific wing mass in the magnitude of only $2\,\mathrm{kg/m^2}$ [181], while Makani's M600 has about $40\,\mathrm{kg/m^2}$ [102]. Yet, a much higher power per wing area is expected for Makani's kite, as visualized in Fig. A.2.

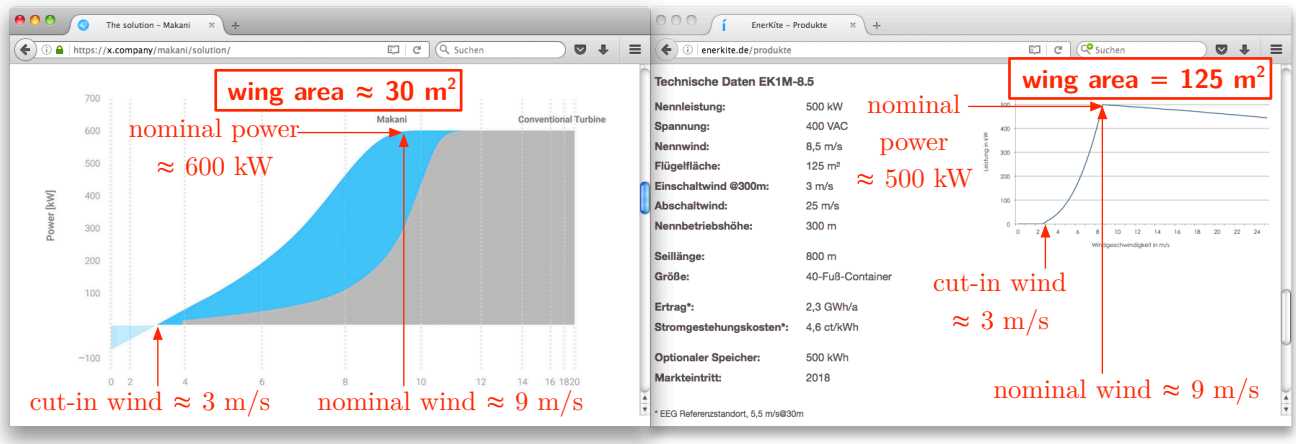

Figure A.2: Screenshots of the Makani and EnerKite company websites showing the power curves of Makani's M600 (drag power, left) and EnerKite's EK1M-8.5 (lift power with rotational arm launch and landing, right) [websites accessed on December 5, 2016], cf. also [151], overlayed by highlighting information in red: drag power can have a much higher power density than lift power despite a higher mass.

Table A.1: Comparison and assessment of rigid kite-based crosswind kite power concepts.
Color-coding: *green* = *advantageous;* *red* = *disadvantageous;* *yellow* = *somewhere in-between;* *white* = *unclear.*

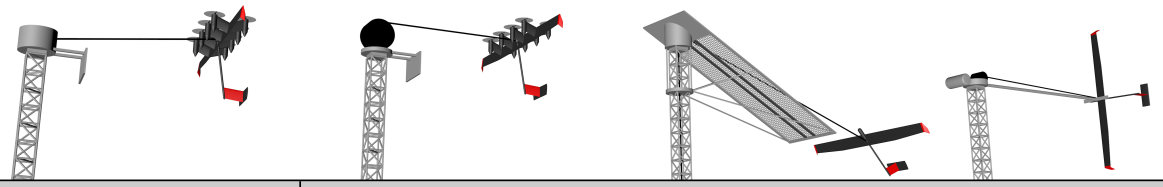

1	concept	generation principle	drag power	lift power		
2		launch & landing principle	multicopter	multicopter	catapult (with propellers for climbing)	rotating arm/rotational
3		number of tethers	1	1...3		
4		example	Makani	TwingTec	Ampyx Power	EnerKite
5	(R1) simplicity	launch & landing control	low speeds, standard multicopter, almost instantaneous transition possible		high speeds, complex control	
6		optimal power control	simple via rotor drag with flat optimum	complicated, optimization over complete reel-out-reel-in cycle required		
7		powertrain speed range	low	high: slow reel-out and fast reel-in		
8		usage of off-the-shelf components	mostly custom designed, at least for airborne parts	many players claim that mostly off-the-shelf components can be used, but it can be doubted that e.g. an industrial winch drive for another application is usable without software changes, which vendors likely will not do for a small customer, such that custom designs are also required		
9		airframe and airfoil design challenge	main requirement is high lift	challenging, high lift during reel-out and low-lift during reel-in required		
10		ground station tether handling design challenge	one low-torque and low-speed winch	high-torque and high-speed winch(es) and corresponding tether guidance system		
11		launch & landing system design challenge for ground station	only heliport or similar	in case of onboard batteries: only heliport or similar	complex catapult and catch mechanism	complex and large rotating arm and catch mechanism
12				additionally for detachable electrical cable: complex trolley mechanism		
13		launch & landing system design challenge for kite	comparatively simple, but bidirectional powertrain and rotors for wind turbine and propeller mode	high mass through batteries or high complexity with detachable electrical cable; drag reduction mechanism for unused propellers in power generation	additional mass through batteries; landing gears and brakes needed; drag reduction mechanism for unused propellers in power generation	attach mechanism needed, but might be mostly accomplished by ground station part
14		powertrain design challenge	high voltage and low mass required	powertrain on ground, so low voltage and high mass possible		
15		power supply for onboard systems	with power from tether	with onboard wind turbine and batteries with necessary battery management		
16		simple and safe testing	full power in machine hall during hovering with safety line	full power only in flight or power-hardware-in-the-loop		

Table A.1: Comparison and assessment of rigid kite-based crosswind kite power concepts. (continued)

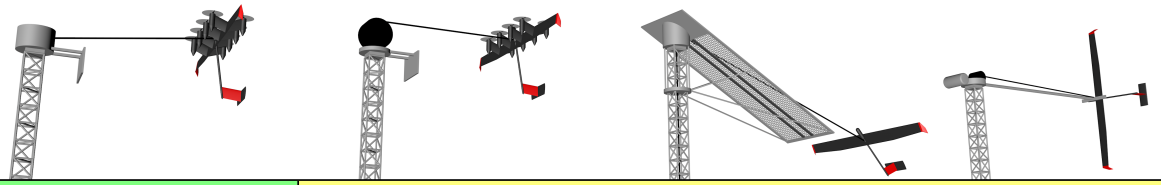

17	(R2) autonomous operation	crosswind flight & power generation	simple crosswind flight with constant tether length, proven experimentally e.g. by Makani	reel-out phase, reel-in phase, and transitions with complex control, but proven experimentally, e.g. by Ampyx Power		
18		launch & landing incl. transitions	*in addition to line 5:* proven experimentally e.g. by Makani and TwingTec		*in addition to line 5:* unproven	
19	(R3) high reliability	fail-safe from crosswind flight	fail-safe to hover		must keep flying	
20		has no single point of failure?	seems possible; proven for powertrain	seems hard if not impossible		
21		lightning protection (apart from landing "at the right time")	tether cables as lightning conductors or lightning conducting sheath around tether seems possible	seems impossible or very hard e.g. with detachable lighting conductor cable		
22		communication between important sensors and actuators	most important ones on kite, and communication over tether (e.g. power line communication) possible	important ones on ground and on kite, communication cables in tether not desirable/hard to design for durability, so real time wireless communication link required		
23		harm from tether	high tension and high speed movements			
24			additionally: high voltage (but isolated and shielded)			
25		safe landing during sudden grid fault	high hover power demand for a short time supplied by batteries on ground	onboard batteries: high hover power demand supplied by existing batteries	low power demand supplied by small batteries on ground	
26				detachable electrical cable: complex interactions and batteries on ground		
27		control in sudden negative gust or low wind	immediate propeller assisted crosswind flight or transit to hover	reverse pumping or transit to hover	immediate propeller assisted crosswind flight or reverse pumping	reverse pumping only
28	(R4) long lifetime	usage of long-life materials for kite	probably no restrictions, also aluminum seems possible	onboard batteries: only very light materials, possibly even flexible materials necessary, because of high battery mass	probably no or only moderate restrictions	only light materials to enable launch and landing on a short and light arm
29				detachable cable: probably no or much lower restrictions		
30		lifetime of tether	high: no tension when reeled on drum	low: high tether tear due to consistently tensioned reeling on drum and over pulleys		

Table A.1: Comparison and assessment of rigid kite-based crosswind kite power concepts. (continued)

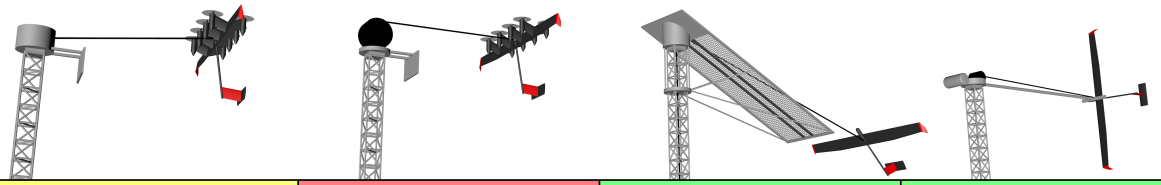

31	(R5) high power- and energy density	**airborne mass**	moderate (onboard generators contribute in the order of 10 % only)	onboard batteries: very high	low (but also onboard batteries and rotors required for climb)	lowest
32				detachable cable: low		
33		**tether mass**	moderate (electrical cables contribute only a fraction)	low		
34		**tether drag**	moderate (electrical cables contribute only a fraction to tether thickness)	1 tether: low		
35				2 tethers: medium		
36				3 tethers: high		
37		**power loss during power cycle**	moderate due to electrical transmission losses over tether	no power generation – even power demand – during reeling-in, i.e. overall moderate losses		
38		**powertrain mass**	low: low torque & high speed	high: high torque & low speed		
39		**powertrain costs**	moderate: low mass and scaling effect due to number of rotors, but custom high-voltage design required	moderate: high mass, but off-the-shelf components (at least for generators, gearboxes, and similar) seem usable		
40		**usage of high lift airfoil**	possible, proven by Makani	onboard batteries: seems challenging, because a very low airframe mass is required, which restricts wing loading	possible, pursued by Ampyx Power and EnerKite, but also very low lift coefficient for reeling-in required which apparently limits the maximum lift coefficient to around two.	
41				detachable electrical cable:		
42		**required ground area**	small			may be large due to long arm
43		**required efforts for continuous power output (may be required for small farms or single systems)**	nothing or small energy storage capacities on ground	high power and energy storage capacities on ground through positive and negative pulsating power		
44		**possibility of multiple kites on shared tether**	thinkable		likely impossible	seems challenging
45	(R6) scalability	**general scalability from small-scale to very large-scale**	scalable, proven by Makani	onboard batteries: square-cube law seriously restricts scaling	scalable	arm scales with wing span and kite mass
46				detachable cable: scalable		
47		**noise (particular by propellers)**	onshore: may be an issue?	except for launch and landing: low		always low
48			offshore: not an issue			

As stated in Sect. 1.1, virtually all researchers and developers start with and still consider lift power as the most promising concept, mainly because they evaluate the mass of the onboard generators for drag power as too high. However, the generators for drag power are at least an order of magnitude lighter compared to lift power generators with same nominal power: This is because of the much lower nominal torque (and instead higher rotational speeds) of the onboard turbines compared to the pulling torque of a lift power kite, as the mass and size of a generator (as well as a gearbox-generator combination) are mainly determined by the nominal load torque. In addition to that, the mass of the kite has no significant effect on the power output, as shown e.g. in Fig. A.2, or by the results of this dissertation in Chap. 5.

It should be noted, that meanwhile many lift power players interestingly pursue also a multicopter launch and landing supplied by onboard batteries, although the power demand for hovering is very high, which in turn requires significant installed propeller power—that remains unused during power generation—, as well as significant battery mass (in case no detachable electrical cable is considered, which would have other drawbacks, cf. also [175, 176]). As also the battery mass has to be lifted, the concept scales very badly, as shown by the author of this dissertation in the prior work [175, 176]. This becomes also apparent by viewing the results of Chap. 3: The mass of the Makani drag power kites is already close to their maximum allowed mass. Even though these kites have a large rotor area and a high installed rotor power, they would likely be way too heavy for hovering if batteries were installed onboard for use in a lift power concept with multicopter launch and landing. As it can be expected, that Makani designs lightweight kites (with a large and skilled team and a large budget), it seems challenging for teams pursuing lift power with multicopter launch and landing with onboard batteries to be able to successfully scale-up their kites (all known teams are smaller and have a far lower budget).

- Row 37 compares the power loss in a power cycle, i.e. one circle or figure eight for drag power and one complete pumping cycle for lift power, respectively. A recent publication [52] considers the effect of the by the kite itself reduced wind speed in the wind field (wake effects), and compares the wind power extraction efficiency of the lift power and drag power concepts (also with a conventional wind turbine). The astonishing result is that a lift power device has a maximum extraction efficiency of only $4/27 \approx 15\,\%$ (even without considering the power-consuming reel-in phase), while a drag power device (as well as a conventional wind turbine) has the *four times higher* well known Betz limit of $16/27 \approx 59\,\%$. This result suggests actually a strong advantage for drag power.
- Noise issues of drag power for onshore, addressed in row 47, are unknown, but may be an issue. However a number of design considerations to limit the rotor noise are available, e.g. a high number of blades, ducts, or concepts like the “bionic loop propeller” [182].

As highlighted by the colors in Tab. A.1 and with the above addenda, drag power is here evaluated as the most promising concept.

A.3 Concluding Remarks

It is hard if not impossible to be entirely objective. Still numerous airborne wind energy concepts are being investigated. One must assume that the different teams did similar comparisons and assessments, but obviously most teams drew different conclusions than presented in the previous sections. A likely reason for the vastly different conclusions is that other assessments are based on different assumptions. For instance, most teams do not assume that the mass of the generators of a drag power kite is relatively small, assume that a high voltage in the tether significantly

increases the danger of the tether, or assume that the efforts for a custom high-voltage powertrain are too high. Different assumptions may also be caused by different backgrounds, e.g. most teams have a much stronger background in mechanical engineering and aerodynamics than in electrical engineering and power electronics (as the author of this dissertation and of the assessment above). Additionally, some of the red and yellow cells in Tab. A.1 may become green with new developments, although it can be assessed that lift power will remain more challenging and less beneficial, and that some of the red cells are fundamental and might never be overcome. Nevertheless, the here presented assessment and statements should be taken with care, critically reviewed, and not be the only basis for choosing a concept over another.

Appendix B

Derivation of the Actuation Equations for Region III(b)

In the following, the actuation equations for the power and airflow speed limitation strategy within the power curve optimization in Region III(b) described in Sect. 2.7.12 are derived analytically. Note that only the airflow speed equation (2.230) and the minimum airfoil lift coefficient condition (2.233) as well as the other actuation bounds have to be satisfied for this task. The airfoil lift coefficient c_L, the actuated drag coefficient $C_\mathrm{D,k,a}$, the azimuth increase $\Delta\varphi_\mathrm{a}$, and the elevation increase $\Delta\vartheta_\mathrm{a}$ are the free variables.

B.1 Region III(b)-1: Airflow Speed Limitation via Airfoil Lift Coefficient

In the first part of Region III(b), only the airfoil lift coefficient is changed, i.e. the other actuations are left at

$$C_\mathrm{D,k,a,III(b)\text{-}1} = 0 \tag{B.1}$$
$$\Delta\varphi_\mathrm{a,III(b)\text{-}1} = 0 \tag{B.2}$$
$$\Delta\vartheta_\mathrm{a,III(b)\text{-}1} = 0. \tag{B.3}$$

By solving (2.230) for $c_\mathrm{L,III(b)} = c_\mathrm{L,III(b)\text{-}1}$, and by defining for sake of compactness

$$k_1 := \cos(\varphi_\mathrm{n} + \Delta\varphi_\mathrm{a,III(b)\text{-}1})\cos(\vartheta_\mathrm{n} + \Delta\vartheta_\mathrm{a,III(b)\text{-}1}) \tag{B.4}$$
$$k_2 := 1 + \frac{2}{\mathit{Æ}} \tag{B.5}$$
$$k_3 := c_\mathrm{D,2} + \frac{1}{\pi e \mathit{Æ}\left(1+\frac{2}{\mathit{Æ}}\right)^2} = c_\mathrm{D,2} + \frac{1}{\pi e \mathit{Æ} k_2^2} \tag{B.6}$$
$$k_4 := c_\mathrm{D,0} + C_\mathrm{D,k,a,III(b)\text{-}1} + C_\mathrm{D,k,o} + C_\mathrm{D,te} + C_\mathrm{D,rot,n(2)}, \tag{B.7}$$

the airfoil lift coefficient in Region III(b)-1 is determined by

$$\begin{aligned} v_\mathrm{a,n} &= \cos(\varphi_\mathrm{n} + \Delta\varphi_\mathrm{a,III(b)\text{-}1})\cos(\vartheta_\mathrm{n} + \Delta\vartheta_\mathrm{a,III(b)\text{-}1}) v_\mathrm{w} \\ &\quad \frac{c_\mathrm{L,III(b)\text{-}1}/\left(1+\frac{2}{\mathit{Æ}}\right)}{c_\mathrm{D,0} + \left[c_\mathrm{D,2} + \frac{1/\left(1+\frac{2}{\mathit{Æ}}\right)^2}{\pi e \mathit{Æ}}\right] c_\mathrm{L,III(b)\text{-}1}^2 + C_\mathrm{D,k,o} + C_\mathrm{D,k,a,III(b)\text{-}1} + C_\mathrm{D,te} + C_\mathrm{D,rot,n(2)}} \\ &= k_1 v_\mathrm{w} \frac{c_\mathrm{L,III(b)\text{-}1}/k_2}{k_3 c_\mathrm{L,III(b)\text{-}1}^2 + k_4} \end{aligned} \tag{B.8}$$

$$
\begin{aligned}
\Leftrightarrow k_3 c_{\mathrm{L,III(b)\text{-}1}}^2 + k_4 &= \frac{k_1 v_\mathrm{w}}{k_2 v_\mathrm{a,n}} c_{\mathrm{L,III(b)\text{-}1}} \\
\Leftrightarrow 0 &= c_{\mathrm{L,III(b)\text{-}1}}^2 - \frac{k_1 v_\mathrm{w}}{k_2 k_3 v_\mathrm{a,n}} c_{\mathrm{L,III(b)\text{-}1}} + \frac{k_4}{k_3} \\
\Leftrightarrow c_{\mathrm{L,III(b)\text{-}1}} &= \frac{k_1 v_\mathrm{w}}{2 k_2 k_3 v_\mathrm{a,n}} \pm \sqrt{\left(\frac{k_1 v_\mathrm{w}}{2 k_2 k_3 v_\mathrm{a,n}}\right)^2 - \frac{k_4}{k_3}} \\
\Rightarrow c_{\mathrm{L,III(b)\text{-}1}} &= \frac{k_1 v_\mathrm{w}}{2 k_2 k_3 v_\mathrm{a,n}} - \sqrt{\left(\frac{k_1 v_\mathrm{w}}{2 k_2 k_3 v_\mathrm{a,n}}\right)^2 - \frac{k_4}{k_3}},
\end{aligned}
\tag{B.9}
$$

whereby only the negative solution is meaningful, otherwise the airfoil lift coefficient would increase with increasing wind speed.

Inserting $c_\mathrm{L} = c_{\mathrm{L,III(b)\text{-}1}}$ into (2.39) and further into (2.15) and (2.178), the total lift coefficient and the parallel force become

$$
C_{\mathrm{L,III(b)\text{-}1}} = \frac{c_{\mathrm{L,III(b)\text{-}1}}}{1 + \frac{2}{\mathit{AR}}} \tag{B.10}
$$

$$
F_{||,\mathrm{III(b)\text{-}1}} = \frac{1}{2} \rho v_\mathrm{a,n}^2 A C_{\mathrm{L,III(b)\text{-}1}}. \tag{B.11}
$$

B.2 Transition between Region III(b)-1 and Region III(b)-2

The wind speed, at which the minimum airfoil lift coefficient $c_\mathrm{L,min}$ (2.233) is reached, is given by solving (B.8) for $v_\mathrm{w} = v_{\mathrm{w,III(b)\text{-}1 \leftrightarrow III(b)\text{-}2}}$ with $c_{\mathrm{L,III(b)\text{-}1}} = c_\mathrm{L,min}$, which is

$$
\begin{aligned}
v_\mathrm{a,n} &= k_1 v_{\mathrm{w,III(b)\text{-}1 \leftrightarrow III(b)\text{-}2}} \frac{\frac{c_\mathrm{L,min}}{k_2}}{k_3 c_\mathrm{L,min}^2 + k_4} \\
\Leftrightarrow v_{\mathrm{w,III(b)\text{-}1 \leftrightarrow III(b)\text{-}2}} &= \frac{k_2 v_\mathrm{a,n} (k_3 c_\mathrm{L,min}^2 + k_4)}{k_1 c_\mathrm{L,min}}.
\end{aligned}
\tag{B.12}
$$

That wind speed at the reference altitude is given by substituting (B.12) into (2.158) and solving for $v_{\mathrm{w},h_\mathrm{ref}} = v_{\mathrm{w},h_\mathrm{ref},\mathrm{III(b)\text{-}1 \leftrightarrow III(b)\text{-}2}}$ which becomes

$$
v_{\mathrm{w},h_\mathrm{ref},\mathrm{III(b)\text{-}1 \leftrightarrow III(b)\text{-}2}} = \frac{v_{\mathrm{w,III(b)\text{-}1 \leftrightarrow III(b)\text{-}2}}}{f_\mathrm{shear}(h)}. \tag{B.13}
$$

If $v_{\mathrm{w},h_\mathrm{ref},\mathrm{cut\text{-}out}} < v_{\mathrm{w},h_\mathrm{ref},\mathrm{III(b)\text{-}1 \leftrightarrow III(b)\text{-}2}}$, then Region III(b)-1 ends already at $v_{\mathrm{w},h_\mathrm{ref},\mathrm{cut\text{-}out}}$ with an airfoil lift coefficient higher than $c_\mathrm{L,min}$, and Region III(b) is not further divided.

B.3 Region III(b)-2: Airflow Speed Limitation via Actuated Drag

In the second part of Region III(b), the flight path is still not changed,

$$
\Delta\varphi_{\mathrm{a,III(b)\text{-}2}} = 0 \tag{B.14}
$$

$$
\Delta\vartheta_{\mathrm{a,III(b)\text{-}2}} = 0, \tag{B.15}
$$

and the airfoil lift coefficient stays at its minimum

$$
c_{\mathrm{L,III(b)\text{-}2}} = c_\mathrm{L,min}, \tag{B.16}
$$

with which the total lift coefficient and parallel force stay at

$$C_{\mathrm{L,min}} := C_{\mathrm{L,III(b)\text{-}2}} = \frac{c_{\mathrm{L,min}}}{1+\frac{2}{\mathit{Æ}}} \tag{B.17}$$

$$F_{||,\mathrm{III(b)\text{-}2}} = \frac{1}{2}\rho v_{\mathrm{a,n}}^2 A C_{\mathrm{L,min}}. \tag{B.18}$$

Only the actuated drag coefficient is increased to limit the airflow speed for increasing wind speeds. By solving (2.230) for $C_{\mathrm{D,k,a,III(b)}} = C_{\mathrm{D,k,a,III(b)\text{-}2}}$ with (B.14), (B.15), and (B.17), the actuated drag coefficient is

$$v_{\mathrm{a,n}} = \cos(\varphi_{\mathrm{n}} + \Delta\varphi_{\mathrm{a,III(b)\text{-}2}})\cos(\vartheta_{\mathrm{n}} + \Delta\vartheta_{\mathrm{a,III(b)\text{-}2}})v_{\mathrm{w}} \frac{c_{\mathrm{L,min}}/\left(1+\frac{2}{\mathit{Æ}}\right)}{c_{\mathrm{D},0} + \left[c_{\mathrm{D},2} + \frac{1/\left(1+\frac{2}{\mathit{Æ}}\right)^2}{\pi e \mathit{Æ}}\right] c_{\mathrm{L,min}}^2 + C_{\mathrm{D,k,a,III(b)}} + C_{\mathrm{D,k,o}} + C_{\mathrm{D,te}} + C_{\mathrm{D,rot,n(2)}}} \tag{B.19}$$

$$\Leftrightarrow C_{\mathrm{D,k,a,III(b)}} = \frac{\cos(\varphi_{\mathrm{n}} + \Delta\varphi_{\mathrm{a,III(b)\text{-}2}})\cos(\vartheta_{\mathrm{n}} + \Delta\vartheta_{\mathrm{a,III(b)\text{-}2}})v_{\mathrm{w}}}{v_{\mathrm{a,n}}} \frac{c_{\mathrm{L,min}}}{1+\frac{2}{\mathit{Æ}}} - \left\{c_{\mathrm{D},0} + \left[c_{\mathrm{D},2} + \frac{1/\left(1+\frac{2}{\mathit{Æ}}\right)^2}{\pi e \mathit{Æ}}\right] c_{\mathrm{L,min}}^2 + C_{\mathrm{D,k,o}} + C_{\mathrm{D,te}} + C_{\mathrm{D,rot,n(2)}}\right\}. \tag{B.20}$$

B.4 Transition between Region III(b)-2 and Region III(b)-3

Region III(b)-2 ends when the actuated drag reaches its maximum. The wind speed at which that happens is given by solving (B.19) for $v_{\mathrm{w}} = v_{\mathrm{w,III(b)\text{-}2\leftrightarrow III(b)\text{-}3}}$ with $C_{\mathrm{D,k,a,III(b)\text{-}2}} = C_{\mathrm{D,k,a,max}}$, which is

$$v_{\mathrm{w,III(b)\text{-}2\leftrightarrow III(b)\text{-}3}} = v_{\mathrm{a,n}} \frac{1}{\cos(\varphi_{\mathrm{n}} + \Delta\varphi_{\mathrm{a,III(b)\text{-}2}})\cos(\vartheta_{\mathrm{n}} + \Delta\vartheta_{\mathrm{a,III(b)\text{-}2}})} \frac{c_{\mathrm{D},0} + \left[c_{\mathrm{D},2} + \frac{1/\left(1+\frac{2}{\mathit{Æ}}\right)^2}{\pi e \mathit{Æ}}\right] c_{\mathrm{L,min}}^2 + C_{\mathrm{D,k,a,max}} + C_{\mathrm{D,k,o}} + C_{\mathrm{D,te}} + C_{\mathrm{D,rot,n(2)}}}{c_{\mathrm{L,min}}/\left(1+\frac{2}{\mathit{Æ}}\right)}. \tag{B.21}$$

That wind speed at the reference altitude is given by substituting (B.21) into (2.158) and solving for $v_{\mathrm{w},h_{\mathrm{ref}}} = v_{\mathrm{w},h_{\mathrm{ref}},\mathrm{III(b)\text{-}2,end}}$ which becomes

$$v_{\mathrm{w},h_{\mathrm{ref}},\mathrm{III(b)\text{-}2\leftrightarrow III(b)\text{-}3}} = \frac{v_{\mathrm{w,III(b)\text{-}2\leftrightarrow III(b)\text{-}3}}}{f_{\mathrm{shear}}(h)}. \tag{B.22}$$

If the flight path should not be changed, i.e. if $\Delta\varphi_{\mathrm{a}}$ and $\Delta\vartheta_{\mathrm{a}}$ should stay at zero, then $v_{\mathrm{w},h_{\mathrm{ref}},\mathrm{III(b)\text{-}2\leftrightarrow III(b)\text{-}3}}$ defines the cut-out wind speed $v_{\mathrm{w},h_{\mathrm{ref}},\mathrm{cut\text{-}out}}$, or, vice-versa, the desired cut-out wind speed defines the required maximum actuated drag coefficient. If $v_{\mathrm{w},h_{\mathrm{ref}},\mathrm{cut\text{-}out}} < v_{\mathrm{w},h_{\mathrm{ref}},\mathrm{III(b)\text{-}2\leftrightarrow III(b)\text{-}3}}$, then Region III(b)-2 ends already at $v_{\mathrm{w},h_{\mathrm{ref}},\mathrm{cut\text{-}out}}$ with an actuated drag lower than $C_{\mathrm{D,k,a,max}}$, and Region III(b) is not further divided.

B.5 Region III(b)-3

If also the flight path can be changed to further limit the airflow speed at very high wind speeds, then $\Delta\varphi_\mathrm{a}$ or/and $\Delta\vartheta_\mathrm{a}$ are increased, while airfoil lift coefficient and actuated drag coefficient stay at their minimum and maximum, respectively,

$$c_{\mathrm{L,III(b)\text{-}3}} = c_{\mathrm{L,min}} \tag{B.23}$$
$$C_{\mathrm{D,k,a,III(b)\text{-}3}} = C_{\mathrm{D,k,a,max}}, \tag{B.24}$$

and therefore also the total lift coefficient and the parallel force stay at

$$C_{\mathrm{L,min}} := C_{\mathrm{L,III(b)\text{-}3}} = \frac{c_{\mathrm{L,min}}}{1+\frac{2}{\mathit{AR}}} \tag{B.25}$$
$$F_{||,\mathrm{III(b)\text{-}3}} = \frac{1}{2}\rho v_{\mathrm{a,n}}^2 A C_{\mathrm{L,min}}. \tag{B.26}$$

Hence, with (2.230), only

$$v_{\mathrm{a,n}} = \cos(\varphi_\mathrm{n}+\Delta\varphi_{\mathrm{a,III(b)\text{-}3}})\cos(\vartheta_\mathrm{n}+\Delta\vartheta_{\mathrm{a,III(b)\text{-}3}})v_\mathrm{w}\frac{C_{\mathrm{L,min}}}{C_{\mathrm{D,max}}} \tag{B.27}$$

must hold true, in which $C_{\mathrm{D,k,max}}$ is defined as[42]

$$C_{\mathrm{D,max}} := c_{\mathrm{D,0}} + \left[c_{\mathrm{D,2}} + \frac{1/\left(1+\frac{2}{\mathit{AR}}\right)^2}{\pi e \mathit{AR}}\right] c_{\mathrm{L,min}}^2 + C_{\mathrm{D,k,a,max}} + C_{\mathrm{D,k,o}} + C_{\mathrm{D,te}} + C_{\mathrm{D,rot,n(2)}}. \tag{B.28}$$

B.5.1 Increase of Azimuth Only

If only $\Delta\varphi_\mathrm{a}$ is increased while leaving $\Delta\vartheta_\mathrm{a}=0$, an analytical solution for the required $\Delta\varphi_\mathrm{a}$ to maintain the airflow speed (2.230) (and force and power) can be readily derived by solving (B.27) for $\Delta\varphi_{\mathrm{a,III(b)\text{-}3}}$ which is

$$\begin{aligned} v_{\mathrm{a,n}} &= \cos(\varphi_\mathrm{n}+\Delta\varphi_{\mathrm{a,III(b)\text{-}3}})\cos(\vartheta_\mathrm{n}+\Delta\vartheta_{\mathrm{a,III(b)\text{-}3}})v_\mathrm{w}\frac{C_{\mathrm{L,min}}}{C_{\mathrm{D,max}}} \\ \Leftrightarrow \frac{v_{\mathrm{a,n}}}{\cos(\vartheta_\mathrm{n})v_\mathrm{w}}\frac{C_{\mathrm{D,max}}}{C_{\mathrm{L,min}}} &= \cos\left(\varphi_\mathrm{n}+\Delta\varphi_{\mathrm{a,III(b)\text{-}3}}\right) \\ \Leftrightarrow \Delta\varphi_{\mathrm{a,III(b)\text{-}3}} &= \arccos\left(\frac{v_{\mathrm{a,n}}}{\cos(\vartheta_\mathrm{n})v_\mathrm{w}}\frac{C_{\mathrm{D,max}}}{C_{\mathrm{L,min}}}\right) - \varphi_\mathrm{n}. \end{aligned} \tag{B.29}$$

Note however, that this might be impractical for a real system particularly when flying figures of eight, because airflow speed, power, and force have to be limited in each time instant, but the kite might still fly through a point close or equal to zero azimuth (remember that φ and ϑ are "effective" values, cf. Sect. 2.1.2).

[42] For a usual/meaningful design, this is the maximum total drag coefficient, which justifies the index, although this is not true in general, e.g. if $r_\mathrm{P}=1$, $C_{\mathrm{D,k,a,max}}=0$, and $c_{\mathrm{L,min}} < c_{\mathrm{L,n}}$, then the maximum drag occurs in Region II.

B.5.2 Increase of Elevation Only or Increase of Elevation and Azimuth

Therefore, an increase of only ϑ, or the combination of increasing both, φ and ϑ, is also considered. For that, Eq. (B.27) is solved for $\Delta\vartheta_{\mathrm{a,III(b)\text{-}3}}$,

$$\begin{aligned} v_{\mathrm{a,n}} &= \cos(\varphi_{\mathrm{n}} + \Delta\varphi_{\mathrm{a,III(b)\text{-}3}}) \cos(\vartheta_{\mathrm{n}} + \Delta\vartheta_{\mathrm{a,III(b)\text{-}3}}) v_{\mathrm{w}} \frac{C_{\mathrm{L,min}}}{C_{\mathrm{D,max}}} \\ \Leftrightarrow \frac{v_{\mathrm{a,n}}}{\cos(\varphi_{\mathrm{n}} + \Delta\varphi_{\mathrm{a,III(b)\text{-}3}}) v_{\mathrm{w}}} \frac{C_{\mathrm{D,max}}}{C_{\mathrm{L,min}}} &= \cos(\vartheta_{\mathrm{n}} + \Delta\vartheta_{\mathrm{a,III(b)\text{-}3}}) \\ \Leftrightarrow \Delta\vartheta_{\mathrm{a,III(b)\text{-}3}} &= \arccos\left(\frac{v_{\mathrm{a,n}}}{\cos(\varphi_{\mathrm{n}} + \Delta\varphi_{\mathrm{a,III(b)\text{-}3}}) v_{\mathrm{w}}} \frac{C_{\mathrm{D,max}}}{C_{\mathrm{L,min}}} \right) - \vartheta_{\mathrm{n}}. \end{aligned} \tag{B.30}$$

An increased elevation changes the altitude h of the kite (2.160) and therefore, if the wind shear is not uniform, v_{w} changes for changed $\Delta\vartheta_{\mathrm{a,III(b)\text{-}3}}$. Note again that this was not the case for all other values in all other regions, as h was constant in all other regions because ϑ and L_{te} were constant. Substituting (2.158) into (B.30) with (2.160) and (2.169) gives

$$\begin{aligned} &\Delta\vartheta_{\mathrm{a,III(b)\text{-}3}} \\ &= \arccos\left(\frac{v_{\mathrm{a,n}}}{\cos(\varphi_{\mathrm{n}} + \Delta\varphi_{\mathrm{a,III(b)\text{-}3}}) v_{\mathrm{w},h_{\mathrm{ref}}} f_{\mathrm{shear}}\left(h_{\mathrm{to}} + L_{\mathrm{te}} \sin(\vartheta_{\mathrm{n}} + \Delta\vartheta_{\mathrm{a,III(b)\text{-}3}})\right)} \frac{C_{\mathrm{D,max}}}{C_{\mathrm{L,min}}} \right) - \vartheta_{\mathrm{n}} \end{aligned} \tag{B.31}$$

which has $\Delta\vartheta_{\mathrm{a,III(b)\text{-}3}}$ on both sides of the equation and, with a non-uniform wind shear, cannot be solved analytically easily (if at all) for $\Delta\vartheta_{\mathrm{a,III(b)\text{-}3}}$. Here, a numerical solution based on a simple grid search is pursued.

It should be noted, if the upper limit of ϑ is $\pi/2$, then Region III(b)-3 can theoretically be infinitely long, i.e. $v_{\mathrm{w},h_{\mathrm{ref}},\mathrm{cut\text{-}out}} \to \infty$, because $\cos(\vartheta) \to 0$ is possible. If the upper bound of ϑ is smaller than $\pi/2$ e.g. to limit the flight altitude h, then that altitude bound defines the (maximum) cut-out wind speed $v_{\mathrm{w},h_{\mathrm{ref}},\mathrm{cut\text{-}out}} < \infty$, whose value, however, can also not easily be found analytically for a non-uniform wind shear.

Appendix C

Derivation of a Higher Fidelity Model

In this appendix chapter, the higher fidelity model is derived which is used to validate at least in part the steady model. It is similar to Diehl's or Fechner's point-mass modeling approach [33, 47] (cf. also works mentioned in Sect. 1.2 and references therein). The model is dynamic, i.e. the kite's flight on a crosswind path such as figure eights or circles is resolved and therefore the model does not make some of the most rough assumptions of the steady model. However, flight controllers have to be derived. The utilized crosswind path controller is similar to Fagiano's approach [41], but has extensions to allow for arbitrary paths, including circles and inside-up figure eights. To fly in all wind speeds of a complete power curve, also a power limitation controller has to be developed which is a new contribution of the author of this dissertation. Core concepts of this appendix chapter are presented in the prior publication [112]. Some figures shown here are identical or only slightly different [112].

The here derived point-mass model applies only for crosswind flight. The hovering case is not covered, or is still modeled as in Chap. 2. Moreover, rotor failures are not considered for sake of simplicity.

This appendix chapter is structured as follows: Sect. C.1 derives the model equations which are different from the ones of the steady model from Chap. 2. This includes highlighting which assumptions are omitted or replaced by less rough ones. Sect. C.2 derives the controllers, which are required to meaningfully run the derived model. Sect. C.3 gives details on the simulation implementation and lists the utilized standard parameters. Sect. C.4 reports and explains simulation results as well as validates the model with measurements of the Makani Wing 7. Sect. C.5 closes with a discussion of the solution and gives concluding remarks.

C.1 Model Derivation

Generally, for the here derived model (and controller), Assumptions 2.1, 2.4, 2.5, 2.33, and 2.35 are not made (unless a re-introduction is stated explicitly), i.e. particularly the kite dynamics submodel is of higher fidelity. Newly introduced assumptions are highlighted within the derivation text.

C.1.1 Point-Mass Dynamics

The following two assumptions are imposed for the dynamics model:

Assumption C.1: *Newtonian mechanics applies.*

Assumption C.2: *The flat earth is an inertial reference frame.*

Clearly, both assumptions are very moderate because, e.g., the kite's speed is much smaller than the speed of light and the Coriolis forces due to earth's rotation and movement are comparably small.

With Assumptions C.1 and C.2, the dynamics of the kite's center of mass (point-mass) is given by Newton's first and second axiom

$$\dot{\boldsymbol{p}}_\mathrm{k} = \boldsymbol{F}_\mathrm{acc}, \qquad \boldsymbol{p}_\mathrm{k}(t_0) = \boldsymbol{p}_{\mathrm{k},0}, \tag{C.1}$$

and the linear kinematics

$$\dot{\boldsymbol{r}}_\mathrm{k} = \boldsymbol{v}_\mathrm{k}, \qquad \boldsymbol{r}_\mathrm{k}(t_0) = \boldsymbol{r}_{\mathrm{k},0}, \tag{C.2}$$

with

$$\boldsymbol{p}_\mathrm{k} = m_\mathrm{a}\boldsymbol{v}_\mathrm{k}, \tag{C.3}$$

where $\boldsymbol{F}_\mathrm{acc}$ is the acceleration force acting on the kite, $\boldsymbol{p}_\mathrm{k}$ is the momentum of the kite with initial value $\boldsymbol{p}_{\mathrm{k},0}$ at initial time t_0, $\boldsymbol{v}_\mathrm{k}$ is the velocity of the kite, m_a is the effective airborne mass defined in Sect. 2.1.6, and $\boldsymbol{r}_\mathrm{k}$ is the position of the kite with initial value $\boldsymbol{r}_{\mathrm{k},0}$. All vectors are given in the flat earth inertial reference frame, which is here defined by the right-handed north-west-up Cartesian axes for the $\boldsymbol{x}$-$\boldsymbol{y}$-$\boldsymbol{z}$ base vectors with origin at the ground station tether connection projected to the flat earth (i.e. origin has zero altitude above ground).

According to Newton's third axiom, $\boldsymbol{F}_\mathrm{acc}$ is the sum of all (external) forces $\boldsymbol{F}_i$ acting on the kite, that is

$$\boldsymbol{F}_\mathrm{acc} = \sum_i \boldsymbol{F}_i = \boldsymbol{F}_\mathrm{g} + \boldsymbol{F}_\mathrm{te} + \boldsymbol{F}_\mathrm{a} \tag{C.4}$$

with gravitational force $\boldsymbol{F}_\mathrm{g}$, tether force $\boldsymbol{F}_\mathrm{te}$, and aerodynamic force $\boldsymbol{F}_\mathrm{a}$. It remains to derive equations for those three forces.

C.1.2 Gravitational Force

Through Assumptions C.1 and C.2, and with the inertial reference frame definition, the gravitational force can be expressed with the gravitational acceleration g as

$$\boldsymbol{F}_\mathrm{g} = m_\mathrm{a}\begin{pmatrix} 0 \\ 0 \\ -g \end{pmatrix}. \tag{C.5}$$

C.1.3 Tether Force

For the tether, Assumption 2.4 is replaced as follows:

Assumption C.3: *Under tension, the straight tether behaves like a spring-damper with massless spring-damper.*

The force magnitude of the tether spring-damper (index "sd") is given by

$$F_\mathrm{te,sd} = \varsigma_\mathrm{te}\Delta r_\mathrm{te} + \xi_\mathrm{te}\Delta v_\mathrm{te}, \tag{C.6}$$

where ς_te is the spring constant, ξ_te is the damper constant, Δr_te is the elongation, defined by

$$\Delta r_\mathrm{te} = ||\boldsymbol{r}_\mathrm{k} - \boldsymbol{r}_\mathrm{to}|| - L_\mathrm{te} \tag{C.7}$$

with the tether connection position at the ground or at the tower $\boldsymbol{r}_\mathrm{to} = \begin{pmatrix} 0 & 0 & h_\mathrm{to} \end{pmatrix}^\top$, and where Δv_te is the elongation speed defined by

$$\Delta v_\mathrm{te} = \boldsymbol{e}_\mathrm{r} \bullet \boldsymbol{v}_\mathrm{k} - \dot{L}_\mathrm{te} \tag{C.8}$$

with radial direction

$$\boldsymbol{e}_\mathrm{r} = \mathrm{dir}(\boldsymbol{r}_\mathrm{k} - \boldsymbol{r}_\mathrm{to}). \tag{C.9}$$

Herein, $||\boldsymbol{x}||$ denotes the Euclidian norm of some vector $\boldsymbol{x}$, $\bullet$ denotes the dot product, and the direction of some vector $\boldsymbol{x}$ is defined by

$$\mathrm{dir}(\boldsymbol{x}) := \begin{cases} \frac{\boldsymbol{x}}{||\boldsymbol{x}||} & \text{for } ||\boldsymbol{x}|| \neq 0, \\ \boldsymbol{0} & \text{otherwise.} \end{cases} \tag{C.10}$$

As the tether can only exert a tension force into the tether direction, the tether force vector is given by

$$\boldsymbol{F}_\mathrm{te} = \begin{cases} -\boldsymbol{e}_\mathrm{r} F_\mathrm{te,sd} & \text{if } \Delta r_\mathrm{te} > 0 \text{ and } F_\mathrm{te,sd} > 0 \\ \boldsymbol{0} & \text{otherwise.} \end{cases} \tag{C.11}$$

C.1.4 Aerodynamic Forces

The aerodynamic forces are defined by

$$\boldsymbol{F}_\mathrm{a} = \boldsymbol{F}_\mathrm{L} + \boldsymbol{F}_\mathrm{D} + \boldsymbol{F}_\mathrm{S} \tag{C.12}$$

$$\boldsymbol{F}_\mathrm{L} = F_\mathrm{L}\,\mathrm{dir}(\boldsymbol{v}_\mathrm{a} \times \boldsymbol{y}_\mathrm{k}) \tag{C.13}$$

$$\boldsymbol{F}_\mathrm{D} = F_\mathrm{D}\,\mathrm{dir}(\boldsymbol{v}_\mathrm{a}) \tag{C.14}$$

$$\boldsymbol{F}_\mathrm{S} = \frac{1}{2}\rho v_\mathrm{a}^2 A C_\mathrm{S}\,\mathrm{dir}(\boldsymbol{F}_\mathrm{D} \times \boldsymbol{F}_\mathrm{L}) \tag{C.15}$$

with F_L and F_D from (2.6) and (2.7), and where $\boldsymbol{F}_\mathrm{S}$ is the side force, C_S is the side force coefficient, $\boldsymbol{v}_\mathrm{a}$ is the airflow velocity (vector), $\boldsymbol{y}_\mathrm{k}$ is the y-axis base vector of the kite-fixed reference frame which points along the main wing span into the starboard direction, and $\times$ denotes the cross product. The lift and drag coefficients remain the same as in Chap. 2.

The airflow speed is given by

$$v_\mathrm{a} = ||\boldsymbol{v}_\mathrm{a}|| \tag{C.16}$$

with the airflow velocity (vector)

$$\boldsymbol{v}_\mathrm{a} = \boldsymbol{v}_\mathrm{w}(\boldsymbol{r}_\mathrm{k}) - \boldsymbol{v}_\mathrm{k}, \tag{C.17}$$

where $\boldsymbol{v}_\mathrm{w}(\boldsymbol{r}_\mathrm{k})$ is the wind velocity at the position (or altitude) of the kite. With the wind shear model (2.158), this becomes

$$\boldsymbol{v}_\mathrm{w}(\boldsymbol{r}_\mathrm{k}) = \boldsymbol{R}_\mathrm{z}(\varphi_\mathrm{w}) \begin{pmatrix} f_\mathrm{shear}(h) v_{\mathrm{w},h_\mathrm{ref}} \\ 0 \\ 0 \end{pmatrix} \tag{C.18}$$

where φ_w is the azimuth angle of the wind (i.e. the azimuth of the wind direction w.r.t. the north or the $\boldsymbol{x}$ unit vector of the inertial reference frame) and with the altitude of the kite above ground

$$h = \boldsymbol{z} \bullet \boldsymbol{r}_\mathrm{k}. \tag{C.19}$$

Herein, rotation matrices for rotations around the x-, y-, and z-axis about some angle # are defined by

$$\boldsymbol{R}_{\mathrm{x}}(\#) = \begin{pmatrix} 1 & 0 & 0 \\ 0 & \cos(\#) & -\sin(\#) \\ 0 & \sin(\#) & \cos(\#) \end{pmatrix}, \tag{C.20}$$

$$\boldsymbol{R}_{\mathrm{y}}(\#) = \begin{pmatrix} \cos(\#) & 0 & \sin(\#) \\ 0 & 1 & 0 \\ -\sin(\#) & 0 & \cos(\#) \end{pmatrix}, \tag{C.21}$$

$$\boldsymbol{R}_{\mathrm{z}}(\#) = \begin{pmatrix} \cos(\#) & -\sin(\#) & 0 \\ \sin(\#) & \cos(\#) & 0 \\ 0 & 0 & 1 \end{pmatrix}. \tag{C.22}$$

C.1.5 Kite Orientation

The lift force depends on $\boldsymbol{y}_{\mathrm{k}}$ which is part of the kite's orientation that remains to be specified. Here, the kite's reference frame is defined as follows: The x-axis base vector $\boldsymbol{x}_{\mathrm{k}}$ points from the nose to the tail, the y-axis base vector $\boldsymbol{y}_{\mathrm{k}}$ points along the main wing span into the starboard direction as mentioned in the previous subsection, and the z-axis base vector $\boldsymbol{z}_{\mathrm{k}}$ points up. This is a right-handed reference frame. The combination of $\boldsymbol{x}_{\mathrm{k}}$, $\boldsymbol{y}_{\mathrm{k}}$, and $\boldsymbol{z}_{\mathrm{k}}$ is one expression of the kite's orientation.[43]

However, by implication, a point-mass has no defined orientation. To define an orientation for the kite, the following assumption is made:

Assumption C.4: *Angle of attack α, angle of sideslip β, and roll angle ψ are stabilized instantaneously with according horizontal and vertical stabilizers or/and with underlying control loops.*

This assumption is justified, as stabilizers and control surfaces are considered for the kite (cf. Sect. 1.5) with which all three angles can be stabilized highly dynamically.

The kite's orientation can therefore be defined as follows: Assumption C.4 and the kite reference frame definition imply with $\alpha = 0$, $\beta = 0$, and $\psi = 0$ (in the following: orientation with prime) that $\boldsymbol{x}'_{\mathrm{k}}$ is parallel to $\boldsymbol{v}_{\mathrm{a}}$, and $\boldsymbol{y}'_{\mathrm{k}}$ is perpendicular to both $\boldsymbol{v}_{\mathrm{a}}$ and the tether radial direction $\boldsymbol{e}_{\mathrm{r}}$. Finally $\boldsymbol{z}'_{\mathrm{k}}$ is perpendicular to both $\boldsymbol{x}'_{\mathrm{k}}$ and $\boldsymbol{y}'_{\mathrm{k}}$. This results in

$$\boldsymbol{x}'_{\mathrm{k}} = \mathrm{dir}(\boldsymbol{v}_{\mathrm{a}}) \tag{C.23}$$

$$\boldsymbol{y}'_{\mathrm{k}} = \mathrm{dir}(\boldsymbol{e}_{\mathrm{r}} \times \boldsymbol{v}_{\mathrm{a}}) \tag{C.24}$$

$$\boldsymbol{z}'_{\mathrm{k}} = \boldsymbol{x}'_{\mathrm{k}} \times \boldsymbol{y}'_{\mathrm{k}}. \tag{C.25}$$

Those vectors can be combined to the orientation matrix

$$\boldsymbol{T}'_{\mathrm{k}} = \begin{pmatrix} \boldsymbol{x}'_{\mathrm{k}} & \boldsymbol{y}'_{\mathrm{k}} & \boldsymbol{z}'_{\mathrm{k}} \end{pmatrix}, \tag{C.26}$$

which is also a transformation matrix, with which any vector given in the kite's primed reference frame coordinates (at $\alpha = 0$, $\beta = 0$, $\psi = 0$) can be transformed into inertial reference frame coordinates.—This can be proven directly by applying $\boldsymbol{T}'_{\mathrm{k}}$ for the unit vectors in the kite's primed

[43] It should be noted that this reference frame definition deviates from the often used convention for aircraft. The here used (arguably unconventional) definition is selected, because it appeared more intuitive, and the same right-handed north-west-up convention is used also for all other reference frames.

reference frame coordinates (at $\alpha = 0$, $\beta = 0$, $\psi = 0$, denoted by $\#^{\text{k'}}$), which clearly are

$$\begin{pmatrix} \boldsymbol{x}_{\text{k}}^{\text{k'}} & \boldsymbol{y}_{\text{k}}^{\text{k'}} & \boldsymbol{z}_{\text{k}}^{\text{k'}} \end{pmatrix} = \left(\begin{pmatrix} 1 \\ 0 \\ 0 \end{pmatrix} \quad \begin{pmatrix} 0 \\ 1 \\ 0 \end{pmatrix} \quad \begin{pmatrix} 0 \\ 0 \\ 1 \end{pmatrix} \right) = \begin{pmatrix} 1 & 0 & 0 \\ 0 & 1 & 0 \\ 0 & 0 & 1 \end{pmatrix} = \mathbf{I}_3 \tag{C.27}$$

where $\mathbf{I}_3$ is the 3×3 identity matrix: Transforming (C.27) with (C.26) (or any of the unit vectors individually) gives

$$\boldsymbol{T}'_{\text{k}} \begin{pmatrix} \boldsymbol{x}_{\text{k}}^{\text{k'}} & \boldsymbol{y}_{\text{k}}^{\text{k'}} & \boldsymbol{z}_{\text{k}}^{\text{k'}} \end{pmatrix} = \boldsymbol{T}'_{\text{k}} \mathbf{I}_3 = \begin{pmatrix} \boldsymbol{x}'_{\text{k}} & \boldsymbol{y}'_{\text{k}} & \boldsymbol{z}'_{\text{k}} \end{pmatrix}. \tag{C.28}$$

For arbitrary α, β, and ψ, the orientation is given again by the analogy of transforming any vector from the kite's reference frame coordinates (denoted by $\#^{\text{k}}$) into inertial reference frame coordinates: $\#^{\text{k}}$ is first rotated by β about the z-axis, then by α about the y-axis, and then by ψ about the x-axis, before it is transformed with $\boldsymbol{T}'_{\text{k}}$, hence

$$\begin{pmatrix} \boldsymbol{x}_{\text{k}} & \boldsymbol{y}_{\text{k}} & \boldsymbol{z}_{\text{k}} \end{pmatrix} = \boldsymbol{T}_{\text{k}} = \boldsymbol{T}'_{\text{k}} \boldsymbol{R}_{\text{x}}(\psi) \boldsymbol{R}_{\text{y}}(\alpha) \boldsymbol{R}_{\text{z}}(\beta). \tag{C.29}$$

This transformation can be proven similarly as above.

C.1.6 Available Actuators under Simplification of Aerodynamics and Orientation

To avoid to define the lift-, drag-, and side force coefficients as function of α and β, but instead to stick with the simplified aerodynamics models derived in Chap. 2, the following two assumptions are made:

Assumption C.5: *Angle of attack α and angle of sideslip β are either both kept at zero, or their effects are only implicitly covered via according values of the aerodynamic coefficients.*

Assumption C.6: *The side force coefficient is always zero.*

Assumption C.5 allows to set $\alpha = 0$ and $\beta = 0$ in (C.29) which simplifies to

$$\begin{pmatrix} \boldsymbol{x}_{\text{k}} & \boldsymbol{y}_{\text{k}} & \boldsymbol{z}_{\text{k}} \end{pmatrix} = \boldsymbol{T}_{\text{k}} = \boldsymbol{T}'_{\text{k}} \boldsymbol{R}_{\text{x}}(\psi). \tag{C.30}$$

With Assumption C.6, the side force (C.15) is zero and (C.12) simplifies to

$$\boldsymbol{F}_{\text{a}} = \boldsymbol{F}_{\text{L}} + \boldsymbol{F}_{\text{D}}. \tag{C.31}$$

The only considered actuations to the model, with which the kite can be controlled, are therefore

- the rotor drag coefficient $C_{\text{D,rot}}$,
- the airfoil lift coefficient c_{L},
- the actuated drag coefficient $C_{\text{D,k,a}}$, and
- the roll angle ψ.

C.1.7 Actuator Dynamics

Another assumption is introduced to model the actuator dynamics:

Assumption C.7: *The dynamics of each of the four actuators can be modeled as a limited first order delay.*

Thus, for an actuation $u \in [C_{\mathrm{D,rot}}, c_{\mathrm{L}}, C_{\mathrm{D,k,a}}, \psi]$,

$$\dot{u} = \frac{1}{T_u}[\mathrm{limit}(u_{\min}, u_{\mathrm{set}}, u_{\max}) - u], \qquad u(t_0) = u_0, \tag{C.32}$$

where T_u is the actuation time constant, u_{set} is the actuation set value, $u_{\min}$ and $u_{\max}$ are the minimum and maximum actuation values, u_0 is the initial value at initial time t_0, and

$$\mathrm{limit}(u_{\min}, u_{\mathrm{set}}, u_{\max}) := \begin{cases} u_{\min} & \text{if } u_{\mathrm{set}} < u_{\min}, \\ u_{\max} & \text{if } u_{\mathrm{set}} > u_{\max}, \\ u_{\mathrm{set}} & \text{otherwise} \end{cases} \tag{C.33}$$

implements actuator constraints.

C.1.8 Power and Power Transmission

The aerodynamic power remains identical to (2.18) and all other powers including the power transmission down to the electrical power remain identical to Chap. 2.

C.1.9 Powertrain Temperature Dynamics

As mentioned at the beginning of this chapter, Assumption 2.35 is not made. However, a temporary overloading of the powertrain might be crucial due to significant power oscillations within the crosswind flight trajectory. Powertrains can usually be overloaded for some time in the order of seconds or tens of seconds with a maximum overloading power in the order of twice the nominal power, until the nominal temperature of a powertrain component is reached, cf. e.g. [183]. Here, the simplest possible temperature dynamics model is employed:

Assumption C.8: *The powertrain temperature dynamics can be modeled with a single thermodynamic time constant.*

With that assumption, the model similar to [183, Sect. III] is utilized:

Theorem C.1 (Per Unit Powertrain Temperature Dynamics with Single Time Constant): *If Assumption C.8 applies, then the powertrain temperature dynamics is given by*

$$\dot{\tau}' = \frac{1}{T_\tau}(P'_{\mathrm{loss}} - \tau' + \tau'_\infty), \qquad \tau'(t_0) = \tau'_0, \tag{C.34}$$

where (i)

$$\tau' = (\tau - \tau_{\infty,\mathrm{n}})/(\tau_{\mathrm{n}} - \tau_{\infty,\mathrm{n}}) \tag{C.35}$$

is the per unit temperature with initial value τ'_0 at initial time t_0, absolute temperature τ, nominal absolute temperature τ_{n}, and nominal ambient temperature $\tau_{\infty,\mathrm{n}}$, (ii)

$$\tau'_\infty = (\tau_\infty - \tau_{\infty,\mathrm{n}})/(\tau_{\mathrm{n}} - \tau_{\infty,\mathrm{n}}) \tag{C.36}$$

is the per unit ambient temperature with absolute ambient temperature τ_∞, and (iii)

$$P'_{\mathrm{loss}} = \begin{cases} \frac{P_{\mathrm{a}}}{P_{\mathrm{a,+,n\text{-}ins}}} & \text{if } P_{\mathrm{a}} \geq 0, \\ \frac{P_{\mathrm{a}}}{P_{\mathrm{a,-,n\text{-}ins}}} & \text{otherwise} \end{cases} \tag{C.37}$$

is the per unit power loss in the powertrain (or its most critical component such as an electrical machine).

Proof. The temperature dynamics of the powertrain (or its most critical component such as an electrical machine) with a single time constant is generally given by

$$C\dot{\tau} = P_{\text{loss}} - H(\tau - \tau_\infty), \qquad \tau(t_0) = \tau_0, \tag{C.38}$$

where C is the heat capacity of the powertrain, P_{loss} is the absolute power loss which is the power that heats up the powertrain, and H is the heat dissipation factor.

By definition, the nominal temperature $\tau = \tau_{\text{n}}$ occurs when the nominal power loss $P_{\text{loss}} = P_{\text{loss,n}}$ is applied at the design ambient temperature $\tau_\infty = \tau_{\infty,\text{n}}$ for a long time such that $\dot{\tau} \to 0$. Therefore, the heat dissipation factor is defined by

$$\begin{aligned} 0 &= P_{\text{loss,n}} - H(\tau_{\text{n}} - \tau_{\infty,\text{n}}) \\ \Leftrightarrow H(\tau_{\text{n}} - \tau_{\infty,\text{n}}) &= P_{\text{loss,n}} \\ \Leftrightarrow H &= \frac{P_{\text{loss,n}}}{\tau_{\text{n}} - \tau_{\infty,\text{n}}}. \end{aligned} \tag{C.39}$$

Substituting (C.39) into (C.38) and rearranging gives

$$\begin{aligned} \dot{\tau} &= \frac{1}{C}\left[P_{\text{loss}} - H(\tau - \tau_\infty)\right] \\ &= \frac{1}{\frac{C}{H}}\left[\frac{P_{\text{loss}}}{H} - (\tau - \tau_\infty)\right] \\ &= \frac{1}{T_\tau}\left[\frac{P_{\text{loss}}}{\frac{P_{\text{loss,n}}}{\tau_{\text{n}} - \tau_{\infty,\text{n}}}} - (\tau - \tau_\infty)\right] \\ &= \frac{1}{T_\tau}\left[\frac{P_{\text{loss}}}{P_{\text{loss,n}}}(\tau_{\text{n}} - \tau_{\infty,\text{n}}) - (\tau - \tau_\infty)\right], \qquad \tau(t_0) = \tau_0, \end{aligned} \tag{C.40}$$

where the thermodynamic time constant of the powertrain

$$T_\tau := \frac{C}{H} \tag{C.41}$$

is inserted.

With the nondimensionalized powertrain temperature (C.35) solved for

$$\tau' = (\tau - \tau_{\infty,\text{n}})/(\tau_{\text{n}} - \tau_{\infty,\text{n}}) \tag{C.42}$$

$$\Leftrightarrow \tau'(\tau_{\text{n}} - \tau_{\infty,\text{n}}) = \tau - \tau_{\infty,\text{n}}$$

$$\Leftrightarrow \tau'(\tau_{\text{n}} - \tau_{\infty,\text{n}}) + \tau_{\infty,\text{n}} = \tau, \tag{C.43}$$

with the nondimensionalized ambient temperature (C.36) solved for

$$\tau'_\infty = (\tau_\infty - \tau_{\infty,\text{n}})/(\tau_{\text{n}} - \tau_{\infty,\text{n}}) \tag{C.44}$$

$$\Leftrightarrow \tau'_\infty(\tau_{\text{n}} - \tau_{\infty,\text{n}}) = \tau_\infty - \tau_{\infty,\text{n}}$$

$$\Leftrightarrow \tau'_\infty(\tau_{\text{n}} - \tau_{\infty,\text{n}}) + \tau_{\infty,\text{n}} = \tau_\infty, \tag{C.45}$$

and with the nondimensionalized power loss

$$P'_{\text{loss}} = P_{\text{loss}}/P_{\text{loss,n}} \tag{C.46}$$

$$\Leftrightarrow P'_{\text{loss}} P_{\text{loss,n}} = P_{\text{loss}} \tag{C.47}$$

all substituted into (C.40), one obtains

$$\begin{aligned}
\dot{\tau} &= \frac{1}{T_\tau}\left[\frac{P_{\text{loss}}}{P_{\text{loss,n}}}(\tau_\text{n}-\tau_{\infty,\text{n}})-(\tau-\tau_\infty)\right] \\
\frac{\mathrm{d}}{\mathrm{d}t}[\tau'(\tau_\text{n}-\tau_{\infty,\text{n}})+\tau_{\infty,\text{n}}] &= \frac{1}{T_\tau}\left\{\frac{P'_{\text{loss}}P_{\text{loss,n}}}{P_{\text{loss,n}}}(\tau_\text{n}-\tau_{\infty,\text{n}})-[\tau'(\tau_\text{n}-\tau_{\infty,\text{n}})\right. \\
&\qquad \left.+\tau_{\infty,\text{n}}-\tau'_\infty(\tau_\text{n}-\tau_{\infty,\text{n}})-\tau_{\infty,\text{n}}]\right\} \\
\dot{\tau}'(\tau_\text{n}-\tau_{\infty,\text{n}}) &= \frac{1}{T_\tau}\left[P'_{\text{loss}}(\tau_\text{n}-\tau_{\infty,\text{n}})-\tau'(\tau_\text{n}-\tau_{\infty,\text{n}})-\tau_{\infty,\text{n}}\right. \\
&\qquad \left.+\tau'_\infty(\tau_\text{n}-\tau_{\infty,\text{n}})+\tau_{\infty,\text{n}}\right] \qquad \big|\cdot(\tau_\text{n}-\tau_{\infty,\text{n}})^{-1} \\
\dot{\tau}' &= \frac{1}{T_\tau}(P'_{\text{loss}}-\tau'+\tau'_\infty), \qquad \tau'(t_0)=\tau'_0.
\end{aligned} \tag{C.48}$$

The nondimensionalized power loss of the powertrain can be further specified by

$$\begin{aligned}
P'_{\text{loss}} &= \frac{P_{\text{loss}}}{P_{\text{loss,n}}} \\
&= \begin{cases} \frac{\eta_+ P}{\eta_+ P_{+,\text{n}}} & \text{if } P \geq 0, \\ \frac{\eta_- P}{\eta_- P_{-,\text{n}}} & \text{otherwise,} \end{cases} \\
&= \begin{cases} \frac{P}{P_{+,\text{n}}} & \text{if } P \geq 0, \\ \frac{P}{P_{-,\text{n}}} & \text{otherwise,} \end{cases}
\end{aligned} \tag{C.49}$$

where P, $P_{\#,\text{n}}$, and $\eta_\#$ are the power, (installed) nominal power, and efficiency of the powertrain as whole or of its critical component. The index "+" and "−" or short "#" take the respective power flow direction into account. As the choice of P is arbitrary, here simply the aerodynamic power $P = P_\text{a}$ is used, with which finally (C.34) with (C.37) is obtained. ■

C.1.10 Sensors

Here, the following simplifying assumption is made:

Assumption C.9: *All states and intermediate values of the model are available exactly to the controllers, i.e. without noise, offset, or delay.*

This assumption is justified for the purpose of the here derived model and controllers, namely to validate the steady model (and not yet to apply the controller on a real kite).

C.1.11 Control Problem Formulation

At this point, the point-mass kite model is derived. It is an explicit system of nonlinear ordinary differential equations with eleven states (momentum $\boldsymbol{p}$ in x-y-z, position $\boldsymbol{r}$ in x-y-z, the four actuations $C_{\text{D,rot}}$, c_L, $C_{\text{D,k,a}}$, ψ, and the temperature τ'). It remains to derive the controllers. This problem can be formulated as follows: Find a control scheme which, over the complete wind speed range,

1. keeps the aerodynamic power P_a, the lift force F_L, the airflow speed v_a, the temperature τ', and the actuations $C_\mathrm{D,rot}$, c_L, $C_\mathrm{D,k,a}$, ψ within their limits,
2. stabilizes the kite on a circular or figure eight flight path, and
3. harvests a good or the maximum possible power.

C.2 Control Method

To solve the stated control problem, the control scheme visualized in Fig. C.1 is utilized. Herein, indices "min", "max", and "set" are for the minimum, maximum, and set values, $P_{\mathrm{a},+,\text{max-}\tau}$ and $P_{\mathrm{a},-,\text{max-}\tau}$ are the maximum generative and consumptive aerodynamic power to satisfy the temperature limits, $F_\mathrm{tan,set}$ is the set value of the tangential force, $F_\mathrm{cen,set}$ is the set value for the centripetal/centrifugal force, and γ_set is the set value of the course angle. Those latter five

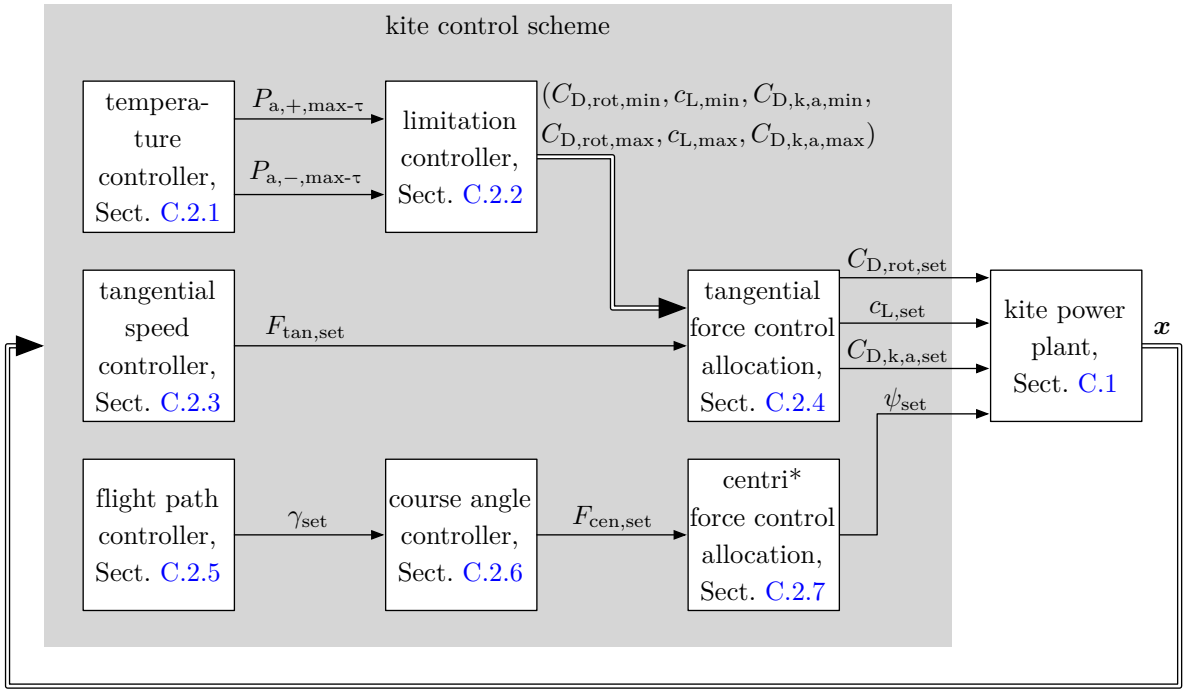

Figure C.1: Block diagram of the kite control scheme.

quantities are introduced within the corresponding control part derivation. The control scheme is based on conventional controllers (e.g. P-controllers) and parts to allocate actuations as well as to invert nonlinearities (e.g. control allocations). The individual parts are relatively simple to understand and to implement, and the computational costs are rather low. Alternatives such as model predictive control (MPC) are not considered here, because of its difficulties which may include a high computational load, the requirement for a good initial solution, and the possibility of failing to find a solution or vice-versa an infinite number of solutions (there might be infinite possibilities for the actuations in Region III(b), cf. Sect. 2.7.12).

The control scheme generally makes the following additional assumption, justified by an according selection of the control computer system:

Assumption C.10: *The control algorithm is executed quasi-continuously, i.e. the inverse of the control frequency is much smaller than the smallest time delay of the plant.*

It should be noted, that no sensor fusion has to be developed and implemented here, because of Assumption C.9 (but the control scheme should be adaptable also otherwise). Moreover, it should be highlighted that possible communication delays and asynchronous communications between sensors, control computers, and actuators are assumed negligibly small due to Assumptions C.7, C.9, and C.10, or are covered (at least in part) by actuation delays through Assumption C.9.

In the following subsections, each controller part is derived in detail.

C.2.1 Temperature Controller

C.2.1.1 General Idea and Controller Equations

The temperature controller is designed with the following rationale: It controls the powertrain's temperature to its nominal temperature with the virtual actuation P_a, cf. (C.34) with (C.37). However, instead of applying the virtual actuation P_a directly, only the maximum value is computed, one for generative power $P_{\mathrm{a},+,\text{max-}\tau}$ and one for consumptive power $P_{\mathrm{a},-,\text{max-}\tau}$. Only in the case if the tangential force control allocation needs a high power (indirectly over $C_{\mathrm{D,rot,set}}$, cf. Fig. C.1), then $P_{\mathrm{a},+,\text{max-}\tau}$ or $P_{\mathrm{a},-,\text{max-}\tau}$, respectively, may indeed be actuated.

A proportional controller is chosen as temperature controller, but with "proportional pre-filter" and "disturbance" cancelation of τ'_∞ to avoid a steady-state error. Moreover, as the purpose of the temperature control is to reduce the instantaneous power $|P_\mathrm{a}|$ from its instantaneous maximum $P_{\mathrm{a},+,\mathrm{max}}$ or $|P_{\mathrm{a},-,\mathrm{max}}|$ down to its nominal value $P_{\mathrm{a,n}} = P_{\mathrm{a},+,\text{n-ins}}$ or $P_{\mathrm{a},-,\text{n-ins}}$ if the temperature limit is reached, a feedforward of the maximum instantaneous power is applied. Finally, the controller's output is limited between the nominal and the maximum instantaneous power. Hence, the controller equations are

$$\Delta\tau' = G_{\mathrm{F},\tau}\tau'_\mathrm{set} - \tau' \tag{C.50}$$

$$P_{\mathrm{a},+,\text{max-}\tau} = \mathrm{limit}(0\ ,\ G_{\mathrm{P},\tau}\Delta\tau' - P_{\mathrm{a},+,\text{n-ins}}\,\tau'_\infty + P_{\mathrm{a},+,\mathrm{max}}\ ,\ P_{\mathrm{a},+,\mathrm{max}}) \tag{C.51}$$

$$|P_{\mathrm{a},-,\text{max-}\tau}| = \mathrm{limit}(0\ ,\ G_{\mathrm{P},\tau}\Delta\tau' - |P_{\mathrm{a},-,\text{n-ins}}|\tau'_\infty + |P_{\mathrm{a},-,\mathrm{max}}|\ ,\ |P_{\mathrm{a},-,\mathrm{max}}|), \tag{C.52}$$

where $\Delta\tau'$ is the temperature error, τ'_set is the set value of the temperature (which is the nominal temperature in per unit, i.e. $\tau'_\mathrm{set} = 1$), $G_{\mathrm{P},\tau}$ is the proportional gain, and $G_{\mathrm{F},\tau}$ is the "proportional pre-filter".[44] The use of absolute values is for sake of simplicity, such that no signs have to be changed.

Fig. C.2 shows the block diagram of the temperature control loop. The part in grey is the controller part. The "actual set value"-block models that $P_{\mathrm{a},+,\text{max-}\tau}$ or $P_{\mathrm{a},-,\text{max-}\tau}$ may not directly be the set-value which is selected by the tangential force control allocation (indirectly over $C_{\mathrm{D,rot,set}}$). Because of that and because at the end only a single P_a value is actually applied, Eqs. (C.51) and (C.52) can be combined to the short form

$$P_{\mathrm{a},\#,\text{max-}\tau} = \mathrm{limit}(0\ ,\ G_{\mathrm{P},\tau}\Delta\tau' - P_{\mathrm{a},\#,\text{n-ins}}\tau'_\infty + P_{\mathrm{a},\#,\mathrm{max}}\ ,\ P_{\mathrm{a},\#,\mathrm{max}}) \tag{C.53}$$

with

$$\begin{pmatrix} P_{\mathrm{a},\#,\text{max-}\tau} & P_{\mathrm{a},\#,\mathrm{max}} & P_{\mathrm{a},\#,\text{n-ins}} \end{pmatrix} = \begin{cases} \begin{pmatrix} P_{\mathrm{a},+,\text{max-}\tau} & P_{\mathrm{a},+,\mathrm{max}} & P_{\mathrm{a},+,\text{n-ins}} \end{pmatrix} & \text{for generative,} \\ \begin{pmatrix} |P_{\mathrm{a},-,\text{max-}\tau}| & |P_{\mathrm{a},-,\mathrm{max}}| & |P_{\mathrm{a},-,\text{n-ins}}| \end{pmatrix} & \text{for consumptive.} \end{cases} \tag{C.54}$$

[44] It should be noted, that alternatives for the lower limits in (C.51) and (C.52) are $P_{\mathrm{a},+,\text{n-ins}}$ and $|P_{\mathrm{a},-,\text{n-ins}}|$, respectively, instead of 0. However, the here proposed lower limit of 0 enables a faster cooling (if demanded) and a proper functioning for $\tau'_\infty > 0$ as well as in case parameters and states are not known exactly.

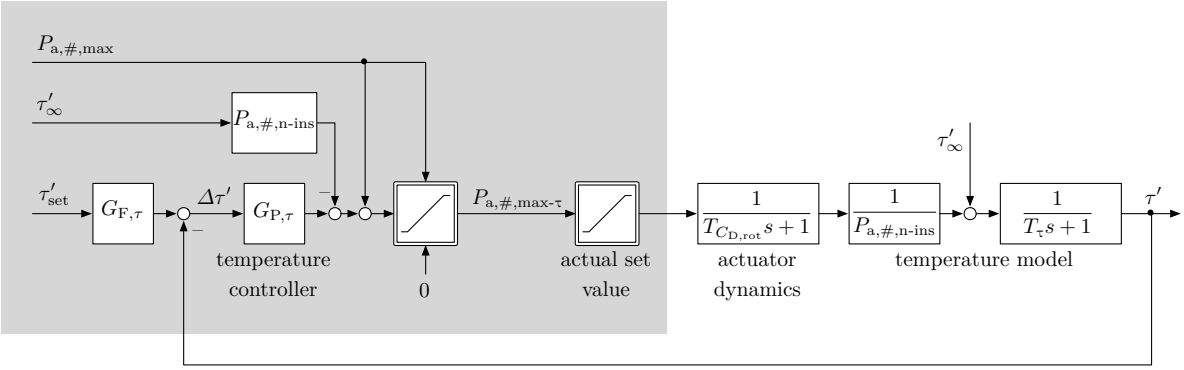

Figure C.2: Block diagram of the temperature control loop.

The other blocks in Fig. C.2 are a visualization of (C.32), (C.34), (C.50), and (C.53), wherein the linear-dynamic subparts are written in the Laplace-domain with complex frequency s. The representation of Fig. C.2 is also used below for the controller parametrization.

C.2.1.2 Maximum Instantaneous Generative Aerodynamic Power

The maximum instantaneous (overloading) generative aerodynamic power can be defined by

$$P_{\mathrm{a},+,\mathrm{max}} = f_{\text{over-P}} P_{\mathrm{a},+,\mathrm{n\text{-}ins}} \tag{C.55}$$

with power overloading (or underloading) factor $f_{\text{over-P}}$. The value of $f_{\text{over-P}}$ depends on the overloading capability of the powertrain (or its most critical component).

Additionally, there are two upper limits for $P_{\mathrm{a},+,\mathrm{max}}$: First, the maximum rotor drag coefficient (2.106) must not be exceeded. Hence, by substituting (2.106) into (2.18),

$$P_{\mathrm{a}} \leq \frac{1}{2}\rho v_{\mathrm{a}}^3 A \frac{8}{9} r_{\mathrm{rot}}. \tag{C.56}$$

Second, the tether transmission power is limited by (2.131). Substituting (2.145)–(2.148) with (2.120) into (2.131), gives the limitation

$$\begin{aligned} \underbrace{\eta_{\mathrm{pe,k},+}\eta_{\mathrm{m},+}\eta_{\mathrm{s},+}\eta_{\mathrm{rot},+}\eta_{\mathrm{a},+}P_{\mathrm{a},+}}_{P_{\mathrm{el,k},+}} &\leq \frac{U_{\mathrm{te,n}}^2}{2R_{\mathrm{te}}} \\ \Leftrightarrow P_{\mathrm{a},+} &\leq \frac{1}{\eta_{\mathrm{pe,k},+}\eta_{\mathrm{m},+}\eta_{\mathrm{s},+}\eta_{\mathrm{rot},+}\eta_{\mathrm{a},+}} \frac{U_{\mathrm{te,n}}^2}{2R_{\mathrm{te}}}. \end{aligned} \tag{C.57}$$

Herein, it is difficult to find the actual value of the upper bound of $P_{\mathrm{a},+}$, because $\eta_{\mathrm{a},+}$ is nonlinearly also a function of $P_{\mathrm{a},+}$, which is virtually the same problem already encountered in Sect. 2.7.14.4. Here, a conservative limit is utilized (also justified by a usually very high upper bound for the transmission power (2.131)): The lowest limit (C.57) would occur if $\eta_{\mathrm{a},+}$ is one (or close to one), for lower $\eta_{\mathrm{a},+}$ the right hand side of (C.57) would be higher compared to $\eta_{\mathrm{a},+} = 1$.

With that, and combining (C.55)–(C.57), Eq. (C.55) is replaced by

$$P_{\mathrm{a},+,\mathrm{max}} = \min\left\{ f_{\text{over-P}} P_{\mathrm{a},+,\mathrm{n\text{-}ins}} \;,\; \frac{1}{2}\rho v_{\mathrm{a}}^3 A \frac{8}{9} r_{\mathrm{rot}} \;,\; \frac{1}{\eta_{\mathrm{pe,k},+}\eta_{\mathrm{m},+}\eta_{\mathrm{s},+}\eta_{\mathrm{rot},+}} \frac{U_{\mathrm{te,n}}^2}{2R_{\mathrm{te}}} \right\}. \tag{C.58}$$

C.2.1.3 Maximum Instantaneous Consumptive Aerodynamic Power (Minimum Aerodynamic Power)

Similarly to (C.55), the maximum instantaneous (overloading) consumptive aerodynamic power, or minimum instantaneous (overloading) aerodynamic power, can be defined by

$$P_{\mathrm{a},-,\max} = f_{\text{over-P}} \hat{P}_{\mathrm{a},-}, \tag{C.59}$$

where $\hat{P}_{\mathrm{a},-}$ is the continuously available (nominal) consumptive aerodynamic power, which is the same as the nominally installed consumptive aerodynamic power $P_{\mathrm{a},-,\text{n-ins}}$ (note, its value is negative). However, $\hat{P}_{\mathrm{a},-}$ is hard to quantify because the actuator disk efficiency also depends on P_{a} (cf. previous subsection and Sect. 2.7.14.4). Nevertheless, the continuously available (nominal) consumptive *rotor* power $\hat{P}_{\mathrm{rot},-}$ is known from (2.254), which is related with $\hat{P}_{\mathrm{a},-}$ by (2.260) and is repeated here for convenience:

$$\hat{P}_{\mathrm{a},-} = \hat{\eta}_{\mathrm{a},-} \eta_{\mathrm{rot},-} \hat{P}_{\mathrm{rot},-}. \tag{2.260}$$

As $\hat{\eta}_{\mathrm{a},-}$ is smaller than one or equal to one,

$$\hat{P}_{\mathrm{a},-} \geq \eta_{\mathrm{rot},-} \hat{P}_{\mathrm{rot},-} \tag{C.60}$$

holds true (note again that the powers are negative; with absolute values this equation would read $|\hat{P}_{\mathrm{a},-}| \leq \eta_{\mathrm{rot},-} |\hat{P}_{\mathrm{rot},-}|$). Again, a conservative limit is utilized. The highest $\hat{P}_{\mathrm{a},-}$ (and thus worst case; this is also the lowest absolute value $|\hat{P}_{\mathrm{a},-}|$) would occur if $\hat{\eta}_{\mathrm{a},-}$ is one (or close to one), for lower $\hat{\eta}_{\mathrm{a},-}$ the right hand side of (C.60) would be lower (and the absolute value higher). Hence,

$$\hat{P}_{\mathrm{a},-} = \eta_{\mathrm{rot},-} \hat{P}_{\mathrm{rot},-}. \tag{C.61}$$

Additionally, there is a lower limit due to the tether power transmission limited (2.135). So, similarly to (C.57), substituting (2.153)–(2.155) into (2.135), gives the limitation

$$\begin{aligned} &\underbrace{\frac{1}{\eta_{\mathrm{pe,k},-}\eta_{\mathrm{m},-}\eta_{\mathrm{s},-}}}_{P_{\mathrm{el,k},-}} P_{\mathrm{rot}} \geq -\frac{U_{\mathrm{te,n}}^2}{4R_{\mathrm{te}}} \\ &\Leftrightarrow P_{\mathrm{rot}} \geq -\eta_{\mathrm{pe,k},-}\eta_{\mathrm{m},-}\eta_{\mathrm{s},-} \frac{U_{\mathrm{te,n}}^2}{4R_{\mathrm{te}}}. \end{aligned} \tag{C.62}$$

Combining (C.59)–(C.62), Eq. (C.59) is replaced by

$$P_{\mathrm{a},-,\max} = \max\left\{ f_{\text{over-P}} \eta_{\mathrm{rot},-} \hat{P}_{\mathrm{rot},-} \ , \ -\eta_{\mathrm{pe,k},-}\eta_{\mathrm{m},-}\eta_{\mathrm{s},-}\eta_{\mathrm{rot},-} \frac{U_{\mathrm{te,n}}^2}{4R_{\mathrm{te}}} \right\}. \tag{C.63}$$

C.2.1.4 Controller Parametrization and Stability

In view of Fig. C.2, the linearized closed loop input-output behavior (i.e. the limitation blocks become 1) is given by

$$\begin{aligned} \tau' &= \frac{1}{T_\tau s+1}\left\{ \tau'_\infty + \frac{1}{P_{\mathrm{a},\#,\text{n-ins}}} \frac{1}{T_{C_{\mathrm{D,rot}}} s+1} [P_{\mathrm{a},\#,\max} - P_{\mathrm{a},\#,\text{n-ins}} \tau'_\infty + G_{\mathrm{P},\tau}(G_{\mathrm{F},\tau}\tau'_{\mathrm{set}} - \tau')] \right\} \\ &= \frac{1}{T_\tau s+1}\tau'_\infty + \frac{1}{T_\tau s+1}\frac{1}{P_{\mathrm{a},\#,\text{n-ins}}}\frac{1}{T_{C_{\mathrm{D,rot}}} s+1} P_{\mathrm{a},\#,\max} - \frac{1}{T_\tau s+1}\frac{1}{T_{C_{\mathrm{D,rot}}} s+1}\tau'_\infty \\ &\quad + \frac{1}{T_\tau s+1}\frac{1}{P_{\mathrm{a},\#,\text{n-ins}}}\frac{1}{T_{C_{\mathrm{D,rot}}} s+1} G_{\mathrm{P},\tau} G_{\mathrm{F},\tau}\tau'_{\mathrm{set}} - \frac{1}{T_\tau s+1}\frac{1}{P_{\mathrm{a},\#,\text{n-ins}}}\frac{1}{T_{C_{\mathrm{D,rot}}} s+1} G_{\mathrm{P},\tau}\tau' \end{aligned}$$

$$
\begin{aligned}
\Leftrightarrow \tau' + \frac{1}{T_\tau s+1}\frac{1}{P_{\mathrm{a},\#,\text{n-ins}}}\frac{1}{T_{C_{\mathrm{D,rot}}}s+1}G_{\mathrm{P},\tau}\tau' &= \frac{1}{T_\tau s+1}\tau'_\infty + \frac{1}{T_\tau s+1}\frac{1}{P_{\mathrm{a},\#,\text{n-ins}}}\frac{1}{T_{C_{\mathrm{D,rot}}}s+1}P_{\mathrm{a},\#,\max} \\
&\quad - \frac{1}{T_\tau s+1}\frac{1}{T_{C_{\mathrm{D,rot}}}s+1}\tau'_\infty \\
&\quad + \frac{1}{T_\tau s+1}\frac{1}{P_{\mathrm{a},\#,\text{n-ins}}}\frac{1}{T_{C_{\mathrm{D,rot}}}s+1}G_{\mathrm{P},\tau}G_{\mathrm{F},\tau}\tau'_{\mathrm{set}} \\
\left(1 + \frac{1}{T_\tau s+1}\frac{1}{P_{\mathrm{a},\#,\text{n-ins}}}\frac{1}{T_{C_{\mathrm{D,rot}}}s+1}G_{\mathrm{P},\tau}\right)\tau' &= \frac{1}{T_\tau s+1}\tau'_\infty + \frac{1}{T_\tau s+1}\frac{1}{P_{\mathrm{a},\#,\text{n-ins}}}\frac{1}{T_{C_{\mathrm{D,rot}}}s+1}P_{\mathrm{a},\#,\max} \\
&\quad - \frac{1}{T_\tau s+1}\frac{1}{T_{C_{\mathrm{D,rot}}}s+1}\tau'_\infty \\
&\quad + \frac{1}{T_\tau s+1}\frac{1}{P_{\mathrm{a},\#,\text{n-ins}}}\frac{1}{T_{C_{\mathrm{D,rot}}}s+1}G_{\mathrm{P},\tau}G_{\mathrm{F},\tau}\tau'_{\mathrm{set}}
\end{aligned}
$$

$$
\Leftrightarrow \tau' = \frac{\frac{1}{T_\tau s+1}\tau'_\infty + \frac{1}{T_\tau s+1}\frac{1}{P_{\mathrm{a},\#,\text{n-ins}}}\frac{1}{T_{C_{\mathrm{D,rot}}}s+1}P_{\mathrm{a},\#,\max} - \frac{1}{T_\tau s+1}\frac{1}{T_{C_{\mathrm{D,rot}}}s+1}\tau'_\infty + \frac{1}{T_\tau s+1}\frac{1}{P_{\mathrm{a},\#,\text{n-ins}}}\frac{1}{T_{C_{\mathrm{D,rot}}}s+1}G_{\mathrm{P},\tau}G_{\mathrm{F},\tau}\tau'_{\mathrm{set}}}{1 + \frac{1}{T_\tau s+1}\frac{1}{P_{\mathrm{a},\#,\text{n-ins}}}\frac{1}{T_{C_{\mathrm{D,rot}}}s+1}G_{\mathrm{P},\tau}}
$$

$$
\begin{aligned}
&= \frac{\frac{P_{\mathrm{a},\#,\text{n-ins}}}{G_{\mathrm{P},\tau}}(T_{C_{\mathrm{D,rot}}}s+1)\tau'_\infty + \frac{P_{\mathrm{a},\#,\max}}{G_{\mathrm{P},\tau}} - \frac{P_{\mathrm{a},\#,\text{n-ins}}}{G_{\mathrm{P},\tau}}\tau'_\infty + G_{\mathrm{F},\tau}\tau'_{\mathrm{set}}}{\frac{P_{\mathrm{a},\#,\text{n-ins}}}{G_{\mathrm{P},\tau}}(T_{C_{\mathrm{D,rot}}}s+1)(T_\tau s+1)+1} \\
&= \frac{\frac{P_{\mathrm{a},\#,\text{n-ins}}}{G_{\mathrm{P},\tau}}(T_{C_{\mathrm{D,rot}}}s+1)\tau'_\infty + \frac{P_{\mathrm{a},\#,\max}}{G_{\mathrm{P},\tau}} - \frac{P_{\mathrm{a},\#,\text{n-ins}}}{G_{\mathrm{P},\tau}}\tau'_\infty + G_{\mathrm{F},\tau}\tau'_{\mathrm{set}}}{\frac{P_{\mathrm{a},\#,\text{n-ins}}T_{C_{\mathrm{D,rot}}}T_\tau}{G_{\mathrm{P},\tau}}s^2 + \frac{P_{\mathrm{a},\#,\text{n-ins}}T_{C_{\mathrm{D,rot}}}}{G_{\mathrm{P},\tau}}s + \frac{P_{\mathrm{a},\#,\text{n-ins}}T_\tau}{G_{\mathrm{P},\tau}}s + \frac{P_{\mathrm{a},\#,\text{n-ins}}}{G_{\mathrm{P},\tau}} + 1} \\
&= \frac{\frac{P_{\mathrm{a},\#,\text{n-ins}}}{G_{\mathrm{P},\tau}}(T_{C_{\mathrm{D,rot}}}s+1)\tau'_\infty + \frac{P_{\mathrm{a},\#,\max}}{G_{\mathrm{P},\tau}} - \frac{P_{\mathrm{a},\#,\text{n-ins}}}{G_{\mathrm{P},\tau}}\tau'_\infty + G_{\mathrm{F},\tau}\tau'_{\mathrm{set}}}{\frac{P_{\mathrm{a},\#,\text{n-ins}}T_{C_{\mathrm{D,rot}}}T_\tau}{G_{\mathrm{P},\tau}}s^2 + \frac{P_{\mathrm{a},\#,\text{n-ins}}(T_{C_{\mathrm{D,rot}}}+T_\tau)}{G_{\mathrm{P},\tau}}s + \left(\frac{P_{\mathrm{a},\#,\text{n-ins}}}{G_{\mathrm{P},\tau}}+1\right)} \\
&= \frac{\frac{P_{\mathrm{a},\#,\text{n-ins}}}{\left(\frac{P_{\mathrm{a},\#,\text{n-ins}}}{G_{\mathrm{P},\tau}}+1\right)G_{\mathrm{P},\tau}}(T_{C_{\mathrm{D,rot}}}s+1)\tau'_\infty + \frac{P_{\mathrm{a},\#,\max}}{\left(\frac{P_{\mathrm{a},\#,\text{n-ins}}}{G_{\mathrm{P},\tau}}+1\right)G_{\mathrm{P},\tau}} - \frac{P_{\mathrm{a},\#,\text{n-ins}}}{\left(\frac{P_{\mathrm{a},\#,\text{n-ins}}}{G_{\mathrm{P},\tau}}+1\right)G_{\mathrm{P},\tau}}\tau'_\infty + \frac{G_{\mathrm{F},\tau}}{\frac{P_{\mathrm{a},\#,\text{n-ins}}}{G_{\mathrm{P},\tau}}+1}\tau'_{\mathrm{set}}}{\frac{P_{\mathrm{a},\#,\text{n-ins}}T_{C_{\mathrm{D,rot}}}T_\tau}{\left(\frac{P_{\mathrm{a},\#,\text{n-ins}}}{G_{\mathrm{P},\tau}}+1\right)G_{\mathrm{P},\tau}}s^2 + \frac{P_{\mathrm{a},\#,\text{n-ins}}(T_{C_{\mathrm{D,rot}}}+T_\tau)}{\left(\frac{P_{\mathrm{a},\#,\text{n-ins}}}{G_{\mathrm{P},\tau}}+1\right)G_{\mathrm{P},\tau}}s + 1} \\
&= \frac{\frac{P_{\mathrm{a},\#,\text{n-ins}}}{P_{\mathrm{a},\#,\text{n-ins}}+G_{\mathrm{P},\tau}}(T_{C_{\mathrm{D,rot}}}\cancel{s+1})\tau'_\infty + \frac{P_{\mathrm{a},\#,\max}}{P_{\mathrm{a},\#,\text{n-ins}}+G_{\mathrm{P},\tau}} \cancel{- \frac{P_{\mathrm{a},\#,\text{n-ins}}}{P_{\mathrm{a},\#,\text{n-ins}}+G_{\mathrm{P},\tau}}\tau'_\infty} + \frac{G_{\mathrm{F},\tau}}{\frac{P_{\mathrm{a},\#,\text{n-ins}}}{G_{\mathrm{P},\tau}}+1}\tau'_{\mathrm{set}}}{\frac{P_{\mathrm{a},\#,\text{n-ins}}T_{C_{\mathrm{D,rot}}}T_\tau}{P_{\mathrm{a},\#,\text{n-ins}}+G_{\mathrm{P},\tau}}s^2 + \frac{P_{\mathrm{a},\#,\text{n-ins}}(T_{C_{\mathrm{D,rot}}}+T_\tau)}{P_{\mathrm{a},\#,\text{n-ins}}+G_{\mathrm{P},\tau}}s + 1} \\
&= \frac{\frac{P_{\mathrm{a},\#,\text{n-ins}}}{P_{\mathrm{a},\#,\text{n-ins}}+G_{\mathrm{P},\tau}}T_{C_{\mathrm{D,rot}}}s\tau'_\infty + \frac{P_{\mathrm{a},\#,\max}}{P_{\mathrm{a},\#,\text{n-ins}}+G_{\mathrm{P},\tau}} + \frac{G_{\mathrm{F},\tau}}{\frac{P_{\mathrm{a},\#,\text{n-ins}}}{G_{\mathrm{P},\tau}}+1}\tau'_{\mathrm{set}}}{\frac{P_{\mathrm{a},\#,\text{n-ins}}T_{C_{\mathrm{D,rot}}}T_\tau}{P_{\mathrm{a},\#,\text{n-ins}}+G_{\mathrm{P},\tau}}s^2 + \frac{P_{\mathrm{a},\#,\text{n-ins}}(T_{C_{\mathrm{D,rot}}}+T_\tau)}{P_{\mathrm{a},\#,\text{n-ins}}+G_{\mathrm{P},\tau}}s + 1}.
\end{aligned}
\tag{C.64}
$$

The control loop is stable, if the denominator polynomial has positive coefficients, because then it is a 2nd order Hurwitz polynomial.

The controller is parametrized by pole-placement by comparing the denominator of (C.64) with that of a second order delay

$$
T_\#^2 s^2 + 2D_\# T_\# s + 1 \tag{C.65}
$$

with time constant $T_\# > 0$ (which is the inverse of the eigen angular frequency, $\omega_\# = T_\#^{-1}$) and damping $D_\# > 0$ (which is sometimes also denoted by $\zeta_\#$): The closed temperature control loop

time constant $T_{\#} = T_{\tau,\circ}$ and damping $D_{\#} = D_{\tau,\circ}$ are then defined by

$$T_{\tau,\circ}^2 = \frac{P_{\mathrm{a},\#,\text{n-ins}} T_{C_{\mathrm{D,rot}}} T_\tau}{P_{\mathrm{a},\#,\text{n-ins}} + G_{\mathrm{P},\tau}} \tag{C.66}$$

and

$$2 D_{\tau,\circ} T_{\tau,\circ} = \frac{P_{\mathrm{a},\#,\text{n-ins}} (T_{C_{\mathrm{D,rot}}} + T_\tau)}{P_{\mathrm{a},\#,\text{n-ins}} + G_{\mathrm{P},\tau}}. \tag{C.67}$$

There is only one degree of freedom, $G_{\mathrm{P},\tau}$, so the control designer chooses $T_{\tau,\circ}$ or $D_{\tau,\circ}$. Here, the latter is used, for which $G_{\mathrm{P},\tau}$ is given by squaring (C.67) and substituting (C.66),

$$\begin{aligned}
2^2 D_{\tau,\circ}^2 T_{\tau,\circ}^2 &= \frac{P_{\mathrm{a},\#,\text{n-ins}}^2 (T_{C_{\mathrm{D,rot}}} + T_\tau)^2}{(P_{\mathrm{a},\#,\text{n-ins}} + G_{\mathrm{P},\tau})^2} \\
4 D_{\tau,\circ}^2 \frac{\cancel{P_{\mathrm{a},\#,\text{n-ins}}} T_{C_{\mathrm{D,rot}}} T_\tau}{\cancel{P_{\mathrm{a},\#,\text{n-ins}} + G_{\mathrm{P},\tau}}} &= \frac{P_{\mathrm{a},\#,\text{n-ins}}^{\cancel{2}} (T_{C_{\mathrm{D,rot}}} + T_\tau)^2}{(P_{\mathrm{a},\#,\text{n-ins}} + G_{\mathrm{P},\tau})^{\cancel{2}}} \\
4 D_{\tau,\circ}^2 T_{C_{\mathrm{D,rot}}} T_\tau &= \frac{P_{\mathrm{a},\#,\text{n-ins}} (T_{C_{\mathrm{D,rot}}} + T_\tau)^2}{P_{\mathrm{a},\#,\text{n-ins}} + G_{\mathrm{P},\tau}} \\
\Leftrightarrow P_{\mathrm{a},\#,\text{n-ins}} + G_{\mathrm{P},\tau} &= \frac{P_{\mathrm{a},\#,\text{n-ins}} (T_{C_{\mathrm{D,rot}}} + T_\tau)^2}{4 D_{\tau,\circ}^2 T_{C_{\mathrm{D,rot}}} T_\tau} \\
\Leftrightarrow G_{\mathrm{P},\tau} &= \frac{P_{\mathrm{a},\#,\text{n-ins}} (T_{C_{\mathrm{D,rot}}} + T_\tau)^2}{4 D_{\tau,\circ}^2 T_{C_{\mathrm{D,rot}}} T_\tau} - P_{\mathrm{a},\#,\text{n-ins}} \\
&= P_{\mathrm{a},\#,\text{n-ins}} \left[\frac{(T_{C_{\mathrm{D,rot}}} + T_\tau)^2}{4 D_{\tau,\circ}^2 T_{C_{\mathrm{D,rot}}} T_\tau} - 1 \right]
\end{aligned} \tag{C.68}$$

with which then the time constant (C.66) becomes

$$\begin{aligned}
T_{\tau,\circ}^2 &= \frac{P_{\mathrm{a},\#,\text{n-ins}} T_{C_{\mathrm{D,rot}}} T_\tau}{P_{\mathrm{a},\#,\text{n-ins}} + \left(\frac{P_{\mathrm{a},\#,\text{n-ins}} (T_{C_{\mathrm{D,rot}}} + T_\tau)^2}{4 D_{\tau,\circ}^2 T_{C_{\mathrm{D,rot}}} T_\tau} - P_{\mathrm{a},\#,\text{n-ins}} \right)} \\
&= \frac{P_{\mathrm{a},\#,\text{n-ins}} T_{C_{\mathrm{D,rot}}} T_\tau}{\frac{P_{\mathrm{a},\#,\text{n-ins}} (T_{C_{\mathrm{D,rot}}} + T_\tau)^2}{4 D_{\tau,\circ}^2 T_{C_{\mathrm{D,rot}}} T_\tau}} \\
&= \frac{4 D_{\tau,\circ}^2 T_{C_{\mathrm{D,rot}}}^2 T_\tau^2}{(T_{C_{\mathrm{D,rot}}} + T_\tau)^2} \\
\Leftrightarrow T_{\tau,\circ} &= \frac{2 D_{\tau,\circ} T_{C_{\mathrm{D,rot}}} T_\tau}{T_{C_{\mathrm{D,rot}}} + T_\tau}.
\end{aligned} \tag{C.69}$$

The steady-state value can be determined by setting $s = 0$ in (C.64),

$$\begin{aligned}
\tau' &= \frac{\frac{P_{\mathrm{a},\#,\text{n-ins}}}{P_{\mathrm{a},\#,\text{n-ins}} + G_{\mathrm{P},\tau}} T_{C_{\mathrm{D,rot}}} \cdot 0 \cdot \tau'_\infty + \frac{P_{\mathrm{a},\#,\max}}{P_{\mathrm{a},\#,\text{n-ins}} + G_{\mathrm{P},\tau}} + \frac{G_{\mathrm{F},\tau}}{\frac{P_{\mathrm{a},\#,\text{n-ins}}}{G_{\mathrm{P},\tau}} + 1} \tau'_{\mathrm{set}}}{\frac{P_{\mathrm{a},\#,\text{n-ins}} T_{C_{\mathrm{D,rot}}} T_\tau}{P_{\mathrm{a},\#,\text{n-ins}} + G_{\mathrm{P},\tau}} \cdot 0^2 + \frac{P_{\mathrm{a},\#,\text{n-ins}} (T_{C_{\mathrm{D,rot}}} + T_\tau)}{P_{\mathrm{a},\#,\text{n-ins}} + G_{\mathrm{P},\tau}} \cdot 0 + 1} \\
&= \frac{P_{\mathrm{a},\#,\max}}{P_{\mathrm{a},\#,\text{n-ins}} + G_{\mathrm{P},\tau}} + \frac{G_{\mathrm{F},\tau}}{\frac{P_{\mathrm{a},\#,\text{n-ins}}}{G_{\mathrm{P},\tau}} + 1} \tau'_{\mathrm{set}}.
\end{aligned} \tag{C.70}$$

Because $\tau' = \tau'_{\text{set}}$ shall be achieved for steady-state, the prefilter $G_{\text{F},\tau}$ must be

$$\begin{aligned}
\tau'_{\text{set}} &= \frac{P_{\text{a},\#,\text{max}}}{P_{\text{a},\#,\text{n-ins}} + G_{\text{P},\tau}} + \frac{G_{\text{F},\tau}}{\frac{P_{\text{a},\#,\text{n-ins}}}{G_{\text{P},\tau}} + 1}\tau'_{\text{set}} \\
\Leftrightarrow \tau'_{\text{set}} - \frac{P_{\text{a},\#,\text{max}}}{P_{\text{a},\#,\text{n-ins}} + G_{\text{P},\tau}} &= \frac{G_{\text{F},\tau}}{\frac{P_{\text{a},\#,\text{n-ins}}}{G_{\text{P},\tau}} + 1}\tau'_{\text{set}} \\
\Leftrightarrow \frac{\frac{P_{\text{a},\#,\text{n-ins}}}{G_{\text{P},\tau}} + 1}{\tau'_{\text{set}}} \left(\tau'_{\text{set}} - \frac{P_{\text{a},\#,\text{max}}}{P_{\text{a},\#,\text{n-ins}} + G_{\text{P},\tau}}\right) &= G_{\text{F},\tau} \\
\frac{P_{\text{a},\#,\text{n-ins}}}{G_{\text{P},\tau}} + 1 - \frac{\left(\frac{P_{\text{a},\#,\text{n-ins}}}{G_{\text{P},\tau}} + 1\right) P_{\text{a},\#,\text{max}}}{\tau'_{\text{set}} \left(P_{\text{a},\#,\text{n-ins}} + G_{\text{P},\tau}\right)} &= G_{\text{F},\tau} \\
\frac{P_{\text{a},\#,\text{n-ins}}}{G_{\text{P},\tau}} + 1 - \frac{\cancel{\left(\frac{P_{\text{a},\#,\text{n-ins}}}{G_{\text{P},\tau}} + 1\right)} P_{\text{a},\#,\text{max}}}{\tau'_{\text{set}} G_{\text{P},\tau} \cancel{\left(\frac{P_{\text{a},\#,\text{n-ins}}}{G_{\text{P},\tau}} + 1\right)}} &= G_{\text{F},\tau} \\
\frac{P_{\text{a},\#,\text{n-ins}}}{G_{\text{P},\tau}} + 1 - \frac{P_{\text{a},\#,\text{max}}}{\tau'_{\text{set}} G_{\text{P},\tau}} &= G_{\text{F},\tau} \\
1 + \frac{1}{G_{\text{P},\tau}} \left(P_{\text{a},\#,\text{n-ins}} - \frac{P_{\text{a},\#,\text{max}}}{\tau'_{\text{set}}}\right) &= G_{\text{F},\tau}.
\end{aligned} \tag{C.71}$$

It should be noted that both, $G_{\text{P},\tau}$ and $G_{\text{F},\tau}$, may differ for the two power flow directions.

C.2.2 Limitation Controller

The limitation controller outputs the limits of the three actuations $C_{\text{D,rot}}$, c_{L}, and $C_{\text{D,k,a}}$ (cf. Fig. C.1) with which (i) not only the actuator limits are satisfied, but also (ii) the maximum instantaneous power limits are satisfied, (iii) the powertrain temperature limit is satisfied, and (iv) the force limits (lift force; tether force implicitly) are satisfied.

C.2.2.1 Rotor Drag Coefficient Upper Limit

The temperature controller outputs the maximum aerodynamic power $P_{\text{a},+,\text{max-}\tau}$ (C.51), which not only already satisfies the temperature limit, but also all instantaneous limits due to (C.58). The upper limit for $C_{\text{D,rot}} = C_{\text{D,rot,max}}$ (which, in this appendix chapter, is the maximum instantaneous rotor drag coefficient, which satisfies all constraints) is readily given by substituting $P_{\text{a}} = P_{\text{a},+,\text{max-}\tau}$ into (2.18) and rearranging to

$$\begin{aligned}
P_{\text{a},+,\text{max-}\tau} &= \frac{1}{2}\rho v_{\text{a}}^3 A C_{\text{D,rot,max}} \\
\Leftrightarrow \frac{P_{\text{a},+,\text{max-}\tau}}{\frac{1}{2}\rho v_{\text{a}}^3 A} &= C_{\text{D,rot,max}},
\end{aligned} \tag{C.72}$$

where v_{a} is the currently measured airflow speed.

C.2.2.2 Rotor Drag Coefficient Lower Limit

Analogously to (C.72), the lower limit of the rotor drag coefficient is given by

$$\begin{aligned} P_{\mathrm{a},-,\text{max-}\tau} &= \frac{1}{2}\rho v_\mathrm{a}^3 A C_{\mathrm{D,rot,min}} \\ \Leftrightarrow \frac{P_{\mathrm{a},-,\text{max-}\tau}}{\frac{1}{2}\rho v_\mathrm{a}^3 A} &= C_{\mathrm{D,rot,min}}. \end{aligned} \tag{C.73}$$

C.2.2.3 Airfoil Lift Coefficient Lower Limit

The lower limit of the airfoil lift coefficient comes from the minimum operational airfoil lift coefficient and from the minimum lift force, which was already derived by (2.233).

C.2.2.4 Airfoil Lift Coefficient Upper Limit

A first upper bound for c_L is the nominal lift coefficient $c_{\mathrm{L,n}}$, cf. (2.167).

A second upper bound for c_L is given via the maximum instantaneous lift force $F_{\mathrm{L,max}}$, which is

$$F_{\mathrm{L,max}} = f_{\text{over-F}} F_{\mathrm{L,n}} \tag{C.74}$$

with force overloading (or underloading) factor $f_{\text{over-F}}$ and nominal lift force $F_{\mathrm{L,n}}$. By substituting $F_\mathrm{L} = F_{\mathrm{L,max}}$ and, via (2.39) $C_\mathrm{L} = c_{\text{L,max-F}}/(1 + 2/\mathit{AR})$, into (2.6), and rearranging, one obtains

$$\begin{aligned} F_{\mathrm{L,max}} &= \frac{1}{2}\rho v_\mathrm{a}^2 A \frac{c_{\text{L,max-F}}}{1 + \frac{2}{\mathit{AR}}} \\ \Leftrightarrow \frac{F_{\mathrm{L,max}}\left(1 + \frac{2}{\mathit{AR}}\right)}{\frac{1}{2}\rho v_\mathrm{a}^2 A} &= c_{\text{L,max-F}}. \end{aligned} \tag{C.75}$$

To satisfy all upper limits, the maximum airfoil lift coefficient is

$$c_{\mathrm{L,max}} = \min\left\{c_{\mathrm{L,n}}, c_{\text{L,max-F}}\right\}. \tag{C.76}$$

Because the currently measured airflow speed v_a is used in (C.75), it is possible that $c_{\mathrm{L,max}} < c_{\mathrm{L,min}}$ during transients, e.g. if there is a gust. To avoid that contradiction, the maximum airfoil lift coefficient also has the minimum airfoil lift coefficient as a lower bound and (C.76) is replaced by

$$c_{\mathrm{L,max}} = \max\left\{ \min\left\{c_{\mathrm{L,n}}, c_{\text{L,max-F}}\right\}, c_{\mathrm{L,min}} \right\}. \tag{C.77}$$

C.2.2.5 Actuated Drag Coefficient Limits

The limits of $C_{\mathrm{D,k,a}}$ are already defined with Assumption 2.14.

C.2.3 Tangential Speed Controller

C.2.3.1 Tangential Direction and Tangential Dynamics

The speed controller is designed for the longitudinal kite dynamics, i.e. the dynamics in the direction "tangential" to the sphere spanned by the tether. This direction can be defined by

$$\boldsymbol{e}_\mathrm{tan} := \boldsymbol{e}_\mathrm{cen} \times \boldsymbol{e}_\mathrm{r}, \tag{C.78}$$

where

$$\boldsymbol{e}_{\mathrm{cen}} := \mathrm{dir}(\boldsymbol{e}_{\mathrm{r}} \times \boldsymbol{v}_{\mathrm{k}}) \tag{C.79}$$

is defined as "centripetal/centrifugal" direction (centripetal direction in left turns/centrifugal direction in right turns; see also Fig. C.4 below), which is reused later.[45]

To express the kite's dynamics into the tangential direction (tangential dynamics), the following two assumptions are introduced:

Assumption C.11: *The effective airborne mass is constant,* $\dot{m}_{\mathrm{a}} = 0$.

Assumption C.12: *The tangential direction and the kite's speed are approximately parallel,* $\boldsymbol{e}_{\mathrm{tan}} || \boldsymbol{v}_{\mathrm{k}}$.

Assumption C.11 can obviously be justified, particularly for a drag power kite during crosswind flight in which the tether length is constant. Assumption C.12 is also justified, because during crosswind flight and tensioned tether the kite essentially moves along the sphere of the tether with little to no speed into the radial direction $\boldsymbol{e}_{\mathrm{r}}$ and by definition with no speed into the centripetal direction. With those two assumptions, the tangential kite dynamics is given as follows:

Theorem C.2 (Tangential Kite Dynamics): *If Assumptions C.1, C.2, C.11, and C.12 apply, then the kite's dynamics w.r.t. to the tangential direction* $\boldsymbol{e}_{\mathrm{tan}}$ *is given by*

$$\dot{v}_{\mathrm{k,tan}} = m_{\mathrm{a}}^{-1} F_{\mathrm{tan}}, \qquad v_{\mathrm{k,tan}}(t_0) = v_{\mathrm{k,tan},0}, \tag{C.80}$$

where $\dot{v}_{\mathrm{k,tan}}$*,* $v_{\mathrm{k,tan}}$*, and* $F_{\mathrm{acc,tan}} = F_{\mathrm{tan}}$ *are the change of speed (i.e. the acceleration), the speed, and the acceleration force into the tangential direction (in short: tangential force* F_{tan}*).*

Proof. With Assumptions C.1, C.2, and C.11, Eq. (C.1) becomes with (C.3) inserted

$$\dot{\boldsymbol{v}}_{\mathrm{k}} = m_{\mathrm{a}}^{-1} \boldsymbol{F}_{\mathrm{acc}}, \qquad \boldsymbol{v}_{\mathrm{k}}(t_0) = \boldsymbol{v}_{\mathrm{k},0} = m_{\mathrm{a}}^{-1} \boldsymbol{p}_{\mathrm{k},0}. \tag{C.81}$$

By expressing the acceleration force and velocity in the non-inertial (i.e. rotating/accelerating) reference frame spanned by the orthogonal (and right-handed) unit vectors $\boldsymbol{e}_{\mathrm{tan}}$, $\boldsymbol{e}_{\mathrm{cen}}$, and $\boldsymbol{e}_{\mathrm{r}}$, which may be called "kinematic reference frame" (in short: kin), and thus with the transformation matrix

$$\boldsymbol{T}_{\mathrm{kin}} = \begin{pmatrix} \boldsymbol{e}_{\mathrm{tan}} & \boldsymbol{e}_{\mathrm{cen}} & \boldsymbol{e}_{\mathrm{r}} \end{pmatrix}, \tag{C.82}$$

one obtains

$$\boldsymbol{F}_{\mathrm{acc}} = \boldsymbol{T}_{\mathrm{kin}} \boldsymbol{F}_{\mathrm{acc}}^{\mathrm{kin}}, \tag{C.83}$$

and

$$\boldsymbol{v}_{\mathrm{k}} = \boldsymbol{T}_{\mathrm{kin}} \boldsymbol{v}_{\mathrm{k}}^{\mathrm{kin}}. \tag{C.84}$$

[45] It should be noted that, if the kite indeed stays on the sphere spanned by the tether (i.e. tether always tensioned) and if the tether length and elongation are constant, then $\boldsymbol{e}_{\mathrm{tan}} = \mathrm{dir}(\boldsymbol{v}_{\mathrm{k}})$. However, Eq. (C.78) and (C.79) do not make those assumptions and are therefore also valid for an untensioned tether or for non-constant tether length, which both may happen during hover-crosswind flight transitions, or for lift power kites during reeling.

Substituting (C.83) and (C.84) into (C.81) and rearranging, while dropping the initial values for sake of brevity, gives

$$\begin{aligned}
\frac{\mathrm{d}}{\mathrm{d}t}(\boldsymbol{T}_{\mathrm{kin}}\boldsymbol{v}_{\mathrm{k}}^{\mathrm{kin}}) &= m_{\mathrm{a}}^{-1}\boldsymbol{T}_{\mathrm{kin}}\boldsymbol{F}_{\mathrm{acc}}^{\mathrm{kin}} \\
\dot{\boldsymbol{T}}_{\mathrm{kin}}\boldsymbol{v}_{\mathrm{k}}^{\mathrm{kin}} + \boldsymbol{T}_{\mathrm{kin}}\dot{\boldsymbol{v}}_{\mathrm{k}}^{\mathrm{kin}} &= m_{\mathrm{a}}^{-1}\boldsymbol{T}_{\mathrm{kin}}\boldsymbol{F}_{\mathrm{acc}}^{\mathrm{kin}} \\
\Leftrightarrow \boldsymbol{T}_{\mathrm{kin}}\dot{\boldsymbol{v}}_{\mathrm{k}}^{\mathrm{kin}} &= m_{\mathrm{a}}^{-1}\boldsymbol{T}_{\mathrm{kin}}\boldsymbol{F}_{\mathrm{acc}}^{\mathrm{kin}} - \dot{\boldsymbol{T}}_{\mathrm{kin}}\boldsymbol{v}_{\mathrm{k}}^{\mathrm{kin}} \qquad | \cdot \boldsymbol{T}_{\mathrm{kin}}^{-1} \\
\dot{\boldsymbol{v}}_{\mathrm{k}}^{\mathrm{kin}} &= m_{\mathrm{a}}^{-1}\boldsymbol{F}_{\mathrm{acc}}^{\mathrm{kin}} - \boldsymbol{T}_{\mathrm{kin}}^{-1}\dot{\boldsymbol{T}}_{\mathrm{kin}}\boldsymbol{v}_{\mathrm{k}}^{\mathrm{kin}}.
\end{aligned} \tag{C.85}$$

As a transformation matrix is orthogonal, its inverse is the transpose, which is with (C.82) given by

$$\boldsymbol{T}_{\mathrm{kin}}^{-1} = \boldsymbol{T}_{\mathrm{kin}}^{\top} = \begin{pmatrix} \boldsymbol{e}_{\mathrm{tan}}^{\top} \\ \boldsymbol{e}_{\mathrm{cen}}^{\top} \\ \boldsymbol{e}_{\mathrm{r}}^{\top} \end{pmatrix}. \tag{C.86}$$

The time derivative of the transformation matrix (C.82) is in general given by

$$\begin{aligned}
\dot{\boldsymbol{T}}_{\mathrm{kin}} &= \begin{pmatrix} \dot{\boldsymbol{e}}_{\mathrm{tan}} & \dot{\boldsymbol{e}}_{\mathrm{cen}} & \dot{\boldsymbol{e}}_{\mathrm{r}} \end{pmatrix} \\
&= \begin{pmatrix} \boldsymbol{\omega} \times \boldsymbol{e}_{\mathrm{tan}} & \boldsymbol{\omega} \times \boldsymbol{e}_{\mathrm{cen}} & \boldsymbol{\omega} \times \boldsymbol{e}_{\mathrm{r}} \end{pmatrix},
\end{aligned} \tag{C.87}$$

with instantaneous angular velocity vector $\boldsymbol{\omega}$. This equation can be explained as follows: As a unit vector always remains a unit vector with unit length, its possible change over time can only be a rotation. As further all unit vectors keep their relative angles, all of them are rotated around the same instantaneous axis and with the same angular velocity. Therefore, the time derivative of a unit vector of a reference frame is the rotation with some angular velocity vector $\boldsymbol{\omega}$.

By expressing that angular velocity vector by

$$\boldsymbol{\omega} = \omega_{\mathrm{tan}}\boldsymbol{e}_{\mathrm{tan}} + \omega_{\mathrm{cen}}\boldsymbol{e}_{\mathrm{cen}} + \omega_{\mathrm{r}}\boldsymbol{e}_{\mathrm{r}} \tag{C.88}$$

without loss of generality, Eq. (C.87) becomes

$$\begin{aligned}
\dot{\boldsymbol{T}}_{\mathrm{kin}} &= \Big((\omega_{\mathrm{tan}}\boldsymbol{e}_{\mathrm{tan}} + \omega_{\mathrm{cen}}\boldsymbol{e}_{\mathrm{cen}} + \omega_{\mathrm{r}}\boldsymbol{e}_{\mathrm{r}}) \times \boldsymbol{e}_{\mathrm{tan}}, \\
&\qquad (\omega_{\mathrm{tan}}\boldsymbol{e}_{\mathrm{tan}} + \omega_{\mathrm{cen}}\boldsymbol{e}_{\mathrm{cen}} + \omega_{\mathrm{r}}\boldsymbol{e}_{\mathrm{r}}) \times \boldsymbol{e}_{\mathrm{cen}}, \\
&\qquad (\omega_{\mathrm{tan}}\boldsymbol{e}_{\mathrm{tan}} + \omega_{\mathrm{cen}}\boldsymbol{e}_{\mathrm{cen}} + \omega_{\mathrm{r}}\boldsymbol{e}_{\mathrm{r}}) \times \boldsymbol{e}_{\mathrm{r}} \Big) \\
&= \Big(\omega_{\mathrm{tan}} \underbrace{\boldsymbol{e}_{\mathrm{tan}} \times \boldsymbol{e}_{\mathrm{tan}}}_{\boldsymbol{0}} + \omega_{\mathrm{cen}} \underbrace{\boldsymbol{e}_{\mathrm{cen}} \times \boldsymbol{e}_{\mathrm{tan}}}_{-\boldsymbol{e}_{\mathrm{r}}} + \omega_{\mathrm{r}} \underbrace{\boldsymbol{e}_{\mathrm{r}} \times \boldsymbol{e}_{\mathrm{tan}}}_{\boldsymbol{e}_{\mathrm{cen}}}, \\
&\qquad \omega_{\mathrm{tan}} \underbrace{\boldsymbol{e}_{\mathrm{tan}} \times \boldsymbol{e}_{\mathrm{cen}}}_{\boldsymbol{e}_{\mathrm{r}}} + \omega_{\mathrm{cen}} \underbrace{\boldsymbol{e}_{\mathrm{cen}} \times \boldsymbol{e}_{\mathrm{cen}}}_{\boldsymbol{0}} + \omega_{\mathrm{r}} \underbrace{\boldsymbol{e}_{\mathrm{r}} \times \boldsymbol{e}_{\mathrm{cen}}}_{-\boldsymbol{e}_{\mathrm{tan}}}, \\
&\qquad \omega_{\mathrm{tan}} \underbrace{\boldsymbol{e}_{\mathrm{tan}} \times \boldsymbol{e}_{\mathrm{r}}}_{-\boldsymbol{e}_{\mathrm{cen}}} + \omega_{\mathrm{cen}} \underbrace{\boldsymbol{e}_{\mathrm{cen}} \times \boldsymbol{e}_{\mathrm{r}}}_{\boldsymbol{e}_{\mathrm{tan}}} + \omega_{\mathrm{r}} \underbrace{\boldsymbol{e}_{\mathrm{r}} \times \boldsymbol{e}_{\mathrm{r}}}_{\boldsymbol{0}} \Big) \\
&= \begin{pmatrix} -\omega_{\mathrm{cen}}\boldsymbol{e}_{\mathrm{r}} + \omega_{\mathrm{r}}\boldsymbol{e}_{\mathrm{cen}} & \omega_{\mathrm{tan}}\boldsymbol{e}_{\mathrm{r}} - \omega_{\mathrm{r}}\boldsymbol{e}_{\mathrm{tan}} & -\omega_{\mathrm{tan}}\boldsymbol{e}_{\mathrm{cen}} + \omega_{\mathrm{cen}}\boldsymbol{e}_{\mathrm{tan}} \end{pmatrix}.
\end{aligned} \tag{C.89}$$

Multiplying (C.86) with (C.89), which is part of (C.85), one obtains

$$\begin{aligned}
\boldsymbol{T}_{\mathrm{kin}}^{-1}\dot{\boldsymbol{T}}_{\mathrm{kin}} &= \begin{pmatrix} \boldsymbol{e}_{\mathrm{tan}}^{\top} \\ \boldsymbol{e}_{\mathrm{cen}}^{\top} \\ \boldsymbol{e}_{\mathrm{r}}^{\top} \end{pmatrix} \begin{pmatrix} -\omega_{\mathrm{cen}}\boldsymbol{e}_{\mathrm{r}} + \omega_{\mathrm{r}}\boldsymbol{e}_{\mathrm{cen}} & \omega_{\mathrm{tan}}\boldsymbol{e}_{\mathrm{r}} - \omega_{\mathrm{r}}\boldsymbol{e}_{\mathrm{tan}} & -\omega_{\mathrm{tan}}\boldsymbol{e}_{\mathrm{cen}} + \omega_{\mathrm{cen}}\boldsymbol{e}_{\mathrm{tan}} \end{pmatrix} \\
&= \begin{pmatrix} \boldsymbol{e}_{\mathrm{tan}}^{\top}(-\omega_{\mathrm{cen}}\boldsymbol{e}_{\mathrm{r}} + \omega_{\mathrm{r}}\boldsymbol{e}_{\mathrm{cen}}) & \boldsymbol{e}_{\mathrm{tan}}^{\top}(\omega_{\mathrm{tan}}\boldsymbol{e}_{\mathrm{r}} - \omega_{\mathrm{r}}\boldsymbol{e}_{\mathrm{tan}}) & \boldsymbol{e}_{\mathrm{tan}}^{\top}(-\omega_{\mathrm{tan}}\boldsymbol{e}_{\mathrm{cen}} + \omega_{\mathrm{cen}}\boldsymbol{e}_{\mathrm{tan}}) \\ \boldsymbol{e}_{\mathrm{cen}}^{\top}(-\omega_{\mathrm{cen}}\boldsymbol{e}_{\mathrm{r}} + \omega_{\mathrm{r}}\boldsymbol{e}_{\mathrm{cen}}) & \boldsymbol{e}_{\mathrm{cen}}^{\top}(\omega_{\mathrm{tan}}\boldsymbol{e}_{\mathrm{r}} - \omega_{\mathrm{r}}\boldsymbol{e}_{\mathrm{tan}}) & \boldsymbol{e}_{\mathrm{cen}}^{\top}(-\omega_{\mathrm{tan}}\boldsymbol{e}_{\mathrm{cen}} + \omega_{\mathrm{cen}}\boldsymbol{e}_{\mathrm{tan}}) \\ \boldsymbol{e}_{\mathrm{r}}^{\top}(-\omega_{\mathrm{cen}}\boldsymbol{e}_{\mathrm{r}} + \omega_{\mathrm{r}}\boldsymbol{e}_{\mathrm{cen}}) & \boldsymbol{e}_{\mathrm{r}}^{\top}(\omega_{\mathrm{tan}}\boldsymbol{e}_{\mathrm{r}} - \omega_{\mathrm{r}}\boldsymbol{e}_{\mathrm{tan}}) & \boldsymbol{e}_{\mathrm{r}}^{\top}(-\omega_{\mathrm{tan}}\boldsymbol{e}_{\mathrm{cen}} + \omega_{\mathrm{cen}}\boldsymbol{e}_{\mathrm{tan}}) \end{pmatrix} \\
&= \begin{pmatrix} 0 & -\omega_{\mathrm{r}} & \omega_{\mathrm{cen}} \\ \omega_{\mathrm{r}} & 0 & -\omega_{\mathrm{tan}} \\ -\omega_{\mathrm{cen}} & \omega_{\mathrm{tan}} & 0 \end{pmatrix}, \qquad \text{(C.90)}
\end{aligned}$$

which is the cross product matrix of the angular velocity rotation vector expressed in the kinematic reference frame, $\boldsymbol{\omega}^{\mathrm{kin}} = \begin{pmatrix} \omega_{\mathrm{tan}} & \omega_{\mathrm{cen}} & \omega_{\mathrm{r}} \end{pmatrix}^{\top}$.

Substituting (C.90) into (C.85), and writing the vector components out, gives

$$\begin{aligned}
\begin{pmatrix} \dot{v}_{\mathrm{k,tan}} \\ \dot{v}_{\mathrm{k,cen}} \\ \dot{v}_{\mathrm{k,r}} \end{pmatrix} &= m_{\mathrm{a}}^{-1} \begin{pmatrix} F_{\mathrm{acc,tan}} \\ F_{\mathrm{acc,cen}} \\ F_{\mathrm{acc,r}} \end{pmatrix} - \begin{pmatrix} 0 & -\omega_{\mathrm{r}} & \omega_{\mathrm{cen}} \\ \omega_{\mathrm{r}} & 0 & -\omega_{\mathrm{tan}} \\ -\omega_{\mathrm{cen}} & \omega_{\mathrm{tan}} & 0 \end{pmatrix} \begin{pmatrix} v_{\mathrm{k,tan}} \\ v_{\mathrm{k,cen}} \\ v_{\mathrm{k,r}} \end{pmatrix} \\
&= \begin{pmatrix} m_{\mathrm{a}}^{-1}F_{\mathrm{acc,tan}} \\ m_{\mathrm{a}}^{-1}F_{\mathrm{acc,cen}} \\ m_{\mathrm{a}}^{-1}F_{\mathrm{acc,r}} \end{pmatrix} - \begin{pmatrix} -\omega_{\mathrm{r}}v_{\mathrm{k,cen}} + \omega_{\mathrm{cen}}v_{\mathrm{k,r}} \\ \omega_{\mathrm{r}}v_{\mathrm{k,tan}} - \omega_{\mathrm{tan}}v_{\mathrm{k,r}} \\ -\omega_{\mathrm{cen}}v_{\mathrm{k,tan}} + \omega_{\mathrm{tan}}v_{\mathrm{k,cen}} \end{pmatrix} \\
&= \begin{pmatrix} m_{\mathrm{a}}^{-1}F_{\mathrm{acc,tan}} + \omega_{\mathrm{r}}v_{\mathrm{k,cen}} - \omega_{\mathrm{cen}}v_{\mathrm{k,r}} \\ m_{\mathrm{a}}^{-1}F_{\mathrm{acc,cen}} - \omega_{\mathrm{r}}v_{\mathrm{k,tan}} + \omega_{\mathrm{tan}}v_{\mathrm{k,r}} \\ m_{\mathrm{a}}^{-1}F_{\mathrm{acc,r}} + \omega_{\mathrm{cen}}v_{\mathrm{k,tan}} - \omega_{\mathrm{tan}}v_{\mathrm{k,cen}} \end{pmatrix}. \qquad \text{(C.91)}
\end{aligned}$$

Finally, with Assumption C.12, the centripetal and radial velocity components are (approximately) zero. Therefore, the first component of (C.91) is

$$\dot{v}_{\mathrm{k,tan}} = m_{\mathrm{a}}^{-1}F_{\mathrm{acc,tan}} + \omega_{\mathrm{r}} \cdot 0 - \omega_{\mathrm{cen}} \cdot 0. \qquad \text{(C.92)}$$

Knowing also that there is some initial velocity in the tangential direction gives (C.80).■

C.2.3.2 Tangential Speed Controller Idea and Equations

The speed controller is derived for the plant (C.80). Herein, $F_{\mathrm{tan,set}}$ is used as a virtual actuation, i.e. the new set values of the actual three actuations $C_{\mathrm{D,rot,set}}$, $c_{\mathrm{L,set}}$, and $C_{\mathrm{D,k,a,set}}$ generate $F_{\mathrm{tan,set}}$, but this function $F_{\mathrm{tan,set}}(C_{\mathrm{D,rot,set}}, c_{\mathrm{L,set}}, C_{\mathrm{D,k,a,set}})$ is inverted by a control allocation in a later step.

For the tangential speed controller, again simply a P-controller is utilized, i.e.

$$\Delta v_{\mathrm{k,tan}} = v_{\mathrm{k,tan,set}} - v_{\mathrm{k,tan}} \qquad \text{(C.93)}$$

$$F_{\mathrm{tan,set}} = G_{\mathrm{P,v}}\Delta v_{\mathrm{k,tan}} \qquad \text{(C.94)}$$

with speed error $\Delta v_{\mathrm{k,tan}}$, speed set value $v_{\mathrm{k,tan,set}}$, and proportional gain $G_{\mathrm{P,v}}$.

Fig. C.3 visualizes the tangential speed control loop. It also visualizes the idea of the tangential force control allocation, which inverts the static nonlinear part of the plant. Here, it is assumed that the control allocation works perfectly:

Assumption C.13: *The control allocation inverts perfectly the tangential force generation of the plant, such that the tangential force actuation can be approximated as first order delay with*

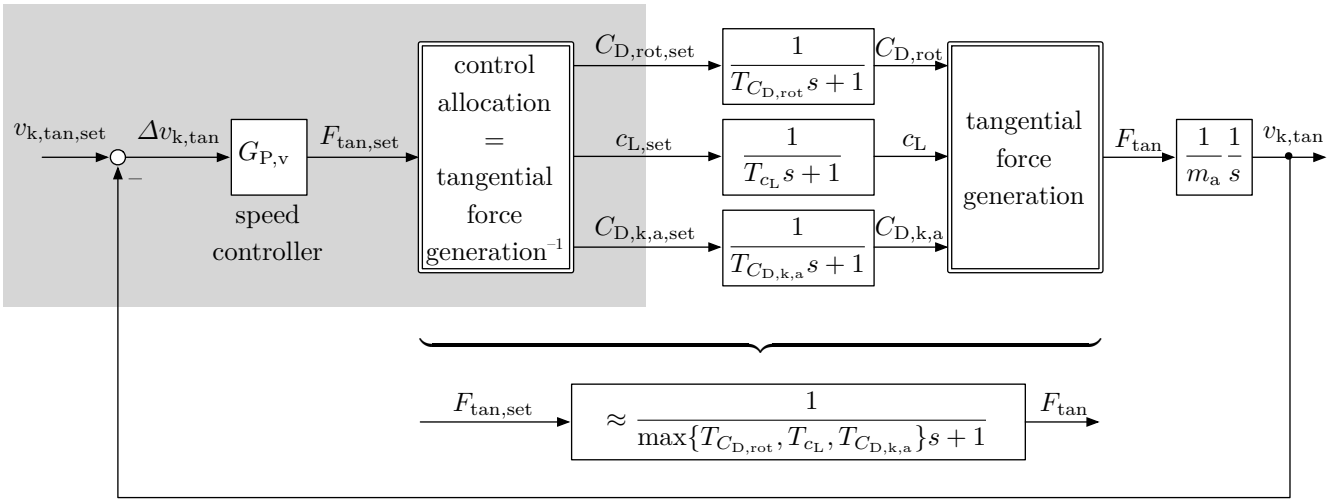

Figure C.3: Block diagram of the tangential speed control loop.

the actuation time constant T_{a} equal to the highest time constant of the actually involved actuators,

$$T_{\mathrm{a}} = \max\{T_{C_{\mathrm{D,rot}}}, T_{c_{\mathrm{L}}}, T_{C_{\mathrm{D,k,a}}}\}. \tag{C.95}$$

This assumption can be justified, because the here utilized simple model can indeed be perfectly inverted (for steady-state) and because the highest actuator time constant defines when F_{tan} is achieved for a set value $F_{\mathrm{tan,set}}$.

C.2.3.3 Controller Parametrization and Stability

In view of Fig. C.3 the closed loop transfer function is

$$\begin{aligned}\frac{v_{\mathrm{k,tan}}}{v_{\mathrm{k,tan,set}}} &= \frac{G_{\mathrm{P,v}}\frac{1}{T_{\mathrm{a}}s+1}\frac{1}{m_{\mathrm{a}}s}}{1+G_{\mathrm{P,v}}\frac{1}{T_{\mathrm{a}}s+1}\frac{1}{m_{\mathrm{a}}s}} \\ &= \frac{1}{\frac{1}{G_{\mathrm{P,v}}}(T_{\mathrm{a}}s+1)m_{\mathrm{a}}s+1} \\ &= \frac{1}{\frac{T_{\mathrm{a}}m_{\mathrm{a}}}{G_{\mathrm{P,v}}}s^2+\frac{m_{\mathrm{a}}}{G_{\mathrm{P,v}}}s+1}.\end{aligned} \tag{C.96}$$

The speed control loop is stable if $G_{\mathrm{P,v}} > 0$, because then the denominator is a 2nd order Hurwitz polynomial due to its positive coefficients.

Analogously to the temperature control loop in Sect. C.2.1.4, the speed control loop is parametrized through pole-placement by comparing the denominator of (C.96) with that of a second order delay (C.65): The closed speed control loop time constant $T_{\#} = T_{\mathrm{v},\circ}$ and damping $D_{\#} = D_{\mathrm{v},\circ}$ are then defined by

$$T_{\mathrm{v},\circ}^2 = \frac{T_{\mathrm{a}}m_{\mathrm{a}}}{G_{\mathrm{P,v}}} \tag{C.97}$$

and

$$2D_{\mathrm{v},\circ}T_{\mathrm{v},\circ} = \frac{m_{\mathrm{a}}}{G_{\mathrm{P,v}}}. \tag{C.98}$$

Again, there is only one degree of freedom, $G_{\mathrm{P,v}}$, so the control designer chooses $T_{\mathrm{v,\circ}}$ or $D_{\mathrm{v,\circ}}$. The latter is used here, for which $G_{\mathrm{P,v}}$ is given by squaring (C.98) and substituting (C.97),

$$\begin{aligned} 2^2 D_{\mathrm{v,\circ}}^2 T_{\mathrm{v,\circ}}^2 &= \frac{m_{\mathrm{a}}^2}{G_{\mathrm{P,v}}^2} \\ 4D_{\mathrm{v,\circ}}^2 \frac{T_{\mathrm{a}} m_{\mathrm{a}}}{G_{\mathrm{P,v}}} &= \frac{m_{\mathrm{a}}^2}{G_{\mathrm{P,v}}^2} \\ 4D_{\mathrm{v,\circ}}^2 T_{\mathrm{a}} &= \frac{m_{\mathrm{a}}}{G_{\mathrm{P,v}}} \\ \Leftrightarrow G_{\mathrm{P,v}} &= \frac{m_{\mathrm{a}}}{4D_{\mathrm{v,\circ}}^2 T_{\mathrm{a}}} \end{aligned} \tag{C.99}$$

with which then the time constant (C.97) becomes

$$\begin{aligned} T_{\mathrm{v,\circ}}^2 &= \frac{T_{\mathrm{a}} m_{\mathrm{a}}}{\frac{m_{\mathrm{a}}}{4D_{\mathrm{v,\circ}}^2 T_{\mathrm{a}}}} \\ &= 4D_{\mathrm{v,\circ}}^2 T_{\mathrm{a}}^2 \\ T_{\mathrm{v,\circ}} &= 2D_{\mathrm{v,\circ}} T_{\mathrm{a}}. \end{aligned} \tag{C.100}$$

C.2.3.4 Tangential Speed Set Value

The set value of the airflow speed $v_{\mathrm{a,set}}$ is given from the optimal airflow speed in Region II via (2.192), but bounded by the minimum and maximum values, i.e.

$$v_{\mathrm{a,set}} = \mathrm{limit}(v_{\mathrm{a,min}}, v_{\mathrm{a,II}}, v_{\mathrm{a,max}}), \tag{C.101}$$

where

$$v_{\mathrm{a,max}} = f_{\text{over-v}} v_{\mathrm{a,n}} \tag{C.102}$$

is the maximum instantaneous airflow speed set value with overloading (or underloading) factor $f_{\text{over-v}}$. From that airflow speed set value, the set airflow velocity is

$$\boldsymbol{v}_{\mathrm{a,set}} = v_{\mathrm{a,set}} \, \mathrm{dir}(\boldsymbol{v}_{\mathrm{a}}), \tag{C.103}$$

where $\mathrm{dir}(\boldsymbol{v}_{\mathrm{a}})$ is the direction of the currently measured airflow velocity. The kite velocity vector is then given by inverting (C.17), i.e.

$$\boldsymbol{v}_{\mathrm{k,set}} = \boldsymbol{v}_{\mathrm{w}}(\boldsymbol{r}_{\mathrm{k}}) - \boldsymbol{v}_{\mathrm{a,set}} \tag{C.104}$$

with the currently measured (or estimated) wind velocity at the kite $\boldsymbol{v}_{\mathrm{w}}(\boldsymbol{r}_{\mathrm{k}})$. Finally the set value of the tangential kite speed is given by

$$v_{\mathrm{k,tan,set}} = \boldsymbol{v}_{\mathrm{k,set}} \bullet \boldsymbol{e}_{\mathrm{tan}} \tag{C.105}$$

with the currently measured tangential direction $\boldsymbol{e}_{\mathrm{tan}}$.

C.2.4 Tangential Force Control Allocation

The control allocation works very similar as motivated in Sect. 2.7.12. As mentioned in the previous section and visualized in Fig. C.3, the tangential force control allocation inverts the

tangential force generation, i.e. it computes the three actuations $C_{\mathrm{D,rot,set}}$, $c_{\mathrm{L,set}}$, and $C_{\mathrm{D,k,a,set}}$ to achieve a given $F_{\mathrm{tan,set}} = F_{\mathrm{tan}}$ in steady-state. Although it should be possible to find an analytical solution for this inversion and for the here utilized model, a numerical solution is pursued for sake of simplicity as well as for the possibility for its use with minimal changes in a more detailed and more nonlinear model. However, because the here utilized model is not very nonlinear, the derived numerical solution is exact.

In the following, first a few functions are defined for later convenient use, then the developed algorithm is detailed step by step.

C.2.4.1 Definition: "force"-function

The "force"-function

$$F_{\mathrm{tan,set}} \leftarrow \mathrm{force}(C_{\mathrm{D,rot,set}}, c_{\mathrm{L,set}}, C_{\mathrm{D,k,a,set}}) \tag{C.106}$$

computes the (steady-state) tangential force (i.e. the tangential set force) subject to the currently measured states for the passed set values of the three actuations $C_{\mathrm{D,rot,set}}$, $c_{\mathrm{L,set}}$, $C_{\mathrm{D,k,a,set}}$, i.e. the equations (2.39), (2.15), (2.6), (C.13), (2.46), (2.42), (2.41), (2.40), (2.33), (2.11), (2.7), (C.14), (C.12), (C.4), and

$$F_{\mathrm{tan}} = F_{\mathrm{acc,tan}} = \boldsymbol{F}_{\mathrm{acc}} \bullet \boldsymbol{e}_{\mathrm{tan}} \tag{C.107}$$

are computed in that order. Note that the straight tether has no force contribution into the tangential direction $\boldsymbol{F}_{\mathrm{te}} \bullet \boldsymbol{e}_{\mathrm{tan}} = 0$, because the tether force is always perpendicular to the tangential direction in the here employed model.

C.2.4.2 Definition: "linpol"-function

The "linpol"-function

$$x \leftarrow \mathrm{linpol}\left(y, \begin{pmatrix} x_1 \\ y_1 \\ x_2 \\ y_2 \end{pmatrix}\right) \tag{C.108}$$

linearly interpolates between two points (x_1, y_1) and (x_2, y_2), and returns the value x for a given y value. The function originates from the equation of a straight line

$$y = c_0 + c_1 x \tag{C.109}$$

with coefficients c_0 and c_1. By inserting the two known points into (C.109) and solving for the coefficients, one obtains

$$\begin{aligned} y_1 &= c_0 + c_1 x_1 \\ y_2 &= c_0 + c_1 x_2 \\ \Rightarrow \begin{pmatrix} y_1 \\ y_2 \end{pmatrix} &= \begin{pmatrix} 1 & x_1 \\ 1 & x_2 \end{pmatrix} \begin{pmatrix} c_0 \\ c_1 \end{pmatrix} \\ \Leftrightarrow \begin{pmatrix} 1 & x_1 \\ 1 & x_2 \end{pmatrix}^{-1} \begin{pmatrix} y_1 \\ y_2 \end{pmatrix} &= \begin{pmatrix} c_0 \\ c_1 \end{pmatrix}. \end{aligned} \tag{C.110}$$

With the known coefficients, x is given by solving (C.109) to

$$x = \frac{y - c_0}{c_1}. \tag{C.111}$$

If $x_1 = x_2$, the matrix in (C.110) is not invertible. In that case, "linpol" simply returns

$$x = x_1. \tag{C.112}$$

C.2.4.3 Definition: "quadpol"-function

The "quadpol"-function

$$x \leftarrow \text{quadpol}\left(y, \begin{pmatrix} x_1 \\ y_1 \\ x_2 \\ y_2 \\ x_3 \\ y_3 \end{pmatrix}\right) \tag{C.113}$$

quadratically interpolates between three points (x_1, y_1), (x_2, y_2), and (x_3, y_3), and returns the value x for a given y value. The function originates from the quadratic equation

$$y = c_0 + c_1 x + c_2 x^2 \tag{C.114}$$

with coefficients c_0, c_1, and c_2. By inserting the three known points into (C.114) and solving for the coefficients, one obtains

$$\begin{aligned} y_1 &= c_0 + c_1 x_1 + c_2 x_1^2 \\ y_2 &= c_0 + c_1 x_2 + c_2 x_2^2 \\ y_3 &= c_0 + c_1 x_3 + c_2 x_3^2 \\ \Rightarrow \begin{pmatrix} y_1 \\ y_2 \\ y_3 \end{pmatrix} &= \begin{pmatrix} 1 & x_1 & x_1^2 \\ 1 & x_2 & x_2^2 \\ 1 & x_3 & x_3^2 \end{pmatrix} \begin{pmatrix} c_0 \\ c_1 \\ c_2 \end{pmatrix} \\ \Leftrightarrow \begin{pmatrix} 1 & x_1 & x_1^2 \\ 1 & x_2 & x_2^2 \\ 1 & x_3 & x_3^2 \end{pmatrix}^{-1} \begin{pmatrix} y_1 \\ y_2 \\ y_3 \end{pmatrix} &= \begin{pmatrix} c_0 \\ c_1 \\ c_2 \end{pmatrix}. \end{aligned} \tag{C.115}$$

With the known coefficients, x is given by solving (C.114) to

$$\begin{aligned} 0 &= \frac{c_0 - y}{c_2} + \frac{c_1}{c_2} x + x^2 \\ \Leftrightarrow x &= -\frac{c_1}{2c_2} \pm \sqrt{\frac{c_1^2}{4c_2^2} - \frac{c_0 - y}{c_2}}. \end{aligned} \tag{C.116}$$

Note that two result values are given. The actual selected value is to be chosen outside "quadpol", i.e. "quadpol" returns two values.

In case $x_1 = x_2$, $x_2 = x_3$, or/and $x_1 = x_3$, the matrix in (C.115) is not invertible. In those cases, "quadpol" falls back to "linpol",

$$x \leftarrow \begin{cases} \text{linpol}\left(y, \begin{pmatrix} x_1 \\ y_1 \\ x_2 \\ y_2 \end{pmatrix}\right) & \text{for } x_1 = x_3 \text{ or } x_2 = x_3, \\ \text{linpol}\left(y, \begin{pmatrix} x_2 \\ y_2 \\ x_3 \\ y_3 \end{pmatrix}\right) & \text{for } x_1 = x_2 \text{ (or } x_1 = x_3). \end{cases} \tag{C.117}$$

C.2.4.4 Tangential Force Control Allocation Algorithm

The tangential force control allocation is defined by the following algorithm, which is executed at each discrete time step:

1. Initialization: Assign optimal actuations, but limited within their bounds, i.e.

$$C_{\mathrm{D,rot,set}} \leftarrow \text{limit}\left(C_{\mathrm{D,rot,min}}, \frac{1}{2}C_{\mathrm{D,eq,n}}, C_{\mathrm{D,rot,max}}\right), \tag{C.118}$$

$$c_{\mathrm{L,set}} \leftarrow \text{limit}(c_{\mathrm{L,min}}, c_{\mathrm{L,n}}, c_{\mathrm{L,max}}), \tag{C.119}$$

$$C_{\mathrm{D,k,a,set}} \leftarrow \text{limit}(C_{\mathrm{D,k,a,min}}, 0, C_{\mathrm{D,k,a,max}}). \tag{C.120}$$

2. Compute the highest achievable tangential force,

$$F_{\mathrm{tan,set},C_{\mathrm{D,rot,min}}} \leftarrow \text{force}(C_{\mathrm{D,rot,min}}, c_{\mathrm{L,set}}, C_{\mathrm{D,k,a,set}}). \tag{C.121}$$

   Note that $c_{\mathrm{L,set}}$ and $C_{\mathrm{D,k,a,set}}$ already have the values to support obtaining the highest achievable force.

3. If $F_{\mathrm{tan,set}} > F_{\mathrm{tan,set},C_{\mathrm{D,rot,min}}}$,

   3.1. then

$$C_{\mathrm{D,rot,set}} \leftarrow C_{\mathrm{D,rot,min}}. \tag{C.122}$$

   A larger tangential force is not achievable, i.e. the tangential speed controller's demand cannot be fully satisfied, because the actuators are at the limit.
   The algorithm ends here (return).

   3.2. Otherwise, continue with next step.

4. Compute the lowest achievable tangential force by changing the rotor drag coefficient only,

$$F_{\mathrm{tan,set},C_{\mathrm{D,rot,max}}} \leftarrow \text{force}(C_{\mathrm{D,rot,max}}, c_{\mathrm{L,set}}, C_{\mathrm{D,k,a,set}}). \tag{C.123}$$

5. If $F_{\mathrm{tan,set},C_{\mathrm{D,rot,max}}} < F_{\mathrm{tan,set}}$,

   5.1. it means that $F_{\mathrm{tan,set}}$ is achievable just by changing the rotor drag coefficient. As from (2.11), (2.7), (C.14), (C.12), (C.4), and (C.107) follows $F_{\mathrm{tan}} = c_0 + c_1 C_{\mathrm{D,rot}}$ with

some values c_0 and c_1, the set value is found (exactly) by a linear interpolation between the two extrema,

$$C_{\mathrm{D,rot,set}} \leftarrow \mathrm{linpol}\left(F_{\mathrm{tan,set}}, \begin{pmatrix} C_{\mathrm{D,rot,max}} \\ F_{\mathrm{tan,set},C_{\mathrm{D,rot,max}}} \\ C_{\mathrm{D,rot,min}} \\ F_{\mathrm{tan,set},C_{\mathrm{D,rot,min}}} \end{pmatrix}\right). \tag{C.124}$$

The algorithm ends here (return).

5.2. Otherwise, it means that $F_{\mathrm{tan,set}}$ is not achievable by changing the rotor drag coefficient alone. It must be set to the maximum

$$C_{\mathrm{D,rot,set}} \leftarrow C_{\mathrm{D,rot,max}}, \tag{C.125}$$

but also further actuation(s) have to be altered.

6. Compute the lowest achievable tangential force by changing additionally the airfoil lift coefficient,

$$F_{\mathrm{tan,set},c_{\mathrm{L,min}}} \leftarrow \mathrm{force}(C_{\mathrm{D,rot,set}}, c_{\mathrm{L,min}}, C_{\mathrm{D,k,a,set}}). \tag{C.126}$$

7. If $F_{\mathrm{tan,set},c_{\mathrm{L,min}}} < F_{\mathrm{tan,set}}$,

7.1. it means that $F_{\mathrm{tan,set}}$ is achievable just by changing additionally the airfoil lift coefficient. As from (2.39), (2.15), (2.6), (C.13), (2.42), (2.46), (2.41), (2.40), (2.33), (2.11), (2.7), (C.14), (C.12), (C.4), and (C.107) follows $F_{\mathrm{tan}} = c_0 + c_1 c_{\mathrm{L}} + c_2 c_{\mathrm{L}}^2$ with some values c_0, c_1, and c_2, the set value is found (exactly) by a quadratic interpolation. For that, three points are required. A first point is the previously computed one at $c_{\mathrm{L,min}}$. A second point is at $c_{\mathrm{L,n}} = c_{\mathrm{L,max}}$, whose force is also already known from

$$F_{\mathrm{tan,set},c_{\mathrm{L,max}}} = F_{\mathrm{tan,set},C_{\mathrm{D,rot,max}}}. \tag{C.127}$$

A third point is computed in-between with

$$c_{\mathrm{L,mid}} = \frac{c_{\mathrm{L,min}} + c_{\mathrm{L,max}}}{2} \tag{C.128}$$

by

$$F_{\mathrm{tan,set},c_{\mathrm{L,mid}}} \leftarrow \mathrm{force}(C_{\mathrm{D,rot,set}}, c_{\mathrm{L,mid}}, C_{\mathrm{D,k,a,set}}). \tag{C.129}$$

The airfoil lift coefficient set value is then

$$c_{\mathrm{L,set}} \leftarrow \mathrm{quadpol}\left(F_{\mathrm{tan,set}}, \begin{pmatrix} c_{\mathrm{L,min}} \\ F_{\mathrm{tan,set},c_{\mathrm{L,min}}} \\ c_{\mathrm{L,mid}} \\ F_{\mathrm{tan,set},c_{\mathrm{L,mid}}} \\ c_{\mathrm{L,max}} \\ F_{\mathrm{tan,set},c_{\mathrm{L,max}}} \end{pmatrix}\right). \tag{C.130}$$

There are two $c_{\mathrm{L,set}}$ values from "quadpol", cf. (C.116). The one is chosen which is within the interval $[c_{\mathrm{L,min}}, c_{\mathrm{L,max}}]$ (and possibly closer to $c_{\mathrm{L,max}}$).
The algorithm ends here (return).

7.2. Otherwise, it means that $F_{\mathrm{tan,set}}$ is not achievable by changing only the rotor drag coefficient and the airfoil lift coefficient. The latter must be set to the minimum

$$c_{\mathrm{L,set}} \leftarrow c_{\mathrm{L,min}}, \tag{C.131}$$

but also further actuation(s) have to be altered.

8. Compute the lowest achievable tangential force by changing additionally the actuated drag coefficient,

$$F_{\mathrm{tan,set},C_{\mathrm{D,k,a,max}}} \leftarrow \mathrm{force}(C_{\mathrm{D,rot,set}}, c_{\mathrm{L,set}}, C_{\mathrm{D,k,a,max}}). \tag{C.132}$$

9. If $F_{\mathrm{tan,set},C_{\mathrm{D,rot,max}}} < F_{\mathrm{tan,set}}$,

9.1. it means that $F_{\mathrm{tan,set}}$ is achievable just by changing additionally the actuated drag coefficient. As from (2.33), (2.11), (2.7), (C.14), (C.12), (C.4), and (C.107) follows $F_{\mathrm{tan}} = c_0 + c_1 C_{\mathrm{D,k,a}}$ with some values c_0 and c_1, the set value is found (exactly) by a linear interpolation between the two extrema,

$$C_{\mathrm{D,k,a,set}} \leftarrow \mathrm{linpol}\left(F_{\mathrm{tan,set}}, \begin{pmatrix} C_{\mathrm{D,k,a,min}} \\ F_{\mathrm{tan,set},C_{\mathrm{D,k,a,min}}} \\ C_{\mathrm{D,k,a,max}} \\ F_{\mathrm{tan,set},C_{\mathrm{D,k,a,max}}} \end{pmatrix}\right), \tag{C.133}$$

where the force at $C_{\mathrm{D,k,a,min}}$ is already known from

$$F_{\mathrm{tan,set},C_{\mathrm{D,k,a,min}}} = F_{\mathrm{tan,set},c_{\mathrm{L,min}}}. \tag{C.134}$$

The algorithm ends here (return).

9.2. Otherwise, it means that $F_{\mathrm{tan,set}}$ is also not achievable with the highest actuated drag coefficient. It must be set to the maximum

$$C_{\mathrm{D,k,a,set}} \leftarrow C_{\mathrm{D,k,a,max}}. \tag{C.135}$$

A lower tangential force is not achievable, i.e. the tangential speed controller's demand cannot be fully satisfied, because the actuators are at the limit.
The algorithm ends here (return).

C.2.5 Flight Path Controller

C.2.5.1 General Idea and Definition of the Course Angle

The here utilized flight path controller is based on target point tracking. Fig. C.4 visualizes the idea: The flight path controller outputs a target point to which the kite shall fly (i.e. which shall be tracked). Once a switching condition is fulfilled, e.g. when the kite is close to that target point, a new target point is selected. If according target points and switching conditions are chosen, the kite can fly e.g. a figure eight.

The direction in which the kite flies is generally three-dimensional. However, as the limitation controller ensures the force limits, during crosswind flight the kite is essentially constrained by the sphere spanned by the tether, which reduces the flight direction to two dimensions. Those two dimensions can be further reduced to a single angle—the course angle γ—as visualized in Fig. C.4, which is defined by

$$\gamma := -\arctan_2(\boldsymbol{e}_{\varphi'} \bullet \boldsymbol{e}_{\mathrm{tan}}, -\boldsymbol{e}_{\vartheta} \bullet \boldsymbol{e}_{\mathrm{tan}}) \tag{C.136}$$

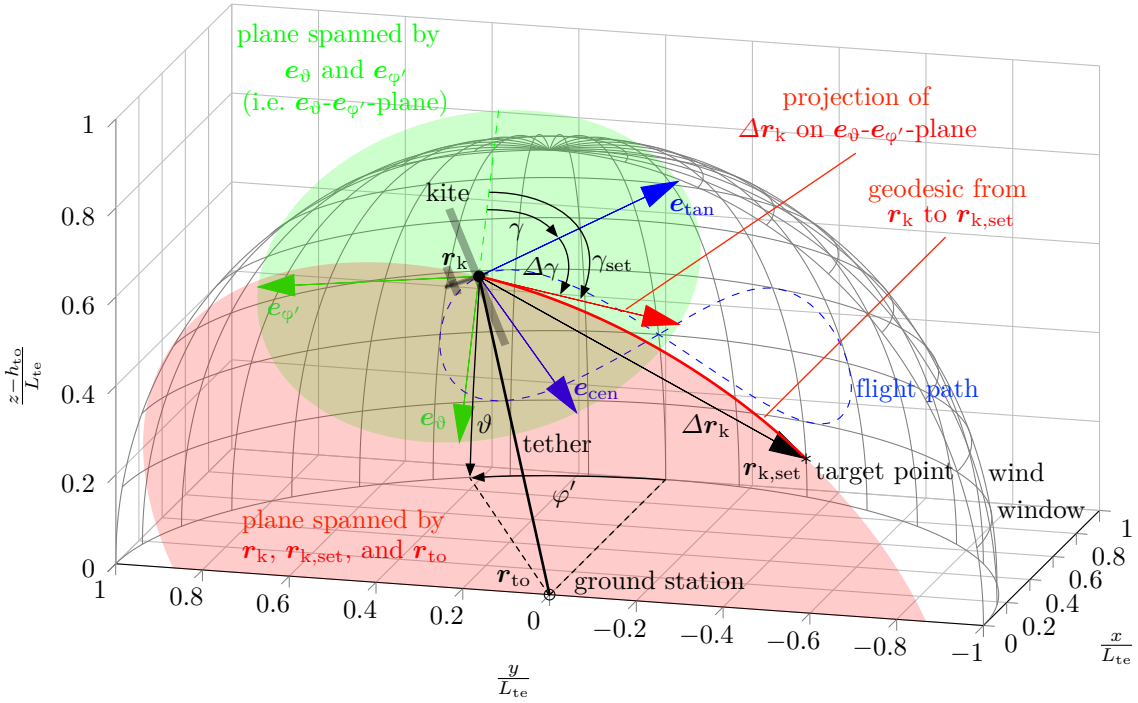

Figure C.4: Visualization of the target point tracking and important quantities.

with

$$\arctan_2(y,x) := \begin{cases} \arctan\left(\frac{y}{x}\right) & \text{if } x > 0, \\ \arctan\left(\frac{y}{x}\right) + \pi & \text{if } x < 0 \text{ and } y \geq 0, \\ \arctan\left(\frac{y}{x}\right) - \pi & \text{if } x < 0 \text{ and } y < 0, \\ +\frac{\pi}{2} & \text{if } x = 0 \text{ and } y > 0, \\ -\frac{\pi}{2} & \text{if } x = 0 \text{ and } y < 0, \\ 0 & \text{if } x = 0 \text{ and } y = 0. \end{cases} \tag{C.137}$$

From the set target point and from the currently measured kite position, the target direction in which the kite shall fly can be determined, i.e. a course angle set value γ_{set} can be determined. The course angle is then controlled by the course angle controller, e.g. by utilizing the actuation of the roll angle ψ_{set}, cf. Fig. C.1.

C.2.5.2 Target Points: Definition and Properties

The flight path controller requires a list of target points. Each target point has

- a target elevation ϑ_{set},
- a target azimuth φ_{set} w.r.t. the wind's azimuth, i.e. the target azimuth in the inertial reference frame (primed azimuth) is

$$\varphi'_{set} = \varphi_{set} + \varphi_w, \tag{C.138}$$

- a threshold value x_{th}, which, when achieved, deactivates the current target point (and activates the next target point),
- a threshold type which declares the meaning of the x_{th} value, and
- a turning direction type, which can be either "Shortest", "Positive", or "Negative".

Tab. C.1 lists the available threshold activation types. Herein,

$$\varphi = \varphi' - \varphi_{\mathrm{w}} \tag{C.139}$$

is the azimuth w.r.t. the wind's azimuth in accordance to (C.138),

$$\varphi' = \arctan_2(\boldsymbol{r}_{\mathrm{k}} \bullet \boldsymbol{y}, \boldsymbol{r}_{\mathrm{k}} \bullet \boldsymbol{x}) \tag{C.140}$$

is the azimuth in the inertial reference frame,

$$\vartheta = -\arctan\left[\frac{(\boldsymbol{r}_{\mathrm{k}} - \boldsymbol{r}_{\mathrm{to}}) \bullet \boldsymbol{z}}{\sqrt{(\boldsymbol{r}_{\mathrm{k}} \bullet \boldsymbol{x})^2 + (\boldsymbol{r}_{\mathrm{k}} \bullet \boldsymbol{y})^2}}\right] \tag{C.141}$$

is the elevation[46], and the "normalized"-function wraps some angle x into the interval $[-\pi, \pi]$ by

$$\mathrm{normalized}(x) := x - 2\pi \left\lfloor \frac{x + \pi}{2\pi} \right\rfloor \tag{C.142}$$

in which $\lfloor x \rfloor$ denotes the rounding-off- or "floor"-function.

Table C.1: Target point deactivation threshold types.

Type	Deactivation Condition
ElevationBelowThreshold	$\vartheta < x_{\mathrm{th}}$
ElevationAboveThreshold	$\vartheta > x_{\mathrm{th}}$
AzimuthBelowThreshold	$\mathrm{normalized}(\varphi) < x_{\mathrm{th}}$
AzimuthAboveThreshold	$\mathrm{normalized}(\varphi) > x_{\mathrm{th}}$
CourseAngleBelowThreshold	$\gamma < x_{\mathrm{th}}$
CourseAngleAboveThreshold	$\gamma > x_{\mathrm{th}}$

C.2.5.3 Target Point Selection State Machine

The state machine simply increments the target point counter, once the deactivation condition of the current target point is true. If the target point counter exceeds the maximum number of target points, it is reset. Note that the completion of a path loop (e.g. circle or figure eight) can be detected by such a target point counter reset.

[46] The sign of this ϑ-definition is opposite compared to the one defined for the steady model, cf. Chap 2 or compare Fig. 2.2 with C.4. This new definition is for sake of consistency, such that all rotations are right-handed positive.

C.2.5.4 "Raw" Course Angle Set Value

The target position from the target point elevation and azimuth is

$$\boldsymbol{r}_{\mathrm{k,set}} = \boldsymbol{R}_{\mathrm{z}}(\varphi'_{\mathrm{set}})\boldsymbol{R}_{\mathrm{y}}(\vartheta_{\mathrm{set}}) \begin{pmatrix} L_{\mathrm{te}} \\ 0 \\ 0 \end{pmatrix} + \boldsymbol{r}_{\mathrm{to}} \tag{C.143}$$

and the position error is

$$\Delta\boldsymbol{r}_{\mathrm{k}} = \boldsymbol{r}_{\mathrm{k,set}} - \boldsymbol{r}_{\mathrm{k}}. \tag{C.144}$$

As visualized in Fig C.4, the kite shall fly towards $\boldsymbol{r}_{\mathrm{k,set}}$ on the shortest way along the sphere spanned by the tether, i.e. on a geodesic. With the target direction $\Delta\boldsymbol{r}_{\mathrm{k}}$ projected onto the $\boldsymbol{e}_{\vartheta}$-$\boldsymbol{e}_{\varphi'}$-plane, the "raw" (primed) course angle set value is

$$\gamma'_{\mathrm{set}} = -\arctan_2(\boldsymbol{e}_{\varphi'} \bullet \Delta\boldsymbol{r}_{\mathrm{k}}, -\boldsymbol{e}_{\vartheta} \bullet \Delta\boldsymbol{r}_{\mathrm{k}}). \tag{C.145}$$

Remark C.1: *There may be reasons to not aim to fly on a geodesic. For example, if $\boldsymbol{r}_{\mathrm{k}}$ and $\boldsymbol{r}_{\mathrm{k,set}}$ are far away from each other (azimuth difference in the order of $\approx \pi$), the geodesic goes to high elevation angles or close to or even through the zenith. This might be undesired and overall a suboptimal path due to the high cosine loss and low speed. Moreover, such a path might violate maximum altitude restrictions or might cause a gimbal lock of tether angle sensors. To avoid that, one possibility is to introduce intermediate target points, if the geodesic from $\boldsymbol{r}_{\mathrm{k}}$ to $\boldsymbol{r}_{\mathrm{k,set}}$ exceeds an altitude or elevation angle limit. Another possibility is to alter (C.145) e.g. to*

$$\gamma'_{\mathrm{set}} = -\arctan_2[\mathrm{normalized}(\varphi'_{\mathrm{set}} - \varphi'), -(\vartheta_{\mathrm{set}} - \vartheta)] \tag{C.146}$$

which targets the shortest path on the "unrolled" φ'-ϑ-grid. However, because the actual position is a nonlinear function of elevation and azimuth angles, Eq. (C.146) may lead to curves of the targeted flight path from $\boldsymbol{r}_{\mathrm{k}}$ to $\boldsymbol{r}_{\mathrm{k,set}}$, e.g. from close to the zenith with negative azimuth for $\boldsymbol{r}_{\mathrm{k}}$ to close to the ground with positive azimuth for $\boldsymbol{r}_{\mathrm{k,set}}$ the path is like a swirl.—It is left to future research to identify appropriate extensions of (C.145) and (C.146) (or combinations thereof) with which further control goals, not mentioned in the problem formulation in Sect. C.1.11, are satisfied or optimized.

C.2.5.5 Course Angle Set Value with Desired Turning Direction

The course angle controller (detailed below, in the next section), drives the difference of the course angle set value and its current value to zero. However, if just the "raw" course angle set value (C.145) or (C.146) is passed on, the desired turning direction might not be satisfied. Therefore, the actual course angle set value is given by

$$\gamma_{\mathrm{set}} = \begin{cases} \gamma'_{\mathrm{set}} + 2\pi & \text{if "Shortest" and } \gamma'_{\mathrm{set}} - \gamma < -\pi \text{ or "Positive" and } \gamma'_{\mathrm{set}} - \gamma < 0, \\ \gamma'_{\mathrm{set}} - 2\pi & \text{if "Shortest" and } \gamma'_{\mathrm{set}} - \gamma > +\pi \text{ or "Negative" and } \gamma'_{\mathrm{set}} - \gamma > 0, \\ \gamma'_{\mathrm{set}} & \text{otherwise.} \end{cases} \tag{C.147}$$

C.2.6 Course Angle Controller

C.2.6.1 Course Angle Dynamics

With the above imposed assumptions and definitions, the course angle dynamics is given as follows:

Theorem C.3 (Course Angle Dynamics): *If Assumptions C.1, C.2, C.11, and C.12 apply, then the dynamics of the course angle γ (C.136) is determined by*

$$\dot{\gamma} = \frac{F_{\text{cen}}}{m_{\text{a}} v_{\text{k,tan}}} + \dot{\varphi}' \sin(\vartheta), \qquad \gamma(t_0) = \gamma_0, \tag{C.148}$$

where $F_{\text{acc,cen}} = F_{\text{cen}}$ is the acceleration force (C.4) into the centripetal/centrifugal direction (C.79) (in short: centripetal/centrifugal force F_{cen}), m_{a} is the (effective) airborne mass, $v_{\text{k,tan}} > 0$ is the speed of the kite into the tangential direction (C.78), φ' is the azimuth angle in the inertial reference frame, ϑ is the elevation angle, and γ_0 is the initial course angle at initial time t_0.

Proof. Taking the time derivative of the course angle (C.136) while neglecting the discontinuity of the $\arctan_2$- and arctan-functions, which is legitimate because angles can generally be expressed also with a $2\pi \cdot \#$ offset where $\# \in \mathbb{Z}$, one obtains

$$\begin{aligned}
\dot{\gamma} &= -\frac{\mathrm{d}}{\mathrm{d}t} \arctan_2(\boldsymbol{e}_{\varphi'} \bullet \boldsymbol{e}_{\text{tan}}, -\boldsymbol{e}_{\vartheta} \bullet \boldsymbol{e}_{\text{tan}}) \\
&= -\frac{\mathrm{d}}{\mathrm{d}t} \arctan\left(\frac{\boldsymbol{e}_{\varphi'} \bullet \boldsymbol{e}_{\text{tan}}}{-\boldsymbol{e}_{\vartheta} \bullet \boldsymbol{e}_{\text{tan}}}\right) \\
&= -\frac{1}{1 + \left(\frac{\boldsymbol{e}_{\varphi'} \bullet \boldsymbol{e}_{\text{tan}}}{-\boldsymbol{e}_{\vartheta} \bullet \boldsymbol{e}_{\text{tan}}}\right)^2} \frac{\mathrm{d}}{\mathrm{d}t} \left(\frac{\boldsymbol{e}_{\varphi'} \bullet \boldsymbol{e}_{\text{tan}}}{-\boldsymbol{e}_{\vartheta} \bullet \boldsymbol{e}_{\text{tan}}}\right).
\end{aligned} \tag{C.149}$$

With the kite's speed into the $\boldsymbol{e}_{\vartheta}$- and into the $\boldsymbol{e}_{\varphi'}$-directions,

$$\begin{aligned}
v_{\text{k},\vartheta} &= (v_{\text{k,tan}} \boldsymbol{e}_{\text{tan}}) \bullet \boldsymbol{e}_{\vartheta} \qquad | : v_{\text{k,tan}} \\
\Leftrightarrow \frac{v_{\text{k},\vartheta}}{v_{\text{k,tan}}} &= \boldsymbol{e}_{\text{tan}} \bullet \boldsymbol{e}_{\vartheta}
\end{aligned} \tag{C.150}$$

and

$$\begin{aligned}
v_{\text{k},\varphi'} &= (v_{\text{k,tan}} \boldsymbol{e}_{\text{tan}}) \bullet \boldsymbol{e}_{\varphi'} \qquad | : v_{\text{k,tan}} \\
\Leftrightarrow \frac{v_{\text{k},\varphi'}}{v_{\text{k,tan}}} &= \boldsymbol{e}_{\text{tan}} \bullet \boldsymbol{e}_{\varphi'},
\end{aligned} \tag{C.151}$$

one further obtains

$$\begin{aligned}
\dot{\gamma} &= -\frac{1}{1 + \left(\frac{v_{\text{k},\varphi'}/v_{\text{k,tan}}}{-v_{\text{k},\vartheta}/v_{\text{k,tan}}}\right)^2} \frac{\mathrm{d}}{\mathrm{d}t} \left(\frac{v_{\text{k},\varphi'}/v_{\text{k,tan}}}{-v_{\text{k},\vartheta}/v_{\text{k,tan}}}\right) \\
&= \frac{1}{1 + \left(\frac{v_{\text{k},\varphi'}}{-v_{\text{k},\vartheta}}\right)^2} \frac{\mathrm{d}}{\mathrm{d}t} \left(\frac{v_{\text{k},\varphi'}}{v_{\text{k},\vartheta}}\right) \\
&= \frac{1}{1 + \frac{v_{\text{k},\varphi'}^2}{v_{\text{k},\vartheta}^2}} \frac{\dot{v}_{\text{k},\varphi} v_{\text{k},\vartheta} - v_{\text{k},\varphi'} \dot{v}_{\text{k},\vartheta}}{v_{\text{k},\vartheta}^2}
\end{aligned}$$

$$= \frac{\dot{v}_{\mathrm{k},\varphi} v_{\mathrm{k},\vartheta} - v_{\mathrm{k},\varphi'} \dot{v}_{\mathrm{k},\vartheta}}{v_{\mathrm{k},\vartheta}^2 + v_{\mathrm{k},\varphi'}^2}$$
$$= \frac{\dot{v}_{\mathrm{k},\varphi'} v_{\mathrm{k},\vartheta} - v_{\mathrm{k},\varphi'} \dot{v}_{\mathrm{k},\vartheta}}{v_{\mathrm{k,tan}}^2} \tag{C.152}$$

in which the Pythagorean theorem

$$v_{\mathrm{k,tan}}^2 = v_{\mathrm{k},\vartheta}^2 + v_{\mathrm{k},\varphi'}^2 \tag{C.153}$$

is inserted.[47] It should be noted, that (C.152) requires $v_{\mathrm{k,tan}} \neq 0$.

As derived in the proof of Theorem C.2, the kite's dynamics are given due to Assumptions C.1, C.2, and C.11 by Eq. (C.81).

The acceleration force and velocity in the non-inertial (i.e. rotating/accelerating) reference frame spanned by the orthogonal unit vectors $\boldsymbol{e}_{\mathrm{r}}$, $\boldsymbol{e}_{\varphi'}$, and $\boldsymbol{e}_{\vartheta}$, which may be called "small earth reference frame" (in short: SE), and thus with the transformation matrix

$$\boldsymbol{T}_{\mathrm{SE}} = \begin{pmatrix} \boldsymbol{e}_{\mathrm{r}} & \boldsymbol{e}_{\varphi'} & \boldsymbol{e}_{\vartheta} \end{pmatrix}, \tag{C.154}$$

$$\text{or equivalently} \quad \boldsymbol{T}_{\mathrm{SE}}(\vartheta, \varphi') = \boldsymbol{R}_{\mathrm{z}}(\varphi') \boldsymbol{R}_{\mathrm{y}}(\vartheta) \begin{pmatrix} 1 & 0 & 0 \\ 0 & 1 & 0 \\ 0 & 0 & -1 \end{pmatrix}, \tag{C.155}$$

are

$$\boldsymbol{F}_{\mathrm{acc}} = \boldsymbol{T}_{\mathrm{SE}} \boldsymbol{F}_{\mathrm{acc}}^{\mathrm{SE}} \tag{C.156}$$

and

$$\boldsymbol{v}_{\mathrm{k}} = \boldsymbol{T}_{\mathrm{SE}} \boldsymbol{v}_{\mathrm{k}}^{\mathrm{SE}}. \tag{C.157}$$

Substituting (C.156) and (C.157) into (C.81) and rearranging gives

$$\begin{aligned}
\frac{\mathrm{d}}{\mathrm{d}t}[\boldsymbol{T}_{\mathrm{SE}}(\vartheta, \varphi') \boldsymbol{v}_{\mathrm{k}}^{\mathrm{SE}}] &= m_{\mathrm{a}}^{-1} \boldsymbol{T}_{\mathrm{SE}}(\vartheta, \varphi') \boldsymbol{F}_{\mathrm{acc}}^{\mathrm{SE}} \\
\dot{\boldsymbol{T}}_{\mathrm{SE}}(\vartheta, \varphi') \boldsymbol{v}_{\mathrm{k}}^{\mathrm{SE}} + \boldsymbol{T}_{\mathrm{SE}}(\vartheta, \varphi') \dot{\boldsymbol{v}}_{\mathrm{k}}^{\mathrm{SE}} &= m_{\mathrm{a}}^{-1} \boldsymbol{T}_{\mathrm{SE}}(\vartheta, \varphi') \boldsymbol{F}_{\mathrm{acc}}^{\mathrm{SE}} \\
\Leftrightarrow \boldsymbol{T}_{\mathrm{SE}}(\vartheta, \varphi') \dot{\boldsymbol{v}}_{\mathrm{k}}^{\mathrm{SE}} &= m_{\mathrm{a}}^{-1} \boldsymbol{T}_{\mathrm{SE}}(\vartheta, \varphi') \boldsymbol{F}_{\mathrm{acc}}^{\mathrm{SE}} - \dot{\boldsymbol{T}}_{\mathrm{SE}}(\vartheta, \varphi') \boldsymbol{v}_{\mathrm{k}}^{\mathrm{SE}} \quad | \cdot \boldsymbol{T}_{\mathrm{SE}}^{-1}(\vartheta, \varphi') \\
\dot{\boldsymbol{v}}_{\mathrm{k}}^{\mathrm{SE}} &= m_{\mathrm{a}}^{-1} \boldsymbol{F}_{\mathrm{acc}}^{\mathrm{SE}} - \boldsymbol{T}_{\mathrm{SE}}^{-1}(\vartheta, \varphi') \dot{\boldsymbol{T}}_{\mathrm{SE}}(\vartheta, \varphi') \boldsymbol{v}_{\mathrm{k}}^{\mathrm{SE}}.
\end{aligned} \tag{C.158}$$

With the help of a computer algebra tool (here, MATLAB Symbolic Toolbox was utilized), the term $\boldsymbol{T}_{\mathrm{SE}}^{-1}(\vartheta, \varphi') \dot{\boldsymbol{T}}_{\mathrm{SE}}(\vartheta, \varphi')$ with (C.155) is solved with the result

$$\boldsymbol{T}_{\mathrm{SE}}^{-1}(\vartheta, \varphi') \dot{\boldsymbol{T}}_{\mathrm{SE}}(\vartheta, \varphi') = \begin{pmatrix} 0 & -\dot{\varphi}' \cos(\vartheta) & -\dot{\vartheta} \\ \dot{\varphi}' \cos(\vartheta) & 0 & -\dot{\varphi}' \sin(\vartheta) \\ \dot{\vartheta} & \dot{\varphi}' \sin(\vartheta) & 0 \end{pmatrix}. \tag{C.159}$$

[47] Eq. (C.152) could have been also derived from the alternative expression of the course angle $\gamma = -\arctan_2(v_{\mathrm{k},\varphi'}, -v_{\mathrm{k},\vartheta})$.

Substituting (C.159) into (C.158), and writing out the vector components, gives

$$\begin{aligned}
\begin{pmatrix} \dot{v}_{\mathrm{k,r}} \\ \dot{v}_{\mathrm{k},\varphi'} \\ \dot{v}_{\mathrm{k},\vartheta} \end{pmatrix} &= m_{\mathrm{a}}^{-1} \begin{pmatrix} F_{\mathrm{acc,r}} \\ F_{\mathrm{acc},\varphi'} \\ F_{\mathrm{acc},\vartheta} \end{pmatrix} - \begin{pmatrix} 0 & -\dot{\varphi}'\cos(\vartheta) & -\dot{\vartheta} \\ \dot{\varphi}'\cos(\vartheta) & 0 & -\dot{\varphi}'\sin(\vartheta) \\ \dot{\vartheta} & \dot{\varphi}'\sin(\vartheta) & 0 \end{pmatrix} \begin{pmatrix} v_{\mathrm{k,r}} \\ v_{\mathrm{k},\varphi'} \\ v_{\mathrm{k},\vartheta} \end{pmatrix} \\
&= \begin{pmatrix} m_{\mathrm{a}}^{-1}F_{\mathrm{acc,r}} \\ m_{\mathrm{a}}^{-1}F_{\mathrm{acc},\varphi'} \\ m_{\mathrm{a}}^{-1}F_{\mathrm{acc},\vartheta} \end{pmatrix} - \begin{pmatrix} -\dot{\varphi}'\cos(\vartheta)v_{\mathrm{k},\varphi'} - \dot{\vartheta}v_{\mathrm{k},\vartheta} \\ \dot{\varphi}'\cos(\vartheta)v_{\mathrm{k,r}} - \dot{\varphi}'\sin(\vartheta)v_{\mathrm{k},\vartheta} \\ \dot{\vartheta}v_{\mathrm{k,r}} + \dot{\varphi}'\sin(\vartheta)v_{\mathrm{k},\varphi'} \end{pmatrix} \\
&= \begin{pmatrix} m_{\mathrm{a}}^{-1}F_{\mathrm{acc,r}} + \dot{\varphi}'\cos(\vartheta)v_{\mathrm{k},\varphi'} + \dot{\vartheta}v_{\mathrm{k},\vartheta} \\ m_{\mathrm{a}}^{-1}F_{\mathrm{acc},\varphi'} - \dot{\varphi}'\cos(\vartheta)v_{\mathrm{k,r}} + \dot{\varphi}'\sin(\vartheta)v_{\mathrm{k},\vartheta} \\ m_{\mathrm{a}}^{-1}F_{\mathrm{acc},\vartheta} - \dot{\vartheta}v_{\mathrm{k,r}} - \dot{\varphi}'\sin(\vartheta)v_{\mathrm{k},\varphi'} \end{pmatrix}. \qquad \text{(C.160)}
\end{aligned}$$

Substituting the second and third component of (C.160) into (C.152) gives

$$\begin{aligned}
\dot{\gamma} &= \frac{[m_{\mathrm{a}}^{-1}F_{\mathrm{acc},\varphi'} - \dot{\varphi}'\cos(\vartheta)v_{\mathrm{k,r}} + \dot{\varphi}'\sin(\vartheta)v_{\mathrm{k},\vartheta}]v_{\mathrm{k},\vartheta} - v_{\mathrm{k},\varphi'}[m_{\mathrm{a}}^{-1}F_{\mathrm{acc},\vartheta} - \dot{\vartheta}v_{\mathrm{k,r}} - \dot{\varphi}'\sin(\vartheta)v_{\mathrm{k},\varphi'}]}{v_{\mathrm{k,tan}}^2} \\
&= \frac{m_{\mathrm{a}}^{-1}F_{\mathrm{acc},\varphi'}v_{\mathrm{k},\vartheta} - m_{\mathrm{a}}^{-1}F_{\mathrm{acc},\vartheta}v_{\mathrm{k},\varphi'}}{v_{\mathrm{k,tan}}^2} + \frac{-\dot{\varphi}'\cos(\vartheta)v_{\mathrm{k,r}}v_{\mathrm{k},\vartheta} + \dot{\vartheta}v_{\mathrm{k,r}}v_{\mathrm{k},\varphi'}}{v_{\mathrm{k,tan}}^2} \\
&\quad + \frac{\dot{\varphi}'\sin(\vartheta)v_{\mathrm{k},\vartheta}v_{\mathrm{k},\vartheta} + \dot{\varphi}'\sin(\vartheta)v_{\mathrm{k},\varphi'}v_{\mathrm{k},\varphi'}}{v_{\mathrm{k,tan}}^2} \\
&= \frac{F_{\mathrm{acc},\varphi'}v_{\mathrm{k},\vartheta} - F_{\mathrm{acc},\vartheta}v_{\mathrm{k},\varphi'}}{m_{\mathrm{a}}v_{\mathrm{k,tan}}^2} + \frac{-\dot{\varphi}'\cos(\vartheta)v_{\mathrm{k,r}}v_{\mathrm{k},\vartheta} + \dot{\vartheta}v_{\mathrm{k,r}}v_{\mathrm{k},\varphi'}}{v_{\mathrm{k,tan}}^2} \\
&\quad + \underbrace{\frac{\dot{\varphi}'\sin(\vartheta)v_{\mathrm{k},\vartheta}^2 + \dot{\varphi}'\sin(\vartheta)v_{\mathrm{k},\varphi'}^2}{v_{\mathrm{k,tan}}^2}}_{=\dot{\varphi}'\sin(\vartheta)\frac{v_{\mathrm{k},\vartheta}^2+v_{\mathrm{k},\varphi'}^2}{v_{\mathrm{k,tan}}^2}=\dot{\varphi}'\sin(\vartheta)\frac{v_{\mathrm{k,tan}}^2}{v_{\mathrm{k,tan}}^2}=\dot{\varphi}'\sin(\vartheta)} \qquad \text{(C.161)}
\end{aligned}$$

in which the Pythagorean theorem (C.153) is inserted.

Knowing further that (cf. Fig. C.4)

$$v_{\mathrm{k},\varphi'} = -v_{\mathrm{k,tan}}\sin(\gamma), \qquad \text{(C.162)}$$

$$v_{\mathrm{k},\vartheta} = -v_{\mathrm{k,tan}}\cos(\gamma), \qquad \text{(C.163)}$$

$$F_{\mathrm{acc},\varphi'} = -F_{\mathrm{acc,cen}}\cos(\gamma), \qquad \text{(C.164)}$$

$$F_{\mathrm{acc},\vartheta} = F_{\mathrm{acc,cen}}\sin(\gamma), \qquad \text{(C.165)}$$

one obtains

$$\begin{aligned}
\dot{\gamma} &= \frac{[-F_{\mathrm{acc,cen}}\cos(\gamma)][-v_{\mathrm{k,tan}}\cos(\gamma)] - [F_{\mathrm{acc,cen}}\sin(\gamma)][-v_{\mathrm{k,tan}}\sin(\gamma)]}{m_{\mathrm{a}}v_{\mathrm{k,tan}}^2} \\
&\quad + \frac{-\dot{\varphi}'\cos(\vartheta)v_{\mathrm{k,r}}[-v_{\mathrm{k,tan}}\cos(\gamma)] + \dot{\vartheta}v_{\mathrm{k,r}}[-v_{\mathrm{k,tan}}\sin(\gamma)]}{v_{\mathrm{k,tan}}^2} \\
&\quad + \dot{\varphi}'\sin(\vartheta) \\
&= \frac{F_{\mathrm{acc,cen}}v_{\mathrm{k,tan}}\cos^2(\gamma) + F_{\mathrm{acc,cen}}v_{\mathrm{k,tan}}\sin^2(\gamma)}{m_{\mathrm{a}}v_{\mathrm{k,tan}}^2}
\end{aligned}$$

$$
\begin{aligned}
&+ \frac{\dot{\varphi}' \cos(\vartheta) v_{\mathrm{k,r}} v_{\mathrm{k,tan}} \cos(\gamma) - \dot{\vartheta} v_{\mathrm{k,r}} v_{\mathrm{k,tan}} \sin(\gamma)}{v_{\mathrm{k,tan}}^2} \\
&+ \dot{\varphi}' \sin(\vartheta) \\
&= \frac{F_{\mathrm{acc,cen}}}{m_{\mathrm{a}} v_{\mathrm{k,tan}}} [\cos^2(\gamma) + \sin^2(\gamma)] \\
&\quad + \frac{v_{\mathrm{k,r}}}{v_{\mathrm{k,tan}}} [\dot{\varphi}' \cos(\vartheta) \cos(\gamma) - \dot{\vartheta} \sin(\gamma)] \\
&\quad + \dot{\varphi}' \sin(\vartheta) \\
&= \frac{F_{\mathrm{acc,cen}}}{m_{\mathrm{a}} v_{\mathrm{k,tan}}} + \frac{v_{\mathrm{k,r}}}{v_{\mathrm{k,tan}}} [\dot{\varphi}' \cos(\vartheta) \cos(\gamma) - \dot{\vartheta} \sin(\gamma)] + \dot{\varphi}' \sin(\vartheta)
\end{aligned} \tag{C.166}
$$

in which the Pythagorean trigonometric identity

$$
\cos^2(\#) + \sin^2(\#) = 1 \tag{C.167}
$$

is inserted.

Finally, Assumption C.12 implies $v_{\mathrm{k,r}} \approx 0$ (or certainly $v_{\mathrm{k,r}} \ll v_{\mathrm{k,tan}}$ such that $v_{\mathrm{k,r}}/v_{\mathrm{k,tan}} \approx 0$). Knowing further that there is an initial course angle due to the initial speeds into the $\boldsymbol{e}_{\vartheta}$- and $\boldsymbol{e}_{\varphi'}$-directions, one obtains (C.148). ■

For sake of simplicity, one further assumption is introduced:

Assumption C.14: *The elevation angle is relatively small and/or the change of the azimuth angle is relatively small, such that* $\dot{\varphi}' \sin(\vartheta) \approx 0$.

This assumption is justified, because, during crosswind flight of a drag power kite, the kite is usually flown far away from the zenith, i.e. $\vartheta \to 0$. Hence, Eq. (C.148) is replaced by

$$
\dot{\gamma} = \frac{F_{\mathrm{cen}}}{m_{\mathrm{a}} v_{\mathrm{k,tan}}}, \qquad \gamma(t_0) = \gamma_0. \tag{C.168}
$$

C.2.6.2 Course Angle Controller Idea and Equations

Similar to the tangential speed controller, $F_{\mathrm{cen,set}}$ is used as a virtual actuation, i.e. the new set value of the actual actuation ψ_{set} generates $F_{\mathrm{cen,set}}$, but this function $F_{\mathrm{cen,set}}(\psi_{\mathrm{set}})$ is inverted by a control allocation in a later step.

Again, a simple P-controller is utilized, i.e.

$$
\Delta\gamma = \gamma_{\mathrm{set}} - \gamma \tag{C.169}
$$

$$
F_{\mathrm{cen,set}} = G_{\mathrm{P},\gamma} \Delta\gamma \tag{C.170}
$$

with course angle error $\Delta\gamma$ and proportional gain $G_{\mathrm{P},\gamma}$.

Fig. C.5 visualizes the course angle control loop. Note the similarity of Fig. C.5 and Fig. C.3. Here, two assumptions need to be introduced:

Assumption C.15: *The control allocation perfectly inverts the centripetal/centrifugal force generation of the plant.*

Assumption C.16: *The tangential speed* $v_{\mathrm{k,tan}} > 0$ *is approximately constant.*

Assumption C.15 can be justified, because the centripetal force generation can indeed be inverted perfectly or with little error. Assumption C.16 is justified, because $v_{\mathrm{k,tan}}$ changes not significantly (the tangential speed controller ensures that v_{a} stays between $v_{\mathrm{a,min}} > 0$ and $v_{\mathrm{a,max}}$, and so $v_{\mathrm{k,tan}}$ stays between some bounds much greater zero) and it changes usually (much) slower than the time constant T_{ψ}.

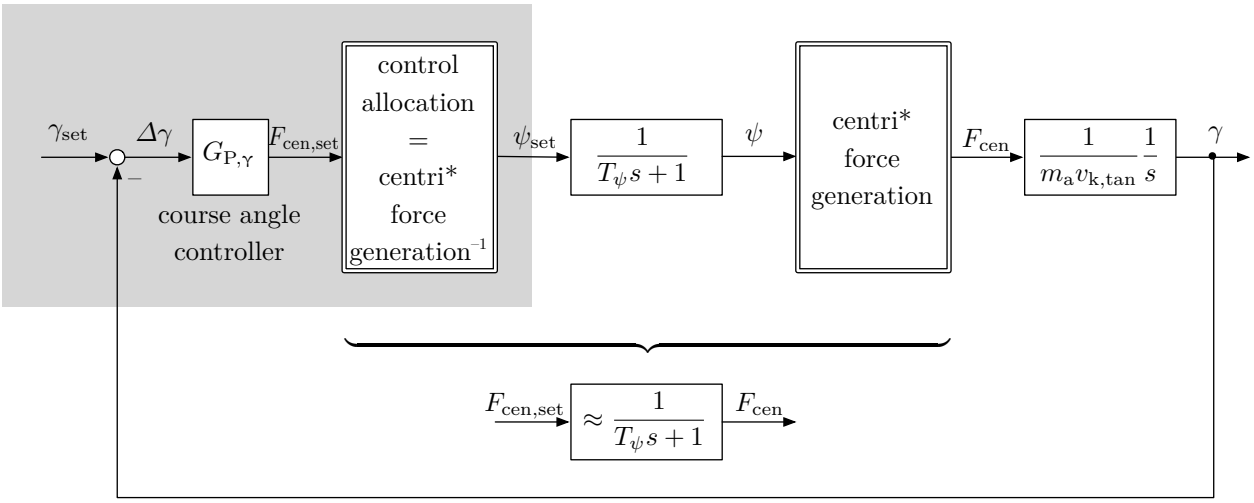

Figure C.5: Block diagram of the course angle control loop.

C.2.6.3 Controller Parametrization and Stability

The course angle controller is tuned with the same method as the temperature controller and the tangential speed controller: In view of Fig. C.5 the closed loop transfer function is

$$\begin{aligned}\frac{\gamma}{\gamma_{\text{set}}} &= \frac{G_{\text{P},\Upsilon}\frac{1}{T_\psi s+1}\frac{1}{m_{\text{a}} v_{\text{k,tan}} s}}{1+G_{\text{P},\Upsilon}\frac{1}{T_\psi s+1}\frac{1}{m_{\text{a}} v_{\text{k,tan}} s}} \\ &= \frac{1}{\frac{1}{G_{\text{P},\Upsilon}}(T_\psi s+1)m_{\text{a}} v_{\text{k,tan}} s+1} \\ &= \frac{1}{\frac{T_\psi m_{\text{a}} v_{\text{k,tan}}}{G_{\text{P},\Upsilon}} s^2 + \frac{m_{\text{a}} v_{\text{k,tan}}}{G_{\text{P},\Upsilon}} s+1}\end{aligned} \tag{C.171}$$

and the control loop is stable if $G_{\text{P},\Upsilon} > 0$, because then the denominator is a 2nd order Hurwitz polynomial due to its positive coefficients. Comparing the denominator of (C.171) with that of a second order delay (C.65), the closed course angle control loop time constant $T_\# = T_{\Upsilon,\circ}$ and damping $D_\# = D_{\Upsilon,\circ}$ are defined by

$$T_{\Upsilon,\circ}^2 = \frac{T_\psi m_{\text{a}} v_{\text{k,tan}}}{G_{\text{P},\Upsilon}} \tag{C.172}$$

and

$$2D_{\Upsilon,\circ}T_{\Upsilon,\circ} = \frac{m_{\text{a}} v_{\text{k,tan}}}{G_{\text{P},\Upsilon}}. \tag{C.173}$$

Again, there is only one degree of freedom, $G_{\text{P},\Upsilon}$, so the control designer chooses $T_{\Upsilon,\circ}$ or $D_{\Upsilon,\circ}$. The latter is used here, for which $G_{\text{P},\Upsilon}$ is given by squaring (C.173) and substituting (C.172),

$$\begin{aligned}2^2 D_{\Upsilon,\circ}^2 T_{\Upsilon,\circ}^2 &= \frac{m_{\text{a}}^2 v_{\text{k,tan}}^2}{G_{\text{P},\Upsilon}^2} \\ 4D_{\Upsilon,\circ}^2 \frac{T_\psi m_{\text{a}} v_{\text{k,tan}}}{G_{\text{P},\Upsilon}} &= \frac{m_{\text{a}}^2 v_{\text{k,tan}}^2}{G_{\text{P},\Upsilon}^2}\end{aligned}$$

$$
\begin{aligned}
4D_{\Upsilon,\mathrm{o}}^2 T_\psi &= \frac{m_\mathrm{a} v_\mathrm{k,tan}}{G_{\mathrm{P},\Upsilon}} \\
\Leftrightarrow G_{\mathrm{P},\Upsilon} &= \frac{m_\mathrm{a} v_\mathrm{k,tan}}{4D_{\Upsilon,\mathrm{o}}^2 T_\psi}
\end{aligned} \tag{C.174}
$$

with which then the time constant (C.172) becomes

$$
\begin{aligned}
T_{\Upsilon,\mathrm{o}}^2 &= \frac{T_\psi m_\mathrm{a} v_\mathrm{k,tan}}{\frac{m_\mathrm{a} v_\mathrm{k,tan}}{4D_{\Upsilon,\mathrm{o}}^2 T_\psi}} \\
&= 4D_{\Upsilon,\mathrm{o}}^2 T_\psi^2 \\
T_{\Upsilon,\mathrm{o}} &= 2D_{\Upsilon,\mathrm{o}} T_\psi .
\end{aligned} \tag{C.175}
$$

It should be noted, that (C.174) is a function of $v_\mathrm{k,tan}$ and thus $G_{\mathrm{P},\Upsilon}$ is an adaptive controller gain.

C.2.7 Centripetal/Centrifugal Force Control Allocation

The centripetal/centrifugal force contributions of actuations can generally originate from the roll angle ψ, from side slipping ($\beta \neq 0$), from vertical wings ($C_\mathrm{S} \neq 0$), or control surfaces which are not horizontal (e.g. vertical wings with flaps, i.e. $C_\mathrm{S} \neq 0$ possibly even for $\beta = 0$). Generally, a similar method as for the tangential force control allocation could then be used. Here, only the roll angle ψ is considered to steer the centripetal/centrifugal force.

One possibility to compute ψ_set from $F_\mathrm{cen,set}$ is again, as for the tangential force control allocation in Sect. C.2.4.4, to first compute the force for ψ_max and ψ_min, and then interpolate between them if $F_\mathrm{cen,set}$ is achievable between those extrema and otherwise set the roll angle to the respective extremum. Instead of a linear interpolation, also a quadratic or higher order interpolation may be used, particularly an interpolation based on the sine-function may lead to exact results.

However, for sake of simplicity, a relatively simple analytical solution is used, by re-introducing Assumption 2.33: With that, the drag force has no centripetal/centrifugal contribution $\boldsymbol{F}_\mathrm{D} \bullet \boldsymbol{e}_\mathrm{cen} = 0$, because it is purely perpendicular to the $\boldsymbol{e}_\mathrm{cen}$ direction. The centripetal/centrifugal contribution of the lift force is in view of Fig. C.4 and from the definition of the roll angle direction (C.29) given by

$$
F_\mathrm{cen,L} = F_\mathrm{L} \sin(\psi). \tag{C.176}
$$

The centripetal/centrifugal force contribution of the straight tether is zero, $\boldsymbol{F}_\mathrm{te} \bullet \boldsymbol{e}_\mathrm{cen} = 0$, because the tether force is always perpendicular to $\boldsymbol{e}_\mathrm{cen}$ due to Assumption 2.3. A final force contribution in the centripetal/centrifugal direction originates from the gravitational force,

$$
F_\mathrm{cen,g} = \boldsymbol{F}_\mathrm{g} \bullet \boldsymbol{e}_\mathrm{cen}, \tag{C.177}
$$

which can, in view of Fig. C.4, also be expressed by

$$
F_\mathrm{cen,g} = m_\mathrm{a} g \sin(\gamma) \cos(\vartheta). \tag{C.178}
$$

Concluding, the total force in the $\boldsymbol{e}_\mathrm{cen}$-direction (with Assumption 2.33) is

$$
\begin{aligned}
F_\mathrm{cen} &= F_\mathrm{cen,L} + F_\mathrm{cen,g} \\
&= F_\mathrm{L} \sin(\psi) + F_\mathrm{cen,g}.
\end{aligned} \tag{C.179}
$$

Substituting the set values into this equation and solving for the set roll angle, one obtains

$$\begin{aligned} F_{\text{cen,set}} &= F_{\text{L}} \sin(\psi_{\text{set}}) + F_{\text{cen,g}} \\ \Leftrightarrow \arcsin\left(\frac{F_{\text{cen,set}} - F_{\text{cen,g}}}{F_{\text{L}}}\right) &= \psi_{\text{set}}. \end{aligned} \tag{C.180}$$

However, as the arcsin-function has real values only in the interval $[-1, 1]$ and as the roll angle shall be limited to the interval $[-\psi_{\max}, \psi_{\max}]$, this equation is altered to

$$\psi_{\text{set}} = \text{limit}\left\{-\psi_{\max}, \arcsin\left[\text{limit}\left(-1, \frac{F_{\text{cen,set}} - F_{\text{cen,g}}}{F_{\text{L}}}, 1\right)\right], \psi_{\max}\right\}. \tag{C.181}$$

C.3 Implementation and Parameters

C.3.1 Simulation Execution

The model and control scheme are implemented as MATLAB-function which computes the time derivatives of all states. Those are then integrated using the forward Euler method in another script file, in which also data loading and saving are handled and figures for debugging are plotted. In additional files, clean publication-ready plots are created.

The simulation is stopped when the trajectory is settled, i.e. when the kite flew the maximum number of path loops. A fall-back is the stopping when the maximum simulation time is reached. With appropriate initial values (particularly of kite position, momentum, and powertrain temperature), the maximum number of path loops can be relatively low. From the last path loop, the mean, minimum, and maximum of important values (e.g. power, force, speed) are computed, which may then be used as a data point in a power curve plot.

C.3.2 Tether Spring-Damper Parameters

Most model parameters are taken from the results of the steady model or are estimated (e.g. actuator time constants). One speciality is implemented for the tether spring-damper constants: Those are not chosen based on the selected materials, because (i) it is hard to estimate the actual values for the compound tether, (ii) a real tether has a mass and a sag and thus effectively has a higher damping and lower spring constant as one would expect from the pure core material properties, and (iii) if high spring and damper constants are chosen, a low time step for the integration is required for numerical stability leading to a high computational load. Instead the spring and damper constants are set based on the following analysis.

The kite's (or point-mass's) dynamics into the radial (or tether) direction is given by combining (C.1)–(C.3), transforming the dynamics into the kinematic reference frame, similar to the proof of Theorem C.2, and then taking the first component of the vector equation, that is

$$m_{\text{a}} \ddot{r}_{\text{k,r}} = F_{\text{acc,r}} + F_{\text{inertia,r}}, \tag{C.182}$$

where $F_{\text{inertia,r}}$ denotes inertial forces into the $\boldsymbol{e}_{\text{r}}$-direction, and in which the initial conditions are dropped for sake of brevity.

Substituting (C.6) into (C.11) under the conditions $\Delta r_{\text{te}} > 0$ and $F_{\text{te,sd}} > 0$, substituting that further into (C.4) and dot-multiply with (C.9), gives the acceleration force in the radial direction

$$\begin{aligned} \boldsymbol{F}_{\text{acc}} &= \boldsymbol{F}_{\text{g}} + \boldsymbol{F}_{\text{a}} - \boldsymbol{e}_{\text{r}} F_{\text{te,sd}} \\ &= \boldsymbol{F}_{\text{g}} + \boldsymbol{F}_{\text{a}} - \boldsymbol{e}_{\text{r}}(\varsigma_{\text{te}} \Delta r_{\text{te}} + \xi_{\text{te}} \Delta v_{\text{te}}) \qquad | \bullet \boldsymbol{e}_{\text{r}} \\ F_{\text{acc,r}} &= F_{\text{g,r}} + F_{\text{a,r}} - \varsigma_{\text{te}} \Delta r_{\text{te}} + \xi_{\text{te}} \Delta v_{\text{te}}, \end{aligned} \tag{C.183}$$

where $F_{\mathrm{g,r}}$ and $F_{\mathrm{a,r}}$ are the gravitational and aerodynamic forces in the $\boldsymbol{e}_{\mathrm{r}}$-direction. Substituting that into (C.182) gives

$$m_{\mathrm{a}}\ddot{r}_{\mathrm{k,r}} = F_{\mathrm{g,r}} + F_{\mathrm{a,r}} - \varsigma_{\mathrm{te}}\Delta r_{\mathrm{te}} + \xi_{\mathrm{te}}\Delta v_{\mathrm{te}} + F_{\mathrm{inertia,r}}. \tag{C.184}$$

As by definition

$$\Delta v_{\mathrm{te}} = \frac{\mathrm{d}}{\mathrm{d}t}\Delta r_{\mathrm{te}} \quad (= \dot{r}_{\mathrm{k,r}} - \dot{L}_{\mathrm{te}}) \tag{C.185}$$

and

$$\begin{aligned} \frac{\mathrm{d}}{\mathrm{d}t}\Delta v_{\mathrm{te}} = \frac{\mathrm{d}^2}{\mathrm{d}t^2}\Delta r_{\mathrm{te}} &= \ddot{r}_{\mathrm{k,r}} - \ddot{L}_{\mathrm{te}} \\ \Leftrightarrow \frac{\mathrm{d}^2}{\mathrm{d}t^2}\Delta r_{\mathrm{te}} + \ddot{L}_{\mathrm{te}} &= \ddot{r}_{\mathrm{k,r}}, \end{aligned} \tag{C.186}$$

Eq. (C.184) becomes

$$\begin{aligned} m_{\mathrm{a}}\left(\frac{\mathrm{d}^2}{\mathrm{d}t^2}\Delta r_{\mathrm{te}} + \ddot{L}_{\mathrm{te}}\right) &= -\varsigma_{\mathrm{te}}\Delta r_{\mathrm{te}} - \xi_{\mathrm{te}}\frac{\mathrm{d}}{\mathrm{d}t}\Delta r_{\mathrm{te}} + F_{\mathrm{g,r}} + F_{\mathrm{a,r}} + F_{\mathrm{inertia,r}} \\ \Leftrightarrow m_{\mathrm{a}}\frac{\mathrm{d}^2}{\mathrm{d}t^2}\Delta r_{\mathrm{te}} &= -\varsigma_{\mathrm{te}}\Delta r_{\mathrm{te}} - \xi_{\mathrm{te}}\frac{\mathrm{d}}{\mathrm{d}t}\Delta r_{\mathrm{te}} + F_{\mathrm{g,r}} + F_{\mathrm{a,r}} + F_{\mathrm{inertia,r}} - m_{\mathrm{a}}\ddot{L}_{\mathrm{te}} \\ &= -\varsigma_{\mathrm{te}}\Delta r_{\mathrm{te}} - \xi_{\mathrm{te}}\frac{\mathrm{d}}{\mathrm{d}t}\Delta r_{\mathrm{te}} + F_{\mathrm{dist,r}}, \end{aligned} \tag{C.187}$$

in which

$$F_{\mathrm{dist,r}} := F_{\mathrm{g,r}} + F_{\mathrm{a,r}} + F_{\mathrm{inertia,r}} - m_{\mathrm{a}}\ddot{L}_{\mathrm{te}} \tag{C.188}$$

is summarized as disturbance or excitation term/force. Eq. (C.187) reads in the Laplace-domain

$$\begin{aligned} m_{\mathrm{a}}s^2\Delta r_{\mathrm{te}} &= -\varsigma_{\mathrm{te}}\Delta r_{\mathrm{te}} - \xi_{\mathrm{te}}s\Delta r_{\mathrm{te}} + F_{\mathrm{dist,r}} \\ \Leftrightarrow m_{\mathrm{a}}\Delta r_{\mathrm{te}}s^2 + \xi_{\mathrm{te}}\Delta r_{\mathrm{te}}s + \varsigma_{\mathrm{te}}\Delta r_{\mathrm{te}} &= F_{\mathrm{dist,r}} \\ \Delta r_{\mathrm{te}}(m_{\mathrm{a}}s^2 + \xi_{\mathrm{te}}s + \varsigma_{\mathrm{te}}) &= F_{\mathrm{dist,r}} \\ \Leftrightarrow \Delta r_{\mathrm{te}} &= \frac{1}{m_{\mathrm{a}}s^2 + \xi_{\mathrm{te}}s + \varsigma_{\mathrm{te}}}F_{\mathrm{dist,r}} \\ &= \frac{\frac{1}{\varsigma_{\mathrm{te}}}}{\frac{m_{\mathrm{a}}}{\varsigma_{\mathrm{te}}}s^2 + \frac{\xi_{\mathrm{te}}}{\varsigma_{\mathrm{te}}}s + 1}F_{\mathrm{dist,r}}. \end{aligned} \tag{C.189}$$

Comparing the denominator with that of a second order delay (C.65), the time constant $T_{\#} = T_{\mathrm{te}}$ and damping $D_{\#} = D_{\mathrm{te}}$ are then defined by

$$T_{\mathrm{te}}^2 = \frac{m_{\mathrm{a}}}{\varsigma_{\mathrm{te}}} \tag{C.190}$$

and

$$2D_{\mathrm{te}}T_{\mathrm{te}} = \frac{\xi_{\mathrm{te}}}{\varsigma_{\mathrm{te}}}. \tag{C.191}$$

Moreover, the elongation $\Delta r_{\mathrm{te}}/L_{\mathrm{te}}$ at steady-state $s = 0$ and in per unit is given by

$$\begin{aligned}
\Delta r_{\mathrm{te}}(s=0) &= \frac{\frac{1}{\varsigma_{\mathrm{te}}}}{\frac{m_{\mathrm{a}}}{\varsigma_{\mathrm{te}}}0^2 + \frac{\xi_{\mathrm{te}}}{\varsigma_{\mathrm{te}}}0 + 1} F_{\mathrm{dist,r}} \\
\Delta r_{\mathrm{te}}(s=0) &= \frac{F_{\mathrm{dist,r}}}{\varsigma_{\mathrm{te}}} && \mid : L_{\mathrm{te}} \\
\frac{\Delta r_{\mathrm{te}}}{L_{\mathrm{te}}}(s=0) &= \frac{F_{\mathrm{dist,r}}}{\varsigma_{\mathrm{te}} L_{\mathrm{te}}} \\
\Delta r'_{\mathrm{te},0} &= \frac{F_{\mathrm{dist,r}}}{\varsigma_{\mathrm{te}} L_{\mathrm{te}}}, && \text{(C.192)}
\end{aligned}$$

where $\Delta r'_{\mathrm{te},0}$ is the per unit steady-state elongation.

Usually, a good estimate tends to be available for the per unit elongation at the nominal forces $\Delta r'_{\mathrm{te,n}}$ (which is rather low) and for the damping D_{te} (which is about the critical value one). With the simplified nominal force in the tether direction $F_{\mathrm{dist,r}} \approx F_{\mathrm{L,n}}$ in (C.192), the spring constant is

$$\begin{aligned}
\Delta r'_{\mathrm{te,n}} &= \frac{F_{\mathrm{L,n}}}{\varsigma_{\mathrm{te}} L_{\mathrm{te}}} \\
\Leftrightarrow \varsigma_{\mathrm{te}} &= \frac{F_{\mathrm{L,n}}}{\Delta r'_{\mathrm{te,n}} L_{\mathrm{te}}}, && \text{(C.193)}
\end{aligned}$$

and the damper constant is given by squaring (C.191), substituting (C.190) and (C.193), and rearranging to

$$\begin{aligned}
\frac{\xi_{\mathrm{te}}^2}{\varsigma_{\mathrm{te}}^2} &= 4 D_{\mathrm{te}}^2 T_{\mathrm{te}}^2 \\
\frac{\xi_{\mathrm{te}}^2}{\cancel{\varsigma_{\mathrm{te}}^2}} &= 4 D_{\mathrm{te}}^2 \frac{m_{\mathrm{a}}}{\cancel{\varsigma_{\mathrm{te}}}} \\
\frac{\xi_{\mathrm{te}}^2}{\varsigma_{\mathrm{te}}} &= 4 D_{\mathrm{te}}^2 m_{\mathrm{a}} \\
\Leftrightarrow \xi_{\mathrm{te}} &= 2 D_{\mathrm{te}} \sqrt{m_{\mathrm{a}} \varsigma_{\mathrm{te}}} \\
&= 2 D_{\mathrm{te}} \sqrt{\frac{m_{\mathrm{a}} F_{\mathrm{L,n}}}{\Delta r'_{\mathrm{te,n}} L_{\mathrm{te}}}}. && \text{(C.194)}
\end{aligned}$$

The time constant (C.190) then becomes

$$\begin{aligned}
T_{\mathrm{te}}^2 &= \frac{m_{\mathrm{a}}}{\frac{F_{\mathrm{L,n}}}{\Delta r'_{\mathrm{te,n}} L_{\mathrm{te}}}} \\
T_{\mathrm{te}} &= \sqrt{\frac{m_{\mathrm{a}} \Delta r'_{\mathrm{te,n}} L_{\mathrm{te}}}{F_{\mathrm{L,n}}}}, && \text{(C.195)}
\end{aligned}$$

which is a measure for the upper limit for the time step of the numerical integration of the system of nonlinear ordinary differential equations to avoid numerical instability.

C.3.3 Parameter Values

The kite power plant parameters (e.g. kite area A or nominal tether force $F_{\mathrm{te,n}} = F_{||,\mathrm{n}}$ etc.) are taken from the parameters and results of the steady model with one exception: The maximum

actuated drag is always set to

$$C_{\mathrm{D,k,a,max}} = 1 \tag{C.196}$$

in order to obtain a reasonable power curve without an elevation and azimuth increase, which is not implemented in the presented control scheme. The kite power plant parameters, which are not existent in the steady model, but required for the point-mass model, are listed in Tab. C.2. Moreover, Tab. C.3 lists the parameters of the target points for three different flight paths.

Table C.2: Standard parameters for simulations of the point-mass model.

Parameter	Value	Comment / Justification
Implementation parameters.		
integration time	$= 0.01\,\mathrm{s}$	estimated good trade-off between accuracy and computational load
maximum time	$= 120\,\mathrm{s}$	estimated enough to complete the maximum amount of path loops
maximum amount of path loops	$= 3$	enough to (approximately) settle flight trajectory
Study-dependent wind parameters.		
$v_{\mathrm{w},h_{\mathrm{ref}}}$	$=$ *depends*	. . . on the actual study (may be several consecutive values)
φ_{w}	$= 0$	any value would be valid
Point-mass model specific plant parameters.		
m_{a}	$=$ *depends*	. . . on the study, may be known (e.g. for the Makani systems), otherwise given as portion of the maximum allowed mass $\hat{m}_{\mathrm{a}}$ computed from the steady model
$\Delta r'_{\mathrm{te,n}}$	$= 0.001$	estimated (and is large enough for numerical stability)
D_{te}	$= 1$	estimated (critical damping)
τ'_{∞}	$= 0$	ambient temperature is nominal ambient temperature
T_{τ}	$= 30\,\mathrm{s}$	estimated, typical time constant for electrical machine
$T_{C_{\mathrm{D,rot}}}$	$= 0.2\,\mathrm{s}$	estimated (for closed rotor speed control loop)
$T_{c_{\mathrm{L}}} = T_{C_{\mathrm{D,k,a}}}$	$= 0.1\,\mathrm{s}$	estimated (for control surfaces)
T_{ψ}	$= 0.2\,\mathrm{s}$	estimated (for closed roll control loop)
$\psi_{\max} = -\psi_{\min}$	$= 30\,^{\circ}$	estimated
Controller parameters.		
$f_{\text{over-P}}$	$= 2$	estimated feasible (and required)
$f_{\text{over-F}}$	$= 1$	no force overloading (or underloading) considered
$f_{\text{over-v}}$	$= 1$	no speed overloading (or underloading) considered
$D_{\tau,\circ}$	$= 1$	critical damping chosen
$D_{\mathrm{v},\circ}$	$= 1$	critical damping chosen
$D_{\Upsilon,\circ}$	$= 1/\sqrt{2}$	subcritical damping chosen for fast reaching of set value, though with slight overshoot in a step response, but amplitude response (Bode plot) has no overshoot with that value

Table C.2: Standard parameters for simulations of the point-mass model. (continued)

Parameter	Value	Comment/Justification
Initial values.		
φ_0	$= 30\,°$	for fast settling
ϑ_0	$= -30\,°$	for fast settling
$v_{\mathrm{k},0}$	$= v_{\mathrm{a,n}}$	for fast settling (note that Assumption 2.33 implies $v_{\mathrm{k}} \approx v_{\mathrm{a}}$)
$C_{\mathrm{D,rot},0}$	$= C_{\mathrm{D,eq,n}}/2$	for most wind speeds close to the final value
$c_{\mathrm{L},0}$	$= c_{\mathrm{L,n}}$	for most wind speeds close to the final value
$C_{\mathrm{D,k,a},0}$	$= 0$	for most wind speeds close to the final value
ψ_0	$= 0$	no roll at beginning
τ_0'	$= 1$	for fast settling at high wind speeds; at low wind speeds, temperature likely drops fast and power is not constrained by the temperature

Table C.3: Standard target point list for three different flight paths.

Note	$\boldsymbol{\varphi}_{\mathrm{set}}$	$\boldsymbol{\vartheta}_{\mathrm{set}}$	Threshold Type	$\boldsymbol{x}_{\mathrm{th}}$	Turn Dir.
Inside-down figure eight with four points.					
bottom right	$-10\,°$	$-30\,°$	AzimuthBelowThreshold	0	Shortest
top right	$-10\,°$	$-50\,°$	CourseAngleBelowThreshold	0	Negative
bottom left	$10\,°$	$-30\,°$	AzimuthAboveThreshold	0	Shortest
top left	$10\,°$	$-50\,°$	CourseAngleAboveThreshold	0	Positive
Inside-up figure eight with four points.					
top right	$-30\,°$	$-60\,°$	AzimuthBelowThreshold	$-10\,°$	Shortest
bottom right	$-10\,°$	$-10\,°$	CourseAngleAboveThreshold	$160\,°$	Positive
top left	$30\,°$	$-60\,°$	AzimuthAboveThreshold	$10\,°$	Shortest
bottom right	$10\,°$	$-10\,°$	CourseAngleBelowThreshold	$-160\,°$	Negative
Clockwise circle with four points.					
top right	$-10\,°$	$-50\,°$	AzimuthBelowThreshold	0	Shortest
bottom right	$-10\,°$	$-30\,°$	ElevationAboveThreshold	$-40\,°$	Shortest
bottom left	$10\,°$	$-30\,°$	AzimuthAboveThreshold	0	Shortest
top left	$10\,°$	$-50\,°$	ElevationBelowThreshold	$-40\,°$	Shortest

The three initial values φ_0, ϑ_0, and $v_{\mathrm{k},0}$ given in Tab. C.2 are not directly initial states ($\boldsymbol{p}_{\mathrm{k},0}$ and $\boldsymbol{r}_{\mathrm{k},0}$ remain to be specified), but the initial states are determined from them by

$$\boldsymbol{r}_{\mathrm{k},0} = \boldsymbol{R}_{\mathrm{z}}(\varphi_0 + \varphi_{\mathrm{w}})\boldsymbol{R}_{\mathrm{y}}(\vartheta_0)\begin{pmatrix} L_{\mathrm{te}} \\ 0 \\ 0 \end{pmatrix} + \boldsymbol{r}_{\mathrm{to}} \tag{C.197}$$

and

$$\boldsymbol{p}_{\mathrm{k},0} = \boldsymbol{R}_{\mathrm{z}}(\varphi_0 + \varphi_{\mathrm{w}})\boldsymbol{R}_{\mathrm{y}}(\vartheta_0)\begin{pmatrix} 0 \\ 0 \\ m_{\mathrm{a}} v_{\mathrm{k},0} \end{pmatrix}. \tag{C.198}$$

All those parameter values are used for all point-mass model simulations, unless stated otherwise.

C.4 Simulation Results and Model Validation with Measurements from the Makani Wing 7

In the following, simulation results of the Makani Wing 7 are reported and discussed in detail. The results are used to validate the point-mass model against the measurements reported in [16].

C.4.1 Parameters

For the Makani Wing 7 simulation, the effective airborne mass is computed from (2.27) with $f_{\text{m-te}}$ and m_{te} from the steady model parameters Tab. 3.1 and results Tab. 3.3, and with the kite mass from [102], i.e.

$$\text{for Makani Wing 7:} \quad m_{\text{k}} = 60\,\text{kg}. \tag{C.199}$$

All other parameters are taken from Tabs. 3.1 and 3.3.

C.4.2 Power Curve Results

The most important question here is how the power curve of the point-mass model compares with that of the steady model and with measurements. So first, the power curve of the point-mass model is recorded. Fig. C.6 shows the results.

It can be seen that the majority of the mean values over a flight path loop match well with those of the steady model. In particular, the most important one, the mean aerodynamic power, is almost identical to the one of the steady model.

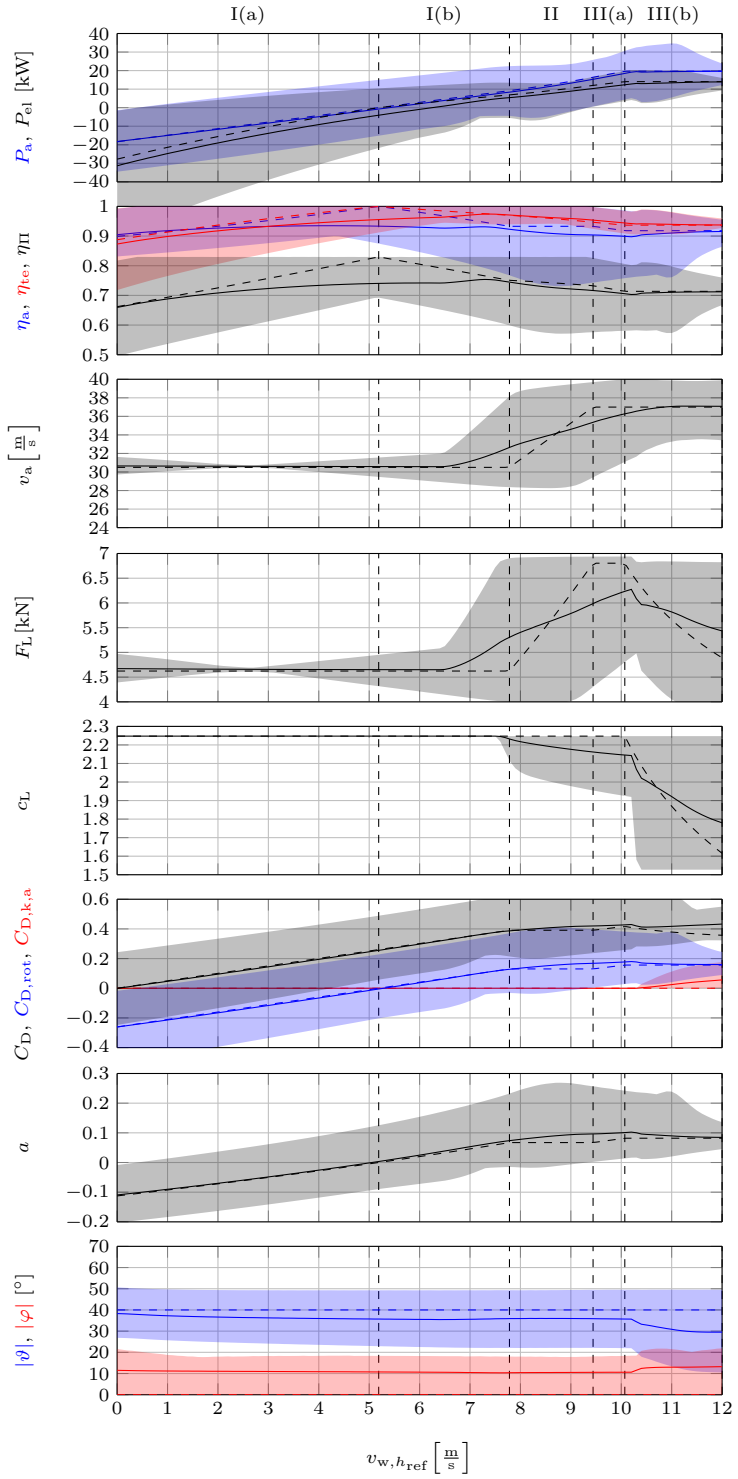

Figure C.6: Power curve results for the Makani Wing 7: steady model in dashed vs. point-mass model with mean values over flight path loop in solid and range of minimum and maximum values over flight path loop as area.

C.4.3 Power Curve: Steady Model vs. Point-Mass Model vs. Reality

Similar to Fig. 3.4, Fig. C.7 shows an overlay of (i) [16, Fig. 28.12], which contains measured powers and simulation results of Makani/Vander Lind, (ii) the computed power curve for the aerodynamic power P_a from Fig. 3.1 (steady model), and (iii) Fig. C.6 (point-mass model), whereby the size, axes, and line thickness are altered for better perception.

It can be seen, that the resulting mean power of the point-mass model is close to the steady model and close to the measurements, as well as close to the static and dynamic simulation results by Makani/Vander Lind. The slightly lower power of the point-mass model can be explained (i) by the non-zero mean azimuth angle assumed in the steady model (cf. Tab. 3.1), while in fact the mean of the absolute values recorded with the point-mass model is $\approx 10\,^\circ$, cf. last row in Fig. C.6, and (ii) by the non-optimized flight path e.g. with maximum power point tracking (MPPT). In fact, slightly changing the flight path parameters of Tab. C.3 results almost exactly in the power curve of the steady model, cf. red line in Fig. C.7. This indicates, that the point-mass

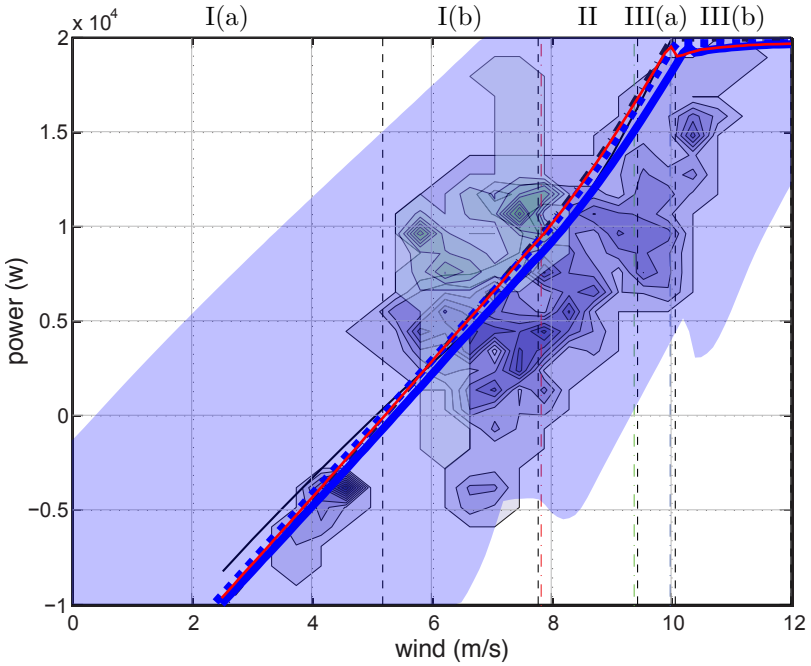

Figure C.7: Overlay of [16, Fig. 28.12], Fig. 3.1 (row 1), and Fig. C.6 (row 1) with size, axes, and line thickness altered: Purple areas show the density of measurements for an early version of Wing 7 and green areas for a later version. The black solid —— and dash-dotted lines -·-·- are Makani's/Vander Lind's simulation results from a simpler steady model [16] and from a dynamic model, respectively. The thick dashed blue line ▪▪▪▪ is the power curve computed with the in this dissertation derived steady model. The thick blue solid line ▬ is the mean power over the flight path loop computed with the point-mass model and the blue areas indicate the range of the minimum and maximum values over a flight path loop. The red line —— shows the mean power over the flight path loop of the point-mass model with a slightly altered flight path (in this case, φ' and ϑ of all target points are $3\,^\circ$ closer to the circle center). All quantities are the aerodynamic power P_a.

model might output suboptimal power curves due to the missing MPP-tracker. It should be noted that an MPP-tracker might not only optimize the flight path, but also the airflow speed set value or the rotor drag coefficient as function of the position within the trajectory.

C.4.4 Flight Trajectories over Wind Speeds

Fig. C.8 visualizes the flight trajectories at different wind speeds. The start and end points of all trajectories are almost identical, which indicates that the trajectory is settled, although the shown trajectories are just the third path loop (cf. Tab. C.2). Apart from the trajectory at $v_{\mathrm{w},h_{\mathrm{ref}}} = 12\,\mathrm{m/s}$, each one is almost a circle (clockwise) with the center point at about $(\varphi, \vartheta) = (0\,^\circ, -40\,^\circ)$. However, the circle is not very smooth, which is caused by the switching behavior of the target point tracking-based flight path controller. This indicates again that there is room for optimizations.

The flight trajectory at $v_{\mathrm{w},h_{\mathrm{ref}}} = 12\,\mathrm{m/s}$ deviates rather significantly from the others: When the kite flies downwards, the potential energy increases the airflow speed which is controlled and limited by the tangential speed controller and the tangential force control allocation, which in turn reduces the airfoil lift coefficient, visible in Fig. C.6. A reduced airfoil lift coefficient reduces the maximum centripetal force and therefore the instantaneous flight path turning radius becomes

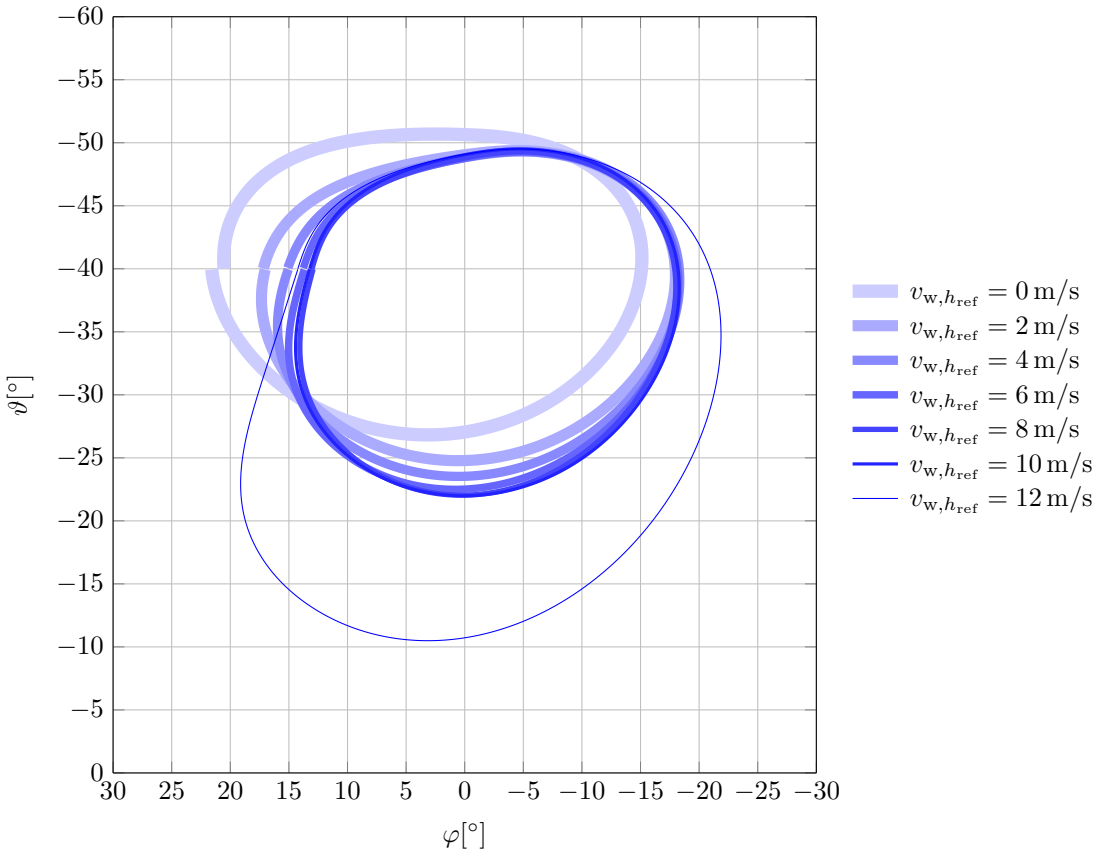

Figure C.8: Flight trajectories of the Makani Wing 7 computed with the point-mass model at different wind speeds.

larger. This phenomenon is expected, as already explained in Sect. 2.7.5 under Assumption 2.36 and in Sect. 2.7.12. Here, the kite reaches dangerously low altitudes which should of course be targeted in improvements of the flight path controller (or its parameters such as altered target points). Alternatively, to circumvent too low altitudes, Makani proposes to use the vertical wings and sideslipping as additional actuation to generate an additional centripetal force contribution, patented in [75].

C.4.5 Time Course of Important Values

To detail at least in part the proper working of the control method, also the time course of important values are reviewed. Here, the results at $v_{\mathrm{w},h_{\mathrm{ref}}} = 10\,\mathrm{m/s}$ for the third flight path loop are focused. Fig. C.9 visualizes the kite's trajectory and Fig. C.10 shows the time course of important values.

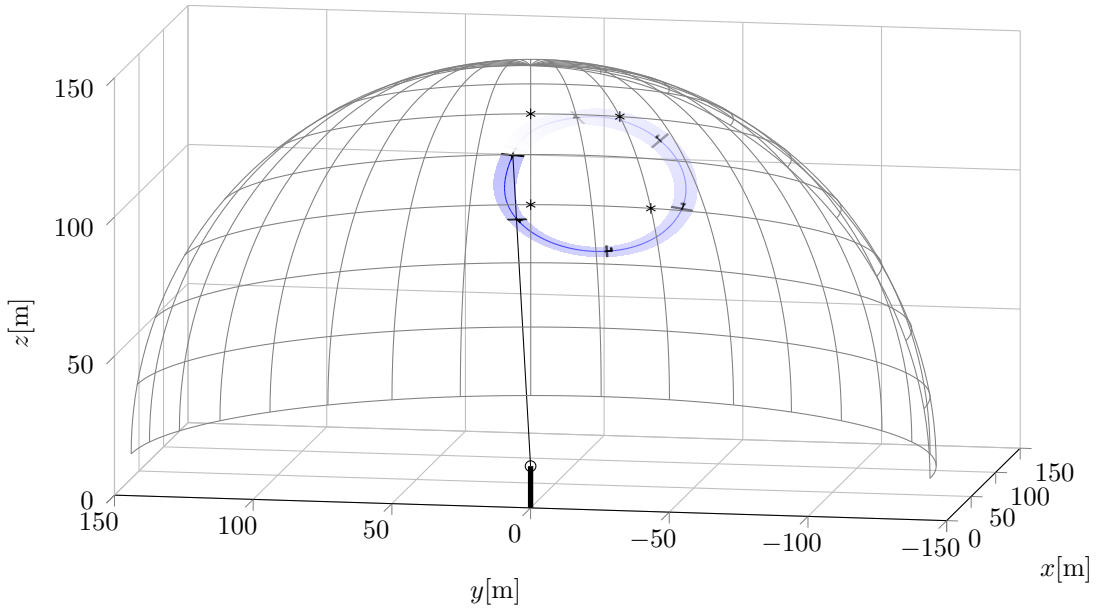

Figure C.9: Flight trajectory of the Makani Wing 7 at $v_{\mathrm{w},h_{\mathrm{ref}}} = 10\,\mathrm{m/s}$ with the flight path target points in * and with the kite's orientation every 1 s before the path loop ends.

A path loop takes just over 6 s. The powers oscillate significantly: When the kite flies downwards the nominal powers are exceeded (overloading) while the powers are well below their nominal values when the kite flies upwards. The airflow speed can be tracked, but with a visible control error, which can be explained by the tangential speed P-controller and its critical dimensioning. However, with a more aggressive gain or a PI-controller, the tangential force control allocation might reduce the airfoil lift coefficient and increase the actuated drag coefficient earlier and more often and thus may reduce the mean power. This is obviously a trade-off between control accuracy and the dimensioning of the plant with enough overloading capability or safety factors. Nevertheless, the important lift force hardly exceeds its nominal value, also visible in Fig. C.6. Therefore, errors in the airflow speed can be tolerated. The proper working of the force control allocations is visible in the last two rows of Fig. C.10, showing a good match of the set values and actual values of the forces. The kite's roll angle is almost all the time at its maximum positive value. Due to gravity, it also has to be reduced for some time in order to regain altitude. Here,

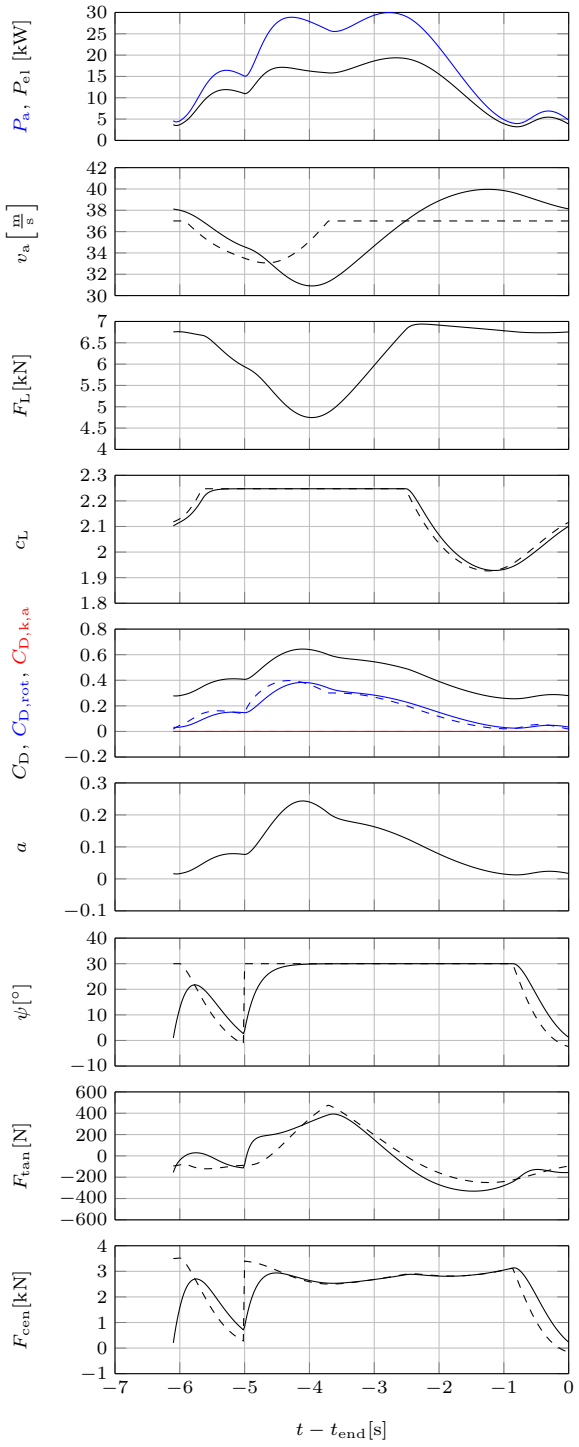

Figure C.10: Time course of important values of the Makani Wing 7 at $v_{w,h_{ref}} = 10\,\mathrm{m/s}$ with limited set values in dashed and actual values in solid.

the switching behavior of the flight path controller is again visible and affects most other values, cf. e.g. Fig. C.10 at $t - t_{\text{end}} \approx -5\,\text{s}$.

C.4.6 Results for Figure Eight Flight Paths

The Makani systems are flown in circles. To not twist the tether while allowing an infinite number of circle loops, a rather complex gimbal system and slip rings are required for the ground station tether connection. To avoid that complexity (which is additionally in part patented by Makani and thus usage might not be allowed by another company), the control scheme shall also enable figure eight paths. Fig. C.11 shows the kite's trajectory for an inside-down figure eight and Fig. C.12 for an inside-up figure eight, both at $v_{\text{w},h_{\text{ref}}} = 10\,\text{m/s}$.

The control scheme stabilizes the kite's trajectory well. However, the inside-up figure eight looks quite distorted. This can be explained by the not-insignificant gravitational force which acts as centrifugal force for a longer time of the turns than it acts as centripetal force. Moreover, when the kite flies downwards, again the lift coefficient is reduced which additionally reduces the maximum actuatable centripetal force. Both is exactly opposite for the inside-down figure eight path, which is an almost perfect eight.

C.4.7 Further Simulations

The prior publication of the author of this dissertation [112] presents two more simulation studies to test the control scheme: a dynamic change of the wind speed and a dynamic change of the powertrain set value. The results are as expected and indicate a proper functioning.[48]

C.5 Discussion and Concluding Remarks

The point-mass model abandons in total four assumptions compared to the steady model, but introduces 16 new assumptions. However, the point-mass model clearly has a higher accuracy, i.e. the new assumptions are (much) less rough. This highlights again, that not the total number of assumptions is important but the total number *and* their roughness altogether.

An addendum to Assumptions C.13 and C.15 should be made (i.e. that both control allocations "work perfectly"): Those imply that both control allocations do not influence each other negatively or that they are independent. This is approximately true, because the actuations act approximately perpendicular to each other and because the tangential force actuators are usually faster. Due to the latter, the centripetal/centrifugal force control allocation could be improved by not using the current (lift) force contributions, but the future ones set by the tangential force control allocation actuators. Another idea is to iterate both control allocations a few times, until both, the set tangential force and the set centripetal/centrifugal force, would be reached almost exactly in steady-state. Yet another idea is to combine both force control allocations into a single one, which achieves the tangential and centripetal/centrifugal force with all four actuators exactly in steady-state. However, for sake of simplicity, none of those ideas are investigated here and are instead left for future research.

The limitation controller does not limit the tether force nor the total drag force. However, if the limitation controller and the speed controller work properly, i.e. if the lift force and the airflow speed are properly bounded, then the tether force and drag force are bounded implicitly. It should be noted, that the tether force is indeed a bit higher than the lift force due to the centrifugal force of the kite caused by its flight on the sphere spanned by the tether. Hence,

[48] It should be noted that the results presented in [112] are slightly different, because slightly different parameter values are used for sake of consistency of the there presented simpler model.

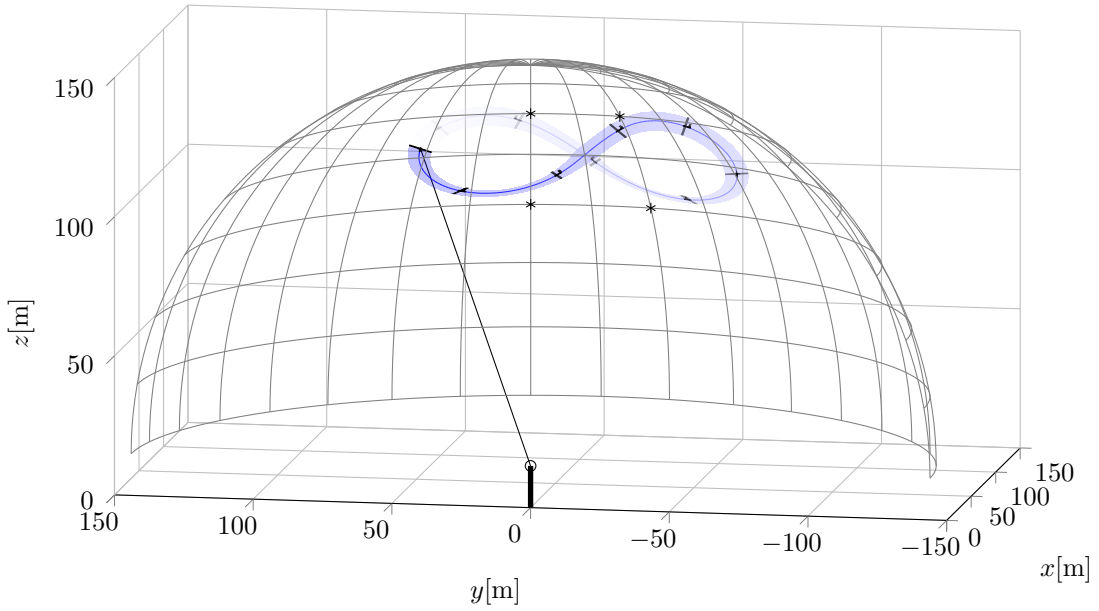

Figure C.11: Inside-down figure eight flight trajectory of the Makani Wing 7 at $v_{\mathrm{w},h_{\mathrm{ref}}} = 10\,\mathrm{m/s}$ with the flight path target points in * and with the kite's orientation every 1 s before the path loop ends.

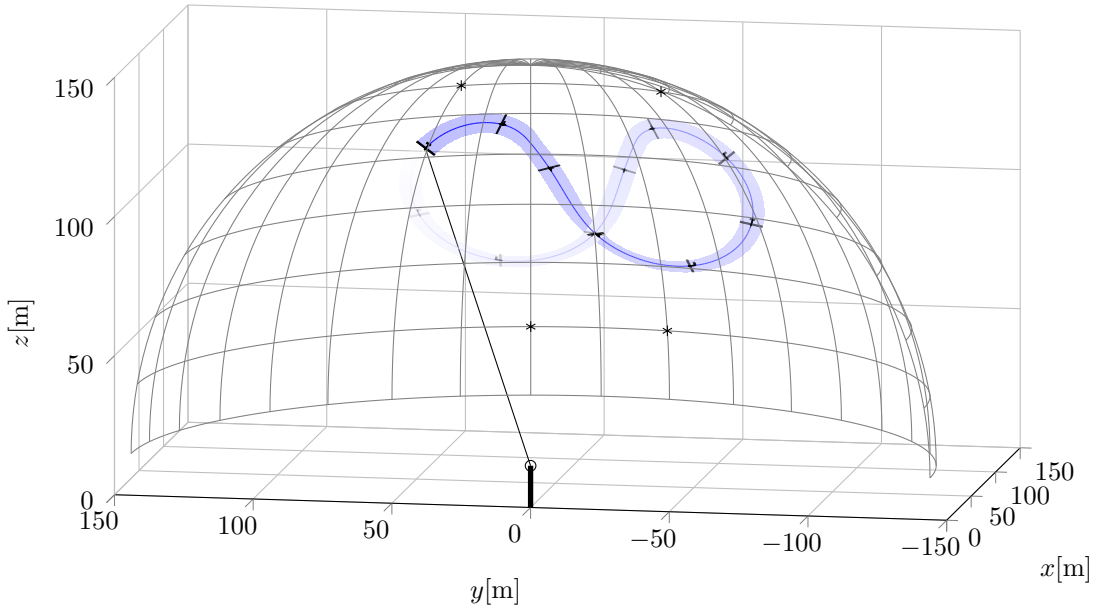

Figure C.12: Inside-up figure eight flight trajectory of the Makani Wing 7 at $v_{\mathrm{w},h_{\mathrm{ref}}} = 10\,\mathrm{m/s}$ with the flight path target points in * and with the kite's orientation every 1 s before the path loop ends.

either the safety factors must have according values, or the limitation controller must be extended accordingly. Here, the first is considered, and the latter is also left for a future work.

All controllers are only P-controllers. Yet, the control scheme stabilizes the kite well, a good amount of power is generated, and the limits are satisfied. This is because the P-controllers are applied for control-oriented plant submodels and the nonlinear parts are canceled out (or linearized) by control allocations. Therefore, the control scheme has a rather low complexity and is rather cheap in terms of computational costs. However, steady-state errors cannot be excluded with P-controllers, particularly also in a real system in which the dynamics, parameters, and states are not exactly available. PI-controllers may improve the control performance, but do also require anti-wind-up, which increases complexity. Of particular interest of future improvements and research is the flight path controller. For instance, further target point properties should be included such as a target rate of the course angle similar to [47]. In particular for circular paths, a flight path controller which is not based on target points as developed in [184] might be the better choice. Moreover, the implementation of a MPP-tracker is of particular interest, e.g. with a similar approach as in [185] or references therein. As an alternative for that, the flight path for each wind speed could be optimized offline. As another alternative, MPC-based controllers or offline optimizations may be suitable. In order to ensure the functioning of the control scheme, a stability proof for the system as a whole (instead of just isolated parts of it with the various assumptions) is of interest. Another idea for future research is the investigation of an intentional power reduction to provide primary control power for the public power grid. Finally, for a control scheme implementation on a real plant, some of the assumptions have to be abandoned, particularly a proper sensor fusion (cf. e.g. [128, 186]) has to be utilized and the actual available actuators (e.g. control surface positions and rotor speed set values) have to be used.

The computational load is dramatically higher for the point-mass model compared to the steady model, which confirms Fig. 1.6: While the computation of a complete power curve with 0.1 m/s wind speed steps using the steady model takes a small fraction of a second on a modern computer (a complete optimization takes a few seconds or a few minutes only), the computation of the power curve for a single parameter set for the point-mass model takes about one hour. Nevertheless, this computation is highly parallelizable, because the result for each wind speed is computed independently from the others. Moreover, a uniform wind speed step size of 0.1 m/s may be avoidable e.g. with far wider steps below the cut-in wind speed or when the nominal power is reached (if the power is the main interest instead of e.g. the proper functioning of the power limitation for a given parameter set). However, such computational efficiency improvements or the execution on a high performance computer cluster introduces further complexity and setup efforts with the model implementation and execution. Because of that, because the flight path should be optimized first (e.g. with MPPT or MPC), and because the steady model already outputs rather accurate results, the inclusion of the point-mass model into the power plant optimization is left to future research.

Appendix D

Ideas for Model Refinements

In this appendix chapter, a few ideas are collected on how the systems engineering model could be refined. None of those refinements are included into the implemented model code, because the complexity and computational load would be increased significantly. The ideas presented here may therefore be considered as an extended outlook.

D.1 General Inclusion of Mass into the Steady Kite Dynamics Model

Sect. 2.1.5 derives a minimum aerodynamic force based on the gravitational force and a nominal roll angle to balance weight. That minimum aerodynamic force is then used to compute the minimum airflow speed in Sect. 2.7.5.

That derivation approach is also valid in general: Fig. D.1 visualizes the kite from the side, which is virtually identical to Fig. 2.4, but for arbitrary flight directions of the kite. Therefore, the kite is drawn as a point (mass) and the angle ψ_w is only a roll angle when the kite flies sidewards.

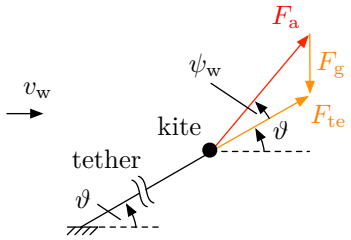

Figure D.1: Sketch of a crosswind flying kite with gravitation, seen from the side.

With the law of sines, one similarly finds

$$\frac{F_\mathrm{a}}{\sin\left(\vartheta+\frac{\pi}{2}\right)} = \frac{F_\mathrm{g}}{\sin(\psi_\mathrm{w})}. \tag{D.1}$$

Substituting (2.24) and (2.5)–(2.7) into (D.1) and rearranging gives

$$\begin{aligned}
\frac{\frac{1}{2}\rho v_\mathrm{a}^2 A\sqrt{C_\mathrm{L}^2+C_\mathrm{D}^2}}{\cos(\vartheta)} &= \frac{m_\mathrm{a} g}{\sin(\psi_\mathrm{w})} \\
\Leftrightarrow \sin(\psi_\mathrm{w}) &= \cos(\vartheta)\frac{m_\mathrm{a} g}{\frac{1}{2}\rho v_\mathrm{a}^2 A\sqrt{C_\mathrm{L}^2+C_\mathrm{D}^2}} \\
\psi_\mathrm{w} &= \arcsin\left[\cos(\vartheta)\frac{m_\mathrm{a} g}{\frac{1}{2}\rho v_\mathrm{a}^2 A\sqrt{C_\mathrm{L}^2+C_\mathrm{D}^2}}\right].
\end{aligned} \tag{D.2}$$

Due to the further rotated aerodynamic force vector against the wind velocity vector, the relation from the similar triangles (2.9) becomes

$$\frac{\cos(\varphi)\cos(\vartheta+\psi_\mathrm{w})v_\mathrm{w}}{v_\mathrm{a}} = \frac{\sqrt{C_\mathrm{L}^2+C_\mathrm{D}^2}}{C_\mathrm{D}}, \tag{D.3}$$

with which the crosswind flight law (2.1) becomes

$$\begin{aligned} v_\mathrm{a} &= \cos(\varphi)\cos(\vartheta+\psi_\mathrm{w})v_\mathrm{w}\frac{\sqrt{C_\mathrm{L}^2+C_\mathrm{D}^2}}{C_\mathrm{D}} \\ &= \cos(\varphi)\cos\left\{\vartheta+\arcsin\left[\cos(\vartheta)\frac{m_\mathrm{a}g}{\frac{1}{2}\rho v_\mathrm{a}^2 A\sqrt{C_\mathrm{L}^2+C_\mathrm{D}^2}}\right]\right\}v_\mathrm{w}\frac{\sqrt{C_\mathrm{L}^2+C_\mathrm{D}^2}}{C_\mathrm{D}}. \end{aligned} \tag{D.4}$$

This result was similarly found already by Costello et al. [51].

A drawback, however, is that the actual airborne mass m_a (not the maximum allowed one) is required and that the airflow speed v_a in (D.4) appears on the left hand side and nonlinearly on the right hand side, which can only be solved numerically. These are the reasons, why this model refinement was not used in the here employed systems engineering model. On the other hand, solving (D.4) numerically is likely much faster than computing the results of the point-mass model from Appendix C, particularly if it is extended with MPP-tracking or optimal control. An interesting future work would be the comparison of the results of these two models.

D.2 Replacement of Maximum Angular Speed in the Steady Kite Dynamics Model: Estimation of Minimum Instantaneous Altitude and Nominal Effective Azimuth

With the known effective airborne mass, known maximum roll angle, and by assuming that the due to rolling tilted lift force is the dominant centripetal force component, then the velocity angle dynamics is defined via (C.179) into (C.168) by

$$\dot{\gamma} = \frac{F_\mathrm{L}\sin(\psi)}{m_\mathrm{a}v_\mathrm{k,tan}}. \tag{D.5}$$

That velocity angle change is identical to the instantaneous angular speed of the kite's turn ω_turn, hence

$$\omega_\mathrm{turn} = \frac{F_\mathrm{L}\sin(\psi)}{m_\mathrm{a}v_\mathrm{k,tan}}. \tag{D.6}$$

As the instantaneous angular turning velocity is related to the turning radius r_turn and tangential speed $v_\mathrm{k,tan}$ by

$$\omega_\mathrm{turn} = \frac{v_\mathrm{k,tan}}{r_\mathrm{turn}}, \tag{D.7}$$

one obtains

$$\begin{aligned} \frac{v_\mathrm{k,tan}}{r_\mathrm{turn}} &= \frac{F_\mathrm{L}\sin(\psi)}{m_\mathrm{a}v_\mathrm{k,tan}} \\ \Leftrightarrow r_\mathrm{turn} &= \frac{m_\mathrm{a}v_\mathrm{k,tan}^2}{F_\mathrm{L}\sin(\psi)}. \end{aligned} \tag{D.8}$$

Substituting (2.6) into (D.8), and knowing that $v_{\mathrm{k,tan}} \approx v_{\mathrm{a}}$ due to Assumption 2.33, yields

$$\begin{aligned} r_{\mathrm{turn}} &= \frac{m_{\mathrm{a}} v_{\mathrm{k,tan}}^2}{\frac{1}{2}\rho v_{\mathrm{a}}^2 A C_{\mathrm{L}} \sin(\psi)} \\ &= \frac{2m_{\mathrm{a}}}{\rho A C_{\mathrm{L}} \sin(\psi)}. \end{aligned} \tag{D.9}$$

The nominal turning radius is given at the nominal lift coefficient $C_{\mathrm{L,n}}$ and at the nominal roll angle ψ_{n} (which may be close to the maximum $\psi_{\max}$),

$$r_{\mathrm{turn,n}} = \frac{2m_{\mathrm{a}}}{\rho A C_{\mathrm{L,n}} \sin(\psi_{\mathrm{n}})}. \tag{D.10}$$

With that, the minimum instantaneous altitude can be estimated by

$$h_{\mathrm{n,min}} \approx h_{\mathrm{n}} - r_{\mathrm{turn,n}} \cos(\vartheta_{\mathrm{n}}). \tag{D.11}$$

Instead of imposing bounds on the nominal effective altitude h_{n}, a lower bound on $h_{\mathrm{n,min}}$, and similarly the maximum one, $h_{\mathrm{n,max}} \approx h_{\mathrm{n}} + r_{\mathrm{turn,n}} \cos(\vartheta_{\mathrm{n}})$, could be applied, in order to avoid the problem of dangerously low altitudes encountered in Sect. 5.1.4.

Similarly, if a circle is chosen as crosswind flight path ($\circ$), then the maximum absolute azimuth angle is

$$\varphi_{\max,\circ} \approx \arctan\left[\frac{r_{\mathrm{turn,n}}}{L_{\mathrm{te}} \cos(\vartheta_{\mathrm{n}})}\right] \tag{D.12}$$

and the nominal one can be estimated as

$$\varphi_{\mathrm{n},\circ} \approx \frac{1}{2}\varphi_{\max,\circ}. \tag{D.13}$$

If a lying figure eight is chosen as crosswind flight path (∞), which is approximately as wide as two circles, then the maximum absolute azimuth angle is

$$\varphi_{\max,\infty} \approx \arctan\left[\frac{2r_{\mathrm{turn,n}}}{L_{\mathrm{te}} \cos(\vartheta_{\mathrm{n}})}\right] \tag{D.14}$$

and the nominal one can be estimated as

$$\varphi_{\mathrm{n},\infty} \approx \frac{1}{2}\varphi_{\max,\infty}. \tag{D.15}$$

With such an approach, no upper bound on ω_{n} has to be estimated and applied. However, a more elaborate effective airborne mass model is required, because then the model needs the actual effective airborne mass value and cannot simply compute vice versa the maximum allowed one.

D.3 Inclusion of Reynolds Number Dependency in Tether Drag Model

As motivated in Remark 2.2, the drop of the cylinder drag coefficient for the tether cross section shape $c_{\mathrm{D,te}}$ at high Reynolds numbers could significantly reduce the overall tether drag $C_{\mathrm{D,te}}$.

To include that Reynolds number dependency, $c_{\mathrm{D,te}} = c_{\mathrm{D,te}}(v_{\mathrm{a},l_{\mathrm{te}}})$, Eq. (2.53) may be solved numerically via

$$\begin{aligned}
F_{\mathrm{D,te}} &= \frac{\int_0^{L_{\mathrm{te}}} l_{\mathrm{te}} \mathrm{d}F_{\mathrm{D,te}}}{L_{\mathrm{te}}} \\
&= \frac{\int_0^{L_{\mathrm{te}}} l_{\mathrm{te}} \frac{1}{2}\rho v_{\mathrm{a},l_{\mathrm{te}}}^2 d_{\mathrm{te}}\, c_{\mathrm{D,te}}(v_{\mathrm{a},l_{\mathrm{te}}})\, \mathrm{d}l_{\mathrm{te}}}{L_{\mathrm{te}}} \\
&= \frac{\int_0^{L_{\mathrm{te}}} l_{\mathrm{te}} \frac{1}{2}\rho \left(\frac{l_{\mathrm{te}}}{L_{\mathrm{te}}} v_{\mathrm{a}}\right)^2 d_{\mathrm{te}}\, c_{\mathrm{D,te}}\left(\frac{l_{\mathrm{te}}}{L_{\mathrm{te}}} v_{\mathrm{a}}\right)\, \mathrm{d}l_{\mathrm{te}}}{L_{\mathrm{te}}} \\
&= \frac{\frac{1}{2}\rho v_{\mathrm{a}}^2 d_{\mathrm{te}} \int_0^{L_{\mathrm{te}}} c_{\mathrm{D,te}}\left(\frac{l_{\mathrm{te}}}{L_{\mathrm{te}}} v_{\mathrm{a}}\right) l_{\mathrm{te}}^3 \mathrm{d}l_{\mathrm{te}}}{L_{\mathrm{te}}^3} \\
&\approx \frac{\frac{1}{2}\rho v_{\mathrm{a}}^2 d_{\mathrm{te}} \sum_{i=1}^{n-1} c_{\mathrm{D,te}}\left(\frac{l_{\mathrm{te},i}}{L_{\mathrm{te}}} v_{\mathrm{a}}\right) l_{\mathrm{te},i}^3 (l_{\mathrm{te},i} - l_{\mathrm{te},i-1})}{L_{\mathrm{te}}^3},
\end{aligned} \tag{D.16}$$

where $l_{\mathrm{te},i}$ is the tether length from the ground station connection to point i with a total of n points. Substituting (2.54) into (D.16) and rearranging gives

$$\begin{aligned}
\frac{1}{2}\rho v_{\mathrm{a}}^2 A C_{\mathrm{D,te}} &= \frac{\frac{1}{2}\rho v_{\mathrm{a}}^2 d_{\mathrm{te}} \sum_{i=1}^{n-1} c_{\mathrm{D,te}}\left(\frac{l_{\mathrm{te},i}}{L_{\mathrm{te}}} v_{\mathrm{a}}\right) l_{\mathrm{te},i}^3 (l_{\mathrm{te},i} - l_{\mathrm{te},i-1})}{L_{\mathrm{te}}^3} \\
\Leftrightarrow C_{\mathrm{D,te}} &= \frac{d_{\mathrm{te}} \sum_{i=1}^{n-1} c_{\mathrm{D,te}}\left(\frac{l_{\mathrm{te},i}}{L_{\mathrm{te}}} v_{\mathrm{a}}\right) l_{\mathrm{te},i}^3 (l_{\mathrm{te},i} - l_{\mathrm{te},i-1})}{A L_{\mathrm{te}}^3}.
\end{aligned} \tag{D.17}$$

If this is now further substituted into (2.11) and further into (2.1), the same challenge as already encountered with (D.4) applies (as also already mentioned in Remark 2.2): the equation cannot be solved analytically for the airflow speed v_{a}. Nevertheless, if the mass is included through (D.4) for which a numerical solution is required anyways, then also (D.17) could be included in a refined model.

D.4 More Elaborate Mass Models

As stated at the end of Sects. D.1 and D.2, if the airborne mass is explicitly included in the model (either in a refinement of the steady model or by utilizing the point-mass model), then a good estimate of the actual airborne mass is required, because it is then not possible anymore to simply compute the maximum allowed airborne mass. The mass of the tether, as one portion of the airborne mass, is already rather well resolved in the derived model. In the following, approaches to model the mass contributions of the kite are sketched.

D.4.1 Empiric Kite Mass from Square-Cube Law

If the mass of a small-scale kite is known, because it is already designed in detail and built, then the mass of a similar kite with another scale can be determined as follows: If a one-dimensional

scale is changed by the factor x_1 (e.g. the wing span or wing chord), then the kite's wing area is changed by x_1^2, its total material volume is scaled by x_1^3, and therefore, with unchanged material densities, its mass is scaled by x_1^3. This is the so called square-cube law: an area of an object scales with the square and the volume and mass scale with the cube of a scale-factor which scales a single dimension of the object. Similarly, if the kite wing area is scaled by the factor x_2, then one-dimensional scales are changed by $\sqrt{x_2} = x_2^{1/2}$, its total material volume is scaled by $x_2^{3/2}$, and therefore its mass is scaled by $x_2^{3/2}$. Hence, the kite's mass can be written as

$$m_\mathrm{k} = \gamma_\mathrm{k,b} b^3 \tag{D.18}$$

or equivalently

$$m_\mathrm{k} = \gamma_\mathrm{k,A} A^{3/2}, \tag{D.19}$$

where $\gamma_\mathrm{k,b}$ is the kite's specific mass w.r.t. the wing span b (cubed) and $\gamma_\mathrm{k,A}$ is the kite's specific mass w.r.t. the wing area A (to the power of 3/2).

Fig. D.2 plots the specific kite mass and the absolute kite mass of the three Makani systems Wing 7, M600, and M5 with data extracted from [102]. It also plots Eqs. (D.18) and (D.19)

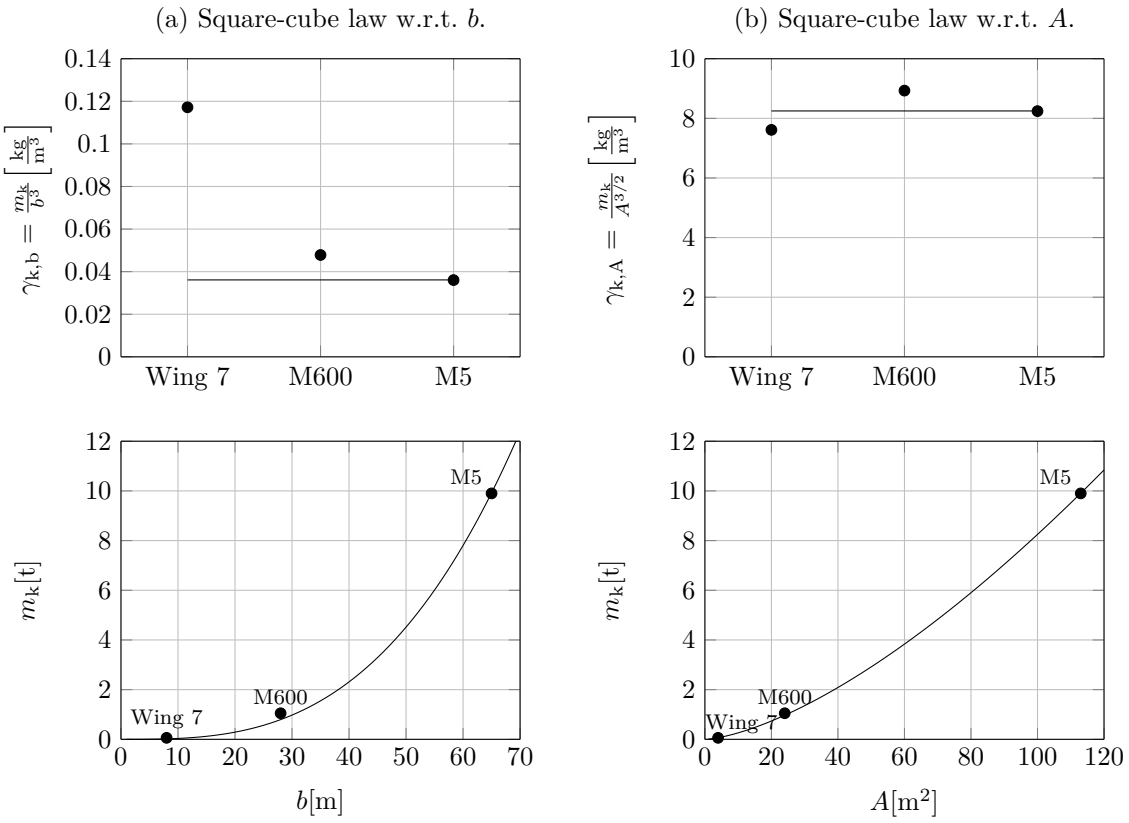

Figure D.2: Square-cube law with the Makani systems, (a) w.r.t. b, (b) w.r.t. A, top: specific mass, bottom: mass. The dots are the data extracted from [102] and solid is the specific mass $\gamma_\mathrm{k,b}$ and $\gamma_\mathrm{k,A}$ (top) and Eqs. (D.18) and (D.19) (bottom), respectively.

in which $\gamma_{\mathrm{k,b}}$ and $\gamma_{\mathrm{k,A}}$ are computed with least squares. A very good match between the models (D.18), (D.19), and the data from Makani is visible.

However, drawbacks of such a modeling approach are obvious: (i) First of all, the basis of Makani's data is unclear. At least the value for the M5 must be based on estimations or models (which indeed could be just the square-cube law). (ii) If no kite is built, its specific mass is unknown. This is particularly the case for the biplane. Though, a good estimate should become available with detailed models e.g. from CAD. (iii) This is an empirical or black-box model. The chosen material for the kite frame (e.g. carbon fiber vs. light metals), the number of rotors, the voltage level, or if gearboxes are used in the drivetrains etc. are all implicitly covered by the specific mass $\gamma_{\mathrm{k,b}}$ or $\gamma_{\mathrm{k,A}}$ and cannot be resolved explicitly.

D.4.2 Empiric Airframe Mass from Square-Cube Law

A better model for the kite's mass is therefore the development of submodels, whose mass sum then defines the kite mass. For the airframe mass m_{af}, again a square-cube law can be used,

$$m_{\mathrm{af}} = \gamma_{\mathrm{af,b}} b^3 \tag{D.20}$$

or equivalently

$$m_{\mathrm{af}} = \gamma_{\mathrm{af,A}} A^{3/2}. \tag{D.21}$$

However, similar drawbacks as just stated above apply, in particular that no data for a biplane airframe would be available. A better modeling approach is therefore a first order modeling e.g. based on beam theory and the actual airframe geometry or approximations thereof. Nevertheless, such a model may be rather complex and complicated, and may have a high number of geometrical parameters, which are then to be optimized.

D.4.3 Mass of Electrical Machines

The mass of electrical machines was modeled as proportional to the (installed) nominal shaft power (2.29). In reality, the mass of an electrical machine is rather proportional to its (installed) nominal (shaft) torque instead, i.e.

$$m_{\mathrm{m,1}} = \gamma_{\mathrm{m,M}} M_{\mathrm{s,n}}, \tag{D.22}$$

where $m_{\mathrm{m,1}}$ is the mass of a single electrical machine[49], $M_{\mathrm{s,n}}$ is the (installed) nominal shaft torque of a machine, and $\gamma_{\mathrm{m,M}}$ is the specific mass of a machine w.r.t. its nominal torque. Though, it should be noted that the previously used simpler model (2.29), mass proportional to power, is approximately valid, because the nominal angular speed remains in a certain range. Tab. D.1 lists the mass, nominal torque, and nominal power for several machines from three different vendors. Fig. D.3 (a) plots the machine specific mass computed by least squares and plots (D.22). Fig. D.3 (b) plots the correlation of the machine mass w.r.t. the nominal machine power. The first variant gives an arguably better fit. That the latter gives also an acceptable fit, is due to the fact that Tab. D.1 lists machines for the same low-weight and high-speed applications, that is permanent magnet rotating field machines for (hybrid) electric vehicles or electric aircraft/kites. This also provides a justification of that model's use in the main part of this dissertation.

The required nominal machine torque is the nominal rotor torque, possibly scaled down with a gearbox in case one is used (a modeling approach for a gearbox is sketched below). The nominal

[49] Throughout this appendix chapter and unlike in the main part, the index "1" is used for "single" instead of "s" to avoid ambiguity with the index "s" for "shaft".

Table D.1: Data of different electrical machines from three vendors.

#	Mass [kg]	Power [kW]	Torque [Nm]	Comment
Remy International, Inc. HVH250 Series Electric Motors [187].				
M1	33.5	60	200	HVH250 Standard
M2	43	60	243	HVH250 HT High Torque
M3	33.5	100	300	HVH250 High Flow Cooling
M4	43	100	440	HVH250 HT High Flow Cooling
Joby Motors [188].				
M5	1.8	8.2	13	JM1S
M6	2.75	13.2	21	JM1
M7	3.35	10.5	40	JM2S
M8	4	14	53	JM2
EMRAX Standard Motors [189].				
M9	7	30	50	EMRAX 188
M10	9.4	40	80	EMRAX 208
M11	12.3	55	125	EMRAX 228
M12	20.3	100	250	EMRAX 268
M13	40	150	500	EMRAX 348

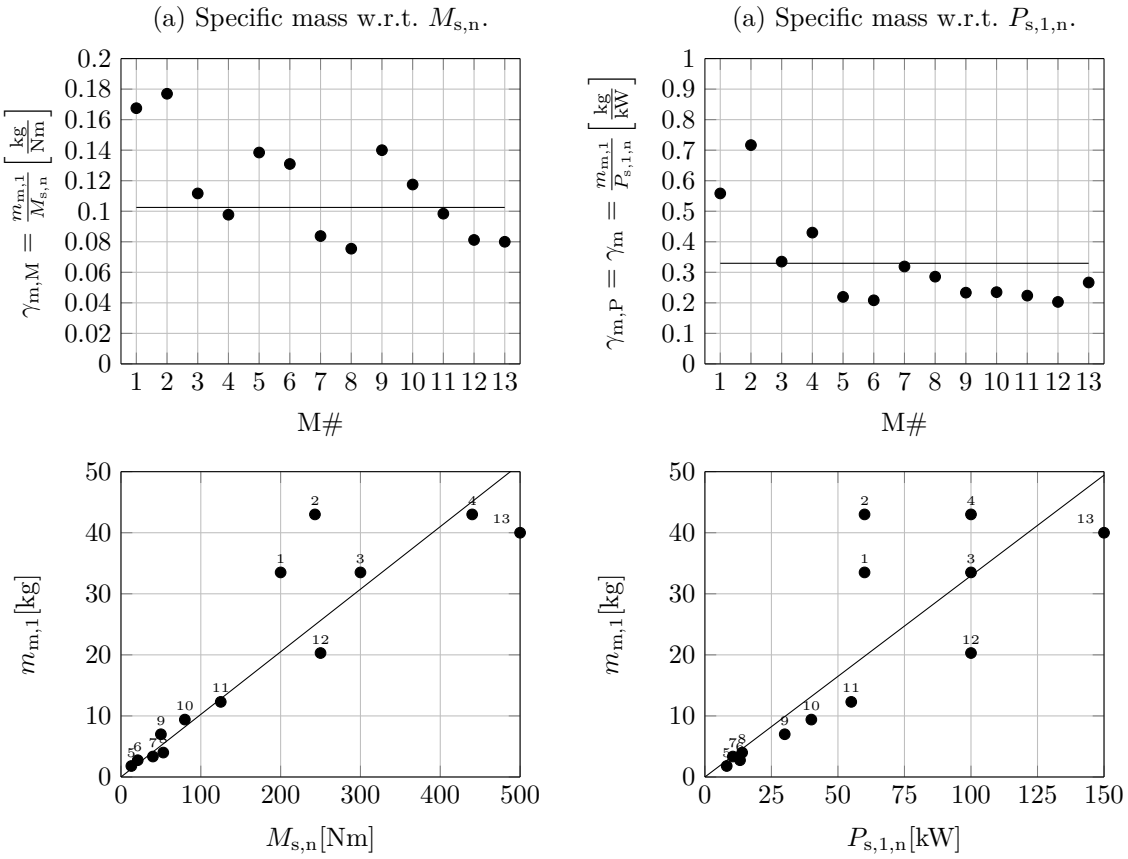

Figure D.3: Correlation of electrical machine mass (a) w.r.t. nominal machine torque $M_{s,n}$, top: specific mass, bottom: mass; for reference, also w.r.t. nominal machine power $P_{s,1,n}$ in (b). The dots are the data of Tab. D.1 and solid is the fitted approximation.

torque and nominal speed of a rotor can be dimensioned via the number of rotor blades, blade chord distribution, blade pitch distribution, blade airfoil (distribution), winglets, duct, etc. For a small nominal torque and thus low machine mass, a high rotor speed is desirable. Nevertheless, this might be in conflict with other goals, such as low noise emissions, and there is some optimal tip speed ratio which maximizes the rotor efficiency.

Generally, the nominal rotor tip speed $v_{\mathrm{tip,n}}$ can be given as nominal portion of the speed of sound $r_{\mathrm{v,n}}$ by

$$v_{\mathrm{tip,n}} = r_{\mathrm{v,n}} c_{\mathrm{snd}}, \tag{D.23}$$

where c_{snd} is the speed of sound. For a good efficiency and acceptable noise, $r_{\mathrm{v,n}} < 1$. A typical value might be $r_{\mathrm{v,n}} = 0.5$. At standard atmosphere with $c_{\mathrm{snd}} = 343\,\mathrm{m/s}$, the nominal tip speed would then be $v_{\mathrm{tip,n}} \approx 170\,\mathrm{m/s} \approx 620\,\mathrm{km/h}$.

With the rotor radius

$$r'_{\mathrm{rot}} = \sqrt{\frac{A_{\mathrm{rot,1}}}{\pi}} \tag{D.24}$$

(not to be confused with the rotor area ratio, which is why there is a prime) in which $A_{\mathrm{rot,1}}$ is the area of a single rotor, the nominal angular rotor speed is

$$\omega_{\mathrm{rot,n}} = \frac{v_{\mathrm{tip,n}}}{r'_{\mathrm{rot}}}. \tag{D.25}$$

With the nominal power of a single rotor $P_{\mathrm{rot,n,1}}$ known, the nominal rotor torque is therefore

$$\begin{aligned} M_{\mathrm{rot,n}} &= \frac{P_{\mathrm{rot,n,1}}}{\omega_{\mathrm{rot,n}}} \\ &= \frac{P_{\mathrm{rot,n,1}}}{\frac{v_{\mathrm{tip,n}}}{r'_{\mathrm{rot}}}} \\ &= \frac{P_{\mathrm{rot,n,1}} \sqrt{A_{\mathrm{rot,1}}/\pi}}{r_{\mathrm{v,n}} c_{\mathrm{snd}}}. \end{aligned} \tag{D.26}$$

The total machine mass is

$$m_{\mathrm{m}} = n_{\mathrm{rot}} m_{\mathrm{m,1}} \tag{D.27}$$

with the total number of rotors n_{rot}.

The rotor torque is scaled down by the gear ratio $r_{\mathrm{g}} \geq 1$ and gear efficiency η_{s}, such that the nominal machine torque must be

$$M_{\mathrm{s,n}} = \frac{1}{r_{\mathrm{g}}} \eta_{\mathrm{s}} M_{\mathrm{rot,n}}. \tag{D.28}$$

In case no gearbox is used, $r_{\mathrm{g}} = 1$ and $\eta_{\mathrm{s}} = 1$.

Substituting (D.26) into (D.28), then into (D.22) and further into (D.27) together with the total rotor area $A_{\mathrm{rot}} = A_{\mathrm{rot,1}} n_{\mathrm{rot}}$ and total rotor power $P_{\mathrm{rot,n}} = P_{\mathrm{rot,n,1}} n_{\mathrm{rot}}$ gives

$$\begin{aligned} m_{\mathrm{m}} &= n_{\mathrm{rot}} \gamma_{\mathrm{m,M}} \frac{1}{r_{\mathrm{g}}} \eta_{\mathrm{s}} \frac{P_{\mathrm{rot,n,1}} \sqrt{A_{\mathrm{rot,1}}/\pi}}{r_{\mathrm{v,n}} c_{\mathrm{snd}}} \\ &= \cancel{n_{\mathrm{rot}}} \gamma_{\mathrm{m,M}} \frac{1}{r_{\mathrm{g}}} \eta_{\mathrm{s}} \frac{\frac{P_{\mathrm{rot,n}}}{\cancel{n_{\mathrm{rot}}}} \sqrt{\frac{A_{\mathrm{rot}}}{n_{\mathrm{rot}}}/\pi}}{r_{\mathrm{v,n}} c_{\mathrm{snd}}} \\ &= \frac{\gamma_{\mathrm{m,M}} \eta_{\mathrm{s}} P_{\mathrm{rot,n}} \sqrt{A_{\mathrm{rot}}/\pi}}{r_{\mathrm{g}} r_{\mathrm{v,n}} c_{\mathrm{snd}}} \frac{1}{\sqrt{n_{\mathrm{rot}}}}. \end{aligned} \tag{D.29}$$

An interesting result can be seen from (D.29): the higher n_{rot}, the lower the total machine mass (for a given rotor area), but the higher n_{rot} the lower the machine mass decrease, due to a scale with $1/\sqrt{n_{\mathrm{rot}}}$. Fig. D.4 plots that scaling.

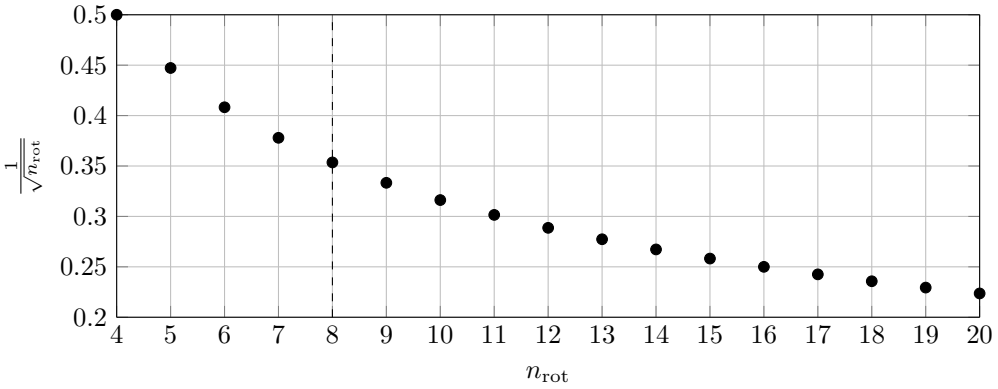

Figure D.4: Plot of $1/\sqrt{n_{\mathrm{rot}}}$. The vertical dashed line highlights the reference scenario, $n_{\mathrm{rot}} = 8$.

A drawback of that machine mass model, is again that it is a black-box model in which e.g. the nominal machine voltage is covered only implicitly by the specific mass $\gamma_{\mathrm{m,M}}$ and cannot be resolved explicitly. A more analytically based modeling approach could be adapted similarly as in [123] and references therein.

D.4.4 Mass of Rotors

A rotor is likely comparably light, particularly if it is made from carbon fiber. It could thus be simply neglected. Another idea is to use the same modeling approach as above. A rotor should scale approximately with its nominal torque,

$$m_{\mathrm{rot,1}} = \gamma_{\mathrm{rot}} M_{\mathrm{rot,n}}, \tag{D.30}$$

where γ_{rot} is the rotor specific mass w.r.t. its nominal torque, and $m_{\mathrm{rot,1}}$ is the mass of one rotor, i.e. the total rotor mass is $m_{\mathrm{rot}} = m_{\mathrm{rot,1}} n_{\mathrm{rot}}$.

D.4.5 Mass of Gearbox

Eq. (D.29) states that the mass of the electrical machines increases with the nominal rotor power and rotor area. Therefore, at some system scale, it might be beneficial or even necessary to use a gearbox to limit the machine mass (with a then much smaller mass of gearbox plus machine, to be meaningful), though with the drawbacks of a reduced conversion efficiency (gearbox efficiency), and increased maintenance costs (the capital costs might not change much due to cost savings with smaller electrical machines but new costs due to gearbox).

If a gearbox is used, a model for its mass is required. In [190, Fig. 7], a correlation of the gearbox (and lubricant) mass as function of rotor power, rotor RPMs, and engine RPMs is found from a number of realized aircraft gearboxes by (with the nomenclature of this dissertation)

$$\tilde{m}_{\mathrm{g,1}}[\mathrm{lbs}] = -37.4262\,\mathrm{lbs} + 116.3297\,\frac{\mathrm{lbs\ RPM}^{0.75}}{\mathrm{hp}^{0.75}} \cdot \underbrace{\left(\frac{P_{\mathrm{rot,n,1}}[\mathrm{hp}]}{\omega_{\mathrm{rot,n}}[\mathrm{RPM}]}\right)^{0.75} r_{\mathrm{g}}^{0.15}}_{\text{“parametric value”}}. \tag{D.31}$$

As expectable, the gearbox mass increases with the nominal rotor torque (the term $P_{\mathrm{rot,n,1}}[\mathrm{hp}]/\omega_{\mathrm{rot,n}}[\mathrm{RPM}]$ is a torque) and with the gear ratio.

If the correlation (D.31) is used directly in an optimization study, it is possible that $m_{\mathrm{g,1}}$ is negative, which is not meaningful. To circumvent that, one possibility is to change the correlation to

$$m_{\mathrm{g,1}}[\mathrm{lbs}] = \gamma_{\mathrm{g}} \underbrace{\left(\frac{P_{\mathrm{rot,n,1}}[\mathrm{hp}]}{\omega_{\mathrm{rot,n}}[\mathrm{RPM}]} \right)^{0.75} r_{\mathrm{g}}^{0.15}}_{\text{“parametric value”}}, \tag{D.32}$$

where γ_{g} is the gearbox specific mass in lbs $\mathrm{RPM}^{0.75}/\mathrm{hp}^{0.75}$ w.r.t. the “parametric value” (same terminology in [190, Fig. 7]). As the two values $-37.4262\,\mathrm{lbs}$ and $116.3297\,\mathrm{lbs}\,\mathrm{RPM}^{0.75}/\mathrm{hp}^{0.75}$ where found with a fitting from real gearboxes with “parametric values” in the range from about 10^0 to 10^2, Eq. (D.32) with the parameter γ_{g} can also be fitted to that. Here, this is done by fitting (D.32) to (D.31) with least squares for the “parametric values” $[10^0, 10^1, 10^2]$. Eq. (D.32) with the resulting γ_{g} then becomes

$$m_{\mathrm{g,1}}[\mathrm{lbs}] = 112.2536\,\frac{\mathrm{lbs}\,\mathrm{RPM}^{0.75}}{\mathrm{hp}^{0.75}} \cdot \underbrace{\left(\frac{P_{\mathrm{rot,n,1}}[\mathrm{hp}]}{\omega_{\mathrm{rot,n}}[\mathrm{RPM}]} \right)^{0.75} r_{\mathrm{g}}^{0.15}}_{\text{“parametric value”}}. \tag{D.33}$$

Fig. D.5 compares (D.31) with (D.33) in a linear and double-logarithmic plot (which is used in [190, Fig. 7]). Obviously, the alternative correlation (D.33) is more pessimistic for small “parametric values” (which can be assumed tolerable).

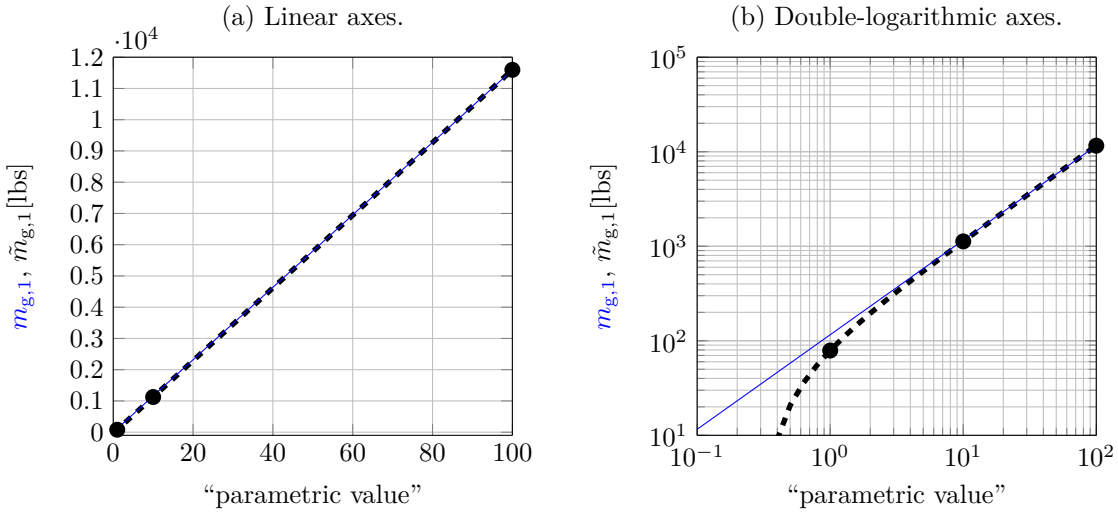

Figure D.5: Plot of $\tilde{m}_{\mathrm{g,1}}$ (D.31) in ▪▪▪▪ and $m_{\mathrm{g,1}}$ (D.33) in ——. The black dots (•) are the points used for the least squares fit of γ_{g}.

In SI-units and with the nominal rotor torque inserted, Eq. (D.33) reads

$$m_{\mathrm{g,1}} = 112.2536 \cdot \frac{0.453592\,\mathrm{kg} \cdot \mathrm{RPM}^{0.75}}{\mathrm{hp}^{0.75}} \cdot \left(\frac{\frac{P_{\mathrm{rot,n,1}}}{745.7\,\mathrm{W/hp}}}{\frac{\omega_{\mathrm{rot,n}}}{\frac{2\pi\,\mathrm{rad}}{60\,\mathrm{s}}/\mathrm{RPM}}} \right)^{0.75} r_{\mathrm{g}}^{0.15}$$

$$
\begin{aligned}
&= 112.2536 \cdot \frac{0.4536\,\mathrm{kg} \cdot \mathrm{RPM}^{0.75} \cdot \left(\frac{2\pi\,\mathrm{rad}}{60\,\mathrm{s}}/\mathrm{RPM}\right)^{0.75}}{\mathrm{hp}^{0.75} \cdot (745.7\,\mathrm{W/hp})^{0.75}} \cdot \left(\frac{P_{\mathrm{rot,n,1}}}{\omega_{\mathrm{rot,n}}}\right)^{0.75} r_{\mathrm{g}}^{0.15} \\
&= 112.2536 \cdot \frac{0.4536\,\mathrm{kg} \cdot \left(\frac{2\pi}{60}\right)^{0.75} \left(\frac{\mathrm{rad}}{\mathrm{s}}\right)^{0.75}}{745.7^{0.75}\mathrm{W}^{0.75}} \cdot M_{\mathrm{rot,n}}^{0.75} r_{\mathrm{g}}^{0.15} \\
&= 0.0657 \frac{\mathrm{kg}}{\mathrm{Nm}^{0.75}} \cdot M_{\mathrm{rot,n}}^{0.75} r_{\mathrm{g}}^{0.15}. \qquad \text{(D.34)}
\end{aligned}
$$

Fig. D.6 plots (D.34) for a range of nominal rotor torques and gear ratios.

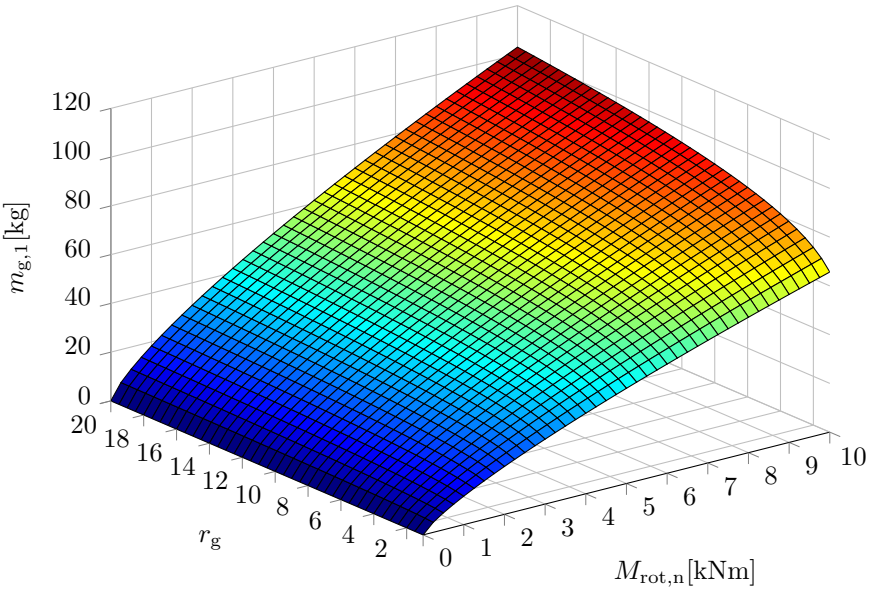

Figure D.6: Plot of $m_{\mathrm{g,1}}$ (D.34) for a range of $M_{\mathrm{rot,n}}$ and r_{g}.

The mass of a gearbox-machine combination obviously is

$$
\begin{aligned}
m_{\mathrm{g\text{-}m,1}} &= m_{\mathrm{g,1}} + m_{\mathrm{m,1}} \\
&= 0.0657 \frac{\mathrm{kg}}{\mathrm{Nm}^{0.75}} \cdot M_{\mathrm{rot,n}}^{0.75} r_{\mathrm{g}}^{0.15} + \gamma_{\mathrm{m,M}} M_{\mathrm{s,n}} \\
&= 0.0657 \frac{\mathrm{kg}}{\mathrm{Nm}^{0.75}} \cdot M_{\mathrm{rot,n}}^{0.75} r_{\mathrm{g}}^{0.15} + \gamma_{\mathrm{m,M}} \frac{1}{r_{\mathrm{g}}} \eta_{\mathrm{s}} M_{\mathrm{rot,n}}. \qquad \text{(D.35)}
\end{aligned}
$$

This equation indicates, that there is some gear ratio i_g, which minimizes $m_{\mathrm{g\text{-}m,1}}$. Though, that gear ratio is likely rather large because of the very different exponents of the two r_{g}-terms in (D.35). Fig. D.7 visualizes (D.35) for the same range of nominal rotor torques and gear ratios as Fig. D.6. It indicates, that the gear ratio should be rather high, or even as high as possible, for a minimal $m_{\mathrm{g\text{-}m,1}}$.

Nevertheless, this gearbox mass model should be taken with care: (i) For high gear ratios, the electrical machines must rotate very fast. Obviously, there is some upper limit for that, e.g. around $10,000\,\mathrm{RPMs}$. Though, in an optimization study, such a constraint can easily be applied. (ii) It should be noted, that only $r_{\mathrm{g}} \geq 1$ is valid, that $r_{\mathrm{g}} = 1$ means no gearbox is used and thus $m_{\mathrm{g,1}} = 0$ and $\eta_{\mathrm{s}} = 1$ (or $\eta_{\mathrm{s}} \approx 1$ if small bearing friction losses are accounted for), and hence the derived gearbox mass equation (D.34) is valid for $r_{\mathrm{g}} > 1$ only. (iii) The here proposed gearbox

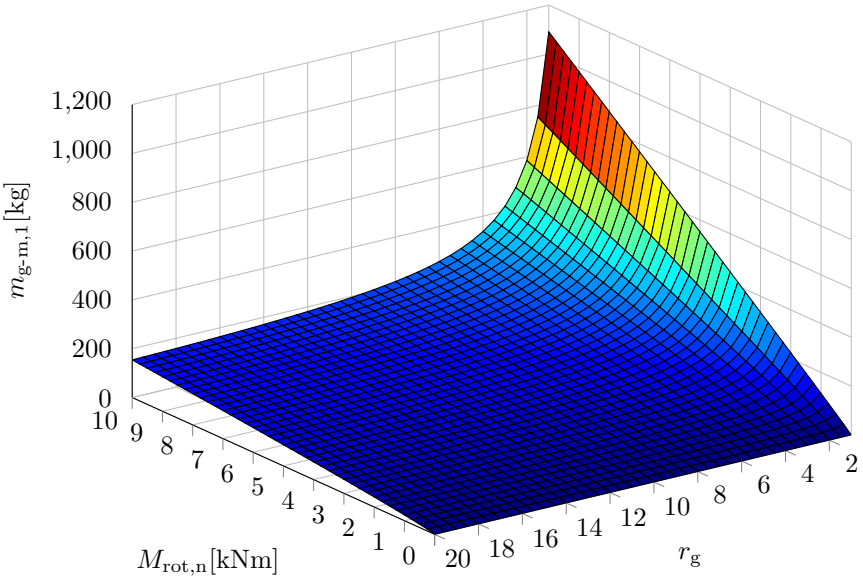

Figure D.7: Plot of $m_{\text{g-m,1}}$ (D.35) for a range of $M_{\text{rot,n}}$ and r_{g}.

model is also a black-box model and is likely valid only for a certain range of $M_{\text{rot,n}}$ and r_{g} (which is not stated in [190]). Likely, the gear ratio should be limited to about $r_{\text{g}} \leq 20$ (which is likely anyways in compliance with a machine RPM limit). For higher gear ratios, several gear stages might be required which might significantly reduce the gearbox efficiency. (iv) The gearbox efficiency and costs should also scale with $M_{\text{rot,n}}$ and r_{g}, for which further data for corresponding black-box models would be required. (v) Again, a more elaborate model would be one that is based on first principles, for which, however, the model complexity and computational load (particularly for optimizations if several geometric parameters are to be optimized) is increased significantly.

D.4.6 Generalized Empiric (or Black-Box) Mass Model for a Component

With the same approach as used for the previously presented mass models, the mass of other parts, such as power electronic components, control surface servos etc. could be modeled. The generalized mass model for a single component # (which may exist $n_{\#}$ times on the kite) reads

$$m_{\#,1} = \gamma_{\#} \prod_i p_i^{c_i}, \tag{D.36}$$

where p_i are parameters of the component which have a significant sensitivity on its mass, c_i are fitting parameters, and $\gamma_{\#}$ is the fitted specific mass w.r.t. $\prod_i p_i^{c_i}$ in the unit kg per $[\prod_i p_i^{c_i}]$.

As one further concrete example, the mass of the kite's onboard power electronics scales not only with the power, but also with the voltage and voltage ratio in case of DC-DC converters. Therefore, the black-box model ansatz could be

$$m_{\text{pe,k}} = \gamma_{\text{pe,k,P\&U}} P_{\text{el,k,n}} \left(\frac{U_{\text{te,n}}}{U_{\text{te,n,ref}}} \right)^{c_{\text{pe,k}}}, \tag{D.37}$$

where $U_{\mathrm{te,n}}$ is the nominal tether voltage, $U_{\mathrm{te,n,ref}}$ is some reference nominal tether voltage (e.g. for which the mass and specific mass are known; or which simply is a fitting parameter), $P_{\mathrm{el,k,n}}$ is the nominal electrical power at the kite, and $c_{\mathrm{pe,k}}$ and $\gamma_{\mathrm{pe,k,P\&U}}$ are fitting parameters.

Yet another example are the mass of the foundation and of the tower. That value has no effect on the power output of the kite, but on its economy, as one can imagine that the costs scale with their mass. One may use the ansatz

$$m_{\mathrm{fdn\&to}} = \gamma_{\mathrm{fdn\&to}} F_{\mathrm{te,n}}^{c_1} h_{\mathrm{to}}^{c_2}, \tag{D.38}$$

where index "fdn&to" stands for foundation and tower.

Generally, such a model may be fitted to actual measurements (i.e. implemented components). As those are not available at the beginning of a (new) development, such models may be fitted to higher fidelity models, e.g. CAD models (which may be reused for the actual detailed component design and optimization). Note that a similar approach was already used with the airfoil polar model, cf. Fig. 2.5.

D.5 Economics Model Refinements

D.5.1 Economics Model for Subsystems

Ideally, each subsystem component with optimization parameters has also an economical model. For example, the gear ratio r_{g} could be an optimization parameter (which is optimized similar to the tether length, nominal tether voltage etc.). With $r_{\mathrm{g}} = 1$, there would be no gearbox and thus no gearbox costs, while $r_{\mathrm{g}} > 1$ implies a gearbox with costs, which likely increases with r_{g}—not only capital costs but particularly in this case also maintenance costs. Clearly, one still may maximize $\hat{K}_{\mathrm{inv,o\&p}}/A$, but without gearbox economics model, the optimizer likely choses a large r_{g} to minimize the kite mass. Because actually the profit should be maximized, the costs of "other parts" in $\hat{K}_{\mathrm{inv,o\&p}}$ should be small and should be as independent from the optimization parameters as possible.

A general black-box model ansatz for the investment cost (capital cost) of component # can be formulated as

$$K_{\mathrm{inv},\#} = k_{\#} m_{\#}, \tag{D.39}$$

i.e. the costs are proportional to the component's mass $m_{\#}$ with proportionality (fitting) factor $k_{\#}$, which was already used for the powertrain costs, cf. Assumption 2.42. In case the mass is not known, or a more complex cost relationship is expectable, a more generalized ansatz similar to (D.36) may be used.

One concrete example, for which an even more complex ansatz is suitable, is the cost of the ground station's uninterruptible power supply (UPS), which is required to enable a safe hover-landing also during a grid fault, cf. [106]. A suitable model is

$$K_{\mathrm{inv,UPS}} = \max\{k_{\mathrm{inv,UPS,P}} P_{\mathrm{el,hov,n}}, k_{\mathrm{inv,UPS,E}} P_{\mathrm{el,hov,n}} t_{\mathrm{land}}\}, \tag{D.40}$$

where $k_{\mathrm{inv,UPS,P}}$ and $k_{\mathrm{inv,UPS,E}}$ are the specific cost of the chosen UPS technology w.r.t. power and w.r.t. energy, respectively, $P_{\mathrm{el,hov,n}}$ is the nominal power required for hovering, and t_{land} is the time required for the hover-landing (incl. some safety margin).

A general black-box model ansatz for the operational costs (maintenance costs) of component # may be

$$k_{\mathrm{op},\#} = c_{\#} E_{\mathrm{el,yr}}, \tag{D.41}$$

where $c_\#$ is a fitting parameter. The proportionality of the costs to the energy yield $E_{\mathrm{el,yr}}$ acknowledges that maintenance costs depend on the operation time and loading of a component.

The general difficulty is to find reasonable fitting values $k_\#$ and $c_\#$. Those values may be highly dependent on time (e.g. due to stock market price changes), on negotiating skills of the kite power manufacturer as well as luck with suppliers, on how many kites are deployed (economy of scale), on the quality of the components, or on the engineering skills of the kite power plant manufacturer (and its employees). Those are the reasons, why such models were not used in the main part of this dissertation.

D.5.2 Cost Savings

If a kite is deployed in an island grid with high diesel generator penetration, it contributes energy that would otherwise have been generated by diesel generators. This means, if the levelized cost of electricity of the kite is e.g. 0.30 EUR/kWh (due to capital and maintenance costs as well as profits of kite power plant manufacturer, utility company, and investors) and that of diesel generators is 0.50 EUR/kWh, then someone saves 0.20 EUR/kWh. That may be the island grid utility company or the electricity customers or a combination of both.

Note that this combination of diesel and renewable energies can be very beneficial: The diesel generators are not replaced (at least not immediately), but instead diesel fuel is saved. The renewable energy systems inject power into the grid (at times where the wind blows and the sun shines) and the diesel generators compensate the difference between renewable power and load, as diesel generators can change their power very dynamically.

The cost savings should be included into the economics model. The saved costs in EUR/yr can be expressed by

$$\begin{aligned} k_{\mathrm{sav}} &= k_{\mathrm{LCOE,o}} E_{\mathrm{el,yr}} - k_{\mathrm{LCOE,k}} E_{\mathrm{el,yr}} \\ &= (k_{\mathrm{LCOE,o}} - k_{\mathrm{LCOE,k}}) E_{\mathrm{el,yr}} \end{aligned} \tag{D.42}$$

where $k_{\mathrm{LCOE,k}}$ is the LCOE of the kite and $k_{\mathrm{LCOE,o}}$ is the LCOE of other generation technologies of the island grid (e.g. of diesel generators).

The simplest possibility can already be used by the derived model, by setting $k_{\mathrm{LCOE,o}} = k_{\mathrm{LCOE,k}}$, i.e. all possible savings go to the kite power plant manufacturer at a first sight. However, if the interest rate I is increased at the same time, then also the investor, which may be the island grid utility company, also benefits significantly from the savings.

Another possibility to acknowledge $k_{\mathrm{sav}} > 0$ is to include it into the static amortization, i.e. replacing (2.301) with

$$\begin{aligned} T_{\mathrm{am}} &= \frac{K_{\mathrm{inv}}}{k_{\mathrm{inv}} - k_{\mathrm{sav}}} \\ &= \frac{K_{\mathrm{inv}}}{K_{\mathrm{inv}} f_{\mathrm{an}} - k_{\mathrm{sav}}}. \end{aligned} \tag{D.43}$$

Yet a further possibility is to include it dynamically by replacing (2.285) with

$$k = k_{\mathrm{inv}} + k_{\mathrm{op}} - \tilde{k}_{\mathrm{sav}}(t) \tag{D.44}$$

where $\tilde{k}_{\mathrm{sav}}$ are the saved costs in EUR/yr, which are discounted for year t, similar to Theorem 2.6 and its proof, by

$$\begin{aligned} \tilde{k}_{\mathrm{sav}}(t) &= \frac{k_{\mathrm{sav}}}{(1+I)^{t/\mathrm{yr}}} \\ &= \frac{(k_{\mathrm{LCOE,o}} - k_{\mathrm{LCOE,k}}) E_{\mathrm{el,yr}}}{(1+I)^{t/\mathrm{yr}}}. \end{aligned} \tag{D.45}$$

D.5.3 Further Economics Model Extensions

Further extensions are required when actual systems are to be sold to customers, for which all involved parties want to have a precise estimate on costs and revenues. Those extensions involve the inclusion of taxes, subsidies, different tariffs for self-consumed energy and grid-injected energy, as well as demolition costs or profits. For utility companies and governments, also the calculation of "levelized avoided cost of electricity" [191] can be an interesting basis for decision making.

D.6 Further Ideas

A few further ideas for improvements of the kite power plant systems engineering model shall be mentioned:

- The tether thermodynamics should be modeled in higher detail. This is particularly interesting, if the actual airborne mass (instead of just the maximum allowed one) is known. Then the tether temperature can be included as a constraint into the optimization.
- If the actual airborne mass is known, then $v_{\mathrm{a,min}}$ can be minimized, such that the actual airborne mass can just be carried in crosswind flight.
- As already mentioned in Appendix C.5, MPC-based controllers or an optimal control approach may be suitable ways to compute the optimal flight path and the maximum achievable power for the point-mass model at a given wind speed. Such an optimization is essential, if the power plant design shall be optimized with the point-mass model, otherwise the power plant design optimization would be done for a suboptimal flight path. To avoid two of the feared difficulties of such an optimal control method, mentioned in Appendix C.2, the here derived point-mass model and controllers may be used to provide a good initial solution, and, more importantly, the here proposed tangential force control allocation may be used to obtain a single solution, i.e. not the actuations $C_{\mathrm{D,rot,set}}$, $c_{\mathrm{L,set}}$, $C_{\mathrm{D,k,a,set}}$ are optimized, but $F_{\mathrm{tan,set}}$ is optimized in each time step and the control allocation is part of the MPC controller's model to optimize for.
- A further approach for a model with mass is to use the point-mass model on prescribed points on a prescribed flight path, which is also called force balance model, an approach already used in [77, 78]. The speeds and actuations are then to be computed such that (C.1)–(C.3) hold true, and at the same time the average power is maximized. As just stated in the previous point, also here the control allocation could be utilized, i.e. not the actuations $C_{\mathrm{D,rot,set}}$, $c_{\mathrm{L,set}}$, $C_{\mathrm{D,k,a,set}}$ are used to find a valid solution which maximizes the power, but $F_{\mathrm{tan,set}}$ is used as variable and the control allocation is part of the model. A good initial solution could be provided by a steady model, similar as the one used within the main part of this dissertation, possibly extended with the kite orientation similar to [48].
- Finally, the optimization could be coupled with sophisticated simulations, e.g. CFD simulations of the airfoil, a blade-element-momentum model for the rotors to also optimize the rotor geometry, an electrical machine geometry model to also optimize the electrical machines, or a rigid body kite model (with flight controllers) to enhance the fidelity of the kite dynamics model. However, such an approach might dramatically increase the computational cost and may not find a solution in due time (within days or weeks of computation), even not on a super computer. A better solution for the subsystem models seems to be to incorporate approximate models of such sophisticated simulations results of components only, i.e. similar to what is discussed in Sect. D.4.

Appendix E

List of Prior Publications and Talks

During the doctoral research time from 2013 to 2021, a number of publications and talks have been contributed by the author of this dissertation. In the following, all these contributions are listed in chronological order of the submission date with a brief description, including the ones already cited within this dissertation. The five most important contributions already briefly described in Sect. 1.9 are highlighted in **bold**.

1. a) Korbinian Schechner, Florian Bauer, and Christoph M. Hackl. "DC-link Control for Airborne Wind Energy Systems During Pumping Mode". In: *Book of Abstracts of the International Airborne Wind Energy Conference 2015*. Ed. by Roland Schmehl. Delft, The Netherlands: Delft University of Technology, 2015, p. 39. ISBN: 978-94-6186-486-4. DOI: 10.4233/uuid:7df59b79-2c6b-4e30-bd58-8454f493bb09. URL: https://repository.tudelft.nl/islandora/object/uuid%3A114710f1-b5ba-4d03-88f5-c5db05f1583b?collection=research (visited on Aug. 2, 2018). Conference video available from: http://www.awec2015.com/ (visited on Aug. 3, 2018).

   b) Korbinian Schechner, Florian Bauer, and Christoph M. Hackl. "Nonlinear DC-link PI Control for Airborne Wind Energy Systems During Pumping Mode". In: *Airborne Wind Energy. Advances in Technology Development and Research*. Ed. by Roland Schmehl. Green Energy and Technology. Springer, Singapore, 2018, pp. 241–276. ISBN: 978-981-10-1946-3. DOI: 10.1007/978-981-10-1947-0_11. URL: https://link.springer.com/chapter/10.1007/978-981-10-1947-0_11 (visited on Aug. 2, 2018).

   This conference abstract, conference talk, and book chapter are co-authored by the author of this dissertation. The main topic is the voltage stabilization of the DC-link of the powertrain of a lift power system.

2. a) Florian Bauer, Christoph M. Hackl, Keyue Smedley, and Ralph M. Kennel. "On Multicopter-Based Launch and Retrieval Concepts for Lift Mode Operated Power Generating Kites". In: *Book of Abstracts of the International Airborne Wind Energy Conference 2015*. Ed. by Roland Schmehl. Delft, The Netherlands: Delft University of Technology, 2015, p. 92–93. ISBN: 978-94-6186-486-4. DOI: 10.4233/uuid:7df59b79-2c6b-4e30-bd58-8454f493bb09. URL: https://repository.tudelft.nl/islandora/object/uuid%3A378559a9-499e-49dd-a357-d7521a338254?collection=research (visited on Apr. 25, 2018). Conference video available from: http://www.awec2015.com/ (visited on Apr. 3, 2018).—Ref. [175].

   b) Florian Bauer, Christoph M. Hackl, Keyue Smedley, and Ralph M. Kennel. "Multicopter-Based Launching and Landing of Lift Power Kites". In: *Airborne Wind Energy. Advances in Technology Development and Research*. Ed. by Roland Schmehl. Green Energy and Technology. Springer, Singapore, 2018, pp. 463–489. ISBN: 978-981-10-1946-3. DOI: 10.1007/978-981-10-1947-0_19. URL: https://link.springer.com/chapter/10.1007%2F978-981-10-1947-0_19 (visited on May 29, 2018).—Ref. [176].

The main topic of this conference abstract, conference talk, and book chapter is the investigation of the possibility to employ a multicopter-based launching and landing for lift power kites. As a result, this approach is only feasible for very light kites. This is one of the reasons why the focus of this doctoral research was shifted towards drag power kites, with which multicopter-based launch and landing is also possible for relatively heavy kites. More details on the comparison between the technologies is given in Appendix A.

3. Florian Bauer, Christoph M. Hackl, Keyue Smedley, and Ralph M. Kennel. "Crosswind Kite Power with Tower". In: *Airborne Wind Energy. Advances in Technology Development and Research*. Ed. by Roland Schmehl. Green Energy and Technology. Springer, Singapore, 2018, pp. 441–462. ISBN: 978-981-10-1946-3. DOI: 10.1007/978-981-10-1947-0_18. URL: https://link.springer.com/chapter/10.1007%2F978-981-10-1947-0_18 (visited on Apr. 25, 2018).—Ref. [14].
This book chapter investigates if a tower for crosswind kite power would have advantages. Results include that a tower can significantly increase the so called cosine efficiency and decrease the complexity of launching and landing the kite. More details are given in Appendix A. Moreover, a tower is considered for the derived model in Chap. 2 and the sensitivity of the tower height on figures of merit are investigated in Chap. 5.

4. Florian Bauer. "Airborne Wind Energy – The Future of Wind Energy?" In: *IDTechEx Show! Energy Harvesting & Storage*. Santa Clara, USA, November 18–19, 2015. URL: https://www.idtechex.com/events/presentations/airborne-wind-energy-the-future-of-wind-energy-007459.asp (visited on Aug. 1, 2018). Slides available from: www.eal.ei.tum.de/fileadmin/tueieal/www/theses/Bauer/Airborne_Wind_Energy_-_The_Future_of_Wind_Energy_.pdf (visited on Aug. 1, 2018).—Ref. [171].
The main topic of this conference talk is a critical comparison of the kite power technologies. Details are given in Appendix A.

5. Florian Bauer, Christoph M. Hackl, Keyue Smedley, and Ralph M. Kennel. "'Virtual'-power-hardware-in-the-loop simulations for crosswind kite power with ground generation". In: *2016 American Control Conference (ACC)*. Boston, USA, 2016, pp. 4071–4076. DOI: 10.1109/ACC.2016.7525561. URL: http://ieeexplore.ieee.org/document/7525561/ (visited on Dec. 9, 2017).—Ref. [177].
This conference paper and conference talk focus on a hardware-in-the-loop simulation for a winch of a lift power kite without the need of another winch to emulate the loads of the kite. Instead, the load is "virtually" generated on the winch of the device under test with a software algorithm.

6. Florian Bauer, Christoph M. Hackl, Keyue Smedley, and Ralph M. Kennel. "Multicopter With Series Connected Propeller Drives". In: *IEEE Transactions on Control Systems Technology* 26.2 (Mar. 2018), pp. 563–574. ISSN: 1063-6536. DOI: 10.1109/TCST.2017.2679071. URL: http://ieeexplore.ieee.org/document/7888441/ (visited on Apr. 3, 2018).—Ref. [131].
This paper proposes to connect propeller drives in series to generate a high voltage with high-efficient low-voltage drives without DC-DC-converters. As preliminary study for the application for drag power kites, only the multicopter operation is considered. A drawback however is, that the control is rather complicated and another more beneficial interconnection of the electrical drives is found (see below, "Fault Tolerant Power Electronic System for Drag Power Kites").

7. **Florian Bauer, Ralph M. Kennel, Christoph M. Hackl, Filippo Campagnolo, Michael Patt, and Roland Schmehl. "Drag power kite with very high lift coefficient". In: *Renewable Energy (Elsevier)* 118.Supplement C (2018), pp. 290–305. ISSN: 0960-**

1481. DOI: 10.1016/j.renene.2017.10.073. URL: http://www.sciencedirect.com/science/article/pii/S0960148117310285 (visited on Nov. 28, 2017).—Ref. [110].
This paper derives a steady drag power kite model and, among others, derives an optimal kite design. It is shown, that the optimal lift coefficient is with > 4 very high. To sustain the high wing loading, a biplane kite is proposed. To achieve such a high lift coefficient, a multi-element airfoil is proposed and a first CFD validation is carried out. It is also shown, that the aerodynamic interference of the biplane wings may be small. Main concepts and major parts of the model derivation are used for this dissertation with further refinements, validations, and more parameter studies.

8. **Florian Bauer, Ralph M. Kennel, Christoph M. Hackl, Filippo Campagnolo, Michael Patt, and Roland Schmehl. "Power Curve and Design Optimization of Drag Power Kites". In: *Book of Abstracts of the Airborne Wind Energy Conference 2017*. Ed. by Moriz Diehl, Rachel Leuthold, and Roland Schmehl. Freiburg, Germany: Albert Ludwigs University of Freiburg and Delft University of Technology, 2017, pp. 72–73. ISBN: 978-94-6186-846-6. DOI: 10.4233/uuid:4c361ef1-d2d2-4d14-9868-16541f60edc7. URL: https://repository.tudelft.nl/islandora/object/uuid:c40f14fc-b4ba-498a-84c4-f2b745b4417b (visited on Apr. 25, 2018). Conference video available from: http://www.awec2017.com (visited on Apr. 3, 2018).—Ref. [104].**
This conference talk further refines the model of the previous paper "Drag power kite with very high lift coefficient". Particularly, the electrical cables in the tether are resolved and are part of the optimization. Major concepts and major parts of the model derivation, validations, and parameter studies are also used for this dissertation.

9. **Florian Bauer and Ralph M. Kennel. "Fault Tolerant Power Electronic System for Drag Power Kites". In: *Journal of Renewable Energy (Hindawi)* 2018 (Apr. 16, 2018). DOI: 10.1155/2018/1306750. URL: https://www.hindawi.com/journals/jre/2018/1306750/ (visited on Apr. 17, 2018).—Ref. [106].**
Based on the finding of the previous study "Power Curve and Design Optimization of Drag Power Kites", which reveals that a high number of electrical cables in the tether is optimal, this paper proposes a fault tolerant power electronic system for a drag power kite, in which e.g. even a short circuit in the tether does not lead to a system failure. The proof-of-concept is demonstrated with a small prototype. Further extensions to obtain a drag power kite system without any single point of failure are discussed.

10. **Florian Bauer and Ralph M. Kennel. "Design Sensitivities of Drag Power Kites". In: *Advances in Energy Transition – 8th Colloquium of the Munich School of Engineering.* July 2018, p. 108. DOI: 10.14459/2018md1449240. url: https://www.mse.tum.de/fileadmin/w00bvc/www/Veranstaltungen/Kolloquien/Kolloquium_2018/MSE_Colloquium_2018_Book_of_Abstacts.pdf (visited on Apr. 7, 2019). Poster available from: https://www.eal.ei.tum.de/fileadmin/tueieal/www/theses/Bauer/Publications/DesignSensitivitiesofDragPowerKites_Poster_FlorianBauer.pdf (visited on Apr. 7, 2019).—Ref. [111].**
This conference abstract and poster presents a preview of the sensitivity analyses results of this dissertation.

11. **Florian Bauer, Daniel Petzold, Ralph M. Kennel, Filippo Campagnolo, and Roland Schmehl. "Control of a Drag Power Kite over the Entire Wind Speed Range". In: *Journal of Guidance, Control, and Dynamics (2018).* Submitted; preprint available from: https://www.eal.ei.tum.de/fileadmin/tueieal/www/theses/Bauer/Publications/ControlofaDragPowerKiteovertheEntireWindSpeedRange_Preprint_FlorianBauer.pdf (visited on Apr. 7, 2019)—Ref. [112].**

This paper proposes a control scheme for drag power kites for the entire wind speed range. It includes a temperature controller allowing for temporary overloading of the powertrain. The underlying model is based on a point-mass model and a simple aerodynamics model. The latter is similar to what was derived in the prior paper "Drag power kite with very high lift coefficient". In particular, the simulation model can compute the entire power curve based on a dynamic kite model. This paper's contents are presented in Appendix C, with more details and extensions.

12. Simon Watson, Alberto Moro, Vera Reis, Charalampos Baniotopoulos, Stephan Barth, Gianni Bartoli, Florian Bauer, Elisa Boelman, Dennis Bosse, Antonello Cherubini, Alessandro Croce, Lorenzo Fagiano, Marco Fontana, Adrian Gambier, Konstantinos Gkoumas, Christopher Golightly, Mikel Iribas Latour, Peter Jamieson, John Kaldellis, Andrew Macdonald, Jimmy Murphy, Michael Muskulus, Francesco Petrini, Luca Pigolotti, Flemming Rasmussen, Philippe Schild, Roland Schmehl, Nafsika Stavridou, John Tande, Nigel Taylor, Thomas Telsnig, Ryan Wiser. "Future emerging technologies in the wind power sector: A European perspective". In: *Renewable and Sustainable Energy Reviews, Volume 113*. 2019. DOI: 10.1016/j.rser.2019.109270. URL: http://www.sciencedirect.com/science/article/pii/S1364032119304782 (visited on Mar. 21, 2021).
This is an overview paper on future emerging wind technologies.

13. Florian Bauer, Hannes Börngen, Ralph M. Kennel. "Power Electronic Topologies of Drag Power Kites". In: *Book of Abstracts of the Airborne Wind Energy Conference 2019*. Ed. by Roland Schmehl, and Oliver Tulloch. Delft University of Technology, and University of Strathclyde Glasgow, 2019, p. 148–151. ISBN: 978-94-6366-213-0. DOI: 10.4233/uuid:57fd203c-e069-11e9-9fcb-441ea15f7c9c. URL: https://repository.tudelft.nl/islandora/object/uuid:57fd203c-e069-11e9-9fcb-441ea15f7c9c?collection=research (visited on Mar. 21, 2021).
This conference abstract and conference talk compares different power electronic topologies for drag power kites based on defined robustness and performance requirements.

Appendix F

List of Supervised Student Works

During the doctoral research time from 2013 to 2021, also a number of works conducted by students were supervised by the author of this dissertation. Many of them had an airborne wind energy focus, but some were also off-topic, about other teaching or research topics of the chair e.g. because students approached the chair to supervise academically their seminar or thesis at a company. Apart from the seminar report by Daniel Petzold who is also a co-author of paper [112], no derivation or result of this dissertation is based on any of those student's works. Nevertheless, many works helped to deepen understanding by conducting surveys, preliminary investigations, challenge ideas in theoretical or simulative studies, prepare the design of test stands, or setting up test stands. To acknowledge all students' efforts, in the following all supervised student works are listed in chronological order[50]:

1. Stephan Bichlmaier. "Simulation and control of a Magnus effect airborne wind energy plant". Seminar report. Technical University of Munich (TUM), Chair of Electrical Drive Systems and Power Electronics, April 2014.
2. Michael Gramatke. "Entwurf einer Schlupfregelung für ein elektrisch angetriebenes Straßenfahrzeug". Bachelor thesis. Technical University of Munich (TUM), Chair of Electrical Drive Systems and Power Electronics, June 2014.
3. Mahmudul Haque Taz. "Power Optimization of a Magnus Effect Plant". Research internship report. Technical University of Munich (TUM), Chair of Electrical Drive Systems and Power Electronics, December 2014.
4. Zhenhan Xu. "Point mass and rigid body models of power generating kites – an overview". Seminar report. Technical University of Munich (TUM), Chair of Electrical Drive Systems and Power Electronics, February 2015.
5. Alejandro Nieto Cuarenta. "A Study on Dynamic Modeling of Soft Kites". Seminar report. Technical University of Munich (TUM), Chair of Electrical Drive Systems and Power Electronics, May 2015.
6. Yuntao Zhang. "Simulative Untersuchung der Lookup-Table-basierten verlustminimalen Momentensteuerung einer Asynchronmashine". Seminar report. Technical University of Munich (TUM), Chair of Electrical Drive Systems and Power Electronics, May 2015.
7. Maximilian Johannes Kneißl. "Power Fluctuations in Airborne Wind Energy Farms with Circulating Kites". Seminar report. Technical University of Munich (TUM), Chair of Electrical Drive Systems and Power Electronics, and Chalmers University of Technology, Department of Signals and Systems, June 2015.
8. Benjamin Prünster. "A Comparative Study between Lift Power Kites and Drag Power Kites". Bachelor thesis. Technical University of Munich (TUM), Chair of Electrical Drive Systems and Power Electronics, January 2016.

[50] This list comprises only those works started before April 2019.

9. Thomas Wildgruber. “Towards Clean Aviation: Today’s Technologies”. Seminar report. Technical University of Munich (TUM), Chair of Electrical Drive Systems and Power Electronics, March 2016.
10. Zhenhan Xu. “Hovering control of a ‘drag power’ kite”. Master thesis. Technical University of Munich (TUM), Chair of Electrical Drive Systems and Power Electronics, April 2016.
11. Alfred Deixler. “Fault Tolerant Control of Multicopters”. Seminar report. Technical University of Munich (TUM), Chair of Electrical Drive Systems and Power Electronics, August 2016.
12. Muhammad Anique Aslam. “Reel-In Phase Control of Power Kites”. Seminar report. Technical University of Munich (TUM), Chair of Electrical Drive Systems and Power Electronics, November 2016.
13. Jannick Pfort. “Model Predictive Control of a Multicopter with Series Connected Propeller Drives”. Research internship report. Technical University of Munich (TUM), Chair of Electrical Drive Systems and Power Electronics, January 2017.
14. Michael Sellner. “Untersuchung der Ausfallsicherheit bei ‘Series Connected Multicopters’”. Seminar report. Technical University of Munich (TUM), Chair of Electrical Drive Systems and Power Electronics, March 2017.
15. Konstantin Wetchy. “Power, Tether Force, and Airspeed Controller for a Drag Power Kite”. Seminar report. Technical University of Munich (TUM), Chair of Electrical Drive Systems and Power Electronics, March 2017.
16. Moritz Blasche. “Modelling and control of series connected current source inverters for airborne wind turbines”. Research internship report. Technical University of Munich (TUM), Chair of Electrical Drive Systems and Power Electronics, June 2017.
17. Moritz Blasche. “Current Source Converter Based Airborne Wind Turbines”. Seminar report. Technical University of Munich (TUM), Chair of Electrical Drive Systems and Power Electronics, July 2017.
18. Sabrina Schlemmer. “Bürstenloser Wechselstrommotor als Bremse im Dauerlaufprüfstand bei Hilti”. Seminar report. Technical University of Munich (TUM), Chair of Electrical Drive Systems and Power Electronics, and Hilti Deutschland AG, September 2017.
19. Sebastian Schranzhofer. “Entwicklung eines automatisierten Motorkennlinienprüfstands”. Bachelor thesis. Technical University of Munich (TUM), Chair of Electrical Drive Systems and Power Electronics, and VIKING GmbH, September 2017.
20. Tadib Jobair. “Evaluation of High Voltage Drive Train of a Power Generating Kite”. Master thesis. Technical University of Munich (TUM), Chair of Electrical Drive Systems and Power Electronics, September 2017.
21. Milos Katanic. “Fault Tolerant Control for Series Connected Multicopters”. Seminar report. Technical University of Munich (TUM), Chair of Electrical Drive Systems and Power Electronics, November 2017.
22. Mengjie Zhao. “CFD Investigation and Experimental Validation of a High-Lift Multi-Element Airfoil for a Drag Power Kite”. Bachelor thesis. Technical University of Munich (TUM), Chair of Wind Energy, and Chair of Electrical Drive Systems and Power Electronics, October 2017.
23. Benjamin Prünster. “Optimisation of a Multi-Element Airfoil for Kite Power Systems using MSES and CMA-ES”. Seminar report. Technical University of Munich (TUM), Chair of Electrical Drive Systems and Power Electronics, January 2018.

24. Daniel Petzold. “Limitation Control of a Drag Power Kite”. Research internship report. Technical University of Munich (TUM), Chair of Electrical Drive Systems and Power Electronics, April 2018.

25. Pol Bosch Faulí. “EMI Filter Optimization for Airborne Wind Turbines”. Master thesis. Technical University of Munich (TUM), Chair of Electrical Drive Systems and Power Electronics, and BRUSA Elektronik AG, May 2018.

26. Moritz Blasche. “Hardware-in-the-Loop Simulation for a Drag Power Kite Demonstrator”. Master thesis. Technical University of Munich (TUM), Chair of Electrical Drive Systems and Power Electronics, May 2018.

27. Maximilian Abele, Alexander Barthel, and Maximilian Löffel. “Market Analysis and Product Conceptualization for a Drag Power Kite”. Project study report. Technical University of Munich (TUM), Dr. Theo Schöller-Stiftungslehrstuhl für Technologie- und Innovationsmanagement, and Chair of Electrical Drive Systems and Power Electronics, August 2018.

28. Markus Sedelmaier. “Sensor Fusion for an Airborne Wind Energy System”. Master thesis. Technical University of Munich (TUM), Chair of Electrical Drive Systems and Power Electronics, September 2018.

29. Benedikt Gummich. “Maximum Power Point Tracking for Drag Power Kites”. Bachelor thesis. Technical University of Munich (TUM), Chair of Electrical Drive Systems and Power Electronics, November 2018.

30. Daniel Petzold. “Modelling and Control of an Oscillating Electric Drivetrain”. Master thesis. Technical University of Munich (TUM), Chair of Electrical Drive Systems and Power Electronics, and Bayerische Motoren Werke (BMW) Aktiengesellschaft, December 2018.

31. Christoph Drexler. “Design by Optimization of a Multi-Element Airfoil for Drag Power Kite”. Master thesis. Technical University of Munich (TUM), Chair of Wind Energy, and Chair of Electrical Drive Systems and Power Electronics, January 2019.

32. Andre Thommessen. “Optimale Regelung eines Drag Power Kites”. Seminar report. Technical University of Munich (TUM), Chair of Electrical Drive Systems and Power Electronics, February 2019.

33. Maximilian Löffel. “Levelized Cost of Electricity for a Drag Power Kite”. Master Thesis. Technical University of Munich (TUM), Chair of Management Accounting, and Chair of Electrical Drive Systems and Power Electronics, April 2019.

34. Sebastiano Brandizzi. “Airfoil Optimization for a Drag Power Kite”. Bachelor thesis. Technical University of Munich (TUM), Chair of Wind Energy, and Chair of Electrical Drive Systems and Power Electronics, *was still in progress in April 2019.*

35. André Frirdich. “Rotor Design Procedure for a Drag Power Kite”. Master thesis. Technical University of Munich (TUM), Chair of Wind Energy, and Chair of Electrical Drive Systems and Power Electronics, *was still in progress in April 2019.*

36. William Barker. “Rotations with Matrices and Quaternions: A Comparison”. Seminar report. Technical University of Munich (TUM), Chair of Electrical Drive Systems and Power Electronics, *was still in progress in April 2019.*

37. Martin Marmsoler. “Sensor Fusion Algorithms for a Drag Power Kite”. Master thesis. Technical University of Munich (TUM), Chair of Electrical Drive Systems and Power Electronics, *was still in progress in April 2019.*

38. Maximilian Abele. “Evaluating Acceptance of Airborne Wind Energy Products”. Master Thesis. Technical University of Munich (TUM), Dr. Theo Schöller-Stiftungslehrstuhl für Technologie- und Innovationsmanagement, and Chair of Electrical Drive Systems and Power Electronics, *was still in progress in April 2019*.
39. Konstantin Lützow. “Design and Implementation of Ground Station Mechanics for a Drag Power Kite”. Seminar report. Technical University of Munich (TUM), Chair of Electrical Drive Systems and Power Electronics, *was still in progress in April 2019*.
40. Andre Thommessen. “Optimierung der Geschwindigkeits- und Flugbahnregelung eines Drag Power Kites durch Anpassung der Sollwerte”. Research internship report. Technical University of Munich (TUM), Chair of Electrical Drive Systems and Power Electronics, *was still in progress in April 2019*.
41. Kareem Abo Gamra. “Design and Implementation of Ground Station Electronics for a Drag Power Kite”. Bachelor thesis. Technical University of Munich (TUM), Chair of Electrical Drive Systems and Power Electronics, *was still in progress in April 2019*.

Bibliography

[1] Thomas Petermann, Harald Bradke, Arne Lüllmann, Maik Poetzsch, and Ulrich Riehm. *Gefährdung und Verletzbarkeit moderner Gesellschaften – am Beispiel eines großräumigen Ausfalls der Stromversorgung (Engl.: Hazards and vulnerability in modern societies – using the example of a large-scale outage in the electricity supply)*. Büro für Technikfolgen-Abschätzung beim Deutschen Bundestag. 2010. URL: http://www.tab-beim-bundestag.de/de/untersuchungen/u137.html (visited on May 22, 2017).

[2] IPCC. *Climate Change 2014: Synthesis Report. Contribution of Working Groups I, II and III to the Fifth Assessment Report of the Intergovernmental Panel on Climate Change*. Ed. by R.K. Pachauri and L.A. Meyer. Geneva, Switzerland, 2015. ISBN: 978-92-9169-143-2. URL: http://www.ipcc.ch/report/ar5/syr/ (visited on May 22, 2017).

[3] IRENA – International Renewable Energy Agency. *Renewable Power Generation Costs in 2014*. 2014. URL: http://www.irena.org/DocumentDownloads/Publications/IRENA_RE_Power_Costs_2014_report.pdf (visited on May 28, 2017).

[4] Kost et al. *Levelized Cost of Electricity – Renewable Energy Technologies*. Fraunhofer Institute for Solar Energy Systems ISE. 2013. URL: https://www.ise.fraunhofer.de/content/dam/ise/en/documents/publications/studies/EN2013_Fraunhofer-ISE_LCOE_Renewable_Energy_Technologies_version%20Nov2013_EN_Stand%2013-04-16_v02.pdf (visited on May 22, 2017).

[5] Christopher Moné, Tyler Stehly, Ben Maples, and Edward Settle. *2014 Cost of Wind Energy Review*. National Renewable Energy Laboratory. 2014. URL: www.nrel.gov/docs/fy16osti/64281.pdf (visited on May 22, 2017).

[6] Giles Hundleby. *The surprising results from the latest UK CfD auction*. BVG Associates. Sept. 15, 2017. URL: https://bvgassociates.com/the-surprising-results-from-the-latest-uk-cfd-auctions/ (visited on Apr. 13, 2018).

[7] Moritz Diehl. "Foreword". In: *Airborne Wind Energy. Advances in Technology Development and Research*. Ed. by Roland Schmehl. Green Energy and Technology. Springer, Singapore, 2018, pp. viii–x. ISBN: 978-981-10-1946-3. DOI: 10.1007/978-981-10-1947-0. URL: http://www.springer.com/de/book/9789811019463 (visited on May 29, 2017).

[8] IRENA – International Renewable Energy Agency. *Innovation Outlook: Offshore Wind*. 2016. URL: http://www.irena.org/DocumentDownloads/Publications/IRENA_Innovation_Outlook_Offshore_Wind_2016.pdf (visited on May 28, 2017).

[9] L. Fagiano and M. Milanese. "Airborne Wind Energy: An overview". In: *American Control Conference (ACC)*. June 2012, pp. 3132–3143. DOI: 10.1109/ACC.2012.6314801. URL: https://ieeexplore.ieee.org/document/6314801/ (visited on Apr. 25, 2018).

[10] U. Ahrens, M. Diehl, and R. Schmehl, eds. *Airborne Wind Energy*. Green Energy and Technology. Springer Berlin Heidelberg, 2013. ISBN: 978-3-642-39964-0. DOI: 10.1007/978-3-642-39965-7. URL: http://link.springer.com/book/10.1007%2F978-3-642-39965-7 (visited on May 22, 2017).

[11] Antonello Cherubini, Andrea Papini, Rocco Vertechy, and Marco Fontana. "Airborne Wind Energy Systems: A review of the technologies". In: *Renewable and Sustainable Energy Reviews* 51 (2015), pp. 1461–1476. ISSN: 1364-0321. DOI: 10.1016/j.rser.2015.07.053. URL: http://www.sciencedirect.com/science/article/pii/S1364032115007005 (visited on May 29, 2017).

[12] Roland Schmehl, ed. *Airborne Wind Energy. Advances in Technology Development and Research*. Green Energy and Technology. Springer, Singapore, 2018. ISBN: 978-981-10-1946-3. DOI: 10.1007/978-981-10-1947-0. URL: http://www.springer.com/de/book/9789811019463 (visited on June 13, 2021).

[13] M.L. Loyd. "Crosswind kite power (for large-scale wind power production)". In: *Journal of Energy* 4.3 (May 1, 1980), pp. 106–111. ISSN: 0146-0412. DOI: 10.2514/3.48021. URL: https://arc.aiaa.org/doi/10.2514/3.48021 (visited on Apr. 19, 2018).

[14] Florian Bauer, Christoph M. Hackl, Keyue Smedley, and Ralph M. Kennel. "Crosswind Kite Power with Tower". In: *Airborne Wind Energy. Advances in Technology Development and Research*. Ed. by Roland Schmehl. Green Energy and Technology. Springer, Singapore, 2018, pp. 441–462. ISBN: 978-981-10-1946-3. DOI: 10.1007/978-981-10-1947-0_18. URL: https://link.springer.com/chapter/10.1007%2F978-981-10-1947-0_18 (visited on Apr. 25, 2018).

[15] M. Erhard and H. Strauch. "Control of Towing Kites for Seagoing Vessels". In: *IEEE Transactions on Control Systems Technology* 21.5 (Sept. 2013), pp. 1629–1640. ISSN: 1063-6536. DOI: 10.1109/TCST.2012.2221093. URL: http://ieeexplore.ieee.org/document/6342904 (visited on Nov. 28, 2017).

[16] Damon Vander Lind. "Analysis and Flight Test Validation of High Performance Airborne Wind Turbines". In: *Airborne Wind Energy*. Ed. by Uwe Ahrens, Moritz Diehl, and Roland Schmehl. Berlin, Heidelberg: Springer Berlin Heidelberg, 2013, pp. 473–490. ISBN: 978-3-642-39965-7. DOI: 10.1007/978-3-642-39965-7_28. URL: https://link.springer.com/chapter/10.1007%2F978-3-642-39965-7_28 (visited on Apr. 25, 2018).

[17] Makani. *All Flight Modes of the Makani AWT*. Youtube. Feb. 28, 2012. URL: https://www.youtube.com/watch?v=9icw1oocUto (visited on May 29, 2017).

[18] Moritz Diehl. "Airborne Wind Energy: Basic Concepts and Physical Foundations". In: *Airborne Wind Energy*. Ed. by Uwe Ahrens, Moritz Diehl, and Roland Schmehl. Berlin, Heidelberg: Springer Berlin Heidelberg, 2013, pp. 3–22. ISBN: 978-3-642-39965-7. DOI: 10.1007/978-3-642-39965-7_1. URL: https://link.springer.com/chapter/10.1007%2F978-3-642-39965-7_1 (visited on May 29, 2017).

[19] Fort Felker. "Progress and Challenges in Airborne Wind Energy". In: *Book of Abstracts of the Airborne Wind Energy Conference 2017*. Ed. by Moriz Diehl, Rachel Leuthold, and Roland Schmehl. Freiburg, Germany: Albert Ludwigs University of Freiburg and Delft University of Technology, 2017, p. 13. ISBN: 978-94-6186-846-6. DOI: 10.4233/uuid:4c361ef1-d2d2-4d14-9868-16541f60edc7. URL: https://repository.tudelft.nl/islandora/object/uuid%3A056d3dd2-bdd1-4bf1-8331-fe5295ce7003?collection=research (visited on Jan. 2, 2018). Conference video recording available from: http://www.awec2017.com (visited on Apr. 3, 2018).

[20] Makani. *Makani's first commercial-scale energy kite*. Youtube. May 16, 2017. URL: https://www.youtube.com/watch?v=An8vtD1FDqs (visited on May 29, 2017).

[21] Fort Felker. *Makani takes to the ocean with Shell*. Medium. Feb. 12, 2019. URL: https://blog.x.company/makani-takes-to-the-ocean-with-shell-5aa74551917a (visited on Apr. 1, 2019). Direct link to figure: https://cdn-images-1.medium.com/max/1000/0*ZLzFqrHriTqbsxfH (visited on Apr. 1, 2019).

[22] Miles Loyd. "Foreword". In: *Airborne Wind Energy*. Ed. by Uwe Ahrens, Moritz Diehl, and Roland Schmehl. Berlin, Heidelberg: Springer Berlin Heidelberg, 2013, p. vii. ISBN: 978-3-642-39965-7. DOI: 10.1007/978-3-642-39965-7. URL: https://link.springer.com/book/10.1007/978-3-642-39965-7 (visited on Apr. 25, 2018).

[23] Anny Key de Souza Mendonça, Caroline Rodrigues Vaz, Álvaro Guillermo Rojas Lezana, Cristiane Alves Anacleto, and Edson Pacheco Paladini. "Comparing Patent and Scientific Literature in Airborne Wind Energy". In: *Sustainability* 9.6 (2017). ISSN: 2071-1050. DOI: 10.3390/su9060915. URL: http://www.mdpi.com/2071-1050/9/6/915 (visited on June 10, 2017).

[24] M.L. Loyd. "Wind driven apparatus for power generation". US Patent 4,251,040. 1981. URL: https://patents.google.com/patent/US4251040 (visited on Apr. 25, 2018).

[25] KitePower. *KitePower*. Delft University of Technology, Section Wind Energy, Faculty of Aerospace Engineering. URL: http://www.kitepower.eu (visited on June 10, 2017).

[26] University of Freiburg. *syscop*. Systems Control and Optimization Laboratory, IMTEK, Faculty of Engineering, University of Freiburg. URL: https://www.syscop.de (visited on June 10, 2017).

[27] X Development LLC. *Makani*. URL: https://x.company/makani/ (visited on June 17, 2017).

[28] Ampyx Power B.V. *Ampyx Power*. URL: https://www.ampyxpower.com/ (visited on June 17, 2017).

[29] EnerKite GmbH. *EnerKite – Flugwindkraftanlagen*. URL: http://enerkite.de/ (visited on June 17, 2017).

[30] SkySails Group GmbH. *SkySails*. URL: https://skysails-group.com/ (visited on June 13, 2021).

[31] Enevate BV. *Kitepower Airborne Wind Energy - Plug & Play Mobile Wind Energy*. URL: https://thekitepower.com/ (visited on June 13, 2021).

[32] TwingTec AG. *Twingtec – Wind Energy 2.0*. URL: http://twingtec.ch/ (visited on June 17, 2017).

[33] Moritz Diehl. "Real-time optimization for large scale nonlinear processes". Ph.D. Dissertation. Ruprecht-Karls-Universität Heidelberg, 2001. DOI: 10.11588/heidok.00001659. URL: http://www.ub.uni-heidelberg.de/archiv/1659 (visited on Feb. 27, 2017).

[34] B. Houska and M. Diehl. "Optimal Control of Towing Kites". In: *Proceedings of the 45th IEEE Conference on Decision and Control*. Dec. 2006, pp. 2693–2697. DOI: 10.1109/CDC.2006.377210. URL: https://ieeexplore.ieee.org/document/4177402/ (visited on Apr. 25, 2018).

[35] B. Houska and M. Diehl. "Optimal control for power generating kites". In: *2007 European Control Conference (ECC)*. July 2007, pp. 3560–3567. URL: https://ieeexplore.ieee.org/document/7068861/ (visited on Apr. 25, 2018).

[36] Paul Williams. "Optimal Wind Power Extraction with a Tethered Kite". In: *AIAA Guidance, Navigation, and Control Conference and Exhibit*. American Institute of Aeronautics and Astronautics, 2006. DOI: 10.2514/6.2006-6193. URL: https://arc.aiaa.org/doi/10.2514/6.2006-6193 (visited on Apr. 25, 2018).

[37] M. Canale, L. Fagiano, M. Ippolito, and M. Milanese. "Control of tethered airfoils for a new class of wind energy generator". In: *2006 45th IEEE Conference on Decision and Control*. Dec. 2006, pp. 4020–4026. DOI: 10.1109/CDC.2006.376775. URL: https://ieeexplore.ieee.org/document/4177614/ (visited on Apr. 25, 2018).

[38] A. Ilzhöfer, B. Houska, and M. Diehl. "Nonlinear MPC of kites under varying wind conditions for a new class of large-scale wind power generators". In: *International Journal of Robust and Nonlinear Control* 17.17 (2007), pp. 1590–1599. ISSN: 1099-1239. DOI: 10.1002/rnc.1210. URL: https://onlinelibrary.wiley.com/doi/abs/10.1002/rnc.1210 (visited on Apr. 25, 2018).

[39] I. Argatov, P. Rautakorpi, and R. Silvennoinen. "Estimation of the mechanical energy output of the kite wind generator". In: *Renewable Energy* 34.6 (2009), pp. 1525–1532. ISSN: 0960-1481. DOI: 10.1016/j.renene.2008.11.001. URL: http://www.sciencedirect.com/science/article/pii/S096014810800400X (visited on June 29, 2017).

[40] I. Argatov and R. Silvennoinen. "Energy conversion efficiency of the pumping kite wind generator". In: *Renewable Energy* 35.5 (2010), pp. 1052–1060. ISSN: 0960-1481. DOI: 10.1016/j.renene.2009.09.006. URL: https://www.sciencedirect.com/science/article/pii/S0960148109004017 (visited on June 29, 2017).

[41] L. Fagiano, A.U. Zgraggen, M. Morari, and M. Khammash. "Automatic Crosswind Flight of Tethered Wings for Airborne Wind Energy: Modeling, Control Design, and Experimental Results". In: *IEEE Transactions on Control Systems Technology* 22.4 (July 2014), pp. 1433–1447. ISSN: 1063-6536. DOI: 10.1109/TCST.2013.2279592. URL: http://ieeexplore.ieee.org/document/6595026 (visited on Nov. 28, 2017).

[42] Jeroen Breukels. "An Engineering Methodology for Kite Design". Ph.D. Dissertation. Delft University of Technology, 2011. ISBN: 9789088912306. URL: http://repository.tudelft.nl/view/ir/uuid%3Acdece38a-1f13-47cc-b277-ed64fdda7cdf (visited on June 27, 2017).

[43] Mario Zanon, Sébastien Gros, Johan Meyers, and Moritz Diehl. "Airborne Wind Energy: Airfoil-Airmass Interaction". In: *IFAC Proceedings Volumes* 47.3 (2014). 19th IFAC World Congress, pp. 5814–5819. ISSN: 1474-6670. DOI: 10.3182/20140824-6-ZA-1003.00258. URL: http://www.sciencedirect.com/science/article/pii/S1474667016425218 (visited on Apr. 9, 2018).

[44] Rachel Leuthold, Sébastien Gros, and Moritz Diehl. "Induction in Optimal Control of Multiple-Kite Airborne Wind Energy Systems". In: *IFAC-PapersOnLine* 50.1 (2017). 20th IFAC World Congress, pp. 153–158. ISSN: 2405-8963. DOI: 10.1016/j.ifacol.2017.08.026. URL: http://www.sciencedirect.com/science/article/pii/S2405896317300381 (visited on Apr. 9, 2018).

[45] Rolf H. Luchsinger. "Pumping Cycle Kite Power". In: *Airborne Wind Energy*. Ed. by Uwe Ahrens, Moritz Diehl, and Roland Schmehl. Berlin, Heidelberg: Springer Berlin Heidelberg, 2013, pp. 47–64. ISBN: 978-3-642-39965-7. DOI: 10.1007/978-3-642-39965-7_3. URL: https://link.springer.com/chapter/10.1007%2F978-3-642-39965-7_3 (visited on Apr. 25, 2018).

[46] Uwe Fechner and Roland Schmehl. "Model-Based Efficiency Analysis of Wind Power Conversion by a Pumping Kite Power System". In: *Airborne Wind Energy*. Ed. by Uwe Ahrens, Moritz Diehl, and Roland Schmehl. Berlin, Heidelberg: Springer Berlin Heidelberg, 2013, pp. 249–269. ISBN: 978-3-642-39965-7. DOI: 10.1007/978-3-642-39965-7_14. URL: https://link.springer.com/chapter/10.1007%2F978-3-642-39965-7_14 (visited on Apr. 25, 2018).

[47] Uwe Fechner. "A Methodology for the Design of Kite-Power Control Systems". Ph.D. Dissertation. Delft University of Technology, 2016. ISBN: 978-94-028-0409-6. DOI: 10.4233/uuid:85efaf4c-9dce-4111-bc91-7171b9da4b77. URL: https://repository.tudelft.nl/islandora/object/uuid:85efaf4c-9dce-4111-bc91-7171b9da4b77?collection=research (visited on Apr. 7, 2019).

[48] Roland Schmehl, Michael Noom, and Rolf van der Vlugt. "Traction Power Generation with Tethered Wings". In: *Airborne Wind Energy*. Ed. by Uwe Ahrens, Moritz Diehl, and Roland Schmehl. Berlin, Heidelberg: Springer Berlin Heidelberg, 2013, pp. 23–45. ISBN: 978-3-642-39965-7. DOI: 10.1007/978-3-642-39965-7_2. URL: https://link.springer.com/chapter/10.1007/978-3-642-39965-7_2 (visited on Apr. 23, 2018).

[49] Roland Schmehl and Rolf van der Vlugt. "Traction Power Generation with Tethered Wings – A Quasi-Steady Model for the Prediction of the Power Output". In: *Book of Abstracts of the International Airborne Wind Energy Conference 2015*. Ed. by Roland Schmehl. Delft, The Netherlands: Delft University of Technology, 2015, p. 39. ISBN: 978-94-6186-486-4. DOI: 10.4233/uuid:7df59b79-2c6b-4e30-bd58-8454f493bb09. URL: https://repository.tudelft.nl/islandora/object/uuid%3A339787a3-415e-4f34-a630-94055585776d (visited on Apr. 25, 2018). Conference video available from: http://www.awec2015.com/ (visited on Apr. 25, 2018).

[50] Rolf van der Vlugt, Roland Schmehl, Anna Bley, and Michael Noom. "Quasi-Steady Model of a Pumping Kite Power System". In: (May 12, 2017). Preprint submitted to Renewable Energy. URL: https://arxiv.org/abs/1705.04133 (visited on Apr. 25, 2018).

[51] S. Costello, C. Costello, G. François, and D. Bonvin. "Analysis of the maximum efficiency of kite-power systems". In: *Journal of Renewable and Sustainable Energy* 7.5 (2015). DOI: 10.1063/1.4931111. URL: https://aip.scitation.org/doi/10.1063/1.4931111 (visited on June 26, 2017).

[52] Marcelo De Lellis, Romeu Reginatto, Ramiro Saraiva, and Alexandre Trofino. "The Betz limit applied to Airborne Wind Energy". In: *Renewable Energy* 127 (2018), pp. 32–40. ISSN: 0960-1481. DOI: https://doi.org/10.1016/j.renene.2018.04.034. URL: http://www.sciencedirect.com/science/article/pii/S0960148118304427.

[53] J. Heilmann. "Technical and Economic Potential of Airborne Wind Energy". Master thesis. Utrecht University, 2012. URL: http://dspace.library.uu.nl/handle/1874/258716 (visited on June 28, 2017).

[54] Jannis Heilmann and Corey Houle. "Economics of Pumping Kite Generators". In: *Airborne Wind Energy*. Ed. by Uwe Ahrens, Moritz Diehl, and Roland Schmehl. Berlin, Heidelberg: Springer Berlin Heidelberg, 2013, pp. 271–284. ISBN: 978-3-642-39965-7. DOI: 10.1007/978-3-642-39965-7_15. URL: https://link.springer.com/chapter/10.1007%2F978-3-642-39965-7_15 (visited on Apr. 25, 2018).

[55] Uwe Fechner and Roland Schmehl. "Downscaling of Airborne Wind Energy Systems". In: *Journal of Physics: Conference Series* 753.10 (2016), p. 102002. URL: http://stacks.iop.org/1742-6596/753/i=10/a=102002 (visited on June 29, 2017).

[56] Ivan Argatov and Valentin Shafranov. "Economic assessment of small-scale kite wind generators". In: *Renewable Energy* 89 (2016), pp. 125–134. ISSN: 0960-1481. DOI: 10.1016/j.renene.2015.12.020. URL: http://www.sciencedirect.com/science/article/pii/S0960148115305231 (visited on Apr. 12, 2018).

[57] Christoph Grete. “Optimization, Scaling and Economics of Pumping Kite Power Systems”. Master thesis. Delft University of Technology, 2014. URL: https://repository.tudelft.nl/islandora/object/uuid%3Ab980aab7-f346-4030-97a3-a3cde13a51d6?collection=education (visited on July 17, 2017).

[58] Pietro Faggiani. “Pumping Kites Wind Farm”. Master thesis. Delft University of Technology, 2014. URL: https://repository.tudelft.nl/islandora/object/uuid%3A66cddbd2-5f50-4fc7-be0b-468853128f37?collection=education (visited on July 17, 2017).

[59] Pietro Faggiani and Roland Schmehl. “Design and Economics of a Pumping Kite Wind Park”. In: *Airborne Wind Energy. Advances in Technology Development and Research*. Ed. by Roland Schmehl. Green Energy and Technology. Springer, Singapore, 2018, pp. 391–411. ISBN: 978-981-10-1946-3. DOI: 10.1007/978-981-10-1947-0_16. URL: https://link.springer.com/chapter/10.1007%2F978-981-10-1947-0_16 (visited on May 29, 2017).

[60] M. De Lellis, A.K. Mendonça, R. Saraiva, A. Trofino, and Á. Lezana. “Electric power generation in wind farms with pumping kites: An economical analysis”. In: *Renewable Energy* 86 (2016), pp. 163–172. ISSN: 0960-1481. DOI: 10.1016/j.renene.2015.08.002. URL: http://www.sciencedirect.com/science/article/pii/S0960148115302020 (visited on Apr. 12, 2018).

[61] A.M.O. Smith. “High-Lift Aerodynamics”. In: *Journal of Aircraft* 12.6 (June 1, 1975), pp. 501–530. ISSN: 0021-8669. DOI: 10.2514/3.59830. URL: https://arc.aiaa.org/doi/10.2514/3.59830 (visited on Nov. 28, 2017).

[62] Flavio Gohl and Rolf H. Luchsinger. “Simulation Based Wing Design for Kite Power”. In: *Airborne Wind Energy*. Ed. by Uwe Ahrens, Moritz Diehl, and Roland Schmehl. Berlin, Heidelberg: Springer Berlin Heidelberg, 2013, pp. 325–338. ISBN: 978-3-642-39965-7. DOI: 10.1007/978-3-642-39965-7_18. URL: https://link.springer.com/chapter/10.1007%2F978-3-642-39965-7_18 (visited on June 29, 2017).

[63] Jeroen Breukels and Wubbo Ockels. “Tethered ‘kiteplane’ design for the Laddermill project”. In: *World Wind Energy Conference, Melbourne, Australia, 2005*. 2005. URL: http://resolver.tudelft.nl/uuid:990f305c-5198-45ff-9f5e-2b166e08b1c0 (visited on June 30, 2017).

[64] Jeroen Breukels and Wubbo Ockels. “Design of a Large Inflatable Kiteplane”. In: *48th AIAA/ASME/ASCE/AHS/ASC Structures, Structural Dynamics, and Materials Conference*. American Institute of Aeronautics and Astronautics, 2007. DOI: doi:10.2514/6.2007-2246. URL: https://arc.aiaa.org/doi/10.2514/6.2007-2246 (visited on Apr. 25, 2018).

[65] B. Lansdorp, B. Remes, and W. Ockels. “Design and testing of a remotely controlled surfkite for the Laddermill”. In: *World Wind Energy Conference, Melbourne, Australia, 2005*. 2005. URL: http://resolver.tudelft.nl/uuid:927a1c12-ae63-4f6f-b2a1-14ac6da22e2e (visited on July 2, 2017).

[66] Bas Lansdorp and Wubbo Ockels. “Design of a 100 MW laddermill for wind energy generation from 5 km altitude”. In: *7th World Congress on Recovery, Recycling and Re-integration, Beijing, 2005*. 2005. URL: http://resolver.tudelft.nl/uuid:2ea1b27b-b92c-4ce9-b097-b17303a1bcf6 (visited on July 2, 2017).

[67] Rolf van der Vlugt, Johannes Peschel, and Roland Schmehl. “Design and Experimental Characterization of a Pumping Kite Power System”. In: *Airborne Wind Energy*. Ed. by Uwe Ahrens, Moritz Diehl, and Roland Schmehl. Berlin, Heidelberg: Springer Berlin Heidelberg, 2013, pp. 403–425. ISBN: 978-3-642-39965-7. DOI: 10.1007/978-3-642-39965-7_23. URL: https://link.springer.com/chapter/10.1007%2F978-3-642-39965-7_23 (visited on Apr. 25, 2018).

[68] Mario Milanese, Franco Taddei, and Stefano Milanese. “Design and Testing of a 60 kW Yo-Yo Airborne Wind Energy Generator”. In: *Airborne Wind Energy*. Ed. by Uwe Ahrens, Moritz Diehl, and Roland Schmehl. Berlin, Heidelberg: Springer Berlin Heidelberg, 2013, pp. 373–386. ISBN: 978-3-642-39965-7. DOI: 10.1007/978-3-642-39965-7_21. URL: https://link.springer.com/chapter/10.1007%2F978-3-642-39965-7_21 (visited on Apr. 25, 2018).

[69] Storm Dunker. “Ram-air Wing Design Considerations for Airborne Wind Energy”. In: *Airborne Wind Energy*. Ed. by Uwe Ahrens, Moritz Diehl, and Roland Schmehl. Berlin, Heidelberg: Springer Berlin Heidelberg, 2013, pp. 517–546. ISBN: 978-3-642-39965-7. DOI: 10.1007/978-3-642-39965-7_31. URL: https://link.springer.com/chapter/10.1007%2F978-3-642-39965-7_31 (visited on Apr. 25, 2018).

[70] Xaver Paulig, Merlin Bungart, and Bernd Specht. “Conceptual Design of Textile Kites Considering Overall System Performance”. In: *Airborne Wind Energy*. Ed. by Uwe Ahrens, Moritz Diehl, and Roland Schmehl. Berlin, Heidelberg: Springer Berlin Heidelberg, 2013, pp. 547–562. ISBN: 978-3-642-39965-7. DOI: 10.1007/978-3-642-39965-7_32. URL: https://link.springer.com/chapter/10.1007%2F978-3-642-39965-7_32 (visited on July 2, 2017).

[71] Ivan Argatov and Risto Silvennoinen. “Structural optimization of the pumping kite wind generator”. In: *Structural and Multidisciplinary Optimization* 40.1 (May 2009), p. 585. ISSN: 1615-1488. DOI: 10.1007/s00158-009-0391-3. URL: https://link.springer.com/article/10.1007%2Fs00158-009-0391-3 (visited on June 29, 2017).

[72] M. Zanon, S. Gros, J. Andersson, and M. Diehl. “Airborne Wind Energy Based on Dual Airfoils”. In: *IEEE Transactions on Control Systems Technology* 21.4 (July 2013), pp. 1215–1222. ISSN: 1063-6536. DOI: 10.1109/TCST.2013.2257781. URL: https://ieeexplore.ieee.org/document/6514616/ (visited on Apr. 25, 2018).

[73] A. Venturato. “Analisi fluidodinamica del profilo alare Clark-Y ed ottimizzazione multi-obbiettivo tramite algoritmo genetico”. Master thesis. Università degli studi di Padova, 2013. URL: http://tesi.cab.unipd.it/44507/1/Tesi_Venturato_Andrea_607493.pdf (visited on Apr. 10, 2017).

[74] Roger J. Coenen, Sil Drenth, Tommy Smits, and Marijn L.W. Veraart. “Design of a Lightweight and Durable Kite for Cost-Effective Traction Power Generation in a Pumping Kite Power System”. In: *Book of Abstracts of the International Airborne Wind Energy Conference 2015*. Ed. by Roland Schmehl. Delft, The Netherlands: Delft University of Technology, 2015, p. 108. ISBN: 978-94-6186-486-4. DOI: 10.4233/uuid:7df59b79-2c6b-4e30-bd58-8454f493bb09. URL: https://repository.tudelft.nl/islandora/object/uuid%3A1128a498-996c-4755-ba18-60405e9329d3 (visited on Apr. 25, 2018). Conference poster available from: http://www.awec2015.com/ (visited on Apr. 25, 2016).

[75] D. Vander Lind. “Kite configuration and flight strategy for flight in high wind speeds”. US Patent 9,896,201. 2018. URL: https://patents.google.com/patent/US9896201B2 (visited on Apr. 25, 2018).

[76] Michiel Kruijff and Richard Ruiterkamp. “A Roadmap Towards Airborne Wind Energy in the Utility Sector”. In: *Airborne Wind Energy. Advances in Technology Development and Research*. Ed. by Roland Schmehl. Green Energy and Technology. Springer, Singapore, 2018, pp. 643–662. ISBN: 978-981-10-1946-3. DOI: 10.1007/978-981-10-1947-0_26. URL: https://link.springer.com/chapter/10.1007%2F978-981-10-1947-0_26 (visited on Apr. 25, 2018).

[77] Maximilian Ranneberg, David Wölfle, Alexander Bormann, Peter Rohde, Florian Breipohl, and Ilona Bastigkeit. "Fast Power Curve and Yield Estimation of Pumping Airborne Wind Energy Systems". In: *Airborne Wind Energy. Advances in Technology Development and Research*. Ed. by Roland Schmehl. Green Energy and Technology. Springer, Singapore, 2018, pp. 623–641. ISBN: 978-981-10-1946-3. DOI: 10.1007/978-981-10-1947-0_25. URL: https://link.springer.com/chapter/10.1007%2F978-981-10-1947-0_25 (visited on Apr. 25, 2018).

[78] Nicholas Tucker and Megan Quick. "A Techno-Economic Analysis of Energy Kites". In: *Book of Abstracts of the Airborne Wind Energy Conference 2017*. Ed. by Moriz Diehl, Rachel Leuthold, and Roland Schmehl. Freiburg, Germany: Albert Ludwigs University of Freiburg and Delft University of Technology, 2017, p. 183. ISBN: 978-94-6186-846-6. DOI: 10.4233/uuid:4c361ef1-d2d2-4d14-9868-16541f60edc7. URL: https://repository.tudelft.nl/islandora/object/uuid:86224277-9cda-417a-aba2-97c9c57dee0e (visited on Jan. 11, 2018).

[79] P.R. Payne and C. McCutchen. "Self-erecting windmill". US Patent 3,987,987. Oct. 1976. URL: https://patents.google.com/patent/US3987987A (visited on Apr. 25, 2018).

[80] Antonello Cherubini and Marco Fontana. *An Assessment of a Megawatt Scale Offshore Wind Energy Drone Generator at Jet Stream Altitude*. Submitted preprint. 2016. URL: http://www.antonellocherubini.com/uploads/4/5/7/1/45719075/cherubini_fontana_jet_stream_wind_drones_v3.pdf (visited on June 29, 2017).

[81] J.W. Kolar, T. Friedli, F. Krismer, A. Looser, M. Schweizer, P. Steimer, and J. Bevirt. "Conceptualization and multi-objective optimization of the electric system of an Airborne Wind Turbine". In: *2011 IEEE International Symposium on Industrial Electronics*. June 2011, pp. 32–55. DOI: 10.1109/ISIE.2011.5984131. URL: http://ieeexplore.ieee.org/document/5984131/ (visited on Jan. 3, 2018).

[82] R.A. Friedemann, F. Krismer, and J.W. Kolar. "Design of a minimum weight dual active bridge converter for an Airborne Wind Turbine system". In: *2012 Twenty-Seventh Annual IEEE Applied Power Electronics Conference and Exposition (APEC)*. Feb. 2012, pp. 509–516. DOI: 10.1109/APEC.2012.6165868. URL: https://ieeexplore.ieee.org/document/6165868/ (visited on Apr. 25, 2018).

[83] C. Gammeter, F. Krismer, and J.W. Kolar. "Weight optimization of a cooling system composed of fan and extruded fin heat sink". In: *2013 IEEE Energy Conversion Congress and Exposition*. Sept. 2013, pp. 2193–2200. DOI: 10.1109/ECCE.2013.6646978. URL: https://ieeexplore.ieee.org/document/6646978/ (visited on Apr. 25, 2018).

[84] C. Gammeter, Y. Drapela, A. Tüysüz, and J.W. Kolar. "Weight optimization of a machine for airborne wind turbines". In: *IECON 2014 - 40th Annual Conference of the IEEE Industrial Electronics Society*. Oct. 2014, pp. 950–958. DOI: 10.1109/IECON.2014.7048616. URL: https://ieeexplore.ieee.org/document/7048616/ (visited on Apr. 25, 2018).

[85] C. Gammeter, F. Krismer, and J.W. Kolar. "Weight Optimization of a Cooling System Composed of Fan and Extruded-Fin Heat Sink". In: *IEEE Transactions on Industry Applications* 51.1 (Jan. 2015), pp. 509–520. ISSN: 0093-9994. DOI: 10.1109/TIA.2014.2336977. URL: https://ieeexplore.ieee.org/document/6850003/ (visited on Apr. 25, 2018).

[86] C. Gammeter, F. Krismer, and J.W. Kolar. "Comprehensive Conceptualization, Design, and Experimental Verification of a Weight-Optimized All-SiC 2 kV/700 V DAB for an Airborne Wind Turbine". In: *IEEE Journal of Emerging and Selected Topics in Power Electronics* 4.2 (June 2016), pp. 638–656. ISSN: 2168-6777. DOI: 10.1109/JESTPE.2015.2459378. URL: https://ieeexplore.ieee.org/document/7163493/ (visited on Apr. 25, 2018).

[87] I. Subotic, C. Gammeter, A. Tüysüz, and J.W. Kolar. "Weight optimization of an axial-flux PM machine for airborne wind turbines". In: *2016 IEEE International Conference on Power Electronics, Drives and Energy Systems (PEDES)*. Dec. 2016, pp. 1–6. DOI: 10.1109/PEDES.2016.7914327. URL: https://ieeexplore.ieee.org/document/7914327/ (visited on Apr. 25, 2018).

[88] J. Adhikari, A.K. Rathore, and S.K. Panda. "Comparison of ZVS based isolated DC-DC converters for high altitude wind power application". In: *2013 IEEE Innovative Smart Grid Technologies-Asia (ISGT Asia)*. Nov. 2013, pp. 1–6. DOI: 10.1109/ISGT-Asia.2013.6698711. URL: https://ieeexplore.ieee.org/document/6698711/ (visited on Apr. 25, 2018).

[89] J. Adhikari, A.K. Rathore, and S.K. Panda. "Modular interleaved ZVS current fed isolated DC-DC converter for harvesting high altitude wind power". In: *IECON 2013 - 39th Annual Conference of the IEEE Industrial Electronics Society*. Nov. 2013, pp. 7187–7192. DOI: 10.1109/IECON.2013.6700327. URL: https://ieeexplore.ieee.org/document/6700327/ (visited on Apr. 25, 2018).

[90] J. Adhikari, A.K. Rathore, and S.K. Panda. "Modelling, design and control of grid connected converter for high altitude wind power application". In: *2014 International Power Electronics Conference (IPEC-Hiroshima 2014 - ECCE ASIA)*. May 2014, pp. 1775–1780. DOI: 10.1109/IPEC.2014.6869824. URL: https://ieeexplore.ieee.org/document/6869824/ (visited on Apr. 25, 2018).

[91] A. Goessling and L.F. Casey. "High frequency bi-directional AC power transmission". US Patent 9,151,272. 2015. URL: https://patents.google.com/patent/US9151272B2 (visited on Apr. 25, 2018).

[92] D. Vander Lind, G. Dolan, and C. Hardham. "Motor control topology for airborne power generation and systems using same". US Patent 9,866,152. 2018. URL: https://patents.google.com/patent/US9866152B2 (visited on Apr. 25, 2018).

[93] A.D. Goessling and E.H.I.I. George. "Motor with multi-phase windings and series-stacked inverter". US Patent 9,698,642. July 2017. URL: https://patents.google.com/patent/US9698642B1 (visited on Apr. 25, 2018).

[94] Windlift. URL: http://windlift.com/ (visited on Jan. 5, 2018).

[95] KiteX IVS. URL: http://kitex.tech/ (visited on Jan. 5, 2018).

[96] Joby Energy, Inc. *Joby Energy*. URL: http://jobyenergy.com/ (visited on July 3, 2017).

[97] Jelle Wijnja, Roland Schmehl, Roeland De Breuker, Kenneth Jensen, and Damon Vander Lind. "Aeroelastic Analysis of a Large Airborne Wind Turbine". In: *Journal of Guidance, Control, and Dynamics* (2018). ISSN: 0731-5090. DOI: 10.2514/1.G001663. URL: https://arc.aiaa.org/doi/10.2514/1.G001663 (visited on Sept. 12, 2018).

[98] Damon Vander Lind. "Developing a 600 kW Airborne Wind Turbine". In: *Book of Abstracts of the International Airborne Wind Energy Conference 2015*. Ed. by Roland Schmehl. Delft, The Netherlands: Delft University of Technology, 2015, pp. 14–17. ISBN: 978-94-6186-486-4. DOI: 10.4233/uuid:7df59b79-2c6b-4e30-bd58-8454f493bb09. URL: https://repository.tudelft.nl/islandora/object/uuid%3Abf8544b8-ef18-45e7-9463-949307e8c095 (visited on Apr. 25, 2018). Conference video recording available from: http://www.awec2015.com (visited on June 28, 2016).

[99] TEDx Talks. *A Different Kind of Wind Power: Damon Vander Lind at TEDxEmbryRiddle*. Youtube. Feb. 7, 2013. URL: https://www.youtube.com/watch?v=gLy13wlclns (visited on June 28, 2017).

[100] Makani. *Makani – Google+*. Google. URL: https://plus.google.com/+makani (visited on June 28, 2017).

[101] Makani. *Makani – Youtube*. Youtube. URL: https://www.youtube.com/channel/UCiMZJ8NppwT2fLwzFWJKOQ (visited on June 28, 2017).

[102] Corwin Hardham. *Response to the Federal Aviation Authority. Docket No.: FAA-2011-1279; Notice No. 11-07. Notification for Airborne Wind Energy Systems (AWES). MAKANI POWER, INC.* Feb. 7, 2012. URL: https://www.regulations.gov/document?D=FAA-2011-1279-0014 (visited on Apr. 25, 2018).

[103] D. Vander Lind. "Airfoil for a flying wind turbine". US Patent 9,709,026. July 2017. URL: https://patents.google.com/patent/US9709026B2 (visited on Apr. 25, 2018).

[104] Florian Bauer, Ralph M. Kennel, Christoph M. Hackl, Filippo Campagnolo, Michael Patt, and Roland Schmehl. "Power Curve and Design Optimization of Drag Power Kites". In: *Book of Abstracts of the Airborne Wind Energy Conference 2017*. Ed. by Moriz Diehl, Rachel Leuthold, and Roland Schmehl. Freiburg, Germany: Albert Ludwigs University of Freiburg and Delft University of Technology, 2017, pp. 72–73. ISBN: 978-94-6186-846-6. DOI: 10.4233/uuid:4c361ef1-d2d2-4d14-9868-16541f60edc7. URL: https://repository.tudelft.nl/islandora/object/uuid:c40f14fc-b4ba-498a-84c4-f2b745b4417b (visited on Apr. 25, 2018). Conference video recording available from: http://www.awec2017.com (visited on Apr. 3, 2018).

[105] D. Vander Lind and J. Felser. "High strength windable electromechanical tether with low fluid dynamic drag and system using same". US Patent 9,230,714. Jan. 2016. URL: https://patents.google.com/patent/US9230714B2 (visited on Apr. 25, 2018).

[106] Florian Bauer and Ralph M. Kennel. "Fault Tolerant Power Electronic System for Drag Power Kites". In: *Journal of Renewable Energy (Hindawi)* 2018 (Apr. 16, 2018). DOI: 10.1155/2018/1306750. URL: https://www.hindawi.com/journals/jre/2018/1306750/ (visited on Apr. 17, 2018).

[107] Joby Energy, Inc. *Technology Innovations*. URL: http://jobyenergy.com/tech/innovations (visited on June 19, 2017).

[108] J. Schlabbach. *Elektroenergieversorgung: Betriebsmittel, Netze, Kennzahlen und Auswirkungen der elektrischen Energieversorgung*. VDE-Verlag, 2009. ISBN: 9783800731084. URL: https://www.vde-verlag.de/buecher/603108/elektroenergieversorgung.html (visited on Apr. 25, 2018).

[109] Kenan Song, Yiying Zhang, Jiangsha Meng, Emily C. Green, Navid Tajaddod, Heng Li, and Marilyn L. Minus. "Structural Polymer-Based Carbon Nanotube Composite Fibers: Understanding the Processing–Structure–Performance Relationship". In: *Materials* 6.6 (2013), pp. 2543–2577. ISSN: 1996-1944. DOI: 10.3390/ma6062543. URL: http://www.mdpi.com/1996-1944/6/6/2543 (visited on June 26, 2017).

[110] Florian Bauer, Ralph M. Kennel, Christoph M. Hackl, Filippo Campagnolo, Michael Patt, and Roland Schmehl. "Drag power kite with very high lift coefficient". In: *Renewable Energy (Elsevier)* 118.Supplement C (2018), pp. 290–305. ISSN: 0960-1481. DOI: 10.1016/j.renene.2017.10.073. URL: http://www.sciencedirect.com/science/article/pii/S0960148117310285 (visited on Nov. 28, 2017).

[111] Florian Bauer and Ralph M. Kennel. "Design Sensitivities of Drag Power Kites". In: *Advances in Energy Transition – 8th Colloquium of the Munich School of Engineering*. July 2018, p. 108. DOI: 10.14459/2018md1449240. URL: https://www.mse.tum.de/fileadmin/w00bvc/www/Veranstaltungen/Kolloquien/Kolloquium_2018/MSE_Colloquium_2018_Book_of_Abstacts.pdf (visited on Apr. 7, 2019). Poster available from: https://www.eal.ei.tum.de/fileadmin/tueieal/www/theses/Bauer/Publications/DesignSensitivitiesofDragPowerKites_Poster_FlorianBauer.pdf (visited on Apr. 7, 2019).

[112] Florian Bauer, Daniel Petzold, Ralph M. Kennel, Filippo Campagnolo, and Roland Schmehl. "Control of a Drag Power Kite over the Entire Wind Speed Range". In: *Journal of Guidance, Control, and Dynamics* (2018). Submitted; preprint available from: https://www.eal.ei.tum.de/fileadmin/tueieal/www/theses/Bauer/Publications/ControlofaDragPowerKiteovertheEntireWindSpeedRange_Preprint_FlorianBauer.pdf (visited on Apr. 7, 2019).

[113] J. Katz and A. Plotkin. *Low-Speed Aerodynamics*. Cambridge Aerospace Series. Cambridge University Press, 2001. ISBN: 9780521665520. URL: https://www.cambridge.org/core/books/low-speed-aerodynamics/077FAF851C4582F1B7593809752C44AE (visited on Apr. 25, 2018).

[114] Robert Roedts. "Design of a Biplane Wing for Small-Scale Aircraft". In: *47th AIAA Aerospace Sciences Meeting including The New Horizons Forum and Aerospace Exposition*. American Institute of Aeronautics and Astronautics, 2009. DOI: 10.2514/6.2009-207. URL: https://arc.aiaa.org/doi/10.2514/6.2009-207 (visited on Apr. 25, 2018).

[115] S.F. Hoerner. *Fluid-dynamic Drag: Theoretical, Experimental and Statistical Information*. Hoerner Fluid Dynamics, 1965. URL: http://hoernerfluiddynamics.com/ (visited on Apr. 5, 2018).

[116] D. Schiktanz and D. Scholz. "Box Wing Fundamentals – An Aircraft Design Perspective". In: *Deutscher Luft- und Raumfahrtkongress 2011, Bremen*. Deutscher Luft- und Raumfahrtkongress, Tagungsband - Manuskripte, 2011, pp. 601–616. URL: http://www.mp.haw-hamburg.de/pers/Scholz/Airport2030/Airport2030_PUB_DLRK_11-09-27.pdf (visited on Apr. 13, 2018).

[117] *Airfoil Tools*. URL: http://airfoiltools.com (visited on Oct. 22, 2017).

[118] Ernesto Benini, Rita Ponza, and Andrea Massaro. "High-Lift Multi-Element Airfoil Shape and Setting Optimization Using Multi-Objective Evolutionary Algorithms". In: *Journal of Aircraft* 48.2 (Mar. 1, 2011), pp. 683–696. ISSN: 0021-8669. DOI: 10.2514/1.C031233. URL: https://arc.aiaa.org/doi/10.2514/1.C031233 (visited on Apr. 25, 2018).

[119] I. Argatov, P. Rautakorpi, and R. Silvennoinen. "Apparent wind load effects on the tether of a kite power generator". In: *Journal of Wind Engineering and Industrial Aerodynamics* 99.10 (2011), pp. 1079–1088. ISSN: 0167-6105. DOI: 10.1016/j.jweia.2011.07.010. URL: http://www.sciencedirect.com/science/article/pii/S0167610511001449 (visited on June 29, 2017).

[120] Lorenzo Fagiano. "Control of Tethered Airfoils for High-Altitude Wind Energy Generation". Ph.D. Dissertation. Politecnico di Torino, 2009. URL: http://lorenzofagiano.altervista.org/docs/PhD_thesis_Fagiano_Final.pdf (visited on July 20, 2017).

[121] J. Adhikari and S.K. Panda. "Overview of high altitude wind energy harvesting system". In: *2013 5th International Conference on Power Electronics Systems and Applications(PESA)*. Dec. 2013. DOI: 10.1109/PESA.2013.6828249. URL: https://ieeexplore.ieee.org/document/6828249/ (visited on Apr. 12, 2018).

[122] J. Adhikari, S.K. Panda, and A.K. Rathore. “Harnessing high altitude wind power using light gas filled blimp”. In: *IECON 2013 - 39th Annual Conference of the IEEE Industrial Electronics Society*. Nov. 2013, pp. 7163–7168. DOI: 10.1109/IECON.2013.6700323. URL: https://ieeexplore.ieee.org/document/6700323/ (visited on Apr. 12, 2018).

[123] J. Adhikari and S.K. Panda. “Generation and Transmission of Electrical Energy in High-Altitude Wind Power Generating System”. In: *IEEE Journal of Emerging and Selected Topics in Power Electronics* 3.2 (June 2015), pp. 459–470. ISSN: 2168-6777. DOI: 10.1109/JESTPE.2015.2388702. URL: https://ieeexplore.ieee.org/document/7004148/ (visited on Apr. 12, 2018).

[124] D.C. Giancoli and O. Eibl. *Physik*. Pearson Studium - Physik Bd. 10. Pearson Studium, 2006. ISBN: 9783827371577.

[125] N.H. Malik, A.A. Al-Arainy, M.I. Qureshi, and F.R. Pazheri. “Calculation of electric field distribution at high voltage cable terminations”. In: *2010 International Conference on High Voltage Engineering and Application*. Oct. 2010, pp. 24–27. DOI: 10.1109/ICHVE.2010.5640873. URL: https://ieeexplore.ieee.org/document/5640873/ (visited on Apr. 25, 2018).

[126] S. Gudmundsson. *General Aviation Aircraft Design: Applied Methods and Procedures*. Elsevier Science, 2013. ISBN: 9780123973290.

[127] T. Burton, N. Jenkins, D. Sharpe, and E. Bossanyi. *Wind Energy Handbook*. Wiley, 2011. ISBN: 9781119993926.

[128] L. Fagiano, K. Huynh, B. Bamieh, and M. Khammash. “On Sensor Fusion for Airborne Wind Energy Systems”. In: *IEEE Transactions on Control Systems Technology* 22.3 (May 2014), pp. 930–943. ISSN: 1063-6536. DOI: 10.1109/TCST.2013.2269865. URL: https://ieeexplore.ieee.org/document/6555854/ (visited on Apr. 25, 2018).

[129] D. Vander Lind. “Bridles for stability of a powered kite and a system and method for use of same”. US Patent 9,630,711. 2017. URL: https://patents.google.com/patent/US9630711 (visited on Apr. 25, 2018).

[130] Thomas Schneider. “Fault-tolerant Multirotor Systems”. Master Thesis. ETH Zürich, 2011. URL: http://students.asl.ethz.ch/upl_pdf/337-report.pdf (visited on Dec. 8, 2016).

[131] F. Bauer, C.M. Hackl, K.M. Smedley, and R.M. Kennel. “Multicopter With Series Connected Propeller Drives”. In: *IEEE Transactions on Control Systems Technology* 26.2 (Mar. 2018), pp. 563–574. ISSN: 1063-6536. DOI: 10.1109/TCST.2017.2679071. URL: http://ieeexplore.ieee.org/document/7888441 (visited on Apr. 3, 2018).

[132] V. Quaschning. *Regenerative Energiesysteme: Technologie - Berechnung - Simulation*. Hanser, 2007. ISBN: 9783446409736.

[133] Cristina L. Archer and Mark Z. Jacobson. “Evaluation of global wind power”. In: *Journal of Geophysical Research: Atmospheres* 110.D12 (2005). ISSN: 2156-2202. DOI: 10.1029/2004JD005462. URL: https://agupubs.onlinelibrary.wiley.com/doi/abs/10.1029/2004JD005462 (visited on Apr. 25, 2018).

[134] Clearingstelle EEG/RELAW GmbH – Gesellschaft für angewandtes Recht der Erneuerbaren Energien. *Erneuerbare-Energien-Gesetz vom 21. Juli 2014 (BGBl. I S. 1066), das durch Artikel 15 des Gesetzes vom 29. August 2016 (BGBl. I S. 2034) geändert worden ist*. URL: https://www.clearingstelle-eeg.de/files/EEG_2014_160829.pdf (visited on Oct. 19, 2017).

[135] Clearingstelle EEG/RELAW GmbH – Gesellschaft für angewandtes Recht der Erneuerbaren Energien. *Erneuerbare-Energien-Gesetz vom 21. Juli 2014 (BGBl. I S. 1066), das zuletzt durch Artikel 1 des Gesetzes vom 17. Juli 2017 (BGBl. I S. 2532) geändert worden ist.* URL: https://www.clearingstelle-eeg.de/files/EEG_2017_170717.pdf (visited on Oct. 19, 2017).

[136] J. Christoffer and M. Ulbricht-Eissing. *Die bodennahen Windverhältnisse in der Bundesrepublik Deutschland*. Berichte des Deutschen Wetterdienstes. Deutscher Wetterdienst, Zentralamt, 1989. ISBN: 9783881482486. URL: https://www.deutsche-digitale-bibliothek.de/binary/MHSFPMJY5BCAJUZKYTWBSSRQV3Q6EXWZ/full/1.pdf (visited on Aug. 10, 2017).

[137] D. Vander Lind and K. Jensen. "Methods and systems for managing power generation and temperature control of an aerial vehicle operating in crosswind-flight mode". US Patent 9,422,918. Aug. 2016. URL: https://patents.google.com/patent/US9422918 (visited on Apr. 25, 2018).

[138] A. Wobben. "Verfahren zum Betreiben einer Windenergieanlage sowie Windenergieanlage". DE19756777 (B4). 2005. URL: https://patents.google.com/patent/DE19756777B4 (visited on Apr. 25, 2018).

[139] Nicolas Boccard. *Capacity Factor of Wind Power: Realized Values vs. Estimates*. 2009. DOI: 10.2139/ssrn.1285435. URL: https://ssrn.com/abstract=1285435 (visited on Aug. 10, 2017).

[140] Walter Short, Daniel J. Packey, and Thomas Holt. *A Manual for the Economic Evaluation of Energy Efficiency and Renewable Energy Technologies*. National Renewable Energy Laboratory (NREL), Mar. 1995. URL: http://www.nrel.gov/docs/legosti/old/5173.pdf (visited on Sept. 4, 2017).

[141] A.C. Lee, J.C. Lee, and C.F. Lee. *Financial Analysis, Planning & Forecasting: Theory and Application*. World Scientific, 2009. ISBN: 9789812706089.

[142] Rigo Bosman, Valerie Reid, Martin Vlasblom, and Paul Smeets. "Airborne Wind Energy Tethers with High-Modulus Polyethylene Fibers". In: *Airborne Wind Energy*. Ed. by Uwe Ahrens, Moritz Diehl, and Roland Schmehl. Berlin, Heidelberg: Springer Berlin Heidelberg, 2013, pp. 563–585. ISBN: 978-3-642-39965-7. DOI: 10.1007/978-3-642-39965-7_33. URL: https://doi.org/10.1007/978-3-642-39965-7_33 (visited on Nov. 9, 2017).

[143] Gruschwitz Textilwerke AG. *Ultra High Molecular Weight Polyethylene Fiber from DSM Dyneema. UHMWPE fiber combines excellent mechanical properties with low density, resulting in high performance-on-weight basis*. URL: http://ea.newscpt.com/_fd/[nl_send_uid]/2711ad8ce5ab4999ec941356eaf00e40.html (visited on Nov. 9, 2017).

[144] MatWeb, LLC. *Online Materials Information Resource - MatWeb*. URL: http://www.matweb.com (visited on Nov. 9, 2017).

[145] DuPont. *Kevlar® Aramid Fiber Technical Guide*. URL: http://www.dupont.com/content/dam/dupont/products-and-services/fabrics-fibers-and-nonwovens/fibers/documents/Kevlar_Technical_Guide.pdf (visited on Nov. 9, 2017).

[146] I.M.L. Ridge, N. O'Hear, R. Verreet, O. Grabandt, and C.A. Das. "High strength fibre cored steel wire rope for deep hoisting applications". In: *Proceedings of the OIPEEC Conference 'How to get the most out of your ropes'*. Sept. 2007, pp. 225–240. ISBN: 978-0-9552500-1-9. URL: http://www.ropetechnology.com/bro_engl/high_strength_fibre_cored_rope.pdf (visited on Nov. 10, 2017).

[147] Guangtong Liu et al. “Highly Dense and Perfectly Aligned Single-Walled Carbon Nanotubes Fabricated by Diamond Wire Drawing Dies”. In: *Nano Letters* 8.4 (2008), pp. 1071–1075. DOI: 10.1021/nl073007o. URL: https://pubs.acs.org/doi/abs/10.1021/nl073007o (visited on Apr. 25, 2018).

[148] Bei Peng, Mark Locascio, Peter Zapol, Shuyou Li, Steven L. Mielke, George C. Schatz, and Horacio D. Espinosa. “Measurements of near-ultimate strength for multiwalled carbon nanotubes and irradiation-induced crosslinking improvements”. In: *Nature Nanotechnology* 3 (Aug. 10, 2008), p. 626. DOI: 10.1038/nnano.2008.211. URL: http://www.nature.com/articles/nnano.2008.211 (visited on Nov. 10, 2017).

[149] T.W. Ebbesen, H.J. Lezec, H. Hiura, J.W. Bennett, H.F. Ghaemi, and T. Thio. “Electrical conductivity of individual carbon nanotubes”. In: *Nature* 382 (July 1996), pp. 54–56. DOI: 10.1038/382054a0. URL: http://www.nature.com/articles/382054a0 (visited on Nov. 10, 2017).

[150] ENERCON GmbH. *WINDBLATT – ENERCON Magazin für Windenergie, Ausgabe 03, 2010*. URL: https://www.enercon.de/fileadmin/Redakteur/Medien-Portal/windblatt/pdf/WB-0310-dt.pdf (visited on Dec. 5, 2017).

[151] Google, Inc. *Makani*. URL: https://x.company/makani/solution (visited on Dec. 5, 2016). *As of January 11, 2018, the website does not show the power curve any more. However, the state of the website showing the power curve is available from the Internet Archive/Wayback Machine via https://web.archive.org/web/20160308201855/http://www.google.com/makani/solution/, respectively https://web.archive.org/web/20160311153634im_/http://www.google.com/makani/images/figures/speed.png for the power curve image. In Fig. A.2 on p. 267 a screenshot is shown that was recorded on December 5, 2016.*

[152] *Wind Energy Online Reader*. URL: http://mstudioblackboard.tudelft.nl/duwind/Wind%20energy%20online%20reader/Static_pages/annual_energy.htm (visited on Aug. 10, 2017).

[153] Nikolaus Hansen. “The CMA Evolution Strategy: A Tutorial”. In: *CoRR* abs/1604.00772 (2016). arXiv: 1604.00772. URL: http://arxiv.org/abs/1604.00772 (visited on Nov. 6, 2017).

[154] Nikolaus Hansen. URL: https://www.lri.fr/~hansen/cmaes_inmatlab.html (visited on Nov. 6, 2017).

[155] Forschungs- und Entwicklungszentrum Fachhochschule Kiel GmbH. *FINO1 - Forschungsplattformen in Nord- und Ostsee Nr. 1*. URL: http://www.fino1.de/standort/standort (visited on Jan. 17, 2018).

[156] J. Roland Ortt, Linda M. Kamp, and Matthew F.A. Doe. “How to Introduce Kite-Based Airborne Wind Energy Systems: The Selection of Niche Strategies to Overcome Barriers to Adoption”. In: *Book of Abstracts of the International Airborne Wind Energy Conference 2015*. Ed. by Roland Schmehl. Delft, The Netherlands: Delft University of Technology, 2015, pp. 64–65. ISBN: 978-94-6186-486-4. DOI: 10.4233/uuid:7df59b79-2c6b-4e30-bd58-8454f493bb09. URL: https://repository.tudelft.nl/islandora/object/uuid%3A9360c003-0bd2-4d0d-abe8-f11df678b70c (visited on Apr. 25, 2018). Conference video recording available from: http://www.awec2015.com (visited on January 18, 2018).

[157] Linda M. Kamp, J. Roland Ortt, and Matthew F.A. Doe. “Niche Strategies to Introduce Kite-Based Airborne Wind Energy”. In: *Airborne Wind Energy. Advances in Technology Development and Research*. Ed. by Roland Schmehl. Green Energy and Technology. Springer, Singapore, 2018, pp. 665–678. ISBN: 978-981-10-1946-3. DOI: 10.1007/978-981-10-1947-0_27. URL: https://link.springer.com/chapter/10.1007%2F978-981-10-1947-0_27 (visited on Apr. 25, 2018).

[158] Deutscher Wetterdienst, Abteilung Klima- und Umweltberatung, Offenbach 2004. *Jahresmittel der Windgeschwindigkeit – 80 m über Grund – in der Bundesrepublik Deutschland*. URL: http://www.dwd.de/DWD/klima/beratung/windkarten/D_0_80.jpg (visited on Jan. 18, 2018).

[159] Christian Bantle (BDEW Bundesverband der Energie- und Wasserwirtschaft e.V.) *BDEW-Strompreisanalyse Januar 2018: Haushalte und Industrie*. Jan. 18, 2018. URL: https://www.bdew.de/service/daten-und-grafiken/bdew-strompreisanalyse/ (visited on Mar. 9, 2018).

[160] U.S. Department of Energy, Office of Energy Efficiency & Renewable Energy. *Island Energy Snapshots Map*. URL: https://www.energy.gov/eere/island-energy-snapshots (visited on Mar. 9, 2018).

[161] European Energy Exchange AG. URL: https://www.eex.com (visited on Mar. 9, 2018).

[162] Airbus S.A.S. *Airbus A380 fatigue test reaches 15,000 flight cycles*. July 19, 2006. URL: http://www.airbus.com/newsroom/press-releases/en/2006/07/airbus-a380-fatigue-test-reaches-15-000-flight-cycles.html (visited on Mar. 12, 2018).

[163] Stratolaunch Systems Corporation. *How we Launch*. URL: http://www.stratolaunch.com/how-we-launch/ (visited on Apr. 7, 2019).

[164] Stratolaunch Systems Corporation. *Stratolaunch Completes Historic First Flight of Aircraft*. URL: https://www.stratolaunch.com/2019/04/13/stratolaunch-completes-historic-first-flight-of-aircraft/ (visited on Apr. 14, 2019).

[165] Flugtechnik & Leichtbau Bürogemeinschaft GbR. *eta: Technische Daten*. URL: http://www.leichtwerk.de/eta/de/daten/index.html (visited on Mar. 13, 2018).

[166] M. Nita and D. Scholz. "Estimating the Oswald Factor from Basic Aircraft Geometrical Parameters". In: *Deutscher Luft- und Raumfahrtkongress 2012, Berlin*. Deutsche Gesellschaft für Luft- und Raumfahrt – Lilienthal-Oberth e.V., Bonn, 2012. URL: http://www.dglr.de/publikationen/2012/281424.pdf (visited on Apr. 12, 2018).

[167] Michael S. Selig and James J. Guglielmo. "High-Lift Low Reynolds Number Airfoil Design". In: *Journal of Aircraft* 34.1 (Jan. 1997), pp. 72–79. ISSN: 0021-8669. DOI: 10.2514/2.2137. URL: https://arc.aiaa.org/doi/abs/10.2514/2.2137?journalCode=ja (visited on Apr. 23, 2018).

[168] Ran Fu, David Feldman, Robert Margolis, Mike Woodhouse, and Kristen Ardani. *U.S. Solar Photovoltaic System Cost Benchmark: Q1 2017*. National Renewable Energy Laboratory. 2017. URL: https://www.nrel.gov/docs/fy17osti/68925.pdf (visited on Mar. 14, 2018).

[169] D. Gianni, A. D'Ambrogio, and A. Tolk. *Modeling and Simulation-Based Systems Engineering Handbook*. Engineering Management. Taylor & Francis, 2014. ISBN: 9781466571457.

[170] Bladed – DNV GL. URL: http://www.dnvgl.com/bladed (visited on Nov. 20, 2017).

[171] Florian Bauer. *Airborne Wind Energy - The Future of Wind Energy?* IDTechEx Show! Energy Harvesting & Storage, Santa Clara, USA. Nov. 18, 2015. URL: https://www.idtechex.com/events/presentations/airborne-wind-energy-the-future-of-wind-energy-007459.asp (visited on Aug. 1, 2018). Slides available from: http://www.eal.ei.tum.de/fileadmin/tueieal/www/theses/Bauer/Airborne_Wind_Energy_-_The_Future_of_Wind_Energy_.pdf (visited on Aug. 1, 2018).

[172] Henrik Stiesdal. "Airborne Wind Energy – Challenges and Opportunities based on Experiences From the Conventional Wind Industry". In: *Book of Abstracts of the Airborne Wind Energy Conference 2017*. Ed. by Moriz Diehl, Rachel Leuthold, and Roland Schmehl. Freiburg, Germany: Albert Ludwigs University of Freiburg and Delft University of Technology, 2017, p. 21. ISBN: 978-94-6186-846-6. DOI: 10.4233/uuid:4c361ef1-d2d2-4d14-9868-16541f60edc7. URL: https://repository.tudelft.nl/islandora/object/uuid:7908247b-583f-49e3-8f17-b276f16a82ec (visited on Jan. 2, 2018).

[173] Michiel Kruijff and Richard Ruiterkamp. "AP-3, a Safety and Autonomy Demonstrator for Utility-Scale Airborne Wind Energy". In: *Book of Abstracts of the Airborne Wind Energy Conference 2017*. Ed. by Moriz Diehl, Rachel Leuthold, and Roland Schmehl. Freiburg, Germany: Albert Ludwigs University of Freiburg and Delft University of Technology, 2017, pp. 16–19. ISBN: 978-94-6186-846-6. DOI: 10.4233/uuid:4c361ef1-d2d2-4d14-9868-16541f60edc7. URL: https://repository.tudelft.nl/islandora/object/uuid:53286eb3-3e58-4f33-accf-c80c4876a60a?collection=research (visited on Apr. 25, 2018). Conference video recording available from: http://www.awec2017.com (visited on Apr. 16, 2018).

[174] Volkan Salma, Richard Ruiterkamp, Michiel Kruijff, M. M. (René) van Paassen, and Roland Schmehl. "Current and Expected Airspace Regulations for Airborne Wind Energy Systems". In: *Airborne Wind Energy. Advances in Technology Development and Research*. Ed. by Roland Schmehl. Green Energy and Technology. Springer, Singapore, 2018, pp. 703–725. ISBN: 978-981-10-1946-3. DOI: 10.1007/978-981-10-1947-0_29. URL: https://link.springer.com/chapter/10.1007%2F978-981-10-1947-0_29 (visited on May 29, 2017).

[175] Florian Bauer, Christoph M. Hackl, Keyue Smedley, and Ralph M. Kennel. "On Multicopter-Based Launch and Retrieval Concepts for Lift Mode Operated Power Generating Kites". In: *Book of Abstracts of the International Airborne Wind Energy Conference 2015*. Ed. by Roland Schmehl. Delft, The Netherlands: Delft University of Technology, 2015, pp. 92–93. ISBN: 978-94-6186-486-4. DOI: 10.4233/uuid:7df59b79-2c6b-4e30-bd58-8454f493bb09. URL: https://repository.tudelft.nl/islandora/object/uuid%3A378559a9-499e-49dd-a357-d7521a338254?collection=research (visited on Apr. 25, 2018). Conference video recording available from: http://www.awec2015.com (visited on Apr. 3, 2018).

[176] Florian Bauer, Christoph M. Hackl, Keyue Smedley, and Ralph M. Kennel. "Multicopter-Based Launching and Landing of Lift Power Kites". In: *Airborne Wind Energy. Advances in Technology Development and Research*. Ed. by Roland Schmehl. Green Energy and Technology. Springer, Singapore, 2018, pp. 463–489. ISBN: 978-981-10-1946-3. DOI: 10.1007/978-981-10-1947-0_19. URL: https://link.springer.com/chapter/10.1007%2F978-981-10-1947-0_19 (visited on May 29, 2017).

[177] F. Bauer, C.M. Hackl, K.M. Smedley, and R.M. Kennel. "'Virtual'-power-hardware-in-the-loop simulations for crosswind kite power with ground generation". In: *2016 American Control Conference (ACC)*. July 2016, pp. 4071–4076. DOI: 10.1109/ACC.2016.7525561. URL: http://ieeexplore.ieee.org/document/7525561/ (visited on Dec. 9, 2017).

[178] Alfred van den Brink. "Design of the e-50 Ground Station". In: *Book of Abstracts of the International Airborne Wind Energy Conference 2015*. Ed. by Roland Schmehl. Delft, The Netherlands: Delft University of Technology, 2015, pp. 34–35. ISBN: 978-94-6186-486-4. DOI: 10.4233/uuid:7df59b79-2c6b-4e30-bd58-8454f493bb09. URL: https://repository.tudelft.nl/islandora/object/uuid%3Ab589dac1-9ed8-4873-9996-085ebba0f6a5?collection=research (visited on Apr. 25, 2018). Conference video recording available from: http://www.awec2015.com (visited on Apr. 3, 2018).

[179] Roderick Read. “Daisy & AWES Networks: Scalable, Autonomous AWES with Continuous Power Output”. In: *Book of Abstracts of the Airborne Wind Energy Conference 2017*. Ed. by Moriz Diehl, Rachel Leuthold, and Roland Schmehl. Freiburg, Germany: Albert Ludwigs University of Freiburg and Delft University of Technology, 2017, pp. 35–38. ISBN: 978-94-6186-846-6. DOI: 10.4233/uuid:4c361ef1-d2d2-4d14-9868-16541f60edc7. URL: https://repository.tudelft.nl/islandora/object/uuid:1c6b790b-79dc-416b-bd07-6887ed45b087?collection=research (visited on Apr. 25, 2018). Conference poster available from: http://www.awec2017.com.

[180] S. Moballegh, S. Madhusoodhanan, and S. Bhattacharya. “Evaluation of high voltage 15 kV SiC IGBT and 10 kV SiC MOSFET for ZVS and ZCS high power DC-DC converters”. In: *2014 International Power Electronics Conference (IPEC-Hiroshima 2014 - ECCE ASIA)*. May 2014, pp. 656–663. DOI: 10.1109/IPEC.2014.6869657. URL: http://ieeexplore.ieee.org/document/6869657/ (visited on Jan. 7, 2018).

[181] EnerKite GmbH. *Rollout einer revolutionären Flügeltechnologie*. URL: http://enerkite.de/news/102-rollout-einer-revolutionaeren-fluegeltechnologie (visited on Jan. 6, 2018).

[182] EvoLogics GmbH. *Bionic Loop Propeller*. URL: http://www.evologics.de/en/products/propeller/index.html (visited on Nov. 23, 2016).

[183] B. Venkataraman, B. Godsey, W. Premerlani, E. Shulman, M. Thakur, and R. Midence. “Fundamentals of a motor thermal model and its applications in motor protection”. In: *Conference Record of 2005 Annual Pulp and Paper Industry Technical Conference, 2005.* June 2005, pp. 11–28. DOI: 10.1109/PAPCON.2005.1502046. URL: https://ieeexplore.ieee.org/document/1502046/ (visited on Apr. 25, 2018).

[184] Claudius Jehle and Roland Schmehl. “Applied Tracking Control for Kite Power Systems”. In: *Journal of Guidance, Control, and Dynamics* 37.4 (2014), pp. 1211–1222. ISSN: 0731-5090. DOI: 10.2514/1.62380. URL: https://arc.aiaa.org/doi/10.2514/1.62380 (visited on Apr. 25, 2018).

[185] S. Costello, G. François, and D. Bonvin. “Real-Time Optimizing Control of an Experimental Crosswind Power Kite”. In: *IEEE Transactions on Control Systems Technology* 26.2 (Mar. 2018), pp. 507–522. ISSN: 1063-6536. DOI: 10.1109/TCST.2017.2672404. URL: http://ieeexplore.ieee.org/document/7883813/ (visited on Apr. 7, 2018).

[186] Kenneth J. Jensen. “Generalized Nonlinear Complementary Attitude Filter”. In: *Journal of Guidance, Control, and Dynamics* 34.5 (Sept. 1, 2011), pp. 1588–1593. ISSN: 0731-5090. DOI: 10.2514/1.53467. URL: https://arc.aiaa.org/doi/10.2514/1.53467 (visited on Sept. 12, 2018).

[187] Remy International, Inc. *HVH250 Series Electric Motors*. URL: http://evwest.com/support/remy250.pdf (visited on Mar. 22, 2018).

[188] Joby Motors. *Products – Joby Motors*. URL: http://www.jobymotors.com/public/views/pages/products.php (visited on July 3, 2017). *As of March 22, 2018, the website is not reachable anymore. However, the previous state of the website is available from the Internet Archive/Wayback Machine via https://web.archive.org/web/20170730193505/http://www.jobymotors.com/public/views/pages/products.php.*

[189] EMRAX d.o.o. *STANDARD MOTORS - EMRAX*. URL: http://emrax.com/standard-emrax-motors/ (visited on Mar. 22, 2018).

[190] Eric Hendricks and Michael Tong. "Performance and Weight Estimates for an Advanced Open Rotor Engine". In: *48th AIAA/ASME/SAE/ASEE Joint Propulsion Conference & Exhibit*. American Institute of Aeronautics and Astronautics, July 30, 2012. DOI: doi:10.2514/6.2012-3911. URL: https://arc.aiaa.org/doi/abs/10.2514/6.2012-3911 (visited on Apr. 25, 2018).

[191] U.S. Energy Information Administration. *Levelized Cost and Levelized Avoided Cost of New Generation Resources in the Annual Energy Outlook 2017*. Independent Statistics & Analysis, U.S. Energy Information Administration. Mar. 2017. URL: https://www.eia.gov/outlooks/aeo/pdf/electricity_generation.pdf (visited on Mar. 26, 2018).

How to Cite This Work

Plain Text-Citation

Florian Bauer. “Multidisciplinary Optimization of Drag Power Kites”. Dissertation. Technical University of Munich. 2021.

BibTeX-Citation

```
@phdthesis{Bauer2021Multidisciplinary,
    author = {Florian Bauer},
    title = {Multidisciplinary Optimization of Drag Power Kites},
    type = {Dissertation},
    school = {Technical University of Munich},
    year = {2021},
}
```

EndNote-Citation

```
%0
%0 Thesis
%A Bauer, Florian
%D 2021
%T Multidisciplinary Optimization of Drag Power Kites
%I Technical University of Munich
%9 Dissertation
%3 phdthesis
%F Bauer2021Multidisciplinary
%^
```

RIS/RefMan-Citation

```
TY  - THES
AU  - Bauer, Florian
T1  - Multidisciplinary Optimization of Drag Power Kites
Y1  - 2021
PB  - Technical University of Munich
ER  -
```